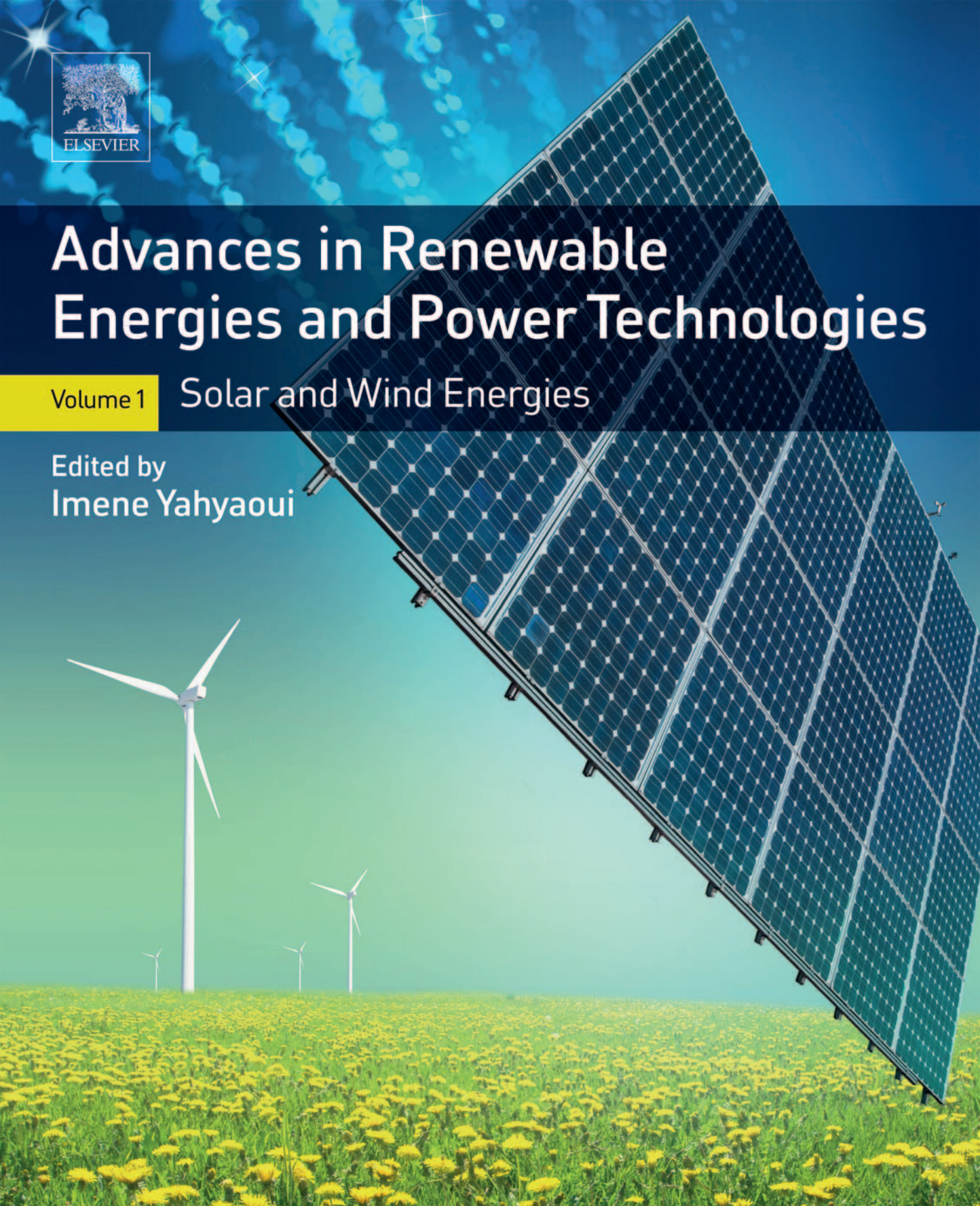

ELSEVIER
Advances in Renewable Energies and Power Technologies
Volume 1
Solar and Wind Energies
Edited by
Imene Yahyaoui

Advances in Renewable Energies and Power Technologies

www.TechnicalBooksPDF.com

This page intentionally left blank

www.TechnicalBooksPDF.com

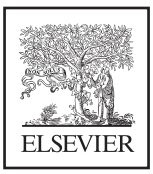
Advances in Renewable Energies and Power Technologies

Volume 1: Solar and Wind Energies

Edited by

Imene Yahyaoui

University Carlos III of Madrid, Spain



www.TechnicalBooksPDF.com

Elsevier
Radarweg 29, PO Box 211, 1000 AE Amsterdam, Netherlands
The Boulevard, Langford Lane, Kidlington, Oxford OX5 1GB, United Kingdom
50 Hampshire Street, 5th Floor, Cambridge, MA 02139, United States

Copyright © 2018 Elsevier Inc. All rights reserved.

No part of this publication may be reproduced or transmitted in any form or by any means, electronic or mechanical, including photocopying, recording, or any information storage and retrieval system, without permission in writing from the publisher. Details on how to seek permission, further information about the Publisher's permissions policies and our arrangements with organizations such as the Copyright Clearance Center and the Copyright Licensing Agency, can be found at our website: www.elsevier.com/permissions.

This book and the individual contributions contained in it are protected under copyright by the Publisher (other than as may be noted herein).

Notices

Knowledge and best practice in this field are constantly changing. As new research and experience broaden our understanding, changes in research methods, professional practices, or medical treatment may become necessary.

Practitioners and researchers must always rely on their own experience and knowledge in evaluating and using any information, methods, compounds, or experiments described herein. In using such information or methods they should be mindful of their own safety and the safety of others, including parties for whom they have a professional responsibility.

To the fullest extent of the law, neither the Publisher nor the authors, contributors, or editors, assume any liability for any injury and/or damage to persons or property as a matter of products liability, negligence or otherwise, or from any use or operation of any methods, products, instructions, or ideas contained in the material herein.

Library of Congress Cataloging-in-Publication Data
A catalog record for this book is available from the Library of Congress

British Library Cataloguing-in-Publication Data
A catalogue record for this book is available from the British Library

ISBN: 978-0-12-812959-3

For information on all Elsevier publications visit our website at
https://www.elsevier.com/books-and-journals



Publisher: Jonathan Simpson
Acquisition Editor: Maria Convey
Editorial Project Manager: Jennifer Pierce
Production Project Manager: Paul Prasad Chandramohan
Designer: Mark Rogers

Typeset by TNQ Books and Journals

www.TechnicalBooksPDF.com

Contents

List of Contributors..... xv
Preface xix
Acknowledgment..... xxi
Introduction.....xxiii

PART 1 PV ENERGY

CHAPTER 1 Solar Cells and Arrays: Principles, Analysis, and Design 3

Abdelhalim Zekry, Ahmed Shaker, Marwa Salem

1. Introduction 4
1.1 General Photovoltaic System 4
1.2 The Solar Radiation 5
1.3 The Incident Solar Radiation "Insolation"..... 6
2. Properties of Semiconductors for Solar Cells 8
2.1 The Energy Gap E_g and Intrinsic Concentration n_i..... 9
2.2 Doping and Conductivity of the Material 10
2.3 The Semiconductor Currents.....11
2.4 Recombination Mechanisms and Minority Carrier Lifetime 12
2.5 Optical Properties 12
3. The Dark p−n Junction Diode..... 15
3.1 Formation of a Field Region in a p−n Junction.....15
3.2 The Ideal Dark $I-V$ Characteristics of the p−n Diode.....16
3.3 Real Dark Diode Characteristics.....18
4. The Solar Cells..... 19
4.1 The PV Effect of a p−n Solar Cell 20
4.2 The $I-V$ Characteristics of the Solar Cell 21
4.3 The Conversion Efficiency of a Solar Cell.....27
4.4 Measurement Results and Practical Considerations.....29
4.5 Manufacturing Solar Cells.....34
4.6 Testing the Solar Cell and Solar Panels.....34
5. The PV Arrays..... 35
5.1 The $I-V$ Characteristics of the Module.....36
5.2 The $I-V$ Characteristics of Mismatched Cells in the Module 38
5.3 Formation of Hot Spots.....39
5.4 Measurement Data and Practical Considerations.....41
5.5 The Solar Cell Array 42

www.TechnicalBooksPDF.com

5.6 The Flat Plate Modules....42
5.7 Failure Modes of the Modules....43
5.8 The Glassing Factor of the Module....44
6. Circuit and Device Simulation of Solar Cells and Modules....45
6.1 Circuit-Level Simulation....45
6.2 TCAD Simulation of Solar Cells....49
References....54
Further Reading....56

CHAPTER 2 Solar PV Power Plants Site Selection: A Review....57
Hassan Z. Al Garni, Anjali Awasthi
1. Introduction to Solar Photovoltaic Land Suitability....57
1.1 Multicriteria Decision-Making Techniques for Photovoltaic Site Selection....58
1.2 Geographical Information System....64
1.3 Dealing With Uncertainties in Photovoltaic Site Selection....65
2. Criteria for Site Selection....65
3. Restriction Factors and Unsuitable Sites....68
4. Conclusions and Future Works....69
Acknowledgments....70
References....70

CHAPTER 3 Forecasting of Intermittent Solar Energy Resource....77
Gilles Notton, Cyril Voyant
1. Introduction....78
2. Intermittent and Stochastic Renewable Energy Production in an Electrical Grid....79
2.1 The Production/Consumption Balance: A Difficult Task Even With Conventional Energy Production Means...79
2.2 Intermittence of Renewable Production and Impact on the Electrical Grid Management....81
3. Need for Solar and Wind Forecast: Forecast Horizon and Time Step....83
4. Cost of Intermittence and Benefit of Forecasting....85
4.1 Cost of Intermittency....85
4.2 Forecasting and Influences on Production Cost....86
5. Forecast Accuracy Evaluation....87
6. Forecasting Methods for Different Forecast Horizons....92
6.1 Temporal Horizon and Resolution − Generalities About Solar Irradiance Forecasting....93

www.TechnicalBooksPDF.com

6.2 Very Short-Term Forecasting in a Temporal Range From 0 to 6 h....96
6.3 Solar Forecasting for Ranges Between 6 h and Days Ahead....104
6.4 Reliability and Accuracy of the Forecasting Models....104
7. The Future of the Renewable Energy Forecasting....106
7.1 Now-Casting....106
7.2 Six Hours Ahead Prediction and More....107
8. Conclusion....108
References....109

CHAPTER 4 Performance of MPPT Techniques of Photovoltaic Systems Under Normal and Partial Shading Conditions....115
Ali M. Eltamaly
1. Introduction....116
1.1 Direct-Coupled Method....117
1.2 Constant-Voltage MPPT....117
1.3 Constant-Current MPPT....118
1.4 Perturb and Observe Technique....118
1.5 Incremental Conductance Technique....118
1.6 Parasitic Capacitance Algorithm....120
1.7 Ripple Correlation Control....120
1.8 Hill Climbing Technique....121
1.9 Fuzzy Logic Controller as MPPT....122
1.10 Particle Swarm Optimization MPPT Technique....122
2. PV System Under Nonshading Conditions....124
2.1 Simulation of PV System....124
2.2 Simulation Results....135
2.3 Experimental Work....137
3. Smart Maximum Power Point Tracker Under Partial Shading Conditions....144
3.1 Partial Shading Effect....144
3.2 Mismatch Power Loss....148
3.3 Simulation of Proposed Systems....150
4. Conclusions....156
References....157

www.TechnicalBooksPDF.com

CHAPTER 5 DMPPT PV System: Modeling and Control Techniques 163
Marco Balato, Luigi Costanzo, Massimo Vitelli
1. Maximum Power Point Tracking of a Photovoltaic Source 163
2. Central Maximum Power Point Tracking and Distributed Maximum Power Point Tracking..... 164
3. Necessity of Joint Adoption of Distributed Maximum Power Point Tracking and Central Maximum Power Point Tracking: Hybrid Maximum Power Point Tracking 167
3.1 HMPPTS Technique.....171
3.2 HMPPTF Technique.....180
References..... 201

CHAPTER 6 Flexible Power Control of Photovoltaic Systems 207
Frede Blaabjerg, Ariya Sangwongwanich, Yongheng Yang
1. Introduction 207
2. Demand to Grid-Connected PV Systems 209
2.1 Overloading of the Grid (Overvoltage) During PV Peak-Power Generation Period.....209
2.2 Grid Voltage Fluctuation Because of Intermittency of PV Energy.....210
2.3 Limited-Frequency Regulation Capability to Stabilize the Grid During Frequency Deviation.....210
3. Possible Solutions for Flexible Power Control of PV Systems..... 211
3.1 Integrating Energy Storage Systems.....211
3.2 Installing Flexible Loads.....212
3.3 Modifying the Control Algorithm of the Power Converters.....213
4. Power Converter Technology and Control for PV Systems 214
4.1 System Diagram of Grid-Connected PV Systems 214
4.2 Control Structure of Grid-Connected PV Systems.....217
4.3 Maximum Power Point Tracking Algorithms.....218
5. Flexible Active Power Control of PV Systems 220
5.1 Power-Limiting Control Algorithm 220
5.2 Power Ramp-Rate Control Algorithm.....221
5.3 Power Reserve Control Algorithm 222
6. Summary..... 225
References..... 226

www.TechnicalBooksPDF.com

CHAPTER 7 Strategies for Fault Detection and Diagnosis of PV Systems..... 231
Santiago Silvestre
1. Introduction 231
2. Performance Parameters of Photovoltaic Systems: Yields and Power Losses 232
3. Supervision and Diagnosis of Photovoltaic Systems 235
4. Automatic Supervision Strategies..... 237
5. Modeling and Simulation of Photovoltaic Systems..... 240
5.1 Modeling Solar Cells, Photovoltaic Modules, and Arrays.....240
5.2 Inverter Model 243
5.3 Parameter Extraction Techniques.....244
5.4 Simulation Tools.....244
6. Fault Detection Procedures 245
6.1 Automatic Supervision and Diagnosis Based on Power Losses Analysis 245
6.2 Supervision and Diagnosis Based on Current and Voltage Indicators.....247
Conclusion 250
References..... 250

CHAPTER 8 Hybrid PV/Batteries Bank/Diesel Generator Solar-Renewable Energy System Design, Energy Management, and Economics..... 257
Ahmad Atieh, Sana Charfi, Maher Chaabene
1. Introduction 258
2. Hybrid Renewable Energy System Modeling 259
2.1 Photovoltaic Cell Model 260
2.2 Lead-Acid Battery Model.....261
2.3 Diesel Generator Model.....262
3. Sizing of Hybrid Photovoltaic/Batteries Bank/Diesel Generator System..... 264
3.1 Description of the Load Investigated.....265
3.2 Renewable Energy System Optimization Process.....266
3.3 Economics of a Hybrid Renewable Energy System: Case Study 276
4. Energy Management of Hybrid Photovoltaic/Batteries Bank/Diesel Generator System 277
4.1 Review of Energy Management Schemes.....278
4.2 Hybrid Renewable Energy System Energy Management: Case Study 279

www.TechnicalBooksPDF.com

5. Economics of Hybrid Photovoltaic/Batteries Bank/Diesel Generator System 284
5.1 Effect of Batteries Depth of Discharge on Hybrid Renewable Energy System Sizing, Cost, and Pollution..... 286
References..... 292

CHAPTER 9 Design Principles of Photovoltaic Irrigation Systems..... 295
Juan Reca-Cardeña, Rafael López-Luque
1. Introduction..... 296
2. Classification of Photovoltaic Irrigation Systems..... 297
2.1 According to the Type of Powering Plant..... 298
2.2 According to the Type of Irrigation System..... 300
3. Photovoltaic Irrigation Systems Components..... 301
3.1 Photovoltaic Power Plants..... 301
3.2 Photovoltaic Irrigation Systems..... 311
4. Modeling and Simulation of Photovoltaic Irrigation System..... 319
4.1 Earth−Sun Geometry and Solar Radiation Modeling 319
5. Design of Photovoltaic Irrigation Systems..... 326
References..... 330
Further Reading..... 333

CHAPTER 10 Scalar and Vector Control of Induction Motor for Online Photovoltaic Pumping..... 335
Imene Yahyaoui, Alvaro Serna Cantero
1. Introduction..... 336
2. Modeling of the System Components..... 337
3. Scalar Control..... 338
4. The Vector Control..... 339
4.1 Estimation of the Torque and the Flux..... 339
4.2 Selection of the Regulators..... 340
4.3 Calculation of the Electric Speed Reference..... 341
5. Results and Discussion..... 342
6. Conclusion..... 346
Annex..... 346
References..... 347

www.TechnicalBooksPDF.com

CHAPTER 11 Energy Management for PV Installations 349
Djamila Rekioua
1. Introduction 350
2. Photovoltaic Principle, Cells Technologies, and Efficiencies 351
2.1 Photovoltaic Principle 351
2.2 Photovoltaic Cell Efficiency 351
3. Energy Management for Photovoltaic Installations 352
3.1 Photovoltaic Systems with Storage 352
3.2 Other Structures 359
4. Conclusions 366
References 367

PART 2 PVT ENERGY

CHAPTER 12 Concentrating Solar Power 373
José J.C.S. Santos, José C.E. Palacio, Arnaldo M.M. Reyes, Monica Carvalho, Alberto J.R. Freire, Marcelo A. Barone
1. Introduction 373
2. Solar Energy Resources: Sun Characteristics and Solar Radiation 377
3. Concentrating Solar Power Plants 381
4. Solar Thermal Energy Storage 391
5. Thermodynamic and Economic Study 395
References 401

CHAPTER 13 Photovoltaic Cooking 403
Antonio Lecuona-Neumann, José I. Nogueira, Mathieu Legrand
1. Introduction 403
1.1 Energy and Cooking 404
1.2 Cooking With Wood and the Associated Health Problems 405
1.3 Cooking With Wood and the Associated Environmental Problems 406
1.4 Cooking With Solar Energy 406
2. Solar Cooking Possibilities 407
3. Fundamentals of Cooking 409
4. Thermal Model of a Photovoltaic Cooker 409
4.1 Some Results of the Model 411

www.TechnicalBooksPDF.com

5. Heat Storage (Thermal Energy Storage) With Solar Cooking..... 414
5.1 Sensible Heat Thermal Energy Storage..... 414
5.2 Latent Heat Thermal Energy Storage..... 416
6. Photovoltaic Solar Cookers 416
7. Conclusions..... 421
Acknowledgments..... 421
References..... 421
Further Reading..... 425

PART 3 WIND ENERGY

CHAPTER 14 Wind Energy FACTS Applications and Stabilization Schemes..... 431

Erhab Youssef, Adel Sharaf, Amr Amin, Adel El Samhey

1. Introduction..... 433
2. Wind Farm Configuration 434
2.1 Fixed-Speed Wind Energy Conversion System..... 434
2.2 Variable-Speed Wind Energy Conversion System 435
2.3 Wind Doubly Fed Induction Generators..... 436
3. Issues of Integrating Wind Energy Into the Grid: An Overview 438
3.1 Issue of Voltage Regulation and Power Quality..... 439
4. Different FACTS Schemes and Applications 441
4.1 FACTS Applications..... 441
5. Wind Energy in Egypt..... 441
6. Wind Farm Modeling..... 443
6.1 Wind Turbine Modeling..... 444
6.2 Modeling of Self-Excited Induction Generator..... 446
6.3 Static Synchronous Compensator Modeling..... 447
6.4 Proposed Controller Design..... 449
6.5 Simulation Results..... 450
7. Conclusions..... 458
Appendix..... 458
References..... 459

CHAPTER 15 Doubly Fed Induction Generator in Wind Energy Conversion Systems..... 461

Domingos S.L. Simonetti, Arthur E.A. Amorim, Flávio D.C. Oliveira

1. Introduction..... 462
1.1 Historical Review of Doubly Fed Induction Generator Technology..... 462

www.TechnicalBooksPDF.com

1.2 Structure 462
1.3 Doubly Fed Induction Generator Singularities..... 464
2. Modeling 465
2.1 Doubly Fed Induction Machine 465
2.2 The Static Model 467
2.3 The Dynamic Modeling 470
2.4 Model for Grid Disturbances 472
3. Control System 476
3.1 Vector Control..... 477
3.2 Control of Grid Side Converter 477
3.3 Control of Rotor Side Converter..... 478
4. Power Electronic Converters..... 480
4.1 The Back-to-Back Voltage Source Converter 480
4.2 The Crowbar and the Chopper 481
4.3 New Trends/Novel Structures..... 482
5. Low-Voltage Ride-Through 483
5.1 Effects of Voltage Dip on Doubly Fed Induction Generator 483
5.2 Grid Code Requirements..... 486
5.3 Crowbar Protection 487
5.4 Complementary Protection 487
5.5 Alternative Solutions 488
References..... 489

CHAPTER 16 Modeling and Characterization of a Wind Turbine Emulator..... 491
Imene Yahyaoui, Alvaro S. Cantero
1. Introduction..... 491
2. Description and Qualities of Wind Energy 492
2.1 Definition of Wind Energy 492
2.2 Main Components of the Wind Turbine 493
3. Types of Wind Turbines..... 494
3.1 Vertical-Axis Wind Turbines..... 494
3.2 Horizontal-Axis Wind Turbines..... 495
4. Modeling of the Wind Turbine..... 495
5. Principle of Wind Turbine Emulator 499
5.1 Modeling and Simulation of the Wind Emulator 500
5.2 Mechanical Speed Control..... 502
6. Results and Interpretations 502
7. Conclusion 507
References..... 507
Index.....509

www.TechnicalBooksPDF.com

This page intentionally left blank

www.TechnicalBooksPDF.com

List of Contributors

Hassan Z. Al Garni
Concordia Institute for Information Systems Engineering, Concordia University, Montreal, QC, Canada

Amr Amin
Electrical Power and Machines Department, Helwan University, Cairo, Egypt

Arthur E.A. Amorim
Electrical Engineering Department, Federal University of Espirito Santo, Vitória, Brazil

Ahmad Atieh
Electrical Engineering Department, The University of Jordan, Amman, Jordan

Anjali Awasthi
Concordia Institute for Information Systems Engineering, Concordia University, Montreal, QC, Canada

Marco Balato
Department of Industrial and Information Engineering, Università degli Studi della Campania "Luigi Vanvitelli", Aversa, Italy

Marcelo A. Barone
Department of Mechanical Engineering, Federal University of Espírito Santo, Vitória, Brazil

Frede Blaabjerg
Department of Energy Technology, Aalborg University, Aalborg, Denmark

Alvaro S. Cantero
University of Valladolid, Valladolid, Spain

Monica Carvalho
Department of Renewable Energy Engineering, Federal University of Paraíba, João Pessoa, Brazil

Maher Chaabene
Machine Control and Power Grid Research Unit, University of Sfax, Sfax, Tunisia

Sana Charfi
Machine Control and Power Grid Research Unit, University of Sfax, Sfax, Tunisia

Luigi Costanzo
Department of Industrial and Information Engineering, Università degli Studi della Campania "Luigi Vanvitelli", Aversa, Italy

www.TechnicalBooksPDF.com

Adel El Samhey
Electrical Power and Machines Department, Helwan University, Cairo, Egypt

Ali M. Eltamaly
Electrical Engineering Department, College of Engineering, King Saud University, Riyadh, Saudi Arabia; Al-Mansoura University, Al-Mansoura, Egypt

Alberto J.R. Freire
Department of Control Engineering and System Analysis, Université Libre de Bruxelles, Brussels, Belgium

Antonio Lecuona-Neumann
Departamento de Ingeniería Térmica y de Fluidos, Universidad Carlos III de Madrid, Madrid, Spain

Mathieu Legrand
Departamento de Ingeniería Térmica y de Fluidos, Universidad Carlos III de Madrid, Madrid, Spain

Rafael López-Luque
Department of Applied Physics, Universidad de Córdoba, Córdoba, Spain

José I. Nogueira
Departamento de Ingeniería Térmica y de Fluidos, Universidad Carlos III de Madrid, Madrid, Spain

Gilles Notton
Renewable energy team - Research Centre Georges Peri - UMR CNRS 6134, University of Corsica Pasquale Paoli, Ajaccio, France

Flávio D.C. Oliveira
Computation and Electronics Engineering Department, Federal University of Espirito Santo, São Mateus, Brazil

José C.E. Palacio
Department of Mechanical Engineering, Federal University of Itajubá, Itajubá, Brazil

Juan Reca-Cardeña
Department of Engineering, Universidad de Almería, Almería, Spain

Djamila Rekioua
Laboratoire LTII, University of Bejaia, Bejaia, Algeria

Arnaldo M.M. Reyes
Department of Mechanical Engineering, Federal University of Itajubá, Itajubá, Brazil

Marwa Salem
Department of Computer Engineering, Computer College, Hail University, Hail, Kingdom of Saudi Arabia

www.TechnicalBooksPDF.com

Ariya Sangwongwanich
Department of Energy Technology, Aalborg University, Aalborg, Denmark

José J.C.S. Santos
Department of Mechanical Engineering, Federal University of Espírito Santo, Vitória, Brazil

Alvaro Serna Cantero
University of Valladolid, Valladolid, Spain

Ahmed Shaker
Department of Engineering Physics and Mathematics, Faculty of Engineering, Ain Shams University, Cairo, Egypt

Adel Sharaf
Electrical and Electronics Engineering Department, New Brunswick University, Fredericton, NB, Canada

Santiago Silvestre
Electronic Engineering Department, Universitat Politècnica de Catalunya-BarcelonaTech., Barcelona, Spain

Domingos S.L. Simonetti
Electrical Engineering Department, Federal University of Espirito Santo, Vitória, Brazil

Massimo Vitelli
Department of Industrial and Information Engineering, Università degli Studi della Campania "Luigi Vanvitelli", Aversa, Italy

Cyril Voyant
Renewable energy team - Research Centre Georges Peri - UMR CNRS 6134, University of Corsica Pasquale Paoli, Ajaccio, France

Imene Yahyaoui
University Carlos 3 of Madrid, Madrid, Spain

Yongheng Yang
Department of Energy Technology, Aalborg University, Aalborg, Denmark

Erhab Youssef
Electrical Power and Machines Department, Helwan University, Cairo, Egypt

Abdelhalim Zekry
Department of Electronics and Communication Engineering, Faculty of Engineering, Ain Shams University, Cairo, Egypt

www.TechnicalBooksPDF.com

This page intentionally left blank

www.TechnicalBooksPDF.com

Preface

This book provides a study of the advances in renewable energies, focusing on solar and wind energies. It is aimed at researchers and experts who want to develop novel results in this exciting subject, as well as newcomers to renewable energies. The book presents explanations about the principle of the solar and wind energies generation and provides ideas for new research applications. Special emphasis is given to the recent innovative applications of solar and wind energies to provide electrical energy, especially on the power control, and the optimum use of energy.

The text is presented in such a way to be accessible to researchers with basic knowledge in renewable energies. The book is divided into two parts: solar and wind energies. Each chapter of the book is devoted to a particular problem, as follows:

- Solar energy
  - Principle and design of solar cells and modules
  - Site selection for installing photovoltaic (PV) plants
  - Forecast of solar energy
  - Maximum Power Point Tracking (MPPT) techniques under normal and shading operation
  - Distributed MPPT techniques
  - Smoothing control of PV power
  - Faults detection and diagnosis in PV plants
  - Energy management and economic study of hybrid PV systems
  - Application of PV energy in irrigation
  - Application of PV energy in water pumping
  - Management strategies for the optimum use of the PV energy
  - Organic Rankine Cycle for generating electricity based on solar concentrators
  - Thermal and solar cookers
- Wind energy
  - Wind energy facts
  - Doubly-fed induction generator (DFIG) in wind energy conversion
  - Wind turbine emulator

These points have been studied in depth by the authors and illustrated using examples. The results are compared with previous results of the literature, whenever is possible. The book contains around (320) figures and (822) compiled references.

This book will open up several interesting research lines, as the results provided can be extended to other problems such as:

- Climatic parameters: prediction and its effect on the power generated
- Integration of PV and wind energies into the grid

www.TechnicalBooksPDF.com

- Faults detection, identification, and correction in PV plants
- Net zero energy buildings
- Economic studies of the viabilities of renewable energies

The Editor

www.TechnicalBooksPDF.com

Acknowledgment

The editor would like to express her sincere respect and gratitude to the authors of the chapters, who gave their valuable cooperation and suggestions from time to time in successfully completing this book. My gratitude and special thanks go for all the persons who helped and advised me while preparing this book.

Inteligencia sin ambición es un pájaro sin alas

Salvador Dalí

www.TechnicalBooksPDF.com

This page intentionally left blank

www.TechnicalBooksPDF.com

Introduction

The exponential growth of industrialization and economic development increases the demand to energy [1]. Energy resources are classified into three categories: the fossil fuels, the renewable resources, and the nuclear resources [2]. While nuclear energy produces toxic substances that threat the human health and the environment and requires the use of huge quantity of water [3], the fossil fuels are limited, their price is variable, and they generate emissions, which cause global warming and climate change [4]. This situation is the main driving force behind the use of renewable energy sources (RESs) [5]. In fact, RESs can be defined as clean sources of energy that minimizes environmental impacts, produces minimum or zero secondary wastes, and is sustainable based on the energetic, economic, and social needs [6]. Indeed, the RES is characterized by the diversity in energy supply options [7], less dependence on fossil fuels [8], the increase in net employment, the creation of export markets [9], the reduction in greenhouse gas emissions, and climate change [10,11]. RESs include, among others, solar, wind, geothermal, biomass, hydropower, and marine energies [12,13].

According to the report of the International Energy Agency (IEA) of 2016, RESs account for a rising share of the world's total electricity supply, and they are the fastest-growing source of electricity generation in the IEO2016 [9]. Indeed, the total generation of electricity from renewable resources increases by 2.9%/year, as the renewable share of world electricity generation grows from 22% in 2012 to 29% in 2040 [9]. Electricity generation from nonhydropower renewables is the predominant source of the increase, rising by an average of 5.7%/year and outpacing increases in natural gas (2.7%/year), nuclear (2.4%/year), and coal (0.8%/year) [9].

The report of IEA confirmed that solar energy is the world's fastest-growing form of renewable energy, with net solar generation increasing by an average of 8.3%/year [9]. Among the 5.9 trillion kWh of new renewable generation added over the projection period, hydroelectric and wind each account for 1.9 trillion kWh (33%), solar energy for 859 billion kWh (15%), and other renewables (mostly biomass and waste) for 856 billion kWh (14%) [9].

This book presents the recent advances in renewable energies field, in particular for solar and wind energies. In fact, the book includes explanations of the renewable energy generation principle first and then presents some technologies related to the power control, fault diagnosis, energy management, and new applications.

This book contains 16 chapters, which are presented by the following preview:

Chapter 1 provides the properties of semiconductors, the operating principles of photovoltaic (PV) cells, and their analysis and design. Fabrication and testing are also presented.

Chapter 2 conducts a literature review on site selection of solar PV power plants. In this chapter, more than 50 papers are studied to identify the site suitability methodologies, decision criteria, and restriction factors and to deal with uncertainty in installing utility-size solar PV.

www.TechnicalBooksPDF.com

Chapter 3 focuses on the prediction of the solar energy resources. In this sense, the authors used numerical models, time series tools, and sky imagery to the forecasting of the stochastic energy generation.

Chapter 4 presents and discusses different techniques for maximum power point tracking (MPPT) techniques under normal and partial shading conditions with their simulation and experimental setup. Then, the performance of the modified particle swarm optimization has been studied and compared with the fuzzy logic controller under partial shading conditions. Then, distributed maximum power point tracking has been studied in Chapter 5, in which hybrid MPPT techniques are detailed.

Chapter 6 deals with the control of the PV power in grid-connected plants. In this chapter, the authors detail how to ensure a smooth and friendly integration between the PV systems and the grid. Thus, control methods have been presented and used to limit the maximum feed-in power, control the maximum power change rate, and provide active power reserve. However, Chapter 7 concentrates in studying the performance parameters of PV systems, as yields and performance ratio. These parameters are used to determine the presence of faults in the studied PV installation.

Chapter 8 presents a method for sizing the elements of a hybrid PV−diesel plant using the particle swarm optimization algorithm. Then, an economic study has been developed by evaluating the overall system' cost and payback period, which have been compared with diesel and PV and battery systems. Chapter 9 is concerned with the PV irrigation systems, in which the authors studied the design and the performance for such systems.

Chapter 10 focuses on a specific application of the PV energy: PV water pumping. In this chapter, the author compared the performance of two methods for the control of an induction machine that powers a water pump. The comparison is basically based on the water volume pumped. However, Chapter 11 presents various energy management algorithms for PV systems that include storage elements or other energy sources, such as wind turbines.

Chapter 12 explains the main fundamentals of the concentrating power plant technologies to convert solar energy resources into electricity and the technologies used for solar thermal energy storage. In this chapter, the authors present a thermodynamic and an economic study of an Organic Rankine Cycle coupled to parabolic trough concentrator. While Chapter 13 proposes a new implementation of photothermal and PV panels for a specific application: solar cooking.

Chapter 14 focuses on the applicability of static synchronous compensators in enhancing the quality of the electrical power in a wind farm and provides the needed reactive power. Chapter 15 studies the control of doubly fed induction generator (DFIG) in wind turbine plants. Moreover, this chapter presents a brief discussion about the DFIG main issue and the corresponding solution. Finally, Chapter 16 presents a simple method to emulate a small-size wind turbine based on the control of a DC machine, which allows to produce the electromagnetic torque and speed of the wind turbine.

The results obtained in every chapter of the book are always illustrated using numerical and experimental examples if possible, showing that they are simple to

www.TechnicalBooksPDF.com

apply and can be solved and reproduced using available software. Generally, the chapters contain proposed future works of the authors, which show the possible research axes that the chapters offer.

REFERENCES

[1] L. Wagner, I. Ross, J. Foster, B. Hankamer, Trading off global fuel supply, CO_2 emissions and sustainable development, PLoS One 11 (3) (2016) e0149406.

[2] J.J. Vidal-Amaro, P.A. Østergaard, C. Sheinbaum-Pardo, Optimal energy mix for transitioning from fossil fuels to renewable energy sources—the case of the Mexican electricity system, Appl. Energy 150 (2015) 80–96.

[3] V.T. Covello, M.W. Merkhoher, Risk Assessment Methods: Approaches for Assessing Health and Environmental Risks, Springer Science & Business Media, 2013.

[4] P.J. Crutzen, A.R. Mosier, K.A. Smith, W. Winiwarter, N_2O release from agro-biofuel production negates global warming reduction by replacing fossil fuels, in: P.J. Crutzen (Ed.), A Pioneer on Atmospheric Chemistry and Climate Change in the Anthropocene, Springer International Publishing, 2016, pp. 227–238.

[5] E.K. Stigka, J.A. Paravantis, G.K. Mihalakakou, Social acceptance of renewable energy sources: a review of contingent valuation applications, Renew. Sustain. Energy Rev. 32 (2014) 100–106.

[6] R.R. Hernandez, S.B. Easter, M.L. Murphy-Mariscal, F.T. Maestre, M. Tavassoli, E.B. Allen, M.F. Allen, Environmental impacts of utility-scale solar energy, Renew. Sustain. Energy Rev. 29 (2014) 766–779.

[7] J. Jewell, A. Cherp, K. Riahi, Energy security under de-carbonization scenarios: an assessment framework and evaluation under different technology and policy choices, Energy Policy 65 (2014) 743–760.

[8] M. Höök, X. Tang, Depletion of fossil fuels and anthropogenic climate change—a review, Energy Policy 52 (2013) 797–809.

[9] M. Bhattacharya, S.R. Paramati, I. Ozturk, S. Bhattacharya, The effect of renewable energy consumption on economic growth: evidence from top 38 countries, Appl. Energy 162 (2016) 733–741.

[10] R.K. Pachauri, M.R. Allen, V.R. Barros, J. Broome, W. Cramer, R. Christ, N.K. Dubash, Climate Change 2014: Synthesis Report, Contribution of Working Groups I, II and III to the Fifth Assessment Report of the Intergovernmental Panel on Climate Change, IPCC, 2014, p. 151.

[11] M. Pacesila, S.G. Burcea, S.E. Colesca, Analysis of renewable energies in European Union, Renew. Sustain. Energy Rev. 56 (2016) 156–170.

[12] F. Manzano-Agugliaro, A. Alcayde, F.G. Montoya, A. Zapata-Sierra, C. Gil, Scientific production of renewable energies worldwide: an overview, Renew. Sustain. Energy Rev. 18 (2013) 134–143.

[13] M. Engelken, B. Römer, M. Drescher, I.M. Welpe, A. Picot, Comparing drivers, barriers, and opportunities of business models for renewable energies: a review, Renew. Sustain. Energy Rev. 60 (2016) 795–809.

www.TechnicalBooksPDF.com

This page intentionally left blank

www.TechnicalBooksPDF.com

PART

1

PV Energy

www.TechnicalBooksPDF.com

This page intentionally left blank

www.TechnicalBooksPDF.com

CHAPTER

1 Solar Cells and Arrays: Principles, Analysis, and Design

Abdelhalim Zekry[1], Ahmed Shaker[2], Marwa Salem[3]

Department of Electronics and Communication Engineering, Faculty of Engineering, Ain Shams University, Cairo, Egypt[1]; Department of Engineering Physics and Mathematics, Faculty of Engineering, Ain Shams University, Cairo, Egypt[2]; Department of Computer Engineering, Computer College, Hail University, Hail, Kingdom of Saudi Arabia[3]

CHAPTER OUTLINE

1. Introduction 4
1.1 General Photovoltaic System 4
1.2 The Solar Radiation 5
1.3 The Incident Solar Radiation "Insolation" 6
2. Properties of Semiconductors for Solar Cells 8
2.1 The Energy Gap E_g and Intrinsic Concentration n_i 9
2.2 Doping and Conductivity of the Material 10
2.3 The Semiconductor Currents 11
2.4 Recombination Mechanisms and Minority Carrier Lifetime 12
2.5 Optical Properties 12
3. The Dark p–n Junction Diode 15
3.1 Formation of a Field Region in a p–n Junction 15
3.2 The Ideal Dark I–V Characteristics of the p–n Diode 16
3.3 Real Dark Diode Characteristics 18
4. The Solar Cells 19
4.1 The PV Effect of a p–n Solar Cell 20
4.2 The I–V Characteristics of the Solar Cell 21
4.3 The Conversion Efficiency of a Solar Cell 27
4.4 Measurement Results and Practical Considerations 29
4.5 Manufacturing Solar Cells 34
4.6 Testing the Solar Cell and Solar Panels 34
5. The PV Arrays 35
5.1 The I–V Characteristics of the Module 36
5.2 The I–V Characteristics of Mismatched Cells in the Module 38
5.3 Formation of Hot Spots 39
5.4 Measurement Data and Practical Considerations 41
5.5 The Solar Cell Array 42

Advances in Renewable Energies and Power Technologies. https://doi.org/10.1016/B978-0-12-812959-3.00001-0
Copyright © 2018 Elsevier Inc. All rights reserved.

www.TechnicalBooksPDF.com

5.6 The Flat Plate Modules 42
5.7 Failure Modes of the Modules 43
5.8 The Glassing Factor of the Module 44
6. Circuit and Device Simulation of Solar Cells and Modules 45
6.1 Circuit-Level Simulation 45
6.1.1 Summary of Mathematical Modeling 45
6.1.2 Parameter Extraction 45
6.1.3 PSpice Model of the Solar Cell 46
6.1.4 Case Studies 48
6.2 TCAD Simulation of Solar Cells 49
6.2.1 Qualitative Analysis for the Novel npn Solar Cell Structure 50
6.2.2 Construction of npn Solar Cell Structure Using Athena 51
6.2.3 Electrical and Optical Characterization for the npn Structure Performance 52
6.2.4 The Simulation of the Effect of Different n^+ Emitter Sidewall Surfaces on the Electrical Performance 53
References 54
Further Reading 56

1. INTRODUCTION

The main energy source in our earth is the sun radiation [1]. The solar radiation amounts to 1.7×10^{17} W; 34% will be reflected back, 42% will be converted to heat directly, 23% is stored in water vapor, wind water waves consumes about 1%, and plants consume 0.023%.

The human consumption comes from fossil fuel, nuclear energy from uranium, and geo heat. Any forms of energy are converted to heat and ultimately to radiation. Till now, there is no appreciable direct conversion path from the solar radiation to the human consumption. This is because:

- There is no efficient conversion machine till now,
- The solar radiation has a low density,
- The solar power is not constant. It varies daily, from season to season, and also from place to place on the earth.

1.1 GENERAL PHOTOVOLTAIC SYSTEM

The photovoltaic (PV) system converts the solar radiation into electricity directly. The block diagram of a general PV system is shown in Fig. 1.1.

It consists of the following building blocks:

1. The PV array: Its function is the conversion of solar radiation into electricity. It is the major unit in the system.

www.TechnicalBooksPDF.com

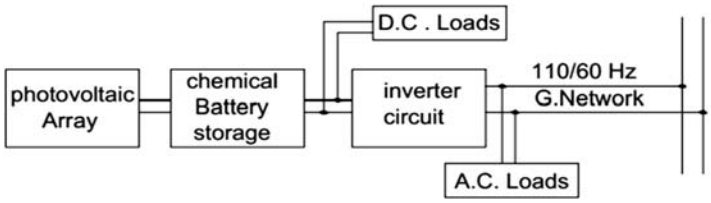


FIGURE 1.1

The general photovoltaic system.

2. Battery storage: To be available at the absence of the solar radiation, the electric energy produced by the array must be partly stored, normally using batteries. So, the second main unit is the battery storage.
3. Power conditioning circuits: According to the nature of the load, the generated electric power must be conditioned using DC/DC converters and DC/AC inverters.

The PV array is composed of solar modules. Each module contains a matrix of solar cells connected in series and parallel to satisfy the terminal properties of the whole generator. Accordingly, the solar cell is the basic element in the PV generator. This element is the basic solar radiation converter into electricity.

1.2 THE SOLAR RADIATION

One must be able to describe the solar radiation as it is the input power source to the PV generators. The sun emits electromagnetic radiations as a black body having a surface temperature of about 6000 K. This is because of the nuclear reaction running in it, where the sun is converting hydrogen into helium. The radius of the sun amounts to 1.39×10^9 m. The total radiation power received from the sun on a unit area perpendicular to the sun rays at the mean earth−sun distance, termed an astronomical unit, is called the solar constant (SC), where 1 astronomical unit = 1 AU = 1.496×10^{11} m. The solar radiation intensity at other distances is expressed in terms of SC with SC = 1.353 kW/m^2 [2]. Like a black body radiation, the sun's radiation covers a wide spectrum of wavelengths from deep ultraviolet to far infrared. The power spectral distribution of the sunlight [3] is shown in Fig. 1.2.

The vertical axis represents the spectral irradiance $I(\lambda)$ while the horizontal axis represents the wavelength in μm. The irradiance $I(\lambda)$ is equal to the incident solar power/m^2/$\delta\lambda$ = [W/m^2/μm], where $\delta\lambda$ is the respective wavelength range in μm. It is clear from this figure that the maximum spectral irradiance lies at $\lambda = 0.5$ μm. The spectral irradiance decreases because of the presence of air in the atmosphere. The air molecules scatter and absorb the solar radiation. There are multiple absorption bands for O_2, H_2O, and CO_2. It is important to notice that the solar irradiance resembles the black body radiation at ∼6000 K represented by the dashed line.

www.TechnicalBooksPDF.com

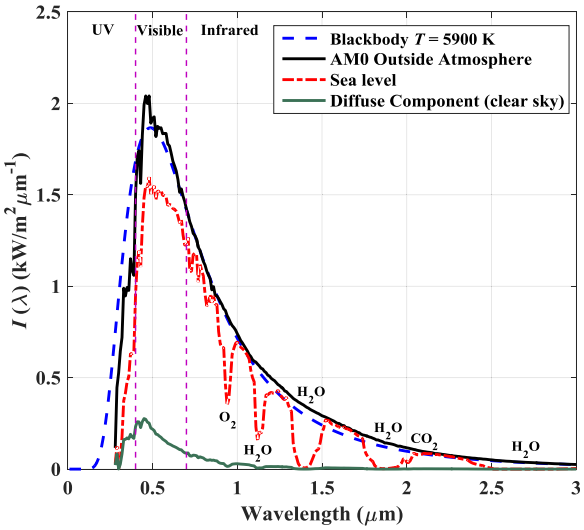


FIGURE 1.2

The power spectral distribution of the sunlight.

The solar power intensity without the effect of the atmosphere or ground surface is called the Air Mass Zero where one AM0 = 1 SC = 135.3 mW/cm^2. The solar power intensity after crossing one air mass perpendicular to the earth is called the air mass 1, AM1. It represents the area under the spectral irradiance curve and amounts to 92.5 mW/cm^2. If θ is the angle of incidence with normal to the earth surface, then the optical path in units of the air mass will be larger. The air mass AM = 1/(cos θ) [4].

1.3 THE INCIDENT SOLAR RADIATION "INSOLATION"

The actual incident solar radiation, the insolation is the incident solar power per unit area at certain location and it varies according to:

1. the position on the earth, because of the earth's spin axes inclination
2. the time of the day because of earth spinning
3. the month of the year because of the earth rotation around the sun
4. the angle of incidence
5. the presence of clouds in the air mass and environmental effects

As an illustration, Fig. 1.3A shows the insolation within the hours of the day in watts per square meter, with the insolation reaching its peak at noon. Moreover, Fig. 1.3B shows the insolation among the months of the year, for Kansas City at latitude 39.1° N, where January has the lowest insolation while July has the highest. Complete measured INSOLATION DATA in a specific place on the earth can be

www.TechnicalBooksPDF.com

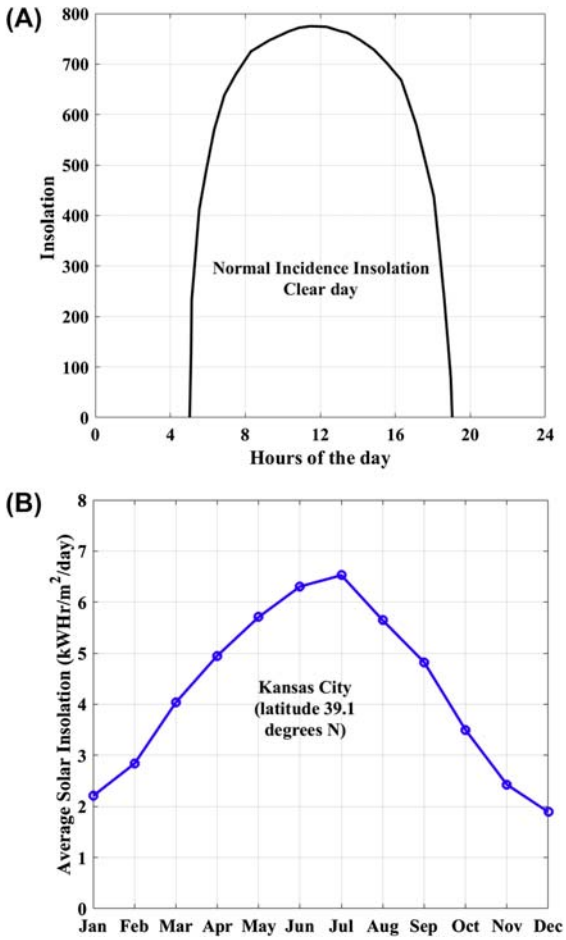


FIGURE 1.3

(A) INSOLATION within the hours of the day and (B) insolation within the months of the year.

obtained from the nearest Regional Climate Centers or from national insolation databases such as the National Solar Radiation Database in the United States [5]. In addition, insolation could be calculated according to the method developed in the Web site [6].

Design considerations

The PV generator must be designed to supply the load safely in smallest Insolation days in winter, and the climatic variations must be taken into consideration in array reliability.

www.TechnicalBooksPDF.com

2. PROPERTIES OF SEMICONDUCTORS FOR SOLAR CELLS

In this section, the properties of semiconductors for solar cells will be introduced. Solar cells are made of semiconductors as the active material. To understand the operation of the solar cells and optimize their characteristics, one has to understand thoroughly their material properties because there is a direct relationship between the cell performance and the material properties.

Semiconductors are a class of materials that have electrical conductivity between the metal and insulators. Accordingly, their electrical characteristics can be controlled by doping and by light. They can be classified according to their chemical structure in elementary form such as Si and Ge, in compound form such as A_{III} B_V and A_{II} B_{VI} [7–9], or molecular form such as the organic semiconductors or the perovskites which are hybrid metal organic molecules [10]. All semiconductors have common distinguished properties that govern their performance. The major properties controlling their electrical and optical behavior will be discussed in the next subsections. The first property is the atomic structures of the materials. It has a large impact on their performance. There are three distinct atomic arrangements for any material:

1. *Crystalline*, where the atoms are perfectly ordered in a three-dimensional array
2. *Amorphous*, where the atoms of the material have random order compared with their original sites in the single crystal
3. *Polycrystalline*, where the material is composed of crystallographic grains joined together by grain boundaries.

Fig. 1.4 shows an illustration of the three possible structures for a semiconductor material. The solar cells made of crystals give the highest efficiency and those made of amorphous materials give the lowest efficiency. But a much thicker layer of crystalline silicon is required to absorb the light ($\sim$300 μm) in comparison with a-Si requiring only $\sim$5 μm. Therefore, there is a considerable material saving using a-Si.

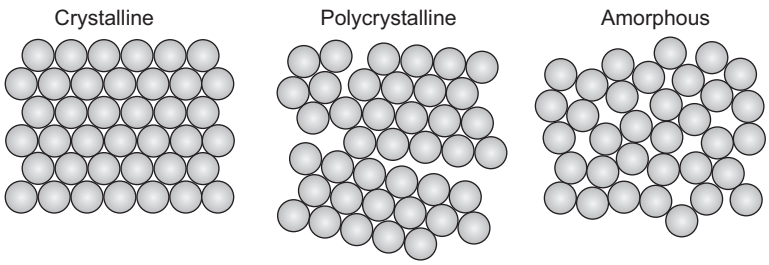


FIGURE 1.4

Three possible structures for a semiconductor material.

www.TechnicalBooksPDF.com

2.1 THE ENERGY GAP E_G AND INTRINSIC CONCENTRATION N_I

A semiconductor has an electron-filled valence band and an empty conduction band. The two bands are separated by an energy gap E_g. It ranges from few tenths of electron-Volts to few electron-Volts. Silicon has an energy gap of 1.1 eV and GaAs $E_g = 1.45$ eV. Elementary semiconductors are characterized by saturated covalent bonds as shown in Fig. 1.5, where each atom is bonded to the neighboring atoms by four covalent bonds.

The valence electrons are shared by the neighboring atoms and are bound by the parent atoms. They are locally fixed and are not capable of conducting electricity. To make such materials conduct electricity we have to free valence electrons. This can be done by doing work sufficient to break the bond. This work can be affected by heating, illuminating the material with a suitable light, and doping the material with suitable impurities.

Any semiconductor material works at room temperature, and hence, it contains heat and bonds will be broken thermally. When a bond is broken, it produces a free hole and a free electron. Both are capable of conducting electricity in the material. The minimum energy required to break a bond and generate an electron−hole (e−h) pair is called the energy gap. The energy gap separates the free electrons from the free holes as illustrated in Fig. 1.6.

The electrons are in the conduction band, where they occupy their lowest allowed energy states with an effective overall density of N_c, whereas the holes with positive charges occupy the allowed electronic states in the top of valence band with an effective density of states N_v. This is illustrated in Fig. 1.6. If the material is pure and its temperature is $T > 0$ K, it contains an electron concentration $n_o = n_i$ and a hole concentration $p_o = n_i$, where n_i is the intrinsic concentration with n_i is the thermally generated electron−hole pairs. It is related to E_g and T by $n_i^2 = N_c N_v \exp(-E_g/k_B T)$. $k_B T$ is the thermal energy = 25.6 meV at room temperature ($T = 300$ K). For silicon, $n_i = 1.5 \times 10^{10}$ cm^{-3} at 300 K.

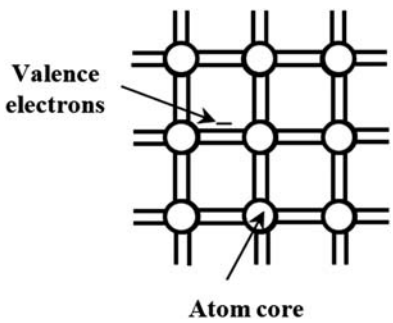


FIGURE 1.5

The covalent bonds in elementary semiconductors.

www.TechnicalBooksPDF.com

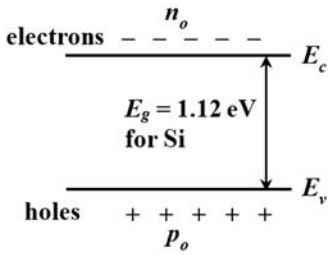


FIGURE 1.6

The illustration of energy gap E_g and energy level diagram.

2.2 DOPING AND CONDUCTIVITY OF THE MATERIAL

One of the main properties of the semiconductors is the possibility to alter their electrical characteristics by doping. Doping is intentional addition of specific impurities to the material to produce n-type or p-type conductors and change the electron and hole concentration in the material. To produce n-type Si, we add pentavalent impurity atoms to Si such as P and As, whereas for p-type Si, we add trivalent atoms such as B, Ga, and Al to Si. The charge picture after doping is illustrated in Fig. 1.7.

The product of the concentration p_o and n_o of any semiconductor at temperature T are given by the relation $n_o p_o = n_i^2$, which is called the mass action law. The conductivity of the semiconductor material can be, generally, expressed by

$$\sigma = q\mu_n n_o + q\mu_p p_o \tag{1.1}$$

where q is the electron charge; μ_n is the electron mobility; and μ_p is the hole mobility. So, the conductivity of the n-type material is

$$\sigma_n \approx q\mu_n n_o = q\mu_n N_D \tag{1.2a}$$

and that of the p-type material is

$$\sigma_p \approx q\mu_p p_o = q\mu_p N_A \tag{1.2b}$$

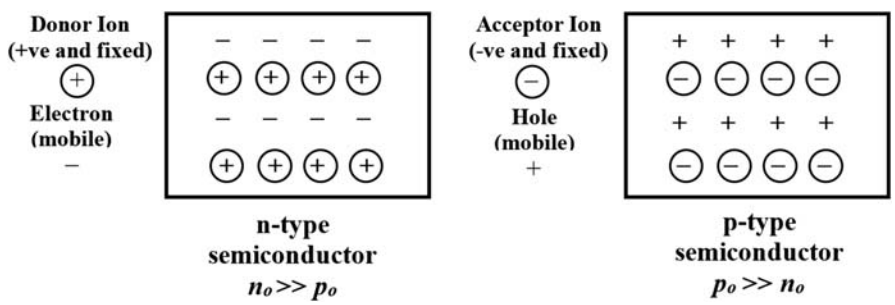


FIGURE 1.7

Charge picture after doping the semiconductor silicon.

www.TechnicalBooksPDF.com

N_D is the donor concentration and N_A, is the acceptor concentration. The conductivity increases by increasing the doping of semiconductor according to Eqs. (1.2a) and (1.2b).

2.3 THE SEMICONDUCTOR CURRENTS

If a voltage V is applied across a semiconductor bar with length L and cross-sectional area A, a current will flow in the bar because of the drift of electrons and holes under the influence of the electric field E developed by the voltage V in the bar as shown in Fig. 1.8.

This current follows the ohm's law for relatively small electric fields, i.e.,

$$I = qA\left(\mu_n n + \mu_p p\right)\left(\frac{V}{L}\right) \equiv AJ_d \tag{1.3}$$

where

$$J_d = \sigma E \text{ and } E = \frac{V}{L}$$

J_d is the drift current density. The mobility μ is the ability of the mobile charges to acquire drift velocities in the presence of the electric field.

Another type of current exists in a semiconductor when concentration differences of mobile changes are present. Such current is termed the diffusion current J_{dif}. This current can be expressed by

$$J_{ndif} = qD_n\frac{\partial n}{\partial x} \text{ for electrons, and} \tag{1.4a}$$

$$J_{pdif} = -qD_p\frac{\partial p}{\partial x} \text{ for holes} \tag{1.4b}$$

where D_n and D_p are the diffusion coefficients for electrons and holes, respectively, and $\frac{\partial n}{\partial x}$ and $\frac{\partial p}{\partial x}$ are the concentration gradients for electrons and holes, respectively. The diffusion coefficient D is related to the mobility by the Einstein equation

$$D = \mu\frac{k_B T}{q} = \mu V_T \tag{1.5}$$

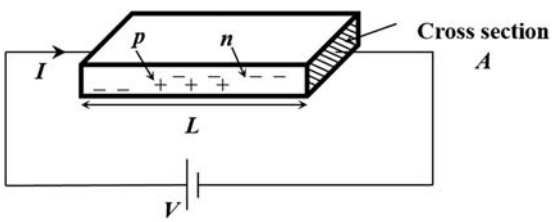


FIGURE 1.8

A drift current I in a semiconductor by applying voltage V.

www.TechnicalBooksPDF.com

with $V_T =$ the thermal voltage $= k_B T/q$. Mobility and the diffusion constant are properties of the semiconductor materials that depend on temperature and doping.

2.4 RECOMBINATION MECHANISMS AND MINORITY CARRIER LIFETIME

The recombination is an intrinsic property of any semiconductor material. In this process, the electron meets a hole and completes a broken bond. Both are going to be lost. There are different recombination mechanisms: the band to band radiative recombination, the band impurity band Shockley−Read−Hall nonradiative recombination, and Auger recombination. Every mechanism has its specific rate equations [11]. Fig. 1.9 illustrates the fact that an excess of electrons and holes $\Delta n = \Delta p$ disappears after an average τ.

So, the recombination rate is $(\Delta n/\tau)$. Any electron hole pair can survive only on the average the lifetime. As they move continuously, electrons and holes travel certain specific distance in their life time called the diffusion length L. The diffusion length is given by $L = \sqrt{D\tau}$. This length is an important property controlling the solar cell performance. For silicon, it amounts to 1−500 μm.

2.5 OPTICAL PROPERTIES

We are interested in understanding the response of the semiconductor to light, i.e., the photoelectric effect. If a light beam is incident on a semiconductor material, part of the light energy will be reflected, a part will be absorbed inside the material after refraction, and the remaining part will be transmitted. According to energy conservation law, we can write

$$I = R + A + T \tag{1.6}$$

Here, I is the incident light energy, R the reflected, A the absorbed and T the transmitted parts. Reflection occurs because of the change of the wave impedance $Z_w = \sqrt{\mu/\varepsilon}$ (where μ and ε are the permeability and permittivity of the medium, respectively), which changes at the surface of the material. The reflectance ρ is given by

$$\rho = \left[\frac{|Z_w - Z_{wa}|}{|Z_w + Z_{wa}|}\right]^2 \tag{1.7}$$

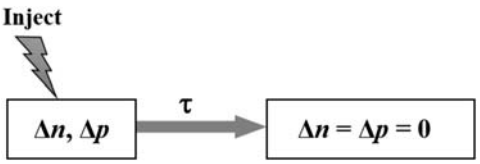


FIGURE 1.9

Illustration of the decay of an excess of electrons and holes.

www.TechnicalBooksPDF.com

where Z_{wa} is the wave impedance of the air $\left(Z_{wa} = \sqrt{\mu_o/\varepsilon_o}\right)$. It is assumed that light is falling perpendicular to the surface. For Si, with $\varepsilon = 12\varepsilon_o$ and $\mu = \mu_o$ the reflectance is $\rho = 0.3$. This means that the reflected part of incident light amounts to 0.3, which is an appreciable part.

The absorption of the light energy is characterized by the absorption coefficient α, where

$$I(x) = I(0)e^{-\alpha x} \tag{1.8}$$

which means that the incident light intensity $I(x)$ decays exponentially with the distance x from the surface of incidence as illustrated in Fig. 1.10.

The intensity decays to $(1/e)$ of the maximum at $x = 1/\alpha$. Therefore, the inverse of α is the average penetration depth of the light in the material, or may be better named the average absorption length. The absorption coefficient depends on the wavelength of the incident light.

It is well established now that light is composed of energy quanta called photons. These photons interact with the electrons and atoms of the material. The photon energy is given by $E_{ph} = hf$, where h is Planck's constant and f is the photon frequency. On the other side, photons are wave packets having a wavelength λ, and velocity $c = 3 \times 10^8$ m/s such that $c = \lambda f$. Therefore, $E_{ph} = h(c/\lambda)$, the photon energy is inversely proportional to the light wavelength. Now, we are able to understand how the light affects the material. Only valence electrons can absorb photons when they can acquire sufficient energy to overcome the energy gap of the material. If this happens, it is called the photon generation process of an electron−hole pair. This process is illustrated in Fig. 1.11.

From Fig. 1.11, the required minimum photon energy for the photogeneration process $E_{ph} \geq E_g$. Energy-rich photons, where $E_{ph} \sim 2\ E_g$, cannot produce 2 e−h

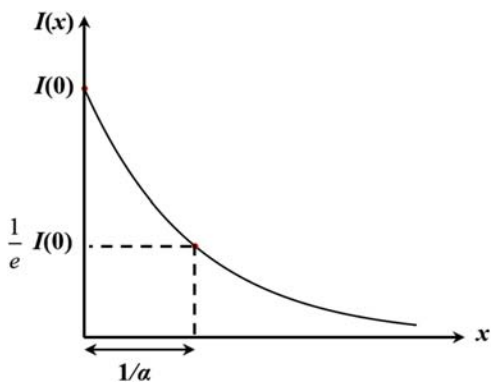


FIGURE 1.10

Decay of light intensity with an absorption coefficient alpha.

www.TechnicalBooksPDF.com

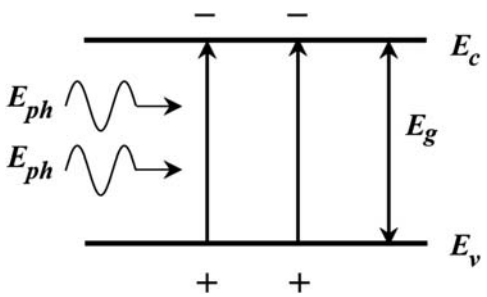


FIGURE 1.11

The process of photogeneration of electron hole pairs.

pairs except with a very small probability as this process requires the collision of photons with two electrons simultaneously if it is a direct process.

The absorption coefficient alpha is a function of the incident wavelength of the photons and it is a material property. Fig. 1.12 shows the absorption coefficient of different semiconductors as a function of the wavelength [12]. The energy gap of the material is also given. It is clear from this figure that materials absorb light appreciably ($\alpha > 10^4\ \mathrm{m}^{-1}$) only if $E_{ph} \geq E_g$. A second important observation is that α of Si rises slowly with decreased wavelength compared with the other materials shown in the diagram. This is because of the indirect nature of band gap of this material.

The longer wavelength photons with smaller alpha need a thicker layer of the semiconductor to be absorbed; otherwise, they can be transmitted across the layer.

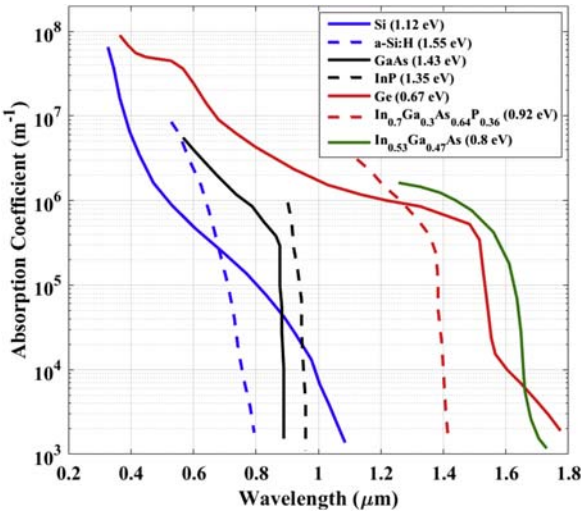


FIGURE 1.12

Absorption coefficient as a function of wavelength for different materials.

www.TechnicalBooksPDF.com

Generally, the minimum semiconductor layer thickness to absorb light can be expressed by

$$D_{\min} \geq \frac{2}{\alpha} \tag{1.9}$$

This simple relation is of a very critical importance for solar cell design. As the semiconductors are expensive, one should use the minimum quantity of to perform the absorption function. In this scenario, one needs thicker crystalline Si-layers as it has the lowest α. This is true for thin-film solar cells. For wafer-based conventional solar cells, the minimum layer thickness is limited by the mechanical rigidity.

3. THE DARK P–N JUNCTION DIODE

The commercial solar cells are basically p–n junction diode structures constructed to receive the solar radiation. To understand the operating principles underlying the solar cell, one has to study first the p–n junction diode. Solar cells are made of either homotype p–n junctions, heterotype junctions, or even multi-junction. The homotype is from the same material, whereas the heterotype is from two different materials. The operating principles are the same. So, we confine ourselves to the homo junctions. The solar cell in darkness is a p–n diode, whose dark characteristics set the limits for the illuminated characteristics. From the principle point of view, an illuminated solar cell = a short circuit cell under light + a dark biased p–n diode.

3.1 FORMATION OF A FIELD REGION IN A P–N JUNCTION

A p–n junction is the metallurgical boundary between an n-type region and a p-type region in a semiconductor as shown schematically in Fig. 1.13 [11].

It can be proved both experimentally and theoretically that a space charge region is formed around the metallurgical junction while the remaining parts of the diode remain neutral under no bias. This layer is formed because of immigration of holes from the p-side to the n-side and the electrons from the n-side to the p-side around

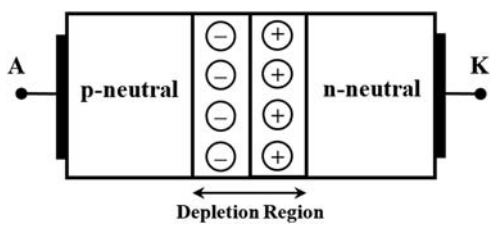


FIGURE 1.13

The p–n junction diode regions.

www.TechnicalBooksPDF.com

the metallurgical junction. They leave behind them un-neutralized acceptor and donor ions as shown in Fig. 1.13. The electric field associated with the charges establishes opposing forces for further migration of holes and electrons, leading to equilibrium such that no net current of either type exists. The width of this field region under no bias is of the order of few tenths of a micrometer depending on the doping concentrations N_A and N_D. There is a potential difference associated with this built-in or internal electric field. The name built-in comes from the fact that this electric field is caused by the material inhomogeneity and not by an external electric source. This built-in potential difference is termed the contact difference of potential pointing out that such potential differences are formed if two dissimilar materials are brought into intimate contact as in a p—n junction where it could be thought that a p—n junction is formed by intimately contacting p- and n-type materials. The contact difference of potential φ can be expressed by

$$\varphi = V_T \ln\left(\frac{N_A N_D}{n_i^2}\right)$$

The contact difference of potential φ separates the two sides of the p—n junction and therefore constitutes a potential barrier. The electromotive force of the solar cell as a photoelectric generator is directly related to φ. As φ increases, the open-circuit voltage of the cell increases. So, the doping concentrations N_A and N_D must be as high as possible. Also, φ can be increased by selecting a material with higher E_g and consequently with lower n_i. The field region is essential for the solar cell operation. It originates the electromotive force of the cell exactly like the chemical battery.

3.2 THE IDEAL DARK *I*—*V* CHARACTERISTICS OF THE P—N DIODE

Let us now study the current conduction in a forward biased p—n diode. To forward bias the diode, a battery with a voltage V_a is connected across the diode with the positive poles connected to the anode attached to the p-side, whereas the negative pole is connected to the cathode attached to the n-side as shown in Fig. 1.14.

On forward biasing the diode, the space charge region contracts and the separation potential decreases. Consequently, holes will be injected from the p-side to the n-side and electrons will be injected from the n-side to the p-side as illustrated in Fig. 1.14. The injected holes Δp diffuses away from the space charge region edge at $x = 0$ towards the metallic contact where they recombine gradually in the n-side. The same happens with electrons injected from n-side to the p-side. The rate of injection of holes across the field region gives a current I_{pi} while that of electrons gives a current I_{ni}. The total diode current

$$I = I_{pi} + I_{ni} \tag{1.10}$$

As illustrated in Fig. 1.14, the injected charges decay exponentially with distance measured from the edges of the field region [11].

www.TechnicalBooksPDF.com

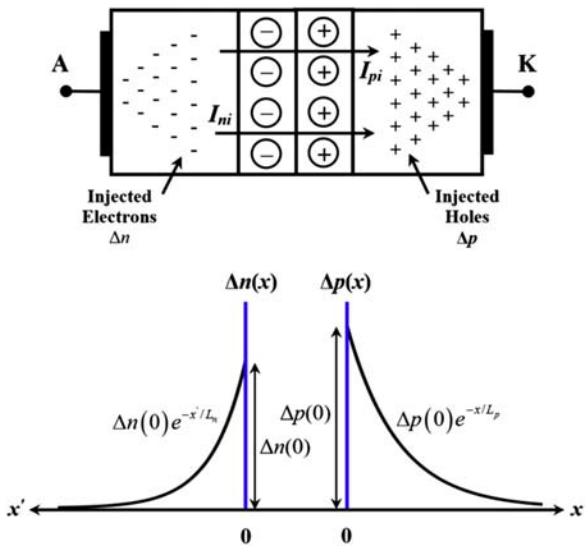


FIGURE 1.14

Distribution of excess electrons and holes in a forward-biased diode.

$$\Delta p(x) = \Delta p(0)e^{-x/L_p} \text{ and} \tag{1.11}$$

$$\Delta n(x) = \Delta n(0)e^{-x/L_n} \tag{1.12}$$

where $\Delta p(0)$ and $\Delta n(0)$ are the injected hole and electron concentration.

$$L_p = \sqrt{D_p \tau_p} \text{ and } L_n = \sqrt{D_n \tau_n} \tag{1.13}$$

L_p and L_n are the diffusion lengths of holes in the n-side and electrons in the p-side. By definition, τ_n is the lifetime of electrons in the p-side and τ_p is that of holes in the n-side. The applied voltage V_a is related to $\Delta p(0)$ and $\Delta n(0)$ by the law of the junction expressed as [11].

$$\Delta p(0) = p_{no}\left(e^{V_a/V_T} - 1\right) \text{ and} \tag{1.14}$$

$$\Delta n(0) = n_{po}\left(e^{V_a/V_T} - 1\right) \tag{1.15}$$

where $p_{no} = n_i^2/N_D$ = the minority carrier concentration in the n-side at no bias, and $n_{po} = n_i^2/N_A$ = the minority electron concentration in the p-side. Then we can get I_{pi} because it is the diffusion current at $x = 0$, i.e.,

$$I_{pi} = -qAD_p \left.\frac{\partial p}{\partial x}\right|_{x=0}$$

www.TechnicalBooksPDF.com

$$\Rightarrow I_{pi} = qA\frac{D_p p_{no}}{L_p}\left(e^{V_a/V_T} - 1\right) \tag{1.16}$$

Similarly, we get I_{ni}

$$I_{ni} = qA\frac{D_n n_{po}}{L_n}\left(e^{V_a/V_T} - 1\right) \tag{1.17}$$

where A is the diode area. Summing up Eqs. (1.16) and (1.17) we obtain the final expression for I in terms of the voltage V_a, i.e.,

$$I = qA\left(\frac{D_p n_i^2}{L_p N_D} + \frac{D_n n_i^2}{L_n N_A}\right)\left(e^{V_a/V_T} - 1\right) \tag{1.18}$$

The current I could be written in the following form:

$$I = I_s\left(e^{V_a/V_T} - 1\right) \tag{1.19}$$

with $I_s =$ the pre-exponential factor of Eq. (1.19), which is termed the reverse saturation current. It is the current which flows in the ideal diode with a reverse bias greater than $3V_T$. In the solar cell mode of the diode, it will be forced to forward bias, which causes energy loss because the current passing through it. This current is a loss current. Therefore, for proper operation in the solar cell mode, the forward diode current must be minimized. This can be achieved according to Eq. (1.18) by increasing the doping concentrations N_A and N_D and the diffusion lengths L_n and L_p and decreasing n_i by selecting a material with higher energy gap. This is in agreement with the requirement for higher φ.

3.3 REAL DARK DIODE CHARACTERISTICS

The solar cell diode contains an Ohmic resistance dropping a part of the applied forward voltage, especially apparent at high diode currents as shown in Fig. 1.15. The leakage current of the diode is much larger than I_s. These nonideal effects are normally modeled by an equivalent circuit consisting of two resistances R_s and R_{sh} along with an ideal diode as will be discussed later, where R_s is the series resistance of the diode and R_{sh} is the shunting resistance of the diode.

In deriving the diode current, the recombination current I_{scr} in the space charge region is neglected as its width is much smaller than the diffusion lengths. In diodes with appreciable space charge width which is compared to the widths of the neutral regions, this recombination current in the space charge region cannot be neglected. I_{scr} can be expressed by [13].

$$I_{scr} = qAn_i\frac{W_{scr}}{T_{scr}}e^{V_j/2V_T} \tag{1.20}$$

where W_{scr} is the width of the space charge region and T_{scr} is the lifetime of carriers in the space charge region. In heterojunctions with high interface state

www.TechnicalBooksPDF.com

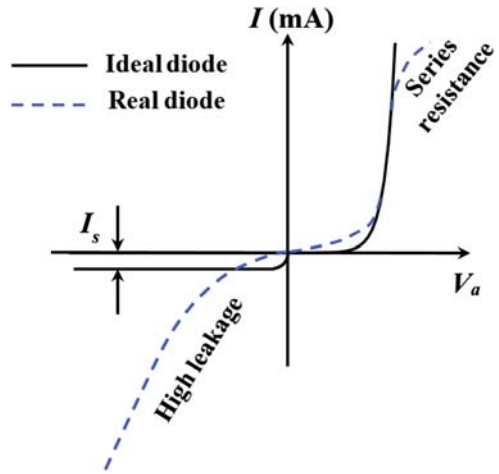


FIGURE 1.15

The nonideal versus ideal diode $I-V$ curves.

density, the interface recombination current I_{irc} must be considered [14]. It can be expressed by

$$I_{scr} = qAn_i v_s e^{V_j/nV_T} \tag{1.21}$$

where v_s is the interface recombination velocity and n is an ideality factor having a value $\geq$1. The ideal diode is represented by the rectifier symbol while the general $I-V$ relation of the diode follows the formula

$$I = I_s\left(e^{V_j/nV_T} - 1\right) \tag{1.22}$$

The temperature affects greatly the diode current for fixed diode voltage. The diode current increases appreciably with the increase in temperature. Keeping the current constant, the diode voltage decreases almost linearly with temperature. These temperature variations can be accounted for by the appreciable increase of I_s with temperature.

4. THE SOLAR CELLS

The solar cell is the basic element in a PV array. It has the vital function of converting the solar radiation into electricity directly. To perform its function satisfactorily, it must have the highest possible conversion efficiency. It has to basically carry out two basic functions:

1. Absorb the incident solar radiation generating at least one hole pair for each photon.

www.TechnicalBooksPDF.com

2. Separate and collect the electrons and holes such that the electrons accumulate at the negative pole while the holes accumulate at the positive pole. The separation potential must be as high as possible.

The device that can perform these functions is the p−n junction diode because its semiconductor material absorbs photons and generates e−h pairs, and it has a separation potential in its transition region, which must be made as high as possible as proved in the previous sections. So, a p−n junction illuminated with the solar radiation can produce electromotive force driving electric loads.

4.1 THE PV EFFECT OF A P−N SOLAR CELL

The construction, of a p−n junction solar cell is shown in Fig. 1.16A. It is a p−n junction structure with full back metallization and partially metallized front to allow the passage of light to the semiconductor while collecting the cell current. The front metallization is in the form of metal fingers with a common bus as shown in Fig. 1.16B. The typical construction parameters of the p−n junction solar cell are [14]: The p-substrate thickness $W_p = 0.20-0.5$ mm, the n^+-layer thickness $W_n = 0.1-0.5$ μm, the doping concentration of the substrate $N_A = 10^{16}-10^{17}$ cm^{-3}, the doping concentration of the emitter n^+-layer $= 10^{18}-10^{19}$/cm^{-3}, the metal thickness $= 5$ μm, and active material is monocrystalline silicon.

The solar cell behaves as a p−n diode in darkness as indicated in Section 1.3. When illuminated, it builds an electromotive force. We are going now to explain this mode of operation. Fig. 1.17 illustrates the PV effect in a solar cell.

When the solar cell is irradiated with the sun light, the photons of light penetrate to different depths where they will be absorbed and generate e−h pairs as shown in Fig. 1.17. The e−h pairs generated within the field region will be separated by this field such that the holes move to the p-side and the electrons to the n-side. Some of the holes accumulate in the field region boundary of the p-side neutralizing part of it.

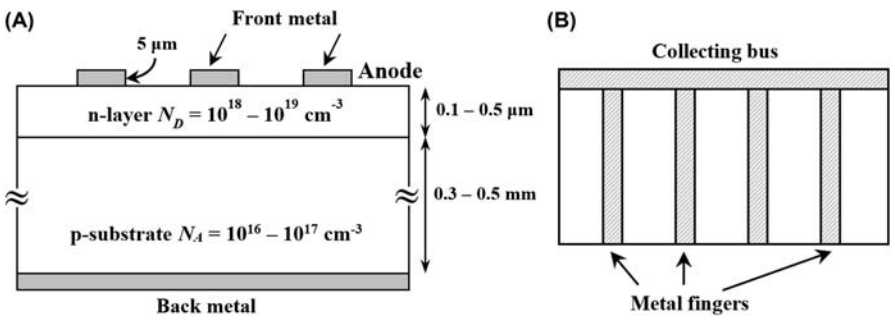


FIGURE 1.16

(A) The solar cell construction and (B) the front metallization.

www.TechnicalBooksPDF.com

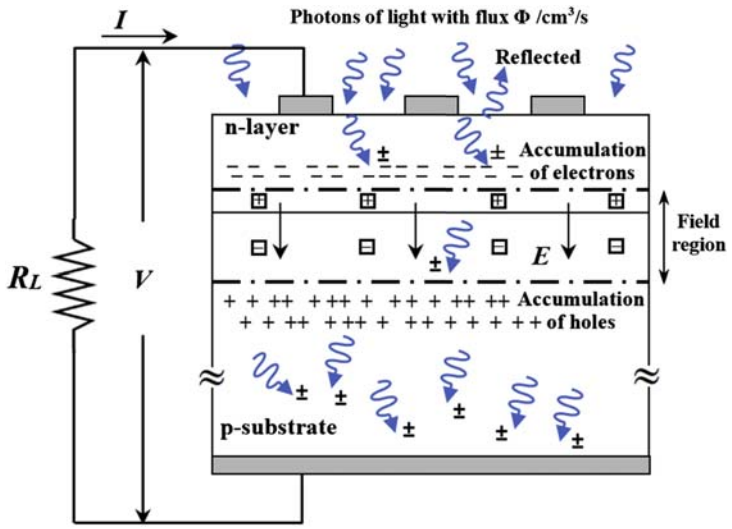


FIGURE 1.17

Illustration of the photovoltaic effect.

The remaining part of the holes flows to the load in the outer circuit. The same happens with electrons where they accumulate partly at the n-side edge of the field region neutralizing part of it while the rest of the electrons flow to the outer load circuit.

The e−h pairs generated outside the field region diffuse toward the field region. Only the e−h pairs generated within a diffusion length from the edges of the field region succeed to reach the field region. The e−h pairs generated outside these diffusion regions are lost by recombination. This means that W_p must be made $\leq L_n$ and W_n must be made $\leq L_p$ such that all the semiconductor volume becomes active.

Metal−semiconductor interfaces must form Ohmic contacts [13] which are characterized by high recombination velocity or tunnel MS contacts. So, the e−h pairs generated near these interfaces survive only for very short times as they recombine there. So, the regions outside the diffusion regions, near the contacts, are dead layers.

Once the diffusing e−h pairs in the neutral regions reach the field region, they act similar to those pairs generated in the field region. They will increase the accumulated charges at the edges of the field region increasing the cell voltage and driving more current in the outer load circuit. From the previous discussion, it is now clear that a solar cell has a voltage across it and drives current in the load connected to its terminal. It acts as a battery. Hence, the name PV generator.

4.2 THE *I*−*V* CHARACTERISTICS OF THE SOLAR CELL

As a source of electricity, the main performance of the solar cell is determined by its *I*−*V* characteristics. The illuminated solar cell characteristics can be considered as a

www.TechnicalBooksPDF.com

superposition of the dark solar cell characteristics and the illuminated cell with short circuit. This superposition principle is almost valid for all commercial solar cells. For experimental solar cells, this principle may not be valid because of the pronounced effect of metal semiconductor contacts and the nonlinear effect of illumination on the dark characteristics. Here, it will be assumed that the superposition principle is applicable. The dark current of the solar cell was treated in detail in Section 1.3. It remains to be determined how the short circuit current is caused by the incident solar radiation.

Assuming a photogeneration rate g_{ph} at an arbitrary point x from the edge of the field region and a minority carrier lifetime τ_n in the p-side, one can express the excess photogenerated electron concentration as

$$\Delta n = \Delta p = g_{ph}\tau \tag{1.23}$$

Assuming τ is constant, one can determine an average Δn knowing the average photogeneration rate g_{ph} such that

$$\Delta n = g_{ph}\tau_n \tag{1.24}$$

Then the collected electron charges Q_n from the p-side by diffusion can be written as

$$Q_n = qA\Delta nL_n = qAg_{ph}\tau_n L_n \tag{1.25}$$

where L_n is the diffusion length of electrons in the p-side. Then the current from the p-side

$$I_n = \frac{Q_n}{\tau_n} = qAg_{ph}L_n \tag{1.26}$$

Similarly, the current from the n-side

$$I_p = \frac{Q_p}{\tau_p} = qAg_{ph}L_p \tag{1.27}$$

The current from the field region

$$I_{fr} = qAg_{ph}W_{scr} \tag{1.28}$$

where W_{scr} is the field region width.

Now, summing up all current components, we get the cell short circuit current I_{sc}

$$I_{sc} = I_{ph} = qAg_{ph}(L_n + L_p + W_{scr}) = qAg_{ph}W_{eff} \tag{1.29}$$

where W_{eff} is the effective thickness of the solar cell.

The spectral irradiance $I(x)$ decreases exponentially as explained in Section 1.2, then, the photon flux Φ_{ph} at any point x can be obtained by dividing Eq. (1.8) by E_{ph},

$$\Phi_{ph} = \Phi_{ph}(0)e^{-\alpha x} \tag{1.30}$$

To get the photons $\Delta\Phi_{ph}$ absorbed in an incremental distance dx at x

$$\Delta\Phi_{ph} = \Phi_{ph}(x) - \Phi_{ph}(x + dx)$$

www.TechnicalBooksPDF.com

$$\Rightarrow \Delta\Phi_{ph} = -\frac{\partial \Phi_{ph}}{\partial x} dx = \alpha \Phi_{ph} dx \tag{1.31}$$

Because each absorbed photon generates an e−h pair, one can determine the photogeneration rate g_{ph}. By definition, g_{ph} = number of generated e−h pairs in certain volume/volume (e−h pairs/cm^3/s). Therefore,

$$g_{ph} = \frac{\Delta\Phi_{ph}}{dx} = \alpha \Phi_{ph} \tag{1.32}$$

The average photogeneration rate g_{pha}

$$g_{pha} = -\int_{x_1}^{x_1+W_{eff}} \frac{\alpha \Phi_{ph}}{W_{eff}} dx = \frac{\Phi_{ph}(0)}{W_{eff}} \left[e^{-\alpha x_1} - e^{-\alpha(x_1+W_{eff})} \right] \tag{1.33}$$

where x_1 is the dead layer in the n-region shown in Fig. 1.18.

Because the incident solar radiation has certain spectral distribution, we can obtain the overall generation rate (g_{pht}) over the whole spectrum, considering that $\alpha \sim 0$ for $E_{ph} \leq E_g$, by integrating Eq. (1.33) once again from $E_{ph} = E_g$ to ∞ or from $\lambda = \lambda_c = hc/E_g$ to $\lambda = 0$, i.e.,

$$g_{pht} = \int_0^{\lambda_c} g_{pha} d\lambda \tag{1.34}$$

Substituting Eq. (1.32) into (1.33)

$$g_{pht} = \int_0^{\lambda_c} \frac{\Phi_{ph}(0) e^{-\alpha x_1}}{W_{eff}} \left[1 - e^{-\alpha W_{eff}} \right] d\lambda \tag{1.35}$$

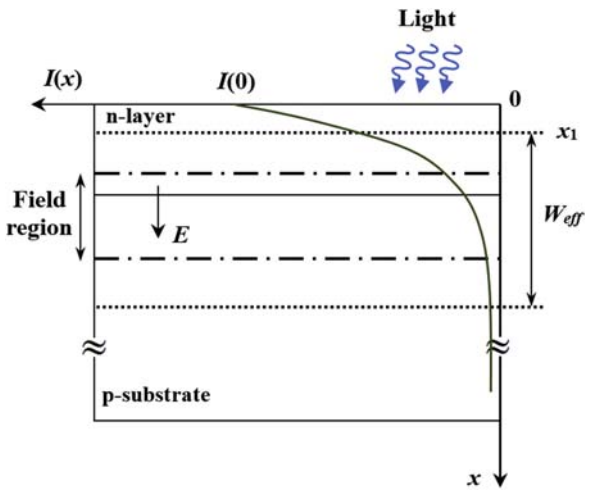


FIGURE 1.18

The effective collection region of the photogenerated carriers.

www.TechnicalBooksPDF.com

Recalling that $\Phi_{ph} = \mathrm{I}/E_{ph}$, one gets

$$g_{pht} = \int_0^{\lambda_c} \frac{I(0)e^{-\alpha x_1}}{E_{ph} W_{eff}} \left[1 - e^{-\alpha W_{eff}}\right] d\lambda \tag{1.36}$$

Combining Eqs. (1.29) and (1.36) we obtain the short circuit current, which is termed also as the photocurrent, i.e.,

$$I_{sc} = I_{ph} = qAg_{pht}W_{eff} = qA \int_0^{\lambda_c} \frac{I(0)e^{-\alpha x_1}}{E_{ph}} \left[1 - e^{-\alpha W_{eff}}\right] d\lambda \tag{1.37}$$

If the solar cell is designed such that $(\alpha W_{eff}) > 1$ and α is dependent of λ, Eq. (1.37) simplifies to

$$I_{scm} = qA \frac{e^{-\alpha x_1}}{hc} \int_0^{\lambda_c} \lambda I(0) d\lambda \tag{1.38}$$

with $E_{ph} = hc/\lambda$. For the highest efficiency, the dead layer under the top surface $x_1 = 0$. Then the highest collected short circuit current from the cell can be written as

$$I_{scm} = qA \frac{1}{hc} \int_0^{\lambda_c} \lambda I(0) d\lambda \tag{1.39}$$

To determine the maximum photocurrent, I_{scm} one integrates the area under the curve of $\lambda I(0)$. To use the spectral irradiance curve one has to subtract from it the reflected part of the light such that

$$I_{scm} = qA \frac{1}{hc} \int_0^{\lambda_c} \lambda(1 - \rho) I(0) d\lambda \tag{1.40}$$

It is clear from Fig. 1.19 that as λ_c increases, the integral increases and consequently I_{scm}. Hence, silicon collects more photons than gallium arsenide and the short circuit current for the Si-cells is larger than that for GaAs. I_{ph} amounts to 30−40 mA/cm^2 for a single-crystal silicon solar cell at AM1.

From the foregoing analysis of the photocurrent of a solar cell, we conclude that

1. as the energy gap of the material decreases, I_{ph} increases,
2. the dead layer directly under the top surface is very harmful for the photons with high absorption coefficient α, because they will be mainly absorbed in this layer. This is true for the energetic photons with high α for all materials,
3. photons with lower α, the low energy photons, must be given sufficient material thickness to be absorbed, i.e., $W_{eff} \geq 1/\alpha$,
4. therefore, the lowest α determines the thickness of the solar cell,
5. the reflectance of the surface must be decreased to increase the photocurrent, ideally $\rho = 0$, and
6. the solar cell has also certain spectral response where the spectral photocurrent depends on the wavelength of the incident light as α depends on λ.

www.TechnicalBooksPDF.com

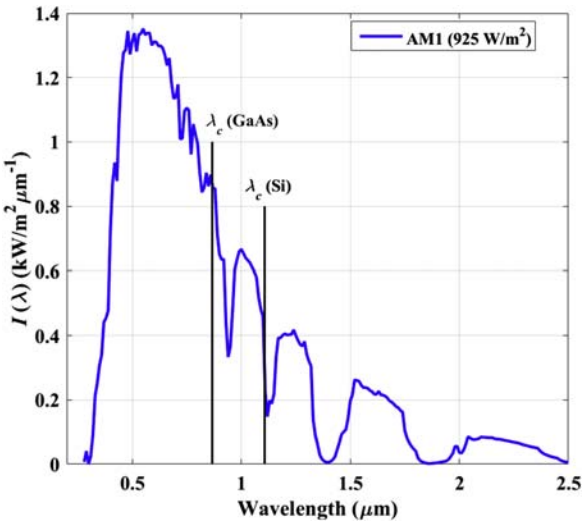


FIGURE 1.19

Choice of semiconductor material according to the cutoff wavelength.

Now, by superposition of the dark solar cell and illuminated short circuit cell currents, we obtain the general case of illuminated and biased solar cell as illustrated in Fig. 1.20. The total current I, at any voltage V, of the cell is then

$$I = I_{ph} - I_d \tag{1.41}$$

Substituting (1.22) in (1.41), we get the $I-V$ of the solar cell

$$I = I_{ph} - I_s\left(e^{V_j/nV_T} - 1\right) \tag{1.42}$$

We should add the effect of bulk resistance R_s. Moreover, there is a loss associated with current leakage through a resistive path that is in parallel with the

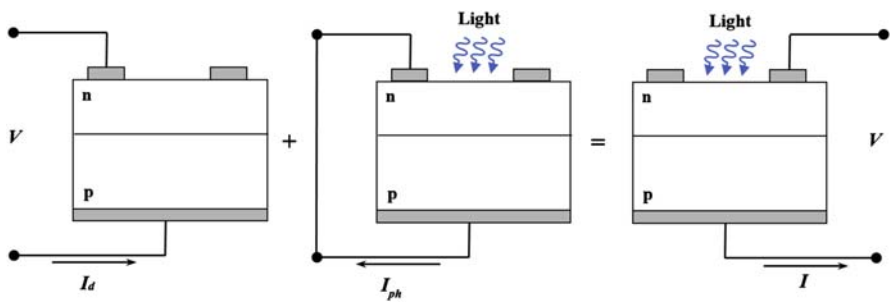


FIGURE 1.20

The illustration of the superposition for the solar cell.

www.TechnicalBooksPDF.com

semiconductor device. This loss can be modeled by a shunt resistance (R_{sh}). Its effect is much less visible in a solar cell compared with the series resistance. Now, the net output current of the cell, considering both effects of R_s and R_{sh}, is given by

$$I = I_{ph} - I_s\left(e^{\frac{(V+IR_s)}{nV_T}} - 1\right) - \frac{V + IR_s}{R_{sh}} \tag{1.43}$$

Eq. (1.43) can be represented by the circuit model in Fig. 1.21. It is the solar cell model recommended to calculate the $I-V$ characteristics of the solar cell under any operating condition.

In this model, the current source represents I_{ph}, the current passing in the diode represents the dark current, while R_s and R_{sh} represents series resistance and the shunt resistance of the solar cell. This equivalent circuit is that of a real diode added to it the photogenerated current I_{ph}. Normally R_{sh} is negligible in solar cell mode. But when the solar cell is reverse biased, R_{sh} must be taken into consideration.

Eq. (1.43) is represented graphically in Fig. 1.22. Here, $I_{ph} = I_{sc}$ as discussed before. V_{oc} is the open circuit voltage of the cell. It can be obtained from Eq. (1.43) by putting $I = 0$ and $V = V_{oc}$ and neglecting R_s ($R_s = 0$) and R_{sh} ($R_{sh} = \infty$)

$$V_{oc} = nV_T \ln\frac{I_{ph}}{I_s} \tag{1.44}$$

The open circuit voltage of an electric source is its driving electromotive force. It must be as high as possible. This can be achieved according to Eq. (1.44) by maximizing I_{ph} and minimizing I_s. The maximization of I_{ph} was discussed in the last section. The minimization of I_s was discussed in Section 1.3. It can be achieved by increasing N_A, N_D, L_n, and L_p and decreasing n_j. It was found that increasing the doping concentration of a semiconductor causes a decrease in L_n and L_p and an increase in its n_i.

Therefore, there are optimum doping concentrations leading to highest open circuit voltage. For Si, e.g., $N_A = 10^{17}/\text{cm}^3$ and $N_D \sim 10^{19}/\text{cm}^{3.}$ To draw the maximum power from a source it must be loaded with a matched load. The matched load is the load to operate the solar cell at its maximum power point where

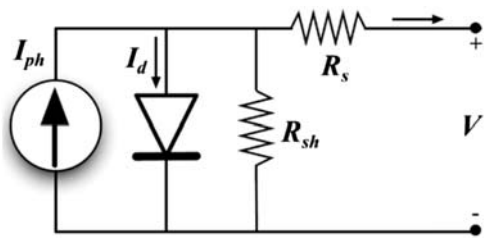


FIGURE 1.21

The equivalent circuit of solar cell.

www.TechnicalBooksPDF.com

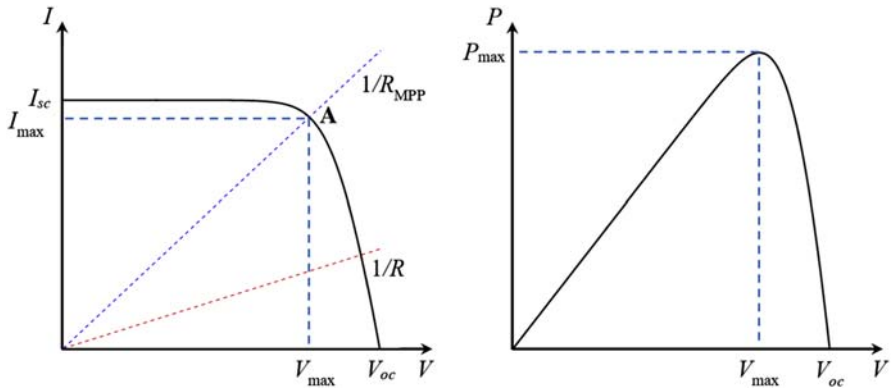


FIGURE 1.22

The *I*–*V* and *P*–*V* characteristics showing maximum power point of the solar cell.

$P = IV =$ maximum. The output power curve is shown in Fig. 1.22. It has a maximum at $P = P_m$, $I = I_m$, and $V = V_m$ as depicted in Fig. 1.22.

4.3 THE CONVERSION EFFICIENCY OF A SOLAR CELL

Now, we are able to determine the conversion efficiency of the solar cell. It is defined as

$$\eta_{\max} = \frac{P_{\max}}{P_{in}} = \frac{V_{\max} I_{\max}}{P_{in}} \tag{1.45}$$

where P_{in} is the incident solar power, for AM1 = 100 mW/cm^2. We also define the fill factor (FF) of the *I*–*V* curve as

$$FF = \frac{V_{\max} I_{\max}}{V_{oc} I_{sc}} \tag{1.46}$$

It is a measure of the squareness of the *I*–*V* curve. As FF increases, the efficiency increases. The solar cell designers try also to maximize the FF. It increases by lowering I_s and R_s and increasing R_{sh}.

Assuming $n = 1$, $R_s = 0$, $R_{sh} = \infty$, $V_j = V$, $I_{ph} = 30.4$ mA, $I_s = 1.66 \times 10^{-12}$ A, and $V_T = 25.6$ mV at 300 K. For this example, the open circuit voltage amounts to 0.605 V for c-Si-cells. The effect of R_s on the *I*–*V* curve of a solar cell is depicted in Fig. 1.23 (taking $R_{sh} = \infty$). We see from this figure that as R_s increases, the short circuit current begins to decrease first at high values of the series resistance, while the open circuit voltage remains constant. The maximum output power decreases because of the power consumption in R_s. So, R_s must be minimized.

Additionally, Fig. 1.24 shows the effect of R_{sh} on the *I*–*V* curve of a solar cell (taking $R_s = 0$). We see from this figure that V_{oc} and the output power decrease

www.TechnicalBooksPDF.com

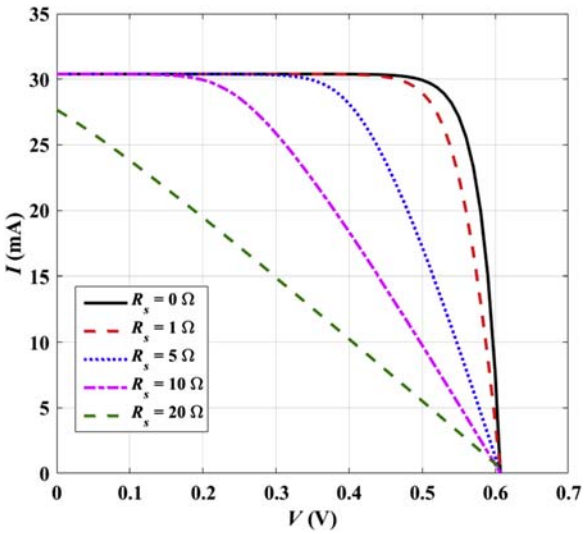


FIGURE 1.23

Effect of R_s on the I–V solar cell characteristics.

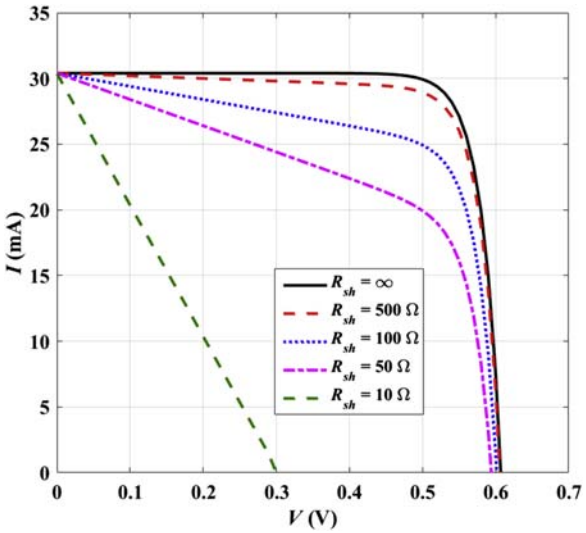


FIGURE 1.24

Effect of R_{sh} on the I–V solar cell characteristics.

www.TechnicalBooksPDF.com

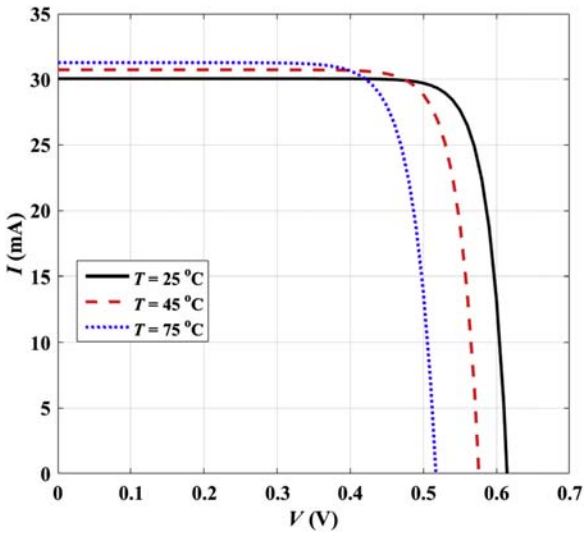


FIGURE 1.25

Effect of temperature on the solar cell characteristics.

because of the power loss in R_{sh}. So, R_{sh} must be increased to the highest suitable value.

As the solar cells are subjected to the environment where the temperature varies in a wide range, the effect of temperature on a solar cell performance must be considered. Fig. 1.25 shows an example for the variations of the $I-V$ curve with temperature.

We can see from this figure that I_{sc} increases with temperature while the open circuit voltage V_{oc} decreases. The combined effect leads to a decrease in the P_m because the decrease in V_{oc} overwhelms the increase of I_{sc}. The increase in I_{sc} is because of the enhancement of photon absorption with increased temperature. The decrease in V_{oc} is dated back to an exponential increase of the reverse saturation current I_s, while the increase in I_{sc} is slight, the decrease in V_{oc} is appreciable. The solar cell manufacturers give data sheets about the temperature coefficients of I_{sc}, V_{oc} and P_m to take these variations in solar cell array design.

4.4 MEASUREMENT RESULTS AND PRACTICAL CONSIDERATIONS

In this subsection, we will introduce some experimental results to demonstrate the different technological parameters effects on the performance parameters of the real solar cells.

- *The solar size:*
  The solar cell size ranges from 2 cm × 2 cm to 25 cm × 25 cm based on whether Si is single crystal, multicrystal, or amorphous. Other types such as CdT and

www.TechnicalBooksPDF.com

CIGS cells are available as commercial products [15]. GaAs cells are used for space applications [16]. This is because the conversion efficiency decreases as the area of the solar cell increases as the defects increase with area.

- *Solar cell material:*
  The efficiency of the solar cell depends on its material as discussed previously. Fig. 1.26 shows the ideal solar cell efficiency as a function of the energy gap of the materials [17]. The efficiency of GaAs cells is slightly higher than that of Si. Most commercial cells are made of Si [15] because the Si technology is the most advanced among all materials.
- *The thickness of the Si-solar cells:*
  As the thickness of the solar cell increases, the cell output power increases for the same illumination intensity. Fig. 1.27 shows the effect of the solar cell thickness on the output power. From this curve, a thickness of about 0.3 mm is sufficient to collect the incident solar radiation. An amorphous layer thickness of 1 μm is also sufficient. Therefore, the a-Si cells are thin film cells.
- *The spectral response of the solar cells:*
  Fig. 1.28 shows the spectral response of solar cells made of different materials. It agrees with the analysis on the short circuit current as a function of the wavelength. It can be noted that silicon solar cell response for ultraviolet radiation is low. This is because of the presence of the dead layer at the top of the cell.
- *Antireflection coating* [18].
  To decrease the reflectance from the surface of the Si-cells, its surface is coated with an antireflection film made of SiO_x and/or TiO_2. These layers have intermediate refractive index between Si and air. They can act also as an interference

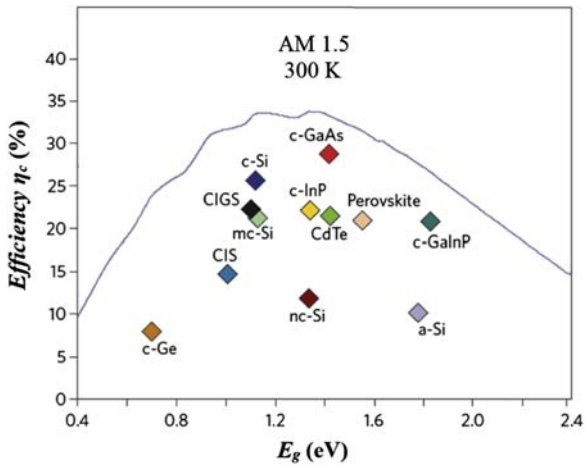


FIGURE 1.26

Theoretical solar cell efficiency as a function of the energy gap.

www.TechnicalBooksPDF.com

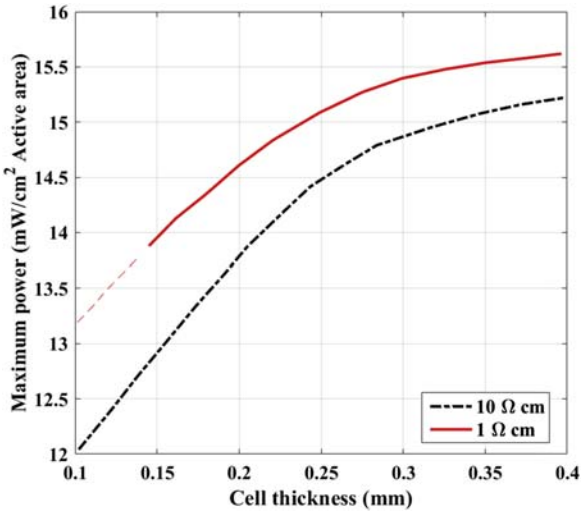


FIGURE 1.27

The effect of the Si solar cell thickness on the output power.

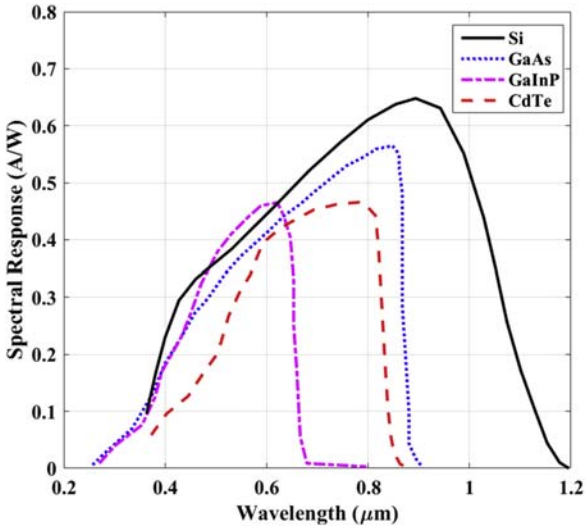


FIGURE 1.28

The spectral response of different solar cells of different materials.

www.TechnicalBooksPDF.com

filter if their thickness is adjusted to $\lambda_a/4$, where λ_a is the wavelength of light in the antireflection coating material. It is given by

$$\lambda_a = \frac{v_{ph}}{f} = \frac{\lambda}{\sqrt{\varepsilon_r}} \tag{1.47}$$

where v_{ph} is the phase velocity of light in the material, ε_r is relative dielectric constant, and λ is the wavelength in free space.

If SiO_2 is used with $\varepsilon_r = 4$ and $\lambda = 0.5$ μm, then $\lambda_a = 0.25$ μm and $\lambda_a/4 =$ the thickness of the antireflection coating $= 0.0625$ μm. For thick layers, thickness of the antireflection coating <1 μm, the optical matching condition is applied to get the suitable antireflection coating:

$$\varepsilon_{ran} = \sqrt{\varepsilon_{ra}\varepsilon_{rSi}} \tag{1.48}$$

where ε_{ran} is the relative dielectric constant of the antireflection coating. ε_{ra} of air is ~ 1 and $\varepsilon_{rSi} = 11.7$. The reflectance can also be decreased by surface texturing [19] as shown in Fig. 1.29A. By surface texturing, the reflected rays will be trapped by the material. Only light will be reflected again after multiple incidence on the surface. Fig. 1.29B depicts the reflectance of Si after antireflection coating and with texturing and antireflection coating.

Remember that ρ of Si $= 0.3$. It is clear from this figure that ρ has been decreased appreciably with this type of surface treatment. There are new developments in antireflective coating such as Al_2O_3 [20].

- *The optimum doping of the layers:*
  The p-Si substrate $\rho = 2.2\ \Omega$ cm − 10 Ω cm.
  The n^+-Si layer $N_D = 10^{18}$−$10^{20}/cm^3$
- *The diffusion lengths:*
  L_n in the substrate ≥200 μm.
  L_p in the n^+ layer ≥0.5 μm
- *The metal grid resistance:*
  It must be much smaller than the lateral resistance of the top layer. The metal grid covers about 10%−20% of the solar cell surface. Thickness of metal = 3−5 μm
- *The short circuit current density* $J_{sc} \sim 30$−$40\ mA/cm^2$ for AM1 illumination.
- *The open circuit voltage* $V_{oc} \sim 0.52$−0.65 V
- FF ∼ 0.8−0.85
- P_{out} maximum, $P_m = (15$−$24)\ mW/cm^2 \times$ F.F. $(0.8) = 12$−$19.2\ mW/cm^2$
- The efficiency $\eta = P_m/P_{in} = (12$−$19)/100 \sim (0.12$−$0.19) = 12\%$−19%.
- The highest efficiency achieved 25.6% for special solar cell constructions:
  - These cells have back surface field p^+-layer at the bottom of the substrate [21].
  - They have very shallow n^+ top layer to minimize the dead top layer and enhance the collection of the e−h generated by the UV radiation.
  - They have double antireflection coating from $SiO_2 + TaO$. The SiO_2 layer also passivates the top layer surface and reduces its recombination velocity.
  - They have surface texturing.
- *Solar cells are connected in circuits, they must be wired.*

www.TechnicalBooksPDF.com

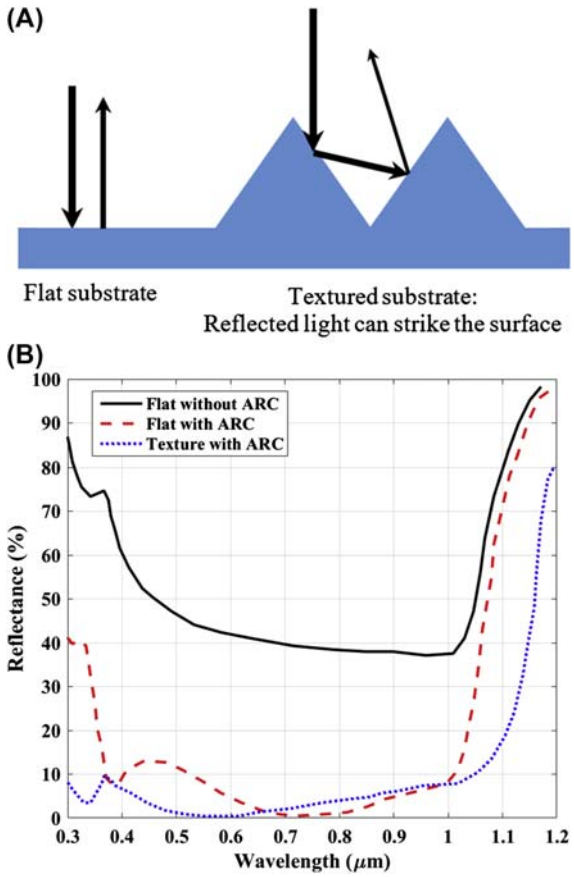


FIGURE 1.29

(A) Surface texturing and (B) effect of antireflective coating and texturing on the reflectivity.

Wire attachment to the solar cells is made by soldering or welding. So, the metallization of the solar cell must be matched to these assembly processes. In addition, it must be corrosion resistive, adhere well to the Si, and form Ohmic contact with it. It must also not diffuse or micro alloy with Si because the shallow junction can be partially shorted. No single metal call satisfies all these requirements. Multi-layer metallization is normally used:

1. Titanium (0.1 μm) + silver (3−5 μm) (sensitive to humidity).
2. Ti (0.1 μm) + Pd (20−50 nm) + silver (3−5 μm) (protect against humidity).
3. Printed silver layer (25 μm).
4. (Cr−Pd−Ag) for space cells.

www.TechnicalBooksPDF.com

4.5 MANUFACTURING SOLAR CELLS

We shall confine ourselves to the manufacturing of the wafer-based, single-crystal and multi-crystal Si solar cells [22]. The major manufacturing steps are as follows:

1. p-type wafers of 1−10 Ω cm resistivity and about 0.2 mm thickness are first diffused with phosphorus to produce an n^+-layer with a thickness of 0.1−0.2 μm. A diffusion furnace is used to carry out this process. The protection gas is nitrogen. The diffusion sources are either solid in the form of discs or liquid spin-on sources. The process may run under oxygen atmosphere.
2. Then the diffused wafers are etched by hydrofluoric acid to remove the diffusion source layers,
3. The wafers are then metallized either by
   a. Evaporation of nickel−palladium−silver using thermal or electron-beam evaporators. The evaporation is carried out through metal masks to save the lithographic step or
   b. Screen printing a thick film of silver (∼25 μm).
4. Back-side metallization using evaporation.
5. The front side is antireflection coated either by spin-on techniques or by evaporation of TaO or TiO and SiO_x. Electron beam evaporator is used.
6. In case of solar cell assembly using solder reflow, the contact areas are coated with solder (Tin + lead + silver).
7. Now the solar cells are ready and are normally stored in cassettes.

4.6 TESTING THE SOLAR CELL AND SOLAR PANELS

To characterize the solar cells, one has to measure its $I-V$ characteristics under different illumination levels [23] and operating temperatures [24]. One may need also to measure the small signal impedance of the solar cell operating at a specified DC operating condition as a function of the small signal frequency [24]. The latter impedance measurements are termed impedance spectroscopy. To get information about the junction in the solar cell, one may measure the capacitance and conductance [25] as a function of the voltage in case of reverse bias. In the development phase, one may need to measure the spectral response of the solar cells represented by external quantum efficiency as a function of the incident radiation wavelength [26]. Within the scope of this book with emphasis on the application side of solar cells, the most important characteristics of interest are the $I-V$ characteristics of modules. So, we will outline such measurements based on a simple electronic circuit for testing the PV modules.

The $I-V$ and $P-V$ characteristics of PV modules are traced using the circuit shown in Fig. 1.30. The circuit is based on MOSFET IRFP260N as a varying electronic load with a heat sink to dissipate the power.

As V_{GS} is less than the threshold voltage V_{th}, the MOSFET will be OFF. When V_{GS} is increased above V_{th}, the MOSFET will operate in the active region and the drain current rises linearly with V_{GS}. The gate voltage is controlled using DAQ

www.TechnicalBooksPDF.com

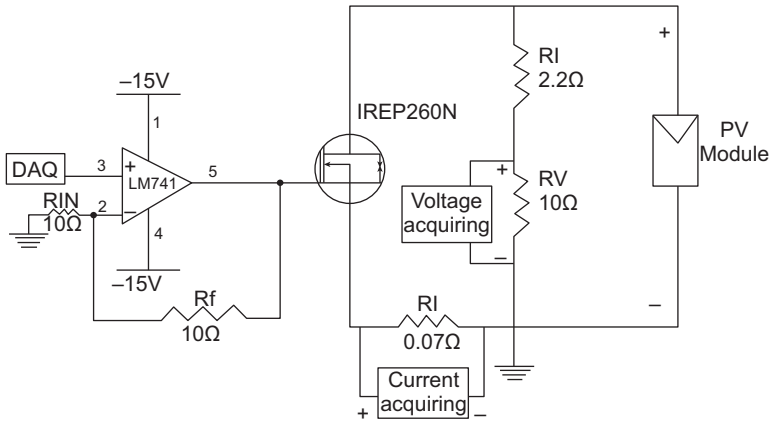


FIGURE 1.30

Testing circuit for the solar cells and modules.

system. This system is based on NI-USB 6008 with a sample rate of 10 Ks/s, laptop and LABVIEW application. The LAPVIEW application is used to generate a saw-tooth signal to vary the gate voltage from 3.4 to 5.5 V through the analog output of the NI-USB 6008. This range cannot be obtained as the analog output maximum voltage swing is 5 V so an amplifier circuit LM741 with gain 2 was used and the voltage generated was adjusted to vary from 1 to 3 V. Because the MOSFET cannot stand a high power for more than some milliseconds, the signal varied with high frequency of about 0.166 Hz and 1000 points per cycle.

The PV voltage is acquired through two high-power resistors (R_I & R_v) with high value comparable with that of the electronic load to draw small current, to not affect the PV operating point. As the maximum input voltage allowed by the DAQ is 10 V, the two resistors are connected as voltage dividers to avoid exceeding the input range. The PV current is acquired through a high-power resistor with low value (R_I) so that its voltage drop could be neglected [27]. A complete testing set up for field supervising the PV array performance on long time was developed based on an electronic load, a DAQ card, and a PC [28].

5. THE PV ARRAYS

In the previous sections, we have seen that the driving voltage of a single solar cell is about 0.55 V, and its current is about 35 mA/cm^2 for AM1 illumination. Conventional loads demand more voltage, more current, and more power. Therefore, we have to combine the solar cells to satisfy the load demand for certain operating voltage, current, power and certain type of current; either DC or AC. The DC loads normally operate from batteries. Therefore, their voltages are known to be 6, 12, 24, or 48 V, which

www.TechnicalBooksPDF.com

are the standard battery voltages. The load current is widely variable according to the power consumption of the load.

In PV systems containing batteries, the batteries themselves are the loads on the system; therefore, the current required is that of the nominal charging current of the batteries. Basically, the solar cells can be combined to satisfy a wide range of the load requirement concerning current, voltage, and power. A large solar cell array is subdivided into smaller arrays called the solar cell panels, which are composed of modules. Then a large array is built from modules. A module has conventionally 12-V and 6-A current with 72-W power under standard test conditions with AM1. Because each cell contributes 0.5 V output, one has to connect at least 24 cells in series to get 12 V. Because the solar cells must drive the load even at solar radiation less than AM1, the reliable module contains 36 cells rather than 24 cells.

The current demand of 6 A can be satisfied by solar cells having an area of 6 A/30 mA = 200 cm^2 and a diameter of 15 cm or 6 in cells.

5.1 THE *I*–*V* CHARACTERISTICS OF THE MODULE

The solar cell module is a unit array in the PV generator. It consists of solar cells connected in series to build the driving force and in parallel to supply the required current. A series-connected group of cells are called a solar cell string. Actually, the strings are connected in parallel as shown in Fig. 1.31.

Assuming that the number of solar cells in the string is n_e and the number of strings in parallel are n_s, then the total number of cells in the module is $n_a = n_e.n_s$. Let us assume further to simplify the problem that the cells in the module are identical having equal voltage drops = V_c and passing the same terminal current I_{st}, the string current. The module voltage is $V_{st} = V_m = V_a$ and the current of the module $I_a = I_m$, where m refers to module. To get $I_m = f(V_m)$, we apply the Kirchhoff's circuit laws and replace each cell by its equivalent circuit as shown in Fig. 1.32.

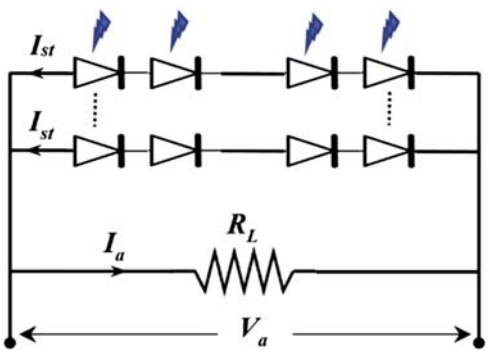


FIGURE 1.31

Basic blocks of the solar cell module.

www.TechnicalBooksPDF.com

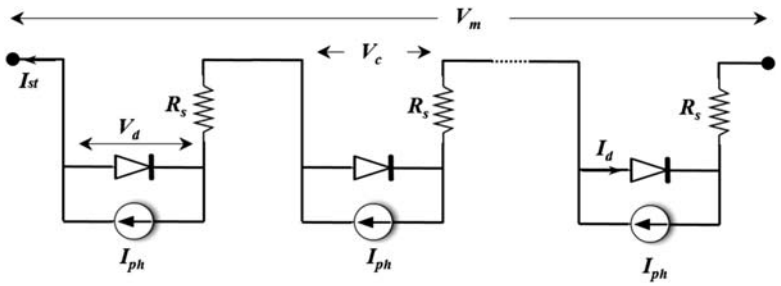


FIGURE 1.32

Equivalent circuit of the module.

Because the cells are identical, they have the same output voltage V_c, and because they are connected in series, they have the same terminal current I_{st}. As

$$V_c = V_j + I_{st}R_s,\ V_j = V_c - I_{st}R_s,\ \text{and}\ I_{st} = I_{ph} - I_d,$$

it follows that

$$I_{st} = I_{ph} - I_s\left(e^{\frac{(V_c + I_{st}R_s)}{nV_T}} - 1\right) \tag{1.49}$$

The overall module voltage is the sum of cell voltages in the module

$$V_m = \sum_{1}^{n_e} V_c = n_e V_c \tag{1.50}$$

Substituting Eq. (1.50) in (1.49), we get the $I-V$ of the string

$$I_{st} = I_{ph} - I_s\left(e^{\frac{(V_m/n_e + I_{st}R_s)}{nV_T}} - 1\right) \tag{1.51}$$

This equation is very simple. To pass the same current in the string, the string voltage must be exactly a multiple of n_e of the cell voltage.

Now let us pay our attention to the parallel connection of n_s strings. Because all cells are identical, the string current is the same in each string while the string voltages are the same, i.e., V_m. Hence,

$$I_m = \sum_{1}^{n_s} I_{st} = n_s I_{st} \tag{1.52}$$

The $I-V$ characteristics of the module can be obtained by substituting Eq. (1.52) in (1.51), i.e.,

$$I_m = n_s I_{ph} - n_s I_s\left(e^{\frac{(V_m/n_e + I_{st}R_s)}{nV_T}} - 1\right) \tag{1.53}$$

www.TechnicalBooksPDF.com

This relationship is the required $I-V$ of the module. It has the form of a single solar cell, with the current multiplied by n_s, the number of strings, and the cell voltage is multiplied by n_e, the number of cells in the string. Because the power output $= IV$, the power output of a single cell will be multiplied by (n_e n_s).

Solar cells with the same type are not identical because of fabrication tolerances. Basically, the produced solar cells from a production line must be sorted to select the matched cells. Matched cells have very high tolerances. On the other hand, if the solar cells are not matched, the string short circuit current will be the smallest short cell current, and the module output voltage under open circuit condition will be equal to the smallest open circuit voltage of the strings connected in parallel and the curve factor of the overall module becomes smaller because of the larger internal losses in the module. Hence, cell mismatch leads to additional internal losses and reduces the efficiency of the array in comparison to that of the single cells [29].

5.2 THE $I-V$ CHARACTERISTICS OF MISMATCHED CELLS IN THE MODULE

Now each cell i has its own parameters, I_{sci}, V_{oci}, FF_i, n_i, I_{si}, I_{phi}, and R_{si}. For a string current I_{st}, the voltage developed on the ith cell can be expressed according to Eq. (1.49) as

$$V_{ci} = n_i V_T \ln\left(\frac{I_{ph} - I_{st} - I_{si}}{I_{si}}\right) + I_{st}R_{si} \tag{1.54}$$

The total string voltage is then

$$V_m = \sum_{1}^{n_e} V_{ci} \tag{1.55}$$

If n_s unmatched strings are connected in parallel with the jth string, which is parametric, then

$$V_{m1} = V_{rn2} = V_{m3\ldots} = V_{mj\ldots} = V_{mns} = V_m \tag{1.56}$$

The string currents I_{st1}, I_{st2}, I_{st3} …, I_{stj}, …, I_{sns} are different. From Eqs. (1.54) and (1.55), the jth string has the characteristics:

$$V_{mj} = \sum_{i=1}^{n_{ej}} V_{ci} = V_m \tag{1.57}$$

This equation can split into (n_s−l) equations in I_{stj}. One needs one additional equation to determine I_{stj}. This equation is the output node equation

$$I_m = \sum_{i=1}^{n_s} I_{stj} \tag{1.58}$$

www.TechnicalBooksPDF.com

For a given I_m, I_{stj} are determined and V_m is calculated from Eqs. (1.54) and (1.55).

These equations can be solved numerically using the mathematical library or Matlab®. Another elegant approach to this problem is to use the circuit simulator PSpice to solve the module circuit under any operating condition and illumination.

In addition to the solar cell mismatch, there is another serious problem of decreasing the output from the module. This problem arises when the module is subjected to nonhomogeneous solar radiation. This problem is termed the partial shadowing of the module [30]. According to the degree of shadowing, photocurrent of some cells is reduced significantly. Partial shadowing comes from flying objects and from moving clouds. If the photocurrent of a cell in a string is made zero, i.e., the cell is dark, no current can pass in the string. This type of shadowing is the most severe one and has two serious consequences:

1. One string cannot deliver power to the load and becomes outage
2. The second is more serious, namely, the shadowed cell will be reverse biased. If this reverse bias is large, it can lead to defective shadowed solar cell by a phenomenon called hot-spot formation.

To see the reverse bias of a shadowed cell, let us estimate the voltage drop on such cell. Referring to Fig. 1.32 and assuming that the kth cell has $I_{ph} = 0$, according to the second Kirchhoff's law

$$V_{sc} = V_m - \sum_{i=1}^{n_e} V_{oci} \tag{1.59}$$

where $n_e \neq k$. Because I_{ph} of the kth cell $= 0$, the string is interrupted and all cells in the string operate under open circuit condition; hence, $V_c = V_{oci}$ for all cells except $i = k$. Inspecting Eq. (1.59), we can differentiate the cases:

1. V_m is that of the maximum power from the module
   $V_m \sim FF\ V_{oc}\ .\ n_e = 0.8 \times 0.6 \times 36 = 17.28$ V.
   Assuming $n_e = 36$, $V_{oc} = 0.6$ V, and $FF = 0.8$.
   $\sum_{i=1}^{n_e} V_{oci} = 36 \times 0.6 = 21$ V, where $n_e \neq k$.
   Substituting these values in Eq. (1.59), we get
   $$V_{cs} = 17.28 - 21 \sim -4V.$$
   This means that the shadowed cell is reverse biased by −4 V.
2. $V_m = 0$, short circuited-module. Then $V_{cs} = -17.28$ V. The shadowed cell is reverse biased with even a much larger voltage of 17.28 V.

5.3 FORMATION OF HOT SPOTS

When we have a diode with soft reverse characteristics and we reverse bias it, hot-spots will be formed. Hot-spots are hotter regions with higher current densities than

www.TechnicalBooksPDF.com

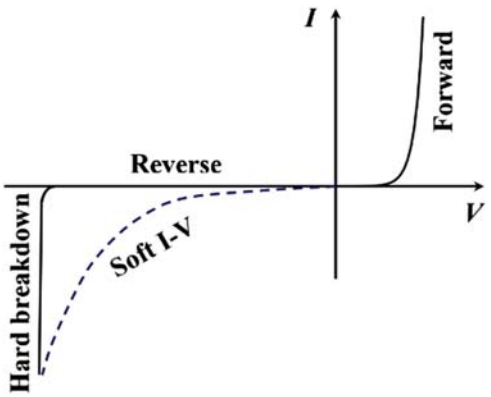


FIGURE 1.33

I—V characteristics showing the soft *I—V* in reverse.

the surrounding regions in the diode. Fig. 1.33 illustrates the reverse characteristics of solar cells. They are soft. It means that the leakage current is large and increases continuously with the reverse voltage. Soft breakdown occurs for shallow p—n junctions as solar cells have points of weak breakdown. Therefore, the breakdown current flows in small spots. Because the current is high and the voltage is high, a relatively large power is consumed in this small area, which becomes hotter as in Fig. 1.34. This effect can lead to thermal breakdown of the cell [31].

To avoid destruction of solar cells, we connect across them a bypass diode back to back as shown in Fig. 1.35. Solar cells can be cracked or disconnected because of unreliable assembly and the effect of environment. This effect is exactly like the shadowing except it is permanent. Protection diodes have an additional vital

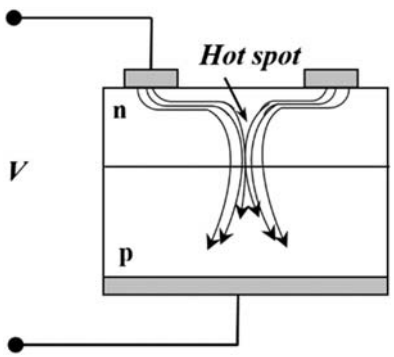


FIGURE 1.34

Hot spot formed in a weak p—n junction region.

www.TechnicalBooksPDF.com

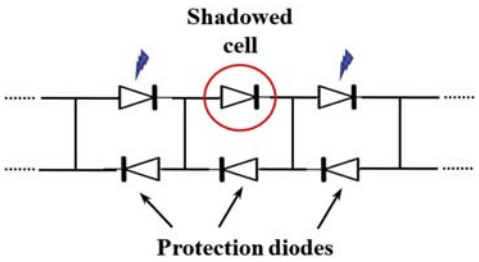


FIGURE 1.35

Solar array with back-connected bypass protection diodes.

function. It conducts the current of the string and prevents the interruption of the current in case of complete cell shadowing or cracking of the interconnect wires or cells.

5.4 MEASUREMENT DATA AND PRACTICAL CONSIDERATIONS

Fig. 1.36 shows the $I-V$ characteristics of a solar module consisting of $n_e = 36$, $n_s = 6$ array solar cells of 2 cm $\times$ 2 cm measured at AM = 100 mW/cm^2 at two different temperatures.

It is clear from this figure, that the shape of the $I-V$ curve of the array is similar to that of a single solar cell as predicted by the previous analysis of the module

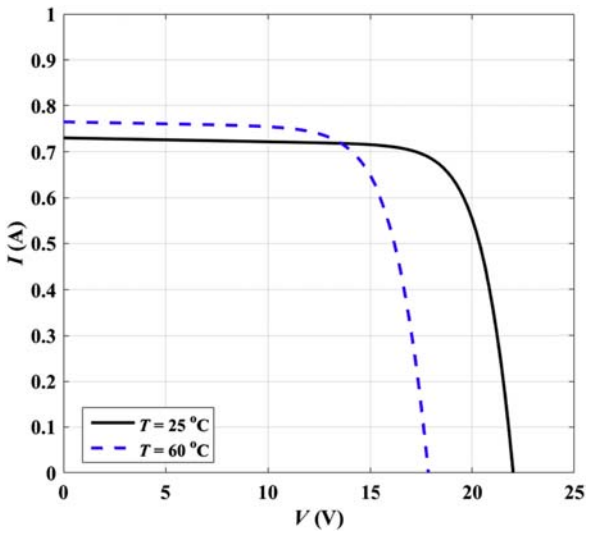


FIGURE 1.36

The $I-V$ characteristics of a solar cell module at different temperatures.

www.TechnicalBooksPDF.com

characteristics. At 20 °C, the short circuit current of the module $I_{sc} = 730$ mA, the open circuit voltage of the module = 22 V, the maximum power $P_m = 12$ W, and the module efficiency = 12%. At 60 °C, $I_{sc} = 770$ rnA, $V_{oc} = 18$ V, $P_m = 10$ W, and $\eta = 10\%$. From the figure, we see further that I_{sc} increases slightly with temperature, V_{oc}, P_m, and η decrease with temperature. This behavior is similar to that of the solar cells, which is expected because the parallel connection is a current multiplication process while the series connection is a voltage multiplication process. The open circuit voltage per cell V_{oc}/cell = $22/n_e = 22/36 = 0.61$ V, and the short circuit current per cell I_{sc}/cell = $730/n_s = 730/6 = 122$ mA. These values are in very close agreement with those of the single cell.

5.5 THE SOLAR CELL ARRAY

The array is composed of solar modules connected according to certain configuration to satisfy the voltage, the current, and the power requirement. If the array voltage is V_a, the array current is I_a, and the array power is P_a, one can determine the number of the modules required and their circuit configuration. As an example, using the modules with the characteristics given in Fig. 1.36, we can design an array with $V_a = 120$ V, $I_a = 4$ A, and an output power ~0.5 kW peak. The number of modules connected in series = 120 V/m = 120 V/20V = 6 and the number of modules strings connected in parallel = 4 A/I_m = 4/0.7 = 6. Then the total number of the modules = $6 \times 6 = 36$ modules. A protection diode may be commented in series with the array to allow the passage of the current to the load only and prevent the back current.

5.6 THE FLAT PLATE MODULES

Solar cells must be encapsulated to protect them against environmental effects and to give them mechanical support for easy handling [32]. The terrestrial modules must be hermetically sealed against the moisture. The following requirements must be satisfied by the encapsulation:

1. rigidly support the mechanically weak solar cells
2. hermetically seal the solar cells against moisture
3. transparent for the solar radiation
4. withstand the environmental effects such as: (1) temperature cycling, (2) wind forces, (3) rain and hail fall.
5. remain reliable for long times to be economically feasible (more than 10 years)
6. as cheap as possible
7. relief temperature cycling leading to thermomechanical stresses on solar cells and interconnectors between them
8. have large area efficiency.
9. conduct the heat of the solar cells.
10. easily fabricated by simple processes.

www.TechnicalBooksPDF.com

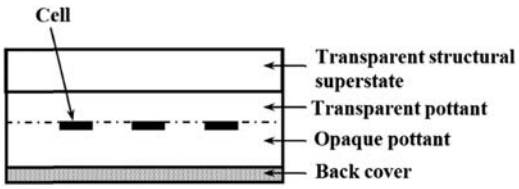


FIGURE 1.37

Cross-section of superstate design for flat-plate photovoltaic modules.

Fig. 1.37 shows the conventional solar cell plate construction for terrestrial applications. It consists of a glass superstrate above the cells and the cells are imbedded in a polymeric adhesive material and covered by an opaque plastic cover.

5.7 FAILURE MODES OF THE MODULES

To raise the reliability of the modules, one has to locate its different failure modes leading to deficient modules. The solar module is subjected during operation in the field to severe environmental effects. These effects may cause failures in the modules. Knowing these failure modes and their origin, we can improve the module construction, the module materials, and assembly processes to produce modules with high reliability. Many investigations [32,33] were made to work out these failure modes. According to this review and other related literature, these failures are as follows:

1. fractured metal interconnects and interconnect contacts
2. cracked cells
3. discoloring, snail formation, and delamination of EVA encapsulant from module
4. potential-induced degradation and dielectric breakdown
5. corrosion
6. Workmanship.

The cause of failures may be [34]

1. deficiency in the module design
2. large temperature excursions with cyclic nature
3. large wind forces
4. nonhermetic sealing against moisture
5. nonoptimized assembly processes
6. nonthermally matched encapsulation materials

Environmental tests on solar modules show that the main cause of failure is the dynamic wind stresses and the second main cause is the temperature cycling with high humidity. For dry climatic conditions, such as that in south Egypt, we developed a three-plate solar cell module [35] to minimize the thermal and wind stresses. This module is shown schematically in Fig. 1.38. Both silicone and silver paste are

www.TechnicalBooksPDF.com

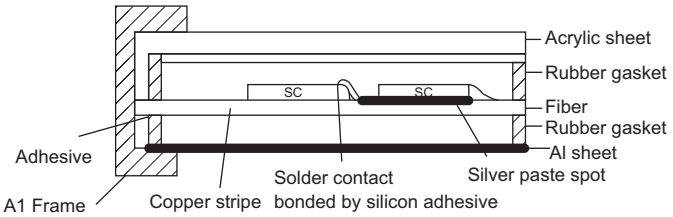


FIGURE 1.38

Flat plate module construction.

relatively soft allowing the bonding of materials with appreciably different linear thermal coefficients.

This structure is characterized by the following:

1. The wind forces do not reach the solar cells because the upper and the lower sheets will reflect the wind and act as barrier or wind shield.
2. Because there is no mechanical requirements on the substrate carryingthe cells, it could be made of thin sheet; therefore, saving in weight and cost.
3. The substrate can be made of material with easy mechanical processing such as fiber, wood, acrylic, printed boards, and plastic sheets. This makes the assembly of the solar cells on the substrate easy.
4. One of the possible ways to assemble the cells is to bond first the interconnect wire strips to the substrate using a glue material, then the solar cells are bonded to the wires from the back side by conducting silver paste. Finally, the wires are soldered to the front of the next solar cell as shown in Fig. 1.39.

One can carry out the first step by using printed circuit boards. If no silver paste is available, one can use the through hole assembly process [36]. One uses soft adhesives for die bond and wire attach to relieve the transfer of stresses between the multilayers. The detailed steps of the fabrication of this module are given in [35].

5.8 THE GLASSING FACTOR OF THE MODULE

The transparent module cover affects the incident solar radiation to the underlying solar cells. It reflects some incident solar radiation and absorbs another

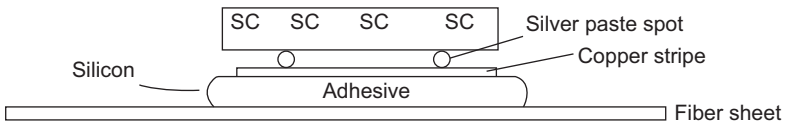


FIGURE 1.39

The assembly of the solar cells (SC) and the interconnected wires to a fiber substrate sheet.

www.TechnicalBooksPDF.com

fraction. Ideally $\rho = 0$, and $\alpha = 0$ for $\lambda = 0.3{-}1$ μm. There is no ideal optical cover. Acrylic absorbs much less than glass. The content of iron in glass affects its transmittance. Especially the overall reflected part of the incident solar radiation on solar cells can be reduced by the cover if the optical matching condition is satisfied. This can be achieved by choosing the encapsulate refractive index $n_e = \sqrt{n_{cover} \times n_{sc}}$, where n_{cover} is the refractive index of the cover and n_{sc} is the refractive index of the antireflective coating of the solar cell. The glassing factor F_g is defined by the ratio of the output power with encapsulation to the output power without encapsulation, i.e., $F_g = (P_o$ with cover)/(P_o without cover) [36]. This factor may be less or slightly greater than 1. It describes the optical performance of the encapsulation.

6. CIRCUIT AND DEVICE SIMULATION OF SOLAR CELLS AND MODULES

6.1 CIRCUIT-LEVEL SIMULATION

The equivalent circuit models are widely used to simulate PV cells and modules. The main advantage of using circuit models is the availability of the standard electrical software such as Matlab® (or Simulink) and PSpice, where the PV model can be easily integrated into a larger system. The choice of any simulation program stands behind the desire of giving the reader the ability of modifying system parameters freely and examining the corresponding effects.

PSpice has become the standard industrial electrical circuit simulator. Most semiconductor devices are modeled such that they can be included in the Pspice library. The models of the PV cell could be implemented by using subcircuit capability found in most PSpice programs [37].

In addition, Matlab® has become an important mathematical tool for simulation in all areas of engineering. Implementation of equations needed for modeling the PV cell is an easy task and can be done either by using Matlab® functions or Simulink models [38]. The purpose of this section is to demonstrate a simple, yet effective way to model solar cells using Matlab® and PSpic.

6.1.1 Summary of Mathematical Modeling

The first step in circuit simulation of solar cells is to build a mathematical model representing the governing equations. Table 1.1 summarizes the basic mathematical equations based on the single-diode model of the solar cell explained in Section 1.4, where the temperature dependence of parameters is also included.

6.1.2 Parameter Extraction

The precise modeling of a solar cell model is based on the accuracy of the extracted parameters in that model. It is necessary to identify the model parameters before the use of the selected model to simulate the cell behavior. According to the model presented above, there are five parameters to be extracted; I_{ph}, I_s, R_s,

www.TechnicalBooksPDF.com

Table 1.1 Summary of Mathematical Equations for the Solar Cell or Module

$$I = I_{ph} - I_s\left(e^{\frac{q(V+IR_s)}{nk_BT}} - 1\right) - \frac{V+IR_s}{R_{sh}}$$

$$I_{ph} = I_{ph(STC)} + K_I(T - T_{STC})$$

$$I_{ph(STC)} = I_{SC(STC)}\left(\frac{G}{G_{STC}}\right)$$

$$V_{oc} = V_{oc(STC)} + K_V(T - T_{STC})$$

$$I_s = I_{s(STC)}\left(\frac{T}{T_{STC}}\right)^3 e^{\frac{-qE_g}{nk_B}\left(\frac{1}{T}-\frac{1}{T_{STC}}\right)}$$

$$I_{s(STC)} = \frac{I_{SC(STC)}}{\left(e^{\frac{qV_{oc(STC)}}{nk_BT_{STC}}} - 1\right)}$$

where, E_g is the band gap energy of the semiconductor; G is the surface irradiance of the cell; G_{STC} is the irradiance under STC (=1000 W/m^2); $I_{s(STC)}$ is the nominal saturation current; $I_{SC(STC)}$ is the short circuit current per cell at T_{STC}; k_B is the Boltzmann's constant; K_I is the temperature coefficient of short-circuit current; K_v is the temperature coefficient of open-circuit voltage; n is the diode ideality factor; STC is standard test conditions (T_{STC} = 25°C); T is the absolute temperature in K.

R_{sh}, and n. In this section, we present two methods that can be implemented using Matlab® to extract the mentioned parameters. The extraction is mainly based on the manufacturer's specification datasheets or experimental data. Most solar cell manufacturers include in the datasheet, at the least, information about the following at STC:

- short circuit current, I_{sc}, and short circuit current/temperature coefficient K_i
- open circuit voltage, V_{oc}, and open circuit voltage/temperature coefficient K_v
- MPP: the optimum operating point at $V = V_{mp}$ and $I = I_{mp}$.

Table 1.2 shows the steps and equations used for extracting the single-diode model parameters using two methods. The first method relies on estimating the ideality factor n, while the other is performed by getting an initial value for the shunt resistance [39,40].

6.1.3 PSpice Model of the Solar Cell

The PSpice model of the subcircuit of an ideal solar cell can be implemented as follows [37]. First, all parameters are defined:

```
.param Isc_STC = 3.87, Ns = 36, n = {ncell*Ns}, ncell = 1.35, G = 1000
+ Rs = 0.1606, Rsh = 385.86, Ki = 2.6e−3 Kv = −0.08, Voc_STC = 21.
```

Temperature and temperature-dependent parameters are also included. For example:

```
.param Tmod = 25
.param Io = {((Rsh+Rs)*Isc_STC − Voc)/(Rsh*exp(Voc/(n*Vtn)))}
.param Iph_STC = {(Isc_STC*(1 + Rs/Rsh) + Io*(exp(Iscn*Rs/(n*Vtn)) − 1))}
.param Iph = {Iph_STC+Ki*(Tmod-25)}, Voc = {Voc_STC + Kv*(Tmod-25)}
+ Vtn = {0.0257*(Tmod + 273)/298}
```

www.TechnicalBooksPDF.com

Table 1.2 Equations and Steps of Two-Parameter Extraction Procedure

1st Method (Estimating n)	2nd Method (Initializing R_{sho})
This can be done by knowing the solar cell material and the number of series cells $n = n_{\text{cell}} \times N_s$ (usually, $1 < n_{\text{cell}} < 1.5$)	This can be done by calculating the slope of the I–V curve at short circuit condition $R_{sho} = -\left(\frac{\partial V}{\partial I}\right)\Big\vert_{I=I_{sc}}$
$\frac{nV_T V_{mp}(2I_{mp} - I_{sc})}{(V_{mp}I_{sc} - (I_{sc} - I_{mp})V_{oc})(V_{mp} - I_{mp}R_s) - nV_T(V_{mp}I_{sc} - V_{oc}I_{mp})} = \exp\left(\frac{V_{mp} + I_{mp}R_s - V_{oc}}{nV_T}\right)$ This equation is an implicit equation of R_s	$R_s = \frac{(A-B)}{(A+B)}\frac{V_{mp}}{I_{mp}} + \frac{B}{A+B}\frac{V_{oc}}{I_{mp}}$ $A = (V_{mp} - (I_{sc} - I_{mp})R_{sho})\log\left(\frac{V_{mp} - (I_{sc} - I_{mp})R_{sho}}{V_{oc} - I_{sc}R_{sho}}\right)$ $B = V_{mp} - I_{mp}R_{sho}$
$R_{sh} = \frac{(V_{mp} - I_{mp}R_s)(V_{mp} - (I_{sc} - I_{mp})R_s - nV_T)}{(V_{mp} - I_{mp}R_s)(I_{sc} - I_{mp}) - nV_T I_{mp}}$, $I_s = \frac{(R_{sh} + R_s)I_{sc} - V_{oc}}{R_{sh}\exp\left(\frac{V_{oc}}{nV_T}\right)}$ and $I_{ph} = \frac{R_{sh} + R_s}{R_{sh}}I_{sc}$	$n = \frac{(V_{mp} - I_{mp}R_s)(V_{mp} - (I_{sc} - I_{mp})R_{sho})}{(V_{mp} - I_{mp}R_{sho})V_T}$

www.TechnicalBooksPDF.com

The equivalent circuit starts with the photogenerated current, which could be assigned to a G-device which is a voltage-controlled current source. Then the circuit may look like:

```
*vbias is added to trace the load current
vbias 1 0 dc 0
*to define the photogenerated current
virrad 2 0 dc {G}
*the PV module is to be defined as a subcircuit model
xPV 0 1 2 PV_mod
```

The subcircuit net list could be written as follows:

```
.subckt PV_mod 100 103 102
girrad 100 101 value = {(Iph/1000)*V(102)}
d1 101 100 diode
.model diode d(is = {Io}, N = {n}, LEVEL = 3)
rs 101 103 {Rs}
rsh 101 100 {Rsh}
.ends PV_mod
```

Finally, many analysis could be done using .TEMP (to sweep the temperature) or .dc (to sweep the voltage) and so on. For example, the following order will sweep the DC bias voltage to get the $I-V$ characteristics.

```
.dc vbias 0 21 0.01
```

Also, we can sweep any parameter to examine its effect on the $I-V$ characteristics. For example, the following orders will sweep the irradiance and the cell ideality factor, respectively, to get different curves at the same time.

```
.step param G list 1000 800 600 400 200
.step param ncell list 1.2 1.35
```

6.1.4 Case Studies

Here, we consider two case studies to validate the modeling and extraction techniques provided in the previous subsections. The first case study is the Photowatt-PWP 201 solar module. The module is composed of 36 solar cells connected in series ($N_s = 36$) and measured at 45°C [41]. This example has been widely used by different authors as benchmark to check for parameter extraction validity. The second case study is the BP MSX-60 solar module, which consists of 36 series solar cells [42]. The measurements of the Photowatt-PWP 201 and the datasheet specifications of the BP MSX-60 are given in Table 1.3.

www.TechnicalBooksPDF.com

Table 1.3 Main Circuit Parameters of the Two Case Studies

Parameter	Photowatt PWP 201	BP MSX-60
I_{sc} (A)	1.0317	3.87
V_{oc} (V)	16.7785	21.1
I_{mp} (A)	0.9120	3.56
V_{mp} (V)	12.6490	17.1
N_s	36	36
K_V (V/K)	NA	−0.08
K_I (A/K)	NA	3×10^{-3}

For the Photowatt-PWP 201, the two extraction methods are applied. Regarding method 1, the ideality factor for the module is estimated to be $n = 45.1958$. Regarding method 2, the initial value of the shunt resistance is $R_{sho} = 561.034$ according to measurements. Table 1.4 shows the extracted parameters using the two methods. Fig. 1.40A shows the $I-V$ characteristics.

Considering BP MSX-60, the first extraction method is only applied because of the difficulty in determining the initial value of the shunt resistance. Here, the ideality factor for the module is estimated to be $n = 46.8$ (1.3×36). Also, Table 1.4 shows the extracted parameters and Fig. 1.40B presents the $I-V$ characteristics for the module at two different temperatures compared with the results obtained from the datasheet. There is good agreement between the simulated and measured characteristics proving that the single-diode model is satisfactory for describing the behavior of the conventional solar cells and modules.

6.2 TCAD SIMULATION OF SOLAR CELLS

It is important to predict the device operation by TCAD (Technology Computer Aided Design) simulations before fabrication. TCAD modeling and simulation plays

Table 1.4 Extracted Model Parameters of the Two Case Studies

	Photowatt PWP 201		BP MSX-60
Parameter	Method 1	Method 2	Method 1
N	45.1958	45.5330	48.6
R_s (Ω)	1.3483	1.3329	0.1606
R_{sh} (Ω)	543.4009	559.7011	385.8654
I_s (A)	1.3278×10^{-6}	1.4690×10^{-6}	1.9080×10^{-7}
I_{ph} (A)	1.0343	1.0342	3.8716

www.TechnicalBooksPDF.com

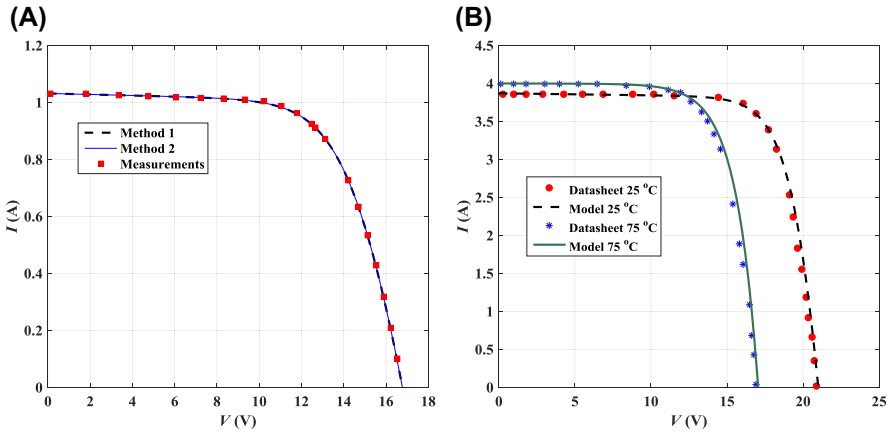


FIGURE 1.40

I–V model curves and experimental data/datasheet of (A) the Photowatt-PWP 201 and (B) MSX-60 solar modules at two different temperatures and $G = 1000$ W/m^2.

a vital role to develop new solar cell structures and predict their performance under various operating conditions. The goal of this section is to clarify the importance of using process and device simulators in the simulation of the solar cells. A novel npn solar cell structure is used as case study [43]. First, a qualitative analysis is carried out for the proposed solar cell structure. Then, the qualitative analysis is quantitatively verified using SILVACO device simulator [44]. In the quantitative analysis, first, an explanation for how to construct the solar cell structure using SILVACO process simulator Athena is presented. Second, the electrical and optical performance parameters are presented using the output from SILVACO device simulator Atlas. Finally, the npn structure performance is simulated for different emitter sidewall treatments introduced.

6.2.1 Qualitative Analysis for the Novel npn Solar Cell Structure

The conventional solar cell structure is planar. As the diffusion length of the minority carriers decreases to become less than the required light absorption depth, the efficiency of the solar cell decreases. This can practically occur when one uses heavily doped single-crystalline silicon, which is relatively a low-cost material [45,46]. A proposed solution to this problem is to use the npn solar cell structure shown in Fig. 1.41. The figure shows the detailed npn structure with the values of its technological and physical parameters as a case study. The light incident on the top surface will be absorbed in the active material and generate electron–hole pairs, which will be collected by the lateral and vertical p–n junctions around the p + substrate silicon material. Thus, the diffusion length can be decreased. To be low cost, the structure could be fabricated using a commercially available highly doped silicon wafer [47].

www.TechnicalBooksPDF.com

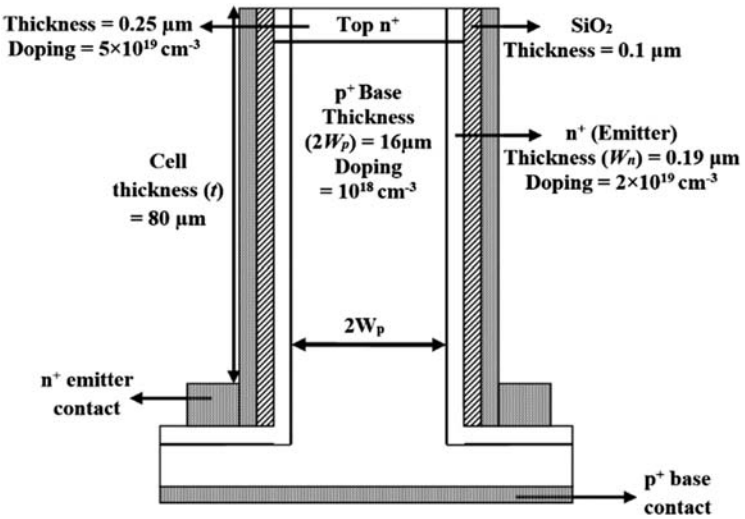


FIGURE 1.41

A two-dimensional cross-sectional view of the proposed npn solar cell structure.

6.2.2 Construction of npn Solar Cell Structure Using Athena

The npn structure is created in SILVACO using Athena process simulator. This process simulator gives the facility to create the structure virtually as fabricating it on a starting p^+ wafer. The starting p^+ substrate is highly doped, with doping in the order of 10^{18} cm^{-3}. Then, one makes deep trenches to produce the fingers with specific widths. Then one produces the n + emitter by diffusion. Then the sidewalls are metalized with a suitable metal. The back side of the wafer receives an aluminum metallic contact. The width of the fingers is called base width, which must be smaller or equal to the diffusion length of the carriers in the base region.

The flow of the code is summarized as follows. First, the definition of the meshing in *x*- and *y*-direction is written. Only half of the structure can be taken into the process simulation at first. Then using the capability of mirror, the whole structure is defined.

```
go athena
line x loc=0    spac=2
line x loc=0.1    spac=2
……..
line x loc=8.5    spac=0.5
#
line y loc=0    spac=0.01
……..
line y loc=80    spac=1
```

www.TechnicalBooksPDF.com

Then the starting material is invoked along with its doping. This process is followed by etching Si wafer to deposit the oxide.

```
init silicon c.boron=1.0e18 orientation = 111
ETCH silicon START X = 8 Y = 0.0
ETCH CONTINUE X = 8.5 Y = 0.0
ETCH CONTINUE X = 8.5 Y = 75
ETCH DONE X = 8 Y = 75
Deposit oxide thickness = 0.1 div = 2
etch oxide right p1.x = 8
```

After that, diffusion of the emitter is performed.

```
Diffuse time = 2 temp = 1000 phosphorus = 2e20
```

The process continues to define the top layer by diffusion. Then the electrodes are defined and finally saving the structure to be used by the device simulator Atlas.-Fig. 1.42 shows the npn structure produced by Athena. The cathode is taken as a contact for n^+ emitter from sidewall. The anode is taken as a contact for p^+ base from back surface. Also, the sidewall n^+ emitter for the two-sidewall n^+ emitter for the npn structures are shown in figure. The top n^+ layer is shown for the structure. It is taken to be 0.25 μm, as for planar solar cell [48].

6.2.3 Electrical and Optical Characterization for the npn Structure Performance

In this subsection, an electrical and optical characterization the npn structure is carried out using Atlas device simulator. Fig. 1.43A shows the npn structure

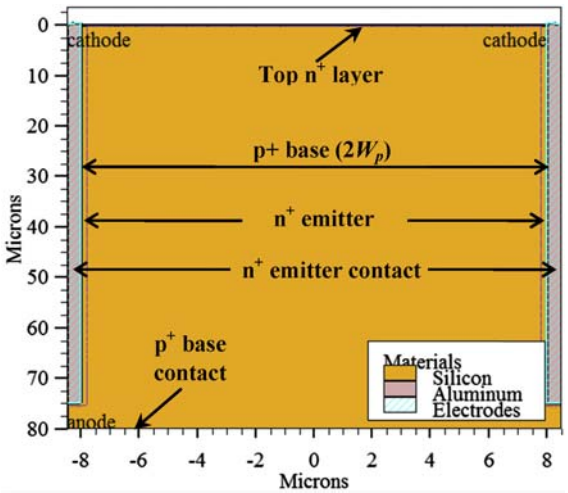


FIGURE 1.42

The npn structure using SILVACO/Athena.

www.TechnicalBooksPDF.com

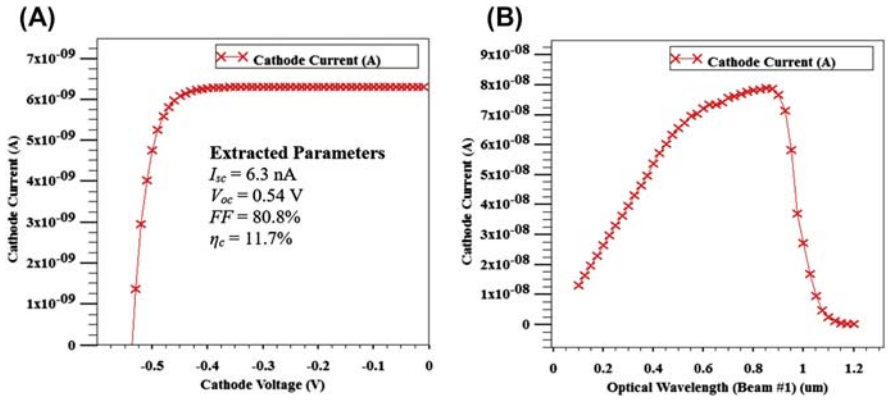


FIGURE 1.43

(A) The *I—V* characteristic of the npn structure, (B) spectral response using SILVACO.

I—V characteristics. The solar cell structure electrical performance parameters are extracted and calculated as shown. Moreover, the simulated optical performance of the npn structure using Atlas is presented. Fig. 1.43B shows the spectral response of the structure. The important data taken from the figure are that the structure responds well to the long-wavelength part of the input solar radiation spectrum, which is the long-wavelength till the silicon cutoff wavelength 1.1 μm. This emphasizes that the vertical pn junction works very well as a long-wavelength collector.

6.2.4 The Simulation of the Effect of Different n^+ Emitter Sidewall Surfaces on the Electrical Performance

In this subsection, the effect of different n^+ emitter sidewall surfaces on the npn structure electrical performance is presented. The objective of this study is to show the effect of different n^+ emitter sidewall surfaces on the structure electrical performance. Two cases for the n^+ emitter sidewall surfaces are studied. In the first case, the sidewalls are passivated with SiO_2. This indicates that it is done with low v_s. The second case is when an aluminum is deposited on the n^+ emitter sidewall. This indicates that the sidewall surface is an Ohmic contact with high v_s. Table 1.5 summarizes the extracted electrical performance parameters for both cases.

Referring to Table 1.5, it is obvious that, I_{sc} and J_{sc} are not greatly affected by the condition of the n^+ emitter sidewall surface treatment. The reason is that the n^+ emitter width W_n equals to 0.18 μm, which is very narrow with respect to the p^+ base width. Thus, the n^+ emitter contribution to the illumination is not important with respect to the p^+ base. As the main objective of the n^+ emitter is to be a good one, the effect of its sidewall surface treatment on the dark characteristics, the reverse saturation current (I_o) and V_{oc}, is more important. In this study, it is important to calculate I_s as its value well clarifies the effect of n^+ emitter sidewall

www.TechnicalBooksPDF.com

Table 1.5 Comparison Between Extracted Electrical Performance Parameters for Two Different Emitter Sidewall Surfaces

Parameter	n^+ Sidewall Surface Is Passivated with SiO_2	Aluminum Is Deposited on n^+ Emitter Sidewall Surface
I_s (A)	2×10^{-18}	1.9×10^{-17}
I_{sc} (V)	6.3	6.2
J_{sc} (A)	35	34.4
V_{oc} (V)	0.54	0.52
FF (%)	80.8	80.7
η_c (%)	11.7	11.1

surface treatment on V_{oc}. It is obvious that V_{oc} is increased when the n^+ sidewall surface is passivated with SiO_2. The reason is that the SiO_2 passivation decreases the gradient of the excess hole distribution. Thus, the reverse saturation current decreases, which in turn increases V_{oc}.

REFERENCES

[1] J. Fricke, W.L. Borst, Essentials of Energy Technology: Sources, Transport, Storage, Conservation, Wiley, 2013.
[2] http://pveducation.org/pvcdrom/2-properties-sunlight/solar-radiation-earths-surface.
[3] https://ntrs.nasa.gov/archive/nasa/casi.ntrs.nasa.gov/19810016493.pdf.
[4] http://www.nrel.gov/docs/legosti/old/3895.pdf.
[5] www.ncdc.noaa.gov/data-access/land-based-station-data/land-based-datasets/solar-radiation.
[6] https://www.researchgate.net/file.PostFileLoader.html?id=553e4871d685ccd10e8b4618&assetKey=AS%3A273765705945088%401442282238044.
[7] https://ocw.tudelft.nl/wp-content/uploads/Solar-Cells-R3−CH3_Solar_cell_materials.pdf.
[8] H.W. Schock, Thin Film Compound Semiconductor Solar Cells: An Option for Large Scale Applications?, in: Tenth E.C. Photovoltaic Solar Energy Conference, 1991, pp. 777−782.
[9] W.C.H. Choy (Ed.), Organic Solar Cells Materials and Device Physics, 2013.
[10] C.C. Stoumpos, M.G. Kanatzidis, Halide perovskites: poor Man's high-performance semiconductors", Adv. Mater. 28 (28) (2016) 5778−5793.
[11] A. Zekry, Electronic Devices: A University Textbook, Ain Shams University, 1998.
[12] H. Zimmerman, Integrated Circuit Optoelectronics, Springer-Verlag Berlin Heidelberg, 2010.
[13] A. Zekry, G. ElDllal, Effect of MS contact on the electrical behavior of solar cells, J. Solid State Electronics 31 (1) (1988) 91−97.
[14] M. Abdelnaby, A. Zekry, F. Elakkad, H.F. Ragaie, Dependence of dark current on zinc concentration in ZnxCd1-xS/ZnTe hetero-junctions, Sol. Energy Mater. Sol. Cells 29 (1993) 97−108.

www.TechnicalBooksPDF.com

[15] https://www.ise.fraunhofer.de/content/dam/ise/de/documents/publications/studies/Photovoltaics-Report.pdf.
[16] T.V. Torchynska, G.P. Polupan, III-V material solar cells for space application, Semicond. Phys. Quan. Electron. Optoelectron." 5 (1) (2002) 63−70.
[17] M.A. Green, S.P. Bremner, Energy conversion approaches and materials for high-efficiency photovoltaics, Nat. Mater. 16 (2017) 23−34.
[18] https://www.sintef.no/contentassets/a7b420c8e5474cc4880c748a9ebb66a1/daniel-n-wright.pdf.
[19] H. Kanda, et al., Al2O3/TiO2 double layer anti-reflection coating film for crystalline silicon solar cells formed by spray pyrolysis, Energy Sci. Eng. 4 (4) (2016) 269−276.
[20] L.A. Dobrzański, M. Szindler, A. Drygała, M.M. Szindler, Silicon solar cells with Al_2O_3 antireflection coating, Central Eur. J. Phys. 12 (9) (2014) 666−670.
[21] S.M. Sze, Physics of Semiconductor Devices, second ed., John Wiley and Sons, 1981.
[22] N. Achara, Solar cell standard and improved manufacturing processes, Int. J. Eng. Innov. Technol. 3 (9) (2014) 162−167.
[23] A. Zekry, A.Y. Al-Mazroo, A distributed SPICE-model of a solar cell, IEEE Trans. Electron Devices 43 (5) (1996) 691−700.
[24] L.A. Hecktheuer, A. Krenzinger, C.W.M. Prieb, Methodology for photovoltaic modules characterization and shading effects analysis, J. Braz. Soc. Mech. Sci. 24 (1) (2002) 26−32.
[25] A. Zekry, M. Abdel-Naby, H.F. Ragaie, F. El Akkad, Capacitance and conductance of $Zn_xCd_{1-x}S$/ZnTe heterojunctions, IEEE Trans. Electron Devices 40 (2) (1993) 259−266.
[26] K. Emery, D. Dunlavy, H. Field, T. Moriarty, 1998"Photovoltaic spectral responsivity measurements" The 2nd World Conference and Exhibition on Photovoltaic Solar Energy Conversion, 6−10 July 1998, Vienna, Austria.
[27] A. Sahbel, N. Hassan, M.M. Abdelhameed, A. Zekry, Experimental performance characterization of photovoltaic modules using DAQ, Energy Procedia 36 (2013) 323−332.
[28] https://www.researchgate.net/publication/236120856_A_full_automatic_measurement_set_up_for_solar_cell_modules.
[29] C.E. Chamberlin, P. Lehman, J. Zoellick, G. Pauletto, Effects of mismatch losses in photovoltaic arrays, Sol. Energy 54 (3) (March 1995) 165−171.
[30] S. Silvestre, A. Chouder, Effects of shadowing on photovoltaic module performance, Prog. Photovoltaics Res. Appl. 16 (2) (2008) 141−149.
[31] H.J. Solheima, H.G. Fjæra, E.A. Sørheima, S.E. Fossa, Measurement and simulation of hot spots in solar cells, Energy Procedia 38 (2013) 183−189.
[32] http://www.isfh.de/institut_solarforschung/files/iea_t13_review_of_failures_of_pv_modules_final.pdf.
[33] http://physics.ucsc.edu/∼galers/stuff/2e3-slides.pdf.
[34] http://www.solar.udel.edu/ELEG620/13_PV_modules.pdf.
[35] A.A. Elshazly, A. Zekry, M.A. ElKoosy, M.S. Farid, Three flat plate terrestrial module fabrication and testing, Renew. Energy 23 (3-4) (July 2001) 509−523.
[36] M.S. Farid, A. Zekry, A.A. El-Shazly, M.A. El-Koosy, Evaluation of optical and thermal behavior of a 3FPT photovoltaic modules, Renew. Energy 23 (3-4) (2001) 429−440.
[37] L. Castaner, S. Silvestre, Modelling Photovoltaic Systems Using Pspice. University Politecnia de Cataluna Barcelona, Spain.

www.TechnicalBooksPDF.com

[38] H. Tsai, C. Tu, Y. Su, Development of generalized photovoltaic model using MATLAB/SIMULINK, in: Proceedings of the World Congress on Engineering and Computer Science 2008, WCECS 2008, October 22-24, 2008, San Francisco, USA, 2008.
[39] J. Cubas, S. Pindado, M. Victoria, On the analytical approach for modeling photovoltaic systems behavior, J. Power Sourc. 247 (2014) 467−474.
[40] M.G. Villalva, J.R. Gazoli, E.R. Filho, Comprehensive approach to modeling and simulation of photovoltaic arrays, IEEE Trans. Power Electron. 24 (5) (May 2009) 1198−1208.
[41] T. Easwarakhanthan, J. Bottin, I. Bouhouch, C. Boutrit, Nonlinear minimization algorithm for determining the solar cell parameters with microcomputers, Int. J. Sol. Energy 4 (1) (1986) 1−12.
[42] BP MSX 60 and BP MSX 64 datasheets. Available online: http://www.troquedeenergia.com/Produtos/LogosModulosSolares/BP-MSX-60-64.pdf.
[43] M.S. Salem, A. Zekry, A. Shaker, M. Abouelatta, Design and simulation of proposed low cost solar cell structures based on heavily doped silicon wafers, in: 43rd IEEE Photovoltaic Specialists Conference (PVSC), Portland, OR, USA, 2016, pp. 2393−2397.
[44] http://www.silvaco.com/.
[45] M.D. Kelzenberg, D.B. Turner-Evans, B.M. Kayes, et al., Single Nanowires SI Solar Cells, California Institute of Technology, 2007.
[46] M.C. Putnam, S.W. Boettcher, M.D. Kelzenberg, et al., Si microwire-array solar cells, Energy Environ. Sci. 3 (April 2010) 1037−1041.
[47] http://www.siltronix.com/wafer.php.
[48] A. Luque, S. Hegedus, Handbook of Photovoltaic Science and Engineering, John Wiley, 2003.

FURTHER READING

[1] http://www.lehigh.edu/imi/teched/SolarWS/T3f_Nositschka.pdf.

www.TechnicalBooksPDF.com

CHAPTER

Solar PV Power Plants Site Selection: A Review

2

Hassan Z. Al Garni, Anjali Awasthi

Concordia Institute for Information Systems Engineering, Concordia University, Montreal, QC, Canada

CHAPTER OUTLINE

1. Introduction to Solar Photovoltaic Land Suitability 57
1.1 Multicriteria Decision-Making Techniques for Photovoltaic Site Selection .. 58
1.2 Geographical Information System 64
1.3 Dealing With Uncertainties in Photovoltaic Site Selection 65
2. Criteria for Site Selection 65
3. Restriction Factors and Unsuitable Sites 68
4. Conclusions and Future Works 69
Acknowledgments 70
References 70

1. INTRODUCTION TO SOLAR PHOTOVOLTAIC LAND SUITABILITY

Compared to other renewable energy sources (RES), solar energy is a low-density power supply that necessitates vast areas for exploitation. Also, solar photovoltaic (PV) technology has enormous potential for deployment where the amount of global solar radiation per year is very high. However, one of the barriers to solar power development is the inconsistency and variability of solar irradiation which can be geographically dissimilar from one site to another. Selecting a suitable site is a crucial step toward developing a feasible utility-scale solar PV project. Though, the utility-scale PV considered as large-scale PV projects which can generate at least 5 MW [1,2].

Throughout solar energy research, a common question exists: What is the optimal site for utility-size solar PV? Performing a comprehensive solar site analysis is the first step toward ensuring a cost-effective and well-performing solar project. In general, the process must consider decision criteria as well as restriction factors that need to be assessed owing to their positive or negative impacts on the performance and cost of the electricity generated. Moreover, knowing the potential sites is a strategic primarily milestone for annual power plant output prediction as well as financial viability [3].

Advances in Renewable Energies and Power Technologies. https://doi.org/10.1016/B978-0-12-812959-3.00002-2
Copyright © 2018 Elsevier Inc. All rights reserved.

www.TechnicalBooksPDF.com

The geographical information system (GIS) is a powerful tool for consulting, analyzing, and editing data, map, and spatial information. In recent years, GIS has become progressively popular as a tool for various site selection studies, in particular for the energy planning. Developing a decision support model that integrates GIS with multicriteria can promote determining the ideal location for solar energy. Consequently, improving the performance of the solar PV projects plays a vital role in maximizing the generated output power, contributing to minimal project costs and assisting in planning future infrastructure projects.

In this chapter, theses, journal papers, and conference proceedings in the last 10 years (2007−17) are reviewed. Table 2.1 summarizes the associated studies with solar PV site selection. It presents the type of RES integrated with solar PV. The methodologies applied to tackle the problem with decision criteria is shown along with a grid-connection option in different contexts.

Solar PV grid-connected systems are linked and deliver power into the public electric grid. Such systems can be either distributed type, serving a certain grid-connected customer or centralized type, acting as a centralized power station and feeding into a transmission grid [43]. More than 80% of researches deal with grid-connected systems. From the location standpoint, China leads the site suitability studies followed by Spain and India as shown in Fig. 2.1.

1.1 MULTICRITERIA DECISION-MAKING TECHNIQUES FOR PHOTOVOLTAIC SITE SELECTION

Given the fact that several criteria can influence site selection, applying multicriteria decision-making (MCDM) methods can help ease site selection for utility-scale PV solar energy systems by considering key factors in the decision process. Various MCDM methods differ in their data requirement and the decision makers' (DM) goals and their respective characteristics. Jankowski explained the integration of GIS and MCDM ways in supporting decision-making [59]. Greene et al. provided an overview of the methods of MCDA and its spatial extension using GIS and suggested improving integration of MCDA with GIS software for increasing accessibility [60]. However, the research of GIS-MCDM has focused on a relatively small number of multicriteria approaches including the weighted linear combination (WLC), ideal points methods, the analytical hierarchy process (AHP), elimination and choice translating reality (ELECTRE), and Technique for Order Preference by Similarity to Ideal Solution (TOPSIS) [61] as shown in Table 2.1. MCDM methods have been successfully applied in many energy-planning projects. Pohekar and Ramachandran [62], Mateo [63], and Wang et al. [64] provide an excellent literature review on application of MCDM approach in the RE planning. According to the survey of AHP literature by Sipahi and Timor [64a], the GIS-AHP applications are among the most often used approaches for integrating AHP with other decision support techniques. The GIS-AHP approach ranks third. It accounts for about 11% of all the AHP-based integrated applications (while the first and second ranking methods, simulation and TOPSIS), account for 15% and 12% [61].

www.TechnicalBooksPDF.com

Table 2.1 Summary of Research Studies Tackling Solar Photovoltaic (PV) Site Selection

No.	References	Applied Technique	Renewable Energy Sources	Grid	Location
1	[4]	AHP	PV	On	Ismailia, Egypt
2	[5]	AHP	Solar farms	On	Konya, Turkey
3	[6]	AHP	PV-Wind	On	South, United Kingdom
4	[7]	AHP	Solar-wind-geothermal	None	Indonesia
5	[8]	AHP	PV	On	South, Morocco
6	[9]	AHP	Solar—wind	On	China
7	[10]	AHP	PV	On	Serbia
8	[11]	AHP	PV	On	Andalusia, Spain
9	[12]	FAHP	PV	On	Iran
10	[13]	FAHP	PV	On	Ulleung, Korea
11	[14]	AHP—TOPSIS	PV	On	Cartagena, Spain
12	[15]	AHP-Fuzzy OWA	PV	On	Oman
13	[16]	AHP-Fuzzy TOPSIS	PV	On	India
14	[17]	AHP-Fuzzy-WLC	Solar farms	On	Isfahan, Iran
15	[18]	FAHP-DEA	PV	On	Taiwan
16	[19]	ELECTRE	PV	On	Murcia, Spain
17	[20]	ELECTRE-II	PV-Wind	On	China
18	[21]	Fuzzy-distance decay	PV	On	La Rioja, Spain
19	[22]	Fuzzy OWA	PV-Wind	On	West, Turkey
20	[23]	Grey Cumulative	PV	On	Northwest, China
21	[24]	Transmitted Energy	Solar farms	None	MENA
22	[25]	Fuzzy ANP and VIKOR	PV	Off	Taiwan
23	[26]	Simulation scenarios	PV	On	India
24	[27]	Matter-Element	PV-Wind	Off	China
25	[28]	SWARA—WASPAS	Solar farms	On	Iran
26	[29]	DEMATEL—DANP	Solar Farms	On	China
27	[30]	Geospatial supply	PV	On	Fujian, China
28	[31]	Axiomatic design	PV	On	Turkey
29	[32]	Binary PSO	PV	On	Jaen, Spain

Continued

www.TechnicalBooksPDF.com

Table 2.1 Summary of Research Studies Tackling Solar Photovoltaic (PV) Site Selection—cont'd

No.	References	Applied Technique	Renewable Energy Sources	Grid	Location
30	[33]	WLC	PV	On	Southwest, USA
31	[34]	WLC	PV	On	EU-28
32	[35]	WLC	PV-Wind	On	Colorado, USA
33	[36]	WLC	PV-CSP-Wind	None	Afghanistan
34	[37]	Generation-demand	PV	On	Malaysia
35	[38]	GIS-Join	PV-Wind-Biomass	On	United States
36	[39]	GIS-Join	Solar Farms	On	United Arab Emirates
37	[40]	GIS- Near	Solar-wind-hydro diesel	On	Nigeria
38	[41]	GIS-Intersect	PV	On	Rajasthan, India
39	[42]	GIS-Overlay	PV	On	East of Morocco
40	[44]	GIS-Overlay	PV	On	Tibet, China
41	[45]	GIS-Overlay	PV-Bioenergy	On	Ontario, Canada
42	[46]	GIS-Overlay	Solar	On	Frosinone, Italy
43	[47]	GIS-Multiply	PV-wind-biomass	On	Appalachian Mountains, United States
44	[48]	GIS-Overlay	PV-wind-hydro-bioenergy	On	Cumbria, United Kingdom
45	[49]	ANN	PV	None	Italy
46	[50]	ANN	Solar farms	None	Indonesia
47	[51]	RETScreen-Solar irradiation	Solar farms	On	Iran
48	[52]	NASA-Solar irradiation	PV	None	India
49	[53]	GIS-Solar irradiation	Solar farms	On	Vietnam
50	[54]	GIS-Solar irradiation	Solar-Wind-Biomass	On	Kujawsko, Poland
51	[55]	GIS-Solar irradiation	PV-CSP	None	India

www.TechnicalBooksPDF.com

Table 2.1 Summary of Research Studies Tackling Solar Photovoltaic (PV) Site Selection—cont'd

No.	References	Applied Technique	Renewable Energy Sources	Grid	Location
52	[56]	GIS-Solar irradiation	Solar-wind-biomass-Hydro	None	Salta, Argentina
53	[57]	GIS-Solar irradiation	PV	On	Andalusia, Spain
54	[58]	GIS-Solar irradiation	Solar farms	None	Brazil

AHP, *analytical hierarchy process;* ELECTRE, *elimination and choice translating reality;* FAHP, *fuzzy analytical hierarchy process;* GIS, *geographical information system;* TOPSIS, *Technique for order preference by similarity to ideal solution;* WLC, *weighted linear combination.*

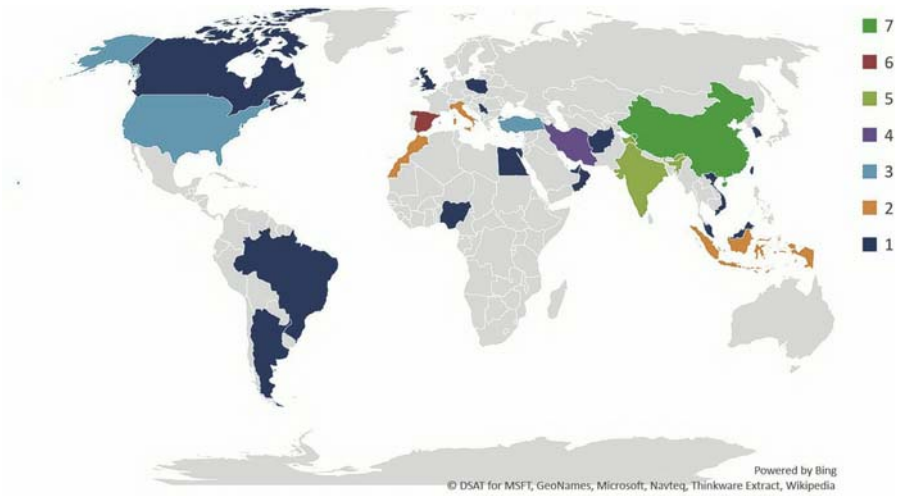


FIGURE 2.1

Utility-size solar photovoltaic (PV) site suitability studies across the globe.

AHP which developed by Saaty and Vargas [65] is the most MCDM tools applied to facilitates the ranking of sites alternatives [4–11]. AHP grasps a combination of qualitative and quantitative inputs. It has been popularly utilized by many authors in several fields, including but is not limited to, renewable and conventional energy planning, energy resources allocation, building energy management, and electricity utility planning [62]. AHP has been criticized for rank reversal, which occurs when adding or removing parameters that influence all other parameters to or from the model [66]. To deal with inaccuracy, AHP employs a consistency test, and hence,

www.TechnicalBooksPDF.com

it can screen out inconsistent judgments. In addition, the availability of commercial software supports the method to overcome the influence of rank reversal. Overall, AHP has been accepted by the international scientific community as a robust and flexible MCDM technique to facilitate solving complex decision problems [67]. Chandio et al. [68] reviewed the GIS-based AHP as MCDA instrument for land suitability assessment and concluded that the integration of GIS using AHP offered DM with an efficient tool for land suitability analysis and proven to improve efficiency from the economic aspect. It is important to notice from the study that the GIS-based AHP application in spatial problems has been growing significantly for the past three decades. In Egypt, Effat [4] used GIS and remote sensing tools along with applying AHP to calculate the criteria weight to spatial multicriteria evaluation model. Similarly, Uyan [5] applied AHP combined with GIS for solar farms site selection in Konya, Turkey. A large area of Southern England was assessed for suitability for the wind and solar farms by Watson and Hudson [6] who incorporates AHP to weigh the criteria and use GIS to find the most suitable lands for both resources. Rumbayan and Nagaska employed AHP and GIS to prioritize renewable energy resources (Solar, Wind, and Geothermal) in 30 provinces in Indonesia [7]. They applied AHP model to determine the weight of each criterion and subcriterion. The GIS-AHP applications are among the most often used approaches for integrating with other decision support techniques. We observed that besides the uses of AHP as a standalone method, some studies exist on AHP integration with other MCDM including TOPSIS, WLC, and fuzzy methods. Noteworthy studies of Charabi and Gastli [15] who conducted an assessment study of the land suitability for large PV farms implementation in Oman. They proposed AHP-WLC using fuzzy quantifiers in GIS toward developing an index for land suitability for PV and CSP farms.

Several authors consider WLC and its models such as simple additive weighting, weighted summation, weighted linear average, and weighted overlay [33–36,42,44–48,61]. The criterion weights, w_k, and value functions, $v(a_{ik})$, are the main parts of this technique. The criterion weight w_k is the allocated importance value of criteria k−th to other criteria while the value function $v(a_{ik})$ is the worth level of the alternative i ($i = 1, 2\ldots m$) with respect to that criterion k ($k = 1, 2\ldots n$). For the k−th criteria to be minimized the following equation applied. The ease of implementation within the GIS environment is the main advantages of WLC since it can easily be implemented using map algebra operations. Accordingly, GIS-WLC has been applied for several studies analyzing the decision. Once the weights obtained, they incorporated with the criteria map layers using a combination rule such as WLC. This method is more suitable for problems holding a large number of alternatives that will be impossible to perform a pairwise comparison of the alternatives. WLC and related models are often applied in site suitability, resource availability, and land-use analysis. Malczewski, in his book titled *Multicriteria Decision Analysis in Geographic Information Science*, stated that "WLC considered as the most often used GIS-MADA"; while he discussed some weakness of this tool including linearity assumptions, generally he highlighted the strength of such approaches including easily understanding how an implementation in GIS

www.TechnicalBooksPDF.com

could incorporate map algebra analysis and availability in several GIS software's (such as IDRISI, ILWIS, and ArcGIS) [61].

Ideal point methods order the decision alternatives based on their separations from some reference point. The chosen alternative should have the shortest distance from the Positive Ideal Solution and the farthest from the Negative Ideal Solution. The final ranking is obtained using the closeness index [14]. The most popular GIS-based ideal point method is the TOPSIS. Sánchez et al. [14] has reduced the studied area by applying restrictive criteria to discard unsuitable areas for solar farms projects. AHP considered weighting criteria and TOPSIS approach applied for alternative assessment according to their degree of adequacy. Sánchez et al. [69] applied AHP model to acquire weights of the criteria and the alternative assessment completed by fuzzy TOPSIS method for the installation of solar thermoelectric power plants.

Outranking Methods are based on pairwise comparison of alternatives on each decision criteria. The major procedure of this approach is applying the concordance and discordance measures. The concordance measure is based on concordance set for which the *i*th alternative is not worse than the competing alternative *j*, on subset of all criteria while the discordance is based on the discordance set for which alternative, *i*, is worse than the competing alternative, *j* [61]. The goal of outranking approaches is to find an alternative that dominate other alternatives while it cannot be dominated by any other alternative. Outranking also requires knowing weights of the criteria to find the best alternative [70]. There are a several formulas existed to calculate the overall score for each alternative based on concordance and discordance measures. The most widely outranking techniques integrated with GIS are the ELECTRE and preference ranking organization method for enrichment evaluation (PROMETHEE) [61]. Jun et al. evaluated seven wind/solar hybrid power stations, weight the indicators by and evaluates these seven regions via ELECTRE [20]. Sánchez et al. [19] integrated ELECTRE with GIS to optimize the solar farms locations according to multiple evaluations criteria. The restricted area excluded using GIS and criteria applied to categorize the potential plots using decision support system. Instead of finding the best suitable site to implement solar farms, the potential locations classified into distinct categories according to multiple evaluation aspects.

Fuzzy Methods is the description of a set of objects that have not shown sharply defined boundaries, and such imprecisely defined sets of objects are called fuzzy sets [71]. The fuzzy criteria and fuzzy constraints are combined to generate a decision where the best alternative is the one with highest grade membership value. In a particular subset + of the universe of discourse *X*, the grade of membership is defined by the membership function $\mu M(x)$. The function represents any elements *x* of *X* partially belonging to *M*, or the grade of membership of *x* in *M*. An object's membership value, which shows the degree to which it belongs to a set, can be any number between one and zero. If $\mu M(x) = 1$ that indicate element *x* obviously belongs to *M* whereas if $\mu M(x) = 0$ it indicates *x* not belong to *M*. The element of higher membership value represents more belong to the set [61]. The fuzzy MCDM has two essential terms: fuzzy number which is a set of real number and

www.TechnicalBooksPDF.com

linguistic variable which represent the state of the fuzzy number. In principle, membership functions can be of different shape but in practice, trapezoidal and triangular types are the most commonly used fuzzy numbers [61,72–74]. Aydin et al. [22] considered mathematical tools of Fuzzy Set Theory with decision-making procedure that deploys ordered weighted averaging algorithm for aggregating multiple objectives and prioritize the most feasible locations for hybrid solar PV-wind systems. Janke [35] applied a multicriteria GIS modeling to identify areas that are more suitable for the wind and solar farms installation in Colorado. The GIS-overlay techniques used to examine the relationship between land cover classes and National Renewable Energy Laboratory solar and wind potential data.

1.2 GEOGRAPHICAL INFORMATION SYSTEM

GIS has demonstrated its ultimate potential for exploiting geographical information to develop a spatial decision support system. The integration of GIS with other techniques develops a better insight for the policy makers to improve their selection and optimize their options by considering various subjective and conflicting criteria. GIS-based MCDM tool is commonly applied in spatial analysis to obtain the most favorable sites for different applications such as landfill site selection [75,76], urban planning [68,77] and renewable energy sites [7,62]. Integrating the two fields brings together their benefits and can offer a fine lens and more reliable decision for the optimal solar site selection. Table 2.1 presents studies applying GIS-based MCDM for utility-size solar PV site suitability in different regions.

The GIS is a computer media (hardware and software) for analysis, editing, consultation, storage and disposal of spatial data for solving complex planning problems [69]. The high-level maturity and advanced embedded tools prompt the GIS to be an excellent tool for strategic planning of solar energy development projects. Building the decision for utility-scale solar PV power plants site selection on extensive information especially from GIS offers significant advantages including [11]:

- Improve the solar project performance by ensuring the high level of solar irradiation and moderate air temperature.
- The orientation of the site can be optimized when the project installed on flat ground, placed toward the south and without a large shadow.
- Minimizing the losses from transportation, power transmission, and production by considering the sites near these utilities and nearby urban areas which is the main consumption points.
- Reduce the environmental, society, and infrastructures impacts.
- Exclude the protected areas and unsuitable sites from the study areas.

The discoveries of the potential solar site can support the new development of infrastructures such as transportation and transmission lines to be near these locations to promote the utilization of free energy. GIS-based approaches are detail-specific, replicable across various regions and can be automated for less hands-on computing. However, they are time-consuming and computer-resource intensive [78].

www.TechnicalBooksPDF.com

1.3 DEALING WITH UNCERTAINTIES IN PHOTOVOLTAIC SITE SELECTION

In many of real-life situations, there is ambiguous and incomplete information due to measurements errors and conceptual inaccuracy; these limitations must be taken into account particularly in the GIS-MCDM analysis. The huge study area along with a large number of alternative sites might have noteworthy uncertainties that had better be considered. Validating the data with ground monitoring devices could reduce the uncertainty. There are several aspects of uncertainty during a solar PV site selection process, uncertainty in the solar irradiation estimation is one of the significant sources of the general energy production uncertainty. Making the composition of accurate data is critical for reducing uncertainty in the solar resource estimate; therefore, it increases the assurance in the project's power estimate [79]. On the other side, two types of uncertainty could be combined with the decision-making process: (1) uncertainty associated with the ambiguous concerning the description of the semantic meaning of the statements and events, and (2) uncertainty related to the limited data about the decision situation and errors within. However, the main source of uncertainty in MCDM tools is related to the criteria weights (DM preferences) and criteria values (criteria maps) [61]. For instance, to deal with uncertainty in the DM evaluation in classic AHP, fuzzy AHP selected to elicit the decision criteria weights in this integration of GIS with AHP for the site selection as shown in Table 2.1.

Comparisons between different methodologies under the same environment could bring insightfulness to the criteria influences and the outcomes. Furthermore, wherever the uncertainty in results designated as a function of the uncertainty of the input, one can develop a framework for MCDA using a simulation method, such as Monte Carlo for generating probability distributions of the inputs [80].

Sensitivity analysis focuses on how uncertainty in the output is affected by the uncertainty in the model input factors. Hence, the influence of varying criterion weights on the MCDA model output is, without a doubt, the most frequently applied form of sensitivity analysis in GIS-based multicriteria modeling [81].

2. CRITERIA FOR SITE SELECTION

To deploy a solar project on a utility-scale, several criteria and factors should be considered with the aim of optimizing the location which will result in more efficient system, more economic to supply the needed customers and less impact on the environment. Typically, the decision criteria are derived based on the study aim, accessibility to the geo-referenced database and the existing literature. The review results in 39 subcriteria assessed mostly under location and climate criteria. Most solar site suitability studies deliberate solar irradiation as the most important decision criteria, as shown in Table 2.2.

www.TechnicalBooksPDF.com

Table 2.2 Associated Criteria for Selected Solar Photovoltaic Site Suitability Studies

Criteria	Subcriteria	References
Environmental	Land use and cover	[5,8,11,12,17,18,25,27,28,32,35,36,37,39,41,42,44,46,49,54]
	Agrological capacity	[14,19,25,29,69]
	Carbon emission savings	[9,20,16,23,27]
Location	Distance to urban areas	[4–6,8,14,11,12,16,17,19,22,27,29,35,36,46,57,69]
	Distance to main roads	[4,5,6,8,11–17,19,29,33–37,39,41,42,69]
	Distance to power lines and substations	[4–6,9,12–19,22,27–29,33–35,37,40–42,45–47,69,82]
	Distance to historical areas	[6]
	Distance to rivers	[33]
	Future capacity expansion	[25]
	Population density	[25,34,35,40,82]
	Distance to wildlife designations	[6,16,18]
Economic	Land cost	[18,25,37,82]
	Initial investment	[18,23,25,28,32,47]
	Total revenue	[23]
	Maintenance cost	[18,20,23,25,27,28,47]
	Transmission Losses	[20,23,24]
	Generated energy	[24,30,32]
	Traffic convenience degree	[20,27]
	Energy saving	[20,27]
	Financial incentives	[26]
	Electricity demand	[20,27,28,46,48]
	Present value and levelized cost of energy	[9,28,32,40]
	Payback period	[9,28]
	Construction cost	[9,16,18,20,25,27,82]
Climatic	Solar irradiation	[4,6–20,22–41,45–57,69,82]
	Average temperature	[7,8,10–14,16,18,19,23,25,26,29,31,39,49,52,56,57,69]
	Relative humidity	[10,12,17,39,52,56]
	Insolation clearness index	[12,52]
	Average annual dusty days	[12,39]
Orography	Slope	[4,5,8,10–19,22,29,33,34,36,37,39,42,44,54,49,55,57,69]
	Orientation	[4,8,10,14,17,19,69,34,39,49,54]
	Elevation	[12,17,18,23,34,39,41]
	Plot area	[14,19,29,36,69]

www.TechnicalBooksPDF.com

Table 2.2 Associated Criteria for Selected Solar Photovoltaic Site Suitability Studies—cont'd

Criteria	Subcriteria	References
Social	Public acceptance	[9,16,20,28]
	Effect on agriculture	[10,16,49]
	Employment and tourism	[16]
Risk	Political and economic risk	[9,28]
	Time delay risk	[28]
	Environmental risk	[28]

Solar irradiation is an essential criterion for large-scale PV solar power projects. Considerable amounts of solar energy play a significant role in producing more electrical power from available resources. Fig. 2.2 shows the top 10 criteria considered in the criteria for selected solar PV site suitability studies.

Furthermore, proximity to power lines and substations prompts adequate accessibility to the grid and aids to avoid the high cost of establishing new lines as well as minimizing power loss in the transmission. Under the orography criteria, the flat terrain is essential for large-scale PV farms so high slope areas are impractical for such projects due to low economic feasibility. However, different slope degrees have been considered in the literature while the most of them considered only 3%−10% to exclude the very steep areas.

Air temperature plays a vital role in PV system performance as the surrounding air cools PV modules and inverters convectively. Hence, improving the PV system efficiency. With respect to the distance to urban areas, certain studies consider locations that are further away from cities more suitable for renewable energy development to avoid negative environmental impact on urban development and to avoid not in my back yard (NIMBY) opposition [5,19,35]. On the other hand, other studies indicate that sites near cities have more economic advantages [4,22]. Undoubtedly,

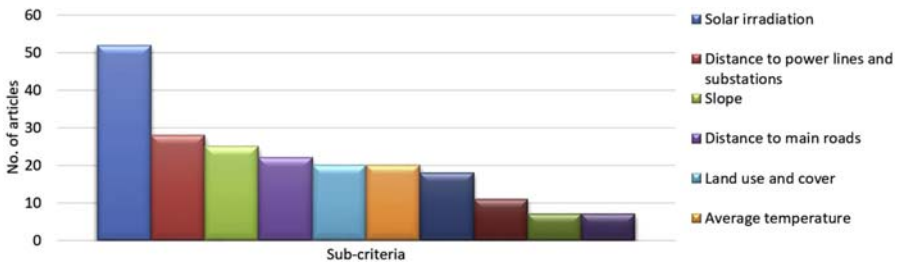


FIGURE 2.2

Top 10 criteria considered in utility-size solar PV studies.

www.TechnicalBooksPDF.com

locating the power plants nearby the adequate consumer is a key factor that should be taking into account for such project. So, establishing the solar farms near the highly populated cities is an advantage.

3. RESTRICTION FACTORS AND UNSUITABLE SITES

The main goal of this stage is to eliminate nonfeasible locations that have impediments to the installation and development of a utility-scale PV plant. Table 2.3 presents restrictions applied to the solar PV site suitability studies.

Table 2.3 Restrictions Used in Solar Energy Studies

No.	Restrictions	References
1	Urban lands	[4–6,8,10,12,13,15,17,19,34, 36,39,54,69]
2	Low solar irradiation	[55]
3	Protected land	[4,5,8,10–13,17,19,22,30,34,35,37, 45,47,49,54,57,69,82]
4	Cultivated and high landscape areas	[4–6,8,10,17,19,22,30,34,35, 37,39,45–47,54,69,82]
5	Water infrastructure	[7,69]
6	Airports and military zones	[5,14,19,69,36,49,45]
7	Wildlife areas	[5,6,13,14,19,45,54,69]
8	Cultural heritage	[6,13–15,19,35,69]
9	Archaeological sites	[5,14,15,19,35,69,82]
10	Paleontological sites	[14,19,69]
11	Roads and railroad network	[4,5,15,19,69,11,10,36,37,17, 12,42,39,57]
12	Sand areas and sand dunes	[15,10,39]
13	Natural disaster areas	[15,54,82]
14	Higher slope areas	[6,12,13,15,30,36,37,39,42,46,47, 49,54,55,82]
15	Elevation	[12,13,37]
16	Mountains	[14,49,69]
17	Soft soil	[36,41,54,82]
18	Community interest sites	[11,14,19,47,57,69,82]
19	Dams	[15]
20	Flight security	[22]
21	Biological significant areas	[5]
22	Watercourses and streams	[10–13,17,30,34,36,37,42,45–47, 49,54,57,69]
23	Coastal zones	[11,10,57,69]
24	The land aspect	[6]
25	Visual impact	[13,16,21]

www.TechnicalBooksPDF.com

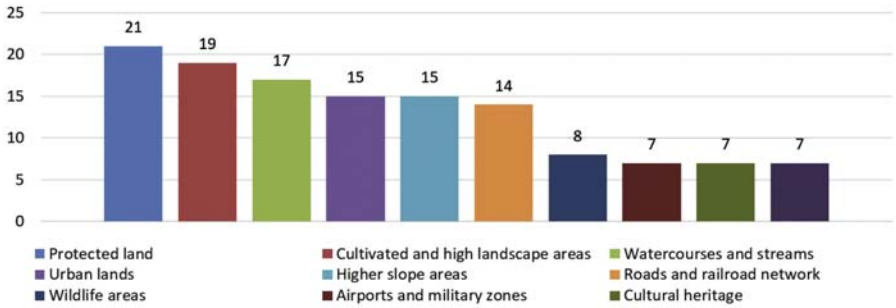


FIGURE 2.3

Top 10 restrictions used in utility-size solar PV studies.

Fig. 2.3 presents the most common applied restriction in solar PV site suitability studies. It can be seen that protected land, cultivated, and high landscape areas along with watercourses and streams are the most excluded areas. Furthermore, high slope areas are not preferable for such projects due to low economic feasibility, so it has been excluded by more than 25% of literature. Additionally, to limit the feasibility analysis many studies discarded urban areas, highway, and railroad networks due to the high density of population and buildings in addition to traffic safety issues.

4. CONCLUSIONS AND FUTURE WORKS

This research offers a critical and in-depth assessment of previous studies in site suitability of utility-scale photovoltaic with the integration of GIS and MCDM tool. GIS-based MCDA continues to expand in research output to offers an efficient decision support system for DM. The proposed review can assist solar energy DM and developers in identifying sites for solar projects that have a significant technical performance along with minimum cost and low environmental impact.

Solar PV site suitability studies considered solar irradiation amount as the highest reported decision criteria followed by the proximity to power lines and land slope, whereas the protected lands and watercourses considered the highest restriction factors described in the literature. For the last 15 years, the deployment of grid-connected PV surpasses the off-grid installation shares worldwide [83]. The exploitation of grid-connected solar PV is proven and has gained favor where vast areas are accessible, and a significant amount of solar irradiation is available. Consequently, more than 80% of literature in this study are concerned with grid-connected solar PV. From the context perspective, China's installed PV capacity doubled in 2016, turning the Republic into the world's largest producer of solar energy by capacity. At the end of 2016, installed PV capacity rose to 77.42 GW with the adding of 34.54 GW over the course of the year while Spain has added 55 MW in 2016, a 1.12% year-on-year increase [84]. As a result of such installation growth in both

www.TechnicalBooksPDF.com

countries, China leads the site suitability studies followed by Spain and India. As per authors' knowledge, this is an original contribution to review site suitability methodologies, decision criteria, and restriction factors for the solar PV.

The limitation of this review is that the findings do not include textbooks and unpublished papers in solar PV site selection literature as well as is limited only to the English journals. This work could be enhanced by considering real projects site assessment and confirming their suitability under different decision criteria if designed in multiple sites. Also, finding common decision criteria and restriction for hybrid solar PV-wind would aid DMs for siting other RES or hybrid RES system toward ensuring cost-effective and well-performing projects.

ACKNOWLEDGMENTS

The first author would like to thank The Royal Commission of Jubail and Yanbu—Jubail Industrial College for the financial support under the scholarship program.

REFERENCES

[1] International Finance Corporation, Utility-scale Solar Photovoltaic Power Plants − A Project Developer's Guide, 2015. Washington, DC.

[2] A. Lopez, B. Roberts, D. Heimiller, N. Blair, G. Porro, U.S. Renewable Energy Technical Potentials : A GIS-based Analysis, National Renewable Energy Laboratory Document, Washington, DC, 2012. NREL/TP-6A20-51946.

[3] M. Sengupta, A. Habte, S. Kurtz, A. Dobos, S. Wilbert, E. Lorenz, T. Stoffel, D. Renné, C. Gueymard, D. Myers, S. Wilcox, P. Blanc, R. Perez, Best Practices Handbook for the Collection and Use of Solar Resource Data for Solar Energy Applications, 2015.

[4] H.A. Effat, Selection of potential sites for solar energy farms in Ismailia Governorate, Egypt using SRTM and multicriteria analysis, Cloud Publ. Int. J. Adv. Remote Sens. GIS 2 (2013) 205−220.

[5] M. Uyan, GIS-based solar farms site selection using analytic hierarchy process (AHP) in Karapinar region, Konya/Turkey, Renew. Sustain. Energy Rev. 28 (2013) 11−17, https://doi.org/10.1016/j.rser.2013.07.042.

[6] J.J.W. Watson, M.D. Hudson, Regional Scale wind farm and solar farm suitability assessment using GIS-assisted multi-criteria evaluation, Landsc. Urban Plan 138 (2015) 20−31, https://doi.org/10.1016/j.landurbplan.2015.02.001.

[7] M. Rumbayan, K. Nagasaka, Prioritization decision for renewable energy development using analytic hierarchy process and geographic information system, in: Advanced Mechatronic Systems (ICAMechS), 2012 International Conference on. IEEE, 2012. Tokyo, Japan, 2012, pp. 36−41.

[8] M. Tahri, M. Hakdaoui, M. Maanan, The evaluation of solar farm locations applying Geographic Information System and Multi-criteria decision-making methods: case study in southern Morocco, Renew. Sustain. Energy Rev. 51 (2015) 1354−1362, https://doi.org/10.1016/j.rser.2015.07.054.

www.TechnicalBooksPDF.com

[9] W. Yunna, S. Geng, Multi-criteria decision making on selection of solar−wind hybrid power station location: a case of China, Energy Convers. Manag. 81 (2014) 527−533, https://doi.org/10.1016/j.enconman.2014.02.056.
[10] D. Doljak, G. Stanojević, Evaluation of natural conditions for site selection of ground-mounted photovoltaic power plants in Serbia, Energy 127 (2017) 291−300, https://doi.org/10.1016/j.energy.2017.03.140.
[11] J. Arán Carrión, A. Espín Estrella, F. Aznar Dols, M. Zamorano Toro, M. Rodríguez, A. Ramos Ridao, Environmental decision-support systems for evaluating the carrying capacity of land areas: optimal site selection for grid-connected photovoltaic power plants, Renew. Sustain. Energy Rev. 12 (2008) 2358−2380, https://doi.org/10.1016/j.rser.2007.06.011.
[12] E. Noorollahi, D. Fadai, M. Akbarpour Shirazi, S. Ghodsipour, Land suitability analysis for solar farms exploitation using GIS and fuzzy analytic hierarchy process (FAHP)—a case study of Iran, Energies 9 (2016) 643, https://doi.org/10.3390/en9080643.
[13] J. Suh, J.R.S. Brownson, Solar farm suitability using geographic information system fuzzy sets and analytic hierarchy processes: case study of Ulleung Island, Korea, Energies 9 (2016), https://doi.org/10.3390/en9080648.
[14] J.M. Sánchez-Lozano, J. Teruel-Solano, P.L. Soto-Elvira, M. Socorro García-Cascales, Geographical Information Systems (GIS) and Multi-Criteria Decision Making (MCDM) methods for the evaluation of solar farms locations: case study in south-eastern Spain, Renew. Sustain. Energy Rev. 24 (2013) 544−556, https://doi.org/10.1016/j.rser.2013.03.019.
[15] Y. Charabi, A. Gastli, PV site suitability analysis using GIS-based spatial fuzzy multi-criteria evaluation, Renew. Energy 36 (2011) 2554−2561, https://doi.org/10.1016/j.renene.2010.10.037.
[16] S. Sindhu, V. Nehra, S. Luthra, Investigation of feasibility study of solar farms deployment using hybrid AHP-TOPSIS analysis: case study of India, Renew. Sustain. Energy Rev. 73 (2017) 496−511, https://doi.org/10.1016/j.rser.2017.01.135.
[17] M. Zoghi, A. Houshang Ehsani, M. Sadat, M. Javad Amiri, S. Karimi, Optimization solar site selection by fuzzy logic model and weighted linear combination method in arid and semi-arid region: a case study Isfahan-Iran, Renew. Sustain. Energy Rev. (2015), https://doi.org/10.1016/j.rser.2015.07.014.
[18] A.H.I. Lee, H.Y. Kang, C.Y. Lin, K.C. Shen, An integrated decision-making model for the location of a PV solar plant, Sustain 7 (2015) 13522−13541, https://doi.org/10.3390/su71013522.
[19] J.M. Sánchez-Lozano, C. Henggeler Antunes, M.S. García-Cascales, L.C. Dias, GIS-based photovoltaic solar farms site selection using ELECTRE-TRI: evaluating the case for Torre Pacheco, Murcia, Southeast of Spain, Renew. Energy 66 (2014) 478−494, https://doi.org/10.1016/j.renene.2013.12.038.
[20] D. Jun, F. Tian-tian, Y. Yi-sheng, M. Yu, Macro-site selection of wind/solar hybrid power station based on ELECTRE-II, Renew. Sustain. Energy Rev. 35 (2014) 194−204, https://doi.org/10.1016/j.rser.2014.04.005.
[21] L.A. Fernandez-Jimenez, M. Mendoza-Villena, P. Zorzano-Santamaria, E. Garcia-Garrido, P. Lara-Santillan, E. Zorzano-Alba, A. Falces, Site selection for new PV power plants based on their observability, Renew. Energy 78 (2015) 7−15, https://doi.org/10.1016/j.renene.2014.12.063.

www.TechnicalBooksPDF.com

[22] N.Y. Aydin, E. Kentel, H. Sebnem Duzgun, GIS-based site selection methodology for hybrid renewable energy systems: a case study from western Turkey, Energy Convers. Manag. 70 (2013) 90–106, https://doi.org/10.1016/j.enconman.2013.02.004.
[23] J. Liu, F. Xu, S. Lin, Site selection of photovoltaic power plants in a value chain based on grey cumulative prospect theory for sustainability: a case study in Northwest China, J. Clean. Prod. 148 (2017) 386–397, https://doi.org/10.1016/j.jclepro.2017.02.012.
[24] R. El-azab, A. Amin, Optimal solar plant site selection, in: IEEE Southeast Con. 2015. Florida, USA, 2015, p. 7132992, https://doi.org/10.1109/SECON.
[25] A. Lee, H.-Y. Kang, Y.-J. Liou, A hybrid multiple-criteria decision-making approach for photovoltaic solar plant location selection, Sustainability 9 (2017) 184, https://doi.org/10.3390/su9020184.
[26] A. Jain, R. Mehta, S.K. Mittal, Modeling impact of solar radiation on site selection for solar PV power plants in India, Int. J. Green. Energy 8 (2011) 486–498, https://doi.org/10.1080/15435075.2011.576293.
[27] Y. Wu, Y. Yi-sheng, F.T. Li-na, L. Wei, F. Luo-jie, Macro-site selection of wind/solar hybrid power station based on ideal matter-element model, Electr. Power Energy Syst. 35 (2013) 194–204, https://doi.org/10.1016/j.rser.2014.04.005.
[28] M. Vafaeipour, S. Hashemkhani Zolfani, M.H. Morshed Varzandeh, A. Derakhti, M. Keshavarz Eshkalag, Assessment of regions priority for implementation of solar projects in Iran: new application of a hybrid multi-criteria decision making approach, Energy Convers. Manag. 86 (2014) 653–663, https://doi.org/10.1016/j.enconman.2014.05.083.
[29] C.R. Chen, C.C. Huang, H.J. Tsuei, A hybrid MCDM model for improving GIS-based solar farms site selection, Int. J. Photoenergy (2014), https://doi.org/10.1155/2014/925370.
[30] Y. Sun, A. Hof, R. Wang, J. Liu, Y. Lin, D. Yang, GIS-based approach for potential analysis of solar PV generation at the regional scale: a case study of Fujian Province, Energy Policy 58 (2013) 248–259, https://doi.org/10.1016/j.enpol.2013.03.002.
[31] F.E. Boran, T. Menlik, K. Boran, Multi-criteria axiomatic design approach to evaluate sites for grid-connected photovoltaic power plants: a case study in Turkey, Energy Source B Econ. Plan. Policy 5 (2010) 290–300, https://doi.org/10.1080/15567240802533831.
[32] M. Gómez, A. López, F. Jurado, Optimal placement and sizing from standpoint of the investor of photovoltaics grid-connected systems using binary particle Swarm optimization, Appl. Energy 87 (2010) 1911–1918, https://doi.org/10.1016/j.apenergy.2009.12.021.
[33] J. Brewer, D.P. Ames, D. Solan, R. Lee, J. Carlisle, Using GIS analytics and social preference data to evaluate utility-scale solar power site suitability, Renew. Energy 81 (2015) 825–836, https://doi.org/10.1016/j.renene.2015.04.017.
[34] C. Perpiña Castillo, F. Batista e Silva, C. Lavalle, An assessment of the regional potential for solar power generation in EU-28, Energy Policy 88 (2016) 86–99, https://doi.org/10.1016/j.enpol.2015.10.004.
[35] J.R. Janke, Multicriteria GIS modeling of wind and solar farms in Colorado, Renew. Energy 35 (2010) 2228–2234, https://doi.org/10.1016/j.renene.2010.03.014.
[36] M.A. Anwarzai, K. Nagasaka, Utility-scale implementable potential of wind and solar energies for Afghanistan using GIS multi-criteria decision analysis, Renew. Sustain. Energy Rev. 71 (2017) 150–160, https://doi.org/10.1016/j.rser.2016.12.048.

www.TechnicalBooksPDF.com

[37] M.L. Sabo, N. Mariun, H. Hizam, M.A. Mohd Radzi, A. Zakaria, Spatial matching of large-scale grid-connected photovoltaic power generation with utility demand in Peninsular Malaysia, Appl. Energy 191 (2017) 663–688, https://doi.org/10.1016/j.apenergy.2017.01.087.

[38] B. Niblick, A.E. Landis, Assessing renewable energy potential on United States marginal and contaminated sites, Renew. Sustain. Energy Rev. 60 (2016) 489–497, https://doi.org/10.1016/j.rser.2015.12.045.

[39] I. Gherboudj, H. Ghedira, Assessment of solar energy potential over the United Arab Emirates using remote sensing and weather forecast data, Renew. Sustain. Energy Rev. 55 (2016) 1210–1224, https://doi.org/10.1016/j.rser.2015.03.099.

[40] D. Mentis, M. Welsch, F. Fuso Nerini, O. Broad, M. Howells, M. Bazilian, H. Rogner, A GIS-based approach for electrification planning—a case study on Nigeria, Energy Sustain. Dev. 29 (2015) 142–150, https://doi.org/10.1016/j.esd.2015.09.007.

[41] G. Khan, S. Rathi, Optimal site selection for solar PV power plant in an indian state using geographical information system (GIS), Int. J. Emerg. Eng. Res. Technol. 2 (2014) 260–266.

[42] A. Alami Merrouni, A. Mezrhab, A. Mezrhab, PV sites suitability analysis in the Eastern region of Morocco, Sustain. Energy Technol. Assess. 18 (2016) 6–15, https://doi.org/10.1016/j.seta.2016.09.006.

[43] K.Y. Kebede, Viability study of grid-connected solar PV system in Ethiopia, Sustain. Energy Technol. Assess. 10 (2015) 63–70, https://doi.org/10.1016/j.seta.2015.02.003.

[44] S. Wang, L. Zhang, D. Fu, X. Lu, T. Wu, Q. Tong, Selecting photovoltaic generation sites in Tibet using remote sensing and geographic analysis, Sol. Energy 133 (2016) 85–93, https://doi.org/10.1016/j.solener.2016.03.069.

[45] K. Calvert, W. Mabee, More solar farms or more bioenergy crops? Mapping and assessing potential land-use conflicts among renewable energy technologies in eastern Ontario, Canada, Appl. Geogr. 56 (2015) 209–221, https://doi.org/10.1016/j.apgeog.2014.11.028.

[46] A. Massimo, M. Dell'Isola, A. Frattolillo, G. Ficco, Development of a geographical information system (GIS) for the integration of solar energy in the energy planning of a wide area, Sustainability 6 (2014) 5730–5744, https://doi.org/10.3390/su6095730.

[47] A.N. Arnette, C.W. Zobel, Spatial analysis of renewable energy potential in the greater southern Appalachian mountains, Renew. Energy 36 (2011) 2785–2798, https://doi.org/10.1016/j.renene.2011.04.024.

[48] A.M. Gormally, J.D. Whyatt, R.J. Timmis, C.G. Pooley, A regional-scale assessment of local renewable energy resources in Cumbria, UK, Energy Policy 50 (2012) 283–293, https://doi.org/10.1016/j.enpol.2012.07.015.

[49] E. Borgogno Mondino, E. Fabrizio, R. Chiabrando, Site selection of large ground-mounted photovoltaic plants: a GIS decision support system and an application to Italy, Int. J. Green. Energy 12 (2014) 515–525, https://doi.org/10.1080/15435075.2013.858047.

[50] M. Rumbayan, A. Abudureyimu, K. Nagasaka, Mapping of solar energy potential in Indonesia using artificial neural network and geographical information system, Renew. Sustain. Energy Rev. 16 (2012) 1437–1449, https://doi.org/10.1016/j.rser.2011.11.024.

www.TechnicalBooksPDF.com

[51] S.M. Besarati, R.V. Padilla, D.Y. Goswami, E. Stefanakos, The potential of harnessing solar radiation in Iran: generating solar maps and viability study of PV power plants, Renew. Energy 53 (2013) 193−199, https://doi.org/10.1016/j.renene.2012.11.012.
[52] S. Chakraborty, P.K. Sadhu, N. Pal, New location selection criterions for solar PV, Int. J. Renew. Energy Res. 4 (2014).
[53] J. Polo, A. Bernardos, A.A. Navarro, C.M. Fernandez-Peruchena, L. Ramírez, M.V. Guisado, S. Martínez, Solar resources and power potential mapping in Vietnam using satellite-derived and GIS-based information, Energy Convers. Manag. 98 (2015) 348−358, https://doi.org/10.1016/j.enconman.2015.04.016.
[54] B. Sliz-Szkliniarz, Assessment of the renewable energy-mix and land use trade-off at a regional level: a case study for the Kujawsko−Pomorskie Voivodship, Land Use Policy 35 (2013) 257−270, https://doi.org/10.1016/j.landusepol.2013.05.018.
[55] R. Mahtta, P.K. Joshi, A.K. Jindal, Solar power potential mapping in India using remote sensing inputs and environmental parameters, Renew. Energy (2014), https://doi.org/10.1016/j.renene.2014.05.037.
[56] S. Belmonte, V. Núñez, J.G. Viramonte, J. Franco, Potential renewable energy resources of the Lerma Valley, Salta, Argentina for its strategic territorial planning, Renew. Sustain. Energy Rev. 13 (2009) 1475−1484, https://doi.org/10.1016/j.rser.2008.09.014.
[57] J.A. Carrión, A. Espín Estrella, F. Aznar Dols, A.R. Ridao, The electricity production capacity of photovoltaic power plants and the selection of solar energy sites in Andalusia (Spain), Renew. Energy 33 (2008) 545−552, https://doi.org/10.1016/j.renene.2007.05.041.
[58] F.R. Martins, E.B. Pereira, S.L. Abreu, Satellite-derived solar resource maps for Brazil under SWERA project, Sol. Energy 81 (2007) 517−528, https://doi.org/10.1016/j.solener.2006.07.009.
[59] J.M.C. Pereira, L. Duckstein, A multiple criteria decision-making approach to GIS-based land suitability evaluation, Int. J. Geogr. Inf. Syst. 7 (1993) 407−424, https://doi.org/10.1080/02693799308901971.
[60] R. Greene, R. Devillers, J.E. Luther, B.G. Eddy, GIS-based multiple-criteria decision analysis, Geogr. Compass 5 (2011) 412−432, https://doi.org/10.1111/j.1749-8198.2011.00431.x.
[61] J. Malczewski, C. Rinner, Multicriteria Decision Analysis in Geographic Information Science, Springer, New York, 2015, https://doi.org/10.1007/978-3-540-74757-4.
[62] S.D. Pohekar, M. Ramachandran, Application of multi-criteria decision making to sustainable energy planning—a review, Renew. Sustain. Energy Rev. 8 (2004) 365−381, https://doi.org/10.1016/j.rser.2003.12.007.
[63] J.R.S.C. Mateo, Multi-criteria Analysis in the Renewable Energy Industry, Springer Science & Business Media, Santander, 2012, https://doi.org/10.2174/97816080528511060101.
[64] J.-J. Wang, Y.-Y. Jing, C.-F. Zhang, J.-H. Zhao, Review on multi-criteria decision analysis aid in sustainable energy decision-making, Renew. Sustain. Energy Rev. 13 (2009) 2263−2278, https://doi.org/10.1016/j.rser.2009.06.021.
[64a] S. Sipahi, M. Timor, The analytic hierarchy process and analytic network process: an overview of applications, Manag. Decis. 48 (5) (2010) 775−808.
[65] T.L. Saaty, L.G. Vargas, Models, Methods, Concepts and Apps of the Analytic Hierarchy Process, second ed., Springer, New York, USA, 2012, https://doi.org/10.1007/978-1-4614-3597-6.
[66] M.A. Elliott, Selecting numerical scales for pairwise comparisons, Reliab. Eng. Syst. Saf. 95 (2010) 750−763, https://doi.org/10.1016/j.ress.2010.02.013.

www.TechnicalBooksPDF.com

[67] F. Elkarmi, I. Mustafa, Increasing the utilization of solar energy technologies (SET) in Jordan, Energy Policy 21 (1993) 978−984, https://doi.org/10.1016/0301-4215(93)90186-J.
[68] I.A. Chandio, A.N.B. Matori, K.B. WanYusof, M.A.H. Talpur, A.-L. Balogun, D.U. Lawal, GIS-based analytic hierarchy process as a multicriteria decision analysis instrument: a review, Arab. J. Geosci. 6 (2013) 3059−3066, https://doi.org/10.1007/s12517-012-0568-8.
[69] J.M. Sánchez-Lozano, M.S. García-Cascales, M.T. Lamata, Evaluation of suitable locations for the installation of solar thermoelectric power plants, Comput. Ind. Eng 87 (2015) 343−355, https://doi.org/10.1016/j.cie.2015.05.028.
[70] K.T. Cho, Multicriteria decision methods: an attempt to evaluate and unify, Math. Comput. Model 37 (2003) 1099−1119, https://doi.org/10.1016/S0895-7177(03)00122-5.
[71] L.A. Zadeh, Fuzzy sets, Inf. Control 8 (1965) 338−353, https://doi.org/10.1016/S0019-9958(65)90241-X.
[72] A. Barua, L.S. Mudunuri, O. Kosheleva, Why trapezoidal and triangular membership functions work so well: towards a theoretical explanation, J. Uncertain. Syst. 8 (2014) 164−168.
[73] K. Chatterjee, S. Kar, Multi-criteria analysis of supply chain risk management using interval valued fuzzy TOPSIS, Opsearch (2016), https://doi.org/10.1007/s12597-015-0241-6.
[74] C.-H. Cheng, Y. Lin, Evaluating the best main battle tank using fuzzy decision theory with linguistic criteria evaluation, Eur. J. Oper. Res. 142 (2002) 174−186, https://doi.org/10.1016/S0377-2217(01)00280-6.
[75] V. Akbari, M. Rajabi, Landfill site selection by combining GIS and fuzzy multi-criteria decision analysis, case study: Bandar Abbas, Iran, World Appl. Sci. J. 3 (2008) 39−47.
[76] S. Sener, E. Sener, B. Nas, R. Karagüzel, Combining AHP with GIS for landfill site selection: a case study in the Lake Beyşehir catchment area (Konya, Turkey), Waste Manag. 30 (2010) 2037−2046, https://doi.org/10.1016/j.wasman.2010.05.024.
[77] M.A. Mohit, M.M. Ali, Integrating GIS and AHP for land suitability analysis for urban development in a secondary city of Bangladesh, J. Alam Bina 8 (2006) 1−20.
[78] J. Melius, R. Margolis, S. Ong, Estimating Rooftop Suitability for PV: A Review of Methods, Patents, and Validation Techniques, NREL Technical Report, 2013.
[79] M. Schnitzer, C. Thuman, Reducing Uncertainty in Mitigating Energy Risk Through. Albany, NY, 2012.
[80] I.N. Durbach, T.J. Stewart, Modeling uncertainty in multi-criteria decision analysis, Eur. J. Oper. Res. 223 (2012) 1−14, https://doi.org/10.1016/j.ejor.2012.04.038.
[81] M. Gómez-Delgado, S. Tarantola, GLOBAL sensitivity analysis, GIS and multi-criteria evaluation for a sustainable planning of a hazardous waste disposal site in Spain, Int. J. Geogr. Inf. Sci. 20 (2006) 449−466, https://doi.org/10.1080/13658810600607709.
[82] A. Kengpol, P. Rontlaong, M. Tuominen, Design of a decision support system for site selection using fuzzy AHP: a case study of solar power plant in North eastern parts of Thailand, in: Proceedings of PICMET'12: Technology Management for Emerging Technologies, 2012, pp. 734−743.
[83] The International Energy Agency (IEA), Trends 2016, in: Photovoltaic Applications, Survey Report of Selected IEA Countries between 1992 and 2015, 2016.
[84] C. Roselund, China claims 34.2 GW of PV Installations in 2016 − PV Magazine International, 2017. https://www.pv-magazine.com/2017/01/17/china-claims-34-2-gw-of-pv-installations-in-2016/.

www.TechnicalBooksPDF.com

This page intentionally left blank

www.TechnicalBooksPDF.com

CHAPTER

Forecasting of Intermittent Solar Energy Resource

3

Gilles Notton, Cyril Voyant
Renewable energy team - Research Centre Georges Peri - UMR CNRS 6134, University of Corsica Pasquale Paoli, Ajaccio, France

CHAPTER OUTLINE

1. Introduction 78
2. Intermittent and Stochastic Renewable Energy Production in an Electrical Grid 79
2.1 The Production/Consumption Balance: A Difficult Task Even With Conventional Energy Production Means 79
2.2 Intermittence of Renewable Production and Impact on the Electrical Grid Management 81
3. Need for Solar and Wind Forecast: Forecast Horizon and Time Step 83
4. Cost of Intermittence and Benefit of Forecasting 85
4.1 Cost of Intermittency 85
4.2 Forecasting and Influences on Production Cost 86
5. Forecast Accuracy Evaluation 87
6. Forecasting Methods for Different Forecast Horizons 92
6.1 Temporal Horizon and Resolution — Generalities About Solar Irradiance Forecasting 93
6.2 Very Short-Term Forecasting in a Temporal Range From 0 to 6 h 96
6.2.1 Sky Imagery 96
6.2.2 Satellite Cloud Image 96
6.2.3 Stochastic Learning Methods or Time Series–Based Method 99
6.3 Solar Forecasting for Ranges Between 6 h and Days Ahead 104
6.4 Reliability and Accuracy of the Forecasting Models 104
7. The Future of the Renewable Energy Forecasting 106
7.1 Now-Casting 106
7.2 Six Hours Ahead Prediction and More 107
7.2.1 Model Output Statistics 107
7.2.2 Nonhydrostatic Atmospheric Models 108
7.2.3 High Accuracy Irradiance Measurement 108
8. Conclusion 108
References 109

Advances in Renewable Energies and Power Technologies. https://doi.org/10.1016/B978-0-12-812959-3.00003-4
Copyright © 2018 Elsevier Inc. All rights reserved.

www.TechnicalBooksPDF.com

1. INTRODUCTION

The market growth of photovoltaic (PV) and wind energy systems over the last decade has reached 50 GWp of PV plants and 62.7 GW of wind turbines installed in 2015 (increasing 25% and 20% for PV and wind energy systems, respectively, over that in 2014). The total capacity, respectively, in Europe and in the world has reached 94.6 and 227 GW for PV [1] and 141.7 and 432.56 GW for wind energy plants at the end of 2015 [2].

As the electricity part produced by PV and wind energy systems increases (Table 3.1), it becomes crucial to integrate these two intermittent and stochastic renewable energies systems (ISRES) into electricity grids.

One of the main challenges for the near-future global energy supply is to maintain safety with a high integration of renewable energy sources [4]. The stochastic and intermittent behavior of solar and wind resources poses numerous problems to the electricity grid operator; they will be reviewed in the first part of this paper. These problems can be partially solved by introducing energy storage means and smart grids within the electrical network and developing and improving production forecasting methods. The interest of forecasting methods for solar and wind production will be discussed in a second paragraph and it will be shown that the development of such methods is fundamental for a good management of the energy flows over the electrical networks and for the energy storage.

The intermittent and stochastic production management has a significant cost, which could be considerably reduced by using a forecasting method by the electricity grid operator. This cost aspect will be treated in the fourth paragraph.

Table 3.1 Intermittent Renewable Energy Production Rate in Some Countries [3]

Country	Installed Capacity (GW) in 2012[a]	Percentage of the Energy Mix (%)	Objective for 2020 (%)
Spain	28.9 22.5 + 0 + 6.3	22	29
Germany	63.9 31 + 0.3 + 32.6	12.4	26
United Kingdom	10.6 5.9 + 3 + 1.7	5.6	22
France	11.6 7.6 + 0 + 4	4.0	12
Italy	24.5 8.1 + 0 + 16.4	9.7	8
United States	67.7 60 + 0 + 7.7	3.7	6
China	83.6 75.3 + 0 + 8.3	2.5	6

[a] *Wind turbine + offshore + PV.*

www.TechnicalBooksPDF.com

After a paragraph on the accuracy evaluation of the models, the various available forecasting methodologies for solar irradiation will be presented according to the forecast horizon. Finally, new perspectives will be reported in a last paragraph.

2. INTERMITTENT AND STOCHASTIC RENEWABLE ENERGY PRODUCTION IN AN ELECTRICAL GRID

It is important to explain why the introduction of intermittent and stochastic electrical power into an electrical network induces some difficulties for the energy manager, to better understand the need to have efficient forecasting tools to estimate the wind and PV powers at various temporal horizons.

Before getting into details, it is worth reminding ourselves some principles on the electrical network management, especially on the challenge to reach at every moment a precise balance between production and consumption.

2.1 THE PRODUCTION/CONSUMPTION BALANCE: A DIFFICULT TASK EVEN WITH CONVENTIONAL ENERGY PRODUCTION MEANS

The produced electricity must be immediately used whenever it is sent to the electrical network. The energy manager must have all the means necessary to produce electrical energy and must especially ensure a precise balance between electricity generation and demand. In a power system, this power balance must be maintained at any moment, i.e., the electricity demand must be balanced by the electricity generation at all times. The electrical network must be working at a stabilized frequency (50 Hz, sometimes 60 Hz); thus, the production systems must adapt their production to the power consumption either in the electrical stations or in the dispatching center at all time.

In normal mode, there is a situation of balance: the production is always equal to the consumption and the electricity frequency slightly fluctuates around the reference frequency as seen in Fig. 3.1.

In case decrease of the electrical production happens suddenly because of the loss of a means of production (or if a shadow of a cloud moves across a PV plant or the wind speed drops off in front of the wind turbine), this balance is broken and the frequency falls below the reference frequency. In these conditions, a rapid increase of the produced electrical power by a connected production means is required (taking into account the ramp rate − rate of power rise) or the start-up of a new production means should be added (according to the start-up time). But the power ramp rate of an energy plant and its starting time are not instantaneous as seen in Table 3.2 [5]. As the run-up time is long, the activation of a new production system should be anticipated; only a hydraulic plant starts rapidly, followed by a light-fuel turbine; internal combustion engines (fuel or gas) need about 45 min before starting to produce electricity (see Table 3.2).

www.TechnicalBooksPDF.com



FIGURE 3.1

Electrical dispatching center (Sofia, Bulgaria) (personal picture).

Without the anticipation of the consumption followed by the start-up of a new energy means, the imbalance remains leading to a load shedding on the one hand. If this load shedding is too slow or insufficient, a risk of blackout arises. On the other hand, if the load is lower than the production (because of an overproduction of a PV plant for instance), the frequency increases and it might present a danger for the

Table 3.2 Characteristics of Electricity Production Plants [5]

Type	Size (MW)	Minimum Power Capacity (%)	Rise Speed in Power Per Min (%)	Start-Up Time (h)
Nuclear power plant	400–1300 per reactor	20	1	40 (cold)-18 h (hot)
Steam thermal plant	200–800 per turbine	50	0.5–5	11–20 h (cold)-5 h (hot)
Fossil-fired power plants	1–200	50–80	10	10 min–1 h
Combined-cycle plant	100–400	50	7	1–4 h
Hydropower plant	50–1300	30	80–100	5 min
Combustion turbine (light fuel)	25	30	30	15–20 min
Internal combustion engine	20	65	20	45–60 min

www.TechnicalBooksPDF.com

electrical machines, the security system stops the electrical machine leading to a power failure in the network.

As demonstrated, the power system is a dynamic system, continuously subject to changing conditions, some variations can be anticipated, while others cannot be predicted [6]. A power system has to meet a continuously varying consumer load. In terms of energy control, the load represents the primary independent variable — the driver whose controllable elements within the power system should be positioned and should respond. It is continuously changing in amplitude at annual, seasonal, daily, minute-to-minute, and second-to-second time steps. The reliability of the system becomes dependent on its ability to accommodate expected and unexpected changes and disturbances while maintaining quality and continuity of service for the customers.

2.2 INTERMITTENCE OF RENEWABLE PRODUCTION AND IMPACT ON THE ELECTRICAL GRID MANAGEMENT

Wind and sun are variable and unforeseeable generating resources. They impact, at all time, the planning and operation processes. The wind and solar variability have their own characteristics and time frames (Fig. 3.2). The variability and unpredictability of wind and solar sources are important as the penetration levels are high [7–9].

The uncertainty and variability of wind and solar resources pose problems for grid operators. This variability requires additional and complex actions to balance the system. The integration of ISRES into an electrical network intensifies the complexity of the grid management [10–12]. A greater flexibility in the system is necessary to accommodate supply-side variability and the relationship between generation levels and loads.

When the renewable electrical power is lower or higher than the power demand, other generation units must compensate the difference, which implies that the global production system should operate with a sufficient reserve margin (electrical systems already in operation but in part-load operation) because most traditional generation units require a considerable start-up time. This allows the system to cover up the loss of generation when needed [13,14].

The introduction of solar or wind systems in the electrical network induces two kinds of constraints [13,15–17]:

- Some constraints related to the source: The power is not guaranteed because of the intermittent and stochastic behavior of the source, leading to the necessity to continuously provide other means in reserve able to compensate the variations of power and to react immediately (in increasing or decreasing their production in a short time). Solar and wind sources are not always available when they are needed and sometimes are present, whereas the network does not require. In this case, their production is in excess. The conventional energy system (as fuel motor) works in part-load mode for the purpose of being able to react rapidly to

www.TechnicalBooksPDF.com

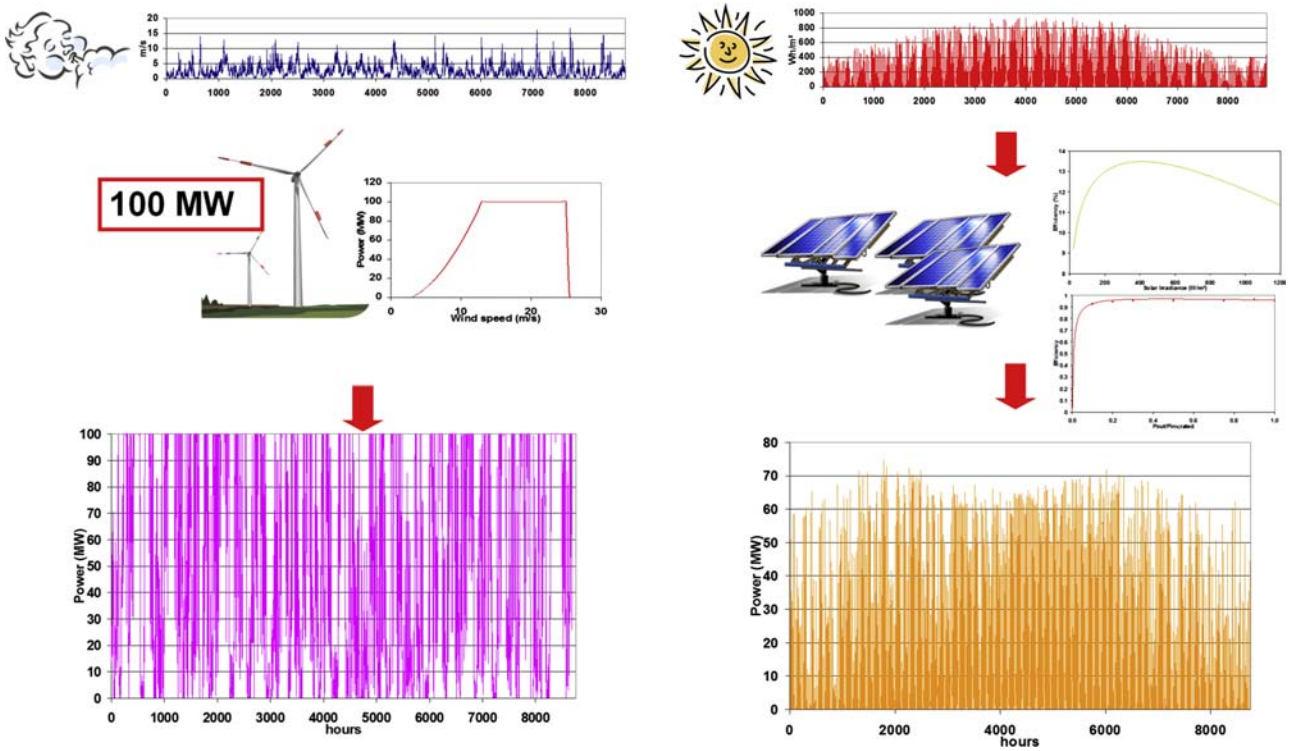


FIGURE 3.2

Example of variability of the solar and wind resources and corresponding renewable production.

www.TechnicalBooksPDF.com

a quick variation of intermittent renewable power (then, with a low efficiency and an increase of the fuel consumption per kWh produced and of the kWh production cost) [11,18].

- Some technical constraints: Wind and PV systems have no inertia and then are sensible to voltage and frequency drops, which cut the production and aggravate the incidents. Moreover they do not participate in the "system service," to the electrical network stability and quality (voltage and frequency regulation, switch-on in autonomous mode or black-start) [19–21]. These systems behave like passive generators from an electrical point of view. Then, some conventional production means with inertia must work permanently to maintain a voltage and frequency regulation provided by conventional electrical plants.

The penetration rate of ISRES, i.e., the power generated by ISRES compared with the total electrical consumption must be limited to guarantee an electrical grid stability and a security of supply. Some feedbacks in Denmark show that for a penetration rate up to 20% or 30% some stability problems can occur. A French directive limits the active power from these plants at 30% of the total active power. The same maximum penetration rate of random renewable electrical systems is used in other countries such as Canary Archipelago (Spain). This ISRES power limitation imposes to develop methodologies for determining the renewable energy absorption capability [22] and need to have a good knowledge of produced and consumed energy fluxes at various temporal horizons.

3. NEED FOR SOLAR AND WIND FORECAST: FORECAST HORIZON AND TIME STEP

Forecasting the ISRES output power is a requirement for a good operation of the power grid and for an optimal management of the energy flows occurring into the ISRES [23]. It is necessary to estimate the reserves, scheduling the power system, and congestion management, for optimally managing the storage and for trading in the electricity market [3,4,21,24–27].

As underlined in paragraph 2.1, even if no ISRES is integrated in the network, energy and power reserves are needed and can be divided in two categories: contingency reserve, used in case of specific event (such as power plant switch-on), and "no-event" reserves used continuously (for instance, because of unreliable load prediction) [28]. These reserves (contingency and no-event ones) are started at various time scales: within 1 min (primary reserve) using spinning generators, from 1 min to 1 h (secondary/tertiary reserves), and more than 1 h [29]. ISRES introduction in an electrical network only affects the nonevent reserve particularly because of the imperfect forecast of their production [28].

Already, it appears that a predicted and anticipated event is easier to manage. The electrical energy operator needs to anticipate the future of the electrical production and consumption at various temporal horizons (Fig. 3.3) [12,30].

www.TechnicalBooksPDF.com

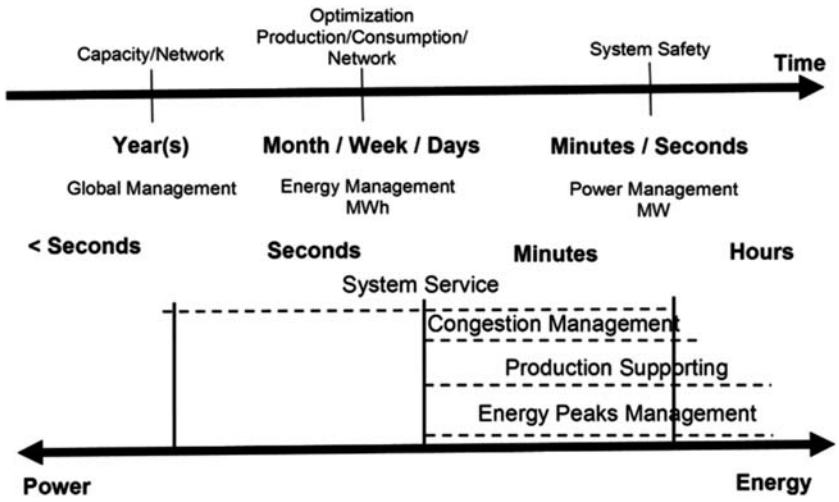


FIGURE 3.3

Prediction scale for energy management in an electrical network.

V. Lara-Fanego, J.A. Ruiz-Arias, D. Pozo-Vázquez, F.J. Santos-Alamillos, J. Tovar-Pescador, Evaluation of the WRF model solar irradiance forecasts in Andalusia (southern Spain), Solar Energy 86 (8) (2012) 2200–2217; H.M. Diagne, M. David, P. Lauret, J. Boland, N. Schmutz, Review of solar irradiance forecasting methods and a proposition for small-scale insular grids, Renew. Sustain. Energy Rev. 27 (2013) 65–76.

A forecast error induces two negative effects: First, the network operator may receive some high penalties because an inaccurate forecast would prevent him to reach a predicted production profile and the use of back-up generators is more important for compensating the gap between predicted and real production [31,32]. A solution consists in using local storage in combination with ISRES to compensate deviations between forecasted and produced electricity [18,23,31,32] or in combining several ISRES spread over a large area in such a way that individual prediction errors of each ISRES would be independent and the overall forecast error reduced (aggregate effect).

The energy storage means appears at various time scales and their management requires to know the power or energy produced by the ISRES and consumed at various temporal horizons: from very short or short (power quality category) to hourly or daily (bulk energy storages) [3]. For the storage management, the forecasting allows to decrease the amount of flexible reserves and to optimize the management of the energy storage by anticipating the charge and discharge phases.

Moreover, the electrical operator needs to know the future production (Fig. 3.3) at various time horizons: from 1−3 days to prepare the production means (and to schedule preventive maintenances), from some minutes to hours to plan the power plants start-up in reserve (between 5 min and 40 h according to the energy production means [5].

www.TechnicalBooksPDF.com

As a result, the overall relevant horizons of forecast should range from 5 min to several days [30]. It is apparent that the time step of predicted data (daily or hourly energy, 10-min or 20-min energy, etc.) varies depending on objectives and on forecasting horizon [25].

4. COST OF INTERMITTENCE AND BENEFIT OF FORECASTING

As seen before, deleting or reducing the "unpredictable" variations of ISRES requires the use of energy storages and back-up energy production means able to compensate immediately the power variations. As a consequence, backup generators must often remain switched-on to maintain the production/consumption balance promptly. Besides, PV and wind energy systems should be switched off, for example, when their electrical production exceeds a certain percentage of the global production (ISRES power curtailment). Such difficulties entail an additional production cost compared with conventional production. The accurate prediction of ISRES intermittence would represent a cost-effective access to these energy resources. As the cost of the intermittence of solar and wind resources is quite important [33,34], a reliable forecasting of these intermittences should not only allow to manage more efficiently the overall electrical system but also significantly reduce the negative cost impact of these ISRES on the electrical network; at last, the cost-effectiveness of PV and wind energy systems is increased.

Evaluation and forecasting of ISRES power appears to be an essential tool for renewable energy power plant developers to identify the location where ISRES could be installed and to decrease the use of conventional electricity production means as much as possible while optimizing the profitability of ISRES.

4.1 COST OF INTERMITTENCY

There are multiple reasons why the ISRES power variations are very troublesome: because the purchase electricity contracts are set up in advance, because back-up generators must be stopped or switched depending on the ISRES production variations, because some of them have to be operating even without producing to compensate instantaneously the short production variations; all of them contribute to the cost linked to variability.

Besides, ISRES production remains uncertain until the last moment, and as electricity trading takes place the day before delivery, the deviations between forecasted and actual production have to be balanced on short notice, which is costly as well [35]. Electrical systems need to incorporate additional flexibilities (new operational practices, storage, demand-side flexibility, flexible generators, etc.) to adapt themselves to the constraints because of the variability of renewables.

The integration costs are evocated as "an increase in power system operating costs" [36], as "the additional cost of accommodating wind and solar" [37], as "the extra investment and operational cost of the non-ISRES part of the power

www.TechnicalBooksPDF.com

system when ISRES power is integrated" [35], as "comprising variability costs and uncertainty costs" [38], or also as "additional costs that are required in the power system to keep customer requirement (voltage, frequency) at an acceptable reliability level" [39] in the literature.

Some references are listed below which will give us an order of magnitude of integration costs or variability costs. Three reviews on integration costs gave a quasisimilar range of 0−6 €/kWh [28,35,40]. The cost of variability depends on the technology and is estimated to be 6.16−8.47 €/MWh for solar PV, 3.85 €/MWh for solar thermal, and about 3.08 €/MWh for wind systems [41]. For wind energy systems, integration costs between 1.57 and 4.22 €/MWh [42,43]. From data obtained by independent systems operators, the integration cost for wind generators were found in the range of 0.34−6.46 €/MWh [44]. The subhourly variability cost for 20 wind plants was 5.93 € ± 0.86 € per MWh in 2008 and 2.81 € ± 0.37 € per MWh in 2009 [38].

4.2 FORECASTING AND INFLUENCES ON PRODUCTION COST

ISRES energy forecasting reduces the uncertainty of variable renewable generation. It helps grid operators more efficiently to commit or decommit generators to accommodate changes in ISRES generation and react to extreme events (ISRES production or load consumption unusually high or low, reducing too the curtailment). Forecasts allow to reduce the amount of operating reserves needed for the system, reducing costs of balancing the system. The forecasting error is a significant parameter in the integration costs [45] and the lack of a good forecasting implies to use larger energy reserves, which cannot be used for other utilizations [46].

With such forecasts, grid operators can schedule and operate other generating capacity efficiently, reducing fuel consumption, operation and maintenance costs, and gas emissions as compared with simply letting variable generation "show up" [47].

Here are a few remarkable examples that already demonstrate the cost improvement:

- one percent point improvement has produced a profit of two million Danish crowns [48].
- six million US$ savings 1 one year as a result of forecasting [49].
- Xcel Energy in reducing its mean average errors in forecasting from 15.7% to 12.2% saved 2.5 M$ [50].
- For GE [51]: the use of production forecasts reduced operating costs by up to 14%, or 5 billion $/year, that is, a reduction of operating cost of 12−20 $/MWh.

An improvement of the forecasting reliability has sometimes a significant influence on the integration cost:

- a 1% Mean Absolute Error (MAE) improvement in a 6-h-ahead forecast induces a reduction of 972 k$ for 6 months (0.05% of the total system cost) and a decrease of wind curtailments by about 35 GWh [52].

www.TechnicalBooksPDF.com

- with a wind penetration of 33% into the Irish electricity system, an improvement from 8% to 4% in MAE has saved 0.5%−1.64% the total system costs and has induced a curtailment reduction of 9% [53];
- a wind forecasting improvement of 20% doubled the savings compared with a 10% improvement [54] (Fig. 3.4). Moreover, at low penetration levels (up to 15%), savings are modest and for higher penetration levels (e.g., 24%), the savings versus the forecasting improvement is not linear as demonstrated by [55]. In Fig. 3.4, the 100% perfect forecast is not possible but shows the maximum possible benefit of a good forecasting on the operating cost [54].

The forecasting improvement on the operating reserve shortfalls (insufficient generation available to serve the load) and on the wind curtailment (because of overproduction of wind turbine or electrical congestion) has also been estimated [54] (Fig. 3.5).

Improved forecasts reduce the amount of curtailment by up to 6% and increase the reliability of power systems by reducing operating reserve shortfalls. A 20% wind forecast improvement could decrease reserve shortfalls by as much as two-thirds with 24% of wind energy penetration.

Solar and wind forecasting is the main solution to manage the variable nature of solar or wind energy production, before establishing the more expensive strategies of energy storage and demand response systems would be put in place. Furthermore, once a forecasting system is in place, it provides additional benefits through the optimized use of these demand-side resources.

A reliable forecasting method for ISRES production has a very positive influence on:

- the reduction of the integration costs
- the decrease of the average annual operating costs
- the decrease of the reserve shortfalls
- the increase of the percentage reduction in curtailments of PV systems or wind turbines.

The improvements impact of a good forecasting depends on the integration level of the renewable systems within the electrical network.

5. FORECAST ACCURACY EVALUATION

Before getting into more detail concerning the various ISRES power forecasting approaches, it is necessary to learn how its performance is evaluated. In the case of forecasting, evaluation is quite particular: For example, during development of a forecasting model, it is a guiding self-assessment leading to improvements in the processing chain; it can also be used as a technique to determine parameters (optimizing the values given by a training set) for certain types of model structures; when studying other models, it aims to make comparisons; and in operation it permits

www.TechnicalBooksPDF.com

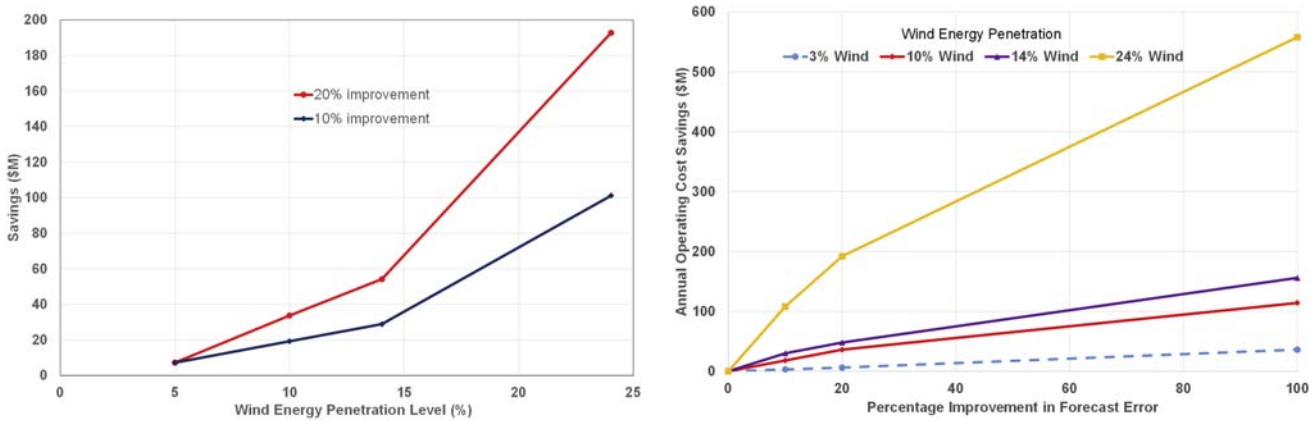


FIGURE 3.4

Left: Average annual operating cost savings versus wind penetration, for 10% and 20% wind forecast improvements — Right: Annual operating cost savings versus wind forecast improvements for 3%, 10%, 14%, and 24% wind energy penetrations [54].

www.TechnicalBooksPDF.com

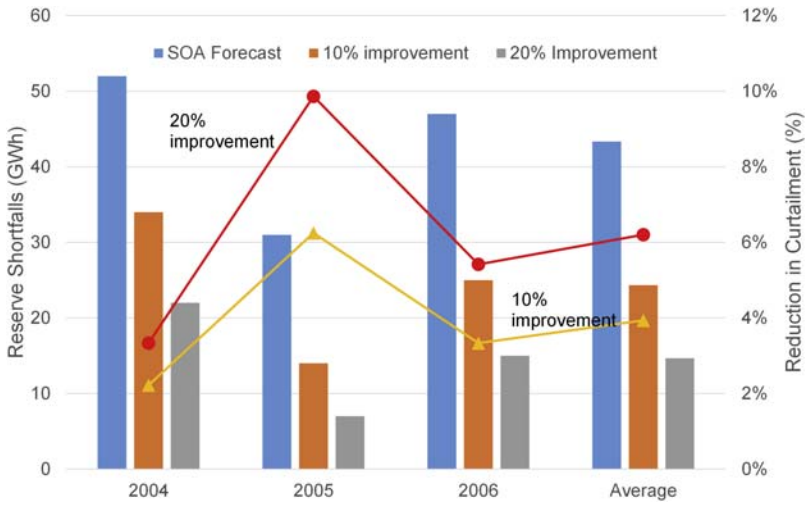


FIGURE 3.5

Reserve shortfalls and percentage reduction in curtailment with improved wind generation forecasts for the 24% WECC (Western Electricity Coordinating Council) wind energy penetration case [54].

tracking how the model is behaving in real conditions. As there are different types of forecasts, evaluation has to be specific for each type of result.

This performance comparison is not easy for multiple reasons such as different time horizons, various time scales of the predicted data and variability of the meteorological conditions from one site to another one. It consists in comparing forecasted outputs y (or predicted time series) with observed data y (or observed or measured time series) which are also measured data themselves linked to an error (or precision) of a measure [56].

Various graphic tools can be used to estimate the adequacy of the model with the experimental measurements (Fig. 3.6):

- Time series of predicted data compared with measured data; it allows to visualize more easily the forecast quality. In Fig. 3.6A, for instance, a high forecast accuracy is observed in clear-sky situations and a low one in partly cloudy situations.
- Scatter plots of predicted data over measured data (Fig. 3.6B): it reveals systematic bias and deviations depending on solar irradiance conditions and gives access to the range of deviations that are related to the forecasts.

There is no well-defined evaluation measurement standard, which makes the forecasting methods difficult to compare. A benchmarking exercise has been realized within the framework of the European Actions Weather Intelligence for Renewable Energies (WIRE) [57] with the objective to evaluate the state-of-the-art

www.TechnicalBooksPDF.com

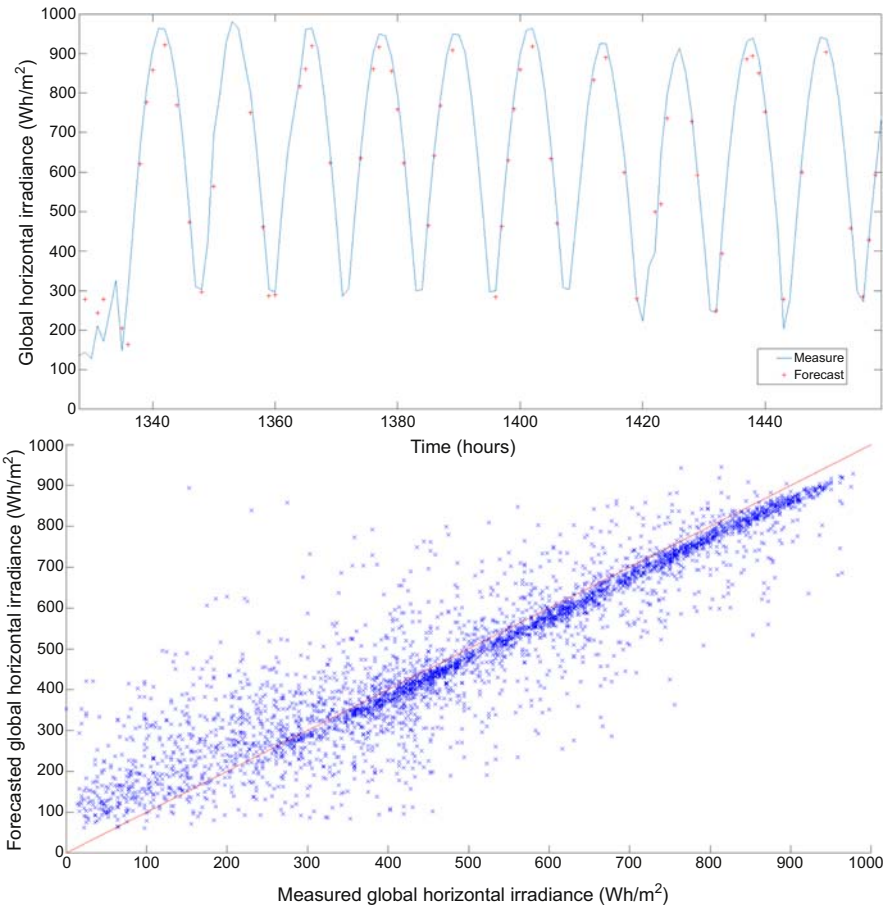


FIGURE 3.6

Upper: Time series of predicted and measured global irradiations — bottom: Scatter plot of predicted vs. measured global irradiations.

concerning models' performances for short-term renewable energy forecasting. They concluded that: "More work using more test cases, data and models needs to be performed to achieve a global overview of all possible situations. Test cases located all over Europe, the US and other relevant countries should be considered, trying to represent most of the possible meteorological conditions." This paper very well illustrates the difficulties associated with performance comparisons.

The usually used statistics include:

- The mean bias error (MBE):

$$\mathrm{MBE} = \frac{1}{N} \times \sum_{i=1}^{N} (\hat{y}(i) - y(i)) \tag{3.1}$$

www.TechnicalBooksPDF.com

$\hat{y}$ being the forecasted outputs (or predicted time series), y the observed data (or observed or measured time series), and N the number of observations. MBE is not a good indicator of the model reliability because the errors often compensate each other, but it allows to see how much it overestimates or underestimates.

- MAE is appropriate for applications with linear cost functions, that is, situations where the costs resulting from a poor forecast are proportional to the forecast error:

$$\mathrm{MAE} = \frac{1}{N} \times \sum_{i=1}^{N} |\hat{y}(i) - y(i)| \tag{3.2}$$

- The mean square error (MSE) uses the square of the difference between observed and predicted values. This index penalizes the highest gaps:

$$\mathrm{MSE} = \frac{1}{N} \times \sum_{i=1}^{N} (\hat{y}(i) - y(i))^2 \tag{3.3}$$

MSE is usually the index minimized by training algorithms [found in Artificial Neural Network (ANN) methods for instance].

- The root mean square error (RMSE) is more sensitive to important forecast errors and hence is suitable for applications where small errors are more tolerable and larger errors lead to costs that are disproportionate, as in the case of utility applications, for example. It is probably the reliability factor that is the most widely used:

$$\mathrm{RMSE} = \sqrt{\mathrm{MSE}} = \sqrt{\frac{1}{N} \times \sum_{i=1}^{N} (\hat{y}(i) - y(i))^2} \tag{3.4}$$

- The mean absolute percentage error is close to the MAE but each gap between observed and predicted data is divided by the observed data to get the relative gap.

$$\mathrm{MAPE} = \frac{1}{N} \times \sum_{i=1}^{N} \left| \frac{\hat{y}(i) - y(i)}{y(i)} \right| \tag{3.5}$$

This index has the disadvantage of being unstable when $y(i)$ is near zero and it cannot be defined for $y(i) = 0$.

Often, these errors are normalized, which is particularly true for the RMSE; the mean value of irradiation is generally used as reference:

$$\mathrm{nRMSE} = \frac{\sqrt{\frac{1}{N} \times \sum_{i=1}^{N} (\hat{y}(i) - y(i))^2}}{\overline{y}} \tag{3.6}$$

www.TechnicalBooksPDF.com

where $\bar{y}$ is the mean value of y. Other indices exist and can be used such as the correlation coefficient R (Pearson coefficient) and the index of agreement (d) normalized between 0 and 1.

When different forecasting methods are evaluated using different data sets, comparisons using score functions are not accurate. Skill scores that relate a specific score function with a base model overcome this problem:

$$\text{SkillScore} = \frac{\text{Metric}_{\text{forecasted}} - \text{Metric}_{\text{reference}}}{\text{Metric}_{\text{perfectforecast}} - \text{Metric}_{\text{reference}}} = 1 - \frac{\text{MSE}_{\text{forecast}}}{\text{MSE}_{\text{reference}}} \tag{3.7}$$

where $\text{Metric}_{\text{forecasted}}$ is the score obtained by the method being evaluated, $\text{Metric}_{\text{perfectforecast}}$ is the score obtained by an optimal forecast (i.e., by using observations as forecasts when computing the score rule), $\text{Metric}_{\text{reference}}$ is the score obtained by a reference model, which is usually found either in climatology (forecast is the average of available measures or of previously obtained average) or persistence (last available measure is used as forecast).

"Trivial" forecast methods can be used as a reference [56]. The most common one is the persistence model ("things stay the same") where the forecast is always equal to the last known data point. The persistence model is also known as the naïve model or the RandomWalk (a mathematical formalization of a path that consists of a succession of random steps).

The solar irradiance has a deterministic component because of the geometrical path of the sun. This component, for example, may be added as a constraint to the most basic form of persistence in considering the measured value of the previous day or the previous hour at the same time as a forecast value. Other common reference forecasts include those based on climate constants and simple autoregressive methods. Such comparison with referenced Numerical Weather Prediction (NWP) model is shown in Fig. 3.7. Generally after 1 h, the forecast is better than the persistence model. For forecast horizons ahead of 2 days, climate averages show lower errors and should be preferred.

6. FORECASTING METHODS FOR DIFFERENT FORECAST HORIZONS

This paragraph presents state-of-the-art approaches to solar irradiance forecasting at different time scales. At first, some generalities concerning time-scale and temporal resolution, about the link between PV production and weather forecast, are developed. Then, very short-term forecasting within a temporal range of 0—6 h and forecasts from 6 h to days ahead will be reviewed.

www.TechnicalBooksPDF.com

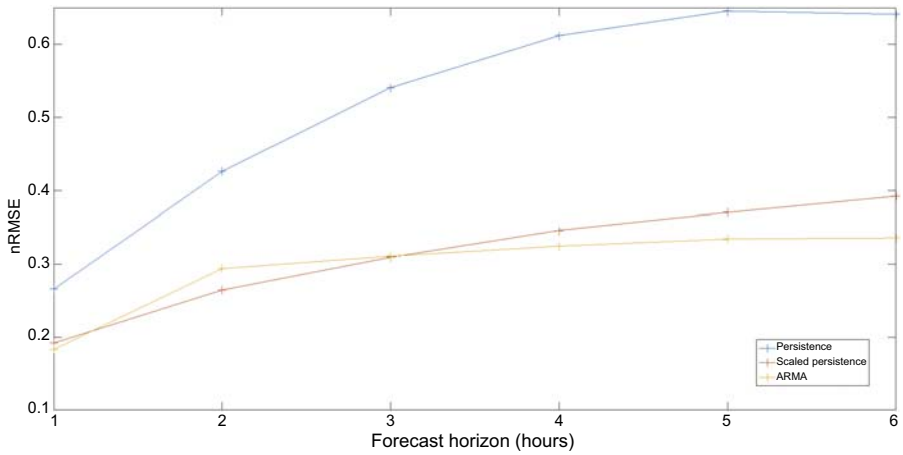


FIGURE 3.7

Relative root mean square error of forecasts (persistence, scaled persistence, autoregressive moving average) depending on the forecast horizon.

6.1 TEMPORAL HORIZON AND RESOLUTION — GENERALITIES ABOUT SOLAR IRRADIANCE FORECASTING

The time scale is linked to the type of application and its time constants (see Figs. 3.3 and 3.8) [4].

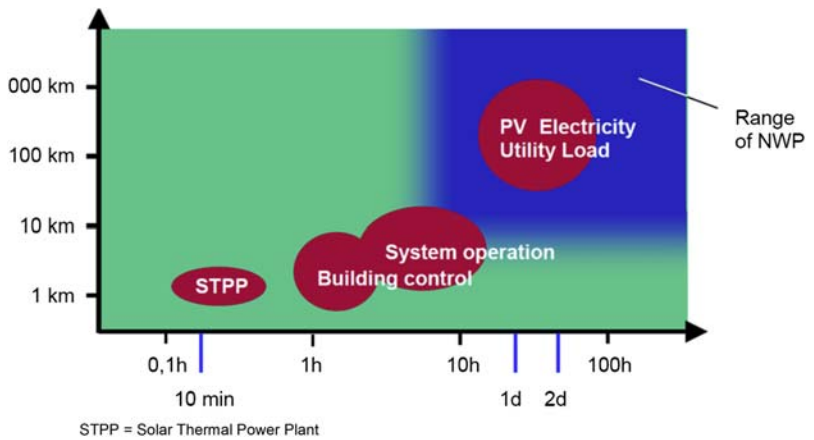


FIGURE 3.8

Typical target applications for solar irradiance forecasting and their respective and temporal scale. The blue area (dark gray in print versions) depicts the range for which the use of numerical weather prediction models is appropriate.

D. Heinemann, E. Lorenz, M. Girodo, Forecasting of Solar Radiation. Solar Energy Resource Management for Electricity Generation from Local Level to Global Scale. Nova Science Publishers, New York, 2006.

www.TechnicalBooksPDF.com

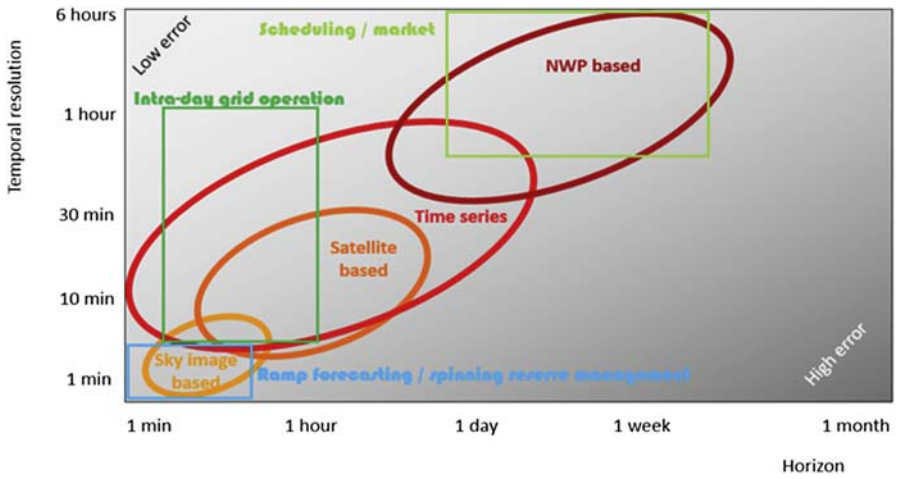


FIGURE 3.9

Forecasting time horizon versus temporal resolution.

H.M. Diagne, M. David, P. Lauret, J. Boland, N. Schmutz, Review of solar irradiance forecasting methods and a proposition for small-scale insular grids, Renew. Sustain. Energy Rev. 27 (2013) 65–76.

Fig. 3.9 summarizes the best uses of the main existing methods (time series–based methods, NWP-based methods, satellite- and image-based methods) according to the forecasting time horizon and the temporal resolution.

The existing methods can be classified in four different categories [30]: (Fig. 3.10):

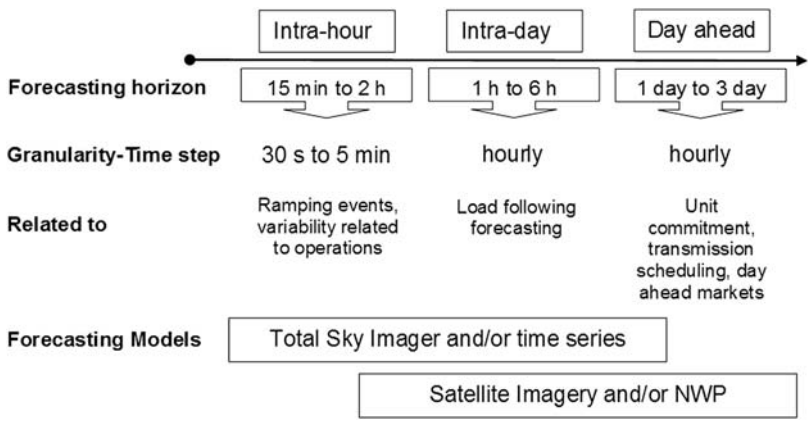


FIGURE 3.10

Relation between forecasting horizons, forecasting models, and the related activities.

H.M. Diagne, M. David, P. Lauret, J. Boland, N. Schmutz, Review of solar irradiance forecasting methods and a proposition for small-scale insular grids, Renew. Sustain. Energy Rev. 27 (2013) 65–76.

www.TechnicalBooksPDF.com

- Time series−based methods: this set holds for approaches based on statistical models solely ground on past measurements;
- NWP-based methods: this set holds for approaches based on weather forecasts provided by a specialized provider ("NWP" is the acronym for "Numerical Weather Forecast");
- Satellite imagery−based methods: methods based on images of the earth taken by satellite;
- Sky images−based methods: based on observations of cloud cover from the ground with an in situ camera.

Strictly speaking, the different categories are not rival and each method is efficient within the range of its own time horizon and even sometimes they can be used together in hybrid methods.

Power prediction of PV systems usually involves several modeling steps to obtain the required forecast information from different kinds of input data [58].

Forecasts may apply to a single PV system or to an aggregation of systems spread over an extended geographic area. The aggregate effect, repartition of ISRES over a large territory, allows to average and to smooth their production; thus, it is easier to predict the production of a country than the production of a region, just as it is easier to predict a production of a region than that of a single PV plant.

Forecasts may focus on the output power of systems or on its rate of change (ramp rate). Forecasting methods also depend on the tools and information available to forecasters, such as data from weather stations and satellites, PV system data, and outputs from NWP models [59] (Fig. 3.9).

Directly forecasting the PV power from an historical PV production data series can be more complicated than predicting solar radiation incident in the PV plant for several reasons:

- in various models as statistical and artificial intelligence ones, a large data set is necessary for the training, which implies that the PV plant has to be installed for a very long time before being able to train the model, which is a rare occurrence;
- the installed power of the PV plant can be increased, some malfunctions may occur (or only a part of the PV plant runs); thus, the historical data set is not more reliable nor homogenous [60].

The main variables influencing PV output power are the irradiance in the plane of the PV array (Global one for nonconcentrating collector and normal beam for concentrated collector), the temperature at the back of the PV modules, and to a lesser extent, the wind speed at the PV modules level.

The PV power forecast is obtained by introducing the irradiance forecast into a PV simulation model. Generally, two models are used in this step: One to calculate the direct current power output and another for modeling the inverter characteristics. Such models are easily available with more or less complexity, but even for simple models, their accuracy is higher than the accuracy of the irradiance forecast.

www.TechnicalBooksPDF.com

The influence of ambient temperature via the cell temperature into the PV power model is low and that of the wind speed even more. For the ambient temperature, often that measured at the previous temporal horizon can be used.

Thus, the accuracy of the PV production forecasting depends mainly on the solar irradiation forecasting.

6.2 VERY SHORT-TERM FORECASTING IN A TEMPORAL RANGE FROM 0 TO 6 H

In the time horizon, three methods are available:

- Total sky imagery (TSI)
- Satellite Cloud Motion Vector Approach
- Stochastic learning methods or Time series−based method

6.2.1 Sky Imagery

TSI is used or real-time forecasting called now-time, up to 10−30 min ahead; it consists in applying image processing and cloud tracking techniques to sky photos (Fig. 3.11). The method generally assumes a persistence of the opacity, direction, and velocity of cloud movements [62].

The cameras have a fish-eye lens that gives a 360-degree vision of the sky above the plant (Fig. 3.11). Clouds are detected and segmented on successive images and their past displacements are estimated so as to anticipate their next moves. The direct sun onto the camera is responsible for one difficulty in such applications. Indeed, it may burn the captors and lead to color saturation for several regions of the sky. Most often, it is solved by applying a mask that follows the path of the sun (but hide some parts of the sky). Several devices have been developed including the whole-sky imager [63], TSI [64] and the infrared sky imager [65], which considers the infrared rays. The Steadysun company has also developed his own camera (Steadysun) [66].

Some works were undertaken to estimate the movement of clouds on an image of the sky [62] or the segmentation and classification of clouds [67,68] (Fig. 3.12). Additional steps were taken for the prediction of global horizontal irradiance [62,69−71] (Fig. 3.12) or to predict the direct normal irradiance [72].

6.2.2 Satellite Cloud Image

Clouds can be detected by satellites using visible and/or infrared images; the cloudiness has a strong impact on surface solar irradiance. A semiempirical method allows to estimate solar irradiance from satellite using a set of cloud index images according to the Heliosat method [73]. To calculate the cloud index image in a first-step motion, vector fields are derived from two consecutive images [4]. The predicted image then is determined by applying the calculated motion vector field to the actual image. Finally, solar surface irradiance is derived from the predicted cloud index images via the Heliosat method. Fig. 3.13 gives an overview of these steps to derive the irradiance forecast.

www.TechnicalBooksPDF.com

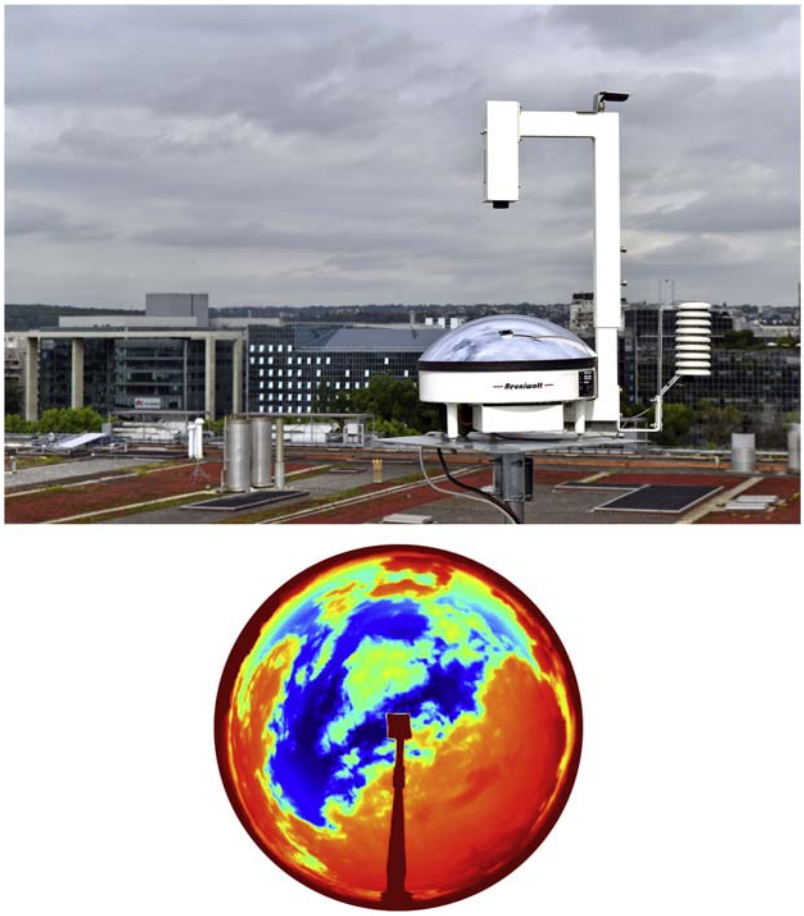


FIGURE 3.11

Example of sky imager [61].

Various methods "Heliosat-1," "Heliosat-2," or "Heliosat-3" [74–78] have been implemented. The spatial resolution of geostationary satellite images is 1 km (GOES) or larger (Meteosat outside high-resolution area), which is much less than ground-based sky images. Most of the clouds cannot be detected excepted the large convective clouds; consequently, the clouds have to be located somewhere within the pixel. The time frequency, the download time, and the images processing are slower than those of the sky imager ones; thus, the forecast cannot be updated as frequently (one image of the full earth about every 30 min).

These spatial and temporal resolutions in the satellite image data reduce the performance of the satellite-based approach compared with the sky imager method associated with very short horizon [59].

www.TechnicalBooksPDF.com

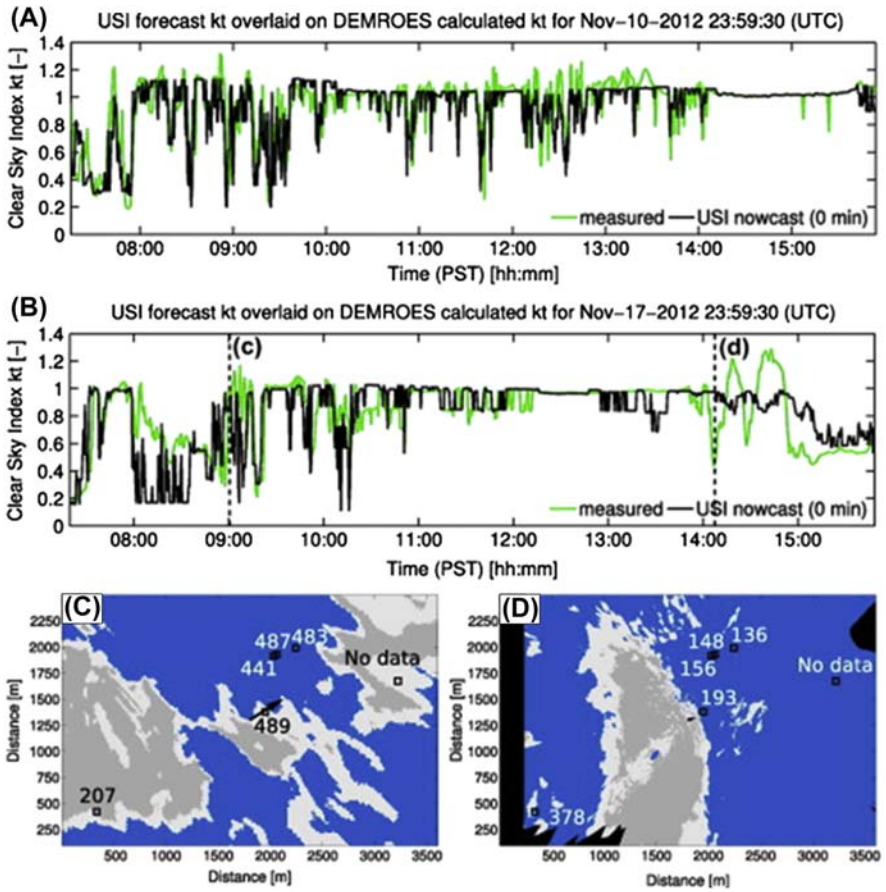


FIGURE 3.12

USI now-cast and measured *kt* averaged covered by the shadow map for (A) November 10, 2012 with cumulus clouds and (B) November 17, 2012 with cumulus clouds (<2 km) followed by altocumulus (2–7 km). *Dashed lines* indicate times corresponding to (c and d). (C) Shadow map [blue (gray in print versions): clear sky, light gray: thin cloud, dark gray: thick cloud, black: no data] corresponding to 09:07:30 PST (Pacific Standard Time) illustrating accurate shadow map. Ground station locations are marked by *black boxes*, with measured irradiance printed nearby in W/m^2. Cloud velocity is indicated by a black vector extending from the center of the shadow map. (D) Shadow map corresponding to 14:07:30 PST illustrating compressed shadow map because of low cloud height of 457 m [71].

www.TechnicalBooksPDF.com

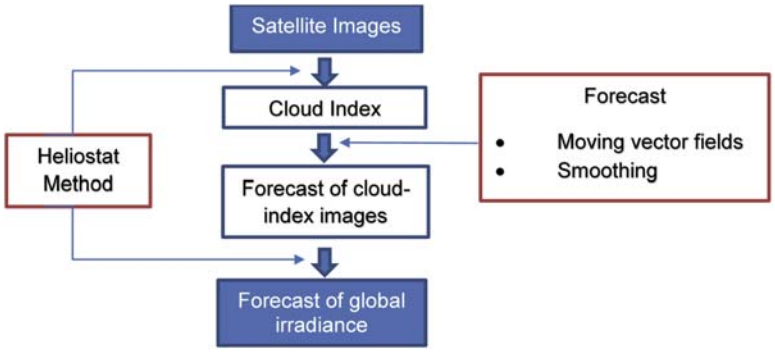


FIGURE 3.13

Short-term forecasting scheme using statistical methods on satellite imagery.

Reprinted from Heinemann D., Lorenz E., Girodo M., 2006. Forecasting of solar radiation. Solar energy resource management for electricity generation from local level to global scale, with permission from Nova Science Publishers, Inc.

As seen in Fig. 3.13, a dimensionless cloud index is calculated for each pixel and a relationship between this cloud index and the ratio of global irradiance to clear-sky irradiance is established. The basis of the forecasting methods relies upon the determination of the cloud structures during the previous recorded time steps. Extrapolation of their motion gives rise to cloud position forecasts (considering the other parameters constant during the time step) and, as a consequence, to the local radiation situation. This method has the advantage to produce a spatial analysis of an area within certain resolution capabilities. Several deriving methods are used for motion vectors [79–81]. The general method is well described in Fig. 3.14 [82].

Perez et al. [83] have compared the results with forecasts based on NWP method and according to their study, they set at approximately 6h the time horizon where NWP-based methods become more efficient than satellite images-based ones. They used infra-red images for determining the possible presence of snow on the ground [84]. Marquez et al. [85] described a hybrid method coupling a time series–based (neural network) and satellite images–based methods.

6.2.3 Stochastic Learning Methods or Time Series–Based Method

A traditional method for forecasting solar radiation is based on the time series of solar energy and sometimes of other meteorological parameters. Autoregressive models (AR) [86], Moving average (MA), Autoregressive Moving Average (ARMA), or Markov chain models are frequently used; more recently, artificial intelligence methods were developed such as ANN, Fuzzy Logic, and other hybrid methods [56,87].

www.TechnicalBooksPDF.com

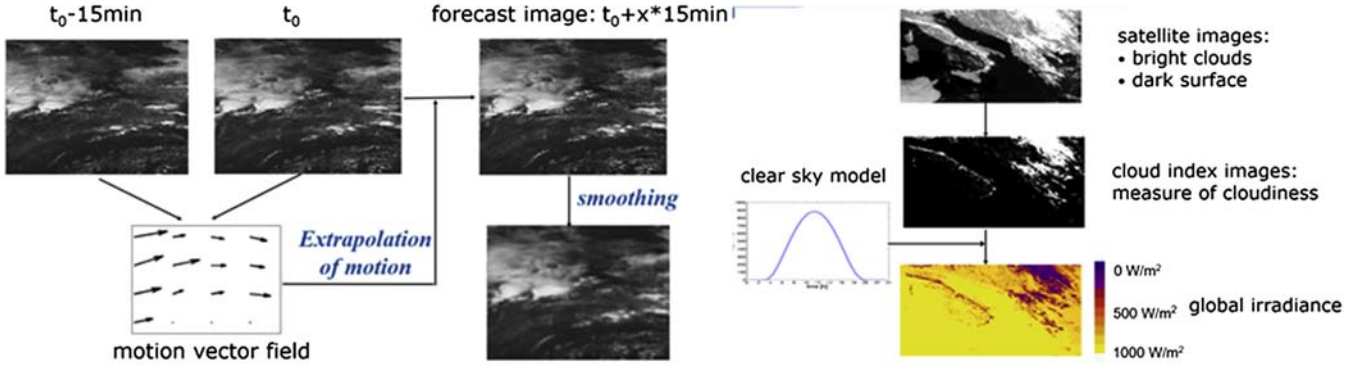


FIGURE 3.14

Forecast of clouds motion and Heliosat method.

E. Lorenz, J. Kühnert, A. Hammer, D. Heinemann, Satellite Based Short Term Forecasting. Summer School "From Renewable Energy Production to End Users" 2.5.2013, Montegut, France, 2013.

www.TechnicalBooksPDF.com

The approach used in such methods consists in predicting the future solar irradiance or irradiation (at different time scales) based on the past observed data [24]. Mathematically, the researched formulation is:

$$G_{t+h} = f(G_t, G_{t-1}, G_{t-2}, G_{t-3}, \ldots, G_{t-p}) \tag{3.8}$$

In other terms, the future time step $(t + h)$ is forecasted based on the observed data at the time $(t, t-1\ldots, t-p)$.

Some of these models are presented below.

6.2.3.1 Persistence and scaled persistence

As said in paragraph 5, the persistence model is often used as a reference for determining the skill factor. It is useful to know if a forecast model provides better results than any trivial reference model, which is the persistence model [24].

The persistence model considers that the solar radiation at $t + 1$ is equal to the solar radiation at t. It assumes that the atmospheric conditions are stationary. It is also called the naïve predictor.

$$G_{t+1} = G_t \tag{3.9}$$

Its accuracy decreases with the time horizon and is generally not adequate for more than 1 h.

An improved version of this model is the scaled persistence model. To take into account the fact that the apparent position of the sun is not identical between t and $t + 1$, the persistence model is corrected with a clear-sky ratio term (see Eq. 3.5) [88] and is then called scaled persistence

$$G_{t+1} = G_t \frac{G_{t+1}^{\text{clear sky}}}{G_t^{\text{clear sky}}} \tag{3.10}$$

6.2.3.2 Autoregressive Moving-Average Model

This model is well-known [89,90] for forecasting the future value of a time series. An ARMA model is composed of an autoregressive part (AR) and a MA; p and q are, respectively, the order of the AR and the MA (Eq. 3.11), and the ARMA (Eq. 12) model is noted as ARMA(p, q) [91,92].

$$\text{MA}(q) \rightarrow G_t = \sum_{i=0}^{q} \theta_i \cdot \varepsilon_{t-i} = \theta(L)\varepsilon(t), \quad \forall t \in \mathbb{Z} \tag{3.11}$$

$$\text{AR}(p) \rightarrow G_t = \sum_{i=1}^{p} \varphi_i \cdot G_{t-i} + \varepsilon_t = [\varphi(L)]^{-1}\varepsilon_t, \quad \forall t \in \mathbb{Z} \tag{3.12}$$

This model uses the statistical properties of the time series and the Box–Jenkins methodology. It has proved its efficiency for time series with a linear structure between the data mainly. To use ARMA model, the time series must be stationary, which is not the case for solar radiation; therefore, a process must be used previously

www.TechnicalBooksPDF.com

in view to obtain a stationary solar radiation time series by removal of the seasonality and trend.

The seasonality is generally deleted by using a clear-sky model, which contains all the seasonal variability. Several models exist to detrend the hourly solar radiation; a good overview of these models is given in [24].

6.2.3.3 Autoregressive Integrated Moving-Average Model

The ARIMA model [93] is a reference model for forecasting solar radiation and is derived from AR and MA models. ARIMA models are fitted to time series data either to better understand the data or to predict future points in the series (forecasting). They are applied in some cases where data exhibit evidence of nonstationarity, where an initial differencing step (corresponding to the "integrated" part of the model) can be applied one or more times to eliminate the nonstationarity.

Nonseasonal ARIMA models are generally denoted ARIMA (p, d, q) where parameters p, d, and q are nonnegative integers, p being the order (number of time lags) of the AR, d is the degree of differencing (the number of times the data have had past values subtracted), and q is the order of the moving-average model. When two out of the three terms are zeros, the model may be referred to based on the nonzero parameter, dropping "AR", "I," or "MA" from the acronym describing the model. For example, ARIMA(1,0,0) is AR(1), ARIMA(0,1,0) is I(1), and ARIMA(0,0,1) is MA(1).

A regression in log has been applied to the inputs of the ARIMA model to predict solar radiation [94]. At 24-h horizon, this model is more accurate than the others.

6.2.3.4 Artificial Neural Network

ANNs are particularly predominant in the field of time series forecasting with nonlinear methods. Indeed, the availability of historical data from the meteorological utility databases added to the fact that NNs are data-driven approaches capable of performing a nonlinear mapping between sets of input and output variables make this modeling tool very attractive. ANNs with d inputs, m hidden neurons, and a single linear output unit define a nonlinear parameterized mapping from an input vector x to an output vector y (see the relationship given in Eq. (3.13) and illustrated in Fig. 3.15).

$$y = y(\mathbf{x}; \mathbf{w}) = \sum_{j=1}^{m} w_j f\left(\sum_{i=1}^{d} w_{ji} x_i\right) \tag{3.13}$$

The m hidden neurons are related to the tangent hyperbolic function $f(x) = (e^x - e^{-x})/(e^x + e^{-x})$. The parameter vector $\mathbf{w} = (\{w_j\}, \{w_{ji}\})$ governs the nonlinear mapping and is estimated during a phase which is called the training or learning phase. During this phase, the NN is trained using the data set D that contains a set of n input and output examples. The second phase, called the generalization phase, consists of evaluating the accuracy of the model on another data set, so

www.TechnicalBooksPDF.com

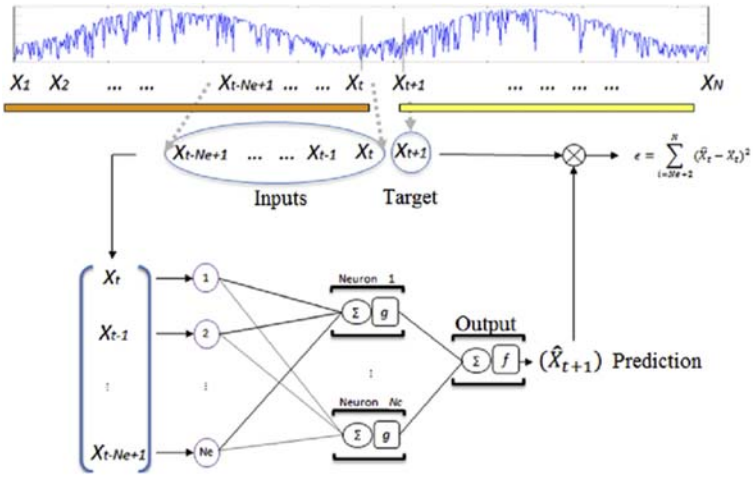


FIGURE 3.15

MLP (multilayer perceptron) for time series prediction with Ne inputs, Nc hidden nodes, and one output.

C. Voyant, P. Randimbivololona, M.L. Nivet, C. Paoli, M. Muselli, 24-hours Ahead Global Irradiation Forecasting Using Multi-layer Perceptron, Meteorological Applications, Wiley, 2013.

that they give correct outputs when confronted to examples that were not treated during the training phase.

For the purpose of our application, the relationship between the output $\widehat{k^*}(t+h)$ and the inputs $\{k^*(t), k^*(t-1), \cdots, k^*(t-p)\}$ has the form given in Eq. (3.14).

$$\widehat{k^*}(t+h) = \sum_{j=1}^{m} w_j f\left(\sum_{i=0}^{p} w_{ji}\, k^*(t-i)\right) \tag{3.14}$$

The NN model is equivalent to a nonlinear AR model for time series forecasting problems. In a similar way as the AR model, the number of past input values p can be calculated using the auto-mutual information technique. Particular attention must be brought to the model establishment. Indeed, a model that is too sophisticated (too many neurons) could overfit the training data. Several techniques like pruning or Bayesian regularization can be employed to control the NN complexity. The Levenberg−Marquardt (approximation to the Newton's method) learning algorithm combined with a max fail parameter before stopping the training is often used to estimate the NN model's parameters. The max fail parameter corresponds to a regularization tool limiting the number of learning steps after a characteristic number of predictions fails: its objective is to control the model complexity [26,92].

A detailed review about artificial intelligence methods applied to solar radiation forecasting is given in [87] and [24].

www.TechnicalBooksPDF.com

6.3 SOLAR FORECASTING FOR RANGES BETWEEN 6 H AND DAYS AHEAD

For an efficient planning and operation of solar energy systems and more specifically for a good management of the electrical grid, forecasts up to 48 h or even beyond have to be provided. NWP models allow to calculate fields of meteorological data as wind speed or radiation in the atmosphere. They use current meteorological data as input in mathematical models based on equations of the atmosphere within the goal to predict solar irradiance up to several days ahead [95,96].

The most used NWP models are the global model of the European Center for Medium-Range Weather Forecasts (ECMWF) and the Global Forecast System model of the National Centers for Environmental Prediction (NCEP) [10]. Because of the complexity of the models, only 14 NWPs are currently operating worldwide [59].

Generally, these models give a forecasting from two to four times a day; the resolution is relatively low because of the limitation of the computing time (in the range of 40−90 km). A mesoscale model covers a limited geographical area with a higher resolution and a best consideration of the local meteorological phenomena. The initial conditions of the mesoscale model are extracted from a global NWP.

Forecast improvements are often performed by comparing outputs to measured data during a training period which is used to develop corrected forecasts. This type of approach is often referred to as Model Output Statistics (MOS) [59]. MOS allows to interpret the outputs of the NWP and to produce site-specific forecasts; it is used to reduce the error of forecasting.

Perez et al. [97] found that the National Digital Forecast Database (NDFD) [a derivative of the operational NWP models of the NCEP] had for a 8- to 26-h forecast horizons an hourly average relative RMSE of 38%, after the application of a local correction function.

Remund et al. [96] evaluated different NWP forecasts for global solar irradiations in the United States; their RMSE values ranged between 20% and 40% for a 24-h forecast horizon. Similar results were reported by Perez et al. [83], evaluating NWP-based irradiance forecasts in several places of the United States [98], and they realized a similar evaluation for NWP-based forecasts in Europe and found nRMSE (normalized Root Mean Square Error) values of about 40% for Central Europe and about 30% for Spain.

6.4 RELIABILITY AND ACCURACY OF THE FORECASTING MODELS

Comparing prediction models is a difficult task also because the meteorological conditions are often very different from a location to another. To overcome this problem, a benchmarking exercise was organized within the framework of "WIRE" with the purpose of evaluating the performance of state-of-the-art models for short-term renewable energy forecasting. The exercise consisted in predicting the power output of two wind farms and two PV power plants, to compare the merits of forecasts based on different modeling approaches and input data [57,58]. As an example,

www.TechnicalBooksPDF.com

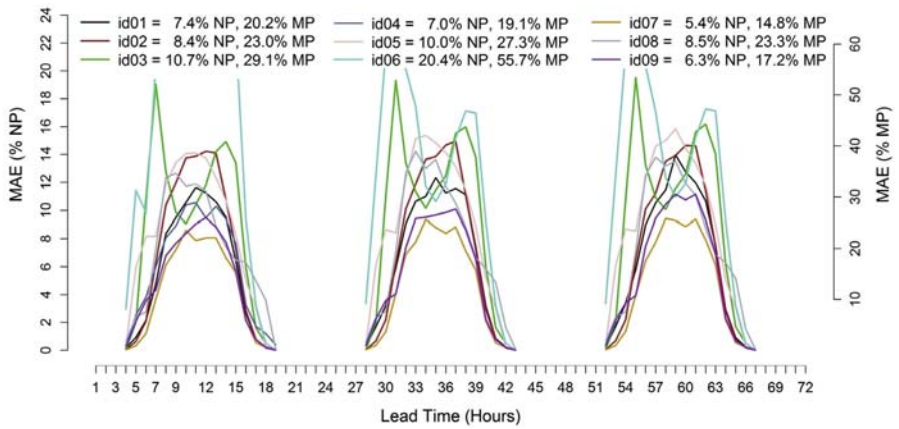


FIGURE 3.16

Error trends of the 1- to 72-h ahead solar power forecasts starting at 0 UTC for the Catania test case (MAE/NP % and MAE/MP %). *MP*, mean power; *NP*, nominal power measured during the test period. Id is the id number identifying each participant to the benchmarking.

S. Sperati, S. Alessandrini, P. Pinson, G. Kariniotakis, The "Weather Intelligence for Renewable Energies" benchmarking exercise on short-term forecasting of wind and solar power generation, Energies 8 (2015) 9594–9619.

Fig. 3.16 shows the MAE trend for the 1- to 72-h ahead, hourly forecasts made for Catania with hourly time steps.

Except for a couple of models that exhibit two peaks during early morning and late afternoon hours, all the others show a maximum MAE around 12 UTC. The differences between the models are quite important and reach about 5%. The model id07 performed better than the others with a 5.4% MAE/NP and 14.8% MAE/MP. The result is particularly good, with almost 1% MAE/NP less than the second best result of 6.3%, achieved by the model id09.

The participants of this COST action concluded that:

- For some applied machine learning techniques, where linear regressions have been the most used, quantile regression provided the best performances despite a low computational effort.
- A substantial source of improvement in the last 10 years should be addressed to the NWP progress. In fact, while testing the same postprocessing technique on older, lower spatial resolution and on newer ones, higher spatial resolution meteorological data lead to better results. It is tricky to draw certain conclusions from a single test case; however, an increase in model performance because of higher resolution and better accuracy appears reasonable

A quasiexhaustive review and comparison of forecasting methods using machine learning methodologies were realized by [56].

www.TechnicalBooksPDF.com

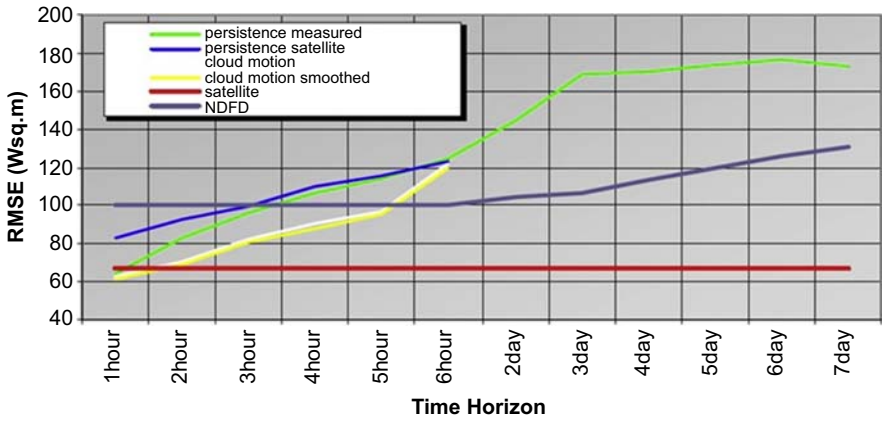


FIGURE 3.17

RMSE of different solar forecasting techniques obtained over a year at seven SURFRAD ground measurement sites (from R. Perez, S. Kivalov, J. Schlemmer, K. Hemker Jr., D. Renné, T.E. Hoff, Validation of short and medium term operational solar radiation forecasts in the US. Solar Energy 84 (2010) 2161–2172). The *red* (dark gray in print versions) *line* shows the satellite now-cast for reference, that is, the satellite "forecast" for the time when the satellite image was taken. Cloud motion forecasts derived from satellite [*yellow* (dark gray in print versions) and *white lines*] perform better than NWP (NDFD) up to 5 h ahead. NWP has similar accuracies for forecast horizons ranging from 1 h to 3 days ahead.

R. Perez, S. Kivalov, J. Schlemmer, K. Hemker Jr., D. Renné, T.E. Hoff, Validation of short and medium term operational solar radiation forecasts in the US, Solar Energy 84 (2010) 2161–2172.

Perez et al. [83] compared several methods of forecasting applied to seven sites; Fig. 3.17 from [59] and drawn from results obtained by [83] shows the RMSE obtained for each method.

7. THE FUTURE OF THE RENEWABLE ENERGY FORECASTING

Machine learning methods give the best results for the now-casting while methods based on NWP are the best fit for longer horizons. However, it is reasonable to imagine that in the future, some improvements would make the predictions gain in efficiency. For the very short term prediction (infra-hour), it is difficult to think that a major breakthrough could happen: the sky imagers and the ad hoc prediction methods already give very good results today.

7.1 NOW-CASTING

The literature shows that Support Vector Machine (SVM), ANN, k-NN, regression tree, boosting, bagging, or random forests systematically give better results than

www.TechnicalBooksPDF.com

classical regression methods [92]. All the methods based on the use of regression trees or similar methods (boosting, bagging, or random forest) are barely used even though they give excellent results. It is not easy at this stage to draw a conclusion, but in the next 5 years, it is probable that these methods might become a reference in terms of irradiation prediction. An alternative to all the previous methods is certainly k-NN, but this should be proved. Actually, it is very difficult to propose a ranking for machine learning methods, although SVR, regression trees, boosting, bagging, and random forest seem the most efficient ones. To overcome this problem, some authors do not hesitate to combine single predictors. There are a lot of solutions that combine predictors. Often ANN is used to construct the predictors [56]. Systematically, the ensemble of predictors gives better results than a single predictor but the best methodology of hybridization is not really defined. Further works are necessary to propose a more robust method, or maybe, to prove that all the methods are equivalent. For the moment, it is not demonstrated! Several methods exist to estimate the solar radiation. Some of them are often used such as ANN, ARIMA, and naïve methods; others are begin used more frequently such as SVM, SVR, and k-mean; and others are rarely used (boosting, regression tree, random forest, etc.). Three methods will be probably used in the few next years: SVM, regression trees and random forests, because the results obtained today with these methods are very promising. The deep learning, which is a branch of machine learning based on a set of algorithms that attempt to model high-level abstractions in data by using model architecture, with complex structures or otherwise, composed of multiple nonlinear transformations, is certainly the kind of prediction models that will be abundantly studied in the near future. This research area is very recent and there is not enough experience, but in the future this kind of methodology may outperform conventional methods, as it is already the case in other predicting domains (air quality, wind, economy, etc.). As a consequence, forecasts reached through various methods can be calculated to satisfy the various needs. A question then arises how they will be put together? The answer is clearly not trivial because the various resulting forecasts show differences on many points. Moreover, some of them will be associated with confidence intervals, which should also be merged.

7.2 SIX HOURS AHEAD PREDICTION AND MORE

Three kinds of improvements should appear in the 10 next years, the first one concerns the MOS [24], the next one the improvement of NWP, and the last one the use of global irradiation measurement through the world to validate models and maybe to propose a robust methodology for all sites and horizons.

7.2.1 Model Output Statistics

MOS is an objective weather forecasting technique that consists of determining a statistical relationship between a measurement and forecast variables by a numerical model at some projection time(s). It is, in fact, the determination of the "weather-related" statistics of a numerical model. Lauret et al. [99] propose an improvement

www.TechnicalBooksPDF.com

of NWP based on a postprocessing technique to reduce systematic forecast errors. The MOS technique consists in using ground irradiance measurements to correct localized errors from NWP models. The technique gives very good results and should allow to generate a global and valuable method coupling machine learning and NWP.

7.2.2 Nonhydrostatic Atmospheric Models

The goal of the NWP use is to produce a model of solar irradiation with an error below 25% (nRMSE). Actually, the global models are not efficient but in the future, local models based on nonhydrostatic equations will allow to obtain very good forecasts (for all the horizons). Note that, with this kind of models, the time and spatial resolution can be increased and the global irradiation is available for an overall territory with a resolution upper than 500 m.

7.2.3 High Accuracy Irradiance Measurement

For all the models tested it is important to validate the output with ground measurement. The problem is obvious, but there is not enough installed sensors to validate all the model through the world map. To overcome this problem, a database such as Helioclim, for instance, should play an important role in the next few years. Indeed, Helioclim-3 regroups time series of radiation components over a horizontal, fix-tilted, and normal plane for the actual weather conditions as well for clear-sky conditions. Geographical coverage corresponds to the Meteosat satellite field of view, that is, it covers Europe, Africa, Atlantic Ocean, and Middle East. The spatial resolution is 3 km at Nadir, and approximately 4−5 km at 45° latitude. Data are available with a time step ranging from 15 min to 1 month. The time coverage is from February 2004 up to current day-2 for HC3v5 and up to day-1 for HC3v4 (http://www.soda-pro.com/fr/home).

8. CONCLUSION

This chapter has demonstrated the fundamental importance of the production forecasting for intermittent and stochastics power plants. Without reliable predictions, renewable energy will not reach a high level of integration as their management would add considerable complexity to the electricity network.

Some information about the intermittence cost, increasing the energy production cost, were introduced and a literature review is in total agreement with the fact that a reliable forecasting of the renewable production at various temporal horizons can decrease these costs and make the intermittent renewable energy more competitive.

The main forecasting methods for solar radiation have been presented and classified according to the temporal horizon. The accuracy of these methods depends on the meteorological characteristics of the site where the solar plant is installed.

At last, new perspectives of the forecasting science were shown and prove that significant progress remains to be made to reach the perfect forecasting model.

www.TechnicalBooksPDF.com

REFERENCES

[1] EurObserv'ER, Photovoltaic Barometer, 2016. April 2016, www.eurobserv-er.org.

[2] EurObserv'ER, Wind Energy Barometer, 2016. February 2016, www.eurobserv-er.org.

[3] J.B. Bart, Grands enjeux du stockage. EDF R&D, Journée MPI "Stockage de l'énergie, Toulouse, November 28, 2013. Available at: http://www.mp-i.fr/wp-content/uploads/2013/12/5_EDF-RD.pdf.

[4] D. Heinemann, E. Lorenz, M. Girodo, Forecasting of Solar Radiation. Solar Energy Resource Management for Electricity Generation from Local Level to Global Scale, Nova Science Publishers, New York, 2006.

[5] M. Saguan, L'analyse économique des architectures de marché électrique. Application au market design du "temps réel" (Ph.D. dissertation), University Paris Sud XI, 2007 (in French).

[6] R. Piwko, X. Bai, K. Clark, G. Jordan, N. Miller, J. Zimberlin, The Effect of Integrating Wind Power on Transmission System Planning, Reliability, and Operation, Prepared for the New York State Energy Research and Development Authority Albany, NY, 2005. Report March 4, 2005.

[7] G. Czisch, B. Ernst, High wind power penetration by the systematic use of smoothing effects within huge catchment areas shown in a European example, in: Proc. Wind Power 2001, AWEA, Washington, 2001.

[8] J.E. Hay, An assessment of the mesoscale variability of solar radiation at the earth's surface, Solar Energy 32 (1984) 425−434.

[9] G. Luther, The regional function energy, in: Proceedings 12th European Community Photovoltaic Solar Energy Conference, 1992, pp. 1313−1316.

[10] B. Espinar, J.L. Aznarte, R. Girard, R. Mbairadjim Moussa, G. Kariniotakis, Photovoltaic forecasting: a state of the art, in: 5th European PV-Hybrid and Mini-grid Conference, OTTI − Ostbayerisches Technologie-Transfer-Institut, Tarragona, Spain, April 2010, ISBN 978-3-941785-15-1, pp. 250−255.

[11] R. Gross, P. Heptonstall, D. Anderson, T. Green, M. Leach, J. Skea, The Costs and Impacts of Intermittency: An Assessment of the Evidence on the Costs and Impacts of Intermittent Generation on the British Electricity Network, UK Energy Research Centre Report, 2006, ISBN 1-90314-404-3.

[12] V. Lara-Fanego, J.A. Ruiz-Arias, D. Pozo-Vázquez, F.J. Santos-Alamillos, J. Tovar-Pescador, Evaluation of the WRF model solar irradiance forecasts in Andalusia (southern Spain), Solar Energy 86 (8) (2012) 2200−2217.

[13] J. Pestourie, Les EnR intermittentes: cas des réseaux insulaires, IEEE P&ES, 25/04/2013, RTE, 2013. La Défense, Paris. (in French).

[14] D. Van Hertem, The Use of Power Flow Controlling Devices in the Liberalized Market, Catholic University of Leuven Report, January 2009, ISBN 978-94-6018-024-8.

[15] EDF, Intermittent Random Renewable Energy in the Insular Energy System: Why a Maximum Integration Rate of 30%, EDF Report, 19/05/2009, CCP SEI, 2009. Available from: http://sei.edf.com/fichiers/fckeditor/Commun/SEI/corp/Pourquoi-30-dans-SEI.pdf (in French).

[16] G. Notton, Importance of islands in renewable energy production and storage: The situation of the French islands, Renew. Sustain. Energy Rev. 47 (2015) 260−269.

www.TechnicalBooksPDF.com

[17] B. Robyns, A. Davigny, C. Saudemont, A. Ansel, V. Courtecuisse, B. Francois, S. Plumel, J. Deuse, J3eA, Impact de l'éolien sur le réseau de transport et la qualité de l'énergie, vol. 5, 2006 (in French).
[18] M. Black, G. Strbac, Value of storage in providing balancing services for electricity generation systems with high wind penetration, J. Power Sources 162 (2006) 949−953.
[19] D. Anderson, M. Leach, Harvesting and redistributing renewable energy: on the role of gas and electricity grids to overcome intermittency through the generation and storage of hydrogen, Energy Policy 32 (14) (2004) 1603−1614.
[20] L. Bird, M. Milligan, D. Lew, Integrating Variable Renewable Energy: Challenges and Solutions, Technical Report, NREL/TP-6A20−60451, Contract No. DE-AC36-08GO28308, 2013.
[21] A. Moreno-Munoz, J.J.G. De la Rosa, R. Posadillo, F. Bellido, Very short term forecasting of solar radiation, in: 33rd IEEE Photovoltaic Specialists Conference, 2008. PVSC '08, 2008.
[22] S.A. Papathanassiou, N.G. Boulaxis, Power limitations and energy yield evaluation for wind farms operating in island systems, Renew. Energy 31 (2006) 457−479.
[23] M. Paulescu, E. Paulescu, P. Gravila, V. Badescu, Weather Modeling and Forecasting of PV Systems Operation, Green Energy and Technology, Springer, London, 2013.
[24] H.M. Diagne, P. Lauret, M. David, Solar irradiation forecasting: state-of-the-art and proposition for future developments for small-scale insular grids, in: Proc. WREF 2012-World Renewable Energy Forum, May 2012, Denver, United States, 2012.
[25] B. Elliston, I. MacGill, The potential role of forecasting for integrating solar generation into the Australian national electricity market, in: Solar 2010: Proc Annual Conference of the Australian Solar Energy Society, 2010.
[26] P. Lauret, C. Voyant, T. Soubdhan, M. David, P. Poggi, A benchmarking of machine learning techniques for solar radiation forecasting in an insular context, Solar Energy 112 (2015) 446−457.
[27] T.C. McCandless, S.E. Haupt, G.S. Young, Short term solar radiation forecast using weather regime dependent artificial intelligence techniques, in: 2th Conference on Artificial and Computational Intelligence and its Applications to the Environmental Sciences. February 02−06, 2014, Atlanta, USA, 2014.
[28] A. Sjoerd Brouwer, M. Van den Broek, A. Seebregts, A. Faaij, Impacts of large-scale intermittent renewable energy sources on electricity systems, and how these can be modeled, Renew. Sustain. Energy Rev. 33 (2014) 443−466.
[29] M. Milligan, P. Donohoo, D. Lew, E. Ela, B. Kirby, H. Holttinen, E. Lannoye, D. Flynn, M. O'Malle, M. Miller, P. Børre Eriksen, A. Gøttig, B. Rawn, M. Gibescu, E. Gómez Lázaro, A. Robitaille, I. Kamwa, Operating reserves and wind power integration: an international comparison preprint, in: 9th Annual International Workshop on Large-Scale Integration of Wind Power into Power Systems as well as on Transmission Networks for Offshore Wind Power Plants Conference Québec, Canada; October 18−19, 2010, 2010.
[30] H.M. Diagne, M. David, P. Lauret, J. Boland, N. Schmutz, Review of solar irradiance forecasting methods and a proposition for small-scale insular grids, Renew. Sustain. Energy Rev. 27 (2013) 65−76.
[31] G. Koeppel, M. Korpås, Improving the network infeed accuracy of non-dispatchable generators with energy storage devices, Elec. Power Syst. Res. 78 (2008) 2024−2036.
[32] D. Masa-Bote, M. Castillo-Cagigal, E. Matallanas, E. Caamaño-Martín, A. Gutiérrez, F. Monasterio-Huelín, J. Jiménez-Leube, Improving photovoltaics grid integration through short time forecasting and self-consumption, Appl. Energy 125 (2014) 103−113.

www.TechnicalBooksPDF.com

[33] M.A. Delucchi, M.Z. Jacobson, Providing all global energy with wind, water, and solar power, Part II: reliability, system and transmission costs, and policies, Energy Policy 39 (2011) 1170–1190.
[34] D. Lew, G. Brinkman, E. Ibanez, B.M. Hodge, M. Hummon, A. Florita, M. Heaney, G. Stark, J. King, N. Kumar, S. Lefton, D. Agan, G. Jordan, S. Venkataraman, Western Wind and Solar Integration Study Phase 2 (WWSIS-2), NREL/TP-5500–55588, National Renewable Energy Laboratory, Golden, CO, 2013.
[35] H. Holttinen, P. Meibom, A. Orths, B. Lange, M. O'Malley, J. Olav Tande, A. Estanqueiro, E. Gomez, L. Söder, J.C. Strbac Smith, F. Van Hulle, Impacts of large amounts of wind power on design and operation of power systems, Wind Energy 14 (2) (2011) 179–192.
[36] M. Milligan, B. Kirby, Calculating Wind Integration Costs: Separating Wind Energy Value from Integration Cost Impacts, 2009. NREL Technical Report TP-550–46275.
[37] M. Milligan, E. Ela, B.M. Hodge, B. Kirby, D. Lew, C. Clark, J. DeCesaro, K. Lynn, Integration of variable generation, cost-causation, and integration costs, Electricity Journal 24 (9) (2011) 51–63.
[38] W. Katzenstein, J. Apt, The cost of wind power variability, Energy Policy 51 (2012) 233–243.
[39] H. Holttinen, M. O'Malley, J. Dillon, D. Flynn, A. Keane, H. Abildgaard, L. Söder, Steps for a complete wind integration study, in: Proc 46th Hawaii International Conference on System Sciences, 2013, pp. 2261–2270.
[40] L. Hirth, I. Ziegenhagen, Balancing power and variable renewables: three links, Renew. Sustain. Energy Rev. 50 (2015) 1035–1051.
[41] C.A. Lueken, Integrating Variable Renewables into the Electric Grid: An Evaluation of Challenges and Potential Solutions (Ph.D. dissertation in Engineering and Public Policy), Carnegie Mellon University, Pittsburgh, PA, December 2012.
[42] J. Logan, S. Mark Kaplan, Wind power in the United States: Technology, Economic and Policy Issues, Congressional Research Service Reports, Paper 58, 2008.
[43] B. Parsons, M. Milligan, J.C. Smith, E. DeMeo, B. Oakleaf, K. Wolf, M. Schuerger, R. Zavadil, M. Ahlstrom, D. Yen Nakafuji, Grid impacts of wind power variability: recent assessments from a variety of utilities in the United States, in: Proc. European Wind Energy Conference. Athens, Greece, 2006.
[44] R. Wiser, M. Bolinger, Wind Technologies Market Report, USDOE, 2008.
[45] E.A. DeMeo, G.A. Jordan, C. Kalich, J. King, M.R. Milligan, C. Murley, B. Oakleaf, M.J. Schuerger, Accommodating wind's natural behaviour, IEEE Power Energy Mag. 5 (6) (2007) 59–67.
[46] P.J. Luickx, E.D. Delarue, W.D. D'haeseleer, Impact of large amounts of wind power on the operation of an electricity generation system: Belgian case study, Renew. Sustain. Energy Rev. 14 (2010) 2019–2028.
[47] K. Porter, J. Rogers, Survey of Variable Generation Forecasting in the West, National Renewable Energy Laboratory, 2012.
[48] C. Hilger, in: Eltra, at the Fuel and Energy Technical Association Conference on "Challenges from the Rapid Expansion of Wind Power" on 3rd April 2005, 2005.
[49] K. Parks, Xcel Energy/NCAR Wind Energy Forecasting System, Talk on the UWIG Forecasting Workshop, Albany (US), February 23–24, 2011.

www.TechnicalBooksPDF.com

[50] Western Governors' Association (WGA), Meeting Renewable Energy Targets in the West at Least Cost: The Integration Challenge, Western Governors' Association, Denver, CO, 2012.
[51] G.E. Energy, Western Wind and Solar Integration Study (WWSIS), NREL/SR-550−47434, National Renewable Energy Laboratory, Golden, CO, 2010.
[52] K. Orwig, B.M. Hodge, G. Brinkman, E. Ela, M. Milligan, V. Banunarayanan, S. Nasir, J. Freedman, Economic evaluation of short-term wind power forecasts in ERCOT: preliminary results, in: 11th Annual International Workshop on Large-Scale Integration of Wind Power into Power Systems as well as on Transmission Networks for Offshore Wind Power Plants Conference, Lisbon, Portugal, November 13−15, 2012, 2012. NREL/CP-5500-56257.
[53] E.V. Mc Garrigle, P.G. Leahy, Quantifying the value of improved wind energy forecasts in a pool-based electricity market, Renew. Energy 80 (2015) 517−524.
[54] D. Lew, M. Milligan, G. Jordan, D. Piwko, The Value of Wind Power Forecasting Preprint, Prepared for the American Meteorological Society Annual Meeting, January 26, 2011. NREL/CP-5500−50814, National Renewable Energy Laboratory, Golden, CO, 2011.
[55] R. Piwko, The value of wind power forecasting, in: Utility Wind Integration Group Workshop on Wind Forecasting Applications for Utility Planning and Operations, February 18−19, 2009, 2009.
[56] C. Voyant, G. Notton, S. Kalogirou, M.L. Nivet, C. Paoli, F. Motte, A. Fouilloy, Machine learning methods for solar radiation forecasting: a review, Renew. Energy 105 (2017) 569−582.
[57] S. Sperati, S. Alessandrini, P. Pinson, G. Kariniotakis, The "Weather Intelligence for Renewable Energies" benchmarking exercise on short-term forecasting of wind and solar power generation, Energies 8 (2015) 9594−9619.
[58] COST, Weather Intelligence for Renewable Energies (WIRE), Current State Report No. ES1002, 2012.
[59] S. Pelland, J. Remund, J. Kleissl, T. Oozeki, K. De Brabandere, Photovoltaic and Solar Forecasting: State of the Art. IEA PVPS Task 14, Subtask 3.1, 2013. Report IEA-PVPS T14-01.
[60] J. Najac, Wind and photovoltaic production forecasting in EDF, in: In'Tech Seminar, INRIA, Grenoble, France, 2012 (in French).
[61] Reuniwatt (2017). Website reuniwatt.com (consulted in April 2017).
[62] C.W. Chow, B. Urquhart, J. Kleissl, M. Lave, A. Dominguez, J. Shields, B. Washom, Intra-hour forecasting with a total sky imager at the UC San Diego solar energy testbed, Solar Energy 85 (11) (2011) 2881−2893.
[63] T. Tooman, Whole Sky Imager Retrieval Guide, U.S. Dept. Energy, Washington, DC, 1997.
[64] C.N. Long, D.W. Slater, T. Tooman, Total Sky Imager Model 880 Status and Testing Results, DOE/SC-ARM/TR-006 Report, U.S. Dept. Energy, 2001.
[65] B. Thurairajah, Thermal Infrared Imaging of the Atmosphere: The Infrared Cloud Imager (Ph.D. dissertation), Montana State University − Bozeman, College of Engineering, 2004.
[66] S. Lespinats, G. Stoops, T. Pistarino, X. Le Pivert, Forecasting the solar production from a plurality of sources, in: 29th European Photovoltaic Solar Energy Conference and Exhibition, 2014.

www.TechnicalBooksPDF.com

[67] M.S. Ghonima, B. Urquhart, C.W. Chow, J.E. Shields, A. Cazorla, J. Kleissl, A method for cloud detection and opacity classification based on ground based sky imagery, Atmos. Meas. Tech. Discuss. 5 (4) (2012) 4535−4569.
[68] B. Thurairajah, J.A. Shaw, Cloud statistics measured with the infrared cloud imager (ICI), Geosci. Rem. Sens. 43 (2005) 2000−2007.
[69] R. Marquez, V.G. Gueorguiev, C.F.M. Coimbra, Forecasting of global horizontal irradiance using sky cover indices, J. Solar Energy Eng. 135 (2013).
[70] D. Yang, P. Jirutitijaroen, W.M. Walsh, Hourly solar irradiance time series forecasting using cloud cover index, Solar Energy 86 (2012) 3531−3543.
[71] H. Yang, B. Kurtz, D. Nguyen, B. Urquhart, C. Wai Chow, M. Ghonima, J. Kleissl, Solar irradiance forecasting using a ground-based sky imager developed at UC San Diego, Solar Energy 103 (2014) 502−524.
[72] R. Marquez, C.F.M. Coimbra, Intra-hour DNI forecasting based on cloud tracking image analysis, Solar Energy 91 (2013) 327−336.
[73] A. Hammer, D. Heinemann, C. Hoyer, R. Kuhlemann, E. Lorenz, R. Müller, H.G. Beyer, Solar energy assessment using remote sensing technologies, Rem. Sens. Environ. 86 (2003) 423−432.
[74] J. Betcke, R. Kuhlemann, A. Hammer, A. Drews, E. Lorenz, M. Girodo, W. Krebs, Energy-Specific Solar Radiation Data from Meteosat Second Generation (MSG): The Heliosat-3 Project, Energy and Semiconductor Research Laboratory, 2006. Technical Report of the Heliosat-3 Project (D17).
[75] K.F. Dagestad, Mean bias deviation of the Heliostat algorithm for varying cloud properties and sun-ground-satellite geometry, Theor. Appl. Technol. 79 (2004) 215−224.
[76] K.F. Dagestad, Estimating Global Radiation at Ground Level from Satellite Images (Ph.D. dissertation), Dept. of Meteorology, University of Bergen, Norway, 2005.
[77] K.F. Dagestad, J.A. Olseth, An Alternative Algorithm for Calculating the Cloud Index, 2005. Heliosat-3 Projekt-Bericht.
[78] R.W. Mueller, K.F. Dagestad, P. Ineichen, M. Schroedter-Homscheidt, S. Cros, D. Dumortier, R. Kuhlemann, J.A. Olseth, G. Piernavieja, C. Reise, L. Wald, D. Heinemann, Rethinking satellite-based solar irradiance modelling: The SOLIS clear-sky module, Rem. Sens. Environ. 91 (2004) 160−174.
[79] K.M. Bedka, J.R. Mecikalski, Application of satellite-derived atmospheric motion vectors for estimating mesoscale flows, J. Appl. Meteor. 44 (2005) 1761−1772.
[80] J.L. Bosch, Y. Zheng, J. Kleissl, Deriving cloud velocity from an array of solar radiation measurements, Solar Energy 87 (2013) 196−203.
[81] C.S. Velden, T.L. Olander, S. Wanzong, The impact of multi-spectral GOES-8 wind information on Atlantic tropical cyclone track forecasts in 1995. Part I: Dataset methodology, description, and case analysis, Mon. Wea. Rev. 126 (1998) 1202−1218.
[82] E. Lorenz, J. Kühnert, A. Hammer, D. Heinemann, Satellite Based Short Term Forecasting, Summer School "From Renewable Energy Production to End Users" 2.5. 2013, Montegut, France, 2013.
[83] R. Perez, S. Kivalov, J. Schlemmer, K. Hemker Jr., D. Renné, T.E. Hoff, Validation of short and medium term operational solar radiation forecasts in the US, Solar Energy 84 (2010) 2161−2172.
[84] R. Perez, S. Kivalov, A. Zelenka, J. Schlemmer, K. Hemker Jr., Improving the performance of satellite-to-irradiance models using the satellite's infrared sensors, in: Proc., ASES Annual Conference, 2010.

www.TechnicalBooksPDF.com

[85] R. Marquez, H.T.C. Pedro, C.F.M. Coimbra, Hybrid solar forecasting method uses satellite imaging and ground telemetry as inputs to ANNs, Solar Energy 92 (2013) 176−188.
[86] P. Bacher, H. Madsen, H.A. Nielsen, Online short-term solar power forecasting, Solar Energy 83 (10) (2009) 1772−1783.
[87] A. Mellit, S.A. Kalogirou, Artificial intelligence techniques for photovoltaic applications: a review, Progr. Energy Combust. Sci. 34 (2008) 547−632.
[88] A. Sfetsos, A.H. Coonick, Univariate and multivariate forecasting of hourly solar radiation with artificial intelligence techniques, Solar Energy 68 (2000) 169−178.
[89] R. Bourbonnais, M. Terraza, Analyse des séries temporelles: application à l'économie et à la gestion, second ed., Dunod Edition, Paris, 2008.
[90] P.J. Brockwell, R.A. Davis, Time Series: Theory and Methods, second ed., Springer-Verlag, New York, 1991.
[91] C. Voyant, P. Randimbivololona, M.L. Nivet, C. Paoli, M. Muselli, 24-hours Ahead Global Irradiation Forecasting Using Multi-layer Perceptron. Meteorological Applications, Wiley, 2013.
[92] C. Voyant, C. Paoli, M. Muselli, M.-L. Nivet, Multi-horizon solar radiation forecasting for Mediterranean locations using time series models, Renew. Sustain. Energy Rev. 28 (2013) 44−52.
[93] J.D. Hamilton, Time Series Analysis, Princeton University Press, 1994, ISBN 0-691-04289-6.
[94] G. Reikard, Predicting solar radiation at high resolutions: a comparison of time series forecasts, Solar Energy 83 (3) (2009) 342−349.
[95] A. Hammer, D. Heinemann, C. Hoyer-Klick, E. Lorenz, B. Mayer, M. Schroedter-Homscheidt, Remote Sensing and Atmospheric Physics for an Efficient Use of Renewable Energies, Status Report 2004−2007, Technical Report, Virtual Institute of Energy Meteorology, 2007.
[96] J. Remund, R. Perez, E. Lorenz, Comparison of solar radiation forecast for the USA, in: 23rd European Photovoltaic Solar Energy Conference, Valencia (Spain), September 1−5, 2008, 2008, pp. 3141−3143.
[97] R. Perez, K. Moore, S. Wilcox, D. Renné, A. Zelenka, Forecasting solar radiation−preliminary evaluation of an approach based upon the national forecast database, Solar Energy 81 (6) (2007) 809−812.
[98] E. Lorenz, J. Remund, S.C. Müller, W. Traunmüller, G. Steinmaurer, D. Pozo, J.A. Ruiz-Arias, V.L. Fanego, L. Ramirez, M.G. Romeo, C. Kurz, L.M. Pomares, C.G. Guerrero, Benchmarking of different approaches to forecast solar irradiance, in: 24th European Photovoltaic Solar Energy Conference, Hamburg, Germany, September 21−25, 2009, 2009.
[99] P. Lauret, M. Diagne, M. David, A neural network post-processing approach to improving NWP solar radiation forecasts, Energy Procedia 57 (2014) 1044−1052.

www.TechnicalBooksPDF.com

CHAPTER

4 Performance of MPPT Techniques of Photovoltaic Systems Under Normal and Partial Shading Conditions

Ali M. Eltamaly[1,2]

Electrical Engineering Department, College of Engineering, King Saud University, Riyadh, Saudi Arabia[1]*; Al-Mansoura University, Al-Mansoura, Egypt*[2]

CHAPTER OUTLINE

1. Introduction 116
1.1 Direct-Coupled Method 117
1.2 Constant-Voltage MPPT 117
1.3 Constant-Current MPPT 118
1.4 Perturb and Observe Technique 118
1.5 Incremental Conductance Technique 118
1.6 Parasitic Capacitance Algorithm 120
1.7 Ripple Correlation Control 120
1.8 Hill Climbing Technique 121
1.9 Fuzzy Logic Controller as MPPT 122
1.10 Particle Swarm Optimization MPPT Technique 122
2. PV System Under Nonshading Conditions 124
2.1 Simulation of PV System 124
2.1.1 Photovoltaic Cell Model 124
2.1.2 Battery and Load Model 128
2.1.3 Boost Converter Model 130
2.1.4 Model of Calculating E *and* ΔE 131
2.1.5 Fuzzy Logic Controller Model 132
2.2 Simulation Results 135
2.3 Experimental Work 137
2.3.1 Hardware Implementation of Boost Circuit 138
2.3.2 Sensors and Driver Circuits 142
3. Smart Maximum Power Point Tracker Under Partial Shading Conditions 144
3.1 Partial Shading Effect 144

Advances in Renewable Energies and Power Technologies. https://doi.org/10.1016/B978-0-12-812959-3.00004-6
Copyright © 2018 Elsevier Inc. All rights reserved.

www.TechnicalBooksPDF.com

3.2 Mismatch Power Loss 148
3.3 Simulation of Proposed Systems 150
4. Conclusions 156
References 157

1. INTRODUCTION

The production of electric energy from photovoltaic (PV) has a lot of applications as in space satellites and orbital stations, solar vehicles, power supply for loads in remote areas, street lighting systems, and generation of electric power in central power stations. PV is environmental friendly and has no emission of harmful gasses as the emission associated with conventional electricity generation.

For each radiation and temperature, the power generated from PV is variable with its terminal voltage as shown in Fig. 4.1. This figure reveals that there is only one maximum power point (MPP) associated with each radiation and temperature. By forcing the PV array to work at the voltage corresponding to MPP will substantially increase the energy produced. This increase in the energy production can be translated into cost reduction of the PV power system, which shows the importance of MPP tracker, maximum power point tracking (MPPT). Tracking MPP needs a fast and smart controller system to counteract the fast change in weather data or load changes.

MPPT consists of two basic components, dc–dc converter and its controller, which is shown in Fig. 4.2. Many techniques have been introduced to catch the MPP. These techniques differ in their complexity, cost, efficiency, response, and robustness. A survey showing comparison of some of PV MPPT techniques is shown

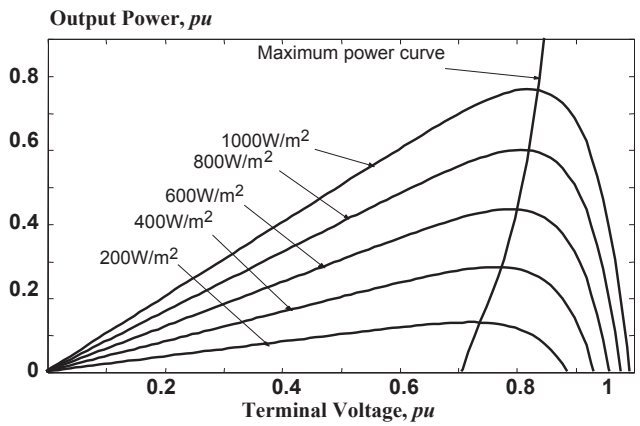


FIGURE 4.1

P–V characteristics of photovoltaic (PV) module.

www.TechnicalBooksPDF.com

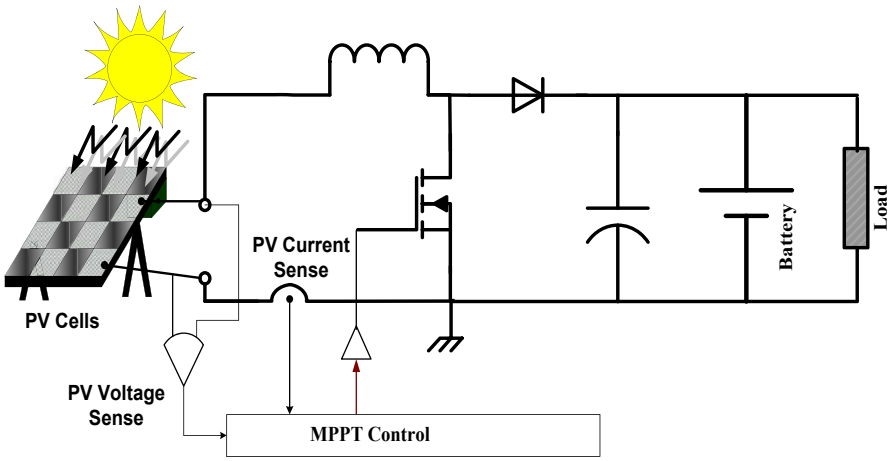


FIGURE 4.2

PV energy system with maximum power point tracking (MPPT) system.

in Esram and Chapman and Salas et al. [1,2], and it will be introduced and discussed in the following sections.

1.1 DIRECT-COUPLED METHOD

In the direct-coupled method [3–5], the PV array is connected directly to the loads without power modifier. To match the MPPs of the solar array as closely as possible, it is important to choose the solar array characteristics according to the characteristics of the load. The direct-coupled method cannot automatically track the MPPs of the solar array when the insulation, temperature, or, load changed.

1.2 CONSTANT-VOLTAGE MPPT

It is clear from the P–V curve of Fig. 4.1 that the ratio of the array's maximum power voltage, V_{mp}, to its open-circuit voltage, V_{oc}, is approximately constant. So, the PV array can be forced to work as a ratio of its open-circuit voltage. The literature reports success with 73%–80% from V_{oc} [6–9]. The implementation of this technique can be obtained by temporarily isolating the solar cells from the MPPT, and a V_{oc} measurement is taken. Next, the MPPT calculates the correct operating point and adjusts the array's voltage until the calculated V_{mp} is reached. This technique is very simple to be implemented but it has two major problems. The first one is the difficulty to choose the optimal value of the constant—the ratio between V_{mp} and V_{oc}—the other one is the momentary interruption of PV power to determine the open-circuit voltage. The later difficulty can be overcome by using pilot cells.

www.TechnicalBooksPDF.com

1.3 CONSTANT-CURRENT MPPT

It is also observed that, the relation between the short-circuit current and the current associated with the maximum power is approximately constant. So, it is possible to use a constant-current MPPT algorithm that approximates the MPP current as a constant ratio of the short-circuit current [10,11]. The short-circuit current is measured and the MPP current is calculated, and the PV array output current is then adjusted by the MPPT until the calculated MPP current is reached. This technique faces the same problems of the constant-voltage technique. However, constant-voltage control is normally favored because the measurement of the open-circuit voltage is much simple than the short-circuit current. The momentary interruption in the constant voltage or current can be avoided by using a pilot cell [12].

1.4 PERTURB AND OBSERVE TECHNIQUE

The Perturb-and-Observe (P&O) technique works by perturbing the PV system by incrementing the array operating voltage and observing its impact on the array output power. Because of constant step width, the system faces high oscillation especially under unstable environmental conditions. Some techniques used waiting time to avoid high oscillation; however, it also makes the MPPT slower to respond to weather changes. Also, this technique suffers from wrong operation, especially in case of multiple local maxima when working in partial shading conditions. A lot of modifications for this technique have been presented in literature [13–21]. P&O is the most frequently used technique to track the maximum power because of its simple structure [22]. The flowchart of P&O is shown in Fig. 4.3 [23]. A common problem in this technique is that the PV module terminal voltage is perturbed every MPPT cycle. Therefore, when the MPP is reached, the output power oscillates around its MPP, resulting in power loss in the PV system. A modified P&O technique has been introduced in [24] to remedy this problem by multiplying the change in the duty ratio by dynamic constant depending on the previous change in the extracted power. Another technique [25] used artificial neural network to predict this multiplying constant. These techniques increase the complexity of the system and may cause more oscillations in stable weather conditions.

1.5 INCREMENTAL CONDUCTANCE TECHNIQUE

Among all the MPPT strategies, the incremental conductance (IncCond) technique is widely used because of the high tracking accuracy at steady state and good adaptability to the rapidly changing atmospheric conditions [26]. The IncCond method [27–31] is based on comparing the instantaneous panel conductance with the incremental panel conductance. The input impedance of the dc–dc converter is matched with optimum impedance of PV panel. This technique requires more sensing equipment and sophisticated control system. The slope of the PV array power curve is zero at the MPP, positive for values of output power smaller than MPP, and negative for values of the output power greater than MPP. The derivative of the PV module power

www.TechnicalBooksPDF.com

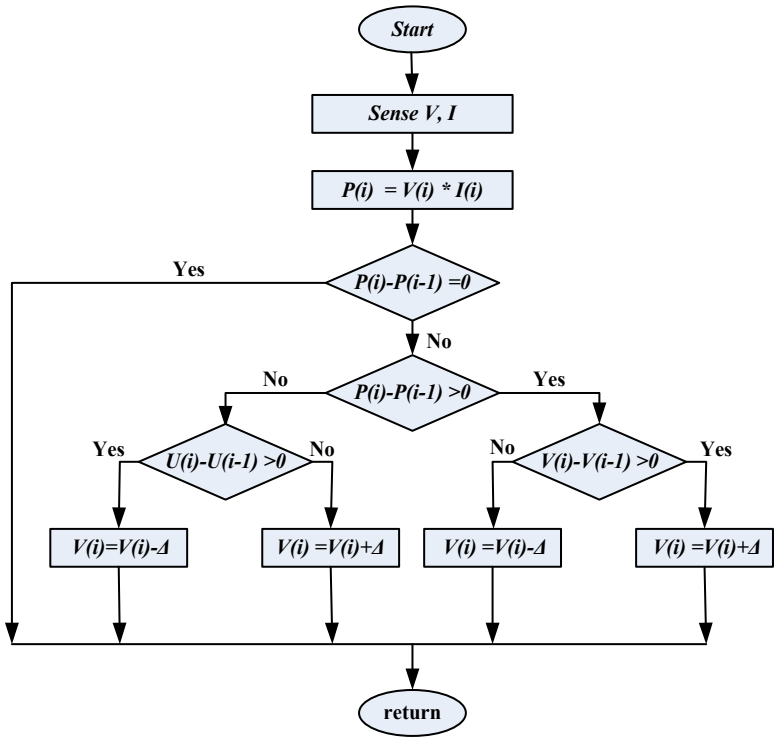


FIGURE 4.3

State flowchart of perturb-and-observe MPPT technique.

is given as in Eq. (4.1), and the resultant equation for the error e is as in Eq. (4.2) [23,32,33]. Tracking the MPP requires the following procedure as shown in Fig. 4.4.

$$\frac{dP}{dV} = \frac{d(V \times I)}{dV} = I + V\,\frac{dI}{dV} = 0 \tag{4.1}$$

also, $$\frac{dI}{dV} + \frac{I}{V} = \frac{I(i) - I(i-1)}{V(i) - V(i-1)} + \frac{I(i)}{V(i)} = 0$$

$$e = \frac{I(i) - I(i-1)}{V(i) - V(i-1)} + \frac{I(i)}{V(i)} \tag{4.2}$$

It can be implemented by a simple discrete integrator with the error signal e considered as the input and a scaling factor. The function of the scaling factor is to adapt the error signal e to a proper range before the integral compensator. Because the error signal e becomes smaller as the operating point approaches the MPP, an adaptive and smooth tracking can be achieved [32]. A modified dynamic change in step size for IncCond is introduced to effectively improve the MPPT speed and accuracy simultaneously [34]. This technique improves the performance of the IncCond technique but it increases the complexity of the control system.

www.TechnicalBooksPDF.com

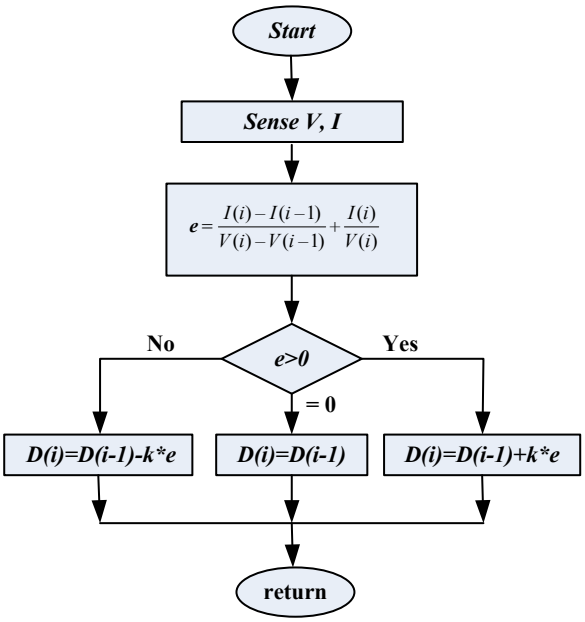


FIGURE 4.4

State-flow chart of Incremental Conductance MPPT technique.

1.6 PARASITIC CAPACITANCE ALGORITHM

The parasitic capacitance algorithm [35] is similar to IncCond technique except that the effect of the solar cells' parasitic junction capacitance, which models charge storage in the p—n junctions of the solar cells, is included.

1.7 RIPPLE CORRELATION CONTROL

Ripple Correlation Control (RCC) [36] uses ripple in PV voltage and current to perform MPPT. RCC correlates the time derivative of the time-varying PV array power with the time derivative of the time-varying PV array current or voltage to drive the power gradient to zero, thus reaching the MPP. Simple and inexpensive analog circuits can be used to implement RCC. An example is given in Midya et al. [37]. Experiments were performed to show that RCC accurately and quickly tracks the MPP, even under varying irradiance levels. The time taken to converge to the MPP is limited by the switching frequency of the power converter and the gain of the RCC circuit. Another advantage of RCC is that it does not require any prior information about the PV array characteristics, making its adaptation to different PV systems straightforward.

www.TechnicalBooksPDF.com

1.8 HILL CLIMBING TECHNIQUE

The advantage of the hill climbing (HC) MPPT technique is its simplicity [38,39]. It uses the duty cycle of boost converter as the judging parameter when the task of the MPPT is implemented. When the condition $dP/dD = 0$ is accomplished, it represents that the MPP has been tracked [38]. The flow diagram of the HC algorithm is shown in Fig. 4.5. The duty cycle in every sampling period is determined by the comparison of the power at present time and previous time. If the incremental power $dP > 0$, the duty cycle should be increased to make $dD > 0$. If $dP < 0$, the duty cycle is then reduced to make $dD < 0$. The main problem associated with this technique is because of the tradeoff between the stability of the system in constant radiation period and the fast response in rapidly changing radiation. Where, the constant radiation period needs very small value of change in duty ratio, ΔD to prevent high oscillation of power around the MPP which reduce the energy captured from PV and the rapidly changing radiation needs higher value of duty ratio for fast tracking the maximum power. A modified HC technique has been introduced [38] to remedy this problem by multiplying the change in the duty ratio by dynamic constant depending on the previous change in the extracted power as shown in Eq. (4.1). The flowchart of this technique is shown in Fig. 4.5.

HC technique can be implemented by using proportional integrator differentiation controller or by using fuzzy logic controller (FLC). This technique requires

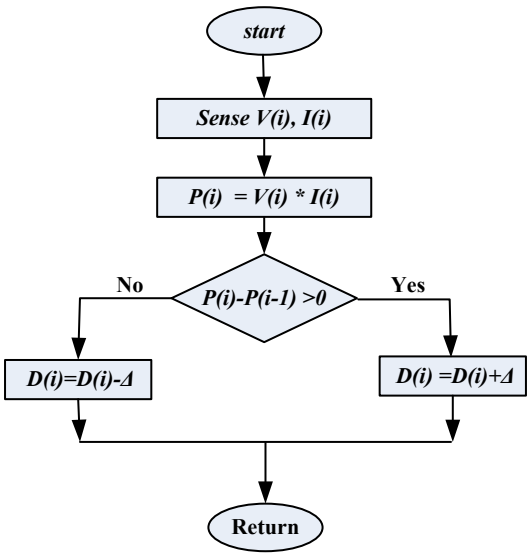


FIGURE 4.5

State flow chart of hill climbing MPPT technique.

www.TechnicalBooksPDF.com

two sensors to measure the PV array voltage and current from which power is computed or only one voltage sensor and the PV array current from the PV array voltage is estimated.

The tuning factor of the change in the duty ratio of modified HC technique can be obtained from the following equation [23]:

$$M = \frac{|\Delta D|}{|\Delta P|} \tag{4.3}$$

where ΔP represents the change of output power and ΔD represents the change in duty ratio.

1.9 FUZZY LOGIC CONTROLLER AS MPPT

FLC has been introduced in many researches as in [40–47] to force the PV to work around MPP. FLC has the advantages of working with imprecise inputs, not needing an accurate mathematical model, and handling nonlinearity. FLC generally consists of three stages: *fuzzification*, *aggregation*, and *defuzzification*. During fuzzification, numerical input variables are converted into a membership function. The output of the systems has linguistic relations with the inputs of the system. These relations are called rules and the output of each rule is a fuzzy set. More than one rule is used to increase conversion efficiency. Aggregation is the process whereby the output fuzzy sets of each rule are combined to make one output fuzzy set. Afterward, the fuzzy set is defuzzified to a crisp output in the defuzzification process.

1.10 PARTICLE SWARM OPTIMIZATION MPPT TECHNIQUE

Particle Swarm Optimization (PSO) is one of the swarm intelligence techniques that uses stochastic variables based on population for solving optimization problems. This technique was first introduced by Eberhart and Kennedy in (1995) [48]. The study to use PSO in MPPT of PV systems was by Miyatake et al. in 2004 [49]. A wide range of studies have been done in the same area. PSOs are inspired by the social swarming behavior of fish schooling or bird's flocking. PSO evolutionary process, potential solutions, called particles, move about the multidimensional search space by following and tracking the current best particle position in the swarm. The operation of PSO technique can be outlined in the following [27]:

Each particle in the swarm has mainly two variables associated with it. These variables are: the position vector $x_i(t)$ and the velocity vector $v_i(t)$ as shown in Eq. (4.4). Thus, each particle $x_i(t)$ is represented by a vector $[x_{i1}(t), x_{i2}(t),\ldots,x_{iD}(t)]$, where i is the index number of each particle in the swarm, D represents the dimension of the search space, and t is the iteration number.

$$x_i(t+1) = x_i(t) + v_i(t+1) \tag{4.4}$$

www.TechnicalBooksPDF.com

The current position $x_i(t)$, the particle velocity $vi(t)$, and the global best position $G_i(t)$ are used to determine the new position of the particle by calculating the velocity as shown in the following equation:

$$v_i(t+1) = \underbrace{\omega(t)v(t)}_{\text{Inertial parameters}} + \underbrace{c_1 r_1 (P_i(t) - x_i(t))}_{\text{Personal best velocity components}} + \underbrace{c_2 r_2 (G_i(t) - x_i(t))}_{\text{Global best velocity component}} \tag{4.5}$$

where $\omega(t)$ is the inertia weight factor that controls the exploration of the search space. The value of $\omega(t)$ can be chosen as a constant value equal to 0.5 or as a variable value to accelerate the GP obtained [50]. c_1 and c_2 are the acceleration constants, which provide a weight for the individual and social components GP, respectively. c_1 is called self-confidence, range: 1.5−2; and c_2 is called swarm confidence, range: 2−2.5 [51].

In using PSO in MPPT of PV system, the duty ratio has been used as particle position and the increment change in duty ratio as the velocity. The fitness function is the model for the PV system.

A modified PSO technique called Deterministic PSO (DPSO) [52,53] has be used to improve the performance of MPPT under partial shading component. In this technique, the random numbers in the acceleration factor of the conventional PSO velocity equation have been removed. Additionally, the change in the velocity values has been restricted to be within a certain value. This research used the experience about P−V curve under partial shading conditions to impose the limits of the maximum velocity of each particle and the maximum allowable duty ratio depending on the resistance of the load and the internal impedance of the PV system, which add a complexity to the proposed technique and may skip GP out of this limits. Also, the preset values need previous experience about the size and configuration of PV system and it may not be suitable for any future extension of the size of the PV system without a modification of the optimization parameter. Also, in this paper hill climbing (HC-MPPT) will be used in uniform distribution of insulation on the PV system but DPSO will be used in case of partial shading conditions. Authors used three branches in parallel and four PV modules in series. They used the current in each branch to distinguish the shading condition depending on the difference in the current between each branch. But shading can exist in each branch in the same pattern, so the criteria will not catch partial shading. The only way to catch shading is to have current and voltage sensors for each PV cell, which may increase the cost of PV system considerably.

Another PSO research [54] proposed a great idea of using some particles to locate the local peak (LP) and some other particles to look for GP. The particle search around the LP will ensure the smooth search of the MPP. Meanwhile, the particle search for GP will ensure the system catches the GP but these particles may cause the system to work in some places away from maximum, which can cause instability of the system and cause unpredicted values away from real GP. This technique needs more consideration about the system stability; also, this

www.TechnicalBooksPDF.com

technique imposed a complexity especially with online systems like MPPT of PV system.

The main problem in the real operation of PSO is the use of random values on the PV system, which can affect the stability of the system. Also, the main concern in using PSO technique in MPPT of PV system is to have lower number of particles to achieve consistent solution. Using conventional PSO will not achieve this requirement as fast as required. So, fast technique to get optimum duty change will be helpful in increasing the stability of the PV system. A modified PSO (MPSO) technique [50,55] has been used to modify the inertia weight, ω using genetic algorithm principals. The modified inertia weight ω can be obtained from the following equation, which increases the value of inertia weight ω for the beginning and reduce it for precise increment at the end of optimization.

$$\omega(k) = \omega_s - (\omega_s - \omega_e)(T_m - k)/T_m \tag{4.6}$$

where ω_s is the initial inertia weight, ω_e is the inertia weight when reaching maximum inertia times, and T_m is the maximum inertia times.

2. PV SYSTEM UNDER NONSHADING CONDITIONS

2.1 SIMULATION OF PV SYSTEM

The proposed system has been simulated using a Simulink that comes with Matlab software package. In the proposed system, the simulation has been carried out using three different techniques for comparison. In the first technique, a Matlab file has been used to calculate the theoretical MPP of the power curve. In the second technique, a constant terminal voltage of the PV is introduced. This voltage is chosen to be the constant voltage that corresponds to the highest possible output power in the normal operating range. In the last technique, an FLC has been used to track the MPP. The simulation model of the proposed system using Matlab/Simulink program is shown in Fig. 4.6. The simulation of the proposed system contains submodels that can be explained in the following sections.

2.1.1 Photovoltaic Cell Model

PV cell is a p−n junction that can absorb photons in the light to generate electric power by the so-called PV effect. The generated power depends on the radiation level of the sunlight, temperature, and the terminal voltage of PV cell. Several kinds of materials have been used to fabricate the PV cells, which differ in their characteristics from one type to another. Crystalline silicon PV cells are the most widely used [56]. Crystalline silicon PV cells have been used for a long time and it became mature technology. Its price became lower and lower especially with mass-fraction production. For this reason, this kind of PV cells will be considered in this paper. Other kind of PV cells have the same analysis but with different performance characteristics.

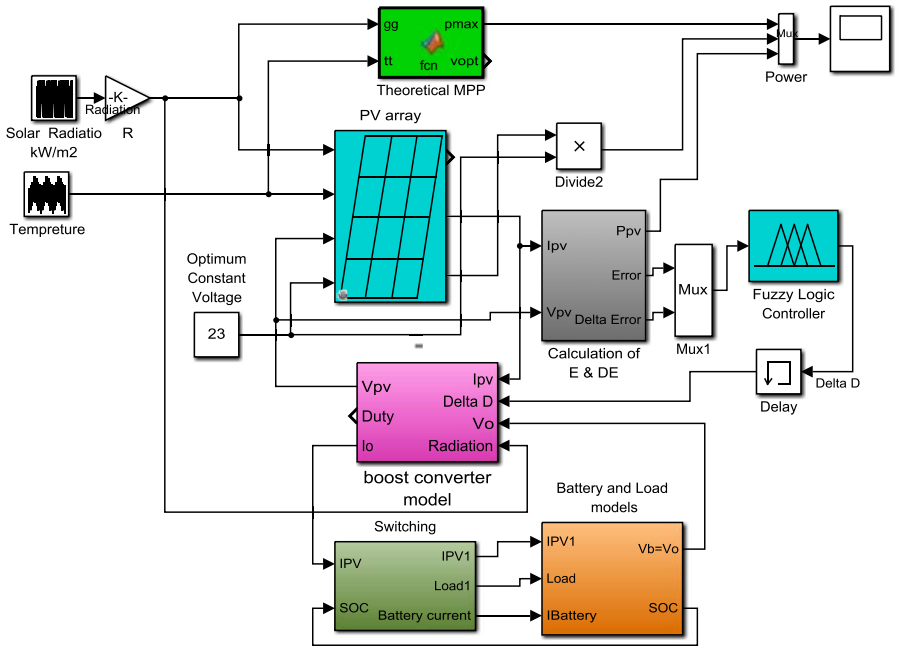


FIGURE 4.6

Simulink simulation model of the PV system with fuzzy logic controller (FLC) as MPPT.

A wide variety of research work have been done to implement a mathematical model for PV cell. The two-diode model has been used in many studies [57–59]. This model of PV cell is shown in Fig. 4.7 and Eq. (4.7). This model is very accurate but it needs intensive mathematical manipulation.

$$I = I_{PH} - I_{sat1} * \left[e^{\left(\frac{q}{KT}(V+R_sI)\right)} - 1 \right] - I_{sat2} * \left[e^{\left(\frac{q}{2KT}(V+R_sI)\right)} - 1 \right] - \frac{V + R_sI}{R_{sh}} \tag{4.7}$$

One-diode model is a widely used model than the two-diode model for PV cell simulation because of its simplicity with acceptable accuracy and its parameter can

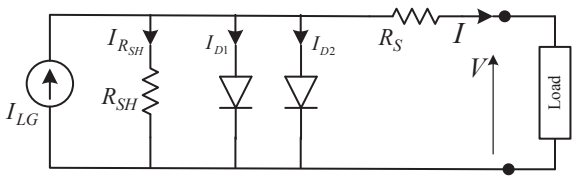


FIGURE 4.7

Equivalent circuit of photovoltaic cell (two diodes model).

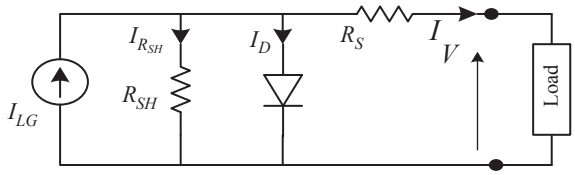


FIGURE 4.8

Equivalent circuit of photovoltaic cell (one diode model).

be obtained experimentally with simple and accurate techniques [52,60]. For this reason, this model will be used in this paper. This model of PV cell is shown in Fig. 4.8 and Eq. (4.8).

$$I = I_{PH} - I_{sat1} * \left[e^{\left(\frac{q}{KT}(V+R_sI)\right)} - 1 \right] - \frac{V + R_sI}{R_{sh}} \tag{4.8}$$

where I, array output current; V, array output voltage; P, array output power; $P_{\max}$, maximum output power; I_{sat1}, I_{sat2}, saturation currents of the first and second diodes; T, array temperature in K; I_{PH}, light-generated current; K, Boltzmann constant; R_s, R_{sh}, series and shunt resistors of PV model; I_{LG}, internal generated current of PV cell; I_{D1}, I_{D2}, currents of the first and second diodes.

The PV simulator uses the radiation, temperature, and output current from PV to determine the corresponding PV curve by using Eq. (4.8) and as shown in Fig. 4.1. The output power from PV is the result from multiplying PV terminal voltage and its output current.

Another method that can be used to model PV cells has been used in some studies such as the piecewise-linear parallel branches that uses linear models to model different parts of the I−V curve of a PV cell [61]. Also, other models are based on driving equation in terms of open-circuit voltage and short-circuit current [62].

The relation between the output power and terminal voltage for different radiations and temperatures is shown in Fig. 4.1, where each curve represents certain radiation and temperature. It is clear from this figure that the MPPs are located at different terminal voltages. For this reason, a wide variety of MPPTs have been developed and discussed in many studies such as that by Rezk and Eltamaly [23]. The PV cell model is based on the single-diode representation of a silicon PV cell as illustrated in Fig. 4.8 [23,63].

The governing equations, which describe the I−V characteristics of a crystalline silicon PV cell as described in [63], are presented as follows:

The PV cell current, I_{PVC} is obtained by applying Kirchhoff's current law to the PV cell circuit shown in Fig. 4.8.

$$I_{\mathrm{PVC}} = I_{\mathrm{LG}} - I_D - I_{R_{sh}} \tag{4.9}$$

The light-generated current is given as:

$$I_{\mathrm{LG}} = I_{\mathrm{SCR}} \times G_N + I_t(T_C - T_r) \tag{4.10}$$

Cell temperature, T_C, can be obtained from the following equation:

$$T_C = T_a + \frac{G}{800}\left(\mathrm{NOCT} - 25^{\circ}\mathrm{C}\right) \tag{4.11}$$

The diode current of the PV cell is similar to the standard diode:

$$I_D = I_o\left[e^{\frac{q}{\mathrm{AKT}_c}(V_{\mathrm{PVC}} + R_S I_{\mathrm{PVC}})} - 1\right] \tag{4.12}$$

The inverse saturation current of the p−n junction can be expressed as:

$$I_o = I_{or}\left(\frac{T_c}{T_r}\right)^3 e^{\frac{qE_G}{AK}\left(\frac{1}{T_r}\frac{1}{T_c}\right)} \tag{4.13}$$

The current caused by the shunt resistance of the PV cell is

$$I_{R_{sh}} = \frac{V_{\mathrm{PVC}} + I_{\mathrm{PVC}}\, R_S}{R_{sh}} \tag{4.14}$$

Substituting Eqs. (4.10)−(4.14) into Eq. (4.9), the cell current can be obtained. From this equation, it can be seen that the PV cell current is a function of itself, forming an algebraic loop, which can be solved conveniently using Simulink as described in Fig. 4.9.

The module voltage can be obtained by:

$$V_M = V_{\mathrm{PVC}} * N_{SC} \tag{4.15}$$

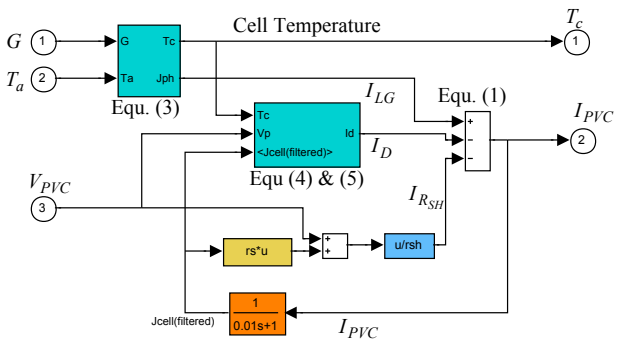


FIGURE 4.9

Simulink model of PV cell.

The module current can be obtained by:

$$I_M = I_{\text{PVC}} * N_{PC} \tag{4.16}$$

PV arrays are represented by the number of modules connected in series, M_S, and the number of modules in parallel, M_P, where the PV array voltage and current are given as:

$$V_{\text{PV}} = V_{\text{PVC}} * N_{SC} * M_S \tag{4.17}$$

$$I_{\text{PV}} = I_{\text{PVC}} * N_{PC} * M_P \tag{4.18}$$

2.1.2 Battery and Load Model

The battery model is shown in many studies and explained in detail in the study by Castaner and Silvestre [64]. The accuracy of this model data is very important in the whole system. The battery model has two modes of operation; charge and discharge as shown in Fig. 4.10. The battery is in charge mode when the current into the battery is positive and in discharge mode when the current is negative. The battery model has the following input parameters:

1. Initial state of charge (SOC_i) (Ah), indicating available charge,
2. Highest and lowest state of charge, SOC_H (Ah) and SOC_L (Ah), respectively.
3. Number of 2-V cells in series.
4. Charge and discharge battery efficiency, K.

The SOC has a linear relationship with the open-circuit terminal voltage of the battery. Initial SOC_i can be estimated based on the current open-circuit terminal voltage of the battery. The battery with about twice the capacity of average daily load power has been chosen in the simulation.

Sizing of the battery bank can be estimated by knowing the average kWh obtained from PV system daily (5.5 kWh) and the number of *days-of-autonomy*

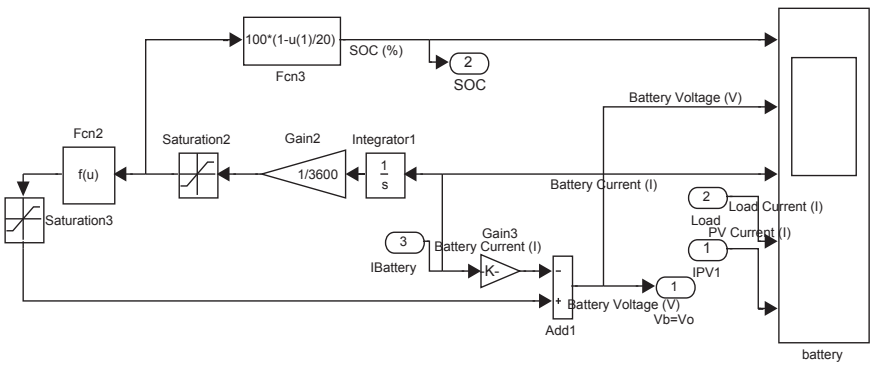


FIGURE 4.10

Simulation model of the battery.

(no-solar radiation in the location, assume it is 2 days). So, the amount of energy storage required can be obtained from Eq. (4.19). For safety, we divide the previous value by allowable level of discharge, SOC_L (90%)

$$E_{\text{rough}} = \frac{\text{Average kWh} * \text{days of autonomy}}{SOC_L} = \frac{5.5 * 2}{0.75} = 14.67 \text{ kWh} \quad (4.19)$$

The capacity of the battery bank in ampere-hours assuming we select a battery voltage of 72 V=(6*12), $C = 14{,}667/72 = 204$ Ah, and according to the selected battery (UB-8D AGM-250 Ah, 12-V dc and a price of $475) [65], the number of batteries needed is six batteries in series.

The battery block implements a generic model parameterized to represent the most popular types of rechargeable batteries.

$$E = E_0 - K\frac{Q}{Q - i_T} + A_x * e^{-B*i_T} \quad (4.20)$$

where $E =$ battery no-load voltage (V); $E_0 =$ battery constant voltage (72 V); $K =$ battery polarization voltage (0.02 V); $Q =$ battery-rated capacity (250 Ah); $A_x =$ battery exponential voltage (0.01 V); $B =$ battery exponential capacity $(2.55\ (\text{Ah})^{-1})$

The State-of-Charge (SOC) of the battery is between 0% and 100%. The SOC for a fully charged battery is 100% and for an empty battery is 0%. The SOC is calculated as shown in the following equation:

$$\text{SOCE} = 100\left(1 - \frac{Q}{\int i\,dt}\right) \quad (4.21)$$

All the parameters of the equivalent circuit can be modified to represent a particular battery type, based on its discharge characteristics. A typical discharge curve is composed of three sections:

The initial State-Of-Charge (SOC_i %) of the battery: This parameter is used as an initial condition for the simulation and does not affect the discharge curve.

The voltage factor (% of the nominal voltage) corresponding to the fully charged voltage, for a given nominal discharge current: For example, a battery cell with a nominal voltage of 1 V and a fully charged voltage factor of 105% has a fully charged voltage of 1.1 V. Note that the fully charged voltage is not the no-load voltage.

The internal resistance of the battery (Ω) is a generic value and is loaded, corresponding to the nominal voltage and the rated capacity of the battery. The resistance is supposed to be constant during the charge and the discharge cycles and does not vary with the amplitude of the current.

The capacity, Q, extracted from the battery until the voltage drops under the nominal voltage: This value should be between 0% and 100%, which is the voltage (% of the nominal voltage) corresponding to the end of the exponential zone.

Control switches are necessary to control the charging and discharging of the battery as shown in Fig. 4.11. These switches are necessary to keep the battery from

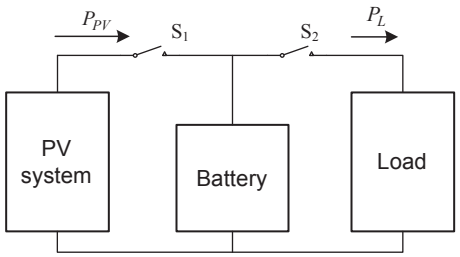


FIGURE 4.11

Block diagram of charging control.

Table 4.1 The Operating Logic Used in the Control Switches

Mode	S_1	S_2	SOC
1	OFF	ON	$SOC \geq SOC_H$
2	ON	OFF	$SOC \leq SOC_L$
3	ON	ON	$SOC_L < SOC < SOC_H$

being overcharged or undercharged, which significantly reduces the battery's lifetime. The operating logic used in the control switches is shown in Table 4.1. Switch S_1 will stay ON unless SOC reaches its maximum value, SOC_H. Switch S_2, will stay ON unless SOC reaches its minimum value, SOC_L. The simulation model of the control switches is shown in Fig. 4.12.

2.1.3 Boost Converter Model

Boost converter block model has been designed as shown in Fig. 4.13. The inputs for this model are the change required in duty ratio, ΔD; radiation, G; and the PV output

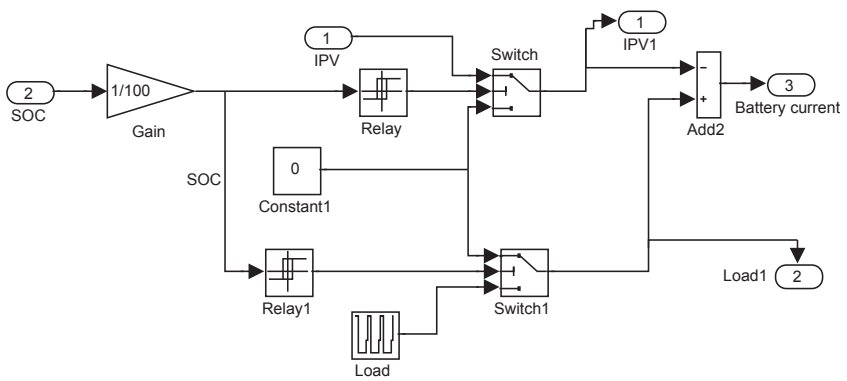


FIGURE 4.12

Simulation model of the switching control.

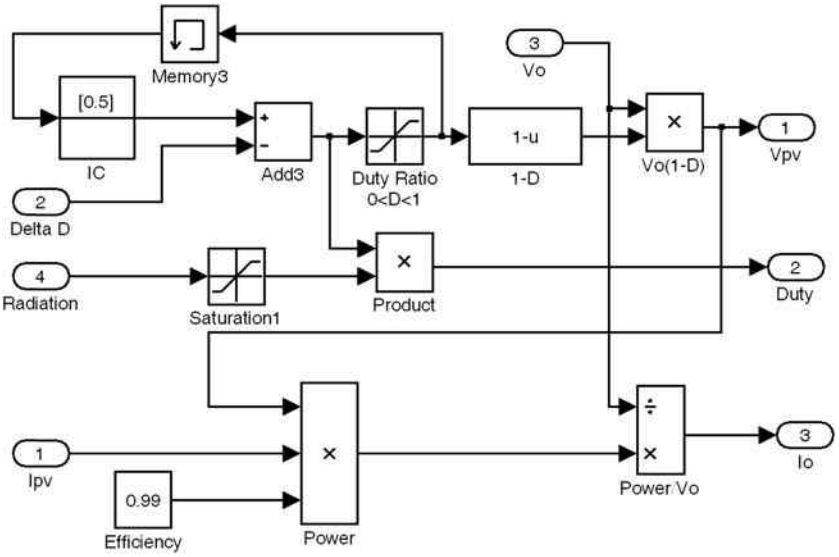


FIGURE 4.13

Simulink model of the boost converter used in the simulation.

current, I_{PV}. The outputs of this model are the PV output voltage, V_{PV}, duty ratio, D, and output current, I_o. In this model the duty ratio can take an initial value or it can be set to zero. The value of ΔD is subtracted from the duty ratio to get the new value of the duty ratio depending on the following equation:

$$D(k+1) = D(k) - \Delta D(k) \tag{4.22}$$

The value of the duty ratio is used to determine the output voltage of the PV array from the following equation:

$$V_{PV} = V_o(1 - D) \tag{4.23}$$

The PV voltage, V_{PV}, obtained from Eq. (4.23) and the output current from PV array obtained from Eq. (4.9) are used to obtain the PV array output voltage. An efficiency factor can be used to determine the corresponding value of the output power. The output current that feeds the battery and load can be obtained from dividing the output power on the output voltage, V_O.

2.1.4 Model of Calculating E and ΔE

The Simulink model of calculating E and ΔE is shown in Fig. 4.14. The input values of this module are PV output current (I_{PV}) and PV output voltage (V_{PV}). These values are used to calculate the power from PV array, P_{PV}. Then, the error signal can be calculated depending on Eq. (4.24). The value of ΔE is calculated as shown in Eq. (4.25).

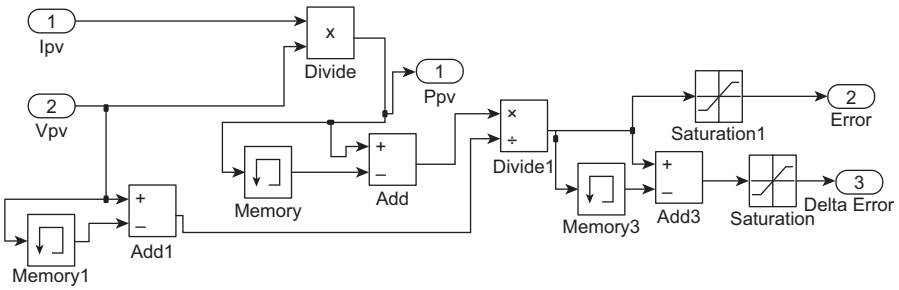


FIGURE 4.14

Simulink model of calculating E and ΔE.

$$E(n) = \frac{P(n) - p(n-1)}{V(n) - V(n-1)} \tag{4.24}$$

$$\Delta E(n) = E(n) - E(n-1) \tag{4.25}$$

2.1.5 Fuzzy Logic Controller Model

FLC uses approximate solution for control problems. In the beginning, Fuzzy logic has been studied since 1920 [66]. By 1965, Zadeh [67] introduced FLC as a controller for real applications [68]. Since then, FLC has been applied to many applications in different fields of science. FLC can be implemented easily in different digital devices such as microcontrollers [69,70], digital signal processors (DSPs) [71,72], and field-programmable gate arrays (FPGAs) [70,73], and it becomes mature technology in the industrial applications. One of the useful application of FLC is its use as MPPT of PV systems [74]. In case of partial shading of PV systems, many LPs and only one GP will be generated in the P−V curve of the PV system as discussed before. FLC controller can stuck with local MPP rather than the global MPP, which will be shown when comparing with the proposed PSO MPPT technique.

HC technique uses a perturbation in the duty ratio of the dc chopper to track the change in power until the change of power reaches almost zero value, which is the MPP. HC technique can be performed using FLC [74]. FLCs have the advantages of working with imprecise inputs, not needing accurate mathematical model, and handling nonlinearity [70].

The output power from the PV system and the voltage are used to determine the error, E, and the change of error, ΔE. In Eqs. (4.16) and (4.17), E and ΔE are based on the range of values of the numerical variable. Predicting the range of error, E, and change of error, ΔE, depends on the experience of the system designer. These variables are expressed in terms of linguistic variables or labels such as PB (Positive Big), PM (Positive Medium), PS (Positive Small), ZE (Zero), NS (Negative Small), NM (Negative Medium), and NB (Negative Big) using basic fuzzy subset. Each of these acronyms is described by a given mathematical membership function. The

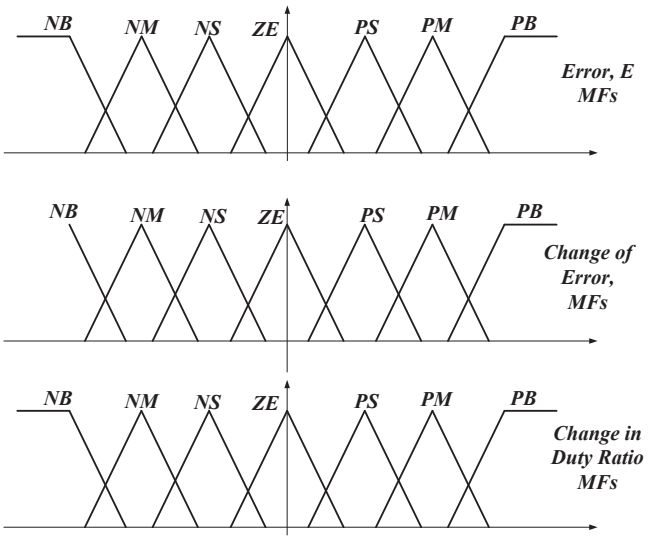


FIGURE 4.15

A fuzzy system with 1 inputs, 1 output, and 7 MFs each.

membership function is sometimes made less symmetric to give more importance to specific fuzzy levels, or it can be symmetric as shown in reference [40]. The inputs to an MPPT FLC are usually an error E and ΔE. Once E and ΔE calculated and converted to the linguistic variables based on membership functions shown in Fig. 4.15, the FLC output, which is typically a change in duty ratio, ΔD of the power converter, can be looked up in a rule base Table 4.2. FLC membership functions for both inputs and output variables can be used as a triangle-shaped function, which is the easiest way to be implemented on the hardware digital control system. The linguistic

Table 4.2 Rules for an FLC System With Two Inputs and One Output With Seven-Membership Functions in PV Applications

E	ΔE						
	NB	**NM**	**NS**	**ZE**	**PS**	**PM**	**PB**
NB	NB	NB	NB	NB	NM	NS	ZE
NM	NB	NB	NB	NM	NS	ZE	PS
NS	NB	NB	NM	NS	ZE	PS	PM
ZE	NB	NM	NS	ZE	PS	PM	PB
PS	NM	NS	ZE	PS	PM	PB	PB
PM	NS	ZE	PS	PM	PB	PB	PB
PB	ZE	PS	PM	PB	PB	PB	PB

variables assigned to ΔD for the different combinations of E and ΔE are based on the power converter being used and also on the knowledge of the user.

These linguistic variables of input and output membership functions are then compared with a set of predesigned values during aggregation stage. The relation between the inputs and output depends on the experience of the system designer. These relations can be tabulated as shown in Table 4.2 [40]. Some researchers proportionate these variables to only five fuzzy subset functions as in Eltamaly [40]. Table 4.2 can be translated into 49 fuzzy rules (IF-THEN rules) to describe the knowledge of control. Some of these rules are shown in the following as an example:

R_{25}: If E is NM and ΔE is PS then ΔD is NS

R_{63}: If E is PM and ΔE is NS then ΔD is PS

…

…

R_{51}: If E is PS and ΔE is NB then ΔD is NM

In the defuzzification stage, the FLC output is converted from a linguistic variable to a numerical variable by using membership function. This provides an analog signal, which is the change in the duty ratio, ΔD, of the boost converter. This value is subtracted from previous value of the duty ratio to get its new value as shown in Eq. (4.14).

Defuzzification is used for converting the fuzzy subset of control form inference back to values. As the output usually required a nonfuzzy value of control, a defuzzification stage is needed. Defuzzification for this system is the height method. The height method is both very simple and very fast method. The height defuzzification method is a system of rules formally given by Eq. (4.26):

$$\Delta D = \frac{\sum_{k=1}^{m} c(k) * W_k}{\sum_{k=1}^{n} W_K} \tag{4.26}$$

where $\Delta D =$ change of control output; $c(k) =$ peak value of each output; $W_k =$ height of rule k.

The FLC is implemented using the fuzzy logic tool box available in MATLAB/Simulink. Fuzzy logic toolbox contains a tool called fuzzy inference system (FIS) editor available with MATLAB/Simulink. The FIS editor is an effective graphical user interface (GUI) tool provided with the fuzzy logic toolbox in Matlab/Simulink to simplify the design of the FLC, which can be used in the system under investigation. The input and output membership functions are designed in the FIS editor.

The relation between the input and output membership functions can be introduced in the aggregation stage. Aggregation stage is carried out in the FIS editor by introducing the rules of Table 4.2 into FIS editor. The rules that come into play for different values of inputs and the corresponding outputs can be viewed using

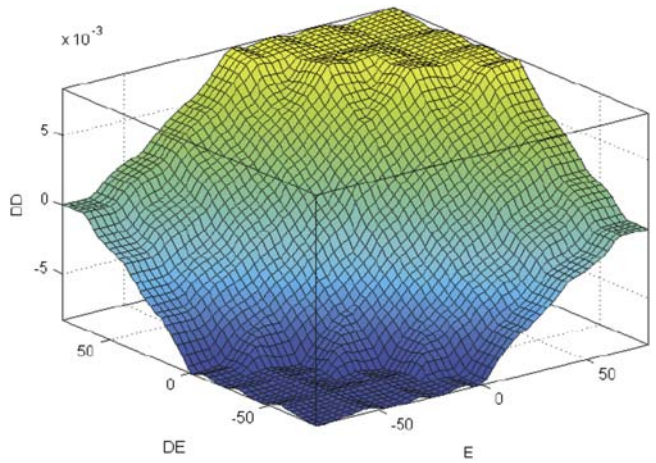


FIGURE 4.16

Surface function of the proposed FLC.

the rule-viewer function. The FLC block outputs the incremental in the duty ratio of the boost converter.

The relation between the inputs and the output of the fuzzy controller can be represented as a 3-D drawing, which is called surface function and is shown in Fig. 4.16. It is clear that the surface function is approximately smooth, which enhances the stability of the fuzzy system.

2.2 SIMULATION RESULTS

The radiation and temperature data used in simulation are from realistic hourly data of the Riyadh city of Saudi Arabia. These data are concentrated in a narrow range of time (640 s), which approves the robustness of the fuzzy-controlled system. Six PV modules have been used in the simulation and each produces 75 W, 12 V, and 4.4 A. The simulation is carried out with FLC and the constant-voltage technique for the purpose of comparison. These two MPPT techniques have been compared with theoretical maximum power from PV module, which can be calculated using a Matlab code. The load is connected with a PV array through a battery. The value of SOC_L of the battery is chosen to be 99% to reduce the time of simulation. Fig. 4.17 shows in the first trace the solar radiation used in the simulation. In the second trace of Fig. 4.17, the output power for FLC (black color) and constant-voltage MPPT technique (blue colored) are compared with the theoretical values of MPPT (red colored). It is clear from second trace that the power output with FLC is following the theoretical MPP exactly but the output power with constant-voltage control is considerably lower than that associated with FLC. Moreover, FLC can restrain any overshooting in the input or output variables.

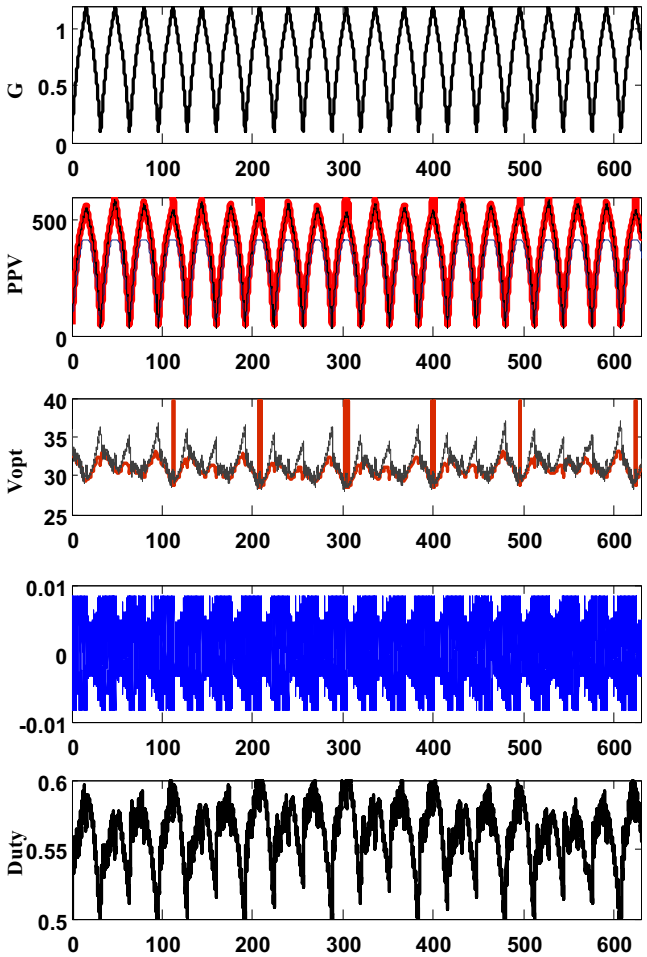


FIGURE 4.17

Simulation results from the Simulink model.

Third trace of Fig. 4.17 shows the value of theoretical value of the optimum voltage and the values obtained from FLC system. It is clear that the optimum voltage from FLC system follows the corresponding values from theoretical calculations.

Fourth trace of Fig. 4.17 shows the change of control output, ΔD, which is the output from FLC. This value can be used to modulate the value of the duty ratio. Last trace of Fig. 4.17 shows the duty ratio of the boost converter.

Output power from PV system using FLC and constant voltage along with the theoretical MPPT are shown in Fig. 4.18 for the purpose of comparison. It is clear

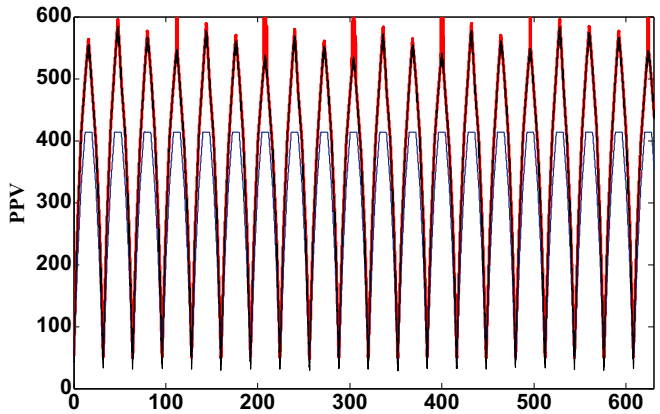


FIGURE 4.18

The output power from PV system using FLC and constant voltage along with the theoretical MPPT.

from Fig. 4.17 that the output power associated with FLC system follows exactly the theoretical MPPT, which proves the superiority of the system.

A zooming in for the E, ΔE, ΔD, D, and optimum voltage, V_{PV} are shown in Fig. 4.19 to simplify the tracking of the logic of the FLC system. The logic shown in Table 4.2 can be explained with the help of this figure.

Fig. 4.20 shows the simulation results from battery and control switches models. The SOC of the battery is shown in the first trace of Fig. 4.20. It is clear from this trace that the SOC is between the preassigned values of SOC_L (99%) and SOC_H (100%). The second trace of Fig. 4.20 shows the battery voltage. It is clear from this trace that the battery voltage directly proportional with the SOC of the battery shown in the first trace of Fig. 4.20. The battery current is shown in the third trace of Fig. 4.20. In the beginning, the battery was supplying the deficit current required for the load unless the SOC is higher than SOC_L. Otherwise, the load switch S_2 will be turned OFF to prevent the battery from overdischarge and the PV current will charge only the battery. The load current is shown in the fourth trace of Fig. 4.20. The load current is existing unless the SOC is higher than SOC_L. Otherwise, the load switch S_2 will be turned OFF to prevent the battery from overdischarge and the PV current will charge only the battery. The PV current is shown in the last trace of Fig. 4.20. It is clear that the battery and load will receive the PV current unless the battery gets overcharged ($SOC > SOC_H$). In this case the PV switch S_1 will be switched OFF to prevent the battery from getting overcharged.

2.3 EXPERIMENTAL WORK

The complete circuit is designed in many stages and connected together to perform the complete function. Two circuits have been implemented, the first one is the

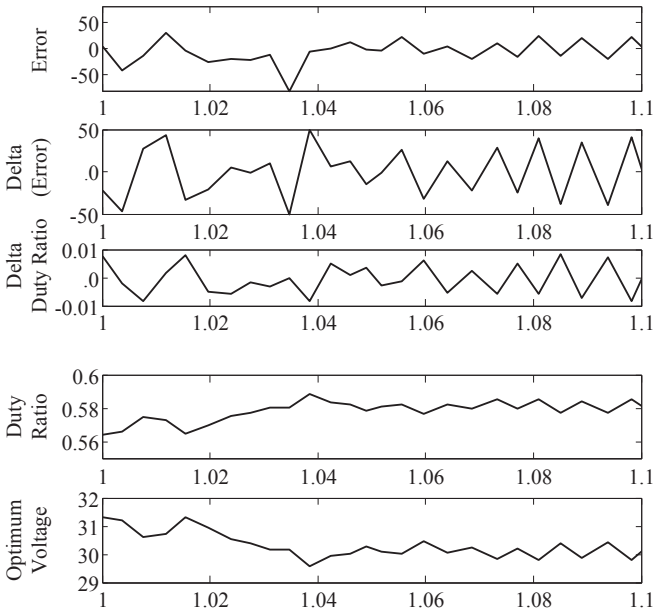


FIGURE 4.19

Simulation results of the FLC system.

power circuit of the boost converter with the isolating circuit and the temporary control signal, and the second one is the circuit of current and voltage sensors, isolating circuits, and switch driver. The details of each component of these two circuits are discussed in detail in the following sections.

2.3.1 Hardware Implementation of Boost Circuit

Boost or step-up converter has an output voltage that is always greater than the input voltage. Fig. 4.21 shows a conceptual diagram of boost converter. The basic operation mechanism is that when the switch is closed, the load is isolated from the input by the diode, and current builds up in the inductor. This current build is effectively storing energy in the field of the inductor. When the switch is opened, the current in the inductor wishes to continue to flow in the same direction and with the same magnitude because of stored energy in the inductor. Therefore, the diode will turn on and the current will immediately flow into the filter capacitor and any connected load.

The control signal has been generated in the beginning by analog circuit to check the operation of the boost converter with PV energy system. After that, the control signals are generated digitally from FPGA board. The control signal should be isolated from the power circuit by using isolating circuit (opto-coupler). Fig. 4.22 shows the circuit diagram of the isolating circuit. In this circuit, the output signal from the control circuit is connected directly to points 1 and 2 of 4n32 opto-

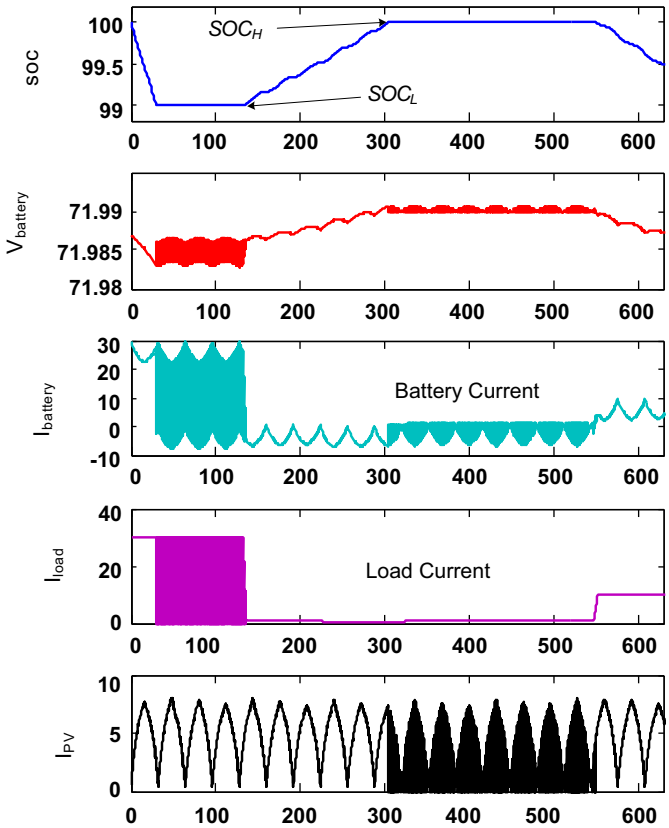


FIGURE 4.20

The simulation results from battery and control switch models.

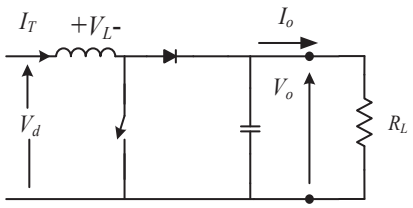


FIGURE 4.21

Step-up dc–dc converter (boost converter).

coupler. Points 5 and 6 are connected to gate and drain of the MOSFET of the boost converter through a current-limiting resistor.

The analog pulse requires two Op-Amp and their power supply is as shown in Fig. 4.27. The power supply supplies +15 V, −15 V, and 0 V to the entire system

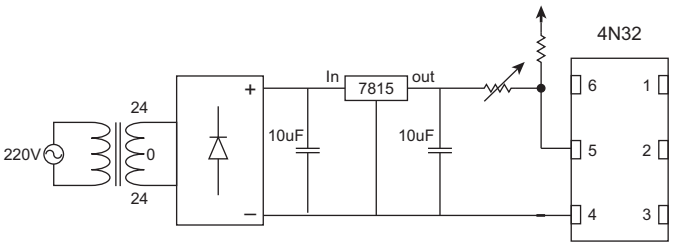


FIGURE 4.22

The circuit diagram of isolating circuit.

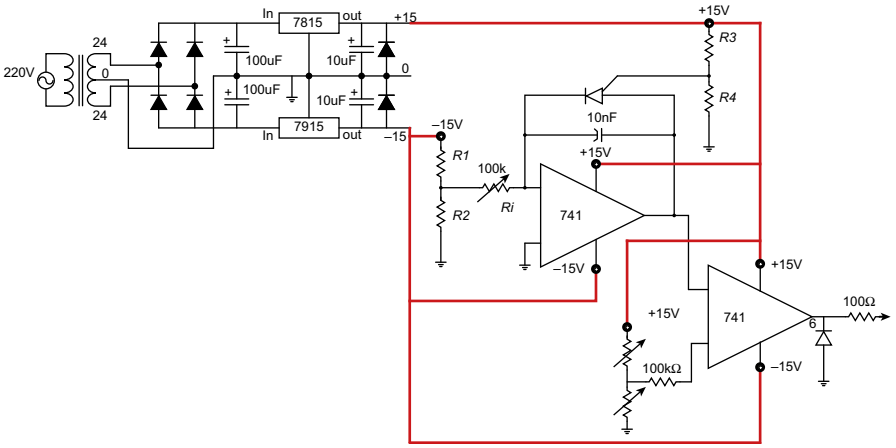


FIGURE 4.23

Schematic diagram of control circuit.

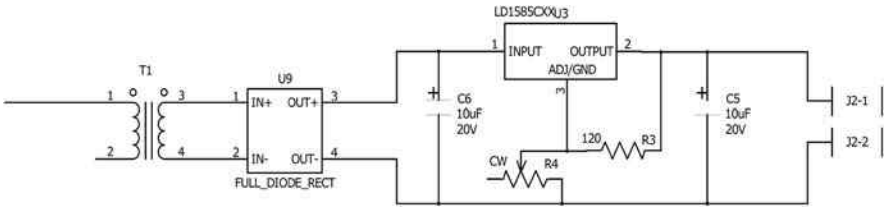


FIGURE 4.24

dc power supply 5 V circuit.

to operate all the integrated circuits. The first Op-Amp work as saw-tooth generator and the other one works as a comparator. The potentiometers are used to control the switching frequency and the duty ratio of the boost converter. After checking the performance of the complete system with the analog circuit of Fig. 4.23, the circuit is replaced by the FPGA.

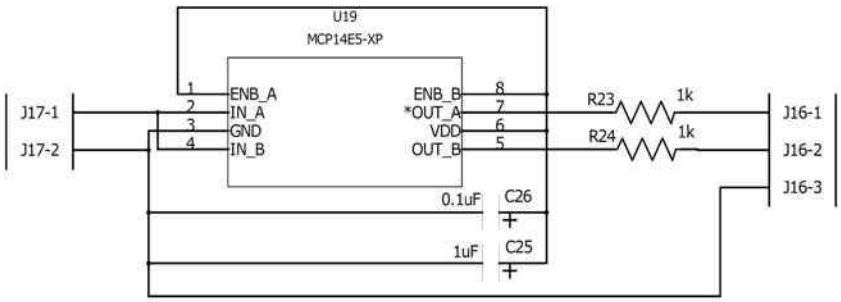


FIGURE 4.25

Boost switch driver circuit.

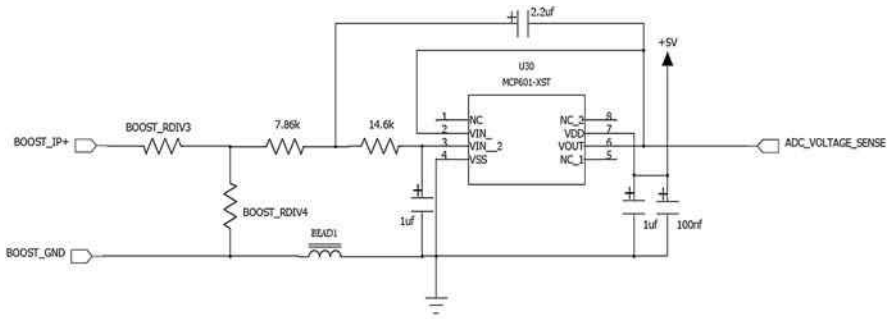


FIGURE 4.26

PV voltage sensing circuit.

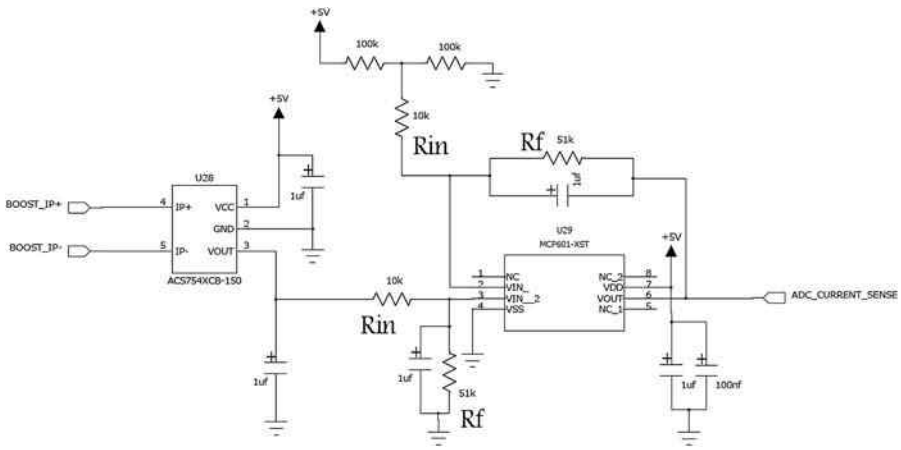


FIGURE 4.27

PV current sensing circuit.

2.3.2 Sensors and Driver Circuits

2.3.2.1 Power Supply Circuits

The voltage and current sensing circuits and switch driver circuit requires +5 V dc power to operate. The required dc power has 0 V ground. The source of power can be either the PV cells directly or any other power source like mains ac power or a battery power. For experimental purpose, ac power has been used for sensing; the switch driver circuits are as shown in Fig. 4.24.

The ac power is first transformed to 12 V ac using a step-down transformer, and then the 12 V ac is rectified using a full-diode bridge rectifier circuit. The output from the rectifier circuit is regulated by the low−drop-out voltage regulator LD1585C. The LD1585C has a maximum of 1.2 V voltage drop (drop between input voltage and output voltage) at full load current of 5 A. The output from the ac rectifier is about +9 V while the regulated output voltage from LD1585C is +5 V, which keeps a margin of +4 V drop between the input and output, this grants a +5 V stable regulated voltage even at the full load current of the LD1585C. The LD1585C output voltage can be adjusted using the resistor R54 ($V_{out} = 1.25*(1 + R54/R53)$). The regulator has a fast response to load current requirements, which makes it suitable to supply fast switching circuits. For more information about LD1585C features and usage requirements, refer to the device datasheet.

2.3.2.2 Boost Switch Driver Circuit

The boost switch (either MOSFET or IGBT) may require a low-resistance and high-power driver to enable it switch on/off while passing a large amount of boost current through it. The FPGA outputs can only supply a current up-to 24 mA at 3.3 V. If the boost switch sinks more current than this amount from the FPGA, then the FPGA output buffer may damage. The circuit here provides a high-power buffer to FPGA output before driving the boost switch gate as shown in Fig. 4.25. The circuit also shifts up the driving level from 3.3 V at FPGA output to 5 V at switch gate. This grants more reliable operations, especially at high boost currents and fast switching frequencies.

The device used here is MCP14E5-XP, which is a high-speed/high-power MOSFET driver with output enable signal. The device has two inputs and two outputs, the first output has the same polarity as the first input and the second output has the inverted polarity of the second input. Connecting the two inputs together will produce two outputs with one of them having the same polarity as the input and the second output having an inverted polarity than the input. The device has a peak output current of 4 A.

2.3.2.3 PV Voltage-Sensing Circuit

The PV voltage has to be sensed and passed to the fuzzy control algorithm by using a PV voltage sensing circuit in Fig. 4.26. The PV voltage is first scaled down to an acceptable voltage level to be fed to analog to digital converter circuits (ADCs). The scaling is achieved by a simple two-resistor voltage divider BOOST_RDIV3 and BOOST_RDIV4. The voltage drops on BOOST_RDIV4 must not exceed the

maximum input voltage acceptable by ADC circuits. The values of BOOS_RDIV3 and BOOST_RDIV4 must be selected to satisfy the following relation:

$$V_{\mathrm{PV}_{\max}} * \frac{\text{Boost\_RDIV4}}{\text{Boost\_RDIV3} + \text{Boost\_RDIV4}} \leq V_{\mathrm{ADC}_{\max}} \tag{4.27}$$

where $V_{\mathrm{PV}_{\max}}$ is the maximum PV output voltage and $V_{\mathrm{ADC}_{\max}}$ is the maximum ADC acceptable input voltage. The scaled voltage is low-pass filtered and buffered using the amplifier circuit shown above before passing to the ADC input. The amplifier device used here is MCP601-XST from Microchip. The MCP601-XST is a low-cost and simple-to-use Op-Amp; it requires a single voltage supply and provides rail-to-rail output. The device has a wide bandwidth and is optimized for ADC circuits driving.

The PV-sensed voltage is the voltage at the PV array terminals, which is the input to the boost circuit. To minimize the noise in the power circuits generated by the high-speed digital circuits (FPGA control board), the PV ground (boost ground) is isolated from the control ground (FPGA board, sensing and switch driving ground) by a ferrite bead as shown above.

2.3.2.4 PV Current-Sensing Circuit

The PV current has to be sensed and passed to the FLC. The PV current is first sensed by a current sensor ACS754XCB-150. This device is a hall effect−based linear current sensor capable of sensing ac and dc currents with a peak up to 150 A. The sensor output is a positive voltage swing between 0 and +5 V proportional to the sensed current. The output of the sensor V_{sens} at a given sensed current I_{sens} can be calculated from the following relation:

$$V_{\mathrm{sens}} = 2.5 + I_{\mathrm{sens}} * \frac{2.5}{150} \tag{4.28}$$

where, I_{sens} can have any value between +150 and −150 A. Because of the fact that the PV array is a dc power supply and the output current cannot have a negative value, the sensible 0 to −150 A current range is not required and can be ignored. The sensor has a sensitivity of 14 mV/A.

The second stage of the current-sensing circuit is an amplifier and low-pass filter circuit. Because the PV array current may not reach the beak of +150 A, the amplifier amplifies the produced output voltage from the current sensor so it's measurable by the ADC circuit.

The amplifier circuit subtracts the +2.5 V offset generated by the current sensor (at 0 A) before amplifying the sensor output and this is why the amplifier is organized as a difference amplifier. The amplification is controlled by two resistors R_{in} and R_f and these resistors can be selected according to the maximum PV current to be sensed and the maximum acceptable ADC input voltage. R_f and R_{in} selected values must satisfy the following relation:

$$\frac{I_{\mathrm{sens}_{\max}} * 14 * R_f}{R_{in}} \leq V_{\mathrm{ADC}_{\max}} \tag{4.29}$$

where $I_{sens_{max}}$ is the maximum PV current to be sensed and $V_{adc_{max}}$ is the maximum input voltage accepted by ADC circuits. The Op-Amp device used in the PV current sensing circuit is the same as the device used in PV voltage-sensing circuit.

The terminals of the current sensor ACS754XCB-150 must be connected in series with the PV array as shown in Fig. 4.27. The current passing through the PV array must enter the sensor from its IP+ terminal and exit the sensor from its IP− terminal. It is suggested to connect sensor's IP+ terminal to the PV array positive terminal and the senor's IP− terminal to one of boost's coil terminal.

3. SMART MAXIMUM POWER POINT TRACKER UNDER PARTIAL SHADING CONDITIONS

3.1 PARTIAL SHADING EFFECT

PV cells should be connected in parallel and series to increase the current and voltage, respectively, to be suitable for the load. Partial shading occurs when one or more PV cells in the PV array are exposed to lower radiation than the rest of the PV array. If partial shading occurs to one or more of series PV cells, it will force the partial shading PV cell to work with current higher than the generated current and it will act as a load for the other PV cells. If the current flow in the shaded PV cell is higher than the generated voltage, it will become negative as shown in Fig. 4.28 for two PV cells in series with 500 and 1000 W/m^2. It is clear from this figure that the first PV cell works at negative terminal voltage for values of terminal voltage lower than the open-circuit cell of the second PV cell. The relation between the generated power from two series PV systems with variation of output voltage

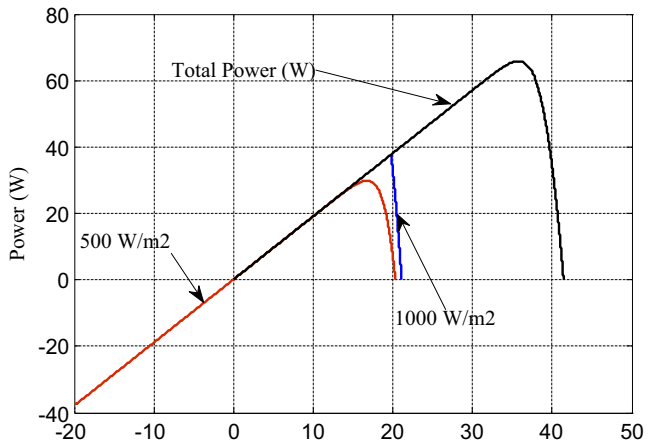


FIGURE 4.28

Terminal voltage across each PV cell of two series PV cells.

along with the radiation of shaded PV cell is shown in Fig. 4.29. It is clear from this figure that the generated power drops considerably with an increase in shading on the PV cell. The relation between the power of shaded PV cell of two series PV system with variation of its terminal voltage along with the radiation of this cell is shown in Fig. 4.30. It is clear from this figure that the PV cell can act as load at certain terminal voltage lower than its open-circuit voltage. If this happens, the PV cell temperature will increase and it may be destroyed especially for higher number of PV cells in series as will be discussed in the following section. The negative power going to the shaded PV cell is called hot-spot point [40].

In case of higher number of series PV cells, the hot spot becomes more serious where high current of the series PV system will pass through the shaded PV cell, which can destroy it. Fig. 4.31 shows the variation in the generated power of the 20 series PV cells with the terminal voltage and radiation on the shaded PV cell when other cells are exposed to 1000-W/m^2 radiation. It is clear from this figure that the generated power of the 20 series PV cells drops considerably with an increase in the shaded strength of only one cell. The shaded PV cell will act as a load for the 19 PV cells and the power consumed by this cell can be the total power generated from the other PV cells, which can easily destroy the shaded PV cell. Fig. 4.32 shows the power of shaded PV cell among 20 series PV cells along with its terminal voltage, and the radiation of this cell, where the rest of PV cells exposed to 1000 W/m^2. It is clear from this figure that for certain values voltage across the shaded PV cell can be the total voltage of the other 19 PV cells, which

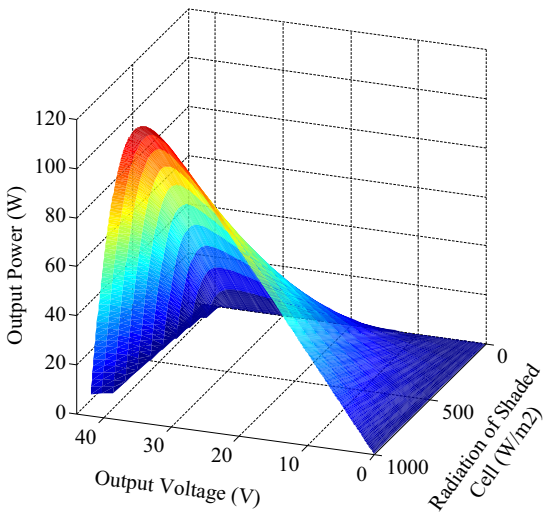


FIGURE 4.29

Total power for two P–V cells without bypass.

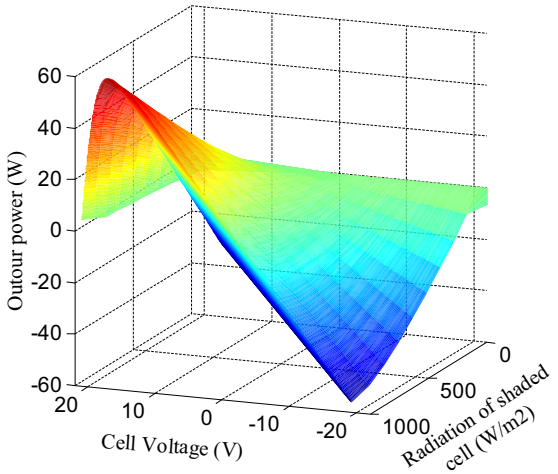


FIGURE 4.30

Power of shaded cell with its voltage and radiation.

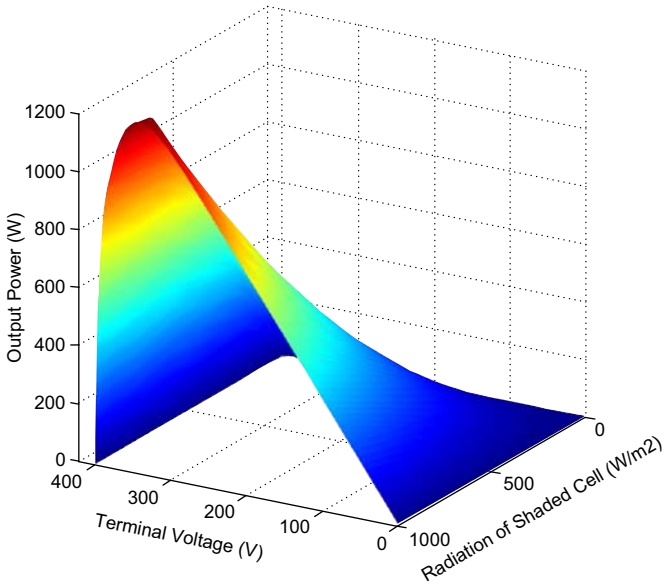


FIGURE 4.31

Total power of 20 series with one shaded PV cell.

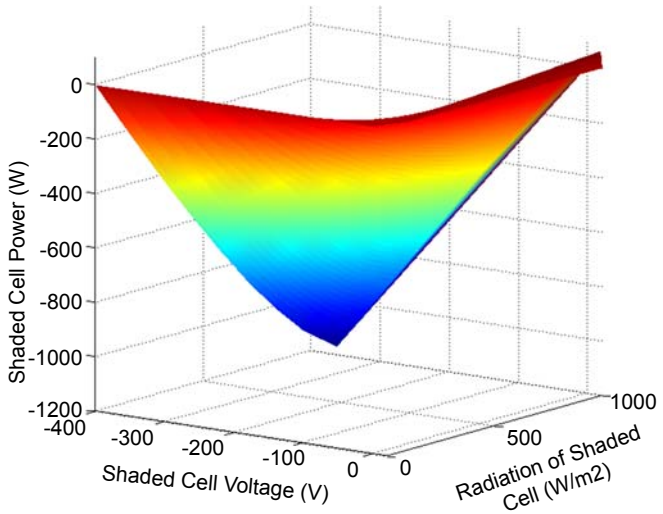


FIGURE 4.32

The power of shaded PV cell among 20 series PV cells.

can easily destroy this shaded PV cell, especially if this voltage is greater than its breakdown reverse voltage. It is clear from the above discussion that the hot spot can be more dangerous for higher number of series PV cells. Some literature work to determine the optimum number of PV cells on series to prevent its hot spot damage [40].

A wide range of studies have been done to remedy the effect of hot spot of PV systems [75,76]. One of the most effective technique is to add bypass diode along with each PV cell or it can be connected to a certain number of PV cells to reduce the cost of PV modules and to reduce the losses of the PV system. In case of using two series PV cells with bypass diodes, the relation between the terminal voltage and output power from these two PV cells with a radiation of 1000 and 500 W/m^2 is shown in Fig. 4.33. It is clear from this figure that when the terminal voltage is lower than the open-circuit voltage of shaded PV cell, it will cause negative terminal voltage across this shaded PV cell. During this period, the bypass diode will become forward and the generated power from the other PV cell will flow through this diode. This situation will cause two peaks in the output power as shown in Fig. 4.33. Fig. 4.34 shows the relation between output power and terminal voltage for two series PV cells with bypass diodes at different shading conditions when the other PV cell radiation is 1000 W/m^2.

In case of 20 series PV cells with bypass diode connected to each one of them, the total generated power for different radiations of shaded PV cell is shown in Fig. 4.35. The rest of the other PV cell radiation is 1000 W/m^2. It is clear from this figure that the shaded PV cell starts working when the terminal voltage forces

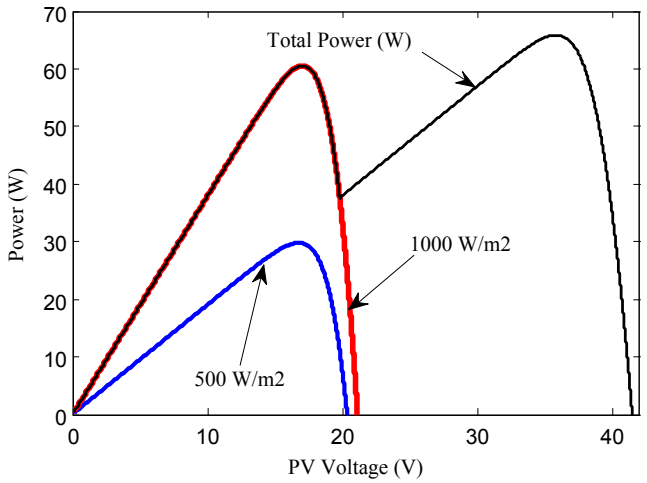


FIGURE 4.33

The relation between output power and terminal voltage for two series PV cells with bypass diodes.

the voltage of the shaded PV cell to be positive. The relation between the output power of shaded PV cell and its voltage for different radiations of this cell is shown in Fig. 4.36.

It is clear from the above discussion that the output power for shaded PV cells with bypass diodes has local MPPs depending on the number of shaded PV cells and the strength of the shade. This local MPP makes the regular MPPT techniques to stick around local MPP. A modified PSO (MPSO) technique has been used to locate the global MPP (Global Peak, GP). This technique has been compared with one of the most effective MPPT techniques, which is FLC. For this reason, three PV cells as an example have been used to study the local and global MPP. The relation between the generated power and terminal voltage in case of three series PV cells at radiations of 1000, 700, 300 W/m^2 is shown in Fig. 4.37. This figure shows three MPPs numbered 1, 2, and 3, where V(1) $<$ V(2) $<$ V(3). The GP is the one corresponding to the point #2. The MPPT system should follow the GP, which is #2 as shown in Fig. 4.37. Most of the MPPT techniques may stick around the LP [40].

3.2 MISMATCH POWER LOSS

Because of the differences in radiation on each PV cell, the generated power from each PV cell varies from one cell to another and multiple MPPs will be generated. The GP is lower than the sum of peaks at all peaks. The relation between the peak power and the sum of peaks is called mismatch loss (MML) and can be mathematically modeled as shown in Eq. (4.30). So, the higher the MML, the higher the

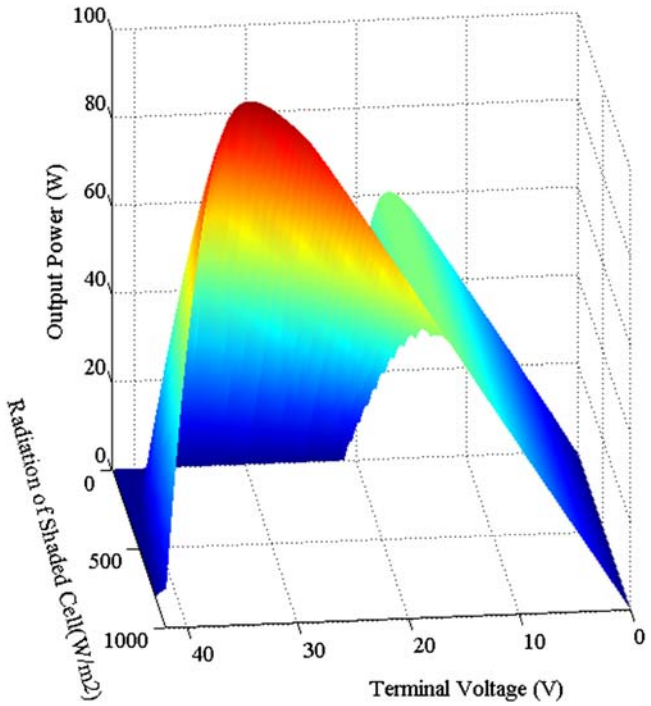


FIGURE 4.34

The relation between output power and terminal voltage for two series PV cells with bypass diodes at different shading conditions.

generated power from PV system. Also, the lower the value of MML factor, the higher the hot spot on the PV cell with lower solar radiation. If the whole PV cells have the same radiation and the whole PV system works at its MPP and each cell works at its own MPP, the MML factor will be 100%. The value of MML factor can be obtained from the following equation:

$$\text{MML} = \frac{\text{Maximum power of whole PVsystem}}{\sum_{i=1}^{N} P\max(i)} * 100 \tag{4.30}$$

where, N is the total number of PV cells in PV system.

So depending on the PV system shown in Fig. 4.37, the MML factor can be obtained as follows.

If the system operates at the MPP #1

$$\text{MML} = \frac{60}{60 + 90 + 64} * 100 = 28.03\%$$

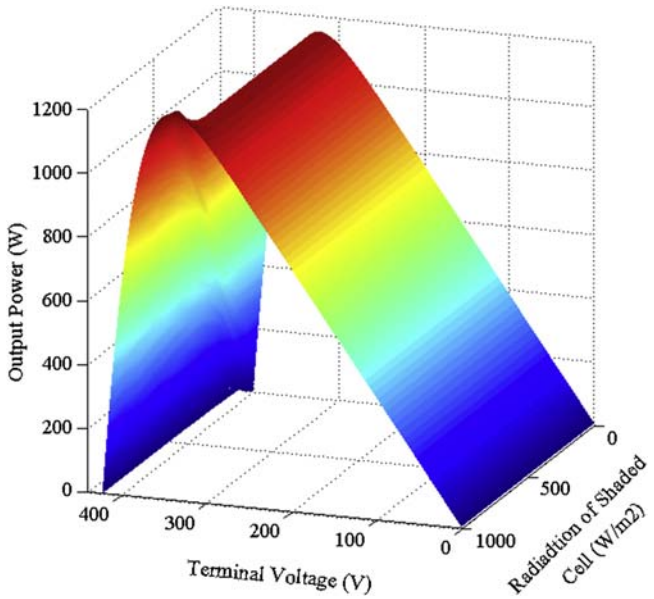


FIGURE 4.35

The total generated power along with terminal voltage for different radiations of shaded PV cell in case of 20 series PV cells with bypass diodes.

If the system operates at the MPP #2

$$\text{MML} = \frac{90}{60+90+64} * 100 = 42.06\%$$

If the system operates at the MPP #3

$$\text{MML} = \frac{64}{60+90+64} * 100 = 29.91\%$$

So, it is clear that the power generated from the PV system can be increased by ((90−60)/60*100) = 50% and ((90−64)/64*100) =·41% if the system works on point #2 instead of points #1 and #3, respectively. Conventional MPPT techniques stick in LP and can not follow the GP. But, MPSO technique has been introduced to actively track the GP power which can increase the generated power considerably and reduce the effect of hot-spot phenomena. In the following section, a comparison between the use of FLC and PSO in MPPT of PV systems under shaded conditions has been introduced in detail.

3.3 SIMULATION OF PROPOSED SYSTEMS

A model of PV module and dc−dc boost converter with FLC and PSO techniques of MPPTs were simulated using PSIM and Simulink software. Co-simulation between

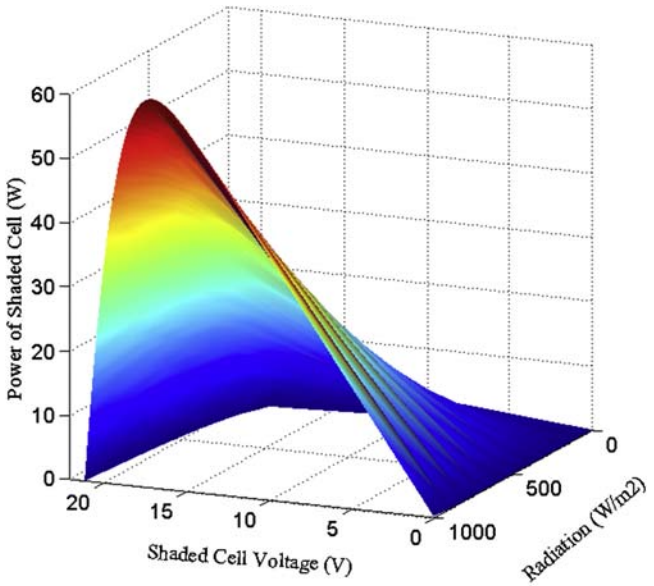


FIGURE 4.36

The relation between the output power of shaded PV cell and its voltage for different radiation of this cell.

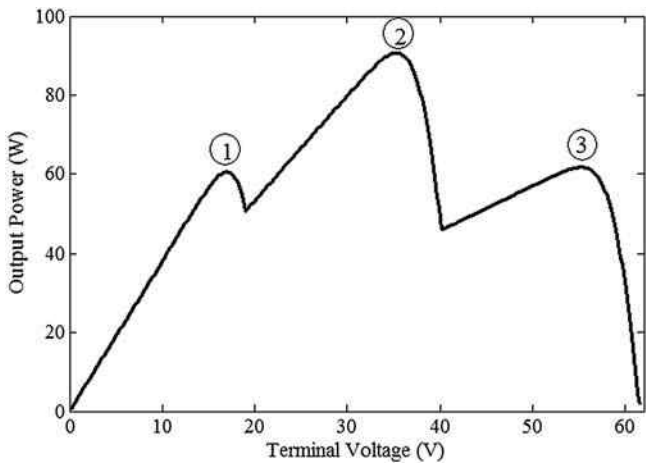


FIGURE 4.37

The relation between the generated power and terminal voltage in case of three series PV cells at radiation of 1000, 700, and 300 W/m^2.

PSIM and Simulink software packages is used. The co-simulation is done to take advantage of each program to handle certain parts of the system. The response of the different MPPT techniques is evaluated in rapidly changing weather conditions.

PSIM model showing the calculation of E and ΔE and the inputs to Simulink is shown in Fig. 4.38. The simulation model showing the output signal from FLC and MPSO in Simulink to PSIM and the switching circuit that controls the switch is shown in Fig. 4.39. The simulation model for three PV modules and boost converter that have been used in FLC and MPSO is shown in Fig. 4.40. The simulation model of the proposed system in Simulink is shown in Fig. 4.41.

The simulation parameters of PV module are shown in Table 4.3.

The simulation results of the MPSO and FLC are shown in Fig. 4.42. The simulation time shown in this figure has been divided to six periods each of which one is 2 s. In each 2 s, the radiation will be changed in two PV modules out of three and the first one will be constant (1000 W/m^2) all the simulation time. The idea of changing the radiation here is to change the GP from right to lift or middle to see the response

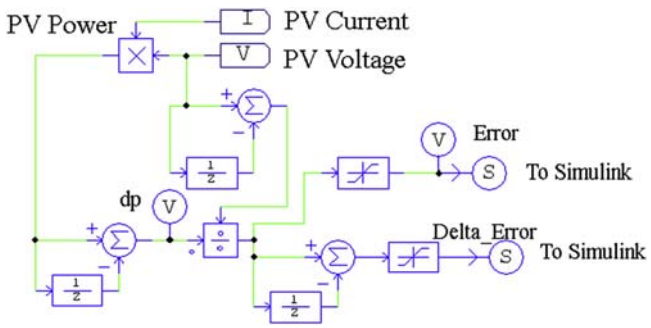


FIGURE 4.38

PSIM model showing the calculation of E and ΔE and the inputs to Simulink.

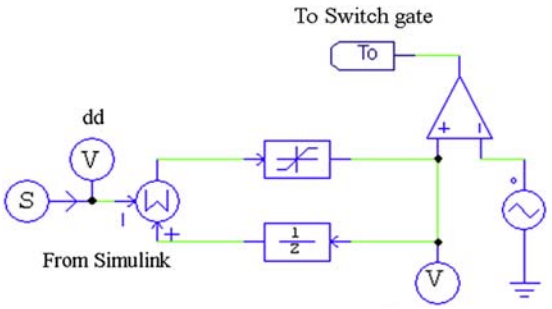


FIGURE 4.39

Simulation model of output signal from FLC in Simulink to PSIM and the switching circuit.

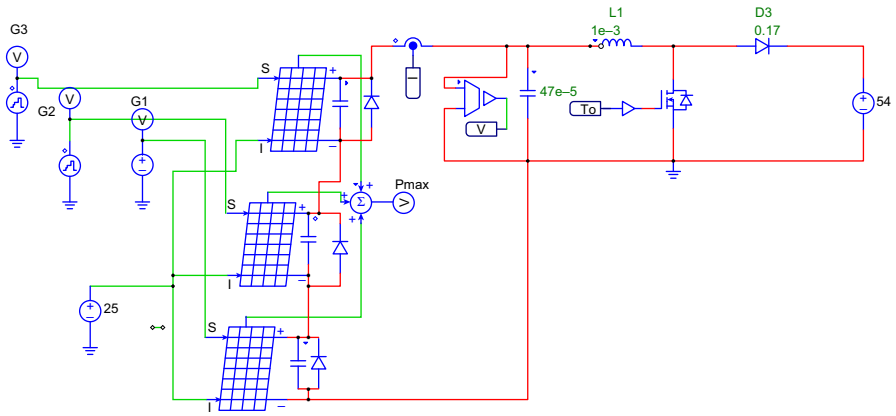


FIGURE 4.40

The simulation model for PV modules and boost converter.

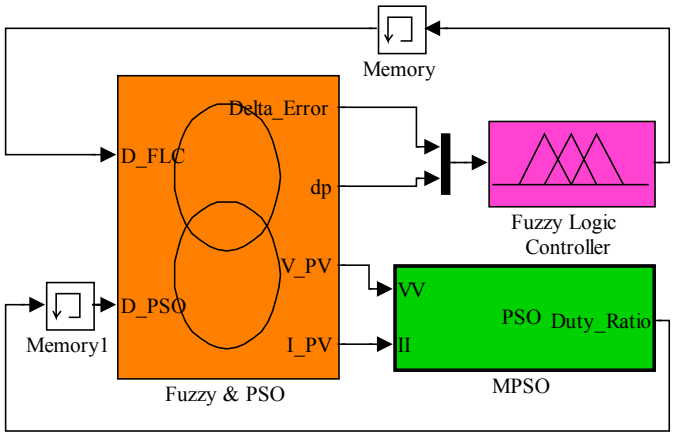


FIGURE 4.41

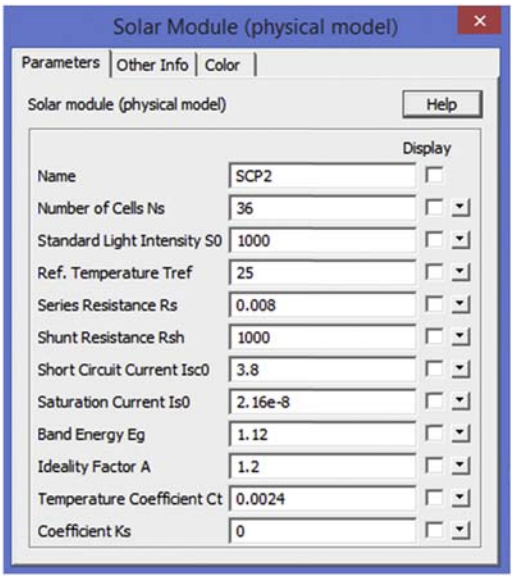
The Simulink model showing the cosimulation between Simulink and PSIM.

of the MPSO and FLC during these changes. The explanation of the simulation results shown in Figs. 4.42 and 4.43 is provided below.

During the *first period from 0 to 2 s* of Fig. 4.42, the radiations of G1, G2, and G3 are 1000 W/m^2 each. In this case, there is only one peak and MPSO and FLC caught the GP, which is also clear in Fig. 4.43 as only one peak of that curve.

In the *second period 2−4 s*, the radiation of each module is 1000, 700, and 200 W/m^2. There are three peaks and the GP is the middle one as shown in Fig. 4.43. It is clear from Figs. 4.42 and 4.43 that MPSO caught the GP with power of 90 W but the FLC stuck around the right LP with power of 41 W. So, in this case

Table 4.3 Simulation Parameters of Each PV Module in PSIM [77]



the MMLs for MPSO and FLC are $90/(90 + 41 + 60) = 47.12\%$ and $41/(90 + 41 + 60) = 21.47\%$, respectively. It is clear from Figs. 4.42 and 4.43 that the generated power from MPSO is 60% greater than the power generated from FLC in this period (2−4 s).

In the *third period 4−6 s*, the radiation of each module is 1000, 900, and 700 W/m^2. There are three peaks and the GP is at the right-hand side. It is clear from Figs. 4.42 and 4.43 that MPSO and FLC caught the GP with power of 140 W. So, in this case the MML for MPSO and FLC is $140/(140 + 112 + 60) = 44.9\%$. It is clear from Figs. 4.42 and 4.43 that the generated power from MPSO FLC is equal in this period (4−6 s).

In the *fourth period 6−8 s*, the radiation of each module is 1000, 400, and 300 W/m^2. There are three peaks and the GP is at the left hand side. It is clear from Figs. 4.42 and 4.43 that MPSO caught the GP with power of 61 W but the FLC stuck on the right LP with power of 60 W. So in this case, the MMLs for MPSO and FLC are $61/(61 + 52 + 60) = 35.26\%$ and $60/(61 + 52 + 60) = 34.68\%$, respectively. It is clear from Figs. 4.42 and 4.43 that the generated power from MPSO is slightly greater than the power generated from FLC in this period (6−8).

In the *fifth period 8−10 s*, the radiation of each module is 1000, 800, 400 W/m^2. There are three peaks and the GP is the middle one. It is clear from Figs. 4.42 and 4.43 that MPSO caught the GP with power of 102 W but the FLC stuck on the right LP with power of 83 W. So, in this case the MMLs for MPSO and FLC are

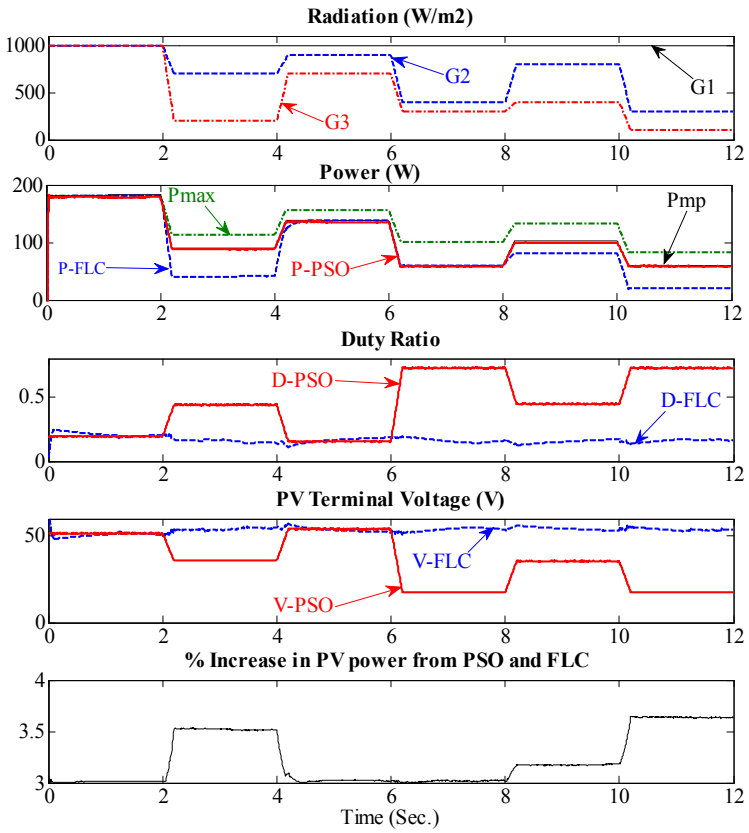


FIGURE 4.42

The simulation results of MPSO and FLC.

$102/(102 + 83 + 61) = 41.46\%$ and $83/(102 + 83 + 61) = 33.7\%$, respectively. It is clear from Figs. 4.42 and 4.43 that the generated power from MPSO is 20% greater than the power generated from FLC in this period (8−10 s).

In the *last period 10−12 s*, the radiation of each module is 1000, 300, and 100 W/m^2. There are three peaks and the GP is at the left hand side. It is clear from Figs. 4.42 and 4.43 that MPSO caught the GP with power of 61 W but the FLC stuck on the right LP with power of 20 W. So, in this case the MMLs for MPSO and FLC are $61/(61 + 40 + 20) = 50.41\%$ and $20/(61 + 40 + 20) = 16.5\%$, respectively. It is clear from Figs. 4.42 and 4.43 that the generated power from MPSO is 60% greater than the power generated from FLC in the last period (10−12 s).

It is clear from the above discussion that the FLC stuck always around local maxima, which sometimes has lower power than the GP which reduces the generated power considerably and participation in the hot spot occurs on shaded PV modules.

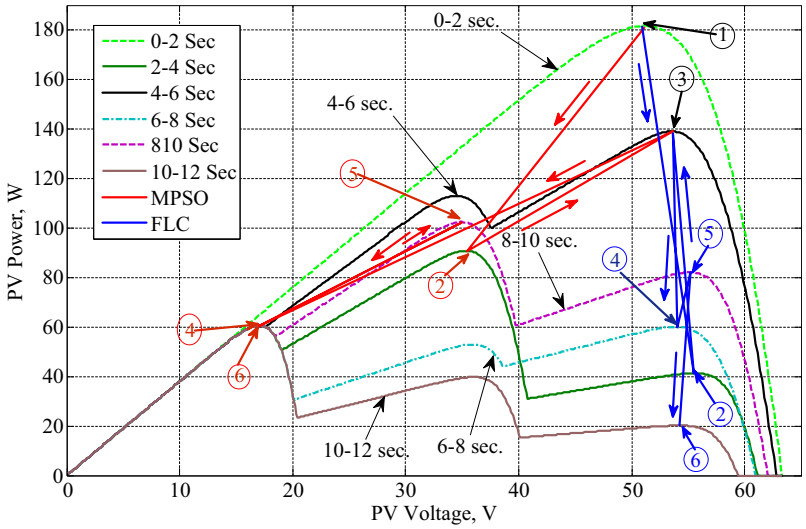


FIGURE 4.43

The relation between the generated power along with terminal voltage and the MPPT response for MPSO and FLC.

4. CONCLUSIONS

The generated power from the PV cells is changing with the operating voltage of the PV cell for each radiation and temperature. There is an MPP at certain voltage of the PV cells for each radiation and temperature. MPPT is used to track this point. Tracking the MPP by using the FLC proves an exact tracking for the MPP even in highly changing weather conditions. Fuzzy logic control system restrains any overshooting in input or output systems and increases a considerable amount of the energy captured. The FLC is implemented using FPGA.

Connecting many PV modules in series and parallel has been used to increase voltage and current to be suitable for the load. Partial shading on some PV modules will reduce the generated voltage of the PV system than the maximum power generated from each module separately. The shaded PV module will work as a load for other PV module, which increases the hot spot on shaded PV module and it may destroy these shaded PV modules. Bypass diodes should be connected across each PV module to remedy the effect of partial shading on shaded PV modules. Connecting several PV modules together will produce multiple peaks (one GP and multiple LPs) on partial shading conditions. Maximum power point tracker techniques (MPPT) have been used to follow the GP. Most of the MPPT techniques stick around LPs. Modified particle swarm optimization (MPSO) technique has been used to follow effectively the GP under all operating conditions with lower number of particles and iterations. This technique has been compared with FLC technique to

assess its operation in catching the GP. These two techniques have been simulated in cosimulation between Matlab/Simulink and PSIM. The simulation results show that the MPSO technique is more effective than FLC in following the GP. The generated power has been increased considerably with MPSO technique in shading condition than FLC. The increase in the generated power in MPSO technique than FLC depends on the level of partial shading conditions. The simulation results show the superiority of MPSO technique during normal and partial shading conditions.

REFERENCES

[1] T. Esram, P.L. Chapman, Comparison of photovoltaic array maximum power point tracking techniques, IEEE Trans. EC 22 (2) (June 2007) 439−449.

[2] V. Salas, E. Olías, A. Barrado, A. Lázaro, Review of the maximum power point tracking algorithms for stand-alone photovoltaic systems, Sol. Energy Mater. Sol. Cells 90 (11) (July 6, 2006) 1555−1578.

[3] A. Balouktsis, T.D. Karapantsios, K. Anastasiou, A. Antoniadis, I. Balouktsis, Load matching in a direct-coupled photovoltaic system-application to Thevenin's equivalent loads, Int. J. Photoenergy 2006 (27274) (2006) 1−7.

[4] K.Y. Khouzam, Optimum load matching in direct-coupled photovoltaic power systems application to resistive loads, IEEE Trans. EC 5 (2) (1990) 265−271.

[5] W.R. Anis, H.M.B. Metwally, Dynamic performance of a directly coupled PV pumping system, Sol. Energy 53 (4) (1994) 369−377.

[6] M.A.S. Masoum, H. Dehbonei, E.F. Fuchs, Theoretical and experimental analyses of photovoltaic systems with voltage and current-based maximum power-point tracking, IEEE Trans. Energy Convers. 17 (4) (December 2002) 514−522.

[7] H.-J. Noh, D.-Y. Lee, D.-S. Hyun, An improved MPPT converter with current compensation method for small scaled PV-applications, in: Proc. 28th Annu. Conf. Ind. Electron. Soc., 2002, pp. 1113−1118.

[8] K. Kobayashi, H. Matsuo, Y. Sekine, A novel optimum operating point tracker of the solar cell power supply system, in: Proc. 35th Annu. IEEE Power Electron. Spec. Conf., 2004, pp. 2147−2151.

[9] B. Bekker, H.J. Beukes, Finding an optimal PV panel maximum power point tracking method, in: 7th AFRICON Conference in Africa, 2004, pp. 1125−1129.

[10] N. Mutoh, T. Matuo, K. Okada, M. Sakai, Prediction-data-based maximum − power - point-tracking method for photovoltaic power generation systems, in: Proc. 33rd Annu. IEEE Power Electron. Spec. Conf., 2002, pp. 1489−1494.

[11] S. Yuvarajan, S. Xu, Photo-voltaic power converter with a simple maximum-power-point-tracker, in: Proc. 2003 Int. Symp. Circuits Syst., 2003 pp. III-399−III-402.

[12] M. Veerachary, T. Senjyu, K. Uezato, Voltage-based maximum power point tracking control of PV system, IEEE Trans. Aerosp. Electron. Syst. 38 (1) (January 2002) 262−270.

[13] N. Fermia, D. Granozio, G. Petrone, M. Vitelli, Predictive & adaptive MPPT perturb and observe method, IEEE Trans. Aerosp. Electron. Syst. 43 (3) (July 2007) 934−950.

[14] M.-L. Chiang, C.-C. Hua, J.-R. Lin, Direct power control for distributed PV power system, in: Proc. Power Convers. Conf., 2002, pp. 311−315.

[15] W. Wu, N. Pongratananukul, W. Qiu, K. Rustom, T. Kasparis, I. Batarseh, DSP-based multiple peak power tracking for expandable power system, Appl. Power Electron. Conf. Expo. (2003).
[16] Y.-T. Hsiao, C.-H. Chen, Maximum power tracking for photovoltaic power system, in: Conf. Record 37th IAS Annu. Meeting Ind. Appl. Conf, 2002, pp. 1035−1040.
[17] Y. Jung, G. Yu, J. Choi, J. Choi, High-frequency DC link inverter for grid-connected photovoltaic system, in: Conf. Record Twenty-ninth IEEE Photovoltaic Spec. Conf, 2002, pp. 1410−1413.
[18] S. Jain, V. Agarwal, A new algorithm for rapid tracking of approximate maximum power point in photovoltaic systems, IEEE Power Electron. Lett. 2 (1) (March 2004) 16−19.
[19] T. Tafticht, K. Agbossou, Development of a MPPT method for photovoltaic systems, in: Canadian Conf. Elect. Comput. Eng., 2004, pp. 1123−1126.
[20] N. Femia, G. Petrone, G. Spagnuolo, M. Vitelli, Optimization of perturb and observe maximum power point tracking method, IEEE Trans. Power Electron. 20 (4) (July 2005) 963−973.
[21] P.J. Wolfs, L. Tang, A single cell maximum power point tracking converter without a current sensor for high performance vehicle solar arrays, in: Proc. 36th Annu. IEEE Power Electron. Spec. Conf., 2005, pp. 165−171.
[22] V.B. Ioan, I. Marcel, Comparative analysis of the perturb-and-observe and incremental conductance MPPT methods, in: 8th International Symposium on Advanced Topics in Electrical Engineering May 23−25, Bucharest, Romania, 2013.
[23] H. Rezk, A.M. Eltamaly, A comprehensive comparison of different MPPT techniques for photovoltaic systems, Sol. Energy 112 (2015) 1−11.
[24] A. Al-Diab, C. Sourkounis, Variable step size P&O MPPT algorithm for PV systems, in: Optimization of Electrical and Electronic Equipment (OPTIM), 12th IEEE International Conference, 2010, pp. 1097−1102.
[25] B. Amrouche, M. Belhamel, A. Guessoum, Artificial intelligence based P&O MPPT method for photovoltaic systems, Rev. Des. Energies Renouvelables ICRESD-07 Telmcen 11−16 (2007).
[26] K. Kobayashi, I. Takano, Y. Sawada, A study on a two stage maximum power point tracking control of a photovoltaic system under partially shaded insolation conditions, in: IEEE Power Eng. Soc. Gen. Meet., 2003, pp. 2612−2617.
[27] M.A. Mohamed, A.M. Eltamaly, A.I. Alolah, PSO-based smart grid application for sizing and optimization of hybrid renewable energy systems, PLoS One 11 (8) (2016) e0159702.
[28] J. Ho Lee, H.S. Bae, Bo H. Cho, Advanced incremental conductance MPPT algorithm with a variable step size, in: Power Electronics and Motion Control Conference, 2006. EPE-PEMC 2006. 12th International at Portoroz, August 2006, pp. 603−607.
[29] J. Kouta, et al., Improving the incremental conductance control method of a solar energy conversion system, Int. Conf. Renew. Energy Power Qual. VI (2008). Santander: [sn].
[30] A.M. Eltamaly, H.H. El-Tamaly, P. Enjeti, An improved maximum power point tracker for photovoltaic energy systems, in: 2nd Minia International Conference for Advanced Trends in Engineering, (MICATE' 2002) Elminia, Egypt, March 16−18, 2002.
[31] K. Siri, K.A. Conner, Parallel-connected converters with maximum power tracking, in: IEEE conf., APEC 2002 vol. 1, March 2002, pp. 419−425.

[32] H. Abouobaida, M. Cherkaoui, Comparative study of maximum power point trackers for fast changing environmental conditions, in: Multimedia Computing and Systems (ICMCS), International Conference, May 10−12, 2012, pp. 1131−1136.
[33] Y.-T. Chen, Z.-H. Lai, R.-H. Liang, A novel auto-scaling variable step-size MPPT method for a PV system, Sol. Energy 102 (2014) 247−256.
[34] L. Fangrui, D. Shanxu, L. Fei, L. Bangyin, K. Yong, A variable step size INC MPPT method for PV systems, IEEE Trans. Ind Electron 55 (7) (2008) 2622−2628.
[35] K. Siri, K.A. Conner, Fault-tolerant scaleable solar power bus architectures with maximum power tracking, in: IEEE conf., APEC 2001 vol. 1, March 2001, pp. 1009−1014.
[36] J.W. Kimball, P.T. Krein, Digital ripple correlation control for photovoltaic applications, in: Power Electronics Specialists Conference, 2007. PESC 2007. IEEE, June 2007, pp. 1690−1694. Orlando, FL.
[37] P. Midya, P.T. Krein, R.J. Turnbull, R. Reppa, J. Kimball, "Dynamic maximum power point tracker for photovoltaic applications, in: Proc. 27th Annu. IEEE Power Electron. Spec. Conf., 1996, pp. 1710−1716.
[38] W. Xiao, W.G. Dunford, A modified adaptive hill climbing MPPT method for photovoltaic power systems, in: Proc. 35th Annu. IEEE Power Electron. Spec. Conf., 2004, pp. 1957−1963.
[39] M. Veerachary, T. Senjyu, K. Uezato, Maximum power point tracking control of IDB converter supplied PV system, in: IEE Proc. Elect. Power Application, 2001, pp. 494−502.
[40] A.M. Eltamaly, Performance of smart maximum power point tracker under partial shading conditions of photovoltaic systems, J. Renew. Sustain Energy 7 (4) (2015) 043141.
[41] S. Lalounia, D. Rekiouaa, T. Rekiouaa, E. Matagneb, Fuzzy logic control of stand-alone photovoltaic system with battery storage, J. Power Sourc. 193 (2009) 899−907.
[42] N. Ammasai Gounden, S. Ann Peter, H. Nallandula, S. Krithiga, Fuzzy logic controller with MPPT using line-commutated inverter for three-phase grid-connected photovoltaic systems, Renew. Energy J. 34 (2009) 909−915.
[43] Chokri Ben Salah, Maher Chaabenea, Mohsen Ben Ammara, Multi-criteria fuzzy algorithm for energy management of a domestic photovoltaic panel, Renew. Energy 33 (2008) 993−1001.
[44] I.H. Altasa, A.M. Sharaf, A novel maximum power fuzzy logic controller for photovoltaic solar energy systems, Renew. Energy 33 (2008) 388−399.
[45] N. Khaehintung, K. Pramotung, B. Tuvirat, P. Sirisuk, RISC microcontroller built-in fuzzy logic controller of maximum power point tracking for solar-powered light-flasher applications, in: Proc. 30th Annu. Conf. IEEE Ind. Electron. Soc., 2004, pp. 2673−2678.
[46] A.D. Karlis, T.L. Kottas, Y.S. Boutalisb, A novel maximum power point tracking method for PV systems using fuzzy cognitive networks (FCN), Electr. Power Syst. Res. 3−4 (March 2007) 315−327.
[47] A.M. Eltamaly, M.A. Mohamed, A novel design and optimization software for autonomous PV/wind/battery hybrid power systems, Math. Problems Eng. 2014 (2014).
[48] J. Kennedy, R. Eberhart, Particle swarm optimization, in: Proceedings of IEEE International Conference on Neural Networks, 1995.

[49] M. Miyatake, T. Inada, I. Hiratsuka, H. Zhao, H. Otsuka, M. Nakano, Control characteristics of a Fibonacci-search-based maximum power point tracker when a photovoltaic array is partially shaded, in: Power Electronics and Motion Control Conference, 2004. IPEMC, 2004.
[50] L. Liu, C. Liu, A novel combined particle swarm optimization and genetic algorithm MPPT control method for multiple photovoltaic arrays at partial shading, J. Energy Resour. Technol 135 (1) (2012) 012002.
[51] M.R. Rad, S.A. Taher, S. Akbari, A maximum power point tracker for photovoltaic arrays with particle swarm optimization technique in cooperation with fuzzy cognitive networks, in: NEEC 2010, 2010.
[52] K. Ishaque, Z. Salam, A deterministic particle swarm optimization maximum power point tracker for photovoltaic system under partial shading condition, Ind. Electron. IEEE Trans. 60 (8) (2013) 3195−3206.
[53] K. Ishaque, Z. Salam, A. Shamsudin, M. Amjad, A direct control based maximum power point tracking method for photovoltaic system under partial shading conditions using particle swarm optimization algorithm, Appl. Energy 99 (2012) 414−422.
[54] Q. Fu, N. Tong, A new PSO algorithm based on adaptive grouping for photovoltaic MPP prediction, in: 2nd International Workshop on Intelligent Systems and Applications (ISA), 2010.
[55] M.A. Hassan, M.A. Abido, Optimal design of microgrids in autonomous and grid-connected modes using particle swarm optimization, IEEE Trans. Power Electron. 26 (3) (2011) 755−769.
[56] B. Kroposki, R. Margolis, D. Ton, Harnessing the sun, Power Energy Mag. IEEE 7 (3) (2009) 22−33.
[57] M. Hejri, H. Mokhtari, On the parameter extraction of a five-parameter double-diode model of photovoltaic cells and modules, Photovoltaics IEEE J. 4 (3) (2014) 915−923.
[58] S.P.J.J. Bikaneria, Modelling and simulation of PV cell based on two-diode model, Int. J. Recent Trends Eng. Technol. 11 (2014).
[59] A.M. Eltamaly, Performance of smart maximum power point tracker under partial shading conditions of PV systems, in: 2015 IEEE International Conference on Smart Energy Grid Engineering (SEGE), IEEE, 2015.
[60] N.M. Shannan, N.Z. Yahaya, B. Singh, Two diode model for parameters extraction of PV module, in: 2014 IEEE Conference on Energy Conversion (CENCON), 2014.
[61] T. Ma, H. Yang, L. Lu, Development of a model to simulate the performance characteristics of crystalline silicon photovoltaic modules/strings/arrays, Sol. Energy 100 (February 2014) 31−41.
[62] M.A. Mohamed, A.M. Eltamaly, A.I. Alolah, Sizing and techno-economic analysis of stand-alone hybrid photovoltaic/wind/diesel/battery power generation systems, J. Renew. Sustain. Energy 7 (6) (2015) 063128.
[63] T. Markvart, L. Castafier, Solar Cells: Materials, Manufacture and Operation, Elsevier Publishing Co., 2005. ISBN:13:978-1-85617-457-1.
[64] L. Castaner, S. Silvestre, Modelling Photovoltaic Systems Using PSpice, John Wiley & Sons Ltd, Chichester, UK, 2002, ISBN 0-470-845279.
[65] www.energymatters.com.au.
[66] J. Łukasiewicz, On three-valued logic, Ruch Filozoficzny 5 (1920) 170−171.
[67] L.A. Zadeh, Fuzzy Sets and Systems, in: System Theory, Polytechnic Press, New York, 1965, pp. 29−39.
[68] L.A. Zadeh, Fuzzy sets, Inf. Control 8 (3) (1965) 338−353.

[69] M. Boukens, A. Boukabou, PD with fuzzy compensator control of robot manipulators: experimental study, in: 2013 3rd International Conference on Systems and Control (ICSC), 2013.
[70] A.M. Eltamaly, A.I. Alolah, M.Y. Abdulghany, Digital implementation of general purpose fuzzy logic controller for photovoltaic maximum power point tracker, in: IEEE, Speedam 2010, Pisa, Italy, 2010.
[71] A.E. Khateb, N.A. Rahim, J. Selvaraj, M.N. Uddin, Fuzzy logic controller based SEPIC converter for maximum power point tracking, IEEE Trans. Ind. Appl. 99 (2014) 1.
[72] S. El Beid, S. Doubabi, DSP-based implementation of fuzzy output tracking control for a boost converter, IEEE Trans. Ind. Electron. 61 (1) (2014) 196−209.
[73] R. Tipsuwanpom, T. Runghimmawan, S. Intajag, V. Krongratana, Fuzzy logic PID controller based on FPGA for process control, in: 2004 IEEE International Symposium, 2004.
[74] A.M. Eltamaly, Modeling of fuzzy logic controller for photovoltaic maximum power point tracker, in: Solar Future 2010 Conf., Istanbul, Turkey, 2010.
[75] Q. Zhang, Y.Z.X. Sun, L. Guo, M. Matsui, Operation mode analysis for solving the partial shadow in a novel PV power generation system, in: Power Electronics Conference (IPEC-Hiroshima 2014-ECCE-ASIA), Hiroshima, 2014.
[76] K. Kim, Hot Spot Detection and Protection Methods for Photovoltaic Systems (Ph.D. dissertation), 2014.
[77] P. U. Manual, PSIM Computer Simulation (Online). Available from: www.power_design.com.

This page intentionally left blank

CHAPTER

DMPPT PV System: Modeling and Control Techniques

5

Marco Balato, Luigi Costanzo, Massimo Vitelli

Department of Industrial and Information Engineering, Università degli Studi della Campania "Luigi Vanvitelli", Aversa, Italy

CHAPTER OUTLINE

1. Maximum Power Point Tracking of a Photovoltaic Source 163
2. Central Maximum Power Point Tracking and Distributed Maximum Power Point Tracking 164
3. Necessity of Joint Adoption of Distributed Maximum Power Point Tracking and Central Maximum Power Point Tracking: Hybrid Maximum Power Point Tracking.... 167
3.1 HMPPTS Technique 171
3.1.1 Modified P&O Distributed Maximum Power Point Tracking Technique 171
3.1.2 CMPPTS Technique 175
3.2 HMPPTF Technique 180
3.2.1 Exact and Approximate I–V and P–V Characteristics of LSCPVUs 180
3.2.2 Distributed Maximum Power Point Tracking and Central Maximum Power Point Tracking Based on Fast Estimate of Maximum Power Voltages 190
3.2.3 Numerical Simulations Concerning Hybrid Maximum Power Point Tracking Techniques 195
References 201

1. MAXIMUM POWER POINT TRACKING OF A PHOTOVOLTAIC SOURCE

It is well known that a photovoltaic (PV) array under uniform irradiance exhibits a power versus voltage (P–V) characteristic with a unique point, called the Maximum Power Point (MPP), where the array provides maximum output power [1]. Because the P–V characteristic of a PV array and hence its MPP change as a consequence of the variation of the irradiance level and of the panels' temperature (which is in turn function of the irradiance level, of the ambient temperature, of the efficiency of the heat exchange mechanism and of the operating point of the panels), it is necessary to track continuously the MPP to maximize the power output from a PV system, for a

Advances in Renewable Energies and Power Technologies. https://doi.org/10.1016/B978-0-12-812959-3.00005-8
Copyright © 2018 Elsevier Inc. All rights reserved.

given set of operating conditions. Many Maximum Power Point Tracking (MPPT) techniques have been presented in the literature [1–8]. Nevertheless, the Perturb and Observe (P&O) and Incremental Conductance (INC) techniques are widely used [8], especially for low-cost implementations. In case of mismatching operating conditions of the PV modules of a given PV array (because of the effects of clouds, shadows of neighboring objects, dirtiness, manufacturing tolerances, different orientation of parts of the PV field, dust, uneven aging, thermal gradients etc.), the P–V characteristic of the PV field may exhibit more than one peak, because of the presence of bypass diodes and/or of PV cells that work in reverse bias conditions, and MPPT algorithms can fail. As a result, a marked reduction of the overall system efficiency occurs [9–14]. Moreover, the absolute maximum power of a mismatched PV field is lower than the sum of the available maximum powers that the mismatched modules would be able to provide if each of them could operate in its own MPP. Therefore, it is evident that the adoption of a PV system architecture able to allow each PV module of the array to operate in its own MPP is highly desirable. Such an architecture can be obtained by choosing one of the two possible following options. The first option is represented by the possibility of using module-dedicated DC/AC converters, often called microinverters, carrying out the MPPT for each PV module [15–25]. Microinverters have their output ports directly connected in parallel to the grid. The second option is represented instead by the possibility of using module-dedicated DC/DC converters, often called microconverters or power optimizers or module maximizers, carrying out the MPPT for each PV module [26–44]. Indeed, as discussed in [44], each bypass diode of a given PV module should be substituted by a microconverter to avoid the drawbacks associated to mismatching operating conditions among strings of cells belonging to the same PV module and put in parallel to different bypass diodes. This chapter is devoted to an in-depth description of exact and approximate modeling techniques of PV systems adopting microconverters. Such modeling techniques are very useful to properly design control techniques allowing the extraction of the maximum available power from PV systems adopting microconverters.

2. CENTRAL MAXIMUM POWER POINT TRACKING AND DISTRIBUTED MAXIMUM POWER POINT TRACKING

In this chapter, the term Distributed MPPT (DMPPT) technique will be used with specific reference to an MPPT technique simultaneously acting on the output of each PV module representing the source of each microconverter. Hereafter, a system composed by a PV module equipped with microcontroller will be called self-controlled PV unit (SCPVU). In the following analysis, without any loss of generality, reference will be made to Lossless SCPVU (LSCPVU). The term “lossless” means not only that all losses occurring in the power stage of DC/DC converters (conduction losses, switching losses, iron losses, etc.) are neglected in the following, but also that, in the sequel, the MPPT efficiency of the DMPPT controllers is

considered equal to one. The schematic representations of DMPPT architectures under investigation are shown in Fig. 5.1 in which grid-connected PV systems adopting microconverter-based DMPPT are reported. Fig. 5.1A refers to boost-based LSCPVUs, Fig. 5.1B refers to buck–boost based LSCPVUs, and Fig. 5.1C refers to buck-based LSCPVUs. It is worth noting that, in each of the above figures, the array of LSCPVUs is indeed represented by means of a single string of N LSCPVUs feeding a central grid-connected inverter. Of course, more strings of LSCPVUs can be put in parallel to feed the central grid-connected inverter. Indeed, a PV inverter can support whatever current in a certain range while keeping its input voltage regulated to a given average value v_b [45,46]. This assumption greatly simplifies the analysis of the PV system because each string of LSCPVUs forms an independent loop with the equivalent DC voltage source v_b representing the model of the input port of the inverter. Hence, because each string of LSCPVUs can be analyzed independently

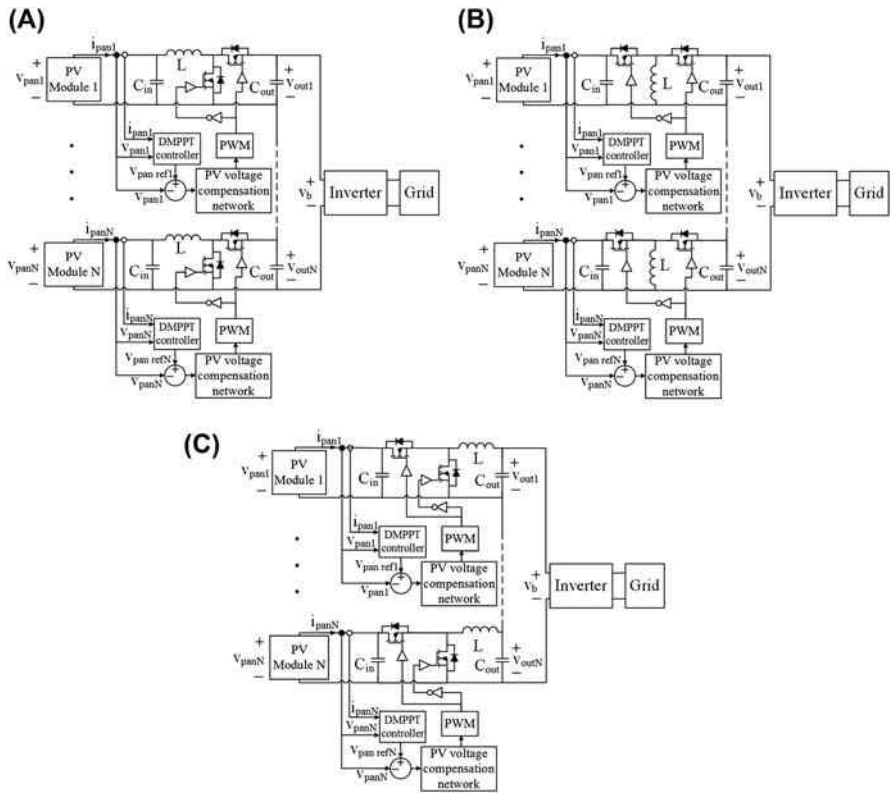


FIGURE 5.1

Grid-connected photovoltaic (PV) system adopting lossless, controlled PV units (LSCPVUs): (A) boost-based LSCPVU, (B) buck–boost based LSCPVU, (C) buck-based LSCPVU.

from all the others, in the rest of this chapter the attention will be focused, without any loss of generality, on techniques for modeling single strings of LSCPVUs. Moreover, in the rest of this chapter, again without any loss of generality, the three basic DC/DC converters (buck, boost, and buck−boost) with synchronous rectification and input-voltage feedback control will be considered [45], as shown in Fig. 5.1. Microconverters based on the above basic topologies are the most widely available on the market [47−51]. The presence of the input voltage feedback controller (PV voltage compensation network) allows to avoid that every disturbance introduced on the output voltage of an LSCPVU, by the inverter and/or by other LSCPVUs, directly propagates on the PV modules' output voltage causing instability or dynamic performance degradation [45,46]. The PV voltage compensation network of Fig. 5.1 processes the error between the k-th PV voltage v_{pank} and the corresponding reference voltage $v_{pan\ ref\ k}$ (k = 1, 2, …,N) provided by the DMPPT controller. The output control signal of the PV voltage compensation network drives the PWM block. If the control loop is fast enough, disturbances acting on the output voltage of a given LSCPVU do not significantly affect its operation [43,45,46]. The meaning which, in this chapter, will be given to the term DMPPT has been already provided above. The term Central MPPT (CMPPT) will be used instead with reference to an MPPT technique acting on the output voltage of a whole string of LSCPVUs.

Of course, such an output voltage also represents the DC input voltage v_b of the grid-connected inverter. Therefore, the CMPPT technique is carried out by a unique controller equipping the central inverter. A great number of grid-connected PV inverter topologies have been presented in the literature [52]. In this chapter, the simple but widespread architecture shown in Fig. 5.2 will be considered [45,46]. The power stage of the inverter is based on the H-bridge topology. The grid current

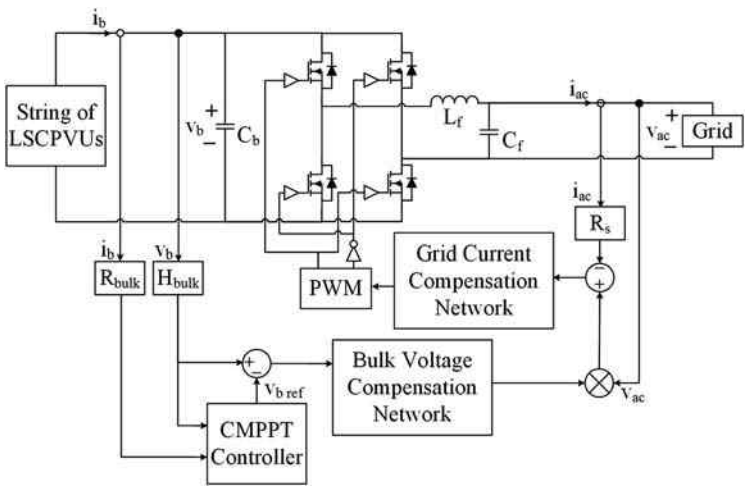


FIGURE 5.2

Grid-connected inverter system.

compensation network of Fig. 5.2 belongs to the wide-bandwidth current controller inner loop, which performs the power factor correction on the AC side [45,46,52,53]. The bulk voltage compensation network belongs instead to the outer low-bandwidth loop, which regulates the low-frequency components of the energy storage capacitor voltage v_b and therefore ensures the balance between the average DC input power and the average AC output power. The CMPPT controller of Fig. 5.2 provides the voltage reference value $v_{b\ ref}$, which must be followed by v_b to maximize the energetic performances of the whole PV system. In fact, in Refs. [54–56] it has been shown that, to get full profit from DMPPT, it is necessary that the bulk inverter voltage belongs to an optimal range whose position and amplitude are functions of the following factors: the number of PV modules and dedicated DC/DC converters in a string, the atmospheric operating conditions characterizing each PV module (irradiance and temperature values), the voltage and current ratings of the physical devices the DC/DC converters are made of, and the adopted DC/DC converter topology. Therefore, to extract as much as energy as possible, not only the PV module voltages but also the bulk inverter voltage v_b must assume specific optimal values that change, case by case, with the atmospheric operating conditions of the PV system.

3. NECESSITY OF JOINT ADOPTION OF DISTRIBUTED MAXIMUM POWER POINT TRACKING AND CENTRAL MAXIMUM POWER POINT TRACKING: HYBRID MAXIMUM POWER POINT TRACKING

The reason why the DMPPT technique alone is not able to lead to the working of each PV module of the field in its MPP, whichever mismatching operating condition, is linked to the limited voltage conversion ratio of the adopted DC/DC converters and to the finite voltage and current ratings of devices of the power stage of LSCPVUs [43,54,55]. In this chapter, the symbol $V_{ds\ max}$ will be used to identify the maximum drain-to-source voltage of the microconverters' switches when they are in the OFF state and the symbol $I_{ds\ max}$ will be used to identify the maximum drain current in the microconverters' switches when they are in the ON state. Because of the series connection of the output ports of N LSCPVUs, it is:

$$v_{outk} = \frac{P_{pank}}{I_{outk}} = \frac{v_b}{\sum_{i=1}^{N} P_{pani}} \cdot P_{pank} \tag{5.1}$$

where P_{pank} is the power extracted from the k-th PV module; v_{outk} and i_{outk}, respectively, are the output voltage and current of the k-th LSCPVU; and v_b is the inverter DC input voltage. From Eq. (5.1), it is clear that, in mismatching conditions, the higher the output power of the LSCPVU, the higher its output voltage that, in certain conditions, may become very large. The voltage across the output capacitor and the

active switch of a boost converter, during its OFF subinterval, is equal to the output voltage [53]. The voltage across the active switch of a buck−boost converter, during its OFF subinterval, is equal to the sum of the input and output voltages [53]. To avoid that the voltage stress of a device of one or more LSCPVUs exceeds $V_{ds\ max}$, an output voltage limitation technique needs to be adopted in the case of boost and buck−boost converters [43,57]. Of course, no output voltage limitation technique is needed in the case of buck converters. In the case of the buck−boost and buck topologies also switch current limitation techniques need to be adopted to avoid that the currents in the switches may exceed $I_{ds\ max}$ [55,57,58]. To limit the currents of the switches of a buck−boost converter or of a buck converter fed by a PV module, it is possible to adopt for the duty-cycle a time-varying lower threshold equal to the ratio $i_{pan}/I_{ds\ max}$, where i_{pan} is the current of the PV module [55]. In this chapter and, in particular, in Section 3.2.3, our attention will be focused on the output voltage limitation technique only, because it deserves particular care in the case of boost-based LSCPVUs, which are the subject of the time-domain numerical simulations discussed in the following. Another parameter imposing additional constraints, which must be fulfilled to avoid limiting the energetic efficiency performances of PV systems adopting microconverters, is represented by the value assumed by the bulk inverter voltage v_b [54−56,58]. To clarify the above statement, the examples reported in Fig. 5.3 should be illumining. SolarWorld SW225 PV modules will be considered throughout this chapter to carry out numerical simulations. Their electrical characteristics in STC (Standard Test Conditions, that is AM = 1.5,

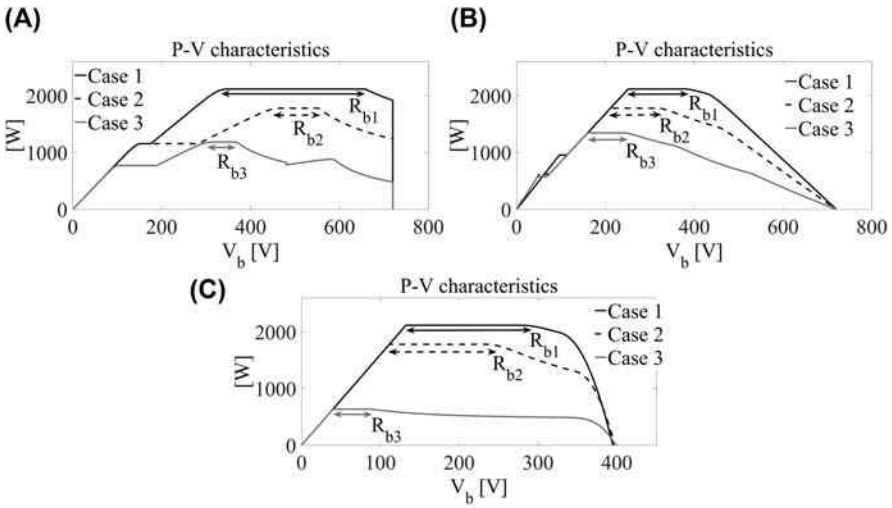


FIGURE 5.3

P−V characteristics of a string of 12 lossless self-controlled photovoltaic units (LSCPVUs): (A) boost-based LSCPVU, (B) buck−boost based LSCPVU, (C) buck-based LSCPVU.

Table 5.1 Electrical Characteristic of the SolarWorld SW225 PV Modules

Open-circuit voltage STC	VOC_STC = 36.8 V
Short-circuit current in STC	ISC_STC = 8.17 A
MPP voltage in STC	VMPP_STC = 29.5 V
MPP current in STC	IMPP_STC = 7.63 A
Nominal operating cell temperature	NOCT = 46°C

irradiance S = 1000 W/m^2, module temperature T_{module} = 25°C) are reported in the Table 5.1.

The curves shown in Fig. 5.3 represent the P−V characteristics of a string composed by 12 LSCPVUs. In particular, Fig. 5.3A refers to 12 boost-based LSCPVUs, Fig. 5.3B refers to 12 buck−boost based LSCPVUs, and Fig. 5.3C refers to 12 buck-based LSCPVUs. The guidelines allowing to obtain the curves that are reported in Fig. 5.3 have been discussed in detail in Vitelli and Femia et al. [54,55] and will be briefly summarized in the subsection "Exact and approximate I−V and P−V characteristics of LSCPVUs". In the sequel, without loss of generality, the LSCPVUs will be ordered in such a manner that the corresponding irradiance levels are sorted in descending order. Based on Eq. (5.1), also their corresponding output voltages form a list in descending order. In particular, Case 1, Case 2, and Case 3 of Fig. 5.3, respectively, refer to the following distributions S of irradiance values characterizing the LSCPVUs: S = [1000 1000 1000 1000 1000 1000 800 800 800 800 800 800] W/m^2, S = [1000 1000 1000 1000 1000 1000 500 500 500 500 500 500] W/m^2, S = [1000 1000 1000 1000 500 500 500 500 200 200 200 200] W/m^2. As for $T_{ambient}$, $V_{ds\ max}$, and $I_{ds\ max}$, their values have been assumed equal, respectively, to 25°C, 60 V, and 16 A. The optimal ranges of v_b, labeled with R_{b1}, R_{b2}, and R_{b3} and evidenced in Fig. 5.3, respectively, refer to Case 1, Case 2, and Case 3. The different position and amplitude of the three optimal ranges (R_{b1}, R_{b2}, and R_{b3}) proves the necessity of the joint adoption of the DMPPT and CMPPT function. It is worth noting that Fig. 5.3 has been obtained by considering the ideal case of LSCPVUs. Of course, if the effect of a realistic power stage efficiency profile is considered, the shape of the P−V curves and hence the amplitude and the position of the optimal operating range R_b are significantly altered but it is always true that the adoption of the CMPPT function in addition to the DMPPT function is necessary in PV systems adopting microconverters. Such a consideration directly leads to the concept of Hybrid MPPT (HMPPT) technique. An HMPPT technique is a control technique allowing the tracking of the whole set of optimal operating points of the PV system. Such a technique is called Hybrid just because it involves not only a proper control of the DC input voltage v_b of the central inverter but also a proper control of all the PV module voltages. The necessity of adoption of a suitable HMPPT technique is not completely clear to all the inverters and/or microconverter manufacturers. In fact, many manufacturers of microconverters or of

central inverters share the wrong opinion that because in PV applications adopting microconverters the MPPT is distributed on the PV modules, the MPPT hardware of the central inverter can be disabled or, better, the central inverter can be without CMPPT control circuitry.

That's why some commercial PV inverters (e.g., SolarEdge), adopted in PV applications using microconverters, operate with a fixed value of the DC input voltage (the value where the inverter exhibits its peak efficiency). Instead, as it will be deeply discussed in the following sections, the adoption of a proper CMPPT technique coupled to a proper DMPPT technique is absolutely necessary. The term proper here means that both the CMPPT technique and the DMPPT technique must be correctly designed to avoid possible errors or malfunctioning during their working. Regarding the DMPPT technique, a modified version of the P&O technique will be adopted. Such a technique is able not only to track the MPP but also to face and solve the problem of the limitation of the LSCPVUs output voltage. To avoid possible errors of the CMPPT technique during the working of the PV system, such a technique must be properly designed to consider the effect played by the particular shape exhibited by the P−V characteristic of the string of LSCPVUs. In fact, the shape of the P−V characteristic of a string of LSCPVUs, in case of mismatching operating conditions, is characterized by the presence of multiple peaks, flat regions, and/or nearly vertical portions [54,55]. Such features are able to lead to the error all the standard MPPT techniques (e.g., P&O, INC, etc.). As an example, by assuming $V_{ds\ max} = 60$ V, $T_{ambient} = 25°C$, and the following distribution S of irradiance values on the 12 boost-based LSCPVUs of the string S = [1000 1000 1000 1000 1000 1000 350 300 250 200 150 150] W/m^2, the corresponding P−V characteristic, which is shown in Fig. 5.4, exhibits the presence of flat regions, suboptimal operating points, and nearly vertical portions.

In the following subsections, two HMPPT techniques will be presented. The first one will be identified with the acronym HMPPTS (hybrid MPPT technique based on the periodic scan of the whole P−V characteristic of the string of LSCPVUs) and it will be discussed in detail in the subsection "HMPPTS technique". The second one will be indicated with the acronym HMPPTF [hybrid MPPT technique based on the

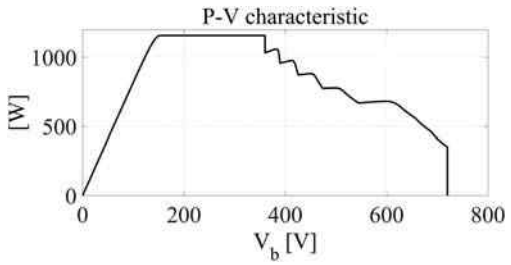


FIGURE 5.4

P−V characteristic of a string of 12 boost-based lossless self controlled photovoltaic units (LSCPVUs).

Fast Estimate of Maximum Power Voltages (FEMPV) algorithm] and will be discussed in depth in the subsection "HMPPTF technique".

3.1 HMPPTS TECHNIQUE

The HMPPTS technique adopts a Modified P&O technique as DMPPT technique and a CMPPT technique, which is based on the periodic scan of the whole P−V characteristic of the string of LSCPVUs. The aim of such a scan is represented by the identification of the best operating value, from the energetic efficiency point of view, of the bulk inverter voltage v_b. Such a CMPPT technique will be indicated in the following with the acronym CMPPTS. In subsection "Modified P&O DMPPT technique", the Modified P&O technique will be explained in detail, and in subsection "CMPPTS technique", it will be shown how to properly optimize the CMPPTS technique. In particular, it will be shown that, despite the seeming great simplicity of the CMPPTS technique, much care is needed to avoid errors because of the peculiar shape assumed, under mismatching operating conditions, by the P−V characteristic of a string of LSCPVUs. Such a P−V characteristic, as seen before (Fig. 5.4), in case of mismatching operating conditions may exhibit the presence of multiple peaks, flat regions, and/or nearly vertical portions, which might easily lead the CMPPTS technique in error, and, consequently, to a more or less consistent waste of the potentially available energy of the PV systems. Therefore, a proper choice of the parameters of the CMPPTS technique is mandatory. In fact, if properly designed, the CMPPTS technique is instead not affected at all by errors, whatever the shape of the P−V characteristic, and therefore the optimization of the energetic performances of the whole PV system is possible.

3.1.1 Modified P&O Distributed Maximum Power Point Tracking Technique

As shown in Fig. 5.1, the output signal of each DMPPT controller is a reference voltage $v_{pan\ ref}$, which is compared with the sensed PV module voltage v_{pan}. The corresponding error drives a PV voltage compensator network. The working principle of the P&O technique is based on the periodic perturbation of the reference voltage $v_{pan\ ref}$ [1]. In particular, the sign of the perturbation of $v_{pan\ ref}$ at the $(k+1)$-th sampling instant is decided on the basis of the following rule: $v_{pan\ ref}((k+1)T_a) = v_{pan\ ref}(kT_a) + \Delta v_{pan\ ref} \cdot \mathrm{sign}(p((k+1)T_a) - p(kT_a))$, where $p(t)$ is the instantaneous power drawn from the PV module, $\Delta v_{pan\ ref}$ is the amplitude of the perturbation of $v_{pan\ ref}$, and T_a is the sampling interval [1]. A suitable modification of the standard P&O MPPT technique allows to avoid that the output voltage of one or more LSCPVUs (those ones providing higher powers, see Eq. 5.1) exceeds $V_{ds\ max}$. Such a modification justifies the adjective "Modified," which has been added to the name of the technique and hence the acronym MP&O, which will be used in the following to label the Modified P&O technique. The limitation of the output voltage of the LSCPVUs, which is obtained by means of the MP&O technique, does not require the adoption of additional control circuitries as it happens instead with the output voltage limitation techniques proposed in Refs. [43,57]. The MP&O

technique works as follows: when the output voltage v_{outk} of the k-th LSCPVU exceeds a guard level $V_{out\ lim}$ ($V_{out\ lim} < V_{ds\ max}$) thus becoming closer to $V_{ds\ max}$, the MPPT function carries out an inversion of direction of tracking (direction of decreasing of output power P_{pank}). Summarizing, when $v_{outk} \leq V_{out\ lim}$, then the MP&O MPPT technique drives the k-th LSCPVU in the direction of increasing output power; instead, when $v_{outk} > V_{out\ lim}$, it drives the k-th LSCPVU in the direction of decreasing output power. It is appropriate to adopt a value of $V_{out\ lim}$, which is as high as possible to profitably exploit the whole voltage rating $V_{ds\ max}$ of LSCPVUs' components. In fact, the adoption of the guard-level voltage $V_{out\ lim}$ is obviously equivalent, in practice, to the choice of LSCPVUs' power components characterized by a voltage rating equal to $V_{out\ lim}$ instead that equal to $V_{ds\ max}$, with $V_{out\ lim} < V_{ds\ max}$. As a rule of thumb, the higher $V_{out\ lim}$, the higher the maximum power which can be extracted from the PV systems adopting microconverters. In fact, as shown in Fig. 5.5, lower values of $V_{out\ lim}$ lead to systems characterized by smaller amplitudes of the optimal range R_b with the additional drawback that R_b may fall outside the allowed inverter input voltage operating range. In Fig. 5.5, the P−V characteristics of a string of 12 LSCPVUs, which have been obtained by assuming an ambient temperature $T_{ambient}$ equal to 25°C, a distribution S of irradiance values equal to [1000 1000 1000 1000 1000 1000 1000 100 100 100 100 100] W/m^2, and three different values of $V_{out\ lim}$ ($V_{out\ lim} = 60$ V, $V_{out\ lim} = 50$ V and $V_{out\ lim} = 40$ V) have been reported together with the corresponding ranges R_b. In particular, Fig. 5.5A refers to 12 boost-based LSCPVUs and Fig. 5.5B refers to 12 buck−boost based LSCPVUs. The allowed inverter input voltage operating range (evidenced by means of the highlighted region of Fig. 5.5) has been assumed to be equal to [360, 660] V, which is a typical range for H-bridge central inverters (see Fig. 5.2) that are connected to electrical grids characterized by an RMS value of the grid voltage equal to 230 V. As shown in Fig. 5.5B, it is evident that when $V_{out\ lim} = 40$ V, the optimal range R_b becomes a single operating point. Of course, it is also evident that, in general, the considered inverter is not suitable in any of the cases of Fig. 5.5B. The maximum "optimal" value to be

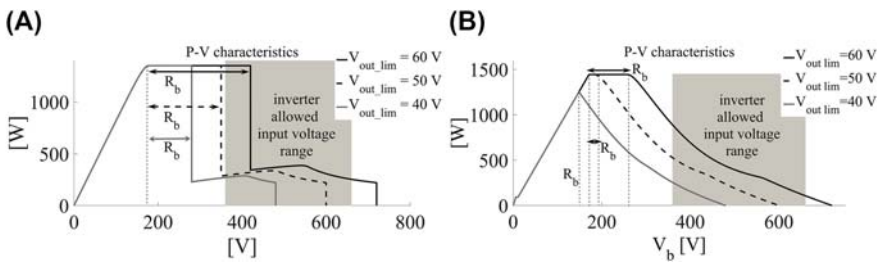


FIGURE 5.5

P−V characteristics of a string of 12 lossless self controlled photovoltaic units (LSCPVUs): (A) boost-based LSCPVU, (B) buck−boost based LSCPVU.

assigned to $V_{out\ lim}$ can be evaluated on the basis of the following considerations. We will consider a string composed by N LSCPVUs and we will assume that all the variations of $v_{pan\ refk}$ (k = 1, 2, …, N), as a worst-case, take place at the same instant t_0 (even if in practical applications they are not synchronous at all). Further, we will consider negligible the settling time of the LSCPVU equipped with a linear input voltage feedback control circuitry. This means that the steady-state variations of all the variables of interest (the powers extracted from the LSCPVUs, their input or output voltages etc.), occurring as a consequence of the variations of $v_{pan\ refk}$, take place immediately at t_0^+. Because of the unit gain of the sensor of the PV voltage and the zero steady-state error, ensured by the action of the PV voltage compensation network, we get: $\Delta v_{pank} = \Delta v_{pan\ ref}$, where Δv_{pank} is the variation of the PV voltage of the k-th LSCPVU (k = 1, 2, …, N). Because the LSCPVUs have been ordered in descending order, with reference to the corresponding values of the irradiance level, the first LSCPVU is characterized by the highest value of the irradiance level, and therefore (see Eq. 5.1), its output voltage is relatively high and may be in the proximity of $V_{out\ lim}$. Therefore, let's assume that at t_0^-, that is, immediately before the occurrence of the variations of $v_{pan\ refk}$ (k = 1, 2, …, N), the value v_{out1} of the output voltage of the first LSCPVU is nearly equal to the guard level $V_{out\ lim}$ ($v_{out1} \approx V_{out\ lim}$).

Further, let us suppose that the variation of $v_{pan\ ref1}$ driven at t_0 by the DMPPT controller of the first LSCPVU causes a positive variation ΔP_{pan1} of the power P_{pan1}. This is certainly possible because it is coherent with the working principle of the MP&O DMPPT technique because it has been assumed that $v_{out1} \approx V_{out\ lim}$ at t_0^-. In addition, let us suppose that all the other power variations ΔP_{pank} (k = 2, …, N), occurring at t_0^+, are negative so that, as suggested by Eq. (5.1), a positive variation Δv_{out1} of v_{out1} takes place. We are interested in evaluating the worst-case value of Δv_{out1}, that is, the highest possible value of Δv_{out1}, because we are searching for conditions granting that the output voltage of the first LSCPVU does not exceeds $V_{ds\ max}$. The worst-case value of Δv_{out1} can be evaluated by assuming that:

$$\Delta P_{pank} = -\Delta P_{pan1\_max} \quad (k = 2, \ldots, N) \tag{5.2}$$

where

$$\begin{aligned} \Delta P_{pan1\_max} &= \left| \frac{\partial P_{pan1}(v, S, T_{module})}{\partial v} \Big|_{S_{max},\, V_{OC},\, T_m} \right| \cdot \Delta v_{pan1} \\ &= \left| \frac{\partial P_{pan1}(v, S, T_{module})}{\partial v} \Big|_{S_{max},\, V_{OC},\, T_m} \right| \cdot \Delta v_{pan\ ref} \end{aligned} \tag{5.3}$$

In Eq. (5.3) ΔP_{pan1_max} is assessed by considering the P−V module characteristic associated to the maximum possible value S_{max} of the irradiance level ($S_{max} = 1000\ W/m^2$) and to a module temperature T_{module} given by [10]:

$$T_{module} = T_{ambient} + (NOCT - 20°C) \cdot \frac{S_{max}}{800} \tag{5.4}$$

By assuming $T_{ambient} = 25°C$ and $NOCT = 46°C$, we get $T_{module} = 57.5°C$. The derivative term appearing in Eq. (5.3) has been evaluated at a voltage equal to V_{oc} (open circuit voltage). In fact, at V_{oc}, the magnitude of the slope of the P−V module characteristic is the highest possible. So that, in correspondence of a given variation $\Delta v_{pan1} = \Delta v_{pan\ ref}$ of the voltage, the corresponding variation ΔP_{pan1} provided by (5.3) assumes its maximum value (ΔP_{pan1_max}). The total variation ΔP_{tot} of the power extracted by the string of N LSCPVUs is given as

$$\Delta P_{tot} = \sum_{k=1}^{N} \Delta P_{pank} = -(N-2)\cdot \Delta P_{pan1\_max} \tag{5.5}$$

Because in practical applications, $N > 2$ (in fact typically $10 < N < 20$) then ΔP_{tot} is < 0. Therefore, it is possible to state that the total variation ΔP_{tot} evaluated by using Eqs. (5.2)−(5.5) assumes the lowest possible value. Summarizing, if the value assumed by ΔP_{pan1} is maximum (ΔP_{pan1_max}), then the value assumed by ΔP_{tot} in Eq. (5.5) is minimum and, as it will be clear in the following, this in turn leads to the highest possible value of Δv_{out1} (see Eq. 5.1). In case of LSCPVUs, we get:

$$\begin{aligned} \Delta P_{pan1} = \Delta P_{pan1\_max} &\approx v_{out1}\cdot \Delta i_{out1} + \Delta v_{out1}\cdot i_{out1} \\ &\approx V_{out\ lim}\cdot \Delta i_{out} + \Delta v_{out1}\cdot i_{out} \end{aligned} \tag{5.6}$$

It is worth noting that, as a result of the series connection of the LSCPVUs, a unique output current flows, so that in Eq. (5.6), the symbol i_{out} has been used in place of i_{out1} and the symbol Δi_{out} in place of Δi_{out1}. From Eq. (5.6) we get:

$$\Delta v_{out1} \approx \frac{\Delta P_{pan1\_max} - V_{out\ lim}\cdot \Delta i_{out}}{i_{out}} \tag{5.7}$$

The inequality that must be fulfilled to avoid exceeding the voltage rating $V_{ds\ max}$ is

$$v_{out1} + \Delta v_{out1} \approx V_{out\ lim} + \Delta v_{out1} \le V_{ds\ max} \tag{5.8}$$

It is worth noting that Eq. (5.8) states an obvious principle: the lower Δv_{out1} (best-case), the higher the value that can be assigned to $V_{out\ lim}$ and, therefore, as discussed at the beginning of this section, the higher the energetic efficiency, which can be obtained by the PV system. From Eqs. (5.7) and (5.8), we get

$$V_{out\ lim} \le \frac{v_{ds\ max} - \dfrac{\Delta P_{pan1\_max}}{i_{out}}}{\left(1 - \dfrac{\Delta i_{out}}{i_{out}}\right)} \tag{5.9}$$

The worst-case (lowest) value of the threshold that must not be exceeded by $V_{out\ lim}$ can be found by minimizing the right-hand side term in Eq. (5.9). This objective can be obtained by exploiting the following equalities:

$$\begin{aligned} i_{out\_min} &= \frac{P_{pan1}}{v_{ds\ max}} \\ \Delta i_{out\_min} &= \frac{\Delta P_{tot}}{N\cdot v_{oc}} \end{aligned} \tag{5.10}$$

By Substituting Eq. (5.10) in (5.9), we get

$$V_{out\ lim} \le \frac{v_{ds\ max} \cdot \left(1 - \frac{-P_{pan1\_max}}{P_{pan1}}\right)}{\left(1 - \frac{\Delta P_{tot}}{N \cdot V_{OC} \cdot \frac{P_{pan1}}{v_{ds\ max}}}\right)} = \frac{v_{ds\ max} \cdot \left(1 - \frac{\Delta P_{pan1\_max}}{P_{pan1}}\right)}{\left(1 - \frac{v_{ds\ max} \cdot (N-2) \cdot \Delta P_{tot}}{N \cdot V_{OC} \cdot P_{pan1}}\right)} \tag{5.11}$$

where P_{pan1} is the maximum power that can be extracted from the first PV module. An additional constraint must be considered in the case of boost-based LSCPVUs. In fact, because the voltage conversion ratio of the boost converter is higher than 1 and the operating voltage of a given PV module is comprised between 0 and V_{oc}, in addition to Eq. (5.11) it must also be:

$$V_{out\ lim} \le V_{OC} \tag{5.12}$$

3.1.2 CMPPTS Technique

The CMPPTS technique is based on the periodic scan of the P−V characteristic of the string of N LSCPVUs to identify the value $V_{b\ opt}$ of the bulk inverter voltage v_b in correspondence of which the power P extracted from the string of LSCPVUs assumes its maximum value. The scan is carried out by means of the CMPPTS controller and by means of the inverter outer feedback loop (Fig. 5.2). The output of the CMPPTS controller, during the scan, is a staircase signal $v_{b\ ref}$, which represents the reference voltage that must be followed by v_b (Fig. 5.6). In the sequel, for the sake of simplicity but without any loss of generality, the gains H_{bulk} and R_{bulk} of the sensors of the bulk voltage v_b and current i_b will be assumed equal to 1. The error between v_b and $v_{b\ ref}$ represents the input signal of the bulk voltage compensation network of Fig. 5.2. The aim of the inverter outer feedback loop is to drive to

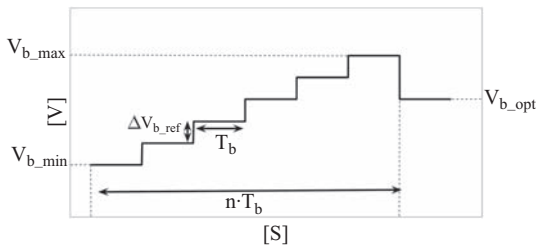


FIGURE 5.6

Staircase reference voltage $v_{b\ ref}$.

zero the DC value of such an error. The instants when the steps of $v_{b\ ref}$ occur will be called sampling instants.Moreover, we will indicate with the symbols $\Delta v_{b\ ref}$ and T_b, respectively, the amplitude and the duration of the steps of $v_{b\ ref}$. The two parameters $\Delta v_{b\ ref}$ and T_b need to be properly chosen to obtain the correct working of the CMPPTS technique. Of course, the initial value $V_{b\ min}$ and the final value $V_{b\ max}$ of $v_{b\ ref}$ must fall within the allowed inverter input voltage operating range. As shown in Fig. 5.6, the waveform of $v_{b\ ref}$ is characterized by n different values: $n = 1 + \frac{v_{b\ max} - v_{b\ min}}{\Delta v_{b\ ref}}$. After the occurrence of each step of $v_{b\ ref}$, the control system waits for an interval of time equal to T_b during which the PV system reaches a new steady-state condition and, in particular, the voltage v_b becomes nearly equal to $v_{b\ ref}$. As a consequence, before driving the new step of $v_{b\ ref}$ at the following sampling instant, the CMPPTS controller is able to record the steady-state value of the total power P extracted from the PV system: $P = v_b \cdot i_b$. In fact, the CMPPTS controller has two inputs: v_b and i_b (see Fig. 5.2). In this way, the n steady-state values of the powers extracted in correspondence of the n different levels assumed by $v_{b\ ref}$ are recorded. After the whole scan from $V_{b\ min}$ to $V_{b\ max}$, the CMPPTS controller sets its output equal to $V_{b\ opt}$, which is the level of $v_{b\ ref}$ in correspondence of which the recorded value of P has assumed its maximum value. Of course, the whole scan requires a total time T_{tot} equal to $n \cdot T_b$. It is evident that only two parameters must be chosen to design the CMPPTS technique: the step amplitude $\Delta v_{b\ ref}$ and the interval of time T_b between two consecutive steps of $v_{b\ ref}$. In the following, the criteria for choosing two parameters are discussed. As concerns the value of $\Delta v_{b\ ref}$, it must be chosen on the basis of a reasonable compromise between two contrasting requirements. The first requirement is strictly linked to the energy storage function carried out by the bulk capacitor C_b placed at the interface between the string of LSCPVUs and the inverter (see Fig. 5.2). It is well-known that the voltage v_b across C_b undergoes an oscillation characterized by a frequency nearly equal to $2 \cdot f_{line}$, where f_{line} is the grid frequency.

In fact, v_b oscillates, that is, it increases or decreases, to allow the capacitor C_b to store or release the energy required for balancing the DC power extracted from the LSCPVUs with the instantaneous power injected into the grid [45,53,54]. As a consequence of such an oscillation, at the end of the scan, the CMPPTS controller may provide a wrong value of $V_{b\ opt}$. In fact, during the scan, when $v_{b\ ref}$ is fixed and assumes one among its n possible levels, said $v_a = V_{b\ min} + k \cdot \Delta v_{b\ ref}$ ($k = 0, 1, \ldots, n-1$), the total steady-state power P extracted from the LSCPVUs is not nearly constant in time but it is characterized by an oscillation at a frequency nearly equal to $2 \cdot f_{line}$. Such a power oscillation acts as a sort of unavoidable and undesired, additional, local scan of the P–V characteristic, caused by the aforementioned oscillation of v_b in a voltage region around v_a. The peak to peak amplitude $\Delta v_{b\ fline}$ of such an oscillation is equal to [45,53,55]: $\Delta v_{b\ fline} = \frac{P}{C_b \cdot 2\pi \cdot f_{line} \cdot v_a}$, where P is the DC power injected into the grid. Therefore, to avoid errors of the CMPPTS controller caused by the aforementioned oscillation of v_b, errors which could

severely compromise the efficiency of the system, it is necessary to adopt enough large values of $\Delta v_{b\ ref}$:

$$\Delta v_{b\ ref} \geq \Delta v_{b\ fline} \tag{5.13}$$

The second requirement for a proper choice of $\Delta v_{b\ ref}$ is strictly linked to the necessity to avoid that, during the scan, the voltage ratings of devices are exceeded. In fact, it must be ensured that the steps of $v_{b\ ref}$, taking place at the sampling instants, during the variation of $v_{b\ ref}$ from $V_{b\ min}$ to $V_{b\ max}$, do not cause that the output voltage of one or more LSCPVUs exceeds $V_{ds\ max}$. In the following analysis, let us consider negligible the settling time of the overall system (worst-case). This means that, as a consequence of the steps of $v_{b\ ref}$, the steady-state variations of v_b and the corresponding variations v_{outk} ($k = 1, 2, \ldots, N$) occur near instantaneously. For simplicity, because a unit gain of the sensor of voltage v_b has been assumed and as a result of the zero steady-state error ensured by the Bulk voltage compensation network, it can be assumed that $\Delta v_b = \Delta v_{b\ ref}$. Of course, at any sampling instant, Δv_b must be shared among the N output voltages of the N LSCPVUs. The ideal situation, from the voltage stress point of view, takes place when Δv_b is uniformly shared among the N output voltages. In such a case, the output voltage v_{outk} ($k = 1, \ldots, N$) will increase of a quantity equal to: $\Delta v_{outk} = \Delta v_{b\ ref}/N$ ($k = 1, \ldots, N$). Unfortunately, this situation occurs only when the LSCPVUs work in the same operating conditions (absence of mismatching operating conditions); but, in mismatching operating conditions, Δv_b is unequally shared among the N output voltages. In particular, under mismatching operating conditions, one or more LSCPVUs may work with their output ports in short circuit conditions; that is, such LSCPVUs are not able to provide power to the grid. Of course, such a situation is undesirable from the voltage stress point of view. In fact, if m ($1 < m < N$) LSCPVUs are working with their output ports in short circuit conditions, then the variation Δv_b must be entirely shared only among a minor number ($N-m$) of LSCPVUs, that is, only among those LSCPVUs that are instead working with their output voltages greater than zero so that the output voltages of such ($N-m$) LSCPVUs may become dangerously high. The occurrence of the aforementioned situation, taking place under mismatching conditions, can be explained on the basis of Eq. (5.1). The worst-case, as concerns the distribution of Δv_b among the N output voltages, takes place of course when the maximum number M of LSCPVUs is working in short circuit conditions. M can be evaluated by considering that the remaining ($N-M$) LSCPVUs must operate with the highest possible output voltage, that is $v_{out} = V_{out\ lim}$. It is worth remembering that, in this chapter, the LSCPVUs are listed in descending order as concerns the corresponding value of the irradiance level. So that the first $N-M$ LSCPVUs are assumed to operate at higher irradiance values, while the remaining M LSCPVUs are assumed to operate at very low irradiance values. Summarizing, in the worst-case, it is $v_{outk} = V_{out\ lim}$ ($k = 1, \ldots, N-M$), while $v_{outk} = 0$ ($k = N-M+1, \ldots, N$). It is $M = N - \frac{v_{b\ min}}{v_{out\ lim}}$. On the basis of the above considerations, we get:

$$\begin{aligned} \Delta v_{outk} &= \frac{\Delta v_b}{N-M} \quad (k = 1, 2, \ldots N-M) \\ \Delta v_{outk} &= 0 \quad (k = N-M+1, \ldots N) \end{aligned} \tag{5.14}$$

Our objective is to ensure that

$$v_{outk} + \Delta v_{outk} \approx v_{out\ lim} + \Delta v_{outk} = v_{out\ lim} + \frac{\Delta v_b}{N - M}$$

$$= v_{out\ lim} + \frac{\Delta v_{bref}}{N - M} \leq v_{ds\ max} \quad (k = 1, 2, \ldots N - M)$$

From which we get

$$\Delta v_{b\ ref} \leq (v_{ds\ max} - v_{out\ lim}) \cdot \frac{v_{b\ min}}{v_{out\ lim}} \tag{5.15}$$

As for the choice of T_b, a preliminary consideration is necessary. In correspondence of an arbitrary value $v_b = v_a$ of the inverter voltage, the working conditions of the N LSCPVUs will depend on the distribution of irradiance values. In particular, some LSCPVUs (those ones characterized by the highest irradiance values) will operate with an output voltage nearly equal to $V_{out\ lim}$. Other LSCPVUs will operate with an output voltage comprised between 0 and $V_{out\ lim}$ and, finally, the remaining LSCPVUs (those characterized by the lowest irradiance values) will operate with output short-circuit conditions. The number of LSCPVUs operating with an output voltage nearly equal to $V_{out\ lim}$ will be indicated with N_{lim}, the number of LSCPVUs operating with an output voltage comprised between 0 and $V_{out\ lim}$ will be indicated with N_r, while the number of LSCPVUs operating with an output voltage equal to 0 will be indicated with N_{SC}. Summarizing, by remembering the adopted ordering rule, we get:

$$\begin{gathered} v_{outk} = v_{out\ lim} \quad 1 \leq k \leq N_{lim} \\ 0 < v_{outk} < v_{out\ lim} \quad N_{lim} + 1 \leq k \leq N_{lim} + N_r \\ v_{outk} = 0 \quad N_{lim} + N_r + 1 \leq k \leq N \end{gathered} \tag{5.16}$$

Of course, it is $N_{lim} + N_r + N_{sc} = N$; moreover, N_{lim}, N_r, and/or N_{sc} can be equal to zero. Let us suppose that, during the scan, v_b must change from v_a to $v_a + \Delta v_{b\ ref}$. In the new steady-state condition, at $v_b = v_a + \Delta v_{b\ ref}$, two or three numbers among N_{lim}, N_r, and N_{sc} may change. In fact, it may happen that, in the new steady-state condition, one or more LSCPVUs (among those ones with index $1 \leq k \leq N_{lim} + N_r$) will reduce their output power; that is, N_{lim} and/or N_r may change. Let us indicate with N_d the number of LSCPVUs that, in the new steady-state condition, will reduce their output power ($N_d \leq N_{lim} + N_r$). Such a power reduction may also allow in turn one or more LSCPVUs to increase their output power and therefore to increase their output voltage. That is, in the new steady-state condition, N_{SC} and/or N_r may change. Let us indicate with N_i the number of LSCPVUs that, in the new steady-state condition, will increase their output power. Of course, the process described so far cannot take place instantaneously. In fact, it needs, in the worst case, the time T_1 necessary to the N_d LSCPVUs to move their input operating voltage in the direction from V_{MPP} to zero, to decrease their output power, plus the time T_2 necessary to the N_i LSCPVUs

to move their input operating voltage in the direction from zero to V_{MPP}, to increase their output power. As a worst case, it is possible to assume that the starting and ending input voltages of the N_d LSCPVUs, respectively, are just V_{MPP} and 0, while the starting and ending input voltages of the N_i LSCPVUs, respectively, are just 0 and V_{MPP}. Of course, the corresponding times T_1 and T_2 represent the worst-case (longest) possible times needed by the aforementioned LSCPVUs to reach the new steady-state condition associated with $v_b = v_a + \Delta v_{b\ ref}$. Moreover, it is worth noting that the inverter itself is characterized by its own dynamics so that it needs a time T_3 to change its input voltage v_b from v_a to $v_a + \Delta v_{b\ ref}$. In conclusion, the whole process associated to the change from the steady-state condition associated to $v_b = v_a$ to the steady-state condition associated to $v_b = v_a + \Delta v_{b\ ref}$ needs, in the worst-case, a time T_{tot} equal to: $T_{tot} = T_1 + T_2 + T_3$. Times T_1, T_2, and T_3 can be estimated as it follows:

$$T_1 = T_2 = \frac{V_{MPP}}{\Delta v_{pan\ ref}} \cdot T_a \tag{5.17}$$

Instead, T_3 can be estimated as the settling time of the step response of the closed-loop transfer function W(s) between v_b and $v_{b\ ref}$: $W(s) = \frac{v_b(s)}{v_{b\ ref}(s)} = \frac{T_{cv}(s)}{1+T_{cv}(s)}$, where $T_{cv}(s)$ is the loop gain of the inverter outer voltage feedback loop [45,46,53]:

$$T_{cv}(s) = G_{cv}(s) \cdot \frac{K}{R_s} \cdot \frac{V_{RMS}^2}{V_b \cdot s \cdot C_b} \tag{5.18}$$

where $G_{cv}(s)$ is the transfer function of the inverter bulk voltage compensation network of Fig. 5.2, V_{RMS} is the RMS value of the grid voltage, V_b is the nominal value of the DC inverter input voltage ($V_{b\ min} < V_b < V_{b\ max}$), R_s is the value of the gain of the sensor of the current injected into the grid by the PV system, K is the gain of the multiplier belonging to the inverter control circuitry. Once the closed-form expression of $T_{cv}(s)$ is known, then the estimate of time T_3 can be carried out in numeric form in Matlab or PSIM environment. As a consequence of the above discussion, it is evident that, to correctly perform the scan of the whole P−V characteristic by correctly evaluating the steady-state values of the power obtained from the string of LSCPVUs, without making under- or overestimation errors, which could lead to a more or less consistent waste of available energy of the PV system, it must be

$$T_b \geq T_{tot} \tag{5.19}$$

The capability of the well-designed CMPPTS technique to not be deceived in the presence of multimodal shape of the P−V characteristic of N LSCPVUs represents its main advantage. The other side of the medal is represented by the quite low speed of tracking of the MPP of the PV system (the whole scan takes a time equal to $n \cdot T_{tot}$) and by the fact that, during the scanning process, a more or less large part of the PV available energy is lost. Of course, the repetition period of the CMPPTS technique (T_r) must be greater than $n \cdot T_{tot}$: $T_r > n \cdot T_{tot}$. The choice of T_r must be made on the

basis of a reasonable compromise because the lower T_r, the higher the rate of change of irradiance variation that can be tracked [1] and, at the same time, the higher the amount of available energy that is wasted during the scan when the operating point of the PV system is not the optimal one.

3.2 HMPPTF TECHNIQUE

In this subsection, the HMPPTF technique is presented and discussed [60,63]. Such a technique is based on the "one-shot" estimate of the optimal operating range of the inverter input voltage and of the optimal operating voltages of the PV modules based on the measurement of the short circuit currents of the PV modules. The main advantage of the proposed technique is just represented by the speed of identification of a set of optimal operating points for the inverter and for the PV modules, which in turn allows to obtain a marked increase of the speed of tracking both of the inverter (which performs the CMPPT function) and of the DC/DC converters (which perform the DMPPT function). Moreover, a further advantage is represented by the possibility to avoid mistakes of the inverter CMPPT technique; that is, the operating value of the inverter input voltage cannot remain trapped in the neighborhood of a suboptimal operating point, as it would happen, in mismatching operating conditions, if standard CMPPT techniques (P&O and/or INC techniques) were adopted. The HMPPTF technique exploits the FEMPV algorithm. To describe in detail the working of such an algorithm, a preliminary discussion related to the modeling of LSCPVUs in terms of I−V and P−V output characteristics is needed and it is the subject of subsections "Boost-based LSCPVUs", "Buck−boost based LSCPVUs," and "Buck-based LSCPVUs".

3.2.1 Exact and Approximate I−V and P−V Characteristics of LSCPVUs

In the following the few, simple guidelines allowing to obtain the I−V and the P−V output static characteristics of LSCPVUs will be provided. The knowledge of such characteristics represents the starting point to develop the I−V and P−V characteristics of strings composed by arbitrary numbers of LSCPVUs with series-connected output ports. In fact, once the I−V characteristics of the N LSCPVUs belonging to a given string are known, the I−V equivalent characteristic of the whole string is obtained by summing, for each value of string current I_b, the corresponding values of the N LSCPVUs' output voltages. From the I−V string characteristic, it is then easy to obtain the corresponding P−V characteristic. Examples of P−V characteristics of strings of LSCPVUs have been already shown in Fig. 5.3. It is worth noting, however that, in practice, as it will be clearer in the following, what is really needed to obtain the efficient working of a PV system equipped with microconverters is the knowledge of the features of the optimal operating range R_b (amplitude, location, and corresponding value of the total power), rather than the detailed P−V characteristic of the whole string of LSCPVUs. Therefore, to get enough accurate information concerning R_b, it is not necessary to deal with the exact I−V characteristics of LSCPVUs, but a proper approximate version of such characteristics is enough.

More precisely, rather than the whole approximate characteristic of all the LSCPVUs belonging to a given string, what is needed by the FEMPV algorithm is the knowledge of the position of a few key points on such a characteristic. This subsection is also devoted to the identification of the guidelines to follow to obtain the approximate version of the I−V characteristic of a given LSCPVU. In particular, subsection "Boost-based LSCPVUs" is devoted to boost-based LSCPVUs, subsection "Buck−Boost based LSCPVUs" to buck−boost based LSCPVUs, and finally, subsection "Buck-based LSCPVUs" to buck-based LSCPVUs. In subsections "Boost-based LSCPVUs", "Buck−Boost based LSCPVUs" and "Buck-based LSCPVUs", V will represent the output voltage and I the output current of an LSCPVU.

3.2.1.1 Boost-Based Lossless Self Controlled Photovoltaic Units

As discussed in detail in [61], the exact I−V and P−V characteristics of a boost-based LSCPVU can be subdivided into three portions. In particular, for $0 \leq V \leq V_{MPP}$, the corresponding portions of the I−V and P−V characteristics of the LSCPVU are, respectively, coincident, with the I−V and P−V characteristics of the adopted PV module in the considered atmospheric conditions (irradiance value and ambient temperature) [54,55]. Instead, for $V_{MPP} \leq V < V_{ds\ max}$, the corresponding portions of I−V and P−V characteristics of the LSCPVU are, respectively, a hyperbole of Eq. $I = P_{MPP}/V$ and a straight line of equation $P = P_{MPP}$, where P_{MPP} is the maximum power that can be provided by the adopted PV module in the considered atmospheric conditions [54,55]. The third portion of the I−V and P−V characteristics are represented by a vertical drop located at $V = V_{ds\ max}$ and caused by the action of the output overvoltage protection circuitry. In Fig. 5.7, as an example, the I−V (Fig. 5.7A) and P−V (Fig. 5.7B) characteristics of a SolarWorld SW225 PV module operating at ambient temperature $T_{amb\ =\ ent} = 25°C$ and at an irradiance value $S = 1000\ W/m^2$ are reported together with the

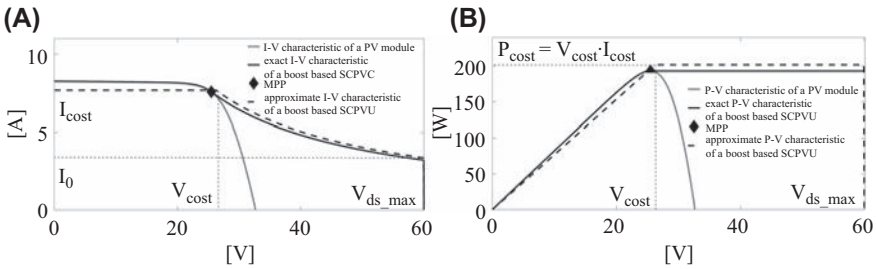


FIGURE 5.7

(A) I−V characteristic of a photovoltaic (PV) module and exact and approximate I−V characteristics of a boost-based lossless self-controlled PV unit (LSCPVU), (B) P−V characteristic of a PV module and exact and approximate P−V characteristics of a boost-based LSCPVU.

corresponding exact and approximated I−V and P−V characteristics of the associated boost-based LSCPVU. The approximated I−V characteristic of the LSCPVU (dashed line in Fig. 5.7A) is obtained by substituting the part of the I−V characteristic for $V \leq V_{MPP}$, part which cannot be expressed in easy explicit form $I = f(V)$ [9,55], with a simpler constant characteristic:

$$I = I_{cost} = \beta \cdot I_{SC} \tag{5.20}$$

where the factor β represents the ratio between I_{MPP_STC} and I_{SC_STC}. In the case of SW225 modules, it is $\beta = 0.93$. This approximation can be justified by considering that the exact I−V characteristic is more or less flat, for $V \leq V_{MPP}$, and it is contained in the quite narrow band $I_{MPP} \leq I \leq I_{SC}$ (usually $I_{MPP}/I_{SC} \approx 0.9$). The hyperbolic equation of the portion of the approximate P−V characteristic for $V_{MPP} \leq V \leq V_{ds\ max}$ is of course $V \cdot I = V_{MPP} \cdot I_{cost}$. It is worth noting that of course other, more accurate, forms of approximation of the I−V curve for $V \leq V_{MPP}$ might be adopted; for example, a piecewise linear approximation. But, as it will be shown in the following, it is not necessary at all. In fact, the use of the simple approximation $I = I_{cost}$ for $V \leq V_{MPP}$ and $V \cdot I = V_{MPP} \cdot I_{cost}$ for $V_{MPP} \leq V \leq V_{ds\ max}$ allows to easily carry out in closed form, with enough accuracy, the calculations needed by the HMPPTF technique to maximize the energetic efficiency of the PV system. Indeed, some additional considerations are needed concerning the values to adopt for V_{MPP}. For a given PV module, V_{MPP} is generally weakly dependent on the irradiance and on the module temperature [9,10]. Usually the variations of V_{MPP} are relatively small. Therefore, because of the approximate nature of the analysis to be carried out, in the following V_{MPP} will be considered constant and not time-varying. In particular, V_{MPP} will be considered equal to the value V_{cost} assumed by the MPP voltage at $S_{max} = 1000\ W/m^2$ and $T_{ambient} = 25°C$. In such conditions, by using Eq. (5.4) it is possible to evaluate the module temperature T_{module}. With specific reference to SW225 modules, it is $T_{module} = 57.5°C$. Hence, the desired value of V_{cost} can be finally obtained [10]:

$$V_{cost} = V_{MPP\_STC}\left[1 + \alpha \cdot \frac{(T_{Module} - 25)}{100}\right] \tag{5.21}$$

where α [%/°K] is a negative temperature coefficient (in the case of SW225 modules, it is $\alpha = -0.34\%/°K$ and hence $V_{cost} = 26.24$ V). It is worth noting that the parameters V_{MPP_STC} and α appearing in Eq. (5.21) are provided by all the PV module manufacturers in their datasheets. In conclusion, V_{cost} can be easily evaluated by using the data extracted from PV module datasheets.

Therefore, I_{cost} is the only time-varying parameter because it depends on I_{SC} ($I_{cost} = \beta\ I_{SC} \approx P_{MPP}/V_{cost}$), which exhibits a strong dependence on irradiance values. The short circuit current I_{SC} of the PV module is a quantity that can be quite easily measured. Therefore, by using the approximate relation $I_{cost} = \beta \cdot I_{SC}$, even I_{cost} can be quite easily evaluated. It is worth noting that also the value of β can

be easily extracted from PV modules datasheets. Moreover, as it will be clear in the sequel, it is useful to define the following current:

$$\begin{aligned} I_0 &= \frac{V_{cost} \cdot I_{cost}}{V_{ds\ \ max}} \\ &= \frac{V_{cost} \cdot \beta \cdot I_{SC}}{V_{ds\ \ max}} < I_{cost} \quad \text{since } (V_{cost} < V_{ds\ \ max}) \end{aligned} \tag{5.22}$$

From Eq. (5.22), it is evident that, if I_{SC} is known not only I_{cost} but also I_0 is known. The meaning of I_0 and I_{cost} are clarified in Fig. 5.7A. As described in detail in [59–62], the set of equations that allow to obtain the I–V and P–V approximate characteristics of a string composed by an arbitrary number N of boost based LSCPVUs are:

$$\begin{aligned} &\text{if} \quad I = I_{0k} = \frac{V_{cost} \cdot I_{costk}}{V_{ds\ max}} = \frac{V_{cost} \cdot \beta \cdot I_{SCk}}{V_{ds\ max}} \\ &V_{tot} = k \cdot V_{ds\ max} + \frac{\sum_{i \in J} V_{cost} \cdot I_{costi}}{I_{0k}} \end{aligned} \tag{5.23}$$

where $k = 1, 2, \ldots, N$ and $J = \{i > k: I_{cost\ i} > I_{0k}\}$. In Eq. (5.23) the set J may also be empty.

$$\begin{aligned} &\text{if} \quad I = I_{costk} = \beta \cdot I_{SCk} \\ &V_{tot} = \left[m \cdot V_{ds\ max} + \frac{\sum_{i \in J} V_{cost} \cdot I_{costi}}{I_{costk}},\ m \cdot V_{ds\ max} + \frac{\sum_{i \in J} V_{cost} \cdot I_{costi}}{I_{costk}} + V_{cost} \right] \end{aligned} \tag{5.24}$$

where, $k = 1, 2, \ldots, N$; $m = \max \{i < k: I_{0i} > I_{costk}\}$; $J = \{m < i < k: I_{costi} > I_{costk}\}$. In Eq. (5.24) the set J may also be empty. Eqs. (5.23) and (5.24) represent the core of the FEMPV algorithm suited for boost-based LSCPVUs. By looking at Eqs. (5.23) and (5.24), it is clear that the key quantities are represented by currents $I_{costk} = \beta\ I_{SCk}$ ($k = 1, 2, \ldots, N$). Once I_{SCk} ($k = 1, 2, \ldots, N$) are known, then the $(3N + 1)$ points of the approximated I–V (and hence the approximated P–V) characteristic of the string of LSCPVUs can be obtained. Finally, the I–V and P–V approximate characteristic can be obtained by connecting, by means of proper segments, the $(3N + 1)$ points obtained by using Eqs. (5.23) and (5.24). As an example, let us consider a string composed by $N = 11$ boost-based LSCPVUs. The set of irradiance values characterizing the N PV modules, operating at $T_{ambient} = 25°C$, are the following [1000, 1000, 600, 600, 400, 400, 200, 200, 100, 100, 100] W/m^2. The corresponding values of $\beta\ I_{SCk}$ and I_{0k} ($k = 1, 2, \ldots, 11$) are, respectively equal to [7.67, 7.67, 4.58, 4.58, 3.05, 3.05, 1.52, 1.52, 0.76, 0.76, 0.76] A and [3.37, 3.37, 2.01, 2.01, 1.34, 1.34, 0.67, 0.67, 0.33, 0.33, 0.33] A. The $3\ N = 33$ points belonging to

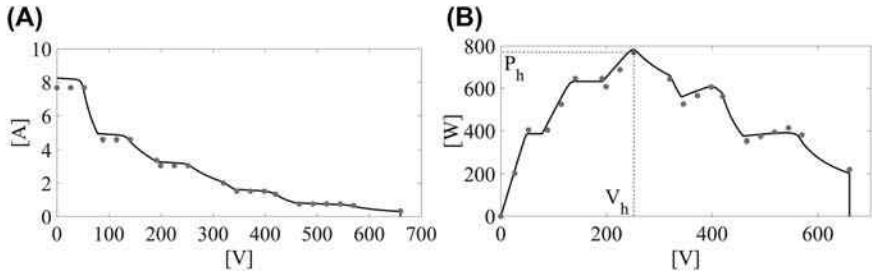


FIGURE 5.8

(A) Exact I–V characteristic of 11 series-connected lossless self-controlled PV units (LSCPVUs). (B) Exact P–V characteristics of 11 series-connected LSCPVUs, points calculated by using Eqs. (5.23) and (5.24) (*grey circle* markers).

the I–V plane, and obtained by using Eqs. (5.23) and (5.24), are indicated in Fig. 5.8A by means of grey circle markers, together with the exact I–V characteristic. Indeed, the number of different circle markers in Fig. 5.8A is lower than 33 because the number of different irradiance values that have been assumed is lower than N and therefore some markers overlap. The corresponding points belonging to the P–V plane are shown in Fig. 5.8B together with the exact P–V characteristic. As can be seen by looking Fig. 5.8, the points obtained by using Eqs. (5.23) and (5.24) provide fairly accurate results in the neighborhood of R_b (region of greatest interest) that, in this case, is characterized by a single point (251.9 V, 767.9 W).

3.2.1.2 Buck–Boost Based Lossless Self-Controlled Photovoltaic Units

In the case of buck–boost based LSCPVUs, V represents the absolute value of the output voltage. Also, the exact I–V and P–V characteristics of a buck–boost based LSCPVU can be subdivided into three portions. In particular, for $0 \leq V \leq V_1$, the corresponding portions of the I–V and P–V characteristics of the LSCPVU are straight lines of Eq. $I = I_{MAX}$ [54,55] for the I–V curve and $P = I_{MAX} \cdot V$ for the P–V curve. Instead, for $V_1 \leq V \leq V_2$, the corresponding portions are a hyperbole of Eq. $V \cdot I = P_{MPP}$ for the I–V curve and a straight line of equation $P = P_{MPP}$ for the P–V curve. Finally, the third portion of the I–V and P–V characteristics, for $V_2 \leq V \leq V_{ds\ max}$, are represented by curves of Eq. $V = P_{pan}(V_{ds\ max} - V)/I$ for the I–V characteristic and $P = P_{pan}(V_{ds\ max} - V)$ for the P–V characteristic, where $P_{pan}(v_{pan})$ is the function expressing the PV module power as a function of the PV module voltage v_{pan}. To explain the meaning of the voltage values V_1 and V_2 and of the current value I_{MAX}, some preliminary considerations are necessary. Continuous Conduction Mode operating conditions of the buck–boost converter and related equations will be referred to in the sequel, because of the synchronous version of the buck–boost, which has been adopted. Because a buck–boost converter is able to reduce its output voltage V with respect to the input voltage and by considering that when the PV module is working in its MPP ($V \cdot I = P_{MPP}$), it

is evident that, while the PV module operating point remains in the MPP, the lower the output voltage the higher the output current. By indicating with $I_{MAX,}$ the maximum allowed value of I, we get:

$$V_1 = \frac{P_{MPP}}{I_{MAX}} \tag{5.25}$$

Therefore, V_1 is the left value of the voltage range where the output characteristic of the buck–boost based LSCPVU is hyperbolic ($V \cdot I = P_{MPP}$) and it can be calculated by using Eq. (5.25) once I_{MAX} is known. As shown in the following, I_{MAX} depends on $I_{ds\ max}$ and I_{MPP}. Without the adoption of a proper overcurrent protection circuitry, values of V lower than V_1 would give rise to output currents I greater than I_{MAX}. So that, for $\leq V \leq V_1$, it is assumed that the output current is limited to I_{MAX} by means of a proper overcurrent protection circuitry and that the PV module operating point moves away from the MPP because the output power becomes of course lower than P_{MPP}. By indicating with D, the duty-cycle of the buck–boost converter, when the PV module operates in the MPP, it is [50]:

$$\begin{aligned} I &= \frac{V_{MPP} \cdot I_{MPP}}{V} = \frac{I_{MPP}}{\left[\frac{D}{1-D}\right]} \\ I_{s\ peak} &= \frac{I_{MPP}}{D} \end{aligned} \tag{5.26}$$

where $I_{s\ peak}$ is the peak current value of the switches of the buck–boost. From Eq. (5.26) it is evident that, while the PV module operating point remains in the MPP, the lower D (and hence the lower V) the higher both the output current and the peak current of the switches. By indicating with D_1 the value of D in correspondence of which the peak current of the switches is equal to $I_{ds\ max}$ and therefore the output current also assumes its maximum value I_{MAX}, from Eq. (5.26) we get:

$$\begin{aligned} I_{MAX} &= \frac{I_{MPP}}{\left[\frac{D_1}{1-D_1}\right]} \\ I_{ds\ max} &= \frac{I_{MPP}}{D_1} \end{aligned} \tag{5.27}$$

From Eq. (5.27) it is easy to get the value of I_{MAX}: $I_{MAX} = I_{ds\ max} - I_{MPP}$. As concerns the value of V_2, by remembering that in a buck–boost the voltage across the switches in the OFF state is equal to the sum of the input voltage and of the output voltage V [53], we get:

$$V_{ds\ max} = V_2 + V_{MPP} \tag{5.28}$$

That is, not only for $V < V_1$ but also for $V > V_2$ the operating point of the PV module cannot be the MPP because of the action of overcurrent or overvoltage protection circuitries, respectively. It is therefore assumed that, for $V > V_2$, the PV

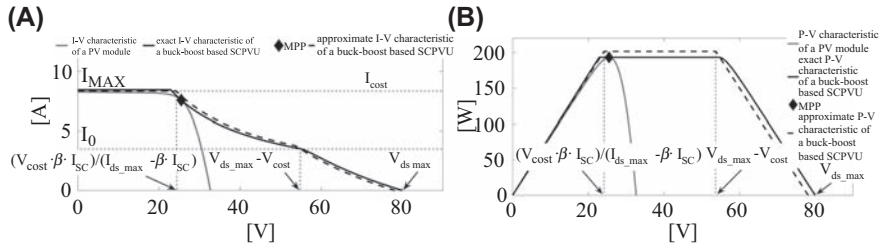


FIGURE 5.9

(A) I–V characteristic of a photovoltaic (PV) module and exact and approximate I–V characteristics of a buck–boost based lossless self-controlled PV unit (LSCPVU), (B) P–V characteristic of a PV module, and exact and approximate P–V characteristics of a buck–boost based LSCPVU.

voltage is equal to $V_{ds\ max} - V$ and hence the output power of the LSCPVU is equal to $P(V_{ds\ max} - V)$. In Fig. 5.9, the I–V (Fig. 5.9A) and P–V (Fig. 5.9B) characteristics of a SolarWorld SW225 PV module ($T_{ambient} = 25°C$, $S = 1000\ W/m^2$) are reported together with the corresponding exact and approximated I–V and P–V characteristics of the associated buck–boost based LSCPVU. Fig. 5.9 has been obtained by assuming $V_{ds\ \ max} = 80\ V$ and $I_{ds\ \ max} = 16\ A$; because it is $V_{MPP} = 25.52\ V$ and $I_{MPP} = 7.56\ A$, we get $V_1 = 22.86\ V$, $V_2 = 54.48\ V$, $I_{MAX} = 8.44\ A$. As concerns buck–boost based LSCPVUs the approximate characteristic, which is needed for the implementation of the HMPPTF technique, is composed by three different portions. The first portion (for $0 \le V \le (V_{cost}\cdot\beta\cdot I_{SC})/(I_{ds\ \ max} - \beta\cdot I_{SC})$) is represented by the constant line of equation:

$$I = I_{cost} = I_{ds\ \ max} - \beta I_{SC} \tag{5.29}$$

The second portion (for $(V_{cost}\cdot\beta\cdot I_{SC})/(I_{ds\ max} - \beta\cdot I_{SC}) \le V \le (V_{ds\ max} - V_{cost})$) is represented by a hyperbole of equation:

$$V\cdot I = V_{cost}\cdot\beta\cdot I_{SC} \tag{5.30}$$

The third portion (for $(V_{ds\ \ max} - V_{cost}) \le V \le V_{ds\ \ max}$) is represented by the curve of equation:

$$V\cdot I = V_{cost}\cdot\beta\cdot I_{SC} - V_{cost}\cdot I_{SC} + (V_{ds\ max} - V)\cdot I_{SC} \tag{5.31}$$

The definition of I_0 in the case of buck–boost based LSCPVU is the following one:

$$I_0 = \frac{V_{cost}\cdot\beta\cdot I_{SC}}{V_{ds\ max} - V_{cost}} \tag{5.32}$$

The meaning of I_0 and I_{cost} is indicated in Fig. 5.9A. By analyzing Eqs. (5.29)–(5.32), it is evident that, also in the case of buck–boost based LSCPVUs, it is enough

to measure I_{SC} to obtain the approximate I–V characteristic. The set of equations that allow to obtain the approximate I–V and P–V characteristics of a string composed by an arbitrary number N of buck–boost based LSCPVUs are given below:

$$\text{if} \quad I = I_{0k} = \frac{V_{cost} \cdot \beta \cdot I_{SCk}}{V_{ds\ max} - V_{cost}}$$

$$V_{tot} = V_{ds\ max} - V_{cost} + \frac{\sum_{i \in J} V_{cost} \cdot \beta \cdot I_{SCi}}{I_{0k}} + \frac{\sum_{y \in T} V_{ds\ max} \cdot \beta \cdot I_{SCy}}{I_{0k} + \beta \cdot I_{SCy}} \tag{5.33}$$

where $k = 1, 2, \ldots, N$; $J = \{i > k: I_{0i} < I_{0k}\}$; $T = \{y < k: I_{0y} > I_{0k}\}$.

$$\text{if} \quad I = I_{costk} = I_{ds\ max} - \beta \cdot I_{SCk}$$

$$V_{tot} = \left[\frac{\sum_{i \in J} V_{cost} \cdot \beta \cdot I_{SCi}}{I_{costk}}, \quad \frac{\sum_{i \in J} V_{cost} \cdot \beta \cdot I_{SCi}}{I_{costk}} + \frac{V_{cost} \cdot \beta \cdot I_{SCk}}{I_{costk}} \right] \tag{5.34}$$

where $J = \{k < i < N: I_{costi} > I_{costk}\}$, $k = 1, 2, \ldots, N$. In Eqs. (5.33) and (5.34), the sets J and T may also be empty. Eqs. (5.33) and (5.34) represent the core of FEMPV algorithm suited for buck–boost based LSCPVUs.

3.2.1.3 Buck-based Lossless Self-controlled Photovoltaic Units

Also, the I–V and P–V characteristics of a buck-based LSCPVU can be subdivided into three portions. In particular, for $0 \le V \le V_1$, the corresponding portions of the I–V and P–V characteristics of the LSCPVU are straight lines of Eq. $I = I_{MAX}$ [54,55] for I–V curve and $P = V \cdot I_{MAX}$ for the P–V curve. Instead, for $V_1 \le V \le V_{MPP}$, the corresponding portion of I–V characteristic of the LSCPVU is a hyperbole of Eq. $V \cdot I = P_{MPP}$ [54,55]. This means that, for $V_1 \le V \le V_{MPP}$, the corresponding portion of P–V characteristic of the LSCPVU is flat and equal to $P = P_{MPP}$. Finally, for $V_{MPP} \le V \le V_{oc}$ the I–V and P–V characteristics of the LSCPVU are coincident with those of the associated PV module [54,55]. The meaning of V_1 and I_{MAX} is the same as for the case of buck–boost based LSCPVUs. Therefore, also in the case of buck-based LSCPVU it is:

$$V_1 = \frac{P_{MPP}}{I_{MAX}} \tag{5.35}$$

Continuous Conduction Mode operating conditions of the buck converter and related equations will be referred to in the sequel because of the synchronous version of the buck which has been considered. Without the adoption of a proper overcurrent protection circuitry, values of V lower than V_1 would give rise to output currents I greater than I_{MAX}. So that, for $V \le V_1$, the output current is limited to I_{MAX} by means of a proper overcurrent protection circuitry and the PV module operating

point moves away from the MPP because the output power becomes lower than P_{MPP}. By indicating with D the duty-cycle of the buck converter, when the PV module operates in the MPP, it is [53]:

$$I = \frac{V_{MPP} \cdot I_{MPP}}{V} = \frac{I_{MPP}}{D}$$
$$I_{s\ peak} = \frac{I_{MPP}}{D} \tag{5.36}$$

where $I_{s\ peak}$, is the peak current value of the switches of the buck. From Eq. (5.36) it is evident that, while the PV module operating point remains in the MPP, the lower D (and hence the lower V) the higher both the output current and the peak current of the switches. By indicating with D_1 the value of D in correspondence of which the peak current of the switches is equal to $I_{ds\ max}$ and therefore the output current also assumes its maximum allowed value I_{MAX} and by considering Eq. (5.36) we get:

$$I_{MAX} = I_{ds\ max} \tag{5.37}$$

In Fig. 5.10, the I–V (Fig. 5.10A) and P–V (Fig. 5.10B) characteristics of a SolarWorld SW225 PV module ($T_{ambient} = 25°C$, $S = 1000\ W/m^2$) are reported together with the corresponding exact and approximated I–V (Fig. 5.10A) and P–V (Fig. 5.10B) characteristics of the associated buck-based LSCPVU. Fig. 5.10 has been obtained by assuming $I_{ds\ max} = 16$ A; because $V_{MPP} = 25.52$ V and $I_{MPP} = 7.56$ A, we get $V_1 = 12.06$ V and $I_{MAX} = 16$ A. The approximate characteristic of LSCPVU based on the buck microconverter, which is needed for the implementation of the HMPPTF technique, is composed of the three following different portions. The first portion (for $0 \le V \le (V_{cost} \cdot \beta \cdot I_{SC})/I_{dsmax}$) is represented by the constant line of equation:

$$I = I_{cost} = I_{ds\ max} \tag{5.38}$$

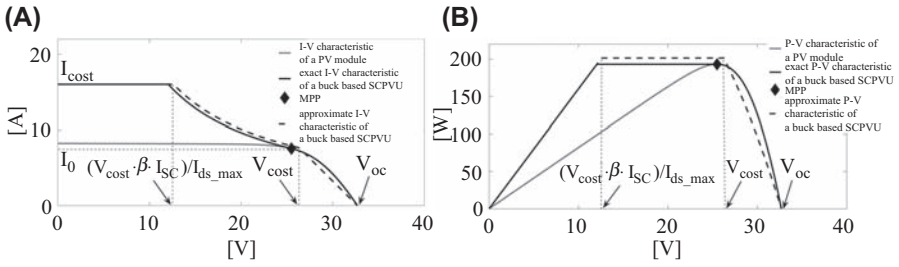


FIGURE 5.10

(A) I–V characteristic of a photovoltaic (PV) module and exact and approximate I–V characteristics of a buck-based lossless self-controlled PV unit (LSCPVU), (B) P–V characteristic of a PV module and exact and approximate P–V characteristics of a buck-based LSCPVU.

The second portion (for $(V_{cost}\cdot\beta\cdot I_{SC})/I_{ds\ max} \le V \le V_{cost}$) is represented by a hyperbole of equation:

$$V\cdot I = V_{cost}\cdot\beta\cdot I_{SC} \tag{5.39}$$

The third portion (for $V_{cost} \le V \le V_{OC}$) is represented by the line of equation:

$$I = \frac{V\cdot\beta\cdot I_{SC}}{V_{cost}-V_{oc}} - \frac{V_{oc}\cdot\beta\cdot I_{SC}}{V_{cost}-V_{oc}} \tag{5.40}$$

The definition of I_0 in the case of buck-based LSCPVUs is the following one:

$$I_0 = \beta\cdot I_{SC} \tag{5.41}$$

The value of V_{OC} (at $S = 1000\ W/m^2$, $T_{ambient} = 25°C$) can be evaluated as [10]:

$$V_{oc} = V_{oc\_STC}\left[1+\alpha\cdot\frac{(T_{Module}-25)}{100}\right] \tag{5.42}$$

where α [%/°K] is a negative temperature coefficient (in the case of SW225 modules, it is $\alpha = -0.34\%/°K$, $T_{module} = 57.5°C$, $V_{OC\_STC} = 36.8\ V$, and hence $V_{OC} = 32.7\ V$). It is worth noting that the parameters V_{OC_STC} and α appearing in Eq. (5.42) and NOCT appearing in Eq. (5.4), needed to evaluate T_{module}, are provided by all the PV module manufacturers in their datasheets. Therefore, also in the case of buck-based LSCPVUs, the measurement of I_{SC} allows to evaluate the whole approximate I−V characteristic. In the case of buck-based LSCPVUs, because I_0 is nearly equal to I_{MPP} and $I_{cost} = I_{dsmax}$ must be greater than I_{MPP}/D (see Eq. 5.38), it is $I_0 < I_{cost}$. The set of equations that allow to obtain the approximate I−V and P−V characteristics of a string composed by an arbitrary number N of buck-based LSCPVUs are:

if $I = I_{0k} = \beta\cdot I_{SCk}$

$$V_{tot} = V_{cost} + (k\text{-}1)\cdot V_{OC} + \frac{\sum_{i\in J}[I_{SCk}\cdot(V_{cost}\text{-}V_{OC})]}{I_{SCi}} + \frac{\sum_{y\in T}\cdot(V_{cost}\cdot I_{SCy})}{I_{SCk}}$$

where $k = 1,\ 2,\ ...,\ N;\ J = \{i < k:\ I_{0i} > I_{0k}\};\ T = \left\{y > k:\ I_{0y} < I_{0k}\right\}$

if $I = I_{costk} = I_{dsmax}$

$$V_{tot} = \left[\sum_{i\in J}\frac{V_{cost}\cdot\beta\cdot I_{SCi}}{I_{costk}},\ \sum_{i\in J}\frac{V_{cost}\cdot\beta\cdot I_{SCi}}{I_{costk}} + \frac{V_{cost}\cdot\beta\cdot I_{SCk}}{I_{costk}}\right]$$

where $k = 1,\ 2,\ ...,\ N;\ J = \{k < i < N:\ I_{costi} > I_{costk}\}$

(5.43)

In Eq. (5.43) the sets J and T may also be empty. Eq. (5.43) represents the core of FEMPV algorithm suited for buck-based LSCPVUs.

3.2.2 Distributed Maximum Power Point Tracking and Central Maximum Power Point Tracking Based on Fast Estimate of Maximum Power Voltages

In this section, it will be explained how the DMPPT control technique and the CMPPT control technique can be jointly used and optimized by means of the knowledge of the approximate P−V characteristic of the string of LSCPVUs. Without any loss of generality, the discussion will refer to the case of boost-based LSCPVUs. The extension to the case of buck−boost and buck-based LSCPVUs is straightforward. As discussed in the previous section, once I_{SCk} (k = 1, 2, …, N) is known, the approximate P−V characteristic of the string of LSCPVUs is easily obtained. So that, I_{SCk} (k = 1, 2, …, N) needs to be measured. In the following, it will be assumed that the measurement of I_{SCk} (k = 1, 2, …, N) takes place synchronously for all the N LSCPVUs. Such a measurement is periodic, with period T_m. The duration of the measurement process will be indicated with Δt (measurement interval). Of course, it is $T_m > \Delta t$. During Δt, all the LSCPVUs are forced to work at a duty-cycle nearly equal to one, because in boost converters this corresponds to short circuit conditions at the input. The value of Δt must be high enough to allow the k-th LSCPVU (k = 1, 2, …, N) to reach the steady-state corresponding to a nearly unit duty-cycle. Nevertheless, the value of Δt must not be higher than strictly necessary, because of course, during the measurement interval, the MPP is not tracked. During Δt, because all the LSCPVUs are forced to work at a duty-cycle nearly equal to one, the currents I_{pank} are nearly equal to I_{SCk} (k = 1, 2, …, N). Therefore, if the input currents of the LSCPVUs are measured, it is possible to evaluate the approximate P−V equivalent characteristic of the string of LSCPVUs and hence the corresponding R_b can be easily estimated in closed form. Each evaluation interval must be followed by a period of time, indicated with T_t: $T_m = \Delta t + T_t$. During T_t, the controller of the inverter (the CMPPT controller of Fig. 5.2) initially sets the reference voltage for v_b equal to V_h (which is the mid-point of R_b) and then refines the operating value of v_b by means of a proper hill-climbing technique. During T_t, also every LSCPVU controller (the DMPPT controllers in Fig. 5.1) initially sets the reference signal $v_{pan\ refk}$ for its input operating voltage equal to the nearly optimal value v_{pk}, which can be evaluated as explained in the following, and successively refines such a voltage by means of a proper hill-climbing technique. The hill-climbing−based refinement phases for v_b and v_{pank} are adopted to compensate for the small, unavoidable errors associated to both the numerical and the theoretical approximations, which have been adopted (e.g., the approximations of the I−V and P−V characteristics, the assumption of lossless DC/DC power stages, the assumption of a unit MPPT accuracy etc.). The choice of T_m must be made on the basis of a reasonable compromise between speed of tracking and energetic efficiency. In fact, the lower T_m, the higher the rate of change of irradiance variation which can be tracked [1] and, at the same time, the higher the amount of available energy that is wasted because of the

nontracking interval Δt. To evaluate v_{pk} ($k = 1, 2, \ldots, N$), it is first necessary to calculate $I_h = P_h/V_h$, where P_h is the power corresponding to V_h in the P−V equivalent characteristic of the string of LSCPVUs. Once I_h is known, it is then possible to evaluate v_{pk} ($k = 1, 2, \ldots, N$) on the basis of the following considerations. In particular, if $I_h \geq \beta\ I_{SCk}$, then $v_{pk} = 0$; instead, if $\beta\ I_{SCk} < I_h \leq I_{0k}$, then $v_{pk} = V_{cost}$; finally, if $I_{0k} < I_h < 0$, then $v_{pk} = V_{ds\ max} \cdot I_h/(\beta\ I_{SCk})$. As an example, let us consider the case shown in Fig. 5.8 in which the optimal range R_b is indeed a single point $V_h = 251.9$ V. Because it is $P_h = 767.9$ W, therefore I_h can be easily evaluated: $I_h = P_h/V_h = 3.05$ A. Finally, the values of v_{pk} ($k = 1, 2, \ldots, 11$) can be obtained as explained above [23.84, 23.84, 26.34, 26.34, 26.34, 26.34, 0, 0, 0, 0, 0] V. The same analysis carried out by using the exact P−V characteristic of the string of LSCPVUs and the exact I−V characteristics of the N LSCPVUs provide instead the following results: $V_h = 250.7$ V, $P_h = 781.9$ W, $I_h = 3.119$ A, v_{pk} ($k = 1, 2, \ldots, 11$) = [23.6, 23.6, 27.1, 27.1, 26.2, 26.2, 0, 0, 0, 0, 0] V. The above results clearly indicate that the suggested procedure is able to provide a quite accurate starting condition for both the DC input inverter voltage and the PV voltages of the LSCPVUs. The values of such voltages can be successively refined by means of a suitable hill-climbing technique. In particular, as concerns the DMPPT controllers, in the following it will be assumed that they carry out an MP&O MPPT technique with starting conditions v_{pk} ($k = 1, 2, \ldots, 11$) provided by the FEMPV algorithm. In the above discussion, it has been assumed that, of course, the inverter is able to operate at a DC input voltage equal to V_h. After the hill climbing refinement step, it is possible to state that LSCPVUs 1 and 2 will operate at $V_{out} = V_{ds\ max}$ because of their high irradiance values; the input operating points of LSCPVUs 3 and 4 will be their MPPs; LSCPVUs 5 and 6 will operate at a PV voltage slightly lower than their own V_{MPP}; and, at last, LSCPVUs 7, 8, 9, 10, and 11 will be short-circuited because of their low irradiance values. The above statement can be easily explained by considering the location, in Fig. 5.11, of the intersections among the horizontal dashed line representing $I_h = 3.119$ A with the I−V output exact characteristics of the various LSCPVUs. In the case of LSCPVUs 1 and 2, such an intersection is found in the vertical portion of the I−V characteristics, at $V = V_{ds\ max}$. Therefore,

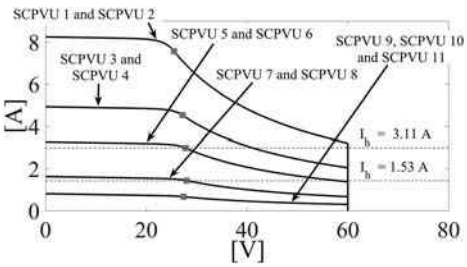


FIGURE 5.11

Exact I−V characteristics of lossless self-controlled photovoltaic units (LSCPVUs). *Grey square* markers indicate maximum power points.

LSCPVUs 1 and 2 will operate at the maximum allowed output voltage. In the case of LSCPVUs 3 and 4, the intersection is found in the hyperbolic portion of the I−V characteristic; therefore, the PV modules of LSCPVUs 3 and 4 will operate in their MPPs. In the case of LSCPVUs 5 and 6, the intersection takes place at a voltage slightly lower than the MPP voltage, as it is clearly shown in Fig. 5.11 where the grey square markers just indicate the position of the MPPs; therefore, the PV modules of LSCPVUs 3 and 4 will operate at a voltage slightly lower than their MPP voltage. Finally, LSCPVUs 7, 8, 9, 10, and 11 will operate in short circuit conditions because I_h is higher than the short circuit currents of their associated PV modules.

In the above case, a voltage nearly equal to 251 V represents the best inverter input operating voltage. But, if the allowed inverter DC input voltage range is, for example, equal to [350, 600] V, then the FEMPV algorithm is of course able to provide the best operating voltage value V_h included in such a range. In the considered case, it is V_h=398.3 V [see Fig. 5.8B), the exact and the approximate optimal values in the range [350, 600] V are nearly coincident]. In correspondence of $V_h = 398.3$ V, from the I−V output exact characteristic of the string of LSCPVUs it is possible to get $I_h = 1.53$ A. By considering the location, in Fig. 5.11, of the intersections among the horizontal dashed line representing $I_h = 1.53$ A with the I−V output exact characteristics of the various LSCPVUs it is possible to draw the following conclusions. In correspondence of a DC inverter input voltage $V_h = 398.3$ V and hence $I_h = 1.53$ A, in the case of LSCPVUs 1, 2, 3, and 4, such an intersection is found in the vertical portion of the I−V characteristics, at $V = V_{ds\ max}$. Therefore, LSCPVUs 1, 2, 3, and 4 will operate at the maximum allowed output voltage. In the case of LSCPVUs 5 and 6, the intersection is found in the hyperbolic portion of the I−V characteristic; therefore, the PV modules of LSCPVUs 5 and 6 will operate in their MPPs. In the case of LSCPVUs 7 and 8, the intersection takes place at a voltage slightly lower than the MPP voltage; therefore, the PV modules of LSCPVUs 7 and 8 will operate at a voltage slightly lower than their MPP voltage. Finally, LSCPVUs 9, 10, and 11 will operate in short circuit conditions because $I_h = 1.53$ A is higher than the short circuit currents of their associated PV modules. Figs. 5.12 and 5.13 refer instead to

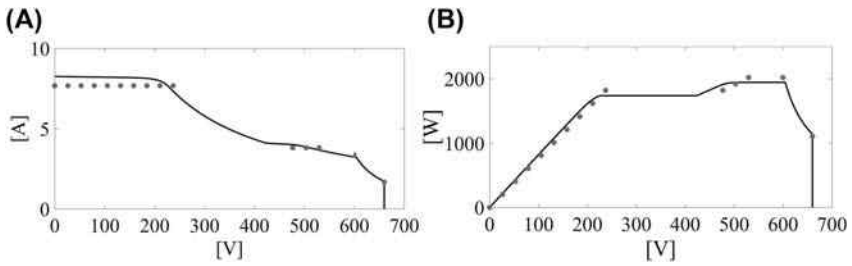


FIGURE 5.12

(A) Exact I−V characteristic of 11 series-connected lossless self-controlled photovoltaic units (LSCPVUs), (B) exact P−V characteristics of 11 series-connected LSCPVUs, points calculated by using Eqs. (5.23) and (5.24) (*grey circle* markers).

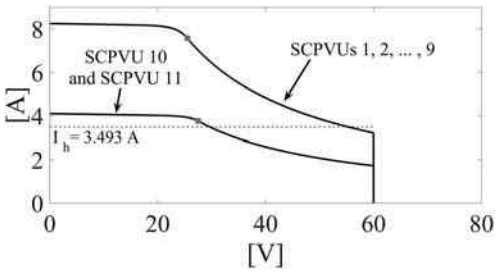


FIGURE 5.13

Exact I–V characteristics lossless self-controlled photovoltaic units (LSCPVUs). *Grey square* markers indicate maximum power points.

the case of the following set of operating conditions and parameters: S = [1000, 1000, 1000, 1000, 1000, 1000, 1000, 1000, 1000, 500, 500] W/m^2; Tambient = 25°C; $V_{ds\ max}$ = 60 V. By assuming that the allowed inverter DC input voltage range is equal to [350, 600] V, the FEMPV-based analysis provides the following value: V_h = 556.6 V; while the exact analysis provides V_h = 564.55 V. Therefore, we assume that the operating inverter voltage will initially be V_h = 556.6 V and, after the hill climbing refinement process, will be V_h = 564.55 V. In correspondence of such a voltage value, from the I–V exact characteristic it is I_h = 3.493 A. As shown in Fig. 5.13, the intersections among the horizontal dashed lines representing I_h = 3.493 A with the I–V output exact characteristics of the various LSCPVUs are found in the hyperbolic portions of the I–V characteristics of all the LSCPVUs. Therefore, in the considered case, the PV modules of all the LSCPVUs will operate in their MPPs.

Finally, Figs. 5.14 and 5.15 refer to the following set of operating conditions and parameters: S = [1000, 1000, 1000, 1000, 1000, 200, 200, 200, 200, 200, 200] W/m^2; $T_{ambient}$ = 25°C; $V_{ds\ max}$ = 60 V. By assuming that, once again, the allowed

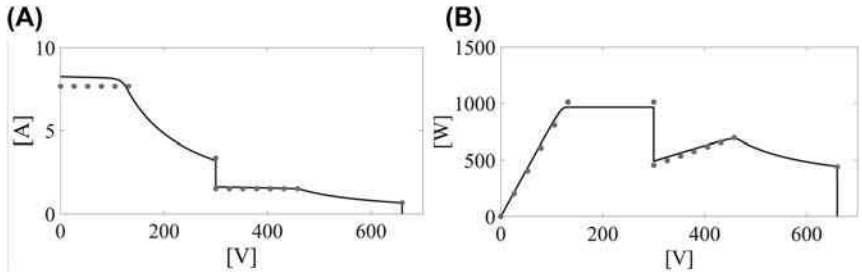


FIGURE 5.14

(A) Exact I–V characteristic of 11 series-connected lossless self-controlled PV units (LSCPVUs), (B) exact P–V characteristics of 11 series-connected LSCPVUs, points calculated by using Eqs. (5.23) and (5.24) (*grey circle* markers).

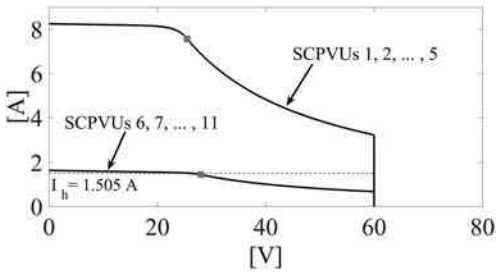


FIGURE 5.15

Exact I–V characteristics of lossless self-controlled PV units. *Grey square* markers indicate maximum power points.

inverter DC input voltage range is equal to [350, 600] V, the FEMPV-based analysis provides the following value: $V_h = 458$ V (which is nearly coincident with the exact one $V_h = 456.75$ V). In correspondence of such a voltage value, from the I–V exact characteristic it is $I_h = 1.505$ A. As shown in Fig. 5.15, the intersections among the horizontal dashed line representing $I_h = 1.505$ A with the I–V output exact characteristics of the various LSCPVUs are located in the vertical portion of the I–V characteristics, at $V = V_{ds\ max}$, for the LSCPVUs 1, 2, …, 5. Therefore, such LSCPVUs will operate at the maximum allowed output voltage. In the case of LSCPVUs 6, 7, …, 11, the intersection takes place at a voltage slightly lower than the MPP voltage; therefore, the PV modules of LSCPVUs 6, 7, …, 11 will operate at a voltage slightly lower than their MPP voltage.

The above examples clearly show that, for a given string of N LSCPVUs, the optimal operating range R_b must be continuously tracked because its amplitude and location are not fixed but strongly depend on the operating conditions of the N PV modules. Therefore, it is clear that it is mandatory to couple the Distributed MPPT (DMPPT) function assigned to the DC/DC converters, with a suitable Centralized MPPT (CMPPT) function carried out by the inverter through a proper control of V_b.

The main advantages of the HMPPTF strategy are:

- The high speed of tracking because of the fast (one-shot) estimation not only of the optimal operating range R_b but also of the k-th optimal PV voltage (k = 1, 2, …, N);
- The high robustness in the presence of multimodal P–V characteristic.

The eventual further refinement of the DC inverter input voltage V_b, with respect to the estimated value V_h, and the further refinement of the N operating voltages of the PV modules with respect to the corresponding estimated optimal values, is necessary to correct the errors associated with the theoretical and numerical approximations made in estimating such optimal values and also to take into account the actual efficiency of the power stage of the SCPVUs. In fact, such an efficiency, which of course modifies the actual shape of the equivalent P–V characteristic

with respect to that one obtained by considering LSCPVUs, is a complicated function of the operating point. It would be nearly impossible to exactly consider it in the analytical evaluation of the estimate of the optimal R_b. A very important, fundamental aspect is the following one: the exact and the approximate P−V characteristics of the strings of LSCPVUs are nearly coincident, in the region of the optimal R_b, where the highest accuracy is necessary. The greatest errors are localized instead in the regions of minor interest, from the point of view of the energetic efficiency of the whole PV system.

3.2.3 Numerical Simulations Concerning Hybrid Maximum Power Point Tracking Techniques

In this section, the performances of the HMPPTF strategy are compared with those of HMPPTS by analyzing two different mismatching scenarios (CASE I and CASE II). The time-domain numerical simulations have been carried out in PSIM environment; PSIM is a well-known simulation environment for power conversion and control. The simulated system is represented by a grid-connected PV system composed of an H-bridge central inverter fed by an array of LSCPVUs adopting boost converters with synchronous rectification (Fig. 5.16).

Fig. 5.16A refers to HMPPTF technique, instead Fig. 5.16B refers to HMPPTS technique. The substantial differences between the two architectures shown in Fig. 5.16A and B are linked to the fact that in the case of HMPPTF (Fig. 5.16A) the DMPPT and CMPPT controllers must be able to exchange useful data to implement the FEMPV algorithm. In particular, the DMPPT controllers must be able to provide the values of I_{SCk} ($k = 1, 2, \ldots, N$) to the CMPPT controller. In fact, such values are needed to evaluate the approximate P−V equivalent characteristic of the string of LSCPVUs. On the other hand, the CMPPT controller must in turn be able to provide the calculated values of v_{pk} ($k = 1, 2, \ldots, N$) to the DMPPT controllers. Such controllers carry out an MP&O technique with starting conditions v_{pk} ($k = 1, 2, \ldots, 11$) obtained, as discussed above, by means of the FEMPV algorithm. As concerns the HMPPTS technique (Fig. 5.16B), the DMPPT and CMPPT controllers are independent of one another.

3.2.3.1 Case I

Case I refers to the following set of values: irradiance distribution $S = [1000\ 1000\ 1000\ 1000\ 1000\ 1000\ 1000\ 200\ 200\ 200\ 200]$ W/m^2, $T_{ambient} = 25°C$. Both the HMPPTS strategy and the HMPPTF strategy adopt the MP&O algorithm as DMPPT technique. The MP&O parameters of the HMPPTS and HMPPTF techniques are reported in the Table 5.2.

The two parameters T_a and $\Delta v_{pan\ ref}$ of the MP&O technique (Table 5.2) have been chosen on the basis of the guidelines provided in [1] by assuming that the maximum rate of change of irradiance level to track without errors is equal to 100 W/(s m^2). As shown in Table 5.2, the main difference between the two DMPPT techniques is represented by the adopted value of $V_{out\ lim}$. In the case of HMPPTS, the value of $V_{out\ lim}$ must fulfill the inequalities of Eqs. (5.11) and (5.12), which are valid whenever the

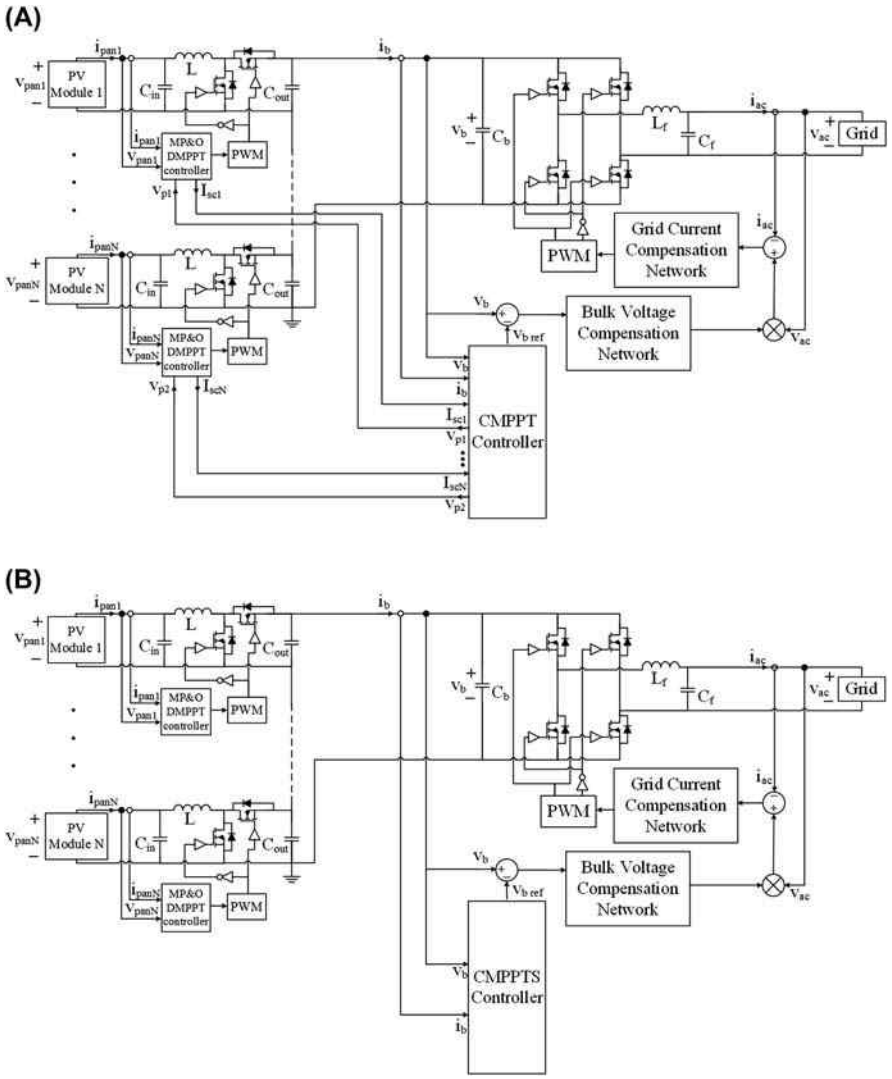


FIGURE 5.16

Grid-connected photovoltaic (PV) system adopting boost-based lossless self-controlled PV units: (A) HMPPTF technique, (B) HMPPTS technique.

Table 5.2 Modified P&O (MP&O) Parameters

Sampling interval of MP&O	$T_a = 1.5$ ms
Amplitude of the perturbation of MP&O	$\Delta v_{pan\ ref} = 0.15$ V
Guard level HMPPTS	$V_{out\ lim} = 53$ V
Guard level HMPPTF	$V_{out\ lim} = 59$ V

HMPPTS technique is adopted in a grid-connected PV system adopting boost-based LSCPVUs. In particular, by taking into account that, for $S_{max} = 1000\ W/m^2$ and $T_{ambient} = 25°C$, the values of P_{pan1}, ΔP_{pan1} and V_{OC} are, respectively, equal to 192 W, 8.89 W, and 36.8 V, we have that the value of $V_{out\ lim}$ must belong to the range [36.8−53.8] V. Because it is convenient to adopt a value of $V_{out\ lim}$ which is as high as possible, $V_{out\ lim}$ has been chosen equal to 53 V. As discussed previously, when adopting the HMPPTF technique, it is possible to estimate in advance the number N_{MPP} of LSCPVUs operating in their MPPs and the number N_{SC} of LSCPVUs operating with an output voltage equal to 0. This is very useful; in fact, the quantity ΔP_{tot} appearing in Eq. (5.11) can be evaluated with greater accuracy with respect to the worst-case value used when adopting the HMPPTS strategy:

$$\Delta P_{tot} = -(N - N_{SC} - N_{MPP}) \cdot \Delta P_{pan1} \cdot N_{MPP} \cdot \frac{\Delta V_{pan}^2}{R_{MPP}} \tag{5.44}$$

where R_{MPP} is the PV module differential resistance evaluated at the MPP [1]. It is worth noting that, thanks to the data obtained by means of the FEMPV algorithm, the quantities P_{pan1} and ΔP_{pan1} appearing in Eq. (5.11) can also be more or less accurately estimated:

$$P_{pan1} = V_{cost} \cdot I_{SC1} \tag{5.45}$$

$$\Delta P_{pan1} = \Delta V_{pan1} \cdot I_{SC1} \tag{5.46}$$

where I_{SC1} is the largest measured short circuit current. Instead, only worst-case values can be assumed in place of P_{pan1} and ΔP_{pan1} when adopting the HMPPTS strategy. In the CASE I, the values of I_{SC1}, N_{SC}, and N_{MPP} are, respectively, equal to 8.17 A, 4, and 7. By using Eqs. (5.11), (5.12), (5.44) and (5.46) we have that the value of $V_{out\ lim}$ must belong to the range [36.8−59.3] V. The value $V_{out\ lim}$ has been chosen equal as 59 V. The P−V exact characteristics of the 11 series-connected LSCPVUs are reported in Fig. 5.17A with reference to $V_{out\ lim} = 53$ V (which is the value adopted in HMPPTS technique) and $V_{out\ lim} = 59$ V (which is

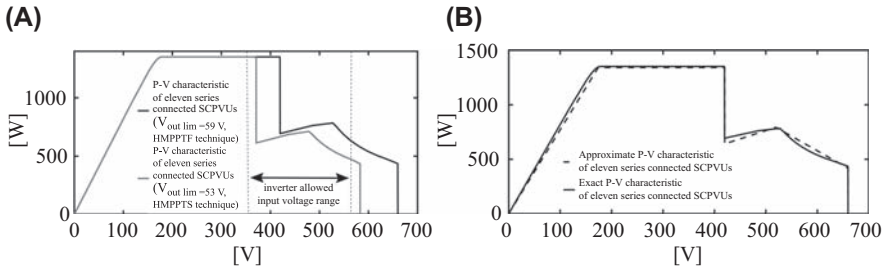


FIGURE 5.17

(A) Exact P−V characteristics of 11 series-connected Lossless Self-Controlled Photovoltaic Units (LSCPVUs) obtained by considering two different values of $V_{out\ lim}$, (B) exact and approximate P−V characteristics of 11 series-connected LSCPVUs ($V_{out\ lim} = 59$ V HMPPTF technique).

the value adopted in HMPPTF technique). The advantages associated with the adoption of a higher value of $V_{out\ lim}$ are clearly evident in Fig. 5.17A. For the sake of completeness, in Fig. 5.17B, both the exact and the approximate P−V characteristics obtained by assuming $V_{out\ lim} = 59$ V are reported. It is worth remembering that, while the approximate characteristic is used by the FEMPV algorithm, the exact characteristic must be considered if one is interested in the accurate verification of the actual power extracted from the PV system. The values of the remaining parameters adopted in HMPPTF technique are: $\Delta t = 1$ s, $V_{cost} = 26.24$ V. The remaining parameters adopted in HMPPTS technique have been chosen on the basis of the guidelines provided by Eqs. (5.13) and (5.15) for the value of $\Delta v_{b\ ref}$ and by Eqs. (5.17) and (5.19) for the value of T_b. By assuming $P = N \cdot V_{MPP} \cdot I_{PMM} = 2475$ W, $f_{line} = 50$ Hz, $V_a = V_{inverter\_min} = 360$ V, and $C_b = 1$ mF and by applying Eqs. (5.13) and (5.15), the allowed range of $\Delta v_{b\ ref}$ can be obtained:

$$21.9\ \text{V} \leq \Delta v_{b\ ref} \leq 47.55\ \text{V} \tag{5.47}$$

On the basis of the above considerations, $\Delta v_{b\ ref}$ has been chosen to be equal to 25 V. As concerns the value of T_b, it must fulfill the following inequalities:

$$T_b \geq T_{tot} = 0.75\ \text{s} \tag{5.48}$$

In this case, T_b has been chosen to be equal to 1 s. More details regarding the calculation of T_{tot} are reported in [62].

The time-domain behavior of the power extracted from the PV system by adopting both the techniques is shown in Fig. 5.18A. Even if, at the steady state, the value of the power extracted by adopting the two techniques is the same, it is evident that the HMPPTF technique is much faster. The HMPPTS technique instead needs to wait the time required for the whole scan before being able to identify the optimal operating point of the PV system. The time-domain behavior of the bulk inverter voltage, taking place when adopting both the techniques, is shown in Fig. 5.18B. The steady-state values of v_b are different in the two cases ($V_{b\ opt} = 380$ V in HMPPTF, $V_{b\ opt} = 360$ V in HMPPTS); in any case, they are in complete agreement

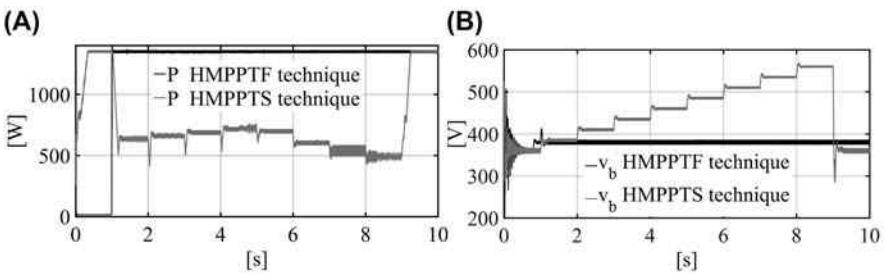


FIGURE 5.18

Time-domain behavior of the power P extracted (A) and of the input inverter voltage (B).

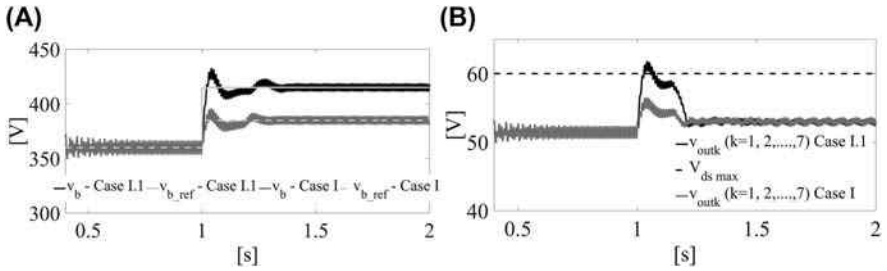


FIGURE 5.19

Time-domain behavior of v_b and $v_{b\ ref}$ (A) and v_{outk} (k = 1,2, …,7) (B).

with the curves shown in Fig. 5.17A and with the working principles of the two hybrid techniques.

Now, to show the effect of an inappropriate choice of $\Delta v_{b\ ref}$ with reference to the HMPPTS technique, Case I.1 has been considered. The set of parameters characterizing Case I.1 is the same as that adopted in Case I except for $\Delta v_{b\ ref.}$ In particular, the value adopted for $\Delta v_{b\ ref}$ in Case I.1 is $\Delta v_{b\ ref} = 55$ V, which does not satisfy the inequality Eq. (5.47). The results of this analysis are summarized in Fig. 5.19 in which the time-domain behavior of v_b, $v_{b\ ref}$ (Fig. 5.19A) and v_{outk} (k = 1, 2, …,7) (Fig. 5.19B) are reported in the time interval [0.4, 2] s. The first aspect which is worth noting is that, in both cases, the amplitude $\Delta v_{b\ ref}$ of the variation of $v_{b\ ref}$, occurring at t = 1 s, is greater than the peak-to-peak amplitude of the 100 Hz oscillation superimposed on v_b. The second aspect to underline is the following one; because the adopted value of $\Delta v_{b\ ref}$ does not fulfill inequality (5.47), it is not possible to ensure that the output voltages of all the LSCPVUs maintain below $V_{ds\ max}$. In fact, as shown in Fig. 5.19B, where the output voltage v_{outk} (k = 1, 2, …, 7) is shown either in Case I or in Case I.1, the threshold voltage $V_{dsmax} = 60$V is exceeded in Case I.1.

3.2.3.2 Case II

The last simulation case (Case II) refers to the following set of values of the parameters: S = [1000 1000 1000 1000 1000 1000 1000 390 390 390 390] W/m^2, $T_{ambient} = 25°C$. The HMPPTS parameters are the same as those considered in Case I except for the value of $\Delta v_{b\ ref}$, which in this case has been chosen equal to 47 V. The new value assumed by the $\Delta v_{b\ ref}$ continues to fulfill the inequality (5.47). As concerns the HMPPTF parameters, the only difference compared with that considered in the previous case concerns the value of $V_{out\ lim}$. In this case, the values of N_{SC} and N_{MPP} are, respectively, equal to 0 and 4. This means that, by using Eqs. (5.11), (5.12), (5.44), and (5.46), we have that the value of $V_{out\ lim}$ must belong to the range [36.8−58.5] V. The value of $V_{out\ lim}$ has been chosen equal to 58.5 V. The P−V exact characteristics of the 11 series-connected LSCPVUs are reported in Fig. 5.20A with reference to $V_{out\ lim} = 53$ V (which is the value adopted in the HMPPTS technique) and $V_{out\ lim} = 58.5$ V (which is the value adopted in

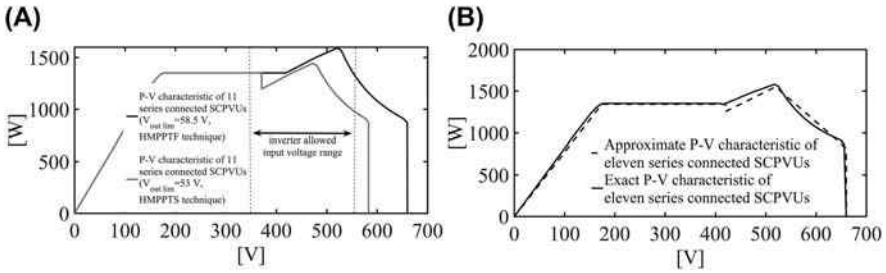


FIGURE 5.20

(A) Exact P–V characteristics of 11 series-connected Lossless Self-Controlled Photovoltaic Units (LSCPVUs) obtained by considering two different values of $V_{out\ lim}$, (B) exact and approximate P–V characteristics of 11 series-connected LSCPVUs ($V_{out\ lim} = 58.5$ V HMPPTF technique).

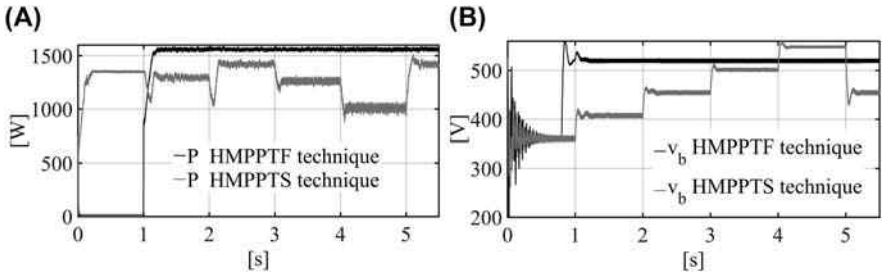


FIGURE 5.21

Time-domain behavior of the power P extracted (A) and of the input inverter voltage (B).

HMPPTF technique). For the sake of completeness, in Fig. 5.20B, both the exact and the approximate P–V characteristics obtained by assuming $V_{out\ lim} = 58.5$ V are reported. The time-domain behavior of the power extracted from the PV system by adopting both the techniques is shown in Fig. 5.21A. Such a figure clearly puts in evidence the superior performances exhibited by the HMPPTF strategy. The time-domain behavior of the bulk inverter voltage, taking place when adopting both the techniques, is shown in Fig. 5.21B. The steady-state optimal values of v_b are different in the two cases ($V_{b\ opt} = 520$ V in HMPPTS, $V_{b\ opt} = 450$ V in HMPPTF).

Now, to show the effect of a wrong choice of T_b with reference to the HMPPTS technique, Case II.1 has been considered. The set of parameters characterizing Case II.1 is the same as that adopted in Case II except for T_b. The value adopted for T_b in Case II.1 is $T_b = 0.1$ s, which does not satisfy the inequality (5.48). The results of this analysis are summarized in Fig. 5.22 in which the time-domain behavior of v_b, $v_{b\ ref}$ (Fig. 5.22A), and P (Fig. 5.22B) are reported. The analysis of the Fig. 5.22 puts in evidence that, when T_b is not enough high ($T_b = 0.1$ s), the optimal value of the bulk voltage that is identified after the scan is wrong. The error of the

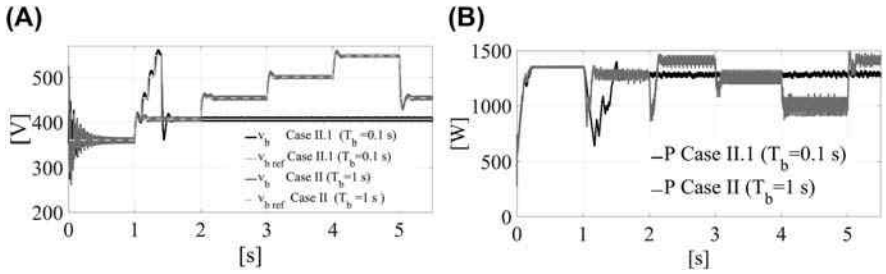


FIGURE 5.22

Time-domain behavior of the input inverter voltage (A) and of the power P extracted (B).

CMPPTS technique is because of the fact that, after each variation of v_b ref, the PV system is not able to reach a new steady-state equilibrium condition before the occurrence of the subsequent variation of v_b ref. In particular, the optimal operating points found by the CMPPTS technique in Case II.1 are (407 V, 1300 W), second point of the scan, when $T_b = 0.1$ s and (454 V, 1400 W), third point of the scan, when $T_b = 1$ s.

REFERENCES

[1] N. Femia, G. Petrone, G. Spagnuolo, M. Vitelli, Optimization of perturb and observe maximum power point tracking method, IEEE Trans. Power Electron. 20 (4) (July 2005) 963–973.

[2] M. Veerachary, T. Senjyu, K. Uezato, Voltage-based maximum power point tracking control of PV system, IEEE Trans. Aerosp. Electron. Syst. 38 (1) (January 2002) 262–270.

[3] M. Balato, L. Costanzo, M. Vitelli, Maximum power point tracking techniques, in: Wiley Online Encyclopedia of Electrical and Electronics Engineering, John Wiley & Sons, New Jersey, February 15, 2016, pp. 1–26, https://doi.org/10.1002/047134608X.W8299.

[4] K.H. Hussein, I. Muta, T. Hoshino, M. Osakada, Maximum photovoltaic power tracking: an algorithm for rapidly changing atmospheric conditions, IEEE Proc. Gener. Transm. Distrib. 142 (1) (January 1995) 59–64.

[5] P. Midya, P.T. Krein, R.J. Turnbull, R. Reppa, J. Kimball, Dynamic maximum power point tracker for photovoltaic applications, in: PESC Record. 27th Annual IEEE Power Electronics Specialists Conference, Baveno, vol. 2, 1996, pp. 1710–1716.

[6] E. Koutroulis, K. Kalaitzakis, N.C. Voulgaris, Development of a microcontroller-based, photovoltaic maximum power point tracking control system, IEEE Trans. Power Electron. 16 (1) (January 2001) 46–54.

[7] W. Wu, N. Pongratananukul, W. Qiu, K. Rustom, T. Kasparis, I. Batarseh, DSP-based multiple peak power tracking for expandable power system, in: Applied Power Electronics Conference and Exposition, 2003. APEC '03. Eighteenth Annual IEEE, Miami Beach, FL, USA, vol. 1, 2003, pp. 525–530.

[8] D.P. Hohm, M.E. Ropp, Comparative study of maximum power point tracking algorithms, Prog. Photovoltaics Res. Appl. 11 (2003) 47−62, https://doi.org/10.1002/pip.459.
[9] G. Petrone, G. Spagnuolo, M. Vitelli, Analytical model of mismatched photovoltaic fields by means of Lambert W-function, Sol. Energy Mater. Sol. Cells 91 (18) (November 6, 2007) 1652−1657. ISSN: 0927−0248, https://doi.org/10.1016/j.solmat.2007.05.021.
[10] L. Shengyi, R.A. Dougal, Dynamic multiphysics model for solar array, IEEE Trans. Energy Convers. 17 (2) (June 2002) 285−294.
[11] E.L. Meyer, E. Ernest van Dyk, The effect of reduced shunt resistance and shading on photovoltaic module performance, in: Conference Record of the Thirty-First IEEE Photovoltaic Specialists Conference, 2005, 2005, pp. 1331−1334.
[12] R. Bruendlinger, B. Bletterie, M. Milde, H. Oldenkamp, Maximum power point tracking performance under partially shaded PV array conditions, in: Twenty-First European Photovoltaic Solar Energy Conference, Dresden, Germany, September 4−8, 2006, 2006, pp. 2157−2160.
[13] T. Oozeki, K. Otani, K. Kurokawa, Accuracy of estimated shading loss ratio by means of the SV method − an extraction algorithm of maximum pattern, in: Conference Record of the Thirty-First IEEE Photovoltaic Specialists Conference, 2005, 2005, pp. 1804−1807.
[14] G. Petrone, G. Spagnuolo, R. Teodorescu, M. Veerachary, M. Vitelli, Reliability issues in photovoltaic power processing systems, IEEE Trans. Ind. Electron. 55 (7) (July 2008) 2569−2580.
[15] B. Burger, B. Goeldi, S. Rogalla, H. Schmidt: "Module integrated electronics − an overview", 25th European Photovoltaic Solar Energy Conference and Exhibition, September 2010, Valencia (Spain), pp. 3700−3707.
[16] Q. Li, P. Wolfs, A review of the single phase photovoltaic module integrated converter topologies with three different DC link configurations, IEEE Trans. Power Electron. 23 (3) (May 2008) 1320−1333.
[17] S.B. Kjaer, J.K. Pedersen, F. Blaabjerg, A review of single-phase grid-connected inverters for photovoltaic modules, IEEE Trans. Ind. Appl. 41 (5) (September−October 2005) 1292−1306.
[18] Website, http://www.exeltech.com.
[19] Website, http://www.greenraysolar.com.
[20] Website, www.petrasolar.com.
[21] Website, www.enecsys.com.
[22] Website, www.enphaseenergy.com.
[23] Website, http://solarbridgetech.com.
[24] Website, http://www.involar.com.
[25] Website, http://www.power-one.com/renewable-energy/products/solar/string-inverters/panel-products/aurora-micro/series-0.
[26] E. Roman, R. Alonso, P. Ibanez, S. Elorduizapatarietxe, D. Goitia, Intelligent PV module for grid-connected PV systems, IEEE Trans. Ind. Electron. 53 (4) (June 2006) 1066−1073.
[27] G.R. Walker, P.C. Sernia, Cascaded DC-DC converter connection of photovoltaic modules, IEEE Trans. Power Electron. 19 (4) (July 2004) 1130−1139.
[28] W. Yao, M. Gao, Z. Ren, M. Chen, Z. Qian, "Improvement of performance and flexibility for photovoltaic module using individual DC/DC converter, in: 2009 IEEE 6th International Power Electronics and Motion Control Conference, Wuhan, 2009, pp. 441−444.

[29] T. Zhao, Z. Ju, H. Wang, X. Wei, X. Li, S. Zhang, The distributed maximum power point tracking method and application in the PV grid-connected Generation, in: 2010 International Conference on Intelligent System design and Engineering Application, Changsha, 2010, pp. 639−642.
[30] A. Elasser, M. Agamy, J. Sabate, R. Steigerwald, R. Fisher, M. Harfman-Todorovic, A comparative study of central and distributed MPPT architectures for megawatt utility and large scale commercial photovoltaic plants, in: IECON 2010-36th Annual Conference on IEEE Industrial Electronics Society, Glendale, AZ, 2010, pp. 2753−2758.
[31] Q. Li, P. Wolfs, A preliminary study of the distributed maximum power point tracker designs for different types of solar cells in solar and electric vehicle arrays, in: 2007 Australasian Universities Power Engineering Conference, Perth, WA, 2007, pp. 1−6.
[32] R. Shao, M. Kaye, L. Chang, Advanced building blocks of power converters for renewable energy based distributed generators, in: 8th International Conference on Power Electronics − ECCE Asia, Jeju, 2011, pp. 2168−2174.
[33] S. Poshtkouhi, J. Varley, R. Popuri, O. Trescases, Analysis of distributed peak power tracking in photovoltaic systems, in: The 2010 International Power Electronics Conference − ECCE Asia −, Sapporo, 2010, pp. 942−947.
[34] R. Alonso, P. Ibáñez, V. Martínez, E. Román, A. Sanz, Analysis of performance of new distributed MPPT architectures, in: 2010 IEEE International Symposium on Industrial Electronics, Bari, 2010, pp. 3450−3455.
[35] D. Ahmadi, S.A. Mansouri, J. Wang, Circuit topology study for distributed MPPT in very large scale PV power plants, in: 2011 Twenty-Sixth Annual IEEE Applied Power Electronics Conference and Exposition (APEC), Fort Worth, TX, 2011, pp. 786−791.
[36] U. Kamnarn, S. Yousawat, S. Sreeta, W. Muangjai, T. Somsak, Design and implementation of a distributed solar controller using modular buck converter with maximum power point tracking, in: 45th International Universities Power Engineering Conference UPEC2010, Cardiff, Wales, 2010, pp. 1−6.
[37] Y.M. Chen, C.W. Chen, Y.L. Chen, Development of an autonomous distributed maximum power point tracking PV system, in: 2011 IEEE Energy Conversion Congress and Exposition, Phoenix, AZ, 2011, pp. 3614−3619.
[38] S. Poshtkouhi, V. Palaniappan, M. Fard, O. Trescases, A general approach for quantifying the benefit of distributed power electronics for fine grained MPPT in photovoltaic applications using 3-D modeling, IEEE Trans. Power Electron. 27 (11) (November 2012) 4656−4666.
[39] G. Petrone, G. Spagnuolo, M. Vitelli, An analog technique for distributed MPPT PV applications, IEEE Trans. Ind. Electron. 59 (12) (December 2012) 4713−4722.
[40] P. Tsao, S. Sarhan, I. Jorio, Distributed maximum power point tracking for photovoltaic arrays, in: PVSC PV Photovoltaic Specialists Conference, 2009, pp. 2293−2298.
[41] R. Giral, C.E. Carrejo, M. Vermeersh, A.J. Saavedra-Montes, C.A. Ramos-Paja, PV field distributed maximum power point tracking by means of an active bypass converter, in: 2011 International Conference on Clean Electrical Power (ICCEP), Ischia, 2011, pp. 94−98.
[42] Z. Cheng, H. Zhou, H. Yang, Research on MPPT control of PV system based on PSO algorithm, in: Chinese Control and Decision Conference, 2010, pp. 887−892.
[43] N. Femia, G. Lisi, G. Petrone, G. Spagnuolo, M. Vitelli, Distributed maximum power point tracking of photovoltaic arrays: novel approach and system analysis, IEEE Trans. Ind. Electron. 55 (7) (July 2008) 2610−2621.

[44] M. Balato, L. Costanzo, P. Marino, G. Rubino, L. Rubino, M. Vitelli, Modified TEODI MPPT technique: theoretical analysis and experimental validation in uniform and mismatching conditions, IEEE J. Photovoltaics 7 (2) (March 2017) 604−613.
[45] N. Femia, G. Petrone, G. Spagnuolo, M. Vitelli, A technique for improving P&O MPPT performances of double-stage grid-connected photovoltaic systems, IEEE Trans. Ind. Electron. 56 (11) (November 2009) 4473−4482.
[46] N. Femia, M. Fortunato, G. Lisi, G. Petrone, G. Spagnuolo, M. Vitelli, Guidelines for the optimization of the P&O technique in grid-connected double-stage photovoltaic systems, in: 2007 IEEE International Symposium on Industrial Electronics, Vigo, 2007, pp. 2420−2425.
[47] Website, http://www.solaredge.com.
[48] Website, http://www.tigoenergy.com.
[49] Website, http://www.xandex.com.
[50] Website, http://eiqenergy.com.
[51] Website, http://solarmagic.com/en/index.html.
[52] F. Blaabjerg, R. Teodorescu, M. Liserre, A.V. Timbus, Overview of control and grid synchronization for distributed power generation systems, IEEE Trans. Ind. Electron. 53 (5) (October 2006) 1398−1409.
[53] Erikson R.W., Maksimovic D., "Fundamentals of Power Electronics", second ed., Kluwer Academic Publishers: Norwell, MA. ISBN: 0-7923-7270-0.
[54] M. Vitelli, On necessity joint adoption both distributed maximum power point tracking and central maximum power point tracking in PV systems, Prog. Photovoltaics Res. Appl. 22 (2014) 283−299, https://doi.org/10.1002/pip.2256.
[55] N. Femia, G. Petrone, G. Spagnuolo, M. Vitelli, Power Electronics and Control Techniques for Maximum Energy Harvesting in Photovoltaic Systems, CRC Press, Taylor & Francis group, 2013.
[56] M. Balato, M. Vitelli, Optimization of distributed maximum power point tracking PV applications: The scan of the power vs. voltage input characteristic of the inverter, Int. J. Electr. Power Energy Syst. 60 (September 2014) 334−346.
[57] C.A. Ramos-Paja, A.J. Saavedra-Montes, M. Vitelli, Distributed maximum power point tracking with overvoltage protection for PV systems. ISSN: 0012-7353, vol. 178, Revista DYNA − Medellin, Centro Editorial − Facultad de Minas, Universidad Nacional de Colombia − year 80, Nro, April 2013, pp. 141−150.
[58] M. Balato, M. Vitelli, N. Femia, G. Petrone, G. Spagnuolo, Factors limiting the efficiency of DMPPT in PV applications, in: 2011 International Conference on Clean Electrical Power (ICCEP), Ischia, 2011, pp. 604−608.
[59] M. Balato, M. Vitelli, A new strategy for the identification of the optimal operating points in PV applications with distributed MPPT, in: 2013 Eighth International Conference and Exhibition on Ecological Vehicles and Renewable Energies (EVER), Monte Carlo, 2013, pp. 1−6.
[60] M. Balato, M. Vitelli, A hybrid MPPT technique based on the fast estimate of the maximum power voltages in PV applications, in: 2013 Eighth International Conference and Exhibition on Ecological Vehicles and Renewable Energies (EVER), Monte Carlo, 2013, pp. 1−7.
[61] M. Balato, M. Vitelli, A new control strategy for the optimization of distributed MPPT in PV applications, Int. J. Electr. Power Energy Syst. ISSN: 0142-0615 62 (November 2014) 763−773, https://doi.org/10.1016/j.ijepes.2014.05.0323.

[62] M. Balato, M. Vitelli, An algorithm for the estimation of the maximum power voltages in microconverters based PV applications, in: 2014 Ninth International Conference on Ecological Vehicles and Renewable Energies (EVER), Monte-Carlo, 2014, pp. 1−11.
[63] H.D. Venable, Practical techniques for analyzing, measuring, and stabilizing feedback control loops in switching regulators and converters, in: Proceedings of POWERCON Conference, March 1980 pp. I2−I1−I2−I17.

This page intentionally left blank

CHAPTER

Flexible Power Control of Photovoltaic Systems

6

Frede Blaabjerg, Ariya Sangwongwanich, Yongheng Yang
Department of Energy Technology, Aalborg University, Aalborg, Denmark

CHAPTER OUTLINE

1. Introduction 207
2. Demand to Grid-Connected PV Systems 209
2.1 Overloading of the Grid (Overvoltage) During PV Peak-Power Generation Period 209
2.2 Grid Voltage Fluctuation Because of Intermittency of PV Energy 210
2.3 Limited-Frequency Regulation Capability to Stabilize the Grid During Frequency Deviation 210
3. Possible Solutions for Flexible Power Control of PV Systems 211
3.1 Integrating Energy Storage Systems 211
3.2 Installing Flexible Loads 212
3.3 Modifying the Control Algorithm of the Power Converters 213
4. Power Converter Technology and Control for PV Systems 214
4.1 System Diagram of Grid-Connected PV Systems 214
4.2 Control Structure of Grid-Connected PV Systems 217
4.3 Maximum Power Point Tracking Algorithms 218
5. Flexible Active Power Control of PV Systems 220
5.1 Power-Limiting Control Algorithm 220
5.2 Power Ramp-Rate Control Algorithm 221
5.3 Power Reserve Control Algorithm 222
6. Summary 225
References 226

1. INTRODUCTION

As a result of environmental and CO_2 emission concerns, renewable energy sources have gained more and more attention worldwide. Several countries have set an ambitious goal for energy production capacity concerning renewable energy sources. As a main market share, the European Council targets 30% of renewable energy by 2030 [1]. With the same milestone, Germany plans to achieve 18% of renewable energy for gross energy consumption [2]. Denmark has also set a goal to be

Advances in Renewable Energies and Power Technologies. https://doi.org/10.1016/B978-0-12-812959-3.00006-X
Copyright © 2018 Elsevier Inc. All rights reserved.

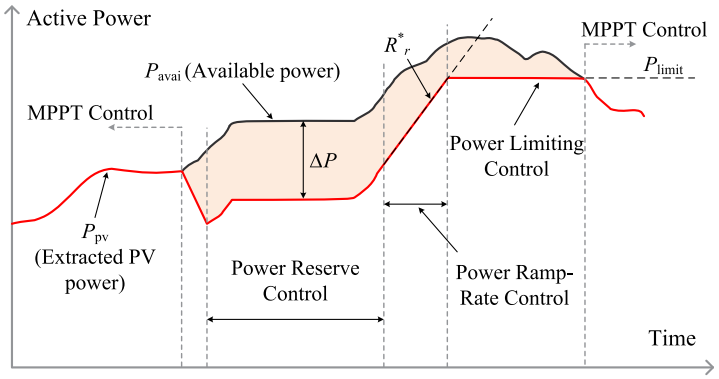


FIGURE 6.1

Active power control strategies for grid-connected PV systems defined in the Danish grid code (P_{pv}: PV power, P_{avai}: available power, P_{limit}: the power limit level, R^*_r: the ramp-rate limit, ΔP: the power reserve level) [17].

independent of fossil fuel by 2050 [3]. With these initiatives, the penetration level of renewable energy such as solar and wind energy has been increasing considerably during the last decades [4].

Among other renewable energy sources, photovoltaic (PV) systems have a potential to become a major source of electricity in the near future because of several merits such as simple installation, modularity, and scalability. In fact, the installation and component cost of PV systems, especially the cost of PV panel, has been significantly declining in the past years [5,6]. As a result, PV systems have been increasingly installed and connected to the power grid during the recent years. However, under a large-scale adoption of grid-connected PV systems, the integration of PV systems into the power grid becomes important. Challenges like overloading of the grid during the PV peak-power generation periods, severed grid voltage fluctuations because of the intermittency of PV energy, and limited grid frequency regulation capability because of more decentralized power generation units have been witnessed in practice with a high-penetration level of grid-connected PV system [6a–10].

To address the above issues and ensure a smooth integration of PV systems into the grid, the grid requirements in some countries have been revised and updated [11–17]. One of the recent requirements is the flexible active power control for the PV system, where the active power generated by the PV systems has to be regulated upon demands, e.g., during grid frequency deviation. An example of active power control strategies for PV systems introduced in the grid code is shown in Fig. 6.1, where various power control functionalities have been defined as:

- Power-Limiting Control (PLC) (also called as Constant Power Generation Control, Absolute Active Power Control): The maximum absolute active power

production from the PV systems is limited to a certain set-point P_{limit} during the operation.
- Power Ramp-Rate Control (PRRC) (also called Power Gradient Control): The maximum change rate of the active power production from the PV systems is limited to a certain rate R_r^*.
- Power Reserve Control (PRC) (also called Delta Power Control): An active power from the PV system P_{pv} is regulated below the maximum available power P_{avai} to provide a certain amount of power reserve ΔP.

By implementing such control functionalities, the PV systems not only are acting as a purely power-generating unit but also are involved in grid supporting by providing flexible power delivery. Therefore, "grid-friendly" integrations can be ensured, and the above technical challenges caused by the intermittency nature of solar energy can be resolved.

In this chapter, the demands for flexible power control in grid-connected PV systems are briefly discussed. An overview of possible control solutions to realize flexible active power control for the PV system is provided. Then, the rest of the chapter focuses on the flexible power control solutions through the modification of the power converter control algorithm. Finally, concluding remarks are provided.

2. DEMAND TO GRID-CONNECTED PV SYSTEMS

Several challenges regarding grid integration of PV system have been reported in recent studies. In this section, three commonly concerned issues related to active power control of the PV system are discussed.

2.1 OVERLOADING OF THE GRID (OVERVOLTAGE) DURING PV PEAK-POWER GENERATION PERIOD

Under a large PV installation scenario, overloading of the grid is one of the associated and the most concerned issues [9]. When many PV systems are connected to the grid, they can introduce a significant peak surplus power during midday (i.e., when the PV power production is highest). This will increase the power losses and lead to overvoltage (if the grid capacity remains the same) and thus should be avoided as it will overstress the equipment in the systems. This issue has been increasingly of concern recently. For instance, it has been reported that parts of the distribution grid in Northern Ireland have experienced a severe overloading because of a high number of PV systems connected to the grid [18]. To solve this problem, the PLC scheme has been introduced in grid regulations, where the active power injected from the PV systems has to be limited to a certain value if demanded, as illustrated in Fig. 6.1. By doing so, the peak-power from PV systems can be avoided. This requirement is currently adopted in Germany through the grid codes [15], where the newly installed PV systems have to be able to limit their maximum feed-in power

(i.e., 70% of the rated power). Similar requirements have also been defined in the grid codes of other countries (e.g., Denmark and Japan).

2.2 GRID VOLTAGE FLUCTUATION BECAUSE OF INTERMITTENCY OF PV ENERGY

Another potential problem caused by PVs is because of the intermittency nature of solar energy. It is well known that the PV power can be fluctuating considerably in the case of cloudy days, where the power production can suddenly drop because of passing clouds. Actually, the change rate of the PV power is also correlated with the system size [19]. For instance, this problem is usually pronounced in small-scale PV systems (rooftop PV applications) because a passing cloud can easily cover a major area of the PV panels [20]. In the case of a wide-scale grid-connected PV system, those sudden changes in the PV power can potentially induce severe grid voltage fluctuations [7], which thus should be addressed.

To reduce the power fluctuation from the PVs, the PRRC is introduced to limit the PV output power change rate [14,17]. Namely, as long as the PV output power changing rate is below a certain limit, the PV system is allowed to continuously operate in the Maximum Power Point Tracking (MPPT) mode (i.e., normal operation). However, once the PV power changing rate reaches the maximum limit, the PV output power should be controlled in a ramp manner, as shown in Fig. 6.1.

2.3 LIMITED-FREQUENCY REGULATION CAPABILITY TO STABILIZE THE GRID DURING FREQUENCY DEVIATION

In the conventional power systems, the grid frequency is normally regulated by large conventional power plants (e.g., coal, gas turbine), which are considered as dispatchable sources of electricity. However, as the installation of grid-connected PV system increases, the system operator will have less capability to stabilize the grid in the case of frequency deviations, as a large portion of PV systems cannot be easily controlled by the system operator. Initially, some grid regulations require the PV systems to be disconnected from the power grid during the frequency deviation. However, as the penetration level of grid-connected PV systems increases, disconnecting the large amount of PV systems during the frequency deviation will challenge the grid stability because of a sudden loss of large power generation [21]. This is known as the 50.2-Hz problem, which is highly concerned in countries with high PV penetration (e.g., Germany) [12].

With the above concerns, the frequency regulation has been implemented in grid codes, where the PV systems are not allowed to immediately disconnect from the grid in response to frequency deviations. Instead, the PV system needs to provide a power reserve by reducing its output power to a certain level (specified by the grid codes), as shown in Fig. 6.1. In this way, the PV systems are requested to contribute to frequency regulations and support the grid during frequency deviation.

3. POSSIBLE SOLUTIONS FOR FLEXIBLE POWER CONTROL OF PV SYSTEMS

To realize a wide-scale adaptation of grid-connected PV system, the above grid integration issues need to be addressed. Therefore, solutions for flexible power control of PV system are demanded. Various solutions to provide the power control flexibility have been introduced for grid-connected PV systems. In this section, an overview of the widely used solutions to achieve flexible active power control functionalities will be presented.

3.1 INTEGRATING ENERGY STORAGE SYSTEMS

Among other possible solutions, integrating PV systems with the energy storage system (ESS) is one of the most widely used approaches [22–25]. For example, the battery technology is considered to be a suitable technology to be used with PV system because of its high energy density and high efficiency. This solution has been adopted with commercial PV systems, and it is commonly referred to as the PV-battery system. In this combination, the extracted PV power from the PV arrays always follows the maximum available power, which fluctuates dynamically according to the solar irradiance and ambient temperature conditions. However, the flexibility of the power injection can be provided by the ESS, where the battery is charged and discharged following the active power demand. Fig. 6.2 demonstrates the control strategy of the PV system with integrated ESS.

One strong benefit of this solution is the increase of the PV energy utilization, where the surplus PV power (e.g., during the PLC) can be stored in the battery and used later during the low PV power production. This offers a possibility to provide an upward frequency regulation during the power reserve when the PV systems are requested to inject the output power higher than the maximum available PV power production, which is achieved by discharging the battery.

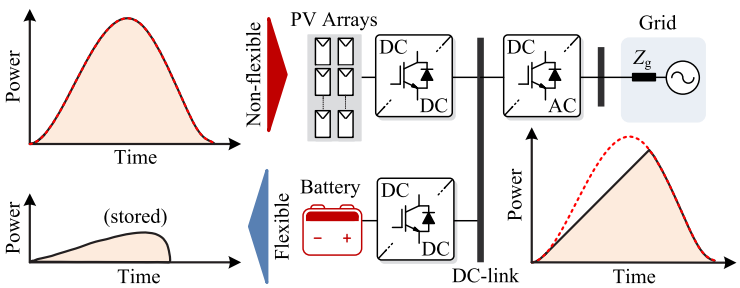


FIGURE 6.2

Flexible active power control solution for grid-connected photovoltaic system by integrating energy storage systems.

A compromise of this solution is the extra cost because of the ESS. Although the cost of battery is continuously decreasing, the total cost of PV systems with integrating ESS is still considerably higher than the conventional PV systems [26]. This is mainly because of the cost of extra equipment such as batteries and battery management systems and also the operation and maintenance costs. With the recent technology, the warranty period of the commercial battery (e.g., lithium ion) is usually limited to less than 5 year [27], whereas the typical PV systems are expected to last for 20–30 years. When looking from the reliability perspective, although the ESSs provide the flexibility in power injection of the PV systems, they also introduce other possible failure mechanisms in the overall PV systems.

3.2 INSTALLING FLEXIBLE LOADS

Another solution to provide the power control flexibility through extra equipment is by installing flexible loads locally. The main idea of this approach is to absorb the surplus PV energy through the demand side management, where the flexibility is provided by the load that absorbs the surplus PV energy locally [24]. The basic control strategy of this approach is presented in Fig. 6.3, which is quite similar to the solution with integrating ESS. The difference is that the surplus PV energy is dissipated or utilized by the local load, instead of being stored in the battery.

The flexible load can be realized by resistors with the power flow controller to control the power dissipation. In this case, it is usually referred to as "dump load" as the excessive PV power is simply dumped in the resistors without being used. Therefore, this approach is not very economically attractive from the user perspective. The utilization of the PV energy can be improved if the local load (e.g., household equipment, electric vehicles) can be adaptively controlled. For instance, the electric vehicles are charged by the surplus PV energy during midday or the washing machine is set to be operated when the PV system produces surplus energy. In this case, the surplus PV energy is not wasted, as it is done with the dump load solution,

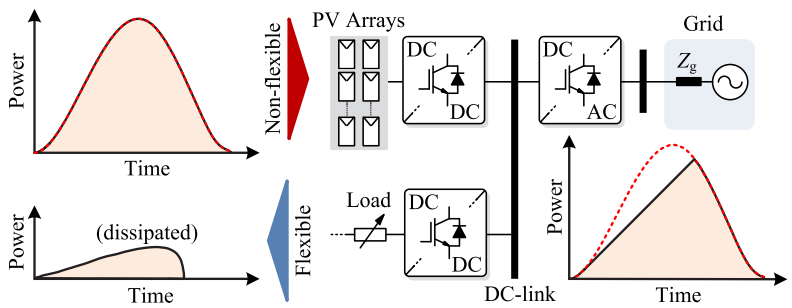


FIGURE 6.3

Flexible active power control solution for grid-connected photovoltaic system by installing flexible loads.

but it is being utilized by the actual loads, which can be flexibly controlled, and they are referred to as "smart load" [28,29].

This solution has been widely discussed with the context of smart grid, where communication network and coordination control between different components are the main focus [29]. However, the requirement of communication network and coordinate control are also shortcomings of this method, which may increase the cost and the complexity of the overall system.

3.3 MODIFYING THE CONTROL ALGORITHM OF THE POWER CONVERTERS

With the recent technology advancement in power electronics, more and more advanced control functionality has been developed for power converters [16,30]. This gives a possibility for the PV system to take the benefit of the advanced control in power converters, which are the key components to control the power delivery of PV systems, to achieve the flexible power control functionality. Conventionally, the MPPT control strategy is implemented in power converters of PV systems for maximizing the energy yield from the PV arrays. However, the MPPT control scheme cannot provide the flexible power injection, as the PV systems under this control scheme always try to extract the maximum available PV power during the operation. In other words, the PV power production with the MPPT control can be fluctuating following the dynamic of the solar irradiance and ambient temperature (e.g., during the cloudy day).

To enable the power control flexibility of the PV systems, the conventional MPPT control algorithm needs to be modified as shown in Fig. 6.4. Instead of always tracking the Maximum Power Point (MPP) of the power−voltage (P−V) curve of the PV arrays, the operating point of the PV system may need to be regulated below the MPP, corresponding to the required amount of output power for certain active power control functionality [31−34]. The operational principle of the modifying MPPT algorithm is illustrated in Fig. 6.5, and this approach is also called active power curtailment in literature.

In this approach, the flexible active power control functionality is realized through the modification of the inherent control algorithm of the power converter

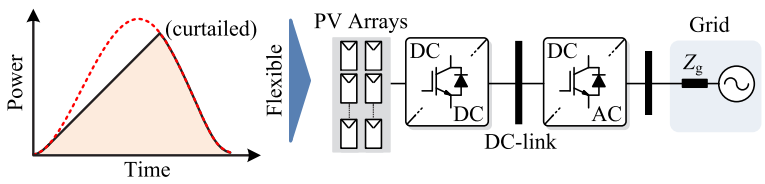


FIGURE 6.4

Flexible active power control solution for grid-connected photovoltaic system by modifying control algorithm of the power converters.

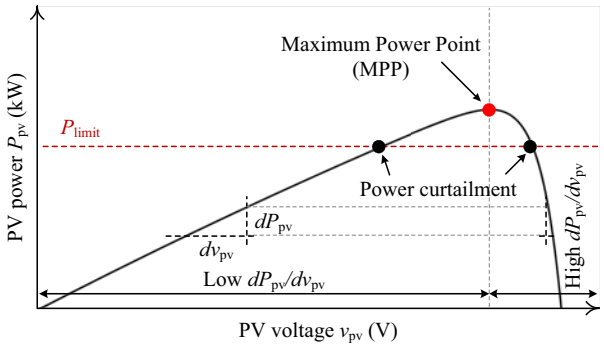


FIGURE 6.5

Possible operating points of the photovoltaic (PV) system in power–voltage curve of the PV arrays with the PV power below the maximum available power.

(i.e., MPPT algorithm). This offers a cost-effective solution in terms of component cost, as there is no extra component (such as battery or dump load). In addition, the reduced number of components in the system also results in a benefit in the reliability aspect because of the lower number of possible failure components in the system. Nevertheless, the shortcoming of this approach is the reduction in the PV utilization as a result of the loss of PV energy yield during the power curtailment because the PV energy is not being stored or used. In some cases, the economic loss because of the reduction in the PV energy yield may overcome the benefit of the reduced equipment cost, which has to be carefully designed [31,35,36].

4. POWER CONVERTER TECHNOLOGY AND CONTROL FOR PV SYSTEMS

4.1 SYSTEM DIAGRAM OF GRID-CONNECTED PV SYSTEMS

A general system diagram of grid-connected PV systems is shown in Fig. 6.6 and consists of three main components: PV panels (or arrays), power converters (PV inverters), and ac grid. As the power generated by the PV arrays is dc power, the power converter, which is a power electronic-based technology, is required to convert the dc power from the PV arrays to the ac power [37]. In other words, power converter plays an important role in controlling the power delivery and at the same time ensuring a proper integration between the PV and the grid. Additionally, other specifications are imposed by the grid requirements to make grid-connected PV systems more resilient and grid-friendly: (1) reliable or secure the power supply; (2) flexible control of active and reactive power; (3) dynamic grid support per demands; (4) system condition monitoring, protection, and communication; and (5) high efficiency and reliability, low cost, and small volume [38–40].

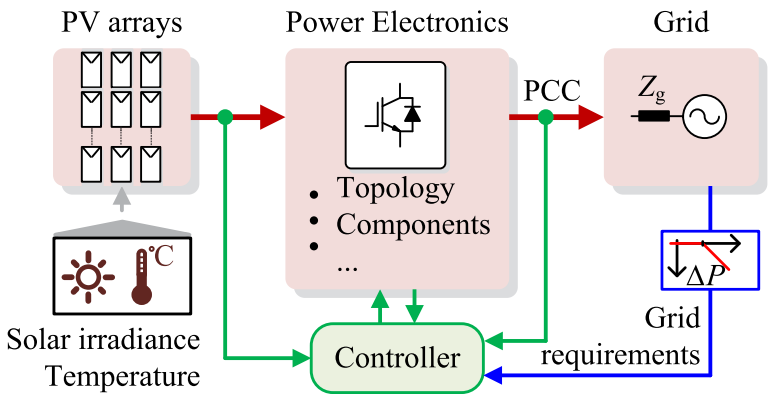


FIGURE 6.6

System diagram of the grid-connected photovoltaic (PV) system, where the PV arrays are the source of input power and power converters are employed to enable the control of the PV system and the integration of the grid, whose control strategy is imposed by the grid requirements.

In the state-of-the art technology, there are three mainstream system configurations of grid-connected PV systems, as summarized in Fig. 6.7 [41,42]. The adaptation of each configuration is mainly dependent on the applications and the power ratings. For example, a small-scale PV system usually employs module PV converters shown in Fig. 6.7A because of the small volume and high scalability. The module PV converter enables individual MPPT tracking at each PV panel, which is the advantage of this configuration due to the increased energy yield. Nevertheless, this configuration requires a dc−dc converter with high conversion ratio, as the PV voltage of the module is usually small because of the limited number of panels, to be able to be connected to the ac grid through the inverter. At the same time, high efficiency needs to be attained over a wide range of operation, which is a challenge of this system configuration. For a medium/large-scale PV systems, string, multistring, or central inverters shown in Fig. 6.7B and C are more promising because of their overall high conversion efficiency. In this case, the PV power can be directly fed to the ac grid without or with a dc−dc converter with a small conversion ratio, as the PV voltage is usually high enough because of the large number of PV panels. As the PV utilization is still at a residential application (e.g., rooftop system), the string and multistring inverters are dominating in market, and the single-phase connection is more often to see [39]. In fact, the string inverter becomes more and more popular in the recent years because of its high scalability, high reliability, and simple installation. This system configuration is expected to be more adopted in the large-scale PV system as a replacement of the central inverter [43,44].

Another way to classify the PV system configuration can be done by considering the number of power conversion stages employed in the system. For a

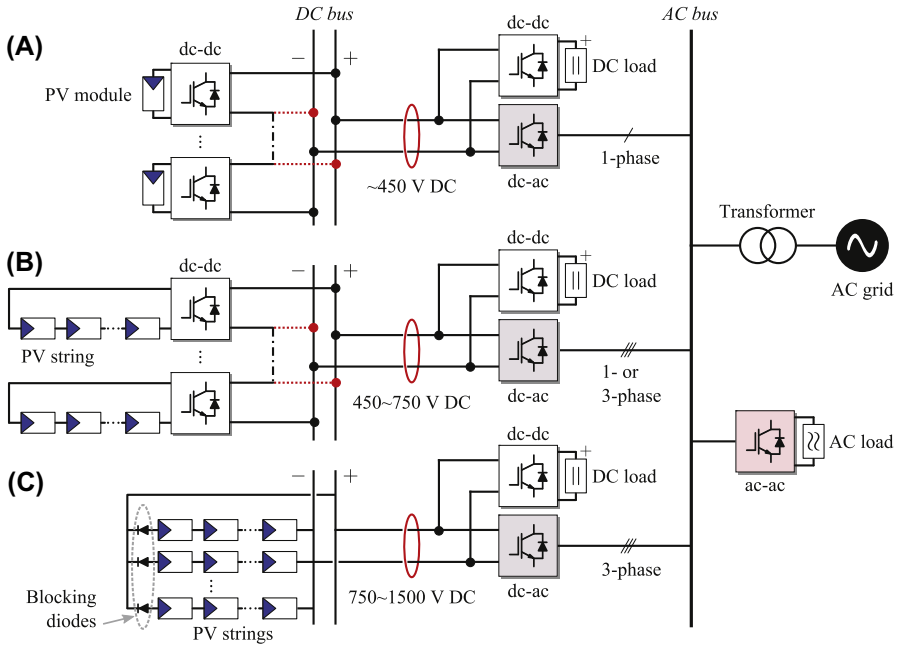


FIGURE 6.7

Different grid-connected photovoltaic inverter structures: (A) module inverters connected to a common dc-bus, (B) string/multistring inverter applied in single- or three-phase systems (residential and commercial applications), and (C) center inverters for commercial or utility-scale applications (high power, e.g., 100 kW).

small-scale PV system (e.g., modular PV converters, string/multi-string inverters), the PV voltage is usually lower than the required dc-link voltage because of the limited number of PV panels connected in series. In this case, a two-stage power conversion is normally required. The first conversion stage is a dc−dc conversion, which is employed to step up the PV voltage to match the minimum required dc-link voltage for grid-connected applications (e.g., dc-link voltage of 450 V for 230 V ac grid). In the case of large-scale PV system, the PV voltage is usually high enough to connect to the grid without the need of the voltage amplification. Therefore, a single-stage conversion can be employed, where the dc−dc conversion stage is not required. The absence of the dc−dc conversion stage can reduce the power loss introduced by the dc−dc converter, which is an important aspect for large-scale PV plants.

In this chapter, the single-phase string inverter configuration is used as an example as a result of its popularity. An example of the two-stage grid-connected PV system with an LCL filter is shown in Fig. 6.8. Moreover, to achieve a higher efficiency, transformer-less PV inverter topologies are favorable. However, the

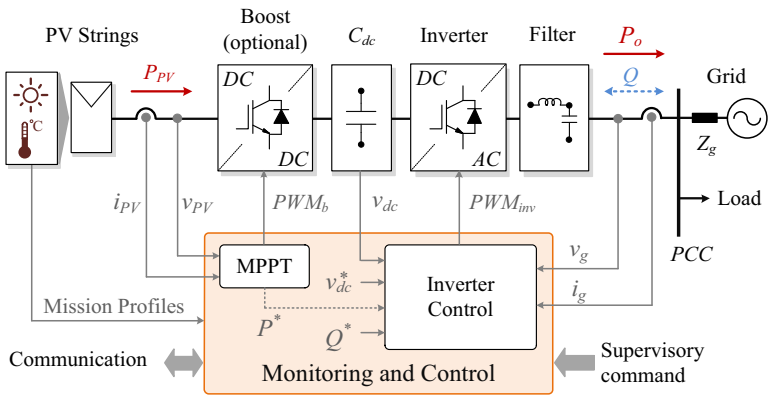


FIGURE 6.8

System configuration of a two-stage, single-phase, grid-connected photovoltaic system.

lack of isolation transformers can compromise the safety of the system because of the generated leakage currents, which may need to be addressed by specifically designing the modulation schemes or bypassing methods [45,46].

4.2 CONTROL STRUCTURE OF GRID-CONNECTED PV SYSTEMS

The control of PV systems is enabled through the power converter, which acts as an interface between the PV and the grid. For the two-stage PV system in Fig. 6.8, the dc−dc conversion stage is responsible for the PV power control, while the dc−ac conversion stage is in charge of grid interactive [46−48]. From the PV side, the dc−dc converter regulates the extracted power from the PV arrays by controlling the operating point of the PV array (e.g., PV voltage) according to the P−V characteristic of the PV array. This can be done by using a proportional-integral controller to regulate the PV voltage, whose reference is determined by the MPPT algorithm, to continuously track the MPP and maximize the energy yield during operation.

As the PV power is controlled by the dc−dc converter, the role of dc−ac conversion stage is to ensure that the extracted power is delivered to the ac grid. One possible way to do so is to regulate the dc-link voltage, as the dc-link voltage should be kept constant when the dc power and ac power is balanced. By doing so, the output of the dc-link voltage controller will give a required amplitude of the grid current $|i_g|$, according to the difference between the reference and the measured dc-link voltage. Then, the reference grid current i_g^* can be obtained by multiplying the grid current amplitude $|i_g|$ with $\sin\theta_g$, where θ_g is the phase angle of the grid voltage provided by a Phase-Locked Loop (PLL). The control structure of the grid-connected PV system can be summarized as shown in Fig. 6.9.

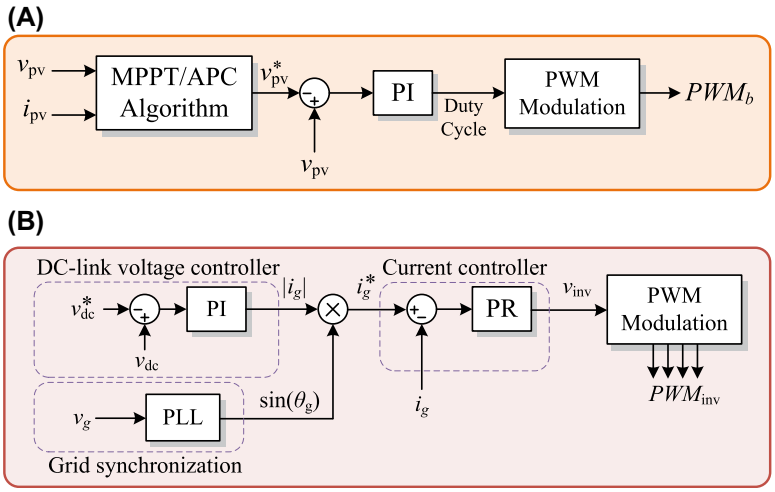


FIGURE 6.9

Control structure of a two-stage, single-phase, grid-connected photovoltaic system: (A) dc–dc converter controller and (B) dc–ac inverter controller. *APC*, active power control; *MPPT*, maximum power point tracking; *PI*, proportional integral; *PLL*, Phase-locked loop; *PR*, proportional resonant; *PWM*, pulse width modulation.

4.3 MAXIMUM POWER POINT TRACKING ALGORITHMS

In PV systems, one main consideration is the efficiency of the power production of the system. It is desirable that the PV systems deliver the maximum available power to the grid all the time because of the fact that PV modules have relatively low conversion efficiency [49–51]. Therefore, in most cases, it is required for PV systems to operate at the maximum power point. As shown in Fig. 6.10A and B, the MPP of the PV arrays varies with the environmental conditions. To maximize the power production of PV systems, maximum power point tracking algorithm, which continuously tracks the MPP during operation, is essential.

Several MPPT algorithms have been proposed, among which the Perturb and Observe (P&O) algorithm is the most widely used method because of its simplicity [52,53]. In this control algorithm, the operating voltage of the PV arrays v_{pv} is "perturbed" intentionally and then the corresponding change in the output power of the PV arrays is "observed" to determine the direction of the next perturbation. If a perturbation of v_{pv} leads to an increase of the PV output power P_{pv}, the next perturbation should be continued in the same direction. Otherwise, if the change of the v_{pv} results in a decrease of the P_{pv}, the perturbation should reverse the direction. An operational principle of the P&O MPPT algorithm is demonstrated in Fig. 6.11, where the initial operating point of the PV system is higher than the MPP (i.e., point A). When the operating point is perturbed from point A → B, the change in the PV power is positive. Thus, the next perturbation is continued in the same direction (i.e.,

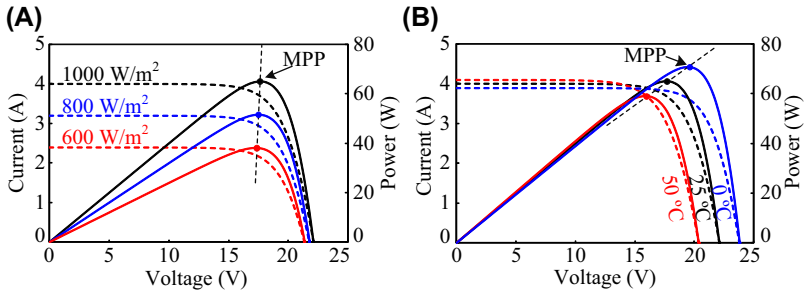


FIGURE 6.10

Power–voltage (P–V) characteristic of photovoltaic arrays with (A) different solar irradiance level at 25°C and (B) different ambient temperature at 1000 W/m^2.

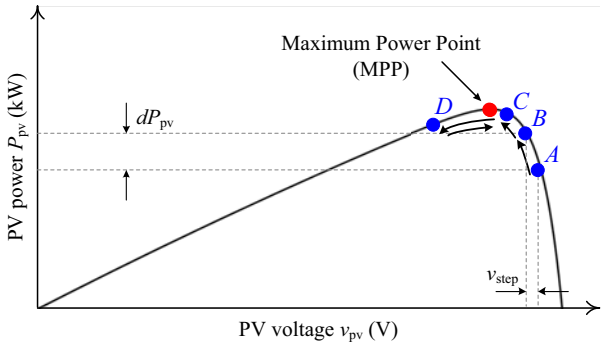


FIGURE 6.11

Operational principle of the Perturb and Observe (P&O) MPPT algorithm. *MPP*, Maximum Power Point, v_{step} is the perturbation step size.

B → C). However, when the perturbation of the operating point results in a decrease in the PV power (i.e., C → D), the perturbation direction should be reserved in the next iteration.

By doing so, the operating point of the PV system will reach and oscillate around the MPP. This power oscillation is one of the main drawbacks of the P&O MPPT algorithm, which results in the power losses during steady-state operation. In addition, the conventional P&O MPPT algorithm is also reported to have poor tracking performance under rapid change environmental conditions, as it is an iteration-based algorithm. Different methods to enhance the P&O MPPT algorithm performance have been proposed. For example, a variable step size can be used to improve dynamic performance of the algorithm. In the study by Serra et al. [54], an extra measurement point between each perturbation is used to reduce the error in the PV power change detection during a fast-changing environmental condition. Nevertheless,

these solutions may introduce more complexity of the algorithm and may reduce the control robustness. As a consequence, the conventional P&O MPPT algorithm is still being widely adopted MPPT algorithm in industry.

5. FLEXIBLE ACTIVE POWER CONTROL OF PV SYSTEMS

In this section, the realization of the flexible active power control strategies by modifying MPPT algorithms is discussed. Following the control structure in Fig. 6.9, the active power control strategy is implemented in the dc−dc converter. This is achieved by determining an appropriate reference PV voltage v_{pv}^* for a certain active power control strategy (e.g., PLC, PRRC, PRC), which will be discussed in the following section.

5.1 POWER-LIMITING CONTROL ALGORITHM

For the PLC strategy, the PV system is not allowed to deliver the output power higher than the power limit value P_{limit}. This condition can be easily fulfilled as long as the available PV power is less than the power limit value (i.e., $P_{avai} \leq P_{limit}$), which usually occurs during the low solar irradiance condition. In that case, the typical MPPT operation is employed, where the reference PV voltage v_{pv}^* is set from the MPPT algorithm (e.g., P&O MPPT), to allow the PV system to inject the maximum available power to the grid (i.e., A→B in Fig. 6.12). However, once the available PV power is reaching and exceeding the level of power limit (i.e., $P_{avai} > P_{limit}$), e.g., because of the solar irradiance level increase, the operating point of the PV system in the P−V curve needs to be regulated below the MPP. More specifically, to keep the PV power to be constant at a certain value, the operating point of the PV system has to be regulated along the horizontal line during the solar

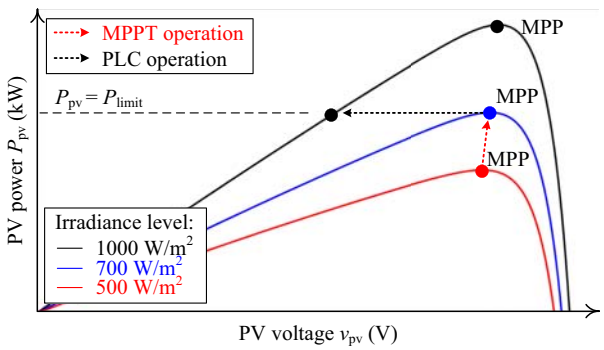


FIGURE 6.12

Operational principle of the Power-Limiting Control (PLC) algorithm: MPPT mode (A → B) and PLC mode (B → C), where P_{limit} is the power limit.

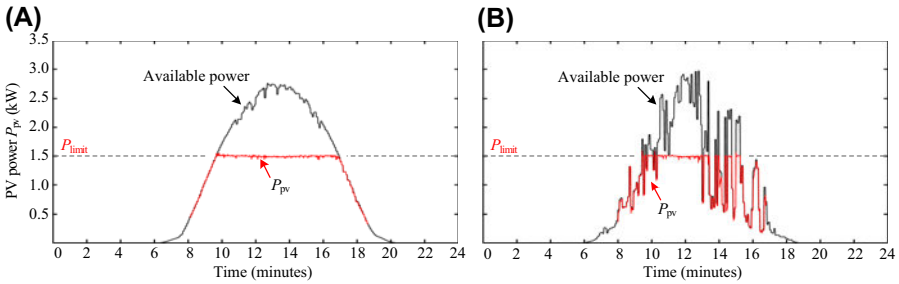


FIGURE 6.13

Photovoltaic output power with the Power-Limiting Control (PLC) strategy under: (A) a clear-day and (B) a cloudy-day irradiance conditions (with an accelerated test to reduce the testing time from 24 h to 24 min), where the power limit level P_{limit} is 1.5 kW.

irradiance change (i.e., B → C in Fig. 6.12) [55,56]. This can be achieved by continuously perturbing the reference PV voltage v_{pv}^* toward the left side of the MPP, i.e., $P_{pv} = P_{limit}$, as illustrated in Fig. 6.12.

Fig. 6.13 demonstrates an example of the PLC operation during the day, where the power limit level P_{limit} is chosen as 1.5 kW. Here, two different cases are considered where the PV system operates under a clear-day condition in Fig. 6.13A and under a cloudy-day condition in Fig. 6.13B. It can be clearly seen in Fig. 6.13A that the PV output power follows the maximum available power during the low solar irradiance condition (i.e., $P_{avai} \leq P_{limit}$), while it is kept constant at the set-point once the available PV power exceeds the power limit level (i.e., $P_{avai} > P_{limit}$). Similarly, the PLC condition is also achieved during the fluctuating solar irradiance condition in Fig. 6.13B. In this case, the operating mode is switched between the MPPT and the PLC depending on the solar irradiance condition. In any case, the maximum PV power injection can be limited according to the set-point and the PLC requirement is fulfilled.

5.2 POWER RAMP-RATE CONTROL ALGORITHM

In the case of the PRRC, the goal of this control strategy is to regulate the change rate of the PV power to a certain limit R_r^*, instead of an absolute PV power like in the PLC strategy. Therefore, the criterion to reduce (or curtail) the PV power is coming from the change rate of the PV power, which can be calculated as

$$R_r(t) = dP_{pv}/dt$$

As long as the change rate in the PV power is below the maximum limit (i.e., $R_r(t) \leq R_r^*$), the PV system is allowed to operate in the MPPT operation, because the power ramp-rate constraint is fulfilled (i.e., A → B in Fig. 6.14). Nevertheless, during a fast increase in the solar irradiance condition (e.g., from 700 to 1000 W/m^2), the PV power change rate can exceed the maximum limit and violate the power

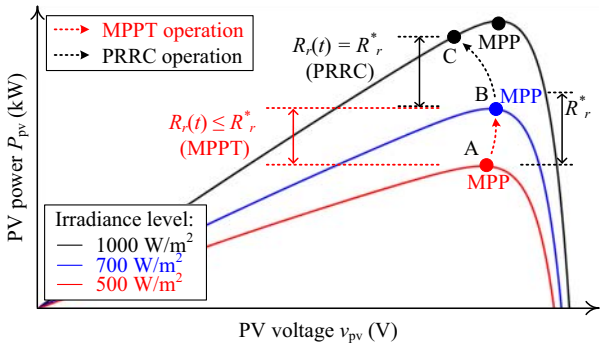


FIGURE 6.14

Operational principle of the Power Ramp-Rate Control (PRRC) algorithm: MPPT mode (A → B) and PRRC mode (B → C), where $R_r(t)$ is the PV power ramp-rate and R^*_r is the ramp-rate limit.

ramp-rate constraint (i.e., $R_r(t) > R^*_r$). In that case, the extracted PV power needs to be reduced to regulate the change rate of the PV power [57]. This can be achieved by perturbing the PV voltage v^*_{pv} toward the left side of the MPP until the PV power change rate is equal to the set-point (i.e., $R_r(t) = R^*_r$), as illustrated in Fig. 6.14.

The performance of the PV system with the PRRC strategy is demonstrated in Fig. 6.15A with a clear-day solar irradiance and ambient temperature condition. The available power and the extracted PV power with the PRRC algorithm are shown in Fig. 6.15A, where it can be seen that the PV power follows a ramp changing manner. The corresponding power ramp-rate with the PRRC strategy is shown in Fig. 6.16A, which verifies that the change rate of the PV power is kept below the maximum limit (i.e., $R_r(t) \le R^*_r$). Another experimental result with a fluctuating solar irradiance (e.g., during a cloudy day) is shown in Fig. 6.15B. In this case, it is more challenging to control the change rate of the PV power because of the rapid change in solar irradiance condition. It can be seen from the ramp-rate result in Fig. 6.16B that the change rate of the PV power can be limited according to the reference in most cases. The PV power ramp-rate limit is only exceeded during very fast transients, whereas the PRRC algorithm requires a number of iterations to reduce the PV power change rate according to the set-point R^*_r. Nevertheless, the experimental results have confirmed that the PRRC algorithm can effectively control the change rate in the PV power according to the demand.

5.3 POWER RESERVE CONTROL ALGORITHM

The idea of the PRC is to keep the PV output power follow the available PV power dynamic with the power difference corresponding to the amount of power reserve ΔP [58,59]. The basic concept of this operation can be expressed as

$$P_{pv} = P_{avai} - \Delta P$$

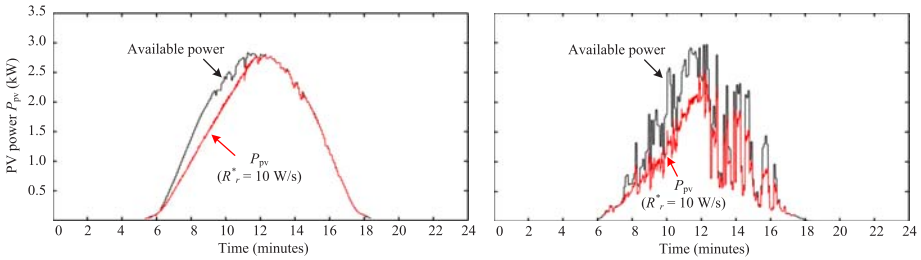


FIGURE 6.15

Photovoltaic (PV) output power with the Power Ramp-Rate Control (PRRC) strategy under: (A) a clear-day and (B) a cloudy-day irradiance conditions (with an accelerated test to reduce the testing time from 24 h to 24 min), where the ramp-rate limit R_r^* is 10 W/s.

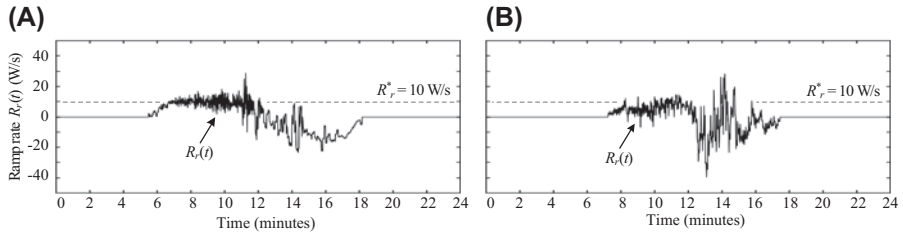


FIGURE 6.16

Measured power ramp-rate of the Power Ramp-Rate Control (PRRC) strategy under: (A) a clear-day and (B) a cloudy-day irradiance conditions (with an accelerated test to reduce the testing time from 24 h to 24 min), where the ramp-rate limit R_r^* is 10 W/s.

where P_{avai} is the available PV power, P_{pv} is the PV output power, and ΔP is the power reserve level. By doing so, the PV system will be able to support the active power to the grid during the operation with the maximum value corresponding to the power reserve level ΔP.

Actually, the PRC strategy can be seen as a special case of the PLC strategy, where the set-point P_{limit} is dynamically changed during the operation to provide a constant power reserve. The power limit level employed in the PRC strategy can be calculated by subtracting the available PV power P_{avai} with the required amount of power reserve as: $P_{\text{limit}} = P_{\text{avai}} - \Delta P$. Therefore, the key of the PRC strategy is to determine (or estimate) the available PV power during the operation. Once the available PV power is known, a similar control algorithm as in (1) can be employed to reduce the PV output power to a certain level of power limit. Fig. 6.17 illustrates the operational principle of the PRC algorithm where it can be seen that the extracted PV power from the PV system is always kept below the MPP with a certain amount of power reserve.

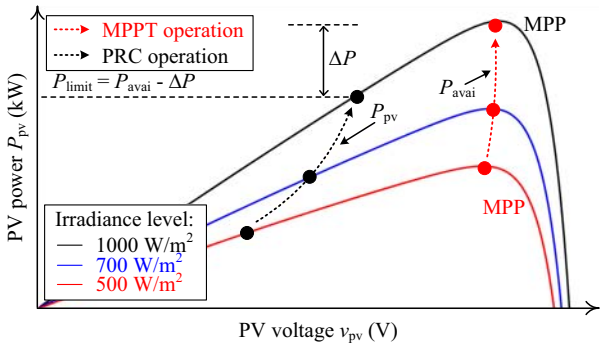


FIGURE 6.17

Operational principle of the Power Reserve Control (PRC) algorithm, where P_{avai} is the available photovoltaic (PV) power and ΔP is the power reserve level.

It is worth to mention that the challenge of the PRC strategy is the estimation of the available PV power, which is needed for calculating the power limit set-point during the operation. There are several approaches proposed in literature to estimate the available PV power:

- Installing solar irradiance measurement or using solar irradiance forecasting data together with the PV array characteristic model [60,61].
- Using curve-fitting approximation of the P−V characteristic [58,62,63].
- Employing a small PV unit to operate in the MPPT mode and use the output power for estimating the total available power of the whole system (assuming that the solar irradiance level is similar for all the PV arrays in the system) [26,59].
- Employing a hybrid operation between the MPPT and the PRC mode in one single PV system [64]

There is a trade-off in terms of cost, complexity, and accuracy among different approaches. The comparison of different approach is beyond the scope of this chapter. Therefore, it will not be discussed here. More detailed analysis can be found in the studies by Sangwongwanich et al. [59,64].

An example of the PV system with the PRC strategy is shown in Fig. 6.18A and B, where the power reserve level is chosen as 200 W. It can be seen from the results in Fig. 6.18A and B that the extracted PV power follows the dynamic in the available PV power with the reduced amount corresponding to the power reserve level once the PRC strategy is activated. Accordingly, the power reserve can be achieved as shown in Fig. 6.19. Notably, the fluctuation in the power reserve during the cloudy-day condition in Fig. 6.19B is because of the fluctuating solar irradiance condition. In that case, the sampling rate of the control algorithm needs to be increased, to improve the dynamic of the PRC algorithm. Nevertheless, the PRC algorithm is effective in terms of providing the power reserve following the demand.

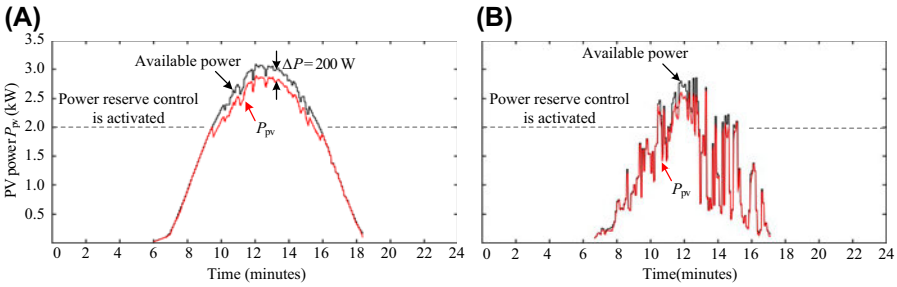


FIGURE 6.18

Photovoltaic (PV) output power of the Power Reserve Control (PRC) strategy under: (A) a clear-day and (B) a cloudy-day irradiance conditions (with an accelerated test to reduce the testing time from 24 h to 24 min), where the reference power reserve level ΔP is 200 W and the PRC strategy is activated when $P_{pv} > 2$ kW.

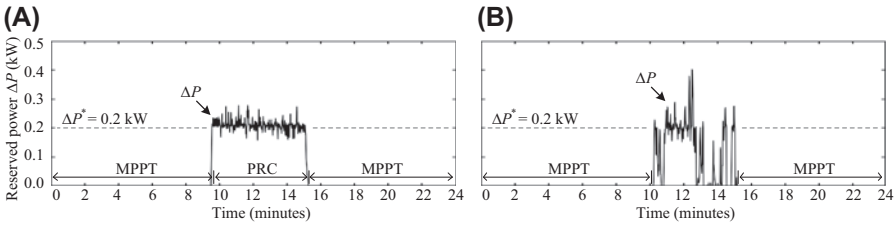


FIGURE 6.19

Measured power reserve of the Power Reserve Control (PRC) strategy under: (A) a clear-day and (B) a cloudy-day irradiance conditions (with an accelerated test to reduce the testing time from 24 h to 24 min), where the power reserve level ΔP is 200 W.

6. SUMMARY

In this chapter, the demands for flexible active power control solution have been discussed. Potential problems associated with a large-scale grid integration of PV systems, such as overloading of the grid, voltage fluctuation, and limited frequency regulation capability, have been presented. To address those issues, the power delivery from PV systems has to be flexible in terms of limiting the maximum feed-in power, limiting the change rate of the PV power, and providing power reserve during the operation. Accordingly, three active power control functionalities: PLC, PRRC, and PRC have been defined in the grid regulations. Among other approaches to achieve these requirements, modifying the inherent MPPT control algorithm of the power converter offers a cost-effective solution in terms of no extra component cost. This approach achieves the flexible power control by continuously regulating the operating point of the PV system below the MPP following the demand of the active power control functionality. The operational principle of three flexible power

control strategies (i.e., PLC, PRRC, and PRC) have been demonstrated on a two-stage grid-connected PV system, where the flexible power control solutions are achieved upon demands. In this way, "grid-friendly" integrations can be ensured, and the above technical challenges caused by the intermittency of solar energy can be resolved.

REFERENCES

[1] EPIA, Global Market Outlook for Photovoltaics 2014−2018, EPIA Report, 2014 (Online). Available, http://www.epia.org/news/publications/global-market-outlook-for-photovoltaics-2014-2018/.

[2] Federal Republic of Germany, National Renewable Energy Action Plan in Accordance with Directive 2009/28/ec on the Promotion of the Use of Energy from Renewable Sources, 2010.

[3] H. Lund, B.V. Mathiesen, Energy system analysis of 100% renewable energy systems—the case of Denmark in years 2030 and 2050", Energy 34 (5) (May 2009) 524−531.

[4] REN21 Renewables, Global Status Report (GRS), 2016 (Online). Available, http://www.ren21.net/.

[5] Solar Power Europe, Global Market Outlook for Solar Power 2016−2020, 2016 (Online). Available, http://www.solarpowereurope.org/.

[6] I.S.E. Fraunhofer, Recent Facts about Photovoltaics in Germany, December 29, 2016 (Online). Available, http://www.pv-fakten.de/.

[6a] J. Von Appen, M. Braun, T. Stetz, K. Diwold, D. Geibel, Time in the sun: the challenge of high pv penetration in the German electric grid, IEEE Power Energy Mag. 11 (2) (March−April 2013) 55−64.

[7] A. Woyte, V.V. Thong, R. Belmans, J. Nijs, Voltage fluctuations on distribution level introduced by photovoltaic systems, IEEE Trans. Energy Convers. 21 (1) (March 2006) 202−209.

[8] Y. Yang, P. Enjeti, F. Blaabjerg, H. Wang, Wide-scale adoption of photovoltaic energy: grid code modifications are explored in the distribution grid, IEEE Ind. Appl. Mag. 21 (5) (September 2015) 21−31.

[9] T. Stetz, J. von Appen, F. Niedermeyer, G. Scheibner, R. Sikora, M. Braun, Twilight of the grids: the impact of distributed solar on Germany's energy transition, IEEE Power Energy Mag 13 (2) (March 2015) 50−61.

[10] M. Karimi, H. Mokhlis, K. Naidu, S. Uddin, A. Bakar, Photovoltaic penetration issues and impacts in distribution network − a review, Renew. Sustain. Energy Rev. 53 (2016) 594−605.

[11] BDEW, Technische richtlinie erzeugungsanlagen am mittelspannungsnetz richtlinie fur anschluss und parallelbetrieb von erzeugungsanlagen am mittelspannungsnetz, June 2008.

[12] E. Troester, New German grid codes for connecting PV systems to the medium voltage power grid, in: Proc. 2nd Int. Workshop Concentrating Photovoltaic Power Plants: Opt. Design, Prod., Grid Connection, 2009.

[13] V. Gevorgian, S. Booth, Review of PREPA Technical Requirements for Interconnecting Wind and Solar Generation, National Renewable Energy Laboratory (NREL), Tech. Rep., 2013.

[14] European Network of Transmission System Operators for Electricity, Network Code for Requirements for Grid Connection Applicable to All Generators, Tech. Rep., March 2013.
[15] T. Stetz, F. Marten, M. Braun, Improved low voltage grid integration of photovoltaic systems in Germany, IEEE Trans. Sustain. Energy 4 (2) (April 2013) 534−542.
[16] E. Reiter, K. Ardani, R. Margolis, R. Edge, Industry perspectives on Advanced Inverters for US Solar Photovoltaic Systems: Grid Benefits, Deployment Challenges, and Emerging Solutions, National Renewable Energy Laboratory (NREL), Tech. Rep, 2015.
[17] Energinetdk, Technical Regulation 3.2.2 for PV Power Plants with a Power Output Above 11 KW, 2015. Tech. Rep. Doc. 14/17997−39.
[18] D. Maxwell, Parts of Northern Ireland's Electricity Grid Overloaded, BBC News NI, 2013 (Online). Available, http://www.bbc.com/.
[19] M.K. Hossain, M.H. Ali, Statistical analysis of ramp rates of solar photovoltaic system connected to grid, in: Proc. of ECCE, September 2014, pp. 2524−2531.
[20] D. Cormode, A.D. Cronin, W. Richardson, A.T. Lorenzo, A.E. Brooks, D.N. DellaGiustina, Comparing ramp rates from large and small PV systems, and selection of batteries for ramp rate control, in: Proc. of PVSC, June 2013, pp. 1805−1810.
[21] B. Kroposki, Can solar save the grid? IEEE Spectr. 53 (11) (November 2016) 42−47.
[22] S.J. Chiang, K.T. Chang, C.Y. Yen, Residential photovoltaic energy storage system, IEEE Trans. Ind. Electron. 45 (3) (June 1998) 385−394.
[23] N. Kakimoto, H. Satoh, S. Takayama, K. Nakamura, Ramp-rate control of photovoltaic generator with electric double-layer capacitor, IEEE Trans. Energy Convers. 24 (2) (Jun. 2009) 465−473.
[24] W.A. Omran, M. Kazerani, M.M.A. Salama, Investigation of methods for reduction of power fluctuations generated from large grid-connected photovoltaic systems, IEEE Trans. Energy Convers. 26 (1) (March 2011) 318−327.
[25] H. Beltran, E. Bilbao, E. Belenguer, I. Etxeberria-Otadui, P. Rodriguez, Evaluation of storage energy requirements for constant production in PV power plants, IEEE Trans. Ind. Electron. 60 (3) (March 2013) 1225−1234.
[26] S. Bacha, D. Picault, B. Burger, I. Etxeberria-Otadui, J. Martins, Photovoltaics in microgrids: an overview of grid integration and energy management aspects, IEEE Ind. Electron. Mag. 9 (1) (March 2015) 33−46.
[27] SMA, Warranty Conditions for the Lithium-ion Battery of the Sunny Boy 3600 Smart Energy and Sunny Boy 5000 Smart Energy Inverters. Tech. Rep. Doc. SBSE-GEBED-en-au-15. (Online). Available: www.SMA-Solar.com/.
[28] H. Kanchev, D. Lu, F. Colas, V. Lazarov, B. Francois, Energy management and operational planning of a microgrid with a pv-based active generator for smart grid applications, IEEE Trans. Ind. Electron. 58 (10) (October 2011) 4583−4592.
[29] P. Palensky, D. Dietrich, Demand side management: demand response, intelligent energy systems, and smart loads, IEEE Trans. Ind. Informat. 7 (3) (August 2011) 381−388.
[30] J. Seuss, M.J. Reno, M. Lave, R.J. Broderick, S. Grijalva, Multi-objective Advanced Inverter Controls to Dispatch the Real and Reactive Power of Many Distributed PV Systems, Sandia National Laboratories Tech (Rep. Doc. SAND2016-0023).
[31] A. Ahmed, L. Ran, S. Moon, J.H. Park, A fast pv power tracking control algorithm with reduced power mode, IEEE Trans. Energy Convers. 28 (3) (September 2013) 565−575.

[32] Y. Yang, H. Wang, F. Blaabjerg, T. Kerekes, A hybrid power control concept for PV inverters with reduced thermal loading, IEEE Trans. Power Electron. 29 (12) (December 2014) 6271−6275.
[33] R.G. Wandhare, V. Agarwal, Precise active and reactive power control of the PV-DGS integrated with weak grid to increase PVpenetration, in: Proc. of PVSC, June 2014, pp. 3150−3155.
[34] L.D. Watson, J.W. Kimball, Frequency regulation of a microgrid using solar power, in: Proc. of APEC, March 2011, pp. 321−326.
[35] V. Poulios, E. Vrettos, F. Kienzle, E. Kaffe, H. Luternauer, G. Andersson, Optimal Placement and Sizing of Battery Storage to Increase the PV Hosting Capacity of Low Voltage Grids. International ETG Congress 2015; Die Energiewende − Blueprints for the New Energy Age, Germany, Bonn, 2015, pp. 1−8.
[36] Y. Yang, E. Koutroulis, A. Sangwongwanich, F. Blaabjerg, Minimizing the levelized cost of energy in single-phase photovoltaic systems with an absolute active power control, IEEE Ind. Appl. Mag. 23 (5) (September/October 2017) 1−10.
[37] F. Blaabjerg, Z. Chen, S.B. Kjaer, Power electronics as efficient interface in dispersed power generation systems, IEEE Trans. Power Electron. 19 (5) (September 2004) 1184−1194.
[38] Y. Yang, F. Blaabjerg, Overview of single-phase grid-connected photovoltaic systems, Electr. Power Compo. Sys. 43 (12) (2015) 1352−1363.
[39] N.A. Rahim, R. Saidur, K.H. Solangi, M. Othman, N. Amin, Survey of grid-connected photovoltaic inverters and related systems, Clean Technol. Environ. Policy 14 (4) (2012) 521−533.
[40] Y. Yang, A. Sangwongwanich, F. Blaabjerg, Design for reliability of power electronics for grid-connected photovoltaic systems, CPSS Trans. Power Electron. Appl. 1 (1) (December 2016) 92−103.
[41] S.B. Kjaer, J.K. Pedersen, F. Blaabjerg, A review of single-phase grid-connected inverters for photovoltaic modules, IEEE Trans. Ind. App. 41 (5) (September−October 2005) 1292−1306.
[42] S. Kouro, J.I. Leon, D. Vinnikov, L.G. Franquelo, Grid-connected photovoltaic systems: an overview of recent research and emerging PV converter technology, IEEE Ind. Electron. Mag. 9 (1) (March 2015) 47−61.
[43] S. Moskowitz, The Next Opportunity for Utility PV Cost Reductions: 1,500 Volts DC. (Online). Available: https://www.greentechmedia.com/articles/read/TheNext-Opportunity-for-Utility-PV-Cost-Reductions-1500-Volts-DC/.
[44] Sungrow Sungrow unveiled new, VDC String and Central Inverters at Solar Power International 2016, 1500 [Online]. Available: http://en.sungrowpower.com/event-press/news/335.html/.
[45] T. Kerekes, R. Teodorescu, P. Rodriguez, G. Vazquez, E. Aldabas, A new high-efficiency single-phase transformerless pv inverter topology, IEEE Trans. Ind. Electron. 58 (1) (Jan. 2011) 184−191.
[46] R. Teodorescu, M. Liserre, P. Rodriguez, Grid Converters for Photovoltaic and Wind Power Systems, Wiley, Hoboken, NJ, USA, 2011.
[47] F. Blaabjerg, R. Teodorescu, M. Liserre, A.V. Timbus, Overview of control and grid synchronization for distributed power generation systems, IEEE Trans. Ind. Electron. 53 (5) (October 2006) 1398−1409.
[48] M. Ciobotaru, R. Teodorescu, F. Blaabjerg, Control of single-stage single-phase PV inverter, in: Proc. EPE, 2005, pp. 1−10.

[49] W. Xiao, W. Dunford, A modified adaptive hill climbing MPPT method for photovoltaic power systems, in: Proc. of. PESC, vol. 3, June 2004, pp. 1957−1963.
[50] C. Hua, J. Lin, C. Shen, Implementation of a DSP-controlled photovoltaic system with peak power tracking, IEEE Trans. Ind. Electron. 45 (1) (February 1998) 99−107.
[51] E. Koutroulis, K. Kalaitzakis, N. Voulgaris, Development of a microcontroller-based, photovoltaic maximum power point tracking control system, IEEE Trans. Power Electron. 16 (1) (January 2001) 46−54.
[52] T. Esram, P. Chapman, Comparison of photovoltaic array maximum power point tracking techniques, IEEE Trans. Energy Convers. 22 (2) (June 2007) 439−449.
[53] N. Femia, G. Petrone, G. Spagnuolo, M. Vitelli, Optimization of perturb and observe maximum power point tracking method, IEEE Trans. Power Electron. 20 (4) (July 2005) 963−973.
[54] D. Sera, R. Teodorescu, J. Hantschel, M. Knoll, Optimized maximum power point tracker for fast-changing environmental conditions, IEEE Trans. Ind. Electron. 55 (7) (July 2008) 2629−2637.
[55] A. Sangwongwanich, Y. Yang, F. Blaabjerg, H. Wang, Benchmarking of constant power generation strategies for single-phase grid-connected photovoltaic systems, IEEE Trans. Ind. Appl. PP (99) (2017) in press.
[56] A. Sangwongwanich, Y. Yang, F. Blaabjerg, High-performance constant power generation in grid-connected PV systems, IEEE Trans. Power Electron. 31 (3) (March 2016) 1822−1825.
[57] A. Sangwongwanich, Y. Yang, F. Blaabjerg, A cost-effective power ramp-rate control strategy for single-phase two-stage grid-connected photovoltaic systems, in: Proc. ECCE, September 2016, pp. 1−7.
[58] S. Nanou, A. Papakonstantinou, S. Papathanassiou, Control of a PV generator to maintain active power reserves during operation, in: Proc. EU PVSEC, 2011, pp. 4059−4063.
[59] A. Sangwongwanich, Y. Yang, F. Blaabjerg, D. Sera, Delta power control strategy for multi-string grid-connected pv inverters, IEEE Trans. Ind. App. 53 (4) (July−August 2017) 3862−3870.
[60] A. Hoke, E. Muljadi, D. Maksimovic, Real-time photovoltaic plant maximum power point estimation for use in grid frequency stabilization, in: Proc. of COMPEL, July 2015, pp. 1−7.
[61] B.I. Craciun, T. Kerekes, D. Sera, R. Teodorescu, Frequency support functions in large PV power plants with active power reserves, IEEE J. Emerg. Sel. Top. Power Electron. 2 (4) (December 2014) 849−858.
[62] H. Xin, Z. Lu, Y. Liu, D. Gan, A center-free control strategy for the coordination of multiple photovoltaic generators, IEEE Trans. Smart Grid. 5 (3) (May 2014) 1262−1269.
[63] A. Hoke, M. Shirazi, S. Chakraborty, E. Muljadi, D. Maksimovic, Rapid active power control of photovoltaic systems for grid frequency support, IEEE J. Emerg. Sel. Top. Power Electron. 5 (3) (September 2017) 1154−1163.
[64] A. Sangwongwanich, Y. Yang, F. Blaabjerg, A sensorless power reserve control strategy for two-stage grid-connected PV systems, IEEE Trans. Power Electron. 32 (11) (November 2017) 8559−8569.

This page intentionally left blank

CHAPTER

Strategies for Fault Detection and Diagnosis of PV Systems

7

Santiago Silvestre

Electronic Engineering Department, Universitat Politècnica de Catalunya-BarcelonaTech., Barcelona, Spain

CHAPTER OUTLINE

1. Introduction 231
2. Performance Parameters of Photovoltaic Systems: Yields and Power Losses 232
3. Supervision and Diagnosis of Photovoltaic Systems 235
4. Automatic Supervision Strategies 237
5. Modeling and Simulation of Photovoltaic Systems 240
5.1 Modeling Solar Cells, Photovoltaic Modules, and Arrays 240
5.2 Inverter Model 243
5.3 Parameter Extraction Techniques 244
5.4 Simulation Tools 244
6. Fault Detection Procedures 245
6.1 Automatic Supervision and Diagnosis Based on Power Losses Analysis 245
6.2 Supervision and Diagnosis Based on Current and Voltage Indicators 247
7. Conclusion 250
References 250

1. INTRODUCTION

The cumulative global photovoltaic (PV) capacity has been growing exponentially in the last decade around the world and will continue growing in the future. In 2015 the total additional installed PV power was about 50.7 GW and the globally installed total PV capacity is estimated at roughly 228 GW at the end of that year [1]. The top three markets in 2015 were located in Asia: China and Japan followed by Europe as a whole and the US market in the third place. Moreover, grid-connected PV systems (GCPVSs) are able to cover 1.2% of the global electricity demand nowadays. As a result of this trend, PV energy production will play a very important role in the global generation of electricity in the future.

On the other hand, while the energy price has been increasing worldwide, PV system prices have shown an important cost reduction. PV generation costs and more precisely recently contracted power purchase agreements below 3 USD cents/kWh

Advances in Renewable Energies and Power Technologies. https://doi.org/10.1016/B978-0-12-812959-3.00007-1
Copyright © 2018 Elsevier Inc. All rights reserved.

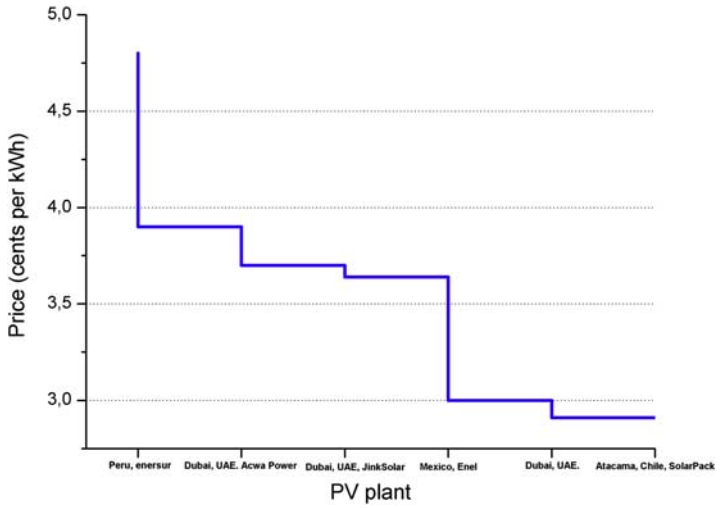


FIGURE 7.1

PV cost reduction in 2016.

have been achieved in 2016, as it can be seen in Fig. 7.1, where the prices correspond to year 2016. As a result of the energy price evolution, most developed countries are entering or in training to achieve the grid parity scenario, when the PV systems can produce electricity at the same or lower price than the price of electricity generated by conventional sources. However, still important efforts remain to be done in terms of cost, performance, and reliability of PV systems, together with lowering the perceived risk of owning and maintaining PV generation plants.

In this context, an important issue within the next few years will be the development of automatic supervision strategies for PV systems that are already requested. Control and supervision systems are always present in big PV plants because the cost associated with the supervision system is not relevant in comparison with the total cost of the PV plant. Normally, monitoring, control, and supervision plants are developed by using SCADA[1] platforms. However, automatic supervision of PV systems will be also incorporated in small- and medium-size PV systems in the near future.

2. PERFORMANCE PARAMETERS OF PHOTOVOLTAIC SYSTEMS: YIELDS AND POWER LOSSES

The aim of any automatic supervision system of GCPVSs is to improve the PV system performance and reliability by optimizing the output of the system to achieve higher yields. Standard methods for performance analysis of GCPVSs take into account some normalized system yields and losses [2,3].

[1]SCADA: Supervisory Control and Data Acquisition.

Four performance parameters established by the International Energy Agency (IEA) Photovoltaic Power System Program and described in the IEC standard 61724 define the overall system performance with respect to the energy production [4], solar resources, rated power, and overall effect of system losses. These performance parameters are, namely, the reference yield (Y_r), array yield (Y_a), final yield (Y_f), and finally the performance ratio (PR). These parameters are given by the following equations:

$$Y_r = \frac{\int_0^{\Delta t} G(t)dt}{G_{ref}} \tag{7.1}$$

where G_{ref} is the irradiance at standard test conditions (STCs), 1000 W/m^2 spectrum Air mass 1.5 (AM1.5), and G is the measured irradiance.

$$Y_a = \frac{\int_0^{\Delta t} E_{dc}(t)dt}{P_o} \tag{7.2}$$

$$Y_f = \frac{\int_0^{\Delta t} E_{ac}(t)dt}{P_o} \tag{7.3}$$

where E_{dc} and E_{ac} are the generated energy at the DC and AC sides, respectively, of the PV system and P_o is the nominal power of the PV array.

The PR is the ratio of the useful energy that would be generated by an ideal PV system working at STC temperature, 25°C, and real irradiance conditions of work. The PR can be evaluated as follows from Eqs. (7.1) and (7.3):

$$PR = \frac{Y_r}{Y_f} \tag{7.4}$$

On the other hand, there are several sources of losses originated by different kind of faults that can be present in a GCPVS. Table 7.1 presents a list of possible origins of faults that may appear in a GCPVS. These faults are divided in terms of their effects in the PV system behavior. Faults can generate permanent energy losses or temporary energy losses. The normalized total inherent losses in the PV system, L, can be calculated by the following expression:

$$L = Y_r(G, T_C) - Y_a(G, T_C) = \frac{H_i}{G_{ref}}(G, Tc) - \frac{E_{dc}}{P_o}(G, Tc) \tag{7.5}$$

where $Yr(G,Tc)$ and $Ya(G,Tc)$ are the reference and array yields, respectively, at real working irradiance, G, and real module temperature, Tc, and H_i is the total plane of array irradiation in Wh/m^2.

These losses can be divided into two groups, the first one associated with thermal effects, L_T, and the second one comprising the rest of possible effects that cause loss of power, miscellaneous losses, L_M, thus:

$$L = L_T + L_M \tag{7.6}$$

Table 7.1 List of Possible Faults and Their Origins That May Affect to the DC Side of the Photovoltaic (PV) System

Fault Type		Affected Components of the PV System	Possible Sources of Faults
Permanent power losses	Degradation [5,6]	Solar Cells PV modules Wiring Contacts	• Deterioration of cells, cracks, hot spots • Penetration of humidity, degradation of interconnections, corrosion of cell's connections • Mismatch • Shorted modules, reversed modules
	Soiling [7,8]	Solar cells PV modules PV array	• Waste, pollution, sand, snow, dust
	Breakdown [6,9]	Solar cells PV modules Monitoring sensors Junction boxes Protection diodes	• Torn or broken module • Short circuit in electrical circuit • Current surges due to lightning storms • Absence or nonoperation of diodes • Reverse diode's polarity, faulty connection
Temporary power losses	Shading [10,11]	Solar cells PV modules, strings and array Irradiance sensors	• Nearby obstacles: buildings, trees, chimneys, etc. • Clouds
	Grid outage Islanding [12]	Cables Inverters PV array	• Faulty wiring • Corrosion of connections and contacts • Destruction of wires • Disconnection of the inverter to prevent islanding
	MPP-tracking [10,13,14]	Inverters DC–DC converters	• Internal error, aging of the component • Temperature effects on the Inverters • Defects in control or communication devices
	Total blackout [15,16]	PV strings PV array	• Disconnection of wiring • Activation of DC-protections (fuses, blocking diodes, etc.)

Normalized thermal losses give the amount of power losses due to the rise of temperature above 25°C. The thermal losses, L_T, can be then determined by the following expression:

$$L_T = Y_a(G, 25^\circ\mathrm{C}) - Y_a(G, T_c) = \frac{E_{dc}}{P_o}(G, 25^\circ\mathrm{C}) - \frac{E_{dc}}{P_o}(G, T_c) \qquad (7.7)$$

where $Y_a(G,25^\circ C)$ is the normalized energy yield at real working irradiance and STC temperature.

3. SUPERVISION AND DIAGNOSIS OF PHOTOVOLTAIC SYSTEMS

Power generation from PV systems is variable in nature due to changes in weather conditions such as solar irradiance, wind, temperature, and other factors. Thus monitoring or forecast of climatic data is essential in the supervision of PV plants.

In PV applications, the supervision systems can be divided into two groups: distributed and centralized supervision systems. In the distributed systems, the supervision system is installed at the PV plant location, whereas centralized supervision systems are based on a remote supervision of the PV system.

Distributed supervision systems include complex monitoring systems and software tools. In this case the cost is not a limitation because these systems are to be applied in big PV generation plants or industrial applications. However, most inverter manufacturers include several monitoring, communications, and specific supervision capabilities that can be used in commercial or residential applications at relatively low costs. Normally, in this kind of low-cost supervision systems, the supervision is just based on the analysis of the energy output or the evaluation of the yields. Therefore, these modest monitoring systems are not able to make a good diagnosis and evaluation of possible failures in the photovoltaic system but can detect when the system is working below its optimum performance.

On the other hand, centralized supervision systems are developed for residential and building-integrated PV (BIPV) systems or commercial applications. These supervision systems minimize the monitoring system at the PV site to reduce the costs. Moreover, the hardware and software needed for the supervision tools are centralized and shared by several PV systems. The communication between the central supervision site and the remote PV systems can be based on the Internet, Ethernet, or Wi-Fi communications, among others. At the supervision site, the PV system performance is evaluated and a basic diagnostic is applied to generate malfunction alarms to be sent to the PV system owners.

The PV energy generation prediction can be based on the forecasting of the global horizontal irradiance and ambient temperature as well as the PV system configuration. Therefore, on-site monitoring is not required and additional cost reduction can be achieved while maintaining a good degree of monitoring accuracy.

Table 7.2 Main Parameters Included in the Monitoring System

Monitored Parameters		PV System Components	Sensors
Climatic parameters	Irradiance in the PV array plane Module and ambient temperature Humidity Wind speed Barometric pressure	PV modules, strings, and arrays	Pyranometers, reference solar cells Thermocouples, resistive temperature sensors Humidity sensors Thermal wind sensors and anemometers Pressure sensors
Electrical parameters	AC and DC: voltage, Current and power Frequency and power factor (AC)	PV strings and arrays Inverters	Voltmeters Ammeters, hall sensors, or active-type CT Power meters, power analyzers

Some centralized supervision systems use as input data satellite monitoring data or weather forecast data [17–19] for the site where the PV system under supervision is located to evaluate the expected energy production and yields. Moreover, for very short-term forecasts, stochastic learning techniques and artificial intelligence methods can be applied [20–23]. Satellite images [24] or local ground measurements of cloud speed [25] can also be used to analyze cloud motion vectors for forecasting.

The best accuracy in the supervision and diagnosis of PV systems is achieved by using real monitored data in combination with specific software tools in both centralized and distributed supervision systems. The monitored data can be grouped in climatic and electrical parameters as shown in Table 7.2.

The most important climatic parameters are the plane of array (POA) irradiance and the PV module temperature. Moreover, relative humidity, barometric pressure, and wind speed also affect the behavior of PV modules and can be included in the monitoring system.

Regarding the electrical parameters, voltages, currents, and power must be monitored at both DC and AC sides of the PV system. It is also important to measure the frequency, power factor, and total harmonic distortion (THD) at the output of the inverters in GCPVSs.

Specific sensors together with data acquisition systems or data loggers can be used for monitoring both electrical and climatic parameters. However, nowadays most inverters include inputs for irradiance and temperature sensors and internal hardware to measure all electrical parameters at its input (DC) and output (AC) and for maximum power point tracking (MPPT) evolution. Moreover, most inverters also include storage capabilities and communication interfaces: Ethernet, RS-485, RS-232, or wireless connection (Bluetooth, Wi-Fi, and GSM), to send the monitored data to the supervision system.

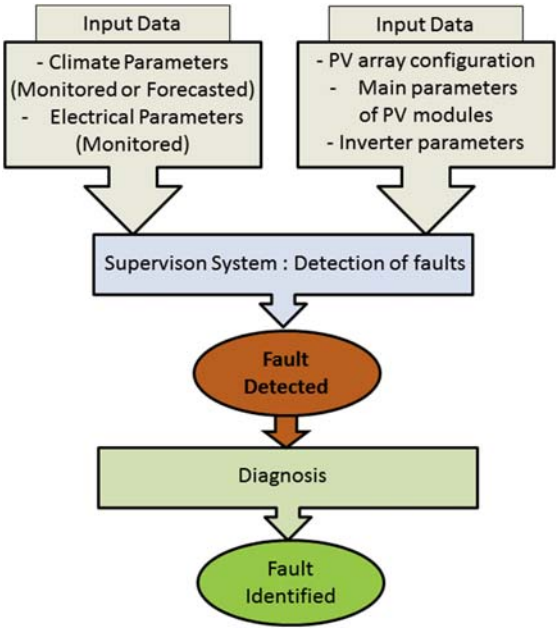


FIGURE 7.2

Supervision and diagnosis procedure.

The PV system supervision and diagnosis procedure has, as input data, the set of climatic parameters obtained from the monitoring system or from forecasting techniques and the set of electrical parameters both DC and AC: current, voltage, and power, normally given by the inverter present in the PV system. Fig. 7.2 shows the flowchart of the supervision and diagnosis procedure. At the first level, the supervision algorithm evaluates the behavior of the PV system taking into account the input data. Once an abnormal behavior is observed, a fault is detected in the PV system. At this point, the diagnosis algorithm starts running and tries to identify the most probable cause of the fault detected by the supervision algorithm.

4. AUTOMATIC SUPERVISION STRATEGIES

As it has been described in the previous section, the supervision system is the procedure responsible to analyze the behavior of the PV system and detect any fault present in the system. Different strategies to achieve this objective exist.

The simplest supervision procedure is based on the evaluation of the energy produced by the PV system by comparing the production of monitored and expected

energy over a given period of time, the daily or monthly evaluation [26–28]. For this purpose, it is necessary to measure the energy produced by the PV system or the corresponding yield, Y_a or Y_f. The values of these yields can be calculated using Eqs. (7.2) and (7.3) respectively, once the energy produced by the PV system has been monitored and taking into account the nominal power of the PV array, P_o. The expected value of the daily array yield, Y_{aE}, can be obtained from the following equation:

$$Y_{aE} = \frac{PSH\ Nsm\ Npm\ \mathrm{Im}\ Vm}{Po} \tag{7.8}$$

where N_{sm} and N_{pm} are the number of PV modules in series per string and strings forming part of the PV array, respectively, and Im and Vm are the current and voltage corresponding to the maximum power point of the PV modules at real operating temperature, given by the manufacturer, respectively. It is considered in the equation that the inverter includes maximum power point tracking (MPPT).

The parameter PSH (Peak Sun-Hours) in Eq. (7.8) refers to the solar daily irradiation that a particular location would receive under STC irradiance, $G_{ref} = 1000\ \mathrm{W/m^2}$ (AM1.5), for a number of PSH hours. This parameter is equivalent to the reference yield, Yr, given by Eq. (7.1) evaluated for a day and it is usually used in sizing PV systems:

$$PSH = \frac{\int_0^{24} G(t)d(t)}{G_{ref}} \tag{7.9}$$

where $G(t)$ is the real profile of the irradiance along the 24 h of the day at the location of the PV array.

On the other hand, the expected daily value of the field yield, Y_{fE}, is given by the following equation:

$$Y_{fE} = \frac{PSH\ Nsm\ Npm\ \mathrm{Im}\ Vm\ \eta}{Po} \tag{7.10}$$

where η is the inverter efficiency.

The supervision system can estimate some kind of faults present in the PV system when relevant differences between the expected and the measured yields are observed. Small deviations between expected and measured yields could be associated with mismatch effects or ohmic losses present in the system [29]. Fig. 7.3 shows the evolution of the expected and monitored array yields in a GCPVS sited in the south of Spain along 15 days of July. As it can be seen in the figure, no relevant discrepancies are observed between both yields. Therefore, the PV system is working free of faults.

The supervision system can also be based on the analysis of the PR [30,31], previously defined in Section 2, that can be evaluated from Eq. (7.2) using Y_r and Y_f.

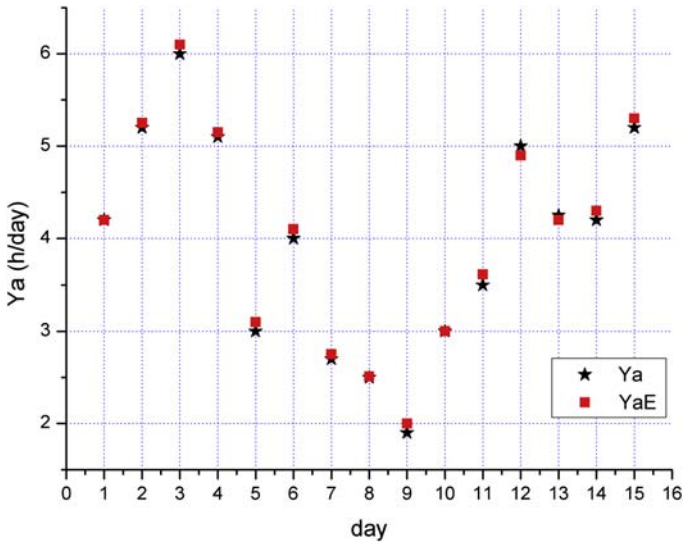


FIGURE 7.3

Comparison between measured and expected array yields.

The expected final yield, Y_{fE}, can be evaluated from Eq. (7.10) and then the absolute error on the PR is calculated as follows:

$$PR_{error} = |PR_{measured} - PR_{expected}| \tag{7.11}$$

where $PR_{measured}$ results from the measured Y_f, and $PR_{expected}$ corresponds to Y_{fE}.

The supervision system will detect a fault present in the PV system if the value of PR_{error} exceeds a fixed threshold.

Other supervision techniques are based on the analysis of the power losses present in the PV system [32–34]. However, most supervision strategies presented in the literature are based on the comparison of the monitored electrical parameters of the PV system at the DC, AC, or both sides of the PV inverter with expected values of these parameters obtained by means of simulation of several models of the PV system in different software environments. Some of the most used PV systems models and simulation techniques are discussed in the following section. The input data used in the simulations include both monitored climate variables and PV system main characteristics: configuration of PV modules, main PV modules, and inverter parameters.

Intelligent systems based on artificial neural networks (ANNs), fuzzy systems, or neuro-fuzzy networks have demonstrated great potential in the supervision of PV systems and are able to localize and identify faults occurring in the PV array [35–39]. The proposed techniques are based on the analysis of a set of attributes

such as currents, voltages, energy at the inverter outputs, and number of peaks present on the I−V curve that can indicate the normal and the faulty operations. Other methodologies for supervision of PV systems are based on the parameterization of metadata and the quality control of PV power output data [40]. Moreover, remote supervision and fault detection on OPC[2]-based monitoring of PV systems [41] was carried out by using indicators of voltage and current as key parameters of the supervision algorithm [42,43].

5. MODELING AND SIMULATION OF PHOTOVOLTAIC SYSTEMS

As it has been described in the previous section, the simulation of the PV system behavior is the key for most supervision and diagnostic methods in automatic fault detection of PV systems. The simulation results give information about the expected evolution of main electrical output parameters of the PV system or try to reproduce the I−V characteristic of PV modules and arrays in real conditions of work. Therefore, these simulations are also useful for forecasting the energy produced by PV systems.

The comparison of the results obtained in the simulations with the real measured data obtained from the monitoring system allows the identification of malfunctions in the PV system and the diagnostic of the most probable fault. For this purpose, it is necessary to work with accurate models of the main GCPVS components such as PV modules and inverters. Nowadays, a wide variety of software tools are available for the simulation of PV systems [44]. These tools present different degrees of complexity depending on the specific tasks that each tool has been developed for. However, the accuracy of the simulation results depends primarily on the models used. Some of the most used models in simulation of PV systems as well as several software environments that can be used in the simulations of these models are introduced in this section.

5.1 MODELING SOLAR CELLS, PHOTOVOLTAIC MODULES, AND ARRAYS

One of the most used solar cell models is the one-diode model also known as the five-parameter model. This model includes a combination of a photogenerated controlled current source I_{PH}, a diode, described by the single-exponential Shockley equation [45], and a shunt resistance R_{sh} and a series resistance R_s modeling the power losses. The equivalent circuit for this model is given in Fig. 7.4.

[2]OPC is an interoperability standard for the secure and reliable exchange of data. It is platform independent and ensures the seamless flow of information among multiple kinds of devices.

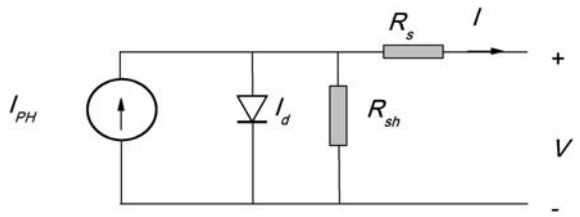


FIGURE 7.4

An equivalent circuit representing the five-parameter model of the solar cell.

The I−V characteristic of the solar cell is given by an implicit and nonlinear equation as follows [46]:

$$I = I_{PH} - I_o\left(e^{\left(\frac{V+R_sI}{nV_t}\right)} - 1\right) - \left(\frac{V+R_sI}{R_{sh}}\right) \tag{7.12}$$

where I_o and n are the reverse saturation current and ideality factor of the diode, respectively, and V_t is the thermal voltage.

The photo-generated current, I_{PH}, can be evaluated for any arbitrary value of irradiance, G, and cell temperature, T_c, using the following equation:

$$I_{PH} = \frac{G}{G_{ref}}I_{sc} + k_i(T_c - T_{ref}) \tag{7.13}$$

where G_{ref} and T_{ref} are, respectively, the irradiance and cell temperature at STC, ki (A/oC) is the temperature coefficient of the current, and I_{sc} is the solar cell short-circuit current at STC.

On the other hand, the reverse saturation current, I_o, is given by the following equation:

$$I_o = \frac{I_{sc}e^{\left(\frac{E_{go}}{V_{to}} - \frac{E_g}{V_t}\right)}}{\left(e^{\left(\frac{V_{oc}}{n\ N_s V_{to}}\right)} - 1\right)}\left(\frac{T_c}{T_{ref}}\right)^3 \tag{7.14}$$

where I_{sc} and V_{oc} are the short-circuit current and the open-circuit voltage of solar cell, respectively, V_{to} is the thermal voltage at STC, E_g is the energy bandgap of the semiconductor, and E_{go} is the energy bandgap at $T = 0$ K.

The value of the energy bandgap of the semiconductor at any cell temperature, T_c, is given by:

$$E_g = E_{go} - \frac{\alpha gap\ T_c^2}{\beta gap + T_c} \tag{7.15}$$

where α_{gap} and β_{gap} are characteristic parameters of the semiconductor.

There are simplified versions of this model. The simplest one includes only the controlled current source giving the photo-generated current and the diode: the three-parameter model [47]. These parameters are I_{PH}, I_o, and n. Moreover, because the shunt resistance, R_{sh}, included in the five-parameter model normally has a very high value, it can be neglected and the power losses are then just modeled by R_s. This model is called the four-parameter model [48]. As mentioned above, the most commonly used is the five-parameter model; however, the three- and four-parameter models can achieve similar or better accuracies in some cases [49].

Commercial PV modules are composed by association of solar cells in series forming a branch and in some cases also include several branches in parallel connection. Considering N_s solar cells in series in each branch, and a number of N_p branches for a PV module, Eq. (7.12) can be conveniently scaled to obtain a similar equation for the I−V characteristic of a PV module, taking into account the following equations [46,49,50]:

$$I_m = N_p\, I \tag{7.16}$$

$$V_m = N_s\, V \tag{7.17}$$

$$R_{sm} = \frac{N_s}{N_p} R_s \tag{7.18}$$

$$R_{shm} = \frac{N_s}{N_p} R_{sh} \tag{7.19}$$

where parameters with subscript m stands for the PV module.

The same procedure can be applied to scale up the model of the PV module to the model of a PV array by taking into account the number of PV modules connected in series by string, N_{sm}, and the number of parallel strings in the PV array, N_{pm} [46]. The coordinates of the MPP of a PV array, I_{mg} and V_{mg}, of arbitrary series-parallel, $N_{sm}\, x\, N_{pm}$, connection of PV modules can be calculated for any condition of G and T_c using the following equations that include parameters of the PV modules forming the PV array [46]:

$$I_{mg} = N_{pm}\left(\frac{I_{mm}}{1000} G + \left(\frac{dI_{scm}}{dT}\right)(T_c - T_{ref})\right) \tag{7.20}$$

$$V_{mg} = N_{sm}\left(N_s V_T \ln\left(1 + \frac{I_{scm} - I_{mm}}{I_{scm}}\left(e^{\frac{V_{ocm}}{N_s V_T}} - 1\right)\right) - I_{mm} R_{sm}\right) \tag{7.21}$$

where I_{scm} and V_{ocm} are the short-circuit current and open-circuit voltage of the PV modules included in the array, respectively.

On the other hand, the ambient air temperature, T_{air}, can be used to find the operating PV module temperature, T_c, at any irradiance conditions using the following equation [51]:

$$T_c = T_{air} + \frac{NOCT - 20}{800} G \tag{7.22}$$

where *NOCT* is the normal operating cell temperature (800 W/m^2 solar irradiance and 20°C air temperature) and G is the actual irradiance.

Another PV array model that was experimentally validated with success and has been used by several authors in the literature is the Sandia Array Performance Model (SAPM). The SAPM model is an empirical model defined by the following equations [52,53].

The model uses the normalized irradiance, E_e, defined as follows:

$$E_e = \frac{G}{G_{ref}} \tag{7.23}$$

Then, the current and voltage of the MPP of the PV array, I_{mg} and V_{mg}, can be calculated by using the following equations:

$$I_{mg} = N_{pm}\left[I_{mpo}\left(C_0 E_e + C_1 E_e^2\right)\left(1 + \alpha_{Imp}(T_c - T_{ref})\right)\right] \tag{7.24}$$

$$V_{mg} = N_{sm}\left[V_{mpo} + C_2 N_s \delta(T_c) ln(E_e) + C_3 N_s (\delta(T_c) ln(E_e))^2 + \beta_{Vmp} E_e (T_c - T_{ref})\right] \tag{7.25}$$

$$\delta(T_c) = \frac{nk(T_c + 273.15)}{q} \tag{7.26}$$

where I_{mpo} and V_{mpo} are the STC PV module current and voltage at the MPP; C_0 and C_1 are empirically determined coefficients that relate *Imp* to the effective irradiance, C_0+C_1=*1*; α_{Imp} is the normalized temperature coefficient for *Imp*; C_2 and C_3 also are empirical coefficients that relate *Vmp* to the effective irradiance; $\delta(T_c)$ is the thermal voltage per cell at temperature T_c; q is the elementary charge; k is the Boltzmann's constant; and β_{Vmp} is the temperature coefficient for module *Vmp* at STC.

5.2 INVERTER MODEL

The inverters convert DC power from the PV array on AC power that can be injected into the grid or used to supply AC loads present in the system. The DC to AC conversion efficiency, η_{inv}, of the inverter is given by the following equation:

$$\eta_{inv} = \frac{E_{AC}}{E_{DC}} = \frac{\int P_{AC} dt}{\int P_{DC} dt} \tag{7.27}$$

where P_{AC} and E_{AC} are the power and energy at the inverter output, respectively, and E_{DC} and P_{DC} the energy and power at the inverter input, output of the PV array.

Several models can be found in the literature introducing different approaches to estimate the energy conversion of inverters in GCPVSs [54,55]. A model that was widely used proposed the following equation to estimate η_{inv} by including electrical losses of the device [56]:

$$\eta_{inv} = \frac{P_{AC}/P_{NOM}}{P_{AC}/P_{NOM} + \left(k_O + k_1 (P_{AC}/P_{NOM}) + k_2 (P_{AC}/P_{NOM})^2\right)} \tag{7.28}$$

where K_0, K_1, and K_2 are mathematical coefficients and P_{NOM} is the nominal power of the inverter.

Another empirical model useful in simulations of inverter for GCPVS applications was proposed by Sandia: the Sandia Inverter Performance Model (SIPM) [57]. The inverter performance is characterized by the following equations:

$$P_{AC} = \left[\frac{P_{ACo}}{A-B} - C(A-B)\right](P_{DC}-B) + C(P_{DC}-B)^2 \tag{7.29}$$

$$A = P_{DCo}[1 + C_1(V_{DC} - V_{DCo})] \tag{7.30}$$

$$B = P_{so}[1 + C_2(V_{DC} - V_{DCo})] \tag{7.31}$$

$$C = C_o[1 + C_3(V_{DC} - V_{DCo})] \tag{7.32}$$

where V_{DC} is the input voltage, P_{ACo} is the maximum AC-power rating of the inverter at nominal operating condition, P_{DCo} and V_{DCo} are the DC-power and DC-voltage levels, respectively, at which the AC-power rating is achieved at the reference operating condition, P_{so} is the DC-power required to start the inversion process, and C_o, C_1, C_2, and C_3 are empirical coefficients.

5.3 PARAMETER EXTRACTION TECHNIQUES

As discussed in the previous sections, the models of PV modules, arrays, and inverters used in the simulation of the PV system behavior include a set of several model parameters. Some of the model parameters can be esteemed in the characterization process of PV modules and inverters. However, others are empirical parameters obtained by fitting techniques to experimental curves. To obtain accurate simulation results, the estimation of the model parameters is crucial. Parameter extraction techniques are used for this purpose. The parameter extraction techniques evaluate the model parameters described in the previous sections, using measured data of solar irradiance and module temperature together with DC and AC output currents and voltages as inputs.

The parameter extraction techniques can be based on different optimization algorithms applied to linear and nonlinear systems. These algorithms define objective functions for optimization of fittings. One of the most widely used algorithms for dealing with data-fitting applications is the Levenberg−Marquardt algorithm (LMA) [29]. Bio-inspired methods based on the Genetic Algorithm (GA) [58], Particle Swarm Optimization (PSO) [59,60], Simulated Annealing (SA) [61], Harmony Search (HS) [62], Pattern Search (PS) [63], Differential Evolution (DE) [64], and Artificial Bee Colony (ABC) [65,66] have proven to be useful in modeling PV systems because of their good accuracy degree [67,68].

5.4 SIMULATION TOOLS

Several simulation tools and different computational environments are available for the simulation of PV systems independently of the models used for this purpose. As

it has been mentioned before, the accuracy of the simulation results depends primarily on the models and the parameter extraction techniques used.

Modeling and simulation of PV systems can be achieved by using Pspice [69]. Pspice is a circuit simulation and analysis tool for analog and mixed-signal circuits integrated in the OrCAD package developed by Cadence. This software tool has demonstrated to be very useful in the simulation of PV systems [46,70–72].

LabVIEW System Design Software is a sophisticated tool widely applied in instruments control, embedded monitoring, and control systems as well as in data acquisition and signal processing [73]. It has been extensively used in monitoring applications of PV systems [74–77] and also in simulation of PV systems [78,79]. ANFIS[3] was also used as a base for modeling and simulation of PV systems [80]. However, MATLAB is probably the most used software in this field [34,41–44,81–86]. MATLAB is a powerful technical computing environment that can be complemented by a wide set of associated toolboxes offered by Mathworks [87]. It allows the modeling and simulation of PV systems and components as well as monitoring PV plants. Moreover, it can also be combined with the Simulink interface, which is a friendly modular graphical environment of simulation, resulting in a very powerful modeling and simulation platform [68,88].

6. FAULT DETECTION PROCEDURES

Two of the most used automatic supervision and fault detection procedures are described in this section. The first one is focused in the analysis of the losses present in the PV system, while the second one is based on the evaluation of current and voltage indicators to detect faults and also identify the most probable fault present in the system.

6.1 AUTOMATIC SUPERVISION AND DIAGNOSIS BASED ON POWER LOSSES ANALYSIS

As it has been discussed in Section 2, the supervision of the PV system can be based on the continuous check of normalized total inherent losses, L, described in Eq. (7.5). For this purpose, theoretical boundaries based on the standard deviation, δ, obtained from a statistical study of simulated losses, L_sim, given in case of clear sky conditions, must be defined.

The simulation of the PV array, having the PV module parameters, the configuration of the PV array, and the measured irradiance and module temperature as input data, gives the expected values of the yields and L_sim as the result. On the other hand, the supervision algorithm evaluates the evolution of the real yields from

[3]Artificial neuro-fuzzy inference systems.

climatic data and electrical parameters obtained from the monitoring system and calculates the actual value of the real losses, *L_meas*.

When the PV system is in normal operation (absence of faults), the measured losses remain into the theoretical boundaries given by the following equation:

$$L\_sim - 2\delta < L\_meas < L\_sim + 2\delta \tag{7.33}$$

When the measured capture losses are above or below the theoretical boundaries, a fault is detected in the PV system. Fig. 7.5 shows the fault detection algorithm based on the power loss analysis.

The fault diagnosis procedure starts when some fault is detected. The flowchart of this procedure is given in Fig. 7.6. To isolate malfunctions detected and determine the most probable fault type, two indicators of the deviation of the DC variables with respect to the simulated ones are evaluated. These indicators are the current, *Rc*, and voltage, *Rv*, ratios given by the following equations [34]:

$$Rc = \frac{I_{dc\_sim}}{I_{dc\_meas}} \tag{7.34}$$

$$Rv = \frac{V_{dc\_sim}}{V_{dc\_meas}} \tag{7.35}$$

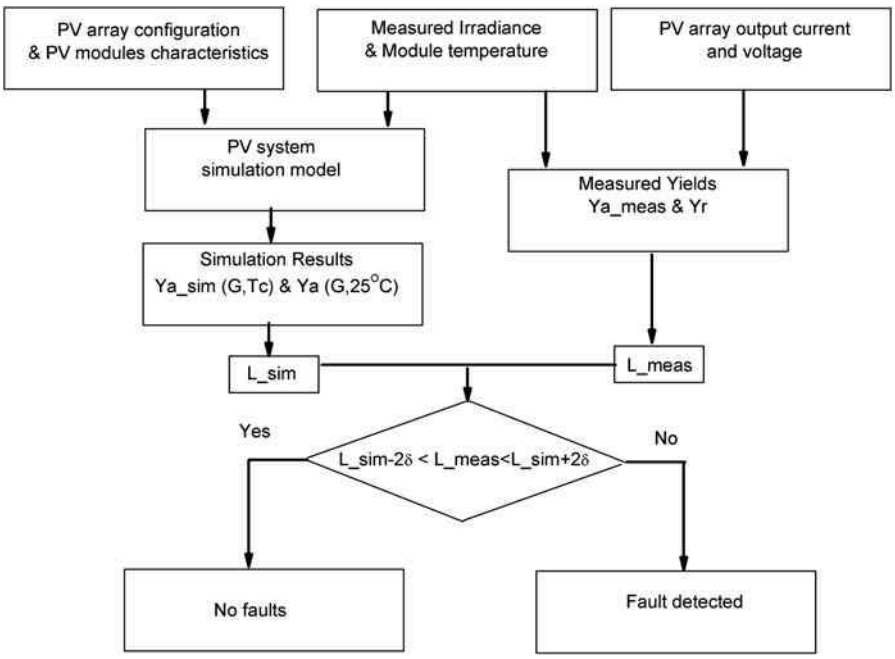


FIGURE 7.5

Fault detection algorithm based on power loss analysis.

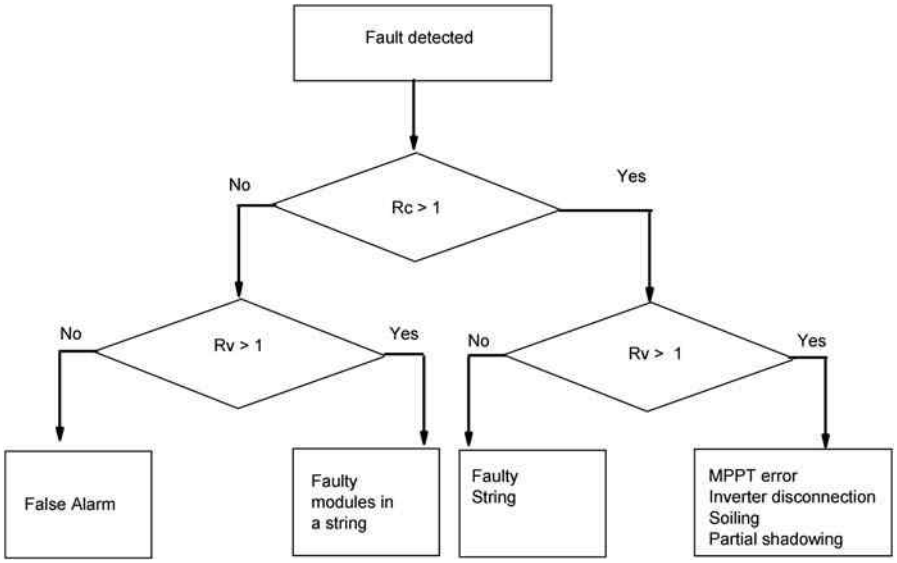


FIGURE 7.6

Diagnosis algorithm based on power loss analysis.

where I_{dc_sim} and I_{dc_meas} are the simulated and measured DC output current, respectively, and $Vdc_{\_sim}$ and $Vdc_{\_meas}$ are the simulated and measured DC output voltages of the PV system.

The evaluation of the simulated and measured losses, as well as the current and voltage ratios, can be carried out practically in real time. This diagnostic procedure was experimentally validated in several GCPVSs [30,34,89,90]. As it can be seen in Fig. 7.6, several faults can be identified: inverter disconnection, partial shadowing operation, short circuits in a PV module forming part of a string, and disconnection of some strings of the PV array.

6.2 SUPERVISION AND DIAGNOSIS BASED ON CURRENT AND VOLTAGE INDICATORS

A second approach for the supervision and diagnosis of PV system based on current and voltage indicators is presented in this section. This procedure is not focused on the system losses but uses two indicators of current, NRc, and voltage, NR_V, similar to the current and voltage ratios presented in Eqs. (7.34) and (7.35) [42]:

$$NRc = \frac{I_m}{I_{sc}} \tag{7.36}$$

$$NR_V = \frac{V_m}{V_{oc}} \tag{7.37}$$

where *Vm* and *Im* are the voltage and current of the MPP at the DC output of the PV generator, respectively, and *Isc* and *Voc* the short-circuit current and open-circuit voltage of the PV array, respectively.

Most inverters incorporate, nowadays, inputs for sensors of irradiance and temperature. Therefore, these indicators could be calculated by the inverter itself from the MPP coordinates available at the inverter input, and the values of *Isc* and *Voc*, of arbitrary series-parallel: $Nsm \times Npm$, connection of PV modules, obtained for actual conditions of irradiance, *G*, and temperature, *Tc*, in real time [46]:

$$Isc = Npm\left(\frac{Iscmr}{1000}G + \left(\frac{dIscm}{dT}\right)(Tc - Tref)\right) \tag{7.38}$$

$$Voc = Nsm\left(Vocmr + \left(\frac{dVocm}{dT}\right)(Tc - Tref) + V_t \ln\left(\frac{Iscm}{Iscmr}\right)\right) \tag{7.39}$$

where *Vocm* and *Iscm* are the open-circuit voltage and short-circuit current of a PV module forming part of the array at STC.

The indicators, *NRco* and *NRvo*, the expected values of *NRc* and *NRv*, in normal operation of the PV system (absence of faults) are given by:

$$NRco = \frac{I_{mo}}{I_{sc}} \tag{7.40}$$

$$NRvo = \frac{V_{mo}}{V_{oc}} \tag{7.41}$$

where the coordinates of the MPP of the PV array, I_{mo} and V_{mo}, are given by Eqs. (7.20) and (7.21), respectively.

The definition of thresholds for current, *TNRcfs*, and voltage, *TNRvbm*, allows detecting both short and open circuits in the PV array. These thresholds were defined by the following equations [42]:

$$TNRcfs = 1.02\ \alpha\ NRco \tag{7.42}$$

$$TNRvbm = 1.02\ \beta\ NRvo \tag{7.43}$$

where α and β are the relationship between the ratios of current in the case of one faulty string and fault-free operation and the ratio between the voltage ratios in the case of one bypassed PV module and fault-free operation, respectively, given by Eqs. (7.7) and (7.8). On the other hand, the constant included in Eqs. (7.42) and (7.43) was fixed by means of statistical procedures to avoid false fault detections as an offset of 2% with respect the *NRco* and *NRvo* values.

The parameters α and β depend only on the number of PV modules forming the array and on the PV array configuration, *Nsm* x *Npm* [42,43]:

$$\alpha = 1 - \frac{1}{Npm} \tag{7.44}$$

$$\beta = 1 - \frac{1}{Nsm} \tag{7.45}$$

When some fault appears in the PV array, the output current and/or the output voltage are reduced. The overall decrease in the output voltage depends on the number of short-circuited PV modules or the number of bypass diodes activated in the PV modules that form the PV array. Moreover, the number of equivalent bypassed modules, *BPmod*, present on the PV array is estimated as follows [41]:

$$BP\ \mathrm{mod} = Nsm\left(1 - \frac{NRv}{NRvo}\right) \tag{7.46}$$

On the other hand it is possible to estimate the equivalent number of faulty strings, *Efs*, in the PV array when a decrease in output current is observed using the following equation [41]:

$$Efs = Npm\left(1 - \frac{NRc}{NRco}\right) \tag{7.47}$$

In normal operation of the PV system the values of the indicators *NRc* and *NRv* should be very close to the values of *NRco* and *NRvo* given by Eqs. (40) and (41) and maintain their values over specific thresholds. When one of the values of the indicators, *NRc* or *NRv*, is below its defined threshold, *TNRcfs* and *TNRvbm*, Eqs. (42) and (43), the supervision system detects a fault in the PV array. The diagnostic of the most probable fault present in the PV system is then evaluated as shown in Table 7.3 based on the values of the ratios *NRc* and *NRv*.

The proportion of DC power losses due to the presence of faults in the PV array, *Ploss*, is also evaluated by the automatic supervision procedure using the following equation:

$$Ploss = \left(1 - \frac{NRc}{NRco}\frac{NRv}{NRvo}\right) \tag{7.48}$$

The supervision and fault detection procedure presented in this section has demonstrated to be effective in several real applications presented in the literature [41–43,91,92]. Main advantages of this procedure are that it can be implemented

Table 7.3 Possible Faults Detected Based on the Values of *NRc* and *NRv*

Possible Fault	*NRc*	*NRv*
No fault Normal Operation	Over threshold	Over threshold
Faulty string	Below threshold	Over threshold
Bypassed modules in a string	Over threshold	Below threshold
Other faults: Partial shadow, inverter disconnection soiling, grid fault, etc.	Below threshold	Below threshold

by the inverter itself offering the evaluation of the PV system in real time, and it is not necessary to involve complex simulation models to make the supervision and diagnostic of the system.

7. CONCLUSION

Main strategies for automatic supervision, fault detection, and diagnosis of PV systems were presented in this chapter.

The simplest supervision procedure is based on the evaluation of the energy produced by the PV system by comparing the production of monitored and expected energy over a given period. This evaluation is based on the analysis of the *PR* and *yields*. The efficiency of this supervision technique in the detection of faults present in the PV system is moderate. However, this procedure is one of the most used because it is able to detect faults that result in relevant decrease in energy harvesting. Moreover, the implementation of these kinds of supervision systems is not very expensive. Nevertheless, the accuracy in the detection of faults depends primarily on the accuracy of the models and simulation tools used to estimate the expected values of the *PR* and *yields*.

The diagnosis techniques are focused on the identification of the most probable fault present in the PV system once a fault was detected. Two diagnosis procedures were presented in this chapter: the first one is based on the power losses analysis, and the second one is based on current and voltage indicators. Both techniques have shown good results and high efficiency in the identification of faults in several real PV systems including different PV module technologies, PV system sizes, and several configurations of inverters present in the system. However, the diagnosis based on the current and voltage indicators is more efficient and offers more information about the origin and the amount of power losses associated with present faults in the PV system. The accuracy of this method in the detection of faults is directly related to the definition of thresholds for current, *TNRcfs*, and voltage, *TNRvbm*. A previous study of the PV system behavior is needed by using statistical procedures to establish a limit of false fault detections. A good commitment between the accuracy in the detection of faults and the probability of false fault detection can be achieved by means of this statistical study and the offsets defined for the *NRco* and *NRvo* values.

REFERENCES

[1] International Energy Agency, IEA, Trends 2016 in Photovoltaic Applications, Report IEA PVPS T1-30, 2016.

[2] CEC, Joint Research Centre/Ispra. Guidelines for the Assessment of Photovoltaic Plants, Document B: Analysis and Presentation of Monitoring Data, June 1993. Issue 4.1.

[3] H. Häberlin, Beutler Ch, Normalized representation of energy and power for analysis of performance and on-line error detection in PV-systems, in: Proceedings of the 13th EU PV Conference on Photovoltaic Solar Energy Conversion, October 1995, Nice, France, 1995, pp. 934−937.
[4] International Electrotechnical Commission, Photovoltaic System Performance Monitoring - Guidelines for Measurement, Data Exchange and Analysis, International Standard IEC 61724, Switzerland, 1998.
[5] M.C. Alonso-García, J.M. Ruiz, F. Chenlo, Experimental study of mismatch and shading effects in the I-V characteristic of a photovoltaic module, Sol. Energy Mater. Sol. Cells 90 (2006) 329−340.
[6] R.M. Smith, D.C. Jordan, S.R. Kurtz, Outdoor PV module degradation of current-voltage parameters, in: World Renew Energy Forum, May 2012; Denver, Colorado, 2012, pp. 1−9.
[7] J. Zorrilla-Casanova, M. Philiougine, J. Carretero, P. Bernaola, P. Carpena, L. Mora-López, M. Sidrach-de-Cardona, Analysis of dust losses in photovoltaic modules, in: World Renewable Energy Congress-Sweden, Linköping University Electronic Press, May 2011, pp. 2985−2992.
[8] F. Touati, M.A. Al-Hitmi, Noor Alam Chowdhury, Jehan Abu Hamad, Antonio J.R. San Pedro Gonzales, Investigation of solar PV performance under Doha weather using a customized measurement and monitoring system, Renew. Energy 89 (2016) 564−577.
[9] A.Z. Bradley, J. Kopchick, B. Hamzavy, Quantifying PV module defects in the service environment, in: Photovoltaic Specialist Conference (PVSC), 2015 IEEE 42nd, IEEE, June 2015, pp. 1−3.
[10] H. Patel, V. Agarwal, Maximum power point tracking scheme for PV systems operating under partially shaded conditions, IEEE Trans. Ind. Electron. 55 (2008) 1689−1698.
[11] K. Lappalainen, S. Valkealahti, Effects of PV array layout, electrical configuration and geographic orientation on mismatch losses caused by moving clouds, Sol. Energy 144 (2017) 548−555.
[12] A. Pigazo, M. Liserre, R.A. Mastromauro, V.M. Moreno, A. Dell'Aquila, Wavelet-based Islanding detection in grid-connected PV systems, IEEE Trans. Ind. Electron. 56 (2009) 4445−4455.
[13] M. Chen, S. Ma, J. Wu, L. Huang, Analysis of MPPT failure and development of an augmented nonlinear controller for MPPT of photovoltaic systems under partial shading conditions, Appl. Sci. 7 (1) (2017) 95.
[14] R.E. Hanitsch, D. Schulz, U. Siegfried, Shading effects on output power of grid connected photovoltaic generator systems, Renew. Energy 93 (2001) 9.
[15] M. Kesraoui, A. Lazizi, A. Chaib, Grid connected solar PV system: modeling, simulation and experimental tests, Energy Procedia 95 (2016) 181−188.
[16] S. Krithiga, N.A. Gounden, Investigations of an improved PV system topology using multilevel boost converter and line commutated inverter with solutions to grid issues, Simul. Model. Pract. Theory 42 (2014) 147−159.
[17] E. Lorenz, J. Hurka, D. Heinemann, H.G. Beyer, Irradiance forecasting for the power prediction of grid-connected photovoltaic systems, IEEE J. Sel. Top. Appl. Earth Observ. Remote Sens. 2 (1) (2009) 2−10.
[18] E. Lorenz, T. Scheidsteger, J. Hurka, D. Heinemann, C. Kurz, Regional PV power prediction for improved grid integration, Prog. Photovoltaics Res. Appl. 19 (7) (2011) 757−771.

[19] M.P. Almeida, O. Perpiñán, L. Narvarte, PV power forecast using a nonparametric PV model, Sol. Energy 115 (2015) 354−368.
[20] R. Marquez, C.F.M. Coimbra, Forecasting of global and direct solar irradiance using stochastic learning methods, ground experiments and the NWS database, Sol. Energy 85 (2011) 746−756.
[21] R. Marquez, V.G. Gueorguiev, C.F. Coimbra, Forecasting of global horizontal irradiance using sky cover indices, J. Sol. Energy Eng. 135 (1) (2013) 011017.
[22] A. Mellit, Artificial Intelligence technique for modelling and forecasting of solar radiation data: a review, J. Artif. Intell. Soft Comput. 1 (2008) 52−76.
[23] S. Daliento, A. Chouder, P. Guerriero, A.M. Pavan, A. Mellit, R. Moeini, P. Tricoli, Monitoring, diagnosis, and power forecasting for photovoltaic fields: a review, Int. J. Photoenergy 2017 (2017) Article ID 1356851, 13 pp. https://doi.org/10.1155/2017/1356851.
[24] E. Lorenz, A. Hammer, D. Heinemann, Short term forecasting of solar radiation based on satellite data, in: Proc. ISES Europe Solar Congress EUROSUN 2004, Freiburg, Germany, 2004.
[25] J.L. Bosch, J. Kleissl, Cloud motion vectors from a network of ground sensors in a solar power plant, Sol. Energy 95 (2013) 13−20.
[26] R. Platon, J. Martel, N. Woodruff, T.Y. Chau, Online fault detection in PV systems, IEEE Trans. Sustain. Energy 6 (4) (2015) 1200−1207.
[27] C. Ventura, G.M. Tina, Development of models for on-line diagnostic and energy assessment analysis of PV power plants: the study case of 1 MW Sicilian PV plant, Energy Procedia 83 (2015) 248−257.
[28] N. Gokmen, E. Karatepe, B. Celik, S. Silvestre, Simple diagnostic approach for determining of faulted PV modules in string based PV arrays, Sol. Energy 86 (2010) 3364−3377.
[29] A. Chouder, S. Silvestre, Analysis model of mismatch power losses in PV systems, J. Sol. Energy Eng. 131 (2) (2009) 024504.
[30] Y. Yagi, H. Kishi, W. Chine, A. Mellit, A.M. Pavan, S.A. Kalogirou, Fault detection method for grid-connected photovoltaic plants, Renew. Energy 66 (2014) 99−110.
[31] D. Trillo-Montero, I. Santiago, J.J. Luna-Rodriguez, R. Real-Calvo, Development of a software application to evaluate the performance and energy losses of grid-connected photovoltaic systems, Energy Convers. Manag. 81 (2014) 144−159.
[32] P. Xu, J.M. Hou, D.K. Yuan, fault diagnosis for building grid-connected photovoltaic system based on analysis of energy loss, in: Advanced Materials Research, vol. 805, Trans Tech Publications, 2013, pp. 93−98.
[33] M. Davarifar, A. Rabhi, A. El-Hajjaji, M. Dahmane, Real-time model base fault diagnosis of PV panels using statistical signal processing, in: 2013 International Conference on Renewable Energy Research and Applications (ICRERA), IEEE, October 2013, pp. 599−604.
[34] A. Chouder, S. Silvestre, Automatic supervision and fault detection of PV systems based on power losses analysis, Energy Convers. Manag. 51 (10) (2010) 1929−1937.
[35] D. Riley, J. Johnson, Photovoltaic prognostics and heath management using learning algorithms, in: Photovoltaic Specialists Conference (PVSC), 2012 38th IEEE, 2012, pp. 001535−001539.
[36] L. Bonsignore, M. Davarifar, A. Rabhi, G.M. Tina, A. Elhajjaji, Neuro-Fuzzy fault detection method for photovoltaic systems, Energy Procedia 62 (2014) 431−441.

[37] K.H. Chao, C.T. Chen, M.H. Wang, C.F. Wu, A novel fault diagnosis method based-on modified neural networks for photovoltaic systems, advances in swarm intelligence, Lect. Notes Comput. Sci. 6146 (2010) 531−539.
[38] S. Vergura, G. Acciani, V. Amoruso, G. Patrono, F. Vacca, Descriptive and inferential statistics for supervising and monitoring the operation of PV plants, IEEE Trans. Ind. Electron. 56 (2009) 4456−4464.
[39] W. Chine, A. Mellit, V. Lughi, A. Malek, G. Sulligoi, A. Massi Pavan, A novel fault diagnosis technique for photovoltaic systems based on artificial neural networks, Renew. Energy 90 (2016) 501−512.
[40] S. Killinger, N. Engerer, B. Müller, QCPV: a quality control algorithm for distributed photovoltaic array power control, Sol. Energy 143 (2017) 120−131.
[41] S. Silvestre, L. Mora-López, S. Kichou, F. Sánchez-Pacheco, M. Dominguez-Pumar, Remote supervision and fault detection on OPC monitored PV systems, Sol. Energy 137 (2016) 424−433.
[42] S. Silvestre, M.A. da Silva, A. Chouder, D. Guasch, E. Karatepe, New procedure for fault detection in grid connected PV systems based on the evaluation of current and voltage indicators, Energy Convers. Manag. 86 (2014) 241−249.
[43] S. Silvestre, S. Kichou, A. Chouder, G. Nofuentes, E. Karatepe, Analysis of current and voltage indicators in grid connected PV (photovoltaic) systems working in faulty and partial shading conditions, Energy 86 (2015) 42−50.
[44] S. Silvestre, Review of System Design and Sizing Tools. Practical Handbook of Photovoltaics: Fundamentals and Applications, Elsevier, Oxford, 2003, p. 543.
[45] C. Sah, R.N. Noyce, W. Shockley, Carrier generation and recombination in P-N junctions and P−N junction characteristics, Proc IRE 45 (1957) 1228−1243.
[46] L. Castaner, S. Silvestre, Modelling Photovoltaic Systems Using PSpice, John Wiley and Sons, 2002.
[47] J. Nelson, The Physics of Solar Cells, Imperial college press, London, 2003.
[48] E. Rodrigues, R. Melício, V. Mendes, J. Catalao, Simulation of a solar cell considering single-diode equivalent circuit model, in: International Conference on Renewable Energies and Power Quality. Spain, 13−15 April 2011, 2011.
[49] A. Dolara, S. Leva, G. Manzolini, Comparison of different physical models for PV power output prediction, Sol. Energy 119 (2015) 83−99.
[50] E. Karatepe, M. Boztepe, M. Çolak, Development of a suitable model for characterizing photovoltaic arrays with shaded solar cells, Sol. Energy 81 (2007) 977−992.
[51] R.P. Kenny, E.D. Dunlop, H.A. Ossenbrink, H. Müllejans, A practical method for the energy rating of c-Si photovoltaic modules based on standard tests, Prog. Photovolt. Res. Appl. 14 (2006) 155−166.
[52] D.L. King, J.A. Kratochvil, W.E. Boyson, Field Experience with a New Performance Characterization Procedure for Photovoltaic Arrays (No. SAND−98-3147C; CONF-980735), Sandia National Labs, Albuquerque, NM (US), 1997.
[53] D.L. King, Photovoltaic module and array performance characterization methods for all system operating conditions, in: C.E. Witt, M. Al-Jassim, J.M. Gee (Eds.), AIP Conference Proceedings, vol. 394 (1), AIP, February 1997, pp. 347−368.
[54] G.A. Rampinelli, A. Krenzinger, F.C. Romero, Mathematical models for efficiency of inverters used in grid connected photovoltaic systems, Renew. Sustain. Energy Res. 34 (2014) 578−587.

[55] J. Guerrero-Perez, E. De Jodar, E. Gómez-Lázaro, A. Molina-Garcia, Behavioral modeling of grid-connected photovoltaic inverters: development and assessment, Renew. Energy 68 (2014) 686−696.
[56] M. Jantsch, H. Schimidt, J. Schmid, Results of the concerted action on power conditioning and control, in: Proceedings of the 11th European Photovoltaic Solar Energy Conference, Montreux, Suiça, 1992, pp. 1589−1593.
[57] D.L. King, S. Gonzalez, G.M. Galbraith, W.E. Boyson, Performance Model for Grid-connected Photovoltaic Inverters, Sandia National Laboratories, Tech. Rep, 2007.
[58] M. Zagrouba, A. Sellami, M. Bouaïcha, M. Ksouri, Identification of PV solar cells and modules parameters using the genetic algorithms: application to maximum power extraction, Sol. Energy 84 (2010) 860−866.
[59] M. Ye, X. Wang, Y. Xu, Parameter extraction of solar cells using particle swarm optimization, J. Appl. Phys. (2009) 105.
[60] M.H. Ali, A. Rabhi, A. El Hajjaji, G.M. Tina, Real time fault detection in photovoltaic systems, Energy Procedia 111 (2017) 914−923.
[61] K.M. El-Naggar, M.R. AlRashidi, M.F. AlHajri, A.K. Al-Othman, Simulated Annealing algorithm for photovoltaic parameters identification, Sol. Energy 86 (2012) 266−274.
[62] A. Askarzadeh, A. Rezazadeh, Parameter identification for solar cell models using harmony search-based algorithms, Sol. Energy 86 (2012) 3241−3249.
[63] M.F. AlHajri, K.M. El-Naggar, M.R. AlRashidi, Al-Othman a. K. Optimal extraction of solar cell parameters using pattern search, Renew. Energy 44 (2012) 238−245, https://doi.org/10.1016/j.renene.2012.01.082.
[64] K. Ishaque, Z. Salam, S. Mekhilef, A. Shamsudin, Parameter extraction of solar photovoltaic modules using penalty-based differential evolution, Appl. Energy 99 (2012) 297−308, https://doi.org/10.1016/j.apenergy.2012.05.017.
[65] D. Oliva, E. Cuevas, G. Pajares, Parameter identification of solar cells using artificial bee colony optimization, Energy 72 (2014) 93−102.
[66] E. Garoudja, K. Kara, A. Chouder, S. Silvestre, Parameters extraction of photovoltaic module for long-term prediction using artifical bee colony optimization, in: 3rd Int Conf Control Eng Inf Technol, 2015, pp. 1−6.
[67] E.E. Ali, M.A. El-Hameed, A.A. El-Fergany, M.M. El-Arini, Parameter extraction of photovoltaic generating units using multi-verse optimizer, Sustain. Energy Technol. Assess. 17 (2016) 68−76.
[68] S. Kichou, S. Silvestre, L. Guglielminotti, L. Mora-López, E. Muñoz-Cerón, Comparison of two PV array models for the simulation of PV systems using five different algorithms for the parameters identification, Renew. Energy 99 (2016) 270−279.
[69] http://www.orcad.com/products/orcad-pspice-designer/overview.
[70] A. Saha, N.N. Nipu, M.F. Khan, PSpice based study of environmental effect on the performance of the solar PV module, in: Development in the in Renewable Energy Technology (ICDRET), IEEE, January 2016, pp. 1−6, 2016 4th International Conference on the.
[71] S. Silvestre, A. Boronat, A. Chouder, Study of bypass diodes configuration on PV modules, Appl. Energy 86 (9) (2009) 1632−1640.
[72] A. Moreno, J. Julve, S. Silvestre, L. Castañer, SPICE macromodeling of photovoltaic systems, Prog. Photovoltaics Res. Appl. 8 (3) (2000) 293−306.
[73] http://sine.ni.com/nips/cds/view/p/lang/en/nid/212669.
[74] H. Rezk, I. Tyukhov, M. Al-Dhaifallah, A. Tikhonov, Performance of data acquisition system for monitoring PV system parameters, Measurement 104 (2017) 204−211.

[75] M. Zahran, Y. Atia, A. Al-Hussain, I. El-Sayed, LabVIEW based monitoring system applied for PV power station, in: Proceedings of the 12th WSEAS International Conference on Automatic Control, Modelling and Simulation (ACMOS'10), May 2010, pp. 65−70.
[76] A.S.K. Bin, S. Weixiang, O.K. Seng, S. Ramanathan, I. Low, Development of a LabVIEW-based test facility for standalone PV systems, in: Electronic Design, Test and Applications, 2006, IEEE, January 2006, p. 6. DELTA 2006. Third IEEE International Workshop on.
[77] M. Vyas, K. Chudasama, M. Bhatt, B. Gohil, Real Time Data Monitoring of PV Solar Cell Using LabVIEW, 2016.
[78] A. Chouder, S. Silvestre, B. Taghezouit, E. Karatepe, Monitoring, modelling and simulation of PV systems using LabVIEW, Sol. Energy 91 (2013) 337−349.
[79] P. Srinivas, K.V. Lakshmi, C. Ramesh, Simulation of incremental conductance MPPT algorithm for PV systems using LabVIEW, Simulation 4 (1) (2016).
[80] A. Mellit, S.A. Kalogirou, ANFIS-based modelling for photovoltaic power supply system: a case study, Renew. Energy 36 (1) (2011) 250−258.
[81] K. Ishaque, Z. Salam, A comprehensive MATLAB Simulink PV system simulator with partial shading capability based on two-diode model, Sol. Energy 85 (9) (2011) 2217−2227.
[82] R. Alik, A. Jusoh, T. Sutikno, Shading effect on photovoltaic modules with proposed P&O checking algorithm, Int. J. Electr. Comput. Eng. 7 (1) (2017).
[83] H. Patel, V. Agarwal, MATLAB-based modeling to study the effects of partial shading on PV array characteristics, IEEE Trans. Energy Convers. 23 (1) (2008) 302−310.
[84] M.E. Ropp, S. Gonzalez, Development of a MATLAB/simulink model of a single-phase grid-connected photovoltaic system, IEEE Trans. Energy Convers. 24 (1) (2009) 195−202.
[85] M. Torres-Ramírez, G. Nofuentes, J.P. Silva, S. Silvestre, J.V. Muñoz, Study on analytical modelling approaches to the performance of thin film PV modules in sunny inland climates, Energy 73 (2014) 731−740.
[86] O. Hachana, G.M. Tina, K.E. Hemsas, PV array fault Diagnostic Technique for BIPV systems, Energy Build. 126 (2016) 263−274.
[87] https://ch.mathworks.com/products/matlab.html.
[88] S. Nema, R.K. Nema, G. Agnihotri, Matlab/simulink based study of photovoltaic cells/modules/array and their experimental verification, Int. J. Energy Environ. 1 (3) (2010) 487−500.
[89] M. Tadj, K. Benmouiza, A. Cheknane, S. Silvestre, Improving the performance of PV systems by faults detection using GISTEL approach, Energy Convers. Manag. 80 (2014) 298−304.
[90] M. Hosseinzadeh, F.R. Salmasi, Determination of maximum solar power under shading and converter faults—a prerequisite for failure-tolerant power management systems, Simul. Model. Pract. Theory 62 (2016) 14−30.
[91] I. Yahyaoui, M.E. Segatto, A practical technique for on-line monitoring of a photovoltaic plant connected to a single-phase grid, Energy Convers. Manag. 132 (2017) 198−206.
[92] M. Bressan, Y. El-Basri, C. Alonso, A new method for fault detection and identification of shadows based on electrical signature of defects, in: Power Electronics and Applications (EPE'15 ECCE-europe), 2015 17th European Conference on, IEEE, September 2015, pp. 1−8.

This page intentionally left blank

CHAPTER

8 Hybrid PV/Batteries Bank/Diesel Generator Solar-Renewable Energy System Design, Energy Management, and Economics

Ahmad Atieh[1], Sana Charfi[2], Maher Chaabene[2]

Electrical Engineering Department, The University of Jordan, Amman, Jordan[1]; Machine Control and Power Grid Research Unit, University of Sfax, Sfax, Tunisia[2]

CHAPTER OUTLINE

1. Introduction 258
2. Hybrid Renewable Energy System Modeling 259
2.1 Photovoltaic Cell Model 260
2.2 Lead-Acid Battery Model 261
2.3 Diesel Generator Model 262
2.3.1 The Diesel Engine Model 262
2.3.2 The Synchronous Generator 263
2.3.3 Excitation System Model 264
3. Sizing of Hybrid Photovoltaic/Batteries Bank/Diesel Generator System 264
3.1 Description of the Load Investigated 265
3.2 Renewable Energy System Optimization Process 266
3.2.1 Optimization Objective Functions 267
3.2.2 Optimization Constraints 269
3.2.3 Methodology 269
3.2.4 Optimization Process Using Particle Swarm Optimization 270
3.2.5 Simulation Result and Discussion 271
3.2.6 Effect of Number of Population and Iteration on PSO Algorithm Conversion 272
3.2.7 PSO Algorithm Results Summary 272
3.3 Economics of a Hybrid Renewable Energy System: Case Study 276
4. Energy Management of Hybrid Photovoltaic/Batteries Bank/Diesel Generator System 277
4.1 Review of Energy Management Schemes 278
4.2 Hybrid Renewable Energy System Energy Management: Case Study 279

Advances in Renewable Energies and Power Technologies. https://doi.org/10.1016/B978-0-12-812959-3.00008-3
Copyright © 2018 Elsevier Inc. All rights reserved.

4.2.1 Batteries Bank Depth of Discharge Control 280
4.2.2 AC Load Prediction 280
4.2.3 Energy Management Process 280
4.2.4 Results and Discussions 282
5. Economics of Hybrid Photovoltaic/Batteries Bank/Diesel Generator System 284
5.1 Effect of Batteries Depth of Discharge on Hybrid Renewable Energy System Sizing, Cost, and Pollution 286
References 292

Nomenclature

C_R	Capacity battery (Amp-h)
G_{STC}	Solar radiation under standard test condition (kWh/m^2)
I_B	Battery current (A)
IphSTC	Photo current in standard test condition (A)
K_3	Current driver (A)
NOCT	Normal operating cell temperature (°K)
STC	Standard Test Condition
T_A	PV cell temperature (°K)
T_{STC}	Ambient temperature under standard test condition (°K)
VOCSTC	Open circuit voltage (V)
V_T	Terminal voltage of PV modules (V)
X'_d	Transient d-axis reactance
X''_d	Subtransient d-axis reactances
X''_q	Subtransient q-axis reactances
X_d	Synchronous d-axis reactance
X_q	Synchronous q-axis reactance
α_{SC}	Temperature coefficient for short circuit current (A/°K)
β_{SC}	Open voltage temperature coefficient (V/°K)

1. INTRODUCTION

Renewable energy sources have been used extensively in the past decade to supplement power production for commercial and residential applications and to reduce greenhouse gases in the globe. These renewable energy sources include solar photovoltaic (PV), solar thermal, wind, geothermal, tide, etc. The choice of renewable energy source(s) depends on the climate and environmental conditions of a country. The renewable energy source(s) can be connected to the grid of the utility company or off the grid. Many countries have laws and regulations that manage the connection of the renewable energy system to the grid. Some countries offer incentives to their residences to encourage them to install renewable energy systems and other countries buy excess produced energy from their

customers at lower prices compared with what they pay for any consumption from the grid. Renewable energy systems that are connected off-grid require supplement energy sources to enable continuous supply of power to the premises. The supplement sources could be either another renewable energy source combined with storage energy subsystem and/or a diesel generator (DG). Available storage energy systems in the market differ depending on the used renewable energy source [1]. Batteries in all kinds are mainly used to store energy for PV and wind energy systems [2]. Different kinds of fluids are also used to store energy for concentrated solar power (CSP) systems that are also known solar thermal systems [3]. Other energy storage subsystems such as hydrosystems [4], supercapacitors [5], and fuel cells [6] are also used to store energy produced by renewable energy sources.

In this chapter, hybrid PV solar energy systems are investigated for off-grid applications. These systems are constructed from PV solar panels, batteries bank, and a DG. The sizing of these renewable energy systems is done for different loads in Tunisia using particle swarm optimization (PSO) algorithm. Optimal sizing of each part of this hybrid renewable energy systems is achieved. The optimization process criterion for these systems is either lower overall system cost or lower CO_2 emission of the system. The main source of pollution in the hybrid energy system is the DG. The optimal depth of discharge (*dod*) value of the batteries bank is also investigated for both conditions of lower cost of the renewable energy system and for lower pollution emission. Energy management of the hybrid renewable energy system is also studied and different proposals are discussed. These proposals are introduced to avoid blackouts that may result when switching the DG ON when the load power requirement is not satisfied by available energy of the PV subsystem and batteries bank. Blackouts typically occur because of an amount of time needed by the DG to reach steady-state power level after it is turned ON. Thus, the DG must be turned ON before the batteries bank *dod* reaches the set value, which is typically 80% [7]. This condition will allow the DG to stabilize before the batteries stored charge reaches the depleted level of 80%.

2. HYBRID RENEWABLE ENERGY SYSTEM MODELING

Fig. 8.1 shows a general block diagram of a hybrid renewable energy system. The main parts used in the system include PV panels, batteries bank, and a DG. Each part of the hybrid energy system is modeled and analyzed in this section. A two-diode nonlinear model that depends on solar irradiation and ambient temperature is used to characterize the PV cells. The battery model includes the *dod* parameter, which is used to characterize the status of charge of the battery. The *dod* parameter is used to control turning ON/OFF the DG. The DG model comprises a diesel engine (DE), a synchronous generator, and an excitation subsystem model.

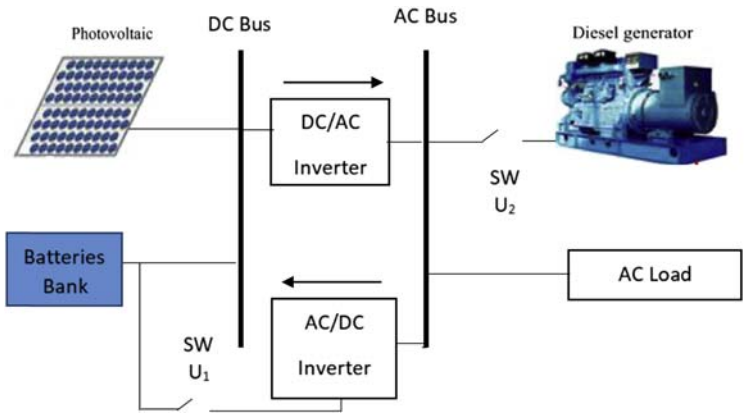


FIGURE 8.1

Block diagram of a hybrid renewable energy system. U_1 and U_2 are switches.

2.1 PHOTOVOLTAIC CELL MODEL

Fig. 8.2 illustrates the block diagram of the two-diode nonlinear circuit used to model the solar PV cell. The PV panel output voltage and power are related through the following equation [8]:

$$P_{\text{pv}} = I_{\text{cell}} \times V_{\text{pv}} \tag{8.1}$$

where V_{pv} is the panel output voltage that is usually connected to the DC bus and I_{cell} is given by:

$$\begin{aligned} I_{\text{cell}} &= I_{\text{ph}} - I_{01} \times \left[\exp\left[\left(\frac{V_{\text{cell}} + I_{\text{cell}} \times R_s}{a_1 \times V_{T1}}\right) - 1\right]\right] \\ &\quad - I_{02} \times \left[\exp\left(\frac{V_{\text{cell}} + I_{\text{cell}} \times R_s}{a_2 \times V_{T2}}\right) - 1\right] - \left(\frac{V_{\text{cell}} + I_{\text{cell}} \times R_s}{R_p}\right) \end{aligned} \tag{8.2}$$

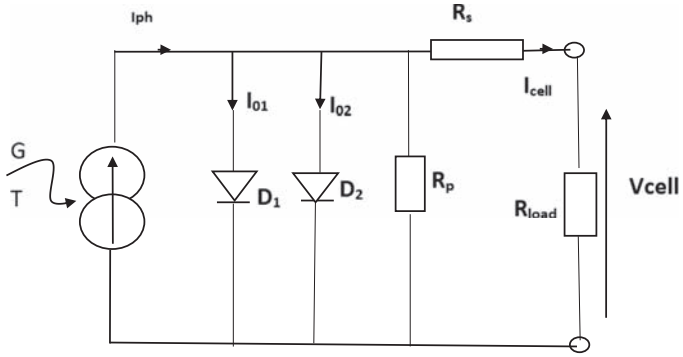


FIGURE 8.2

Circuit diagram of a two-diode model of a photovoltaic cell. G, solar radiation; I_{ph}, photocurrent; R_p, parallel resistance; R_s, series resistance; T, ambient temperature.

where a_1 and a_2 are the diode ideal constants, V_{T1} and V_{T2} are the thermal voltages of a PV module that has many cells, while the cell photocurrent I_{ph} as a function of temperature and irradiance is given by:

$$I_{\text{ph}} = \left(I_{\text{ph}_{\text{STC}}} + \alpha_{\text{SC}} \times \Delta T\right) \times \frac{G}{G_{\text{STC}}} \tag{8.3}$$

where α_{sc} is the temperature coefficient for short circuit current and ΔT is defined as:

$$\Delta T = T_A - T_{\text{STC}} \quad (\text{K}). \tag{8.4}$$

The diodes D_1 and D_2 saturation currents are given by:

$$I_{o_{(1,2)}} = I_o = \frac{I_{\text{pv}_{\text{STC}}} + \alpha_{\text{SC}} \times \Delta T}{\exp[[(V_{\text{oc}_{\text{STC}}} + \beta_{\text{oc}} \times \Delta T) \times V_T] - 1]} \tag{8.5}$$

Maximum power point trackers are mainly used to enable operating the PV panel at maximum power generation [9]. Typically, many solar cells are connected in series to increase the PV panel DC output voltage and in parallel to increase its achieved current. Then, PV panels are connected in strings of series and parallel combinations to produce certain amount of power in Watts that would satisfy the load needs. However, this produced power will not satisfy the load requirements every hour during the day because of limitations in available sun radiation. Therefore, supplement energy sources are installed in conjunction with the PV subsystem.

2.2 LEAD-ACID BATTERY MODEL

Researchers are investigating different energy storage solutions to enable storing excess energy produced by renewable sources [1]. Stored energy can be used during periods when there is no energy generated by the PV subsystem. Lead-acid batteries are used to store excess energy produced either by the PV solar system or by the DG. Lead-acid batteries are chosen because of their lower initial cost and wide availability in the market. The instantaneous *dod* parameter of the batteries is determined using a nonlinear dynamic model. Fig. 8.3 shows the equivalent circuit

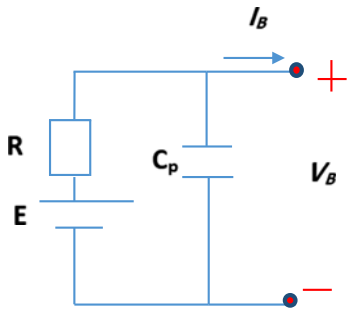


FIGURE 8.3

Equivalent circuit of a lead-acid battery cell. C_p, Peukert capacity; E, battery open circuit voltage; I_B, output current; V_B, output voltage of battery.

diagram of a battery cell. The battery *dod* parameter value is related to the battery capacity by:

$$dod = \frac{C_R}{C_p} \tag{8.6}$$

where

$$C_p = I_B^K \times T \tag{8.7}$$

K is the Peukert coefficient that equals to 1.12, and T is the constant current discharge time. The instantaneous capacity of the battery is given by:

$$\frac{\Delta C_R}{\Delta t} = \frac{I_B^K}{3600} \tag{8.8}$$

where the battery current I_B is given by:

$$I_B = \frac{P_B}{V_B} \tag{8.9}$$

where P_B is the power supplied by the battery to the load.

2.3 DIESEL GENERATOR MODEL

Many models have been published in the literature to model the DG [10−14]. Practically, the DG is composed of three main parts that enable electricity generation. Fig. 8.4 shows the main parts of the DG, which are the DE, the synchronous generator, and the excitation system.

2.3.1 The Diesel Engine Model

The DE block diagram used in the simulation is described in Fig. 8.5. The DE model is characterized by a gain parameter K_2 and time-constant parameter τ_2, which are variables. However, their variations are insignificant in small time intervals [12]. Table 8.1 shows the parameters used in the modeling of the DE [15]. Typically, the DE model is composed of a speed controller to guarantee constant speed of

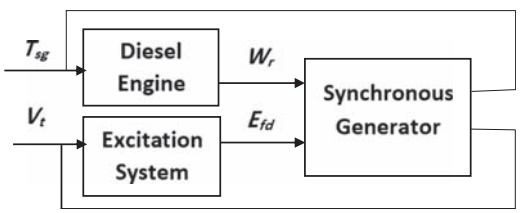


FIGURE 8.4

Diesel generator (DG) block diagram. E_{fd}, exciter field voltage; T_{sg}, generator torque; V_t, terminal voltage phasor; W_r, angular speed of a flywheel.

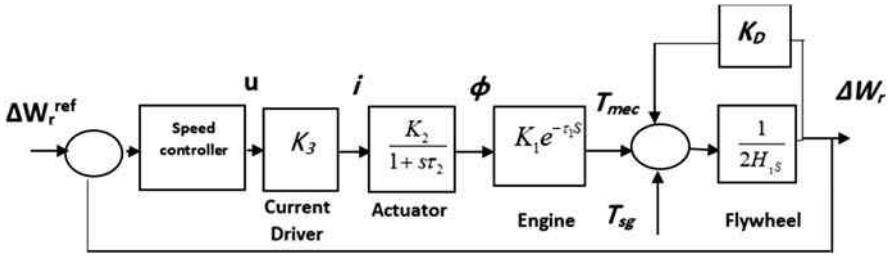


FIGURE 8.5

Typical diesel engine model block diagram. H_1, inertia constant; K_D, damping factor; T_{mec}, mechanical torque; T_{sg}, generator torque;.

Table 8.1 Parameters Used in the Diesel Engine Model

Parameter	Value	Unit	Definition
K_1	1.15	pu	Engine torque constant
K_2	1	pu	Actuator torque constant
K_3	1	pu	Current driver constant
τ_1	0.5	s	Engine delay time
τ_2	0.125	s	Actuator time constant
H_1	1.666	s	Inertia constant
K_D	0.1	pu	Damping factor

the internal combustion engine. The control of the speed is achieved by changing the quantity of fuel consumed by the motor using an actuator that can be a mechanical or electromechanical device. The actuator controls the engine speed by relating the intake of fuel and flywheel speed that represent the complex dynamic effects of the engine inertia. The engine converts the fuel flow ϕ into a mechanical torque T_{mec} after a delay time τ_1 with an engine torque constant K_1. The DE mechanical motion is governed by [16]:

$$T_{\text{mec (s)}} = K_1 e^{-\tau_1 s}\ \phi(\text{s}) \tag{8.10}$$

2.3.2 The Synchronous Generator

The parameters of a synchronous generator with model number E1S13M F/4 are adopted in the numerical simulation. A two-axis dq-model is used to represent the synchronous generator. The relative equations used in the model are obtained from Park equations. The generator electromagnetic torque equation is given as:

$$T_{sg} = E''_d I_d + E''_q I_q - (X'd - X''q) I_d I_q \tag{8.11}$$

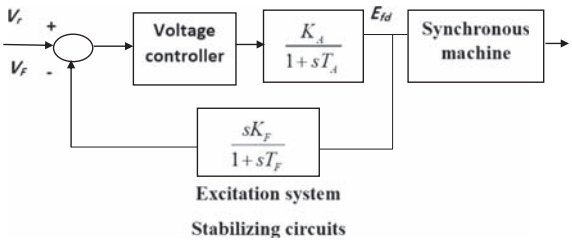


FIGURE 8.6

Functional block diagram of excitation system.

where I_d and I_q are the currents flowing in the generator stator winding. The equations that describe the rotor winding dynamics are [16]:

$$E''_d = \frac{X_q - X''_q}{1 + \tau''_{q0}s} I_q \tag{8.12}$$

$$E''_q = \frac{1}{1 + \tau''_{d0}s} E'_q - \left(\frac{X'_d - X''_d}{1 + \tau''_{d0}s}\right) I_d \tag{8.13}$$

$$E'_q = \frac{1}{\left(\frac{x_d - x''_d}{x'_d - x''_d}\right) + \tau'_{d0}s} E_{fd} + \frac{\left(\frac{x_d - x'_d}{x'_d - x''_d}\right)}{\left(\frac{x_d - x''_d}{x'_d - x''_d}\right) + \tau'_{d0}s} E''_q \tag{8.14}$$

where τ'_{d0} is the open circuit transient time constant and parameters τ''_{d0} and τ''_{q0} are the open circuit subtransient time constants.

2.3.3 Excitation System Model

The excitation system has a powerful impact on the DG dynamic performance and functionality. The main functions of the excitation system are to provide variable DC current with short time overload capability and to control the terminal voltage with suitable accuracy. The block diagram of the excitation control system is illustrated in Fig. 8.6. The excitation system is represented by a first-order system. The DC excitation system provides current flow to the rotor, which will generate an alternating current in the stator.

3. SIZING OF HYBRID PHOTOVOLTAIC/BATTERIES BANK/ DIESEL GENERATOR SYSTEM

The process of finding optimal number of each part used in the hybrid renewable energy system is called sizing. It is important to use minimum number of PV panels

and batteries and to operate the DG for minimum periods at lower output powers. Reducing the periods of operating the DG enables using lower quantities of diesel, thus reducing the amount of emitted pollution. The process of system sizing should guarantee minimum overall system cost and/or minimum produced pollution emitted by the DG.

The PV solar panels supply the required power to the load and provide excess produced power to the batteries bank during daytime. However, the batteries supply power to the load during periods when no sunlight is available, during night times, and during transition periods when turning ON the DG. Conversely, the DG supplies power to the load and provides some excess power to charge the batteries whenever the load required power is not satisfied during either the day or night times. It is assumed in the simulations that the PV solar subsystem and the batteries storage bank are the main energy supply sources to the load, while the DG operates only when both the PV panels and batteries bank available powers are not sufficient to satisfy the load demanded power. The loss of load probability (LLP) parameter is used in the optimization process to guarantee supplying the load with power 24 h a day [17,18]. It is set to zero for the hybrid energy system.

$$\text{LLP } \% = \frac{\sum_{t=0}^{t_{\text{sim}}} \text{Power supplied} - P_{\text{load}}}{\sum_{t=0}^{t_{\text{sim}}} P_{\text{load}}} \tag{8.15}$$

3.1 DESCRIPTION OF THE LOAD INVESTIGATED

The load used in the investigation of this chapter represents a typical house in the Middle East. It has five major rooms (three bedrooms, one guest room, and one living room), two bathrooms, kitchen, and basement [19]. The list of equipment and parts used in the house and their relative power consumption per hour are shown in Table 8.2. The number of each part used per room in the house is described in Table 8.3. Note that it is assumed that all bedrooms have the same parts. The power consumption is calculated for every day in a week for each room based on the following process. The 24-h of the day are divided into hourly intervals of operation, except the period in the night time between 11:00 p.m. and 6:00 a.m., which is defined as a single interval. Each part in the house contributing to the power consumption in every time interval is identified and its usage period is used in the hourly load calculation. The power consumption per hour is identified based on common usage of equipment and parts in the house. The power consumption calculation in each interval is performed over one full week to address load variation in a full day during working days and weekend days. The total power consumption in a week is then averaged over 7 days to find the average power consumption in each interval. Finally, to find the total average monthly power consumption, the total average daily power consumption is multiplied by the number of days of each

Table 8.2 List of Parts and Equipment Used in the Investigated House and Their Relevant Power Consumption

Equipment/Part	Power Consumed per Hour (W)	Brand
Light bulbs	36	Fluorescent lamp
A/C	1500	General company
Mobile	17	Sony Xperia
TV	150	Benq
Sucking Fan	200	No name
PC	170	Hp
Printer	110	Hp
Receiver	15	Humax
PS3	110	Sony
Chandeliers	120	No name
Shaver	30	Panasonic
Water heater	5000	Cornell
Refrigerator	350	Goldstar
Microwave oven	1450	Sharp
Dish washer	1800	LG
Blinder	127	Braun
Coffee Maker	1200	Panasonic
Washing machine	512	Samsung
Dryer	1500	Samsung
Vacuum cleaner	800	Sanyo

month. Excel spreadsheets are used to calculate the power consumption in each month. Fig. 8.7 illustrates the average power consumption per day for the lowest and highest power consuming months in the year, which are January and August, respectively. These 2 months are the coldest and hottest moths of the year. Typically, air conditioners are used at maximum power in August, which makes it the most power-consuming month. The maximum calculated hourly current consumption in August is 78 A for a 220-V power system, which sets an absolute maximum requirement on current for the desired renewable energy system. A summary of the monthly average power consumption of the house is shown in Fig. 8.8.

3.2 RENEWABLE ENERGY SYSTEM OPTIMIZATION PROCESS

As mentioned earlier, the PV panels array and the batteries bank supply the power needed to the load during the daytime. However, when the produced power by the PV array and available power stored in the batteries bank are not enough to meet the load needs, the DG must supply the balance of the required power to avoid possible blackouts. It is important to determine the optimal size of each part used

Table 8.3 Number of Each Part Used per Room in the Investigated House

Part	Bedroom	Living Room	Guest Room	Bathroom	Kitchen	Basement
Light bulbs	4	8	4	2	6	6
A/C	1	1	1	0	0	0
Mobile	1	0	2	0	0	0
TV	0	1	0	0	0	0
Fan	0	0	0	1	1	1
PC	1	1	0	0	0	0
Printer	0	1	0	0	0	0
Receiver	0	1	0	0	0	0
PS3	0	1	0	0	0	0
Chandeliers	0	0	2	0	0	0
Shaver	0	0	0	1	0	0
Water heater	0	0	0	1	0	0
Refrigerator	0	0	0	0	1	0
Microwave oven	0	0	0	0	1	0
Dish washer	0	0	0	0	1	0
Blinder	0	0	0	0	1	0
Coffee Maker	0	0	0	0	1	0
Washing machine	0	0	0	0	0	1
Dryer	0	0	0	0	0	1
Vacuum cleaner	1	1	1	0	0	1

in the renewable energy system taking into account the parts' cost, maintenance requirement of each part including replacement, lifetime of each component, and the pollution produced by the DG. Thus, it is necessary to conduct an optimization process to achieve the best system size for all parts used. The sizing problem includes finding the number of PV panels, the number of batteries, the DG output power, and the time of operating the DG.

3.2.1 Optimization Objective Functions

The objective function used in the optimization process is given by:

$$\min_c = \text{cost}_{\text{PV}} + \text{cost}_{\text{battery}} + \text{cost}_{\text{DG}} \tag{8.16}$$

The overall cost of the hybrid renewable energy system is composed of initial cost of the system, replacement costs of PV panels and batteries during the system lifetime

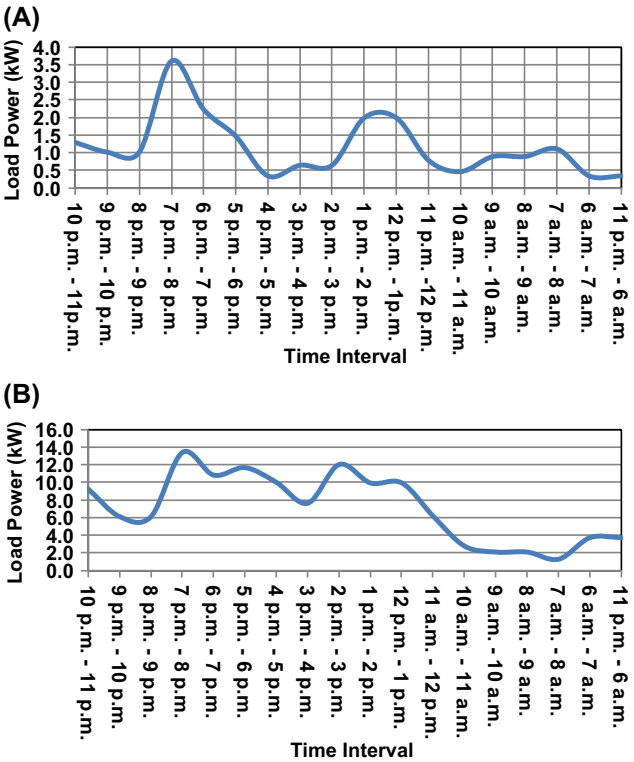


FIGURE 8.7

Average hourly power consumption of the house in (A) January and (B) August.

Month	Load Power Consumption (kW/day)	Load Power Consumption (kW/month)
January	23.3	722.3
February	23.8	690.2
March	72.6	2250.6
April	126.6	3924.6
May	131.6	4079.6
June	138.4	4152.0
July	139.7	4330.7
August	151.0	4681.0
September	142.4	4272.0
October	135.9	4212.9
November	127.1	3813.0
December	23.5	728.5
Total	**1235.90**	**37857.40**

FIGURE 8.8

Monthly average power consumption of the house.

of 20 years, and initial cost of the DG including used fuel cost. These costs are implemented in the following set of equations:

$$\text{cost}_{\text{PV}} = (\text{cost of investement} + 20 * \text{cost of maintenance}) \times N_{\text{pv}} \tag{8.17}$$

$$\text{cost}_{\text{battery}} = (\text{cost of investement} + y * \text{cost of investement}) \times N_{\text{bat}} \tag{8.18}$$

$$\text{cost}_{\text{DG}} = C_{\text{DE}} + C_{\text{oil}} + C_{\text{fuel}} \tag{8.19}$$

where y represents the number of battery replacements during 20 years of system operation, C_{DE} is the capital cost of the DG, C_{oil} is the cost of lubricating oil used in the DE, and C_{fuel} is the cost of diesel fuel consumed.

3.2.2 Optimization Constraints

The following set of constraints is used in the sizing optimization process of the hybrid PV/batteries bank/DG renewable energy system:

$$7\ \text{kW} \leq P_d \leq 15\ \text{kW} \tag{8.20}$$

$$55 \leq N_{\text{pv}} \leq 66 \tag{8.21}$$

$$6 \leq N_{\text{bat}} \leq 10 \tag{8.22}$$

$$\text{LLP} = 0 \tag{8.23}$$

These ranges give the best performance in the optimization process. The choice of each range affects the conversion of the optimization algorithm and the obtained results. The optimization algorithm was executed many times and the results of each run were used in determining the ranges of each parameter that gives best hybrid energy system size.

3.2.3 Methodology

PSO algorithm is used to optimally size the hybrid PV/batteries bank/DG renewable energy system. The optimization process is achieved for both minimum overall system cost and pollution criteria. Typically, PSO algorithms do not always guarantee optimal solution. In fact, achieving algorithm conversion and optimal solution depends mainly on the chosen range of each part used in the hybrid system. In addition, the final achieved solution depends on the used optimization strategy for the hybrid system.

The strategy used in the optimization process consists of three phases. The first phase is introduced to size both the PV panels array that supplies the load during the daytime and the batteries bank that supplies the load when produced PV power is not sufficient to meets the load needs especially during sunset and sunrise. In this step, the optimal numbers of PV panels and batteries are found. Typically, the number of PV panels should be maximized, while the number of batteries should be minimized

(because of high prices of batteries and their short lifetime) to achieve lower overall system cost.

The second phase of optimization strategy is applied at the nighttime where the DG supplies the load when the energy stored in the batteries bank is not sufficient to meet the load needs. The batteries *dod* parameter is the main criterion used to decide when to stop using the batteries bank and use the DG instead. The maximum *dod* value typically used at which the DG is turned ON is 80%. However, the minimum typical value of *dod* parameter at which the DG is turn OFF is 20%. The maximum and minimum *dod* values affect the hybrid energy system overall cost. Thus, optimal range of *dod* values is crucial to optimally size the hybrid renewable energy system. Generally, minimizing CO_2 emission requires maximizing the number of batteries to minimize the operational time of the DG. Thus, the optimal number of batteries found in the first two phases is contradictory. The same number of batteries cannot be used to achieve minimum cost and minimum pollution emission rates at the same time. Hence, in the third and last phase of optimization process, the results obtained in the first two phases are used to get optimal values of the number of PV panels, the number of batteries, the DG output power, and operational time over 24 h. It is clear that the optimization-sizing process is a nonlinear optimization problem.

3.2.4 Optimization Process Using Particle Swarm Optimization

The PSO algorithm is a stochastic technique that was developed in 1995 by Kennedy and Eberhart [20–22]. It is based on a set of population of birds called swarm that is generated randomly. Each particle of the swarm is considered as a potential solution for the optimization problem. It is characterized by its position vector $\overrightarrow{x_i} = (x_{i1},\ x_{i2}, \ldots,\ x_{in})$ and its velocity vector $\overrightarrow{v_i} = (v_{i1},\ v_{i2}, \ldots,\ v_{in})$, where n represents the number of population in the swarm and i represents the number of variables of the optimization process. Each particle remembers its own best position $\overrightarrow{Pbest_i} = (Pbest_1,\ Pbest_2 \ldots\ Pbest_{in})$, the best swarm global experience vector $\overrightarrow{gbest_i} = (gbest_1,\ gbest_2 \ldots\ gbest_{in})$ and its previous velocity vector as described in the following equations:

$$v_{i,j}^{t+1} = wv_{i,j}^{t} + c_1 r_{1i,j}^{t} * \left(p\text{best}_{i,j}^{t} - x_{i,j}^{t}\right) + c_2 r_{2i,j}^{t} * \left(g\text{best}_{i,j}^{t} - x_{i,j}^{t}\right),\ \ j \in \{1,2,\ldots n\} \tag{8.24}$$

$$x_{i,j}^{t+1} = x_{i,j}^{t} + v_{i,j}^{t+1},\ \ j \in \{1,2,\ldots n\} \tag{8.25}$$

where t is the iteration index, the variables i and j are indices of the optimization vector, $r_{1i,j}^{t}$ and $r_{2i,j}^{t}$ are random variables with values in the range [0,1], the variables c_1 and c_2 are acceleration constants with value usually equal to 2, w is the inertia weight, $w_{\max}$ and $w_{\min}$ are the initial and final inertia weights, and $\max_{\text{iter}}$ is the maximum number of iterations. To improve the algorithm conversion process, the

inertia weight is assumed to decrease linearly from $w_{\max}$ value to $w_{\min}$ value as described in the following equation:

$$w^t = w_{\min} + (w_{\max} - w_{\min}) * \frac{t}{\max_{\text{iter}}} \tag{8.26}$$

In [23], a tightening coefficient χ is introduced to improve the convergence of the optimization process. This technique is known as constriction PSO (CPSO). The velocity vector equation becomes:

$$\begin{aligned} v_{i,j}^{t+1} = \chi\Big(v_{i,j}^t + \varphi_1 r_{1i,j}^t * \left(p\text{best}_{i,j}^t - x_{i,j}^t\right) \\ + \varphi_2 r_{2i,j}^t * \left(g\text{best}_{i,j}^t - x_{i,j}^t\right)\Big), \quad j \in \{1, 2, \ldots n\} \end{aligned} \tag{8.27}$$

where χ is the constriction coefficient defined as:

$$\chi = \frac{2}{\varphi - 2 + \sqrt{\varphi^2 - 4\varphi}} \tag{8.28}$$

where $\varphi = \varphi_1 + \varphi_2$, $\varphi > 4$. Typically, $\varphi = 4.1$ and $\varphi_1 = \varphi_2$, so $\chi = 0.7298844$.

3.2.5 Simulation Result and Discussion

A standalone hybrid PV/batteries bank/DG renewable energy system has been designed to supply the load of a house in a remote area in Tunisia, which is off-grid connected. The structure of the house and its load are assumed similar to what is described in Section 3. PSO algorithm has been used to optimally size the hybrid energy system. The PSO algorithm is coded using Matlab software. The average daily load of the house investigated is shown in Fig. 8.7B, which represents the maximum daily load. It is assumed that the solar irradiation and the load power are constant during each hourly time interval. Figs. 8.9 and 8.10 show the sun solar radiation and ambient temperature in Tunisia in the month of March.

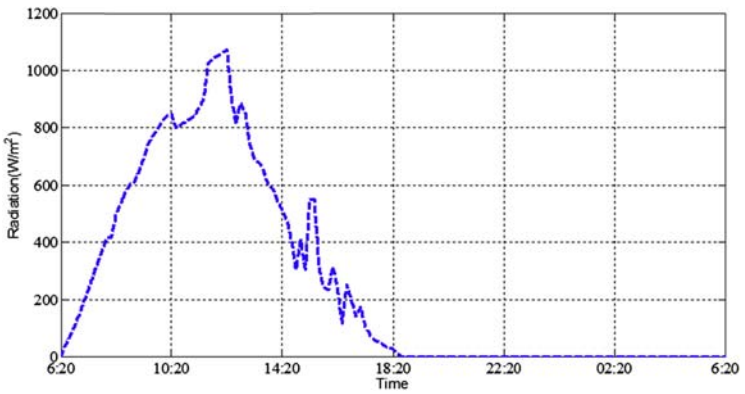


FIGURE 8.9

Sun irradiation in Tunisia for an arbitrary day in March.

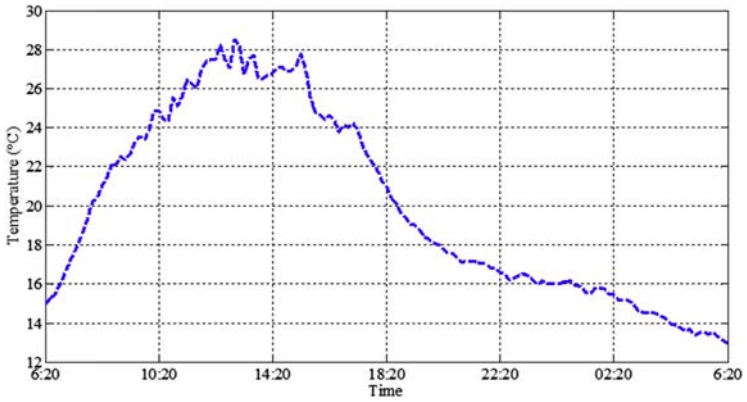


FIGURE 8.10

Ambient temperature of a day in March in Tunisia.

3.2.6 Effect of Number of Population and Iteration on PSO Algorithm Conversion

Fig. 8.11 illustrates the effect of number of population on the conversion of the PSO algorithm. It is clear that the optimization algorithm does not converge at population value that equals to 10. This can be deduced from the fact that the fitness function is not varying during changing the iteration number. However, it converges at population values of 20 and 30, where the fitness function varies during changing the iteration number and then settles to a specific value. The population value of 20 is used in the hybrid system sizing because there is clear variation of the fitness function at different iteration numbers, which is not the case for population value of 30. Fig. 8.12 shows the effect of maximum number of iterations on the conversion of the PSO algorithm. A maximum number of 30 is used in the hybrid system sizing because there is clear variation of the fitness function occurring at different iterations, which is not there for the other choices of maximum number of iterations of 20 and 35. The system sizing results differ for each chosen iteration and population values. An excel spreadsheet was created to monitor the results of the hybrid system sizing. The optimal parameters chosen for the different parts of the hybrid energy system are summarized in Table 8.4 after choosing an iteration value of 30 and a population value of 20.

3.2.7 PSO Algorithm Results Summary

The population and iteration values affect the results achieved for the PSO algorithm. Table 8.4 summarizes the optimal solutions achieved for an iteration value of 30 and a population value of 20 when the optimization constraint is either minimum emitted CO_2 pollution or overall system cost. It is clear that the overall cost of the hybrid energy system when optimized using minimum pollution criterion is higher by about 0.3% compared with the system when optimized using minimum

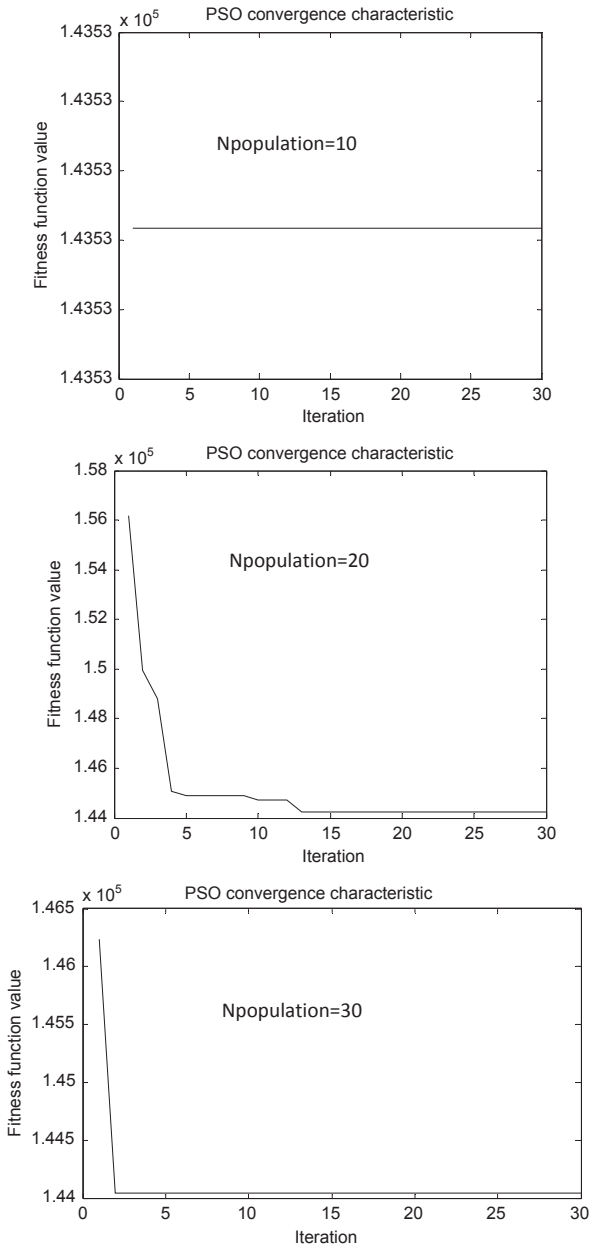


FIGURE 8.11

Effect of the number of populations on the conversion of PSO algorithm.

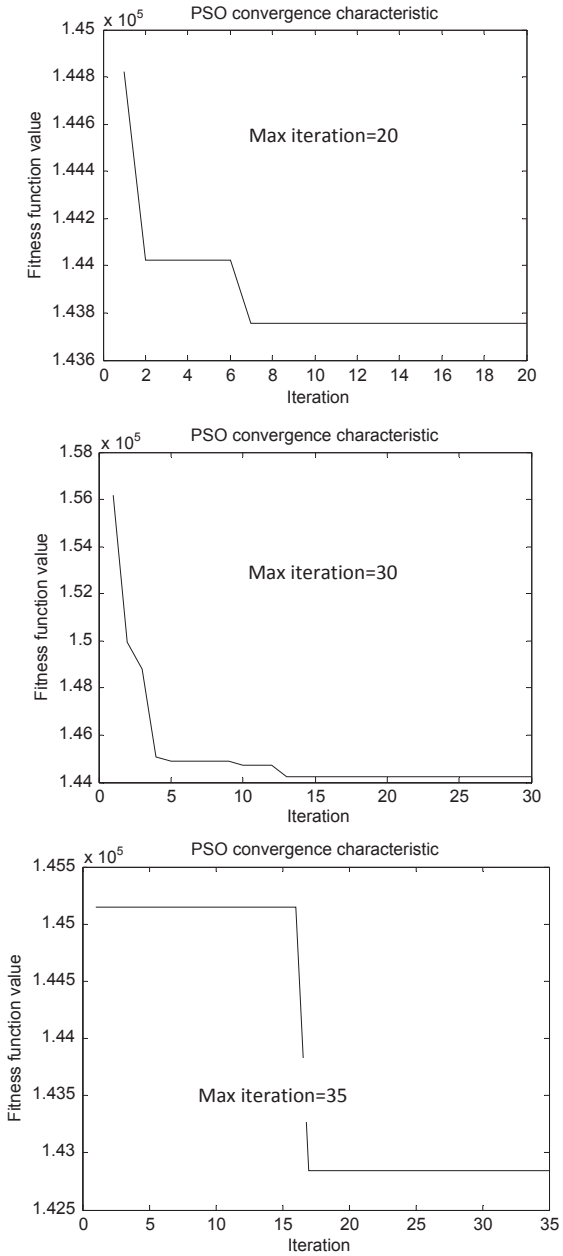


FIGURE 8.12

Effect of the number of iterations on the conversion of PSO algorithm.

Table 8.4 Optimal Values Obtained for Different Parts of Hybrid Renewable Energy System

Constraint	Batteries	PV	DE (kW)	No. of Cycles DG	DG Operation Time	Cost of System (k$ US)	Diesel Consumption (L/day)	CO_2 Emission (kg/day)
Minimum pollution	10	64	13.6	2	5 h 42 min	144.1	18.217	13.11
Minimum cost	6	65	12.4	3	6 h 36 min	139.7	19.232	13.84

overall system cost criterion. However, the choice of optimization condition depends on the requirement of the system deployment: minimum cost or minimum pollution.

3.3 ECONOMICS OF A HYBRID RENEWABLE ENERGY SYSTEM: CASE STUDY

Electricity can be supplied to a load using a DE alone, using PV and storage batteries alone, or by using a hybrid PV/batteries bank/DG system. To compare the economics of these three different options, a case study of an off-grid connected load located in Tunisia is considered [9]. Forty-two 300-W PV solar panels and 120 batteries each of 12 V/100 Ah are used in the analysis of this study case. The cost of a PV solar panel and a battery are assumed to be $270 US and $272 US, respectively. Details of the case study are described in Section 5.

The overall system cost of each option of power supply to the load are calculated, analyzed, and compared in three different countries: Tunisia, Jordan, and Saudi Arabia. Jordan is chosen because it has similar economic situation like Tunisia while Saudi Arabia is chosen because the oil price is subsidized there. The load power during every hour, solar irradiation, and ambient temperature are considered as inputs to the simulation algorithm while the PV output power, batteries *dod* value, and the DG power (Pdiesel) are considered as outputs. Fig. 8.9 shows the sun irradiation and Fig. 8.10 illustrates the ambient temperature for an arbitrary day in the month of March in Tunisia. Fig. 8.13 depicts the PV output power and the required power of the load for that specific day in Tunisia. Fig. 8.14 represents the batteries *dod* when using PV and battery storage bank only to supply power to the load. The batteries *dod* values for the hybrid PV/batteries bank/DG option is shown in Fig. 8.15. The DG output power and the amount of operational time for the hybrid energy system are shown in Fig. 8.16.

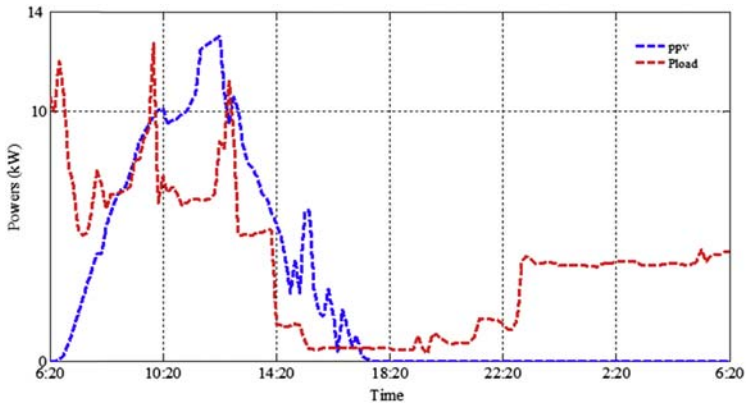


FIGURE 8.13

PV output power and power consumed by the load for a day in March.

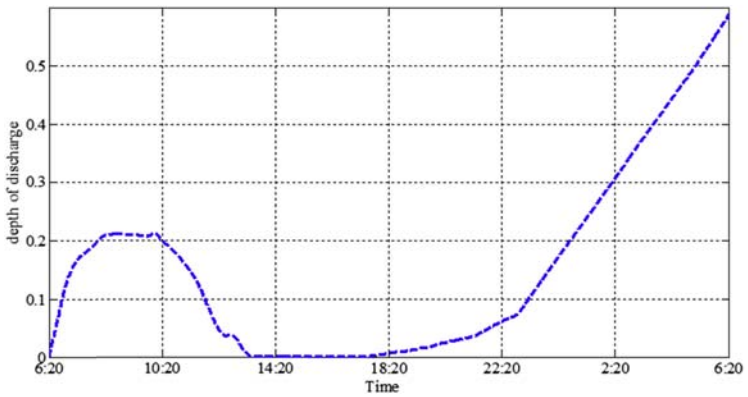


FIGURE 8.14

Batteries depth of discharge when using PV and battery storage bank only.

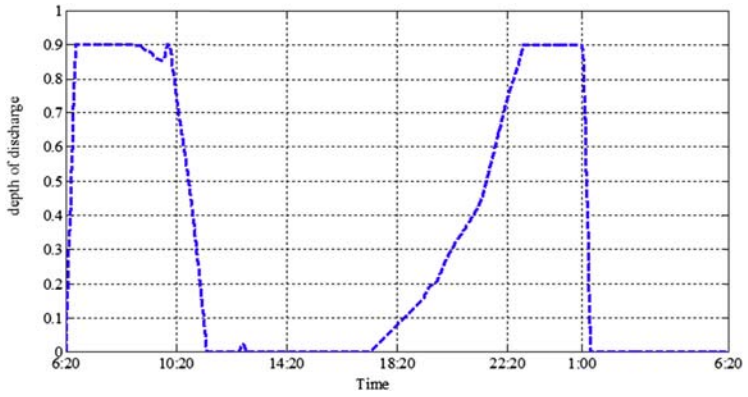


FIGURE 8.15

Batteries depth of discharge for hybrid renewable energy system.

4. ENERGY MANAGEMENT OF HYBRID PHOTOVOLTAIC/ BATTERIES BANK/DIESEL GENERATOR SYSTEM

Using only solar energy to supply electricity to the load in an off-grid system is not viable due to lack of continuous and stable supply of renewable energy all the times during the day. Consequently, supplement energy sources like DGs and batteries storage bank are recommended in these cases to cope with a lack or insufficient availability of solar power. DGs with small output powers up to 20 kW usually operate from cold start. Therefore, they require sometime to reach stable output power levels. In addition, batteries stored energy is not totally used to supply energy to the load. In fact, batteries typically operate in a *dod* ranging from 20% to 80%.

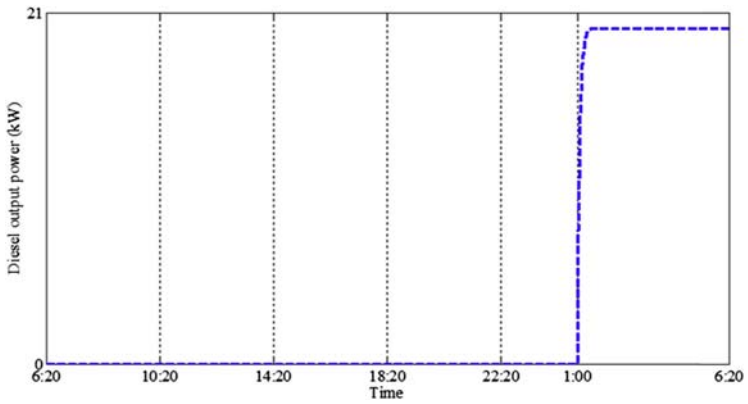


FIGURE 8.16

Produced power and time of operation of the diesel generator of the hybrid energy system.

Also, batteries suffer from shorter lifetimes especially in high-temperature environments, where elevated temperatures play a major factor in electrodes corrosion, which affect batteries lifetime [6]. Hence, an extra cost is acquired by users because of frequent battery replacements. In addition to that, leaving batteries at low state of charge for long periods and using batteries at high voltage reduces their lifetime [7]. All these factors dictate on users to manage energy stored in the batteries and manage the time of turning ON the DG to maximize using stored energy from batteries and minimize using the DG.

4.1 REVIEW OF ENERGY MANAGEMENT SCHEMES

Many authors have focused on the demand side management of renewable energy systems to improve system efficiency. In their study, Ameen et al. [24] investigated energy management of a hybrid system consisting of PV, DG, and batteries bank. Charging cycle that follows the load was the main control strategy used. In his study, Tazvinga [25] adopted a new switched model predictive control strategy for energy dispatching of a hybrid PV/Battery/DG system. The presented PV/Battery/DG system had unified linear multiple-input multiple-output model. Note that in the studies by Ameen et al. and Tazvinga [24,25], the DG was used when required based on the management scheme. While in the studies by Pourmousavi et al., Mishrae et al., and Yin et al.[26–28], the DG was operated continuously to maintain the power balance of the system. This technique suffers at low demanded power levels of the load because of waste of fuel consumption that keeps continuous operation of the DG.

The control strategy of energy management in the previously published work consisted of designing an algorithm aimed to maintain the DC bus voltage constant under various operating conditions [24–28]. However, the management scheme

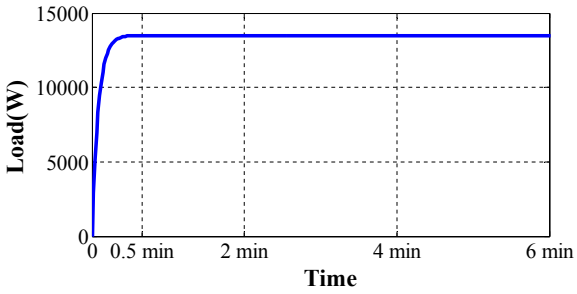


FIGURE 8.17

Time required for the diesel generator to supply stable power to the load.

does not consider the time between turning the DG ON and reaching its steady-state operation. The DGs requires certain time to reach its steady-state output power depending on starting conditions of the prime movers (cold start or warm start). The adopted DG model showed that it needs about 30 s to deliver stable output power as shown in Fig. 8.17. Typically, in the field 2 min are budgeted for the DG to reach steady output. This time must be taken into account when designing power management scheme for a renewable system to avoid power blackouts. Thus, the DG must be turned ON before the batteries *dod* reaches a maximum set value (e.g., 80%) to avoid blackout. Optimal values of *dod* are found in this section for different load demands at which the DG is turned ON before the batteries state of charge reaching a maximum *dod* value. The optimal values are found for the system that was sized in Section 3 [9].

4.2 HYBRID RENEWABLE ENERGY SYSTEM ENERGY MANAGEMENT: CASE STUDY

Fig. 8.18 illustrates a standalone hybrid PV/batteries bank/diesel generator renewable energy system. The hybrid system of this case study is designed such that PV panels and batteries bank only supply the load during the daytime while the DG operates only at night. The batteries are used to minimize the DG operational time to minimize cost and emitted pollution. A novel energy management strategy is used during the night to control when to turn ON the DG to avoid blackout. The *dod* maximum value used in the literature is 80% and the DG is turned ON when the batteries bank *dod* reaches 80%. However, the DG has slow dynamic behavior while starting as shown in Fig. 8.17. Thus, the DG must not wait until the *dod* value reaches 80% because that will cause blackout. On the other hand, a *dod* value of 70%, for example, cannot be used because there will be huge waste of power available in the batteries bank which will result in an extra consumption of fuel. Consequently, an optimal *dod* value must be found for each load required power at which the DG must be turned ON before batteries *dod* reaches 80% value.

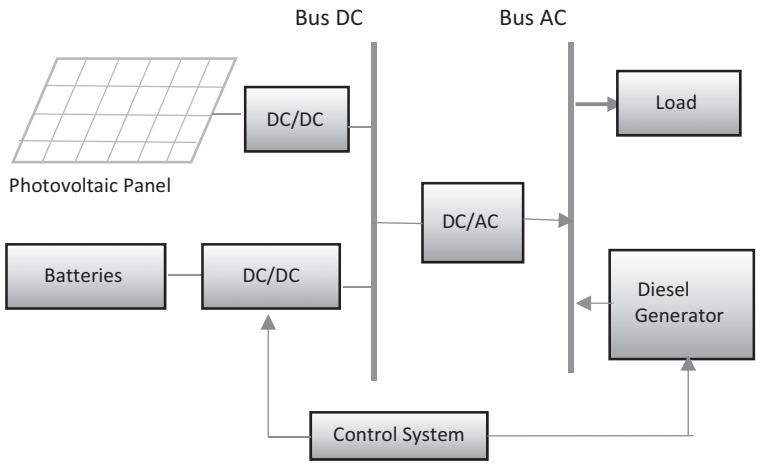


FIGURE 8.18

Hybrid PV/batteries bank/diesel generator renewable energy system block diagram.

4.2.1 Batteries Bank Depth of Discharge Control

Lead-acid batteries are used in the hybrid renewable energy system to store electrical power. Typically, batteries maximum *dod* value is set to 80% to protect batteries from over discharging, which affect the batteries lifetime. On the other hand, the minimum *dod* value at which the DG is turned OFF needs to be adjusted to achieve the best cost/pollution results [7]. Thus, the *dod* value must be in the range defined as:

$$dod_{\min} < dod < dod_{\max} \tag{8.29}$$

The battery *dod* value is computed using Eq. (8.6).

4.2.2 AC Load Prediction

The load used in this management scheme represents a typical house in Tunisia as described in Section 3. The required load power can be supplied during the night by the DG through the AC bus or by the batteries storage bank through a DC/AC inverter as shown in Fig. 8.18. An autoregressive moving average (ARMA) scheme associated with a Kalman filter is adopted in this management process to forecast the load every 2 min ahead of the actual load value. During the day, the actual measured load at each 2 min are used as input to the ARMA algorithm. The obtained modeled values and actual load values are used in Kalman filter to predict the load every 2 min ahead of operation. Fig. 8.19 describes the steps of the ARMA prediction algorithm.

4.2.3 Energy Management Process

PSO algorithm is used for sizing the investigated hybrid renewable energy system as described above [9]. The achieved optimal system sizing for minimum overall system cost and emitted pollution corresponds to 10 batteries with total capacity of

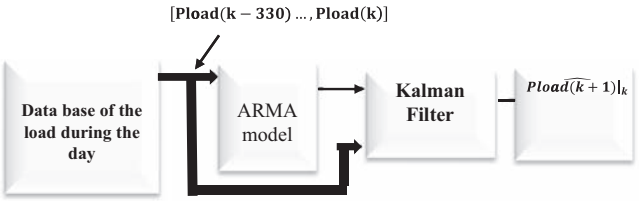


FIGURE 8.19

ARMA scheme associated with Kalman filter to predict the load every 2 min ahead of operation.

2100 Ah and DG output power of 13.5 kW. The obtained optimal *dod* range is between 22% and 80% [7]. The aim of this management scheme is to find optimal maximum *dod* value at which the DG should be turned ON before the *dod* value reaches 80% to avoid blackouts. In fact, all available energy in the batteries bank must be exploited to minimize the DG operational time. Thus, reduce the DG produced pollution and operational cost. The power produced by the hybrid energy system should always satisfy the load at any time.

Usually, the load power is varying during the daytime and the batteries bank available power varies depending on available solar power. Thus, the amount of stored power in the batteries bank by the end of the daytime is not fixed. Also, the time when the DG should be turned ON in the night time depends on the batteries bank *dod* value. Therefore, it is important to know the batteries *dod* value at any time during the day and the time it will take for the batteries to reach maximum *dod* value. The load prediction scheme of the management algorithm discussed in this section calculates future load value every 2 min, then the time it will take the batteries *dod* to reach 0.8 from different initial *dod* values is calculated. Fig. 8.20 depicts the estimated time needed by the batteries bank to reach 0.8 *dod* value from different initial *dod* values of 0.7, 0.75, 0.78, and 0.79 for different loads in the range from 0.5 to 20 kW. The larger the load demanded power, the faster the batteries *dod* to reach maximum value of 0.8. The DG needs about 30 s to reach its steady-state output power as shown in Fig. 8.17. However, a margin of 2 min is considered in the field to ensure stable power supply to the load. It is clear in Fig. 8.20 that the time needed to reach 0.8 *dod* increases when decreasing the initial *dod* value. This will provide longer time before turning ON the DG. It is also clear that for some loads, the time estimated for *dod* to reach 80% will take less than 2 min. Thus, a blackout will occur during this period for that load demanded power. Hence, it is necessary to decrease the *dod* value at which the DG is turned ON. As a conclusion from Fig. 8.20, the optimal *dod* value at which the DG should be turned ON can be set for different load power ranges as follows:

$$\begin{cases} \text{if } 0.5\text{ kW} \le P_{\text{load}} < 8.5\text{ kW}, \text{ the } dod_{\text{OPT}} = 0.79 \\ \text{if } 8.5\text{ kW} \le P_{\text{load}} < 16\text{ kW}, \text{ the } dod_{\text{OPT}} = 0.78 \\ \text{if } 16\text{ kW} \le P_{\text{load}} \le 20\text{ kW}, \text{ the } dod_{\text{OPT}} = 0.75 \end{cases} \tag{8.30}$$

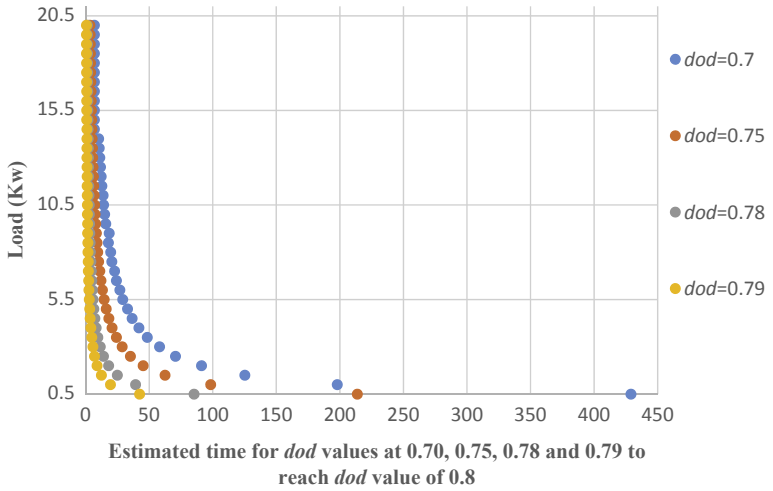


FIGURE 8.20

Estimated time in minutes for different initial *dod* values (0.75–0.78 and 0.79) to reach *dod* value of 0.8 calculated at different load power in the range between 0.5 and 20 kW.

4.2.4 Results and Discussions

Numerical simulations are conducted to validate the energy management scheme. Two cases are considered in the validation for an-off grid load in Tunisia. The first case is investigated when there is no energy management scheme used for the DG and batteries bank and when the DG is turned ON at *dod* value of 0.7. The second case uses the proposed management scheme where the maximum *dod* set value is optimized and used to manage the time at which the DG is turned ON. The load is predicted every 2 min as described above using Kalman filter associated with ARMA model. Fig. 8.21 shows the actual and predicted load values in full day. As noticed, the load reaches its peak of 13.4 kW at 7:00 p.m. The errors of predicted load values are assessed by computing the normalized mean bias error (NRMSE) factors using the following equation:

$$\mathrm{NRMSE} = \sum_{i=1}^{N} \frac{\mathrm{estimated}_{\mathrm{value}}(i) - \mathrm{measured}_{\mathrm{value}}(i)}{\mathrm{measured}_{\mathrm{value}}(i)} * 100\% \tag{8.31}$$

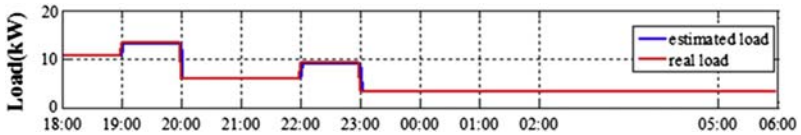


FIGURE 8.21

Load demanded power and its prediction used in energy management of hybrid energy system.

The calculated forecasted error of the investigated load equals to about 0.2%. At sunset, the *dod* value of the hybrid renewable energy system equals 0.69 as depicts in Fig. 8.22. The estimated load by the Kalman filter is input to the management algorithm while the *dod* value is checked if it is less than 0.75. If so, the batteries continue to supply the load and the DG is kept OFF. Once the *dod* value reaches 0.75, the load should be checked to which range it belongs according to Eq. (8.30) to decide whether to turn ON the DG or not. If the load is in the range of 0.5 kW inclusive and 16 kW exclusive, the batteries bank continues to supply the load with energy. Else, if the load is more than 16 kW, the DG should be turn ON. Fig. 8.22 shows also the diesel output power at different values of load power. At the beginning, when the load power equals to 10.82 kW while the *dod* value does not reach 0.75, the DG is kept OFF. After that, the load equals to 13.4 kW, while the *dod* value reaches 0.78, thus DG is turned ON. The load is supplied by the DG and the batteries are also charged by the DG until their *dod* value reaches 0.22. At that time, the DG is turned OFF and the load is supplied by the batteries bank until 00 h 45 min as shown in Fig. 8.22. At this time, the load power equals to 3.725 kW and when the *dod* reaches 0.79, the DG is turned ON. The DG is kept ON supplying the load and charging the batteries bank until their *dod* reaches 0.22 again (02 h 10 min). Typically, the DG provides power over what the load requires by 25% to enable charging the batteries. Once the batteries have sufficient power, they are used to supply the load to reduce DG emitted pollution.

Fig. 8.22 also shows the case when no energy management is used for the batteries and the DG. The achieved results for the two cases are summarized in Table 8.5. The system with energy management has a DG operational time of 3 h 06 min, which is less than the system without energy management (3 h 49 min). Thus, energy management leads to lower diesel consumption compared with the system without

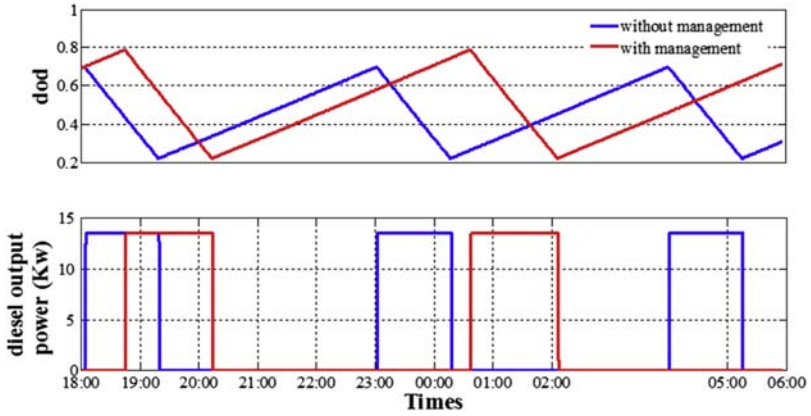


FIGURE 8.22

The *dod* value and diesel generator output power of hybrid energy system with and without energy management.

Table 8.5 Summary of Achieved Results for Two Investigated Management Cases

	No Energy Management	With Energy Management
Diesel operation time	3 h 49min	3 h 06 min
Diesel consumption/night	12.108	9.54l
CO_2 emission (kg/day)	8.718	6.875
Number of cycles of DG	3	2
Wlost(kWh)	18.09	No losses

energy management. In fact, for the case with no energy management, the diesel consumption during the night equals 12.108 L, whereas for the case with energy management the diesel consumption is 9.54 L. The decrease of diesel consumption leads to a decrease of CO_2 emission. Actually, CO_2 emission equals 8.718 kg with no energy management while it is only 6.875 kg with energy management. In addition, the system with energy management has other advantages such as it has less number of cycles for turning ON/OFF the DG (two cycles) and it does not incur any energy losses, whereas the system without energy management has about 18.09 kWh of energy losses.

5. ECONOMICS OF HYBRID PHOTOVOLTAIC/BATTERIES BANK/DIESEL GENERATOR SYSTEM

There are few assumptions used in the analysis of this section such as the power produced by the DG is fixed during its operation. The load considered here is described in Section 3.1. The depreciation cost of the DG is assumed negligible in the calculations. The DG charges the batteries bank from 1:00 a.m. to 6:00 a.m. There is no energy management considered in the analysis of this section.

The general specifications of the used DG are described in Table 8.6. Based on these specifications, 8443 L of diesel are required to supply the required load power when using DG only. The cost of supplying the load by DG for only in three different countries Tunisia, Jordan, and KSA is shown in Table 8.7 [19]. The cost is calculated based on the price of a liter of diesel in these countries as listed in Table 8.8 and published at the global petrol prices Web site at the time of writing the article [29].

The cost analysis when using PV panels and batteries only to supply the load is based on using forty-two 300-W PV panels and one hundred twenty 12-V 100-Ah batteries. The cost of a PV panel and a battery are assumed to be $270 US and $272 US, respectively. As a result, the investment cost is over $125,000 US, which makes it impractical to use PV and batteries bank only to supply the load.

When using a hybrid PV/batteries bank/DG system to power up the load, 9 years are needed to balance the cost of the system compared with that of operating a DG

Table 8.6 General Specifications for Operating the Diesel Generator

Initial Cost of 20-kW Diesel Engine	$ 5000.00	US $
Assume 100% load, the diesel consumption	4.7	L/h
Rated DG power	20,000	W
DE needs 15W40 oil every 3 months	8	L
Cost of 1 L of 15W40 oils with labor	$ 6.00	US $

Table 8.7 Summary for Cost of Investment and Operational of DG Only

Country	Yearly Diesel Cost (US $)	Yearly Oil Cost (US $)	Total Diesel Yearly Cost (US $)	No. of Operational Years	Total Investment and Operational Cost (US $)
Tunisia	$ 5994.24	$ 192.00	$ 6186.24	9	$ 60,676.15
Jordan	$ 5740.96	$ 192.00	$ 5932.96	9.5	$ 61,363.14
KSA	$ 590.98	$ 192.00	$ 782.98	96	$ 80,166.21

Table 8.8 Cost of 1 L of Diesel in Different Countries

Price of 1 L Diesel in US $	
Tunisia	$ 0.71
Jordan	$ 0.68
KSA	$ 0.07

only as shown in Table 8.9. The diesel consumption of the DG of the hybrid energy system in the period between 1:00 a.m. and 6:00 a.m. and is only 1696 L compared with 8443 L when using DG only. After the 9-years period, the hybrid system will be more economical as it will save money on the cost of diesel and it saves the environment. If the rules in a country allow the hybrid energy system to feed excess produced power to the grid, then more saving is achieved and the payback period of the hybrid energy system would drop down. Note that any PV renewable energy system is not practical in KSA because the diesel cost is hugely subsidized in the country. It is evident that about 100 years are needed for the hybrid energy system to balance the cost of operating DG only. Thus, the driver to use renewable energy systems in Saudi Arabia should not be saving money but saving the environment. It is known that each liter of diesel has 720 g of CO_2 and requires 1920 g of O_2 to combust. As a result, a 20-kW DG would produce a pollutant of about 620.4 gCO_2/kWh [30].

Table 8.9 Cost of Operating Hybrid PV/DE/Batteries Bank System

		Unit Price US $	Total Price US $
No. of 12-V/100-Ah batteries	120	$ 272.32	$ 32,678.40
No. of 300-W PV panels	42	$ 270.00	$ 11,340.00
Yearly operation of DE in Tunisia	9	$ 1396.16	$ 12,565.45
Yearly operation of DE in Jordan	9	$ 1345.28	$ 12,107.53
Yearly operation of DE in KSA	100	$ 310.72	$ 31,072.01
DG initial cost			$ 5000.00
Total investment and operational cost		Tunisia	$ 61,583.85
		Jordan	$ 61,125.93
		KSA	$ 80,090.41

5.1 EFFECT OF BATTERIES DEPTH OF DISCHARGE ON HYBRID RENEWABLE ENERGY SYSTEM SIZING, COST, AND POLLUTION

The battery *dod* range setting is considered a key parameter to guarantee lower overall system cost and minimum system pollution emission. Different *dod* range setting values (0%−80%, 20%−80% and 40%−80%) are investigated here to compare the overall system cost and pollution emission. Typically, it is important to keep the DG idle to minimize diesel consumption and eventually produced pollution. However, when batteries *dod* reaches 80%, the DG operates at a set power level that guarantees satisfying the load power requirement and charging the batteries bank. The batteries minimum *dod* level is set to different values: 0%, 20%, and 40% to find the optimal *dod* range. At these minimum *dod* values, the DG is turned OFF.

The hybrid energy system is optimized to achieve either minimum overall cost or minimum pollution over the system lifetime of 20 years for different *dod* ranges. The DG produces extra power over the load requirements to charge the batteries bank. The DG fuel consumption F_{DG} (L/h) is expressed using the following equation [31]:

$$F_{DG} = B_{DG} * P_{DG_{rat}} + A_{DG} * P_{DG_{out}} \tag{8.32}$$

where the parameters B_{DG} and A_{DG} (l/kW) are the fuel consumption curve coefficients which are defined by the DG manufacturer. The values of B_{DG} and A_{DG} are 0.08154 and 0.246 L/kWh, respectively [8]. The $P_{DG_{rat}}$ is the rated DG power (kW) and $P_{DG_{out}}$ is the DG output power (kW).

The load in this section can be supplied at any time by the PV panels, batteries bank, or the DG depending on power availability. However, the main energy sources are the PV and batteries bank while the secondary source is the DG, which complements the main power sources. The hybrid renewable energy system size is optimized for different *dod* ranges to minimize the system overall cost and operational time of the DG over the system lifetime. PSO algorithm is used for the hybrid energy system sizing optimization. Two different optimal solutions

Table 8.10 Summary of Optimal Solutions Obtained Using PSO Algorithm for Hybrid System for *dod* in the Range 20%–80%

	Minimum Pollution	Minimum Cost
Number of batteries	9	6
Number of PV panels	64	65
DG power (kW)	12.6	11.5
System cost ($k US)	141.32	136.15
Diesel consumption/day	19.246	20.268
CO_2 emission (kg/day)	13.587	14.593

were obtained when using minimum overall system cost conditions and when applying minimum DG operational time condition (minimum CO_2 pollution). Table 8.10 summarizes the optimal solutions for the two cases for batteries *dod* values in the range of 20%–80%.

The system cost is calculated during lifetime of 20 years as:

$$\text{system cost} = \text{cost}_{\text{PV}} + \text{cost}_{\text{battery}} + \text{cost}_{\text{DG}} \tag{8.33}$$

where the cost of each part is defined as:

$$\text{cost}_{\text{PV}} = (\text{cost of investement} + 20 * \text{cost of maintenance}) \times N_{\text{pv}} \tag{8.34}$$

$$\text{cost}_{\text{battery}} = (\text{cost of investement} + y * \text{cost of investement}) \times N_{\text{bat}} \tag{8.35}$$

$$\text{cost}_{\text{DG}} = C_{\text{DE}} + C_{\text{oil}} + C_{\text{fuel}} \tag{8.36}$$

where y is the number of times a battery is replaced during 20-year of system operation.C_{DE} is the capital cost of the DE, and C_{oil} is the cost of lubricating oil used in the DE.

Three different cases of *dod* range set values are investigated for minimum pollution condition and minimum cost condition of optimized hybrid energy system. The simulation is carried out over a period of 36 h to cover cases where the DG will continue to work after 6:00 a.m.

- **Case 1**: $0\% < dod < 80\%$

Table 8.11 summarizes the achieved results for minimum pollution analysis condition for *dod* range 0%–80%. The obtained discharging cycles of the batteries are five cycles. The number of discharging cycles typically affects the lifetime of the batteries, which was calculated based on 2000 cycles. Fig. 8.23 shows the different curves for the load power requirements over 36 h, *dod* status of the batteries bank, and the DG output power.

Table 8.12 illustrates the achieved results for minimum cost analysis case when the *dod* range is 0%–80%. The number of discharging cycles of the batteries is six cycles. Fig. 8.24 shows the different curves for the load power requirements over 36 h; *dod* status of the batteries bank, and the DG output power.

Table 8.11 Summary of Hybrid System Operation Results for *dod* Set Range Value of 0%–80% for Minimum Pollution Analysis Condition

Number of discharging cycles of batteries	5
Diesel engine operation time	7 h 36 min
Number of cycles of DG	2
Diesel consumption (L)	23.688
CO_2 emission (Kg)	17.055

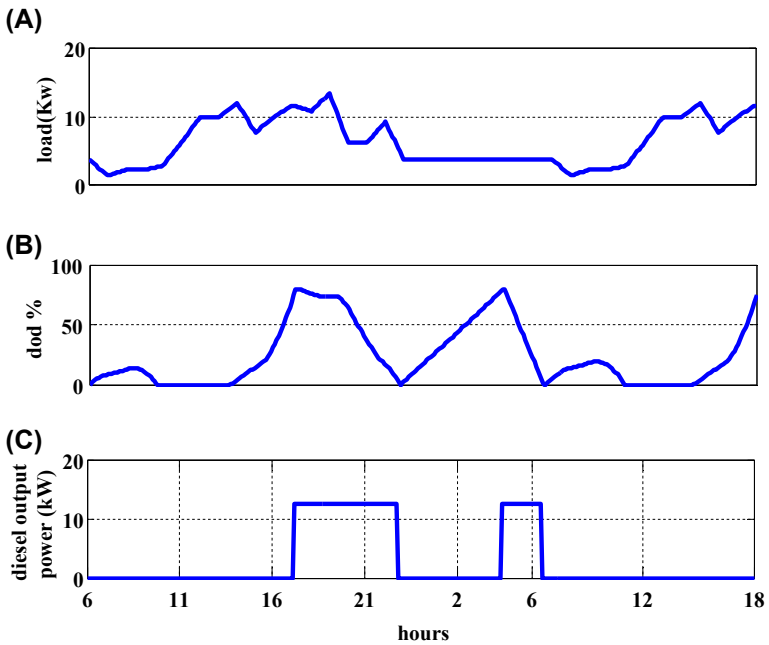


FIGURE 8.23

Results for *dod* range of 0%–80% when minimum pollution analysis condition. (A) AC load power requirements over 36 h. (B) *dod* status of the batteries. (C) diesel generator (DG) output power.

Table 8.12 Summary of Hybrid System Operation Results for *dod* Set Range Value of 0%–80% for Minimum Cost Analysis Condition

Number of cycles of operating the batteries	6
Diesel engine operation time (h)	9
Number of cycles of DG	4
Diesel consumption (L)	24.32
CO_2 emission (kg)	17.51

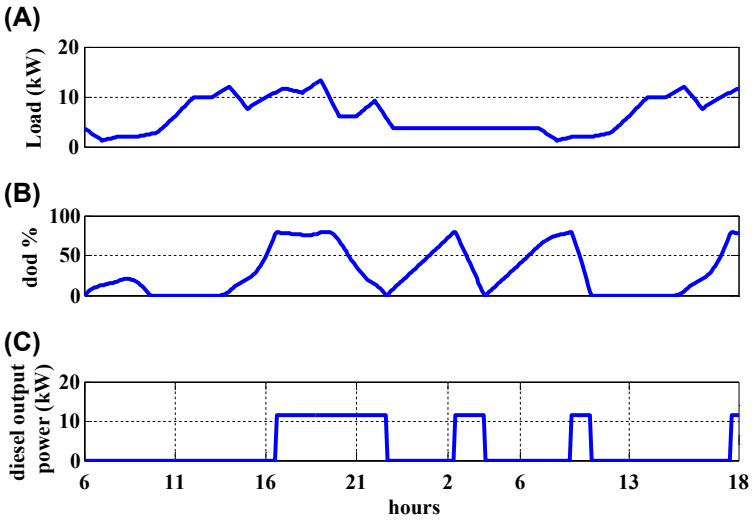


FIGURE 8.24

Results for *dod* range of 0%–80% when minimum cost analysis. (A) AC load power requirements over 36 h. (B) *dod* status of the batteries. (C) DG output power.

- **Case 2**: $20\% < dod < 80\%$

Table 8.13 summarizes the achieved results for minimum pollution analysis condition for *dod* set range value of 20%–80%. The number of discharging cycles of the batteries is six cycles. Table 8.14 summarizes the achieved results for minimum cost analysis condition. The number of discharging cycles of the batteries is eight cycles.

- **Case 3**: $40\% < dod < 80\%$

Table 8.15 shows the achieved results for minimum pollution analysis condition for *dod* set range value of 40%–80%. The number of discharging cycles of the batteries is seven cycles. Table 8.16 summarizes the achieved results for minimum cost condition. The number of discharging cycles of the batteries is 10 cycles.

Table 8.13 Summary of Hybrid System Operation Results for *dod* Set Range Value of 20%–80% for Minimum Pollution Analysis Condition

Number of cycles of operating the batteries	6
Diesel engine operation time	8 h 06 min
Number of cycles of DG	4
Diesel consumption (L)	23.894
CO_2 emission (kg)	17.203

Table 8.14 Summary of Hybrid System Operation Results for *dod* Set Range Value of 20%–80% for Minimum Cost Analysis Condition

Number of cycles of operating the batteries	8
Diesel engine operation time	9 h 12 min
Number of cycles of DG	5
Diesel consumption (L)	24.863
CO_2 emission (kg)	17.901

Table 8.15 Summary of Hybrid System Operation Results for *dod* Set Range Value of 40%–80% for Minimum Pollution Analysis Condition

Number of cycles of operating the batteries	7
Diesel engine operation time	10 h 06 min
Number of cycles of DG	6
Diesel consumption (L)	29.9061
CO_2 emission (kg)	21.532

Table 8.16 Summary of Hybrid System Operation Results for *dod* Set Range Value of 40%–80% for Minimum Cost Analysis Condition

Number of cycles of operating the batteries	10
Diesel engine operation time	10 h 06 min
Number of cycles of DG	7
Diesel consumption (L)	20.727
CO_2 emission (kg)	14.923

The amount of CO_2 emission for the three *dod* set range cases based on minimum pollution analysis and minimum system cost conditions is depicted in Figs. 8.25 and 8.26, respectively. It is clear that minimum CO_2 emission is achieved for the first analysis condition of minimum pollution at *dod* range of 0%–80% as shown in Fig. 8.25. While, *dod* range of 40%–80% set value gives minimum CO_2 emission when the minimum cost analysis condition is applied as shown in Fig. 8.26. When plotting both curves in a single graph, an intersection point is obtained which represents the *dod* optimal minimum value as shown in Fig. 8.27. Thus, a *dod* setting in the range of 22%–80% ensures minimum CO_2 pollution and minimum cost.

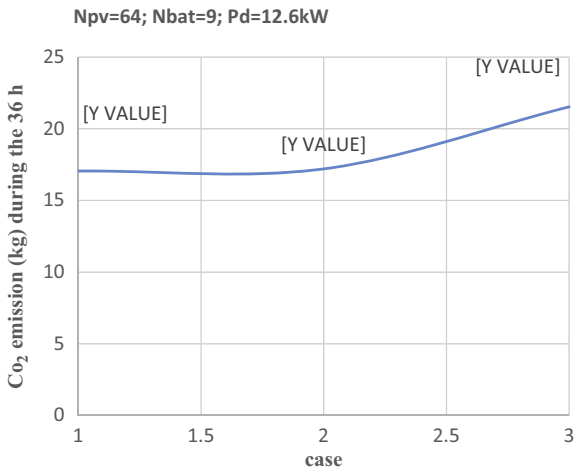


FIGURE 8.25

Calculated CO_2 emission for minimum pollution analysis condition at different *dod* range setting.

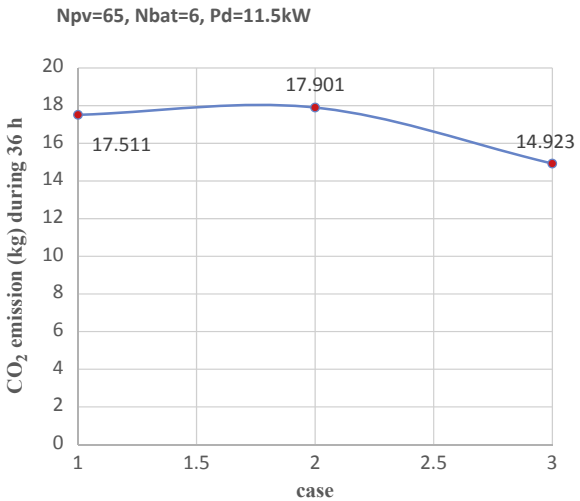


FIGURE 8.26

Calculated CO_2 emission for minimum cost analysis condition at different *dod* range settings.

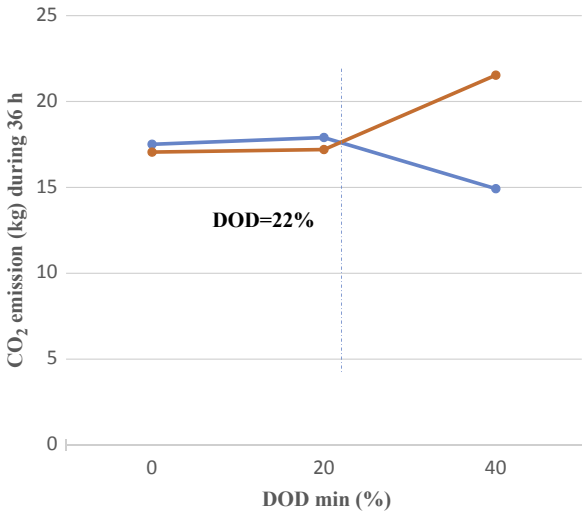


FIGURE 8.27

Calculated CO_2 emission for minimum cost analysis condition and minimum pollution analysis conditions at different *dod* range setting.

REFERENCES

[1] S.O. Amrouche, D. Rekioua, T. Rekioua, S. Bacha, Overview of energy storage in renewable energy systems, Int. J. Hydrogen Energy 41 (45) (December 2016) 20914–20927.

[2] O. Palizban, K. Kauhaniemi, Energy storage systems in modern grids-matrix of technologies and applications, J. Energy Storage 6 (2016) 248–259.

[3] R. Sioshansi, P. Denholm, The Value of Concentrating Solar Power and Thermal Energy Storage, February 2010. Technical Report NREL-TP-6A2-45833.

[4] S. Rehman, L.M. Al-Hadhrami, Md M. Alam, Pumped hydro energy storage system: a technological review, Renew. Sustain Energy Rev. 44 (2015) 586–598.

[5] L. Zhang, J. Song, J.Y. Zou, N. Wang, High voltage super-capacitors for energy storage devices applications, in: Electromagnetic Launch Technology Symposium, Victoria, BC, Canada, June 2008, https://doi.org/10.1109/ELT.2008.102.

[6] Y. Zhang, P.E. Campana, A. Lundblad, J. Yan, Comparative study of hydrogen storage and battery storage Ingrid connected photovoltaic system: storage sizing and rule-based operation, Appl. Energy 201 (September 2017) 397–411.

[7] S. Charfi, A. Atieh, M. Chaabene, The effect of batteries DOD range setting values on diesel engine generator pollution and overall cost of a hybrid solar/diesel/battery system, in: 5th International Renewable and Sustainable Energy Conference (IRSEC), Marrakech, Morocco, November 2016.

[8] K. Ishaque, Z. Salam, et al., Simple, fast and accurate two-diode model for photovoltaic modules, Sol. Energy Mater. Sol. Cells 95 (2) (February 2011) 586–594.

[9] S. Charfi, A. Atieh, M. Chaabene, Modeling and cost analysis for different PV/Battery/Diesel operating options driving a load in Tunisia, Jordan and KSA, Sustainable Cities Soc. J. 25 (August 2016) 49–56, https://doi.org/10.1016/j.scs.2016.02.006.
[10] Y. Zoka, H. Sasaki, N. Yorino, K. Kawahara, C.C. Liu, An interaction problem of distributed generators installed in a microgrid, in: Proc. Of IEEE on Electric Utility Deregulation, Restructuring and Power Technologies Conference, Hong Kong vol. 2, April 2004, pp. 795–799.
[11] G.S. Stavrakakis, G.N. Kariniotakis, A general simulation algorithm for the accurate assessment of isolated diesel-wind turbines systems interaction. A general multimachine power system model, IEEE Trans. Energy Convers. 10 (3) (September 1995) 577–583.
[12] B. Kuang, Y. Wang, Y.L. Tan, An H∞ controller design for diesel engine systems, in: Power System Technology, International Conference Proceedings vol. 1, December 2000, pp. 61–66.
[13] S. Roy, O.P. Malik, G.S. Hope, A least squares based model fitting identification technique for diesel prime movers with unknown dead time, IEEE Trans. Energy Convers. 6 (2) (June 1991) 251–256.
[14] S. Roy, O.P. Malik, G.S. Hope, An adaptive control scheme for speed control of diesel driven power-plants, IEEE Trans. Energy Convers. 6 (4) (December 1991) 605–611.
[15] M.S. Yazic, H.A. Yavasoglu, M. Eroglu, A mobile off-grid platform powered with photovoltaic/wind/battery/fuel cell hybrid power systems, Int. J. Hydrogen Energy 38 (26) (2013) 11639–11645.
[16] J. Salazar, F. Tadeo, C. de Prada, L. Palacin, Modeling and simulation of auxiliary energy systems for off-grid renewable energy installations, Int. Renew. Energy Congr. (2011).
[17] S. Diaf, G. Notton, M. Belhamel, M. Haddadi, A. Louche, Design and techno-economical optimization for hybrid PV/wind system under various meteorological conditions, Appl. Energy 85 (2008) 968–987.
[18] H. Yang, W. Zhou, L. Lu, Z. Fang, Optimal sizing method for stand-alone hybrid solar–wind system with LPSP technology by using genetic algorithm, Sol. Energy 82 (2008) 354–367.
[19] A. Atieh, S. Al Shariff, Case study on the return on investment (ROI) for using renewable energy to power-up typical house in Saudi Arabia, Sustain. Cities Soc. J. 17 (2015) 56–60.
[20] J. Kennedy, R. Eberhart, Particle swarm optimization, Proc. IEEE Int. Conf. Neural Netw. 4 (1995) 1942–1948.
[21] R. Eberhart, J. Kennedy, A new optimizer using particle swarm theory, Proc. Sixth Int. Symp. Micro Mach. Hum. Sci. (1995) 39–43.
[22] X. Hu, Y. Shi, R. Eberhart, Recent advances in particle swarm, Evol. Comput. 1 (2004) 90–97.
[23] N. Encinas, D.A. Alfonso, C. lvarez, D. Alfonso, A. Perez-Navarro, F. Garcia-Franco, Energy market segmentation for distributed energy resources implementation purposes, Gener. Transm. Distrib. 1 (2007) 324–330.
[24] A.M. Ameen, J. Pasupuleti, T. Khatib, Simplified performance models of photovoltaic/diesel generator/battery system considering typical control strategies, Energy Convers. Manage 99 (2015) 313–325.

[25] H. Tazvinga, Switched model predictive control for energy dispatching of a photovoltaic-diesel-battery hybrid power system, IEEE Trans. Control Syst. Technol. 23 (2015) 1229−1236.
[26] S.A. Pourmousavi, M.H. Nehrir, R.K. Sharma, Multi-timescale power management for islanded microgrids including storage and demand response, IEEE Trans. Smart Grid 6 (2015) 1185−1195.
[27] S. Mishra, D. Ramasubramanian, P.C. Sekhar, A seamless control methodology for a grid connected and isolated PV-diesel microgrid, IEEE Trans. Power Syst. 28 (2013) 4393−4404.
[28] C. Yin, H. Wu, F. Locment, M. Sechilariu, Energy management of DC microgrid based on photovoltaic combined with diesel generator and supercapacitor, Energy Convers. Manage 132 (2017) 14−27.
[29] http://www.globalpetrolprices.com/diesel_prices/.
[30] M.A. Elhadidy, Performance evaluation of hybrid (wind/solar/diesel) power systems, Renew. Energy 26 (3) (2002) 401−413.
[31] M. Khalid, A. Ahmadi, A.V. Savkin, V.G. Agelidis, Minimizing the energy cost for microgrids integrated with renewable energy resources and conventional generation using controlled battery energy storage, Renew. Energy 97 (November 2016) 646−655.

CHAPTER

Design Principles of Photovoltaic Irrigation Systems

9

Juan Reca-Cardeña[1], Rafael López-Luque[2]

Department of Engineering, Universidad de Almería, Almería, Spain[1]; Department of Applied Physics, Universidad de Córdoba, Córdoba, Spain[2]

CHAPTER OUTLINE

1. Introduction 296
2. Classification of Photovoltaic Irrigation Systems 297
2.1 According to the Type of Powering Plant 298
2.1.1 Stand-alone Plants 298
2.1.2 Grid-Connected Plants 299
2.1.3 Hybrid Systems 299
2.2 According to the Type of Irrigation System 300
2.2.1 Pumping to an Elevated Tank 300
2.2.2 Direct Pumping 300
3. Photovoltaic Irrigation Systems Components 301
3.1 Photovoltaic Power Plants 301
3.1.1 Photovoltaic Modules 301
3.1.2 Solar Tracking Systems 304
3.1.3 Other Types of Photovoltaic Array Arrangements 308
3.1.4 Inverter 309
3.2 Photovoltaic Irrigation Systems 311
3.2.1 Pumping System 312
3.2.2 On-Farm Irrigation Network 312
4. Modeling and Simulation of Photovoltaic Irrigation System 319
4.1 Earth–Sun Geometry and Solar Radiation Modeling 319
4.1.1 Solar Position 319
4.1.2 Angle of Incidence of the Solar Rays With Respect to the Photovoltaic Modules 320
4.1.3 Solar Irradiance Components 321
4.1.4 Power Calculations 325
5. Design of Photovoltaic Irrigation Systems 326
References 330
Further Reading 333

Advances in Renewable Energies and Power Technologies. https://doi.org/10.1016/B978-0-12-812959-3.00009-5
Copyright © 2018 Elsevier Inc. All rights reserved.

1. INTRODUCTION

Today, in the 21st century, humanity faces multiple, closely interrelated global challenges, such as the increasing world population. In 2017, world population surpassed 7.4 billion inhabitants (https://www.populationmatters.org/). This growing population requires food and energy, and, as a result, food security has become a global concern. Malnutrition affects many countries on the planet and constitutes a major obstacle to both global food security and sustainable development worldwide. One out of three people in the world is undernourished, and it is expected that this figure will reach one out of two in 2030 [1,2]. In addition to the need for food, energy needs have seen a 3% annual growth rate over the last 15 years [3]. The gradual depletion of fossil fuel resources [4] and its associated effects have encouraged the use of new, clean, and renewable energy sources [5–7], such as solar energy.

Other major concerns for humankind are climate change and global warming. They threaten with undesirable consequences such as biodiversity loss, desertification, lack of freshwater and migratory flows, and abandonment of many regions in the world affected by the said problems.

Agriculture, as a fundamental primary activity for the planet, should contribute to the mitigation of the consequences of the abovementioned problems. A paradigm shift would then be required regarding agricultural activity in general; it must become not only a fully sustainable and more energy-efficient activity but also a source of energy rather than a sink. This change of paradigm must be supported by scientific and technical developments. Recent approaches such as Precision Agriculture, Agriculture 4.0, and Agrivoltaic Production are currently laying the foundation of a new agricultural model. Agrivoltaic production approach has been defined and studied by many authors [8–13], and it entails an alliance of both agricultural and renewable energy production, namely photovoltaic (PV). The intrinsic efficiency of the photosynthetic process is currently quite low (about 3%), while the commercially available monocrystalline PV solar panels have an average efficiency of 16%. Agrivoltaic production entails combining solar panels and food crops on farms in such a way that the economic return is optimized. The results of the preliminary studies indicate that the agrivoltaic systems can significantly increase the productivity of farms. Dupraz et al. [13] report that this increase may reach a value between 35% and 73% of the land productivity. Thus, new agriculture should not only be self-sufficient energetically but it should also generate an energy surplus. At the same time, agrivoltaic production must take into account environmental issues, such as water and carbon footprints, as well as social and economic considerations.

PV irrigation is one of the most promising alternatives for rural electrification. The idea of using solar energy to meet the water needs of crops began in the 1970s. The first PV irrigation installations carried out at that time used pumps coupled to direct current (DC) motors, connected directly to the PV array. In

some specific cases, these systems had solar trackers, but electrochemical storage batteries were not needed, as energy was stored by lifting water to an elevated tank. These early PV irrigation systems were low-power installations (<6 kW) whose size was limited by the high cost of PV modules and the need for specific DC pumping groups. The commercial development of these solutions was scarce, which meant that the variety of products was limited. On the contrary, the grid-based irrigation systems that used asynchronous motors did have much more commercial success.

Great efforts have been made over the last 50 years to develop more efficient solar-based water pumping systems. Among the first PV irrigation installations, the very first was that of Campana, built in the 1970s in Corsica. This facility served as the basis for installing 25 PV pumps under the "Mali Aqua Viva" project. Since then, there has been a stable market for small power (<10 kW) PV pumping systems dedicated to irrigation and water supply for rural settlements.

Several factors have made it possible for the existing PV irrigation systems to be profitable in Mediterranean climate conditions. One of them is the gradual decline in the price of the PV Watt Peak (Wp), which reached the value of 0.5 €/Wp in 2015. Another is the fast-paced evolution of electronic solutions that allow the conversion of DC into alternative current (AC) (inverters and frequency inverters) at increasingly competitive prices.

PV pumping systems are currently gaining interest due to their numerous advantages:

- They do not depend on the existence of an electricity distribution network.
- They do not rely on portable electric generators that consume fuels, which either pollute the environment or are expensive and difficult to obtain.
- Their design is simple, as it does not require a battery bank.
- They have a long life, are highly reliable, and require minimal maintenance.

Many scientific research works have been performed in the last two decades with the aim of improving PV irrigation systems. Table 9.1, adapted from Chandel et al. [23], summarizes some of these recent studies.

2. CLASSIFICATION OF PHOTOVOLTAIC IRRIGATION SYSTEMS

PV irrigation systems are composed of two primary and highly interrelated subsystems, namely the PV subsystem, which is responsible for supplying the energy required, and the irrigation subsystem, which demands energy. For the PV irrigation systems to perform properly, the relationship between these two subsystems has to be established by applying rational and scientifically based methods. A primary classification can be made according to the characteristics of both PV and irrigation subsystems.

Table 9.1 Recent Studies Regarding Photovoltaic (PV) Irrigation Systems

Author/s	Country	Summary
Pande et al. [14]	India	The average return period of PV irrigation facilities was 6 years.
Bhave [15]	India	The economic profitability of PV irrigation was demonstrated.
Chaurey et al. [16]	India	The actual performance of PV irrigation systems working long time was analyzed.
Mahmoud and Nather [17]	Egypt	The higher efficiency of PV pumping systems versus conventional pumping systems was proven.
Yu et al. [18]	China	The PV irrigation performance for the production of grass was analyzed.
Al Ali et al. [19]	Saudi Arabia	Crop water requirements were optimized and an automatic PV irrigation system was developed.
Mokeddem [20]	Algeria	The efficiency of PV direct pumping for small irrigation farms was demonstrated.
Hamidat [21]	Algeria	The efficiency of PV direct pumping for small irrigation farms was demonstrated.
López-Luque et al. [22]	Spain	The profitability of PV irrigation for olive orchards was analyzed and the concept of PV opportunity irrigation (PVOI) was introduced.
Reca et al. [24]	Spain	The profitability and optimal design of PV irrigation systems for greenhouse crops was analyzed.

2.1 ACCORDING TO THE TYPE OF POWERING PLANT

2.1.1 Stand-alone Plants

Stand-alone plants are those that are not connected to the grid and consist of PV panels and, occasionally, a storage system that guarantees electric energy supply when insolation is low or at nighttime. Because PV produces DC, an inverter is necessary to convert the DC into AC.

Stand-alone plants are advantageous in isolated areas where the electrical grid is not near, both from technical and economic points of view. They can efficiently replace the generator sets powered by internal combustion engines.

One of the main issues that must be addressed in renewable energy–based irrigation system sizing is the seasonal demand pattern of crops [25] and the variability of renewable energy production. To overcome this problem, some PV systems make use of batteries to accumulate the electric energy produced by the PV system to match energy production and demand [26]. However, the use of batteries has several disadvantages, such as the increase in the investment costs of the system, the space needed to store the batteries, and environmental concerns related to the disposal of the batteries. In the case of PV irrigation plants, the use of batteries can be avoided by storing the energy in the form of potential energy by pumping and accumulating water in an elevated storage tank.

2.1.2 Grid-Connected Plants

Grid-connected plants can draw power from the grid during the hours when the PV generator cannot produce enough energy to satisfy the needs of the consumer. On the contrary, when the PV system produces more energy than required, the surplus can be injected into the grid, which, in turn, operates as a large accumulator. Therefore, in most cases, grid-connected systems do not need to use accumulator banks. Furthermore, such plants offer the advantage of distributed rather than centralized generation.

We can classify grid-connected plants into two categories depending on the type of energy management.

2.1.2.1 Net Metering

Net metering is an energy management model that allows the energy produced to be injected into the grid but not immediately consumed. In this model, the energy is not sold, but the grid is used as power "storage" facility. Excess power that is produced, but not self-consumed, can be transferred to the grid, and the consumer may make use of the grid when the PV plant does not generate enough power to meet their demands.

An annual energy balance is required to account for the energy injected into and drawn from the grid. The following data must be taken into account:

- The amount of energy exchanged with the grid
- The equivalent value, in Euros, of the electrical energy supplied to the grid
- The value, in Euros, of the rates paid for the energy drawn from the grid, divided into energy charges and service charges

Net metering is an advantageous system for the consumer because the annual payment is based on monetary value rather than on energy. Thus, both the prices of the energy injected into and drawn from the network and the cost paid by the user to access the grid must be considered.

2.1.2.2 Self-consumption

In this type of system, the generated PV energy can only be consumed if the demand is simultaneous with energy production. However, such systems cannot use the public grid as a power storage facility and, therefore, the energy surplus produced is lost.

2.1.3 Hybrid Systems

Other systems combine PV power plants with other sources of energy to cope with the problem of energy supply security [26]. Carroquino et al. [27] used a hybrid PV-Diesel system to irrigate Mediterranean crops. Panayiotu et al. [28] compared both a stand-alone PV system and a hybrid PV-Wind installation for a household application. They concluded that neither of them was preferable to the other, as the appropriate type of renewable energy system was dependent on the specific location and climate.

2.2 ACCORDING TO THE TYPE OF IRRIGATION SYSTEM

PV irrigation systems are usually composed of one pump, or one set of pumps operating in parallel, which transfers water to either an elevated storage tank or directly to the irrigation water distribution system. Therefore, two basic typologies can be distinguished.

2.2.1 Pumping to an Elevated Tank

Storing the pumped water into an elevated storage tank is a sound procedure for matching the renewable energy production to the crop irrigation demand. Water can subsequently be distributed to the plants by gravity [21,29,30] (Fig. 9.1).

However, in many cases, there is no location with enough elevation to build a reservoir to take advantage of the gravitational energy to distribute the irrigation water. In this case, a booster station is required to provide the energy required to discharge water through the emitters. In other cases, the elevated locations can be relatively far and the construction cost of these elevated reservoirs can be unaffordable.

2.2.2 Direct Pumping

To avoid the abovementioned drawbacks, in this work a stand-alone direct pumping PV irrigation system that pumps water directly to the irrigation distribution network rather than lifting it to an elevated reservoir is proposed. In addition, with the aim of matching energy production to irrigation demand, we propose a new approach that is different to that used in other works on PV irrigation systems design [31–35] (Fig. 9.2).

In both cases, the segmentation of the pumping stage into several units and the use of frequency variation and frequency drives all help the system to operate efficiently under variable working conditions.

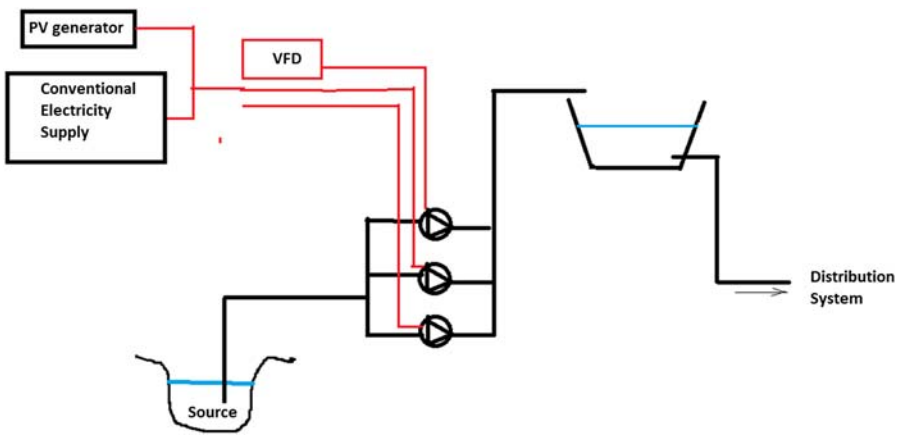


FIGURE 9.1

Scheme of a grid-connected photovoltaic (PV) pumping to an elevated tank system.

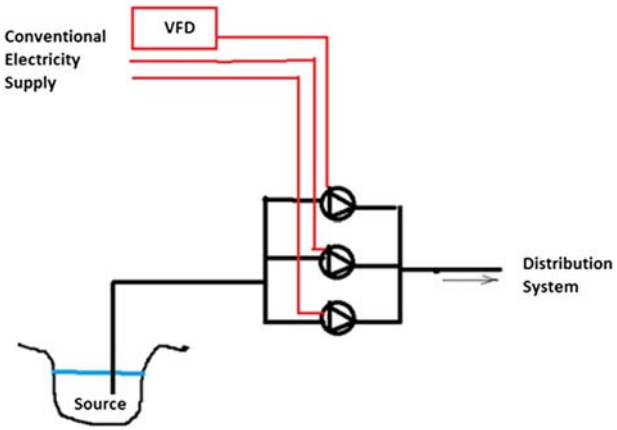


FIGURE 9.2

Scheme of a grid-connected photovoltaic irrigation system with direct pumping.

3. PHOTOVOLTAIC IRRIGATION SYSTEMS COMPONENTS

PV irrigation systems are composed of two main and highly interrelated subsystems, namely the PV subsystem, which is responsible for supplying the energy required, and the irrigation subsystem, which demands energy.

3.1 PHOTOVOLTAIC POWER PLANTS

The main components of a PV power plant are the following:

- PV modules
- Solar trackers
- DC to AC inverters or converters

3.1.1 Photovoltaic Modules

The group of PV cells is known as the PV module. PV panels consist of an array of solar cells connected to form a circuit "in series" to increase the output voltage up to the desired value. The main function of the PV array is to produce a DC between its two terminals when they are illuminated by sunlight (Fig. 9.3).

The i−V performance curve of a common PV module receiving an irradiance of 1000 W/m^2 is depicted in the following figure.

Several characteristic points or values can be distinguished on this curve:

- **Short-circuit current**, $\boldsymbol{I_{sc}}$: The current that is obtained from the cell when the voltage at its terminals is 0 V (V = 0).
- **Open circuit voltage**, $\boldsymbol{V_{oc}}$: The voltage for which the current drawn from the cell is zero (i = 0). If the device is kept in an open circuit, it will self-polarize with a



FIGURE 9.3

Solar module.

certain voltage that is the largest it can withstand in the generation region, or voltage to open circuit V_{oc}. It is the maximum voltage achieved by a solar cell in silicon cells

- **Peak Power**, **PP**: Because the power is supplied as a DC, the power delivered to the load will be $P = i \cdot V$. There will be an operating point (i_M, V_M) with a voltage value between 0 and V_{oc} for which the delivered power is the maximum amount possible (Fig. 9.4).
- **Fill Factor**, **FF**: An indicator of the shape of the characteristic curve and is defined as the peak power (PP) divided by the open circuit voltage (V_{OC}) and the short circuit current (i_{SC}).

$$\mathrm{FF} = \frac{i_M V_M}{i_{SC} V_{OC}} \tag{9.1}$$

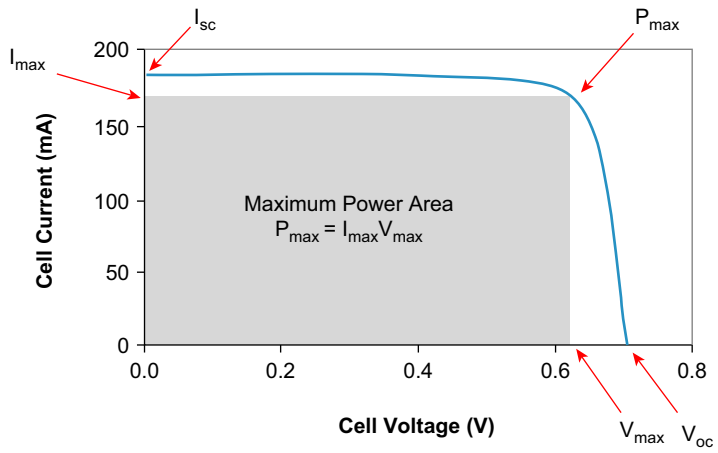


FIGURE 9.4

Solar module i–V characteristic curve.

The sharper the characteristic curve of the cell is, the higher the FF will be.

$$\mathrm{PP} = \mathrm{FF}\ i_{SC} V_{OC} \tag{9.2}$$

- **Energy conversion efficiency, η**: The ratio between the maximum power delivered (PP) and the input radiant power to the PV module, calculated as the product of panel area times the reference irradiance (A·1000 W/m^2).

$$\eta = \frac{\mathrm{FF}\ i_{SC} V_{OC}}{1000\ \mathrm{A}} \tag{9.3}$$

If the efficiency is considered constant for any irradiance value, the following relationship can be written:

$$\mathrm{PPV} = \frac{I_\beta \cdot \mathrm{PP}}{1000} \tag{9.4}$$

The curve in Fig. 9.4 can be fitted to the following mathematical equation:

$$i = i_{sc}\left[1 - \exp\left(\frac{e(V_{OC} - V)}{mkT}\right)\right] \tag{9.5}$$

where "e" is the charge of the electron, "m" is the so-called *diode ideality factor* $1 < m < 2$, "k" is the Boltzman constant, and T is the absolute temperature.

3.1.1.1 Photovoltaic Modules Arrangement

The modules are electrically arranged into different series-parallel or parallel-series combinations to obtain the intensity and voltage values suitable for each application. The set of modules with its own connections, framework, etc. constitutes the PV generator.

Both the modules and the cells are not always identical and knowing the i−V characteristic of the set or generator can become a difficult problem. With N_p and N_s being the number of modules connected in parallel and series, respectively, as shown in Fig. 9.5, the current supplied by the generator should be N_p times higher than that of a module ($i_G = i \cdot N_p$) and the voltage of the generator should be N_s times higher ($V_G = V \cdot N$). Thus, the characteristic curve of the generator i_G−V_G is given by Eq. (9.6):

$$i_G = N_P i_{sc}\left[1 - \exp\left(\frac{e(V_{OC} - V_G/N_S)}{mkT}\right)\right] \tag{9.6}$$

The i−V response of the PV generator as a function of the temperature is described by three coefficients. These coefficients are called α, β, and γ, respectively, and their typical values for monocrystalline silicon modules are given below:

$$\alpha = \partial I_{SC}/\partial T = +0.04\%;\ \ \beta = \partial V_{oc}/\partial T = -0.37\%;\ \ \gamma = \partial \mathrm{PP}/\partial T = -0.44\%. \tag{9.7}$$

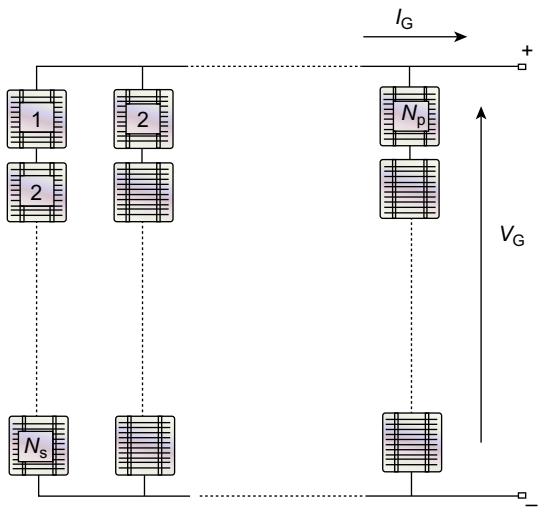


FIGURE 9.5

Scheme of a photovoltaic generator.

For a 100 cm^2 PV cell, the values of these parameters are $\alpha \approx 1.5$ mA/°C; $\beta \approx -2.3$ mV/°C; $(1/P_{max})\ \gamma \approx -0.00441$/°C.

It is assumed that the generator efficiency is equal to that of its PV cells. Global efficiency for the complete PV plant must be calculated depending on the total effective area that is actually covered by cells (A_t) and neglecting the area shadowed by the PV structure and the space between modules. The overall efficiency for the complete PV plant (η_p) is given by the following equation:

$$\eta_p = \frac{PP}{A_t \cdot I} \tag{9.8}$$

where PP is the maximum power generated by the PV plant, A_t is the total area covered, and I is the incoming solar irradiance.

3.1.2 Solar Tracking Systems

A solar tracking system is a specific device intended to move the PV modules in such a way that they continuously face the sun with the aim of maximizing the irradiation received by the PV array. A solar tracking system is composed of three well-differentiated components: the mechanism, the driving motors, and the tracking controller.

3.1.2.1 Mechanism

The mechanism is the part of the tracking system responsible for providing the follower with precision in tracking. This part must be designed to withstand harsh weather conditions and it must also have an estimated useful life equal to or similar to that of the PV module (Fig. 9.6).



FIGURE 9.6

Tracker structure.

Taking into account the type of mechanism, solar tracking systems can be classified into one-axis trackers or two-axis trackers.

3.1.2.1.1 One-Axis Tracker Because solar tracking implies moving parts and control systems that tend to be expensive, single-axis tracking systems seem to be the best solution for small PV power plants. A single-axis solar tracking system uses a tilted PV panel mount and one electric motor to move the panel on an approximate trajectory relative to the Sun's position. The rotation axis can be horizontal, vertical, or oblique. Fig. 9.7 shows a general scheme of a one-axis tracker showing both the rotation axis (unit vector e) and the collector plane (unit vector normal to the collector plane). The angle between these two unit vectors is usually kept constant in this type of tracker.

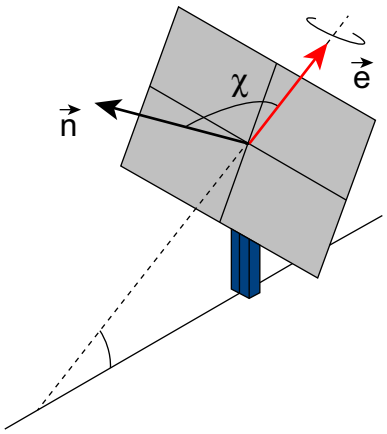


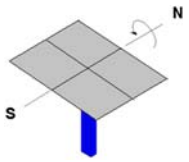
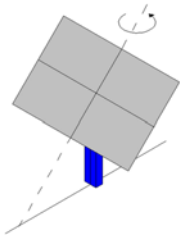
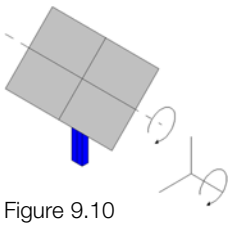
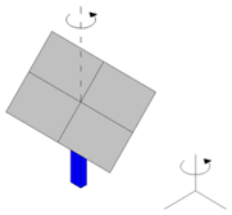
FIGURE 9.7

Characteristic vectors in a one-axis tracker.

Several types of one-axis tracking can be distinguished. These types (Figures 9.8–9.11) are shown in Table 9.2.

3.1.2.1.2 Two-Axis Trackers Using two-axis trackers, maximum energy collection can be achieved because, due to its total freedom of movement (north–south and east–west), the tracker can face the sun's rays throughout the day (Fig. 9.12).

Table 9.2 Types of One-Axis Tracking

North–South horizontal axis tracking The axis is horizontal and its direction is North–South and $\chi = 90$ degrees.	 Figure 9.8
Polar tracking: North–South polar axis tilted on an angle equal to the latitude of the site The rotation is adjusted in such a way that the tracker follows the meridian of the earth containing the sun. The angular velocity is 15 degrees/h. With this configuration, the solar tracker can be used both in northern latitudes and in places near the equator.	 Figure 9.9
East–West horizontal axis tracking In this configuration, the rotation axis is placed parallel to the ground and in an east–west direction. In this way, the panels can rotate only to follow the Sun at its altitude angle, correcting the position of the panels every day due to the Sun's declination. This configuration is not commonly used because the energy collected is much lower than that obtained with other configurations.	 Figure 9.10
Azimuthal axis tracking The tilting angle of the surface is constant and equal to the latitude of the site. The simple and robust mechanics of the azimuthal trackers can trade off the smaller collection of radiation with respect to the two axes trackers, making them the most widely used in practice.	 Figure 9.11

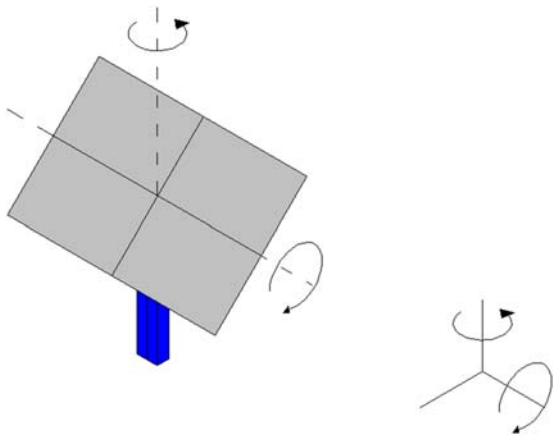


FIGURE 9.12

Characteristic movements in a two-axis tracker.

3.1.2.2 Driving Motor

Depending on the driving mechanism, solar trackers can be classified into active or passive solar trackers. Active driving mechanism can be based on electric motors (DC or AC) or hydraulic systems, whereas passive ones are based on gravitational systems.

The most common driving mechanism is an electric motor because it allows a simpler and precise control of the movement. AC electric motors are more widely used than DC ones. For one-axis trackers, only one motor is required, whereas for two-axis trackers, two motors are needed.

3.1.2.3 Solar Tracker Control

Depending on their control, solar trackers can be classified into solar tracking systems that orient the PV panels based on previously computed sun trajectories (open-loop control) and solar trackers that used a solar radiation sensor to control the orientation of the system (closed-loop control).

3.1.2.3.1 Feedback Controllers These controllers are based on the use of direct solar sensors to detect the position of the Sun. For this purpose, the sensors are composed of photosensitive elements mounted on the panel. Both at dawn and under low insolation conditions (cloudy days), the trackers controlled by photosensors may become disoriented. Therefore, it is essential to use an auxiliary tracking system, which controls the rotation of the motors until the orientation is restored again.

3.1.2.3.2 Open-Loop Controllers This control technique also uses a microprocessor, but it does not need any sensor to determine the position of the Sun. The movement of the Sun can be predicted using astronomic relationships, which are programmed in the microprocessor so that the microprocessor itself can calculate the Sun's position at any time. This type of control is not affected by cloudiness or other low radiation circumstances that may lead to errors in accuracy.

3.1.3 Other Types of Photovoltaic Array Arrangements

In intensive crop farms or greenhouses farms, the lack of space to lay the PV system is an important problem that must be faced because the price of land is usually high and most of the surface area is occupied by farm facilities such as greenhouses, reservoirs, warehouses, and irrigation facilities. The development of PV energy generation technology currently offers different alternatives to cope with this problem. Different research works have proposed mounting the PV cells on greenhouse rooftops. In this way, the excessive sunlight irradiating greenhouses could be used to produce both crops and energy (Fig. 9.13).

Several research works analyzing the effect of partial shading on crop yield [36–39] have pointed out that moderate partial shading does not have a significant effect on crop yield reduction. Kitta et al. [40] recommended a shading factor no higher than 20% for sweet pepper in Mediterranean climate conditions.

Different types of materials and technical solutions have been proposed to integrate solar-based energy generation systems into greenhouses, from conventional opaque flat hard or planar flexible PV modules with various arrangements (straight line and checkerboard) to semitransparent PV modules [41–47] (Fig. 9.14).

More recently, progress in PV cell technologies has provided new possibilities for solar cell applications. Biancardo et al. [48] developed a semitransparent PV module composed of spherical solar microcells, characterized by its small size and isotropic ability for photoreception. Yano et al. [49] subsequently tested the performance of this new type of PV System on a greenhouse. These studies showed that although conscientious design is necessary, it is possible to generate enough electricity for the control of greenhouse environment appliances using PV systems that are compatible with plant cultivation [41,44,45] (Fig. 9.15).

Another alternative is to cover the irrigation reservoirs with floating solar modules so that, in addition to producing solar energy, water losses from evaporation and algae formation in the water could be reduced (Fig. 9.16).

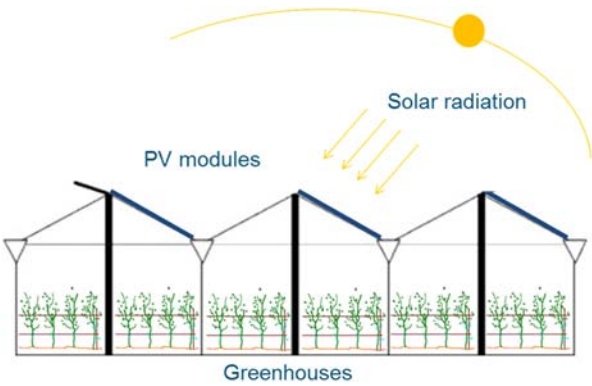


FIGURE 9.13

Photovoltaic (PV) generator on the greenhouse rooftops.

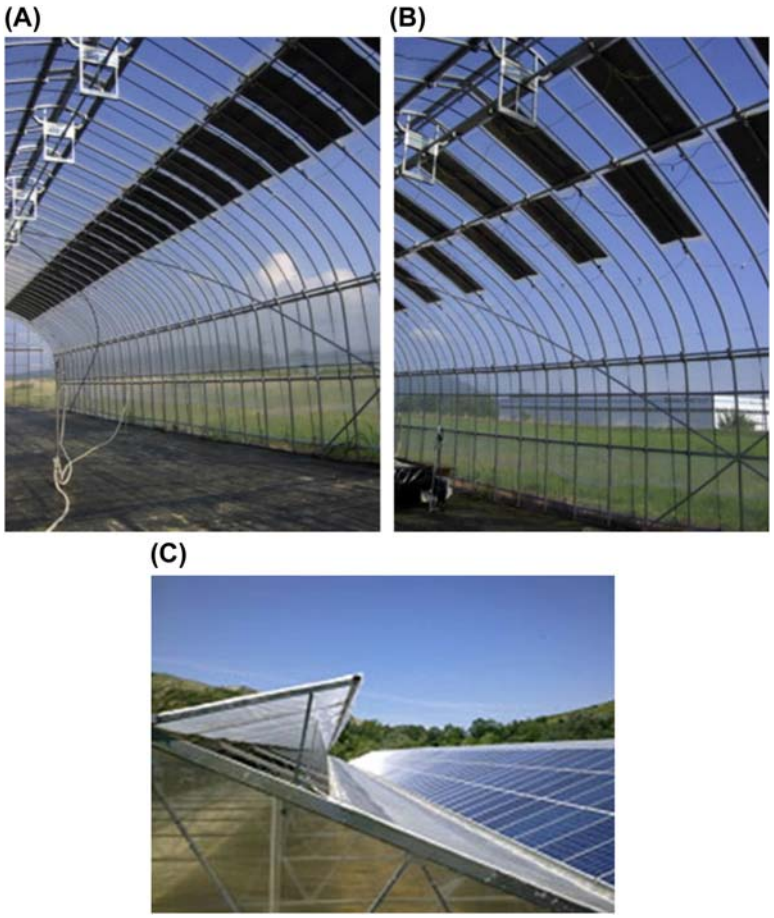


FIGURE 9.14

Opaque flexible PV modules mounted on a roof with straight-line (A) and chessboard (B) arrangements and opaque rigid module on zenithal ventilation windows (C).

Pictures taken from M. Pérez, J.A. Sánchez, Energías renovables en los inviernaderos, in: Innovación en Estructuras Productivas y Manejo de Cultivos en Agricultura Protegida, vol. 3, Cuadernos de Estudios Agroalimentarios, CAJAMAR. Almería (Spain), 2012, pp. 181–210. ISSN:2173-7568.

3.1.4 Inverter

The inverter is the electronic device intended to convert the DC supplied by the PV array into AC, which is generally used in most consumers' facilities (Fig. 9.17).

The main characteristic parameters of an inverter are the following:

- *Nominal voltage*: the voltage that should be applied to the input terminals of the inverter



FIGURE 9.15

Semitransparent photovoltaic modules mounted on the roof.

Pictures taken from M. Pérez, J.A. Sánchez, Energías renovables en los inviernaderos, in: Innovación en Estructuras Productivas y Manejo de Cultivos en Agricultura Protegida, vol. 3, Cuadernos de Estudios Agroalimentarios, CAJAMAR. Almería (Spain), 2012, pp. 181–210. ISSN:2173-7568.



FIGURE 9.16

Photovoltaic modules mounted on a floating structure and covering an agricultural reservoir.

Courtesy of Isigenere Renovables, http://www.renovables.isigenere.com/site/en.

- *Nominal power*: the power that can be supplied by the inverter in a continuous way
- *Overloading*: the ability of the inverter to deliver a power that is considerably higher than the nominal, as well as the time that this situation can be maintained
- *Distortion waveform*: the effective voltage and frequency of the output waveform
- *Efficiency*: the ratio, usually expressed as a percentage, between the output and the input powers. It is dependent on the loading conditions, that is, on the total power of the consumer devices



FIGURE 9.17

STP 10000 TL inverter. SMA Solar Technology source.

3.2 PHOTOVOLTAIC IRRIGATION SYSTEMS

Irrigation systems are usually composed of the following parts:

- A source of water: a reservoir, an uptake from a collective water distribution network or a well
- Water storage facilities, such as tanks or reservoirs
- A system head that comprises both the pumping system and other complementary equipment such as fertigation, filtration, and measurement and control devices
- An on-farm irrigation network that conveys the irrigation water to the emitters
- The irrigation application method. In PV irrigation, pressurized irrigation methods are commonly used, namely, sprinkler or drip irrigation

Most of the components of a PV irrigation system do not differ substantially, neither in their design, nor in their management, from those used in other conventional irrigation system. The design and management of any irrigation system depends on the type of crop and cropping techniques, climatic conditions, soils, water availability and quality, and other technical and socioeconomic constraints.

In this chapter, we are going to focus on those differential aspects that must be taken into consideration regarding the design and management of PV irrigation systems that are not connected to the grid.

3.2.1 Pumping System

Pumping systems are usually composed of one or more than one centrifugal pumps arranged in parallel. Early PV pumping systems used fixed speed pumps driven by electric motors, and their design and management was considerably simpler.

Today, to pump variable flowrates to different total heads efficiently, variable speed pumps are commonly used in these systems. Variable speed pumps are powered by an asynchronous motor and an electronic frequency converter that allows the pump to work under different angular velocities. The frequency converter can be considered as an inverter that is able to modulate the output signal to the desired frequency and amplitude.

Because the power supplied by the PV array is variable throughout the day depending on the incoming radiation, the power required by the pump can be modified by modifying the angular velocity of the pump to match the incoming power.

To select the most appropriate pump for a specific application, the performance curves (Discharge-Head-Efficiency) of the pump provided by the manufacturer and the affinity laws that relate the shaft power, P, the head (H), and the discharge, Q, provided by the pump to its rotation speed (n) are required.

By simultaneously applying the affinity laws (Eq. 9.9) to an operating point, H_1-Q_1, belonging to the Discharge-Head curve of a pump working at a specific pump speed ($N1$), the new operating point, H_2-Q_2, of that pump at another specific velocity ($N2$) can be calculated. The efficiency of the pump is assumed to be constant in these two homologous operating points.

$$\frac{Q_2}{Q_1} = \frac{N_2}{N_1}\frac{H_2}{H_1} = \frac{N_2^2}{N_1^2}\frac{P_2}{P_1} = \frac{N_2^3}{N_1^3}\frac{\eta_2}{\eta_1} = 1 \tag{9.9}$$

where subscripts 1 and 2 refer to two different rotation speeds.

Considering that the rotational speed of the pump is proportional to the frequency of electric current, affinity laws can be expressed as a function of the frequency rather than the speed of the pump.

$$\frac{Q_2}{Q_1} = \frac{f_2}{f_1}\frac{H_2}{H_1} = \frac{f_2^2}{f_1^2}\frac{P_2}{P_1} = \frac{f_2^3}{f_1^3}\frac{\eta_2}{\eta_1} = 1 \tag{9.10}$$

Assuming that the H_0-Q_0 performance curve of a commercial pump is given by the manufacturer at a nominal AC frequency (f_0) (which in EU countries is 50 Hz), the generalized H-Q performance curve of the pump for any other frequency, f, can be obtained from the nominal H_0-Q_0 curve by applying the affinity laws. The generalized H-Q equation is given in Eq. (9.11) and the resulting H-Q curves are depicted in Fig. 9.18.

$$H = A\left(\frac{f}{f_o}\right) - BQ^2 \tag{9.11}$$

3.2.2 On-Farm Irrigation Network

To calculate the operating point (discharge and head) of the PV irrigation system as a function of the power supplied by the PV plant, not only the Head-Discharge of the

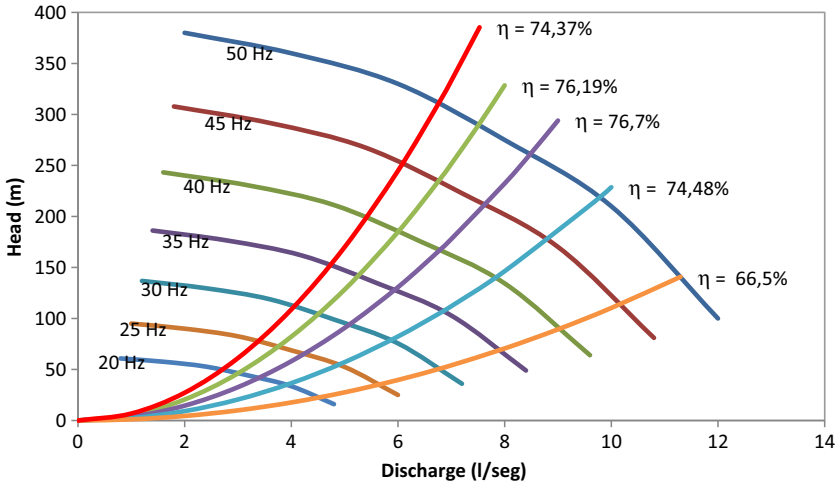


FIGURE 9.18

Head-Discharge performance curves for different AC frequencies and isoefficiency curves for a commercial pump.

pump but also the irrigation network system curve must be known. Two different cases can be distinguished depending on the type of irrigation system.

3.2.2.1 Pumping to an Elevated Tank

There are some irrigation systems in which water is lifted, generally drawn from a deep well, to an elevated tank. If the elevation of this tank is high enough, water can then be distributed to the irrigation network by gravity with the required pressure, and there is no need to pump the water again.

When pumping to an elevated tank, obtaining the system curve is a straightforward task. The total energy head (H), which should be provided by the pump to supply a discharge Q, can be calculated by the following expression:

$$H = \Delta z + hf \tag{9.12}$$

where Δz is the static head, that is, the elevation difference between the groundwater level in the well and the water level in the elevated tank, and hf is the friction head, or the head losses throughout the discharge pipe system. If there are no substantial groundwater level changes, the static head can be considered constant in this type of system.

The friction losses are a function of the discharge using an appropriate head loss equation, such as the Darcy−Weisbach equation. The relationship between the friction losses and the discharge using a generic head loss equation is given in Eq. (9.13).

$$hf = R_s \cdot Q^m \tag{9.13}$$

where R_s is the resistance coefficient of the discharge pipe, Q is the total discharge of the pumping system, and m is the hydraulic exponent of the head loss equation. Assuming that the flow regime is turbulent, it can be supposed that m is equal to 2 (Eq. 9.13). In this equation, the resistance coefficient, R_s, should include not only the uniformly distributed losses in the pipe but also the local or minor head losses.

Finally, the *system curve* is given in the following equation.

$$H = \Delta z + R_s Q^2 \tag{9.14}$$

The shaft power supplied to the pump, P, can be calculated as a function of the PV power, P_{PV}, provided by the PV array.

$$P = P_{\mathrm{PV}} \cdot \eta_M \cdot \eta_C \tag{9.15}$$

where η_M and η_C are the efficiencies of the electric motor and the frequency converter, respectively.

The shaft power can also be expressed as a function of the net power transferred by the pump to the water, which depends on the head, the discharge supplied by the pump, and the pump efficiency, η_P (Eq. 9.16).

$$P = P_{\mathrm{PV}} \cdot \eta_M \cdot \eta_C = \gamma \cdot Q \cdot H / \eta_P \tag{9.16}$$

where γ is the specific weight of the water.

Finally, solving the set of three equations made up by the generalized H-Q curve of the pump (Eq. 9.11), the system curve (Eq. 9.14), and the power supplied by the PV array (Eq. 9.16), the three unknown variables required to control the pumping system can be calculated. These required variables are the output frequency of the AC provided by the inverter (f), the discharge (Q) lifted by the pump when working at this specific frequency, and the head (H) supplied by the pump in these working conditions.

3.2.2.2 Direct Pumping

The simplest and most widely used procedure to control PV irrigation and match renewable energy production to crop irrigation demand is to pump water to an elevated storage tank and then distribute it to the plants by gravity. However, in some cases, farms may be relatively flat, so perhaps no appropriate location is available to build a tank with sufficient elevation to take advantage of the gravitational energy to distribute irrigation water. In any case, the construction costs must be taken into account. To overcome these drawbacks, direct pumping PV irrigation systems can be used.

Regarding the type of the emitters in drip irrigation systems, two different groups of emitters can be distinguished. Noncompensating emitters vary their discharge according to the operating pressure. The inconvenience of noncompensating emitters is that they may produce low irrigation uniformity when pressure variability in the irrigation sector is high. To avoid this drawback, compensating emitters are used that keep the discharge constant regardless of their working pressure. In these cases, the

total flow in the irrigation sector is constant as well and can be calculated by multiplying the emitter discharge by the number of emitters per sector. In the case of compensating emitters, the system curve is $Q = \text{constant}$, and the discharge does not vary even though the pump speed is changed. To overcome these limitations, different procedures to regulate flow as a function of the incoming power have been suggested. The first procedure is based on using variable speed pumps and non-compensating emitters that vary their discharge depending on the pressure. The second procedure is based on subdividing the farm into smaller-sized irrigation sectors and irrigating a variable number of sectors depending on the power supplied by the PV system. With these two configurations, the discharge of the irrigation system can be varied to adjust the power consumed by the irrigation system to the power produced by the PV array. Both procedures can also be applied at the same time (Fig. 9.19).

The irrigation distribution system is composed of a pumping system that boosts water directly into the irrigation distribution network. In this case, obtaining the system curve and controlling the PV irrigation system can be a complex task because the system curve depends on the network layout and sizing, the type and discharge of the emitters, and the number and size of the irrigation sectors. A hydraulic simulation of the irrigation network would be required to accurately derive the system curve for every possible network configuration.

The authors propose a simplified generic representation of the water distribution network to estimate the system curve with sufficient accuracy. The total head (H)

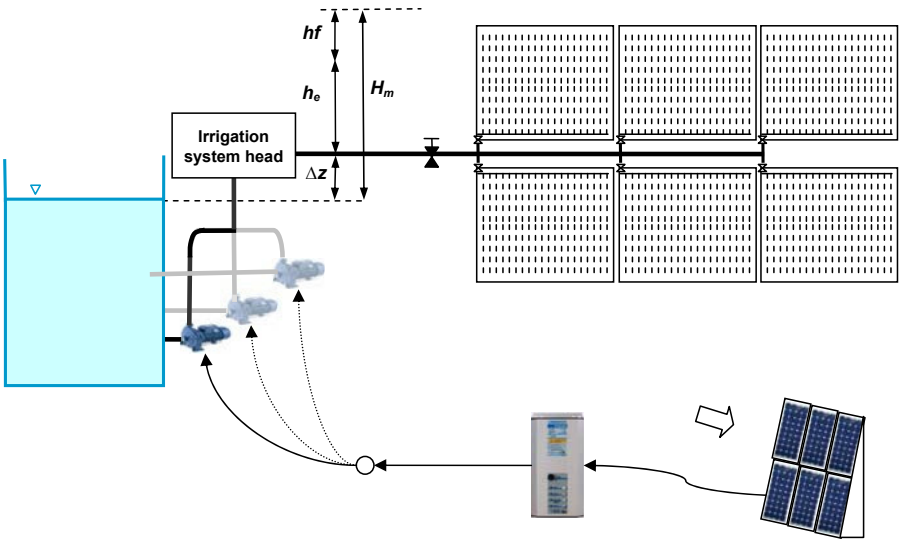


FIGURE 9.19

Scheme of a photovoltaic direct pumping system with six sectors and several pumps in parallel [24].

required by the distribution system to supply a discharge Q can be decomposed into the following components:

$$H = \Delta z + hf + h \tag{9.17}$$

where Δz is a constant value that represents the elevation change from the reservoir to the most restricted point in the irrigation subunits (in meters), *hf* is the estimated head losses in the network path between the head of the system and the most restricted point (in meters), and h is the average pressure head of the emitters of the system (in meters). If the system is composed of several heterogeneous irrigation subunits, a different system curve should be calculated for each irrigation subunit. If the irrigation subunits are relatively homogeneous, the system curve can be valid for all of them. Head losses in this simplified system scheme will able to be calculated by using a general head loss equation as a function of the pump discharge, as explained in Eq. (9.13).

The discharge in a noncompensating emitter varies according to its working pressure. The relationship between these two variables is given by the discharge equation of the emitter [50]:

$$q = k\ h^x \tag{9.18}$$

where k is the emitter discharge coefficient, which is a constant dependent on the unit system used, h is the working pressure head at the emitter (in meters), x is the emitter discharge exponent (nondimensional), and q is the discharge of the emitter. Conventional labyrinth-type emitters usually work in a turbulent regime; therefore the value of their exponent is close to 0.5. In the simplified irrigation scheme proposed, an average h value is considered and the hydraulic variability in the irrigation unit is neglected.

The total discharge in the irrigation system can be calculated by multiplying the number of emitters in operation by their average discharge, which can be calculated with Eq. (9.19).

$$Q = q \cdot n_e = n_e \cdot k \cdot h^x \tag{9.19}$$

Solving for the pressure head in Eq. (9.19), the average pressure at the emitters can be expressed as a function of the total discharge of the system.

$$h = \left(\frac{1}{n_e\ k}\right)^2 Q^2 = K \cdot Q^2 \tag{9.20}$$

And finally, substituting h in Eq. (9.17), the following equation for the system curve can be derived:

$$H = \Delta z + (R_s + K) \cdot Q^2 \tag{9.21}$$

Having identified the system curve (Eq. 9.21), the generalized *H-Q* performance curve of the pump (Eq. 9.11), and the incoming power for the PV plant (Eq. 9.16), the output frequency of the converter and the head and discharge of the pumping

system can be calculated following a procedure similar to that explained in the previous section.

However, in some direct pumping systems on flat farms, when the source of water is superficial, the elevation difference term Δz may be low in comparison with the variable term in Eq. (9.21), which includes both the head losses in the system and the pressure of the emitters. In this case, the authors demonstrated that the operating point follows an isoefficiency curve and can be approximated by applying the affinity laws.

The working point for the maximum speed of the pump ($f = f_o$) can be obtained from the intersection of the nominal H-Q performance curve and the system curve. Once this nominal operating point (Q_M, H_M) is known, the new frequency of the converter and the new operating point for any other value of shaft power provided by the PV array can be calculated by applying the following affinity laws:

$$Q = Q_M \left(\frac{P}{P_M}\right)^{1/3} \tag{9.22}$$

$$f = f_o \left(\frac{Q}{Q_M}\right) \tag{9.23}$$

$$H = H_M \left(\frac{f}{fo}\right) \tag{9.24}$$

In this system, the maximum flow supplied by the pumping system working at its maximum speed is Q_M and the power required in this situation is P_M. The minimum power required to start the irrigation operation depends on the allowable working pressure of the emitters. Let r_h be the ratio of the minimum working pressure of the emitter (h_m) to the maximum one (h_M). Applying the affinity law, the relationship between the maximum power (P_M) and the minimum (P_m) is the following:

$$\frac{P_m}{P_M} = \left(\frac{H_m}{H_M}\right)^{3/2} = {r_h}^{3/2} \tag{9.25}$$

For shaft power provided by the PV system lower than P_m, the irrigation system has to be stopped because the pressure of the emitters would be lower than their minimum working pressure.

The set of equations governing the irrigation system for a unique irrigation sector is the following:

$$\left.\begin{array}{ll} \text{a)} & \text{If } P < P_m = \dfrac{P_M}{{r_h}^{3/2}} \Rightarrow Q = 0 \\ \text{b)} & \text{If } P_m \le P \le P_M \Rightarrow Q = Q_M \left(\dfrac{P}{P_M}\right)^{1/3} \\ \text{c)} & \text{If } P > P_M \Rightarrow Q = Q_M \end{array}\right\} \tag{9.26}$$

Another complementary way to regulate the system and to optimize the use of the generated energy for irrigating the crop is to design more than one irrigation sector. When the farm is divided into a number of sectors (n_s) greater than 1, the discharge and power needed to irrigate each sector can be obtained by dividing the maximum discharge and the maximum power by n_s.

In this case, the system can start irrigating with a shaft power that is n_s times lower than when only one sector is considered. Two different strategies can be applied in this type of system:

1. To irrigate with only one irrigation sector in operation
2. To irrigate with multiple irrigation sectors in operation simultaneously

In the first scenario, only one pump is required as the same pump would be used to irrigate all the irrigation sectors. In the second scenario, the number of pumps would have to be equal to the number of sectors that are irrigated simultaneously.

Generalizing, when a number "n_j" of sectors out of n_s are operating simultaneously, the net power generated by the PV system (P) must be distributed among the n_j pumps in operation ($P_i = P/n_j$). Thus, the total discharge of the system is represented by Eq. (9.27):

$$\left.\begin{array}{ll} \text{a)} & \text{If } \dfrac{P}{n_j} < \dfrac{P_m}{n_s} \Rightarrow Q_i = 0 \\ \text{b)} & \text{If } \dfrac{P_m}{n_s} \le \dfrac{P}{n_j} \le \dfrac{P_M}{n_s} \Rightarrow Q_i = n_j \dfrac{Q_M}{n_s} \left(\dfrac{P_i}{n_j} \dfrac{n_s}{P_M} \right)^{1/3} \\ \text{c)} & \text{If } \dfrac{P}{n_j} > \dfrac{P_M}{n_s} \Rightarrow Q_i = \dfrac{Q_M}{n_s} \cdot n_j \end{array}\right\} \tag{9.27}$$

For the sake of illustration, Fig. 9.20 depicts the discharge of the pumping system as a function of the incoming power for an irrigation system composed of a total of four sectors. In this example, the type of greenhouse farm considered was 1 ha in size, using emitters with a discharge equal to 3 L/h and 2 emitters/m^2, which is a very common arrangement in greenhouse irrigation systems in the south of Spain. This results in a total discharge per hectare (Q_M) equal to 60,000 L/h or 16.67 L/s. The total head (H_M) assumed for this maximum discharge is 40 m (including the three terms in Eq. 8). The pumping efficiency has been considered equal to 0.75. The maximum power (P_M) per hectare proves to be equal to 8720 W. It was supposed that the ratio between minimum and maximum working pressure of the emitter was equal to 1/4 (5/20 m/m). Applying affinity laws in Eq. (9.19), the minimum power required per hectare (P_m) is found to be equal to one-eighth of the maximum power (P_M/8). With these data, and applying Eq. (9.22), the discharge has been calculated for a number of sectors in operation ranging from 1 to 4.

Dashed lines represent the variation of the discharge of the system as a function of the incoming power when only one, two, three, or all four sectors are in operation.

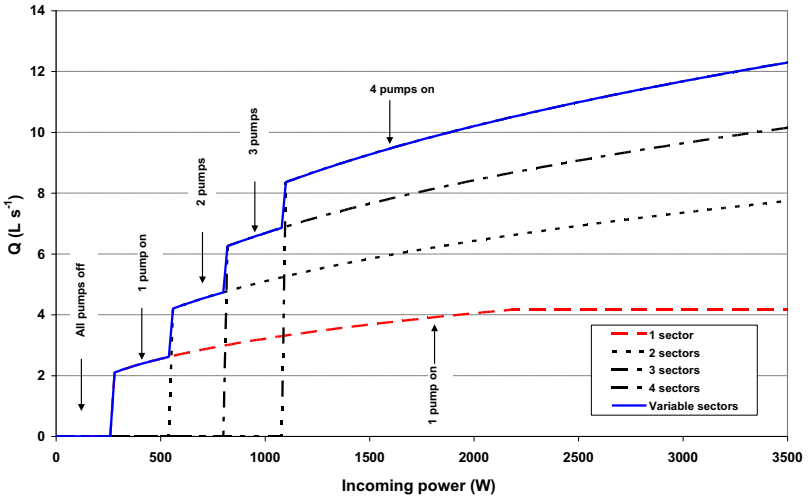


FIGURE 9.20

Discharge—power diagram for a PV irrigation system composed of a total of four sectors [24].

Continuous lines indicate the operational strategy to maximize the discharge of the system for every generated power value.

4. MODELING AND SIMULATION OF PHOTOVOLTAIC IRRIGATION SYSTEM

4.1 EARTH—SUN GEOMETRY AND SOLAR RADIATION MODELING

Rotational movement is what makes the earth turn on a rotation axis that passes through its poles. A complete revolution lasts 23 h, 56 min, and 4 s and is called sidereal day. In addition to the rotation, the planet Earth rotates around the Sun following an orbit in a movement that is called translation movement. It takes the Earth 365 days and 6 h to perform a complete rotation around the Sun. Accumulating these 6 h a year, it is entailed that, every 4 years, the Earth takes an additional complete day. Taking the Sun as a reference, the so-called tropic year is the period necessary for the repetition of the seasons of the year. This tropic year lasts 365 days, 5 h, 48 min, and 45 s. The orbit of the Earth around the sun is elliptical.

4.1.1 Solar Position

The position of an observer located on the Earth's surface will be given by its geographical coordinates, namely, Latitude and Longitude. The position of the

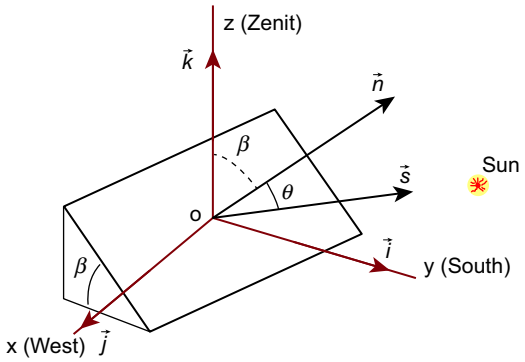


FIGURE 9.21

Terrestrial coordinate system.

sun with respect to an observer located on the Earth's surface is given by the following position vector:

$$\vec{s} = \begin{cases} (\text{sen}\ \Omega\, t \cdot \cos\delta)\ \vec{i} \\ (\cos\Omega\, t \cdot \cos\delta * \text{sen}\ L - \text{sen}\ \delta \cdot \cos L)\ \vec{j} \\ (\cos\Omega\, t \cdot \cos\delta * \cos L + \text{sen}\ \delta \cdot \text{sen}\ L)\ \vec{k} \end{cases} \tag{9.28}$$

Eq. (9.28) is referenced to a Cartesian reference system whose OXY plane is the horizontal plane; therefore the Oz axis will be normal to the earth and will coincide with the zenith; the Oy axis is oriented to the south, whereas the Ox axis points west, as illustrated in Fig. 9.21. Eq. (9.28) is the expression of the unitary solar position vector $\vec{s}$, which points directly to the Sun.

The orientation of this vector depends on the solar declination (δ), the latitude (L), the angular velocity of the Earth (Ω), and the solar time (t).

4.1.2 Angle of Incidence of the Solar Rays With Respect to the Photovoltaic Modules

To know the angle of incidence of the solar rays with respect to the PV modules surface, the unit vector, $\vec{n}$, perpendicular to the surface is used. This vector depends on the angles γ (azimuthal orientation of the surface) and β (inclination of the PV modules) (Fig. 9.22).

$$\vec{n} = \begin{cases} (-\text{sen}\ \beta \cdot \text{sen}\ \gamma)\ \vec{i} \\ (\text{sen}\ \beta \cdot \cos\gamma)\ \vec{j} \\ (\cos\beta)\ \vec{k} \end{cases} \tag{9.29}$$

The scalar product between the solar vector $\left(\vec{s}\right)$ and the unit vector of the modules $\left(\vec{n}\right)$ is directly related to the solar angle of incidence (Fig. 9.23).

$$\cos\theta = \vec{s} \cdot \vec{n} \tag{9.30}$$

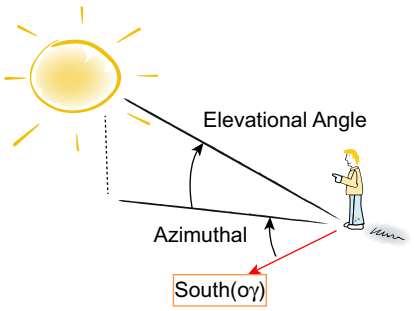


FIGURE 9.22

Azimuthal and elevation angles.

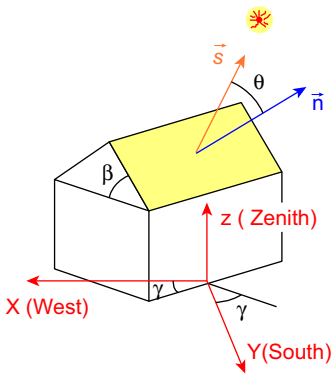


FIGURE 9.23

Incidence angle of solar rays over a plane.

4.1.3 Solar Irradiance Components

The incoming solar radiation on a terrestrial surface is the sum of three different components, namely, direct, diffuse, and reflected radiation. The actual percentage of each of these components varies depending on the weather, location, and other atmospheric conditions (Fig. 9.24):

- Beam irradiance: Comes directly from the Sun.
- Diffuse irradiance: Received from the atmosphere as a consequence of the diffusion of a fraction of the global solar radiation. This energy accounts for about 15% of the global radiation on clear sunny days. However, on cloudy days, radiation is dispersed by the clouds and therefore direct radiation percentage is very low, whereas diffuse radiation accounts for a much higher percentage.

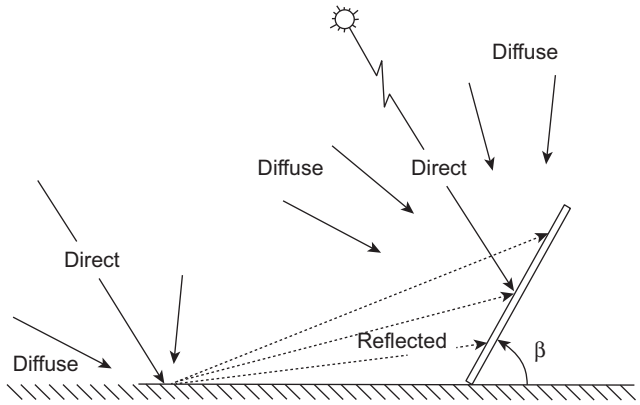


FIGURE 9.24

Solar radiation components.

- Reflected irradiance: Reflected by the earth's surface. The amount of reflected radiation depends on the reflection coefficient of the surface, also termed albedo.

However, these solar radiation components are not usually known when designing a PV project; therefore it is necessary to estimate them using commonly available data, namely, global daily surface radiation, H, which is the incoming radiant energy per square meter throughout a whole day. Fig. 9.25 shows the evolution of H in the city of Cordoba (Spain) throughout the year.

The Clarity Index (K_t) is the ratio between the measured global daily radiation (H) at a specific location and the maximum or extraterrestrial radiation (H_o) that

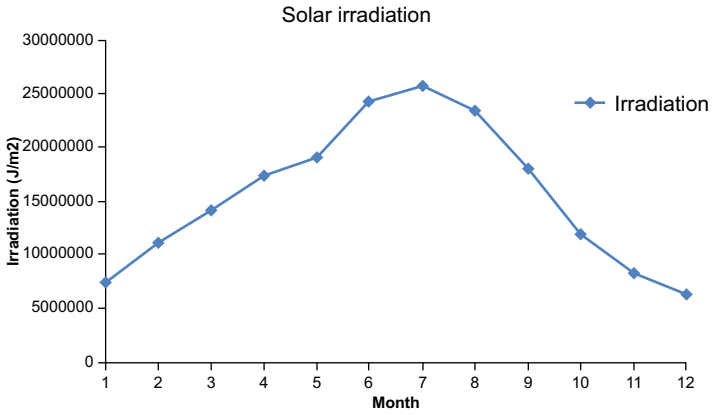


FIGURE 9.25

Monthly Mean irradiation measured in Cordoba (Spain).

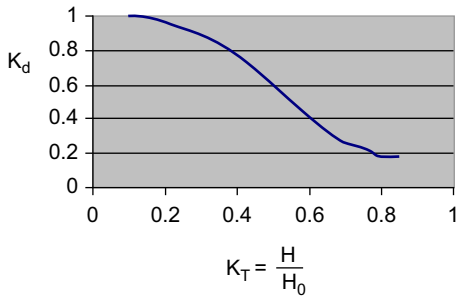


FIGURE 9.26

K_d versus K_T relationship.

could reach that location if there was no atmosphere (Eq. 9.31). K_t measures the transparency of the atmosphere and constitutes the basis of most methods for estimating radiation on inclined surfaces.

$$K_T = \frac{H}{H_o} \tag{9.31}$$

The fraction of diffuse radiation, K_d, can be calculated from the K_t fraction using the relationships proposed by Erbs et al. O Collares-Pereira depicted in Fig. 9.26.

The direct and diffuse components of radiation can be estimated by applying Eqs. (9.32) and (9.33).

$$H_b = (1 - K_d\ )H \tag{9.32}$$

$$H_d = K_d\, H \tag{9.33}$$

The Collares-Pereira and Rabl formula is used to disaggregate the daily global irradiation into hourly values (Eqs. 9.34–9.36).

$$r = \frac{\pi}{24}(a + b\cos\omega)\left(\frac{\cos\omega - \cos\omega_S}{\sin\omega_S - \omega_S\cos\omega_S}\right) \tag{9.34}$$

$$a = 0.409 + 0.516\sin\left(\omega_S - \frac{\pi}{3}\right) \tag{9.35}$$

$$a = 0.6609 - 0.4767\sin\left(\omega_S - \frac{\pi}{3}\right) \tag{9.36}$$

And for the diffuse irradiance, the equation by Liu and Jordan is used:

$$a = 0.409 + 0.516\sin\left(\omega_S - \frac{\pi}{3}\right) \tag{9.37}$$

Therefore, the instantaneous global irradiance (sum of direct and diffuse) is given by the following equation:

$$I = (I_b + I_d) = rH \tag{9.38}$$

where the diffuse and direct components are:

$$I_d = r_d H_d \tag{9.39}$$

$$I_b = (rH - r_d H_d) \tag{9.40}$$

4.1.3.1 Irradiance on a Fixed or Tracked Collector Plane

To calculate the irradiance on a collector plane, direct, diffuse, and global irradiance must be calculated on a horizontal surface every short period of time on a characteristic day of each month. The following input parameters must be defined to perform these calculations: Julian day, latitude, irradiation (H), and timer. The global irradiance in a horizontal plane is the sum of direct irradiance and diffuse irradiance:

Then, both the direct and diffuse irradiance on the tilted PV modules must be calculated taking into account both the unit solar vector $\left(\overrightarrow{s}\right)$ and the unit vector of the collector plane $(\overline{n})$.

- *Direct irradiance received by the modules* $\left(I_{b\beta}\right)$: The most widely accepted approach for estimating the direct daily radiation on a sloped surface considers the geometric position of the Sun and the collector and is based on the hypothesis of proportionality between the fractions of direct and extraterrestrial radiation.

$$I_{b\beta} = I_b \cdot \frac{\cos\theta}{\cos\theta_Z} \tag{9.41}$$

- *Diffuse irradiance received by the modules* $\left(I_{d\beta}\right)$: The estimation of this parameter is based on the isotropic model, which assumes that the distribution of the diffuse radiation is independent of the azimuth and the zenith angle; therefore radiation from any point in the celestial hemisphere has the same intensity.

$$I_{d\beta} = I_d\left(\frac{1+\cos\beta}{2}\right) \tag{9.42}$$

- *Reflected irradiance received by the modules* $\left(I_{r\beta}\right)$: It is usually assumed that the terrain behaves as a horizontal and infinite surface that reflects radiation in an isotropic way.

$$I_{r\beta} = (I_d + I_b)\cdot\rho\cdot\left(\frac{1-\cos\beta}{2}\right) \tag{9.43}$$

  where ρ is the albedo of the ground, which is highly variable and depends on the soil type. A constant value ($\rho = 0.2$) is supposed in many works.
- Total irradiance received by the modules (I_β): It is the sum of the three radiation components:

$$I_\beta = I_{b\beta} + I_{d\beta} + I_{r\beta} \tag{9.44}$$

The total irradiance on a sloped plane is then given by the following equation:

$$I_\beta = I_b \cdot \frac{\cos\theta}{\cos\theta_z} + I_d\left(\frac{1+\cos\beta}{2}\right) + (I_d + I_b)\cdot\rho\cdot\left(\frac{1-\cos\beta}{2}\right) \tag{9.45}$$

Considering that the position of the PV array at a specific moment is described by the vector $\vec{n}$, normal to the collector plane:

$$\cos\theta = \vec{n}\cdot\vec{s} \tag{9.46}$$

$$\cos\beta = \vec{n}\cdot\vec{k} \tag{9.47}$$

The equation for estimating the irradiance is:

$$I_\beta = I_b \cdot \frac{\vec{n}\cdot\vec{s}}{\cos\theta_z} + I_d\left(\frac{1+\vec{n}\cdot\vec{k}}{2}\right) + (I_d + I_b)\cdot\rho\cdot\left(\frac{1-\vec{n}\cdot\vec{k}}{2}\right) \tag{9.48}$$

If the PV array is mounted on a one-axis tracker, vector $\vec{n}$ moves and, in this case, its instantaneous expression is given by Eq. (9.49).

$$\vec{n} = \left(\cos\chi - \sin\chi\sqrt{\frac{(\vec{e}\cdot\vec{s})^2}{1-(\vec{e}\cdot\vec{s})^2}}\right)\vec{e} + \left(\sin\chi\sqrt{\frac{1}{1-(\vec{e}\cdot\vec{s})^2}}\right)\vec{s} \tag{9.49}$$

where the $\vec{e}$ and χ values depend on the type of tracking, as shown in Table 9.3.

For a two-axis tracker:

$$\vec{n} = \vec{s} \tag{9.50}$$

4.1.4 Power Calculations

The main objective of a PV installation is to produce the power required by the pumps to lift or inject the water into the irrigation system.

4.1.4.1 Electric Power Generated by the Photovoltaic Modules

This power can be calculated by applying the following equation:

$$P_{\mathrm{PV}} = \frac{I_\beta \cdot \mathrm{PP}}{1000} \tag{9.51}$$

Table 9.3 $\vec{e}$ and χ for Different Types of One-Axis Tracking

Tracking Type	$\vec{e}$	χ
Vertical axis	$0\vec{i} + 0\vec{j} + 1\vec{k}$	β
E–W horizontal axis	$1\vec{i} + 0\vec{j} + 0\vec{k}$	$\pi/2$
N–S horizontal axis	$0\vec{i} + 1\vec{j} + 0\vec{k}$	$\pi/2$
N–S inclined axis	$0\vec{i} - \sin\tau\vec{j} + \cos\tau\vec{k}$	$\pi/2$
Polar	$0\vec{i} - \sin\varphi\vec{j} + \cos\varphi\vec{k}$	$\pi/2$

where I_β is the total irradiance over the inclined plane where the PV modules are arranged and PP is the peak power of the PV system. With the equations discussed in this chapter, this parameter can be calculated at different times of the year.

4.1.4.2 Power Transmitted to the Pump Shaft

The shaft power supplied to the pump, P, can be calculated as a function of the PV power, $P_{PV,}$ provided by the PV array by applying Eq. (9.52).

$$P = P_{PV} \cdot \eta_M \cdot \eta_C \tag{9.52}$$

where η_C is the efficiency of the converter. This value is higher than 0.95 for most commercial converters. η_M is the efficiency of the asynchronous motor, and this efficiency increases as the frequency of the electrical current diminishes. A constant value of 0.8 can be used as a conservative criterion.

4.1.4.3 Net Power Transmitted to the Water Flow

The power transferred to the water flow can be calculated by multiplying the shaft power by the pump efficiency, η_P.

$$P_u = \gamma \cdot Q \cdot H = P/\eta_P \tag{9.53}$$

where γ is the specific weight of the water.

5. DESIGN OF PHOTOVOLTAIC IRRIGATION SYSTEMS

The procedure recommended by the authors to the design and size the PV irrigation system is based on performing a simulation of the system performance. This simulation is based on the equations that describe both the PV generation subsystem and the irrigation subsystem that have been discussed in this chapter. The following stages in the design process should be considered.

First of all, the study period must be defined. This study period may be a whole year or the period in which the PV is going to operate (cropping cycle). The study period should be disaggregated into shorter periods (weeks, months) for which the invariance of the main variables of the system, such as irradiance, solar position, irrigation requirements, etc., will be assumed. The shorter the selected period, the more precise the simulation will be. A simulation of the system is then performed for a representative day within this period (for example, the middle of the period). This simulation includes the following stages:

1. **Input data and initialization of the design variables.** The first stage in the design process is to initialize the parameters and variables required in the simulation of the PV irrigation system:
   - Type of PV plant and initial PP
   - Type of irrigation system: number of pumps and performance curve of the pumps, total area to irrigate, number of irrigation sectors, type and discharge of the emitters, crops, etc.

- Economic data: installation costs of the PV and irrigation equipment, price of energy and products, discount rate and useful life of the system, etc.

2. **Simulation of the energy received and power supplied by the PV array**:
   - Determination of direct, diffuse, and global irradiance on the horizontal plane.
   - Determination of the three components of the solar vector ($\vec{s}$) for every period.
   - Determination of the three components of the normal vector to the collector plane ($\vec{n}$), applying the right equation depending on whether it is fixed or not.
   - Calculation of the PV power produced by the PV array and the shaft power transferred to the pumps by the electric motor.
3. **Calculation of the operating point of the pumping system.** This depends on the type of irrigation system: pumping to an elevated tank or direct irrigation. In the latter case, the use of noncompensating emitters, the number of irrigation sectors, and the number of sectors in operation have to be considered. In this stage, the frequency of the AC, the discharge, and head of the pumping system are determined.
4. **Calculation of the irrigation water requirements.** This is to estimate the irrigation application time and the volume of water that has to be pumped by the pumping system. The irrigation water requirements depend on many factors, such as the weather conditions of the area, the type of crop and cropping systems, and the efficiency of the irrigation system. The FAO approach [51] has been widely used worldwide to calculate these crop water requirements because of its good level of precision and ease of use. According to this methodology, crop evapotranspiration (ET_c) is calculated by the following equation:

$$ET_c = ET_o \times K_c \tag{9.54}$$

   where ET_o is the reference evapotranspiration for a standardized crop whose canopy characteristics do not change. ET_o depends on climate conditions. K_c is the crop coefficient, which is the ratio between the evapotranspiration of a specific crop and the evapotranspiration of the reference crops. ET_o can be calculated using the Penman–Monteith equation [51]. Appropriate values for the K_c must be chosen depending on the type of crop. Calculating the irrigation water needs is a complex task; therefore consulting specific literature on this issue is recommended for this purpose.

5. **Establishing a water and energy balance.** Both water and energy balances can be established. As a result, the total volume of irrigation water pumped by the pumping system and the total energy consumed can be calculated.

6. **Calculation of technical and economic performance of the system.** From the water and energy balance results, performance indicators of the system can be calculated. These performance indicators allow the technical and economic evaluation of the designed system. Technical indicators include the efficiency of water and energy use, that is, the fraction of the irrigation needs that have been satisfied and the fraction of the produced energy that has been used. Economic indicators, such as the net present value (NPV), payback period, profitability index, or internal rate of return are useful to evaluate the economic profitability of the designed system.
7. **Repeating the simulation process for other PP values and other design parameters.** Once the complete simulation (steps 1 to 6) of the system has been performed for one set of parameters, the process must be repeated by changing the set of input parameters. The main variable that must be considered to optimize the PV irrigation system is the PP of the PV plant. To perform the required iterations quickly, a computer simulation program must be developed. The authors have developed a software program on an Excel spreadsheet to automate the process.

For the sake of illustration of the procedure discussed in this section, Table 9.4 shows the results of a daily simulation of a simple PV pumping system consisting of a fixed speed pump that lifts water to a tank. In this example, 3-min periods are considered and the water pump is put into operation when the produced PV power is higher than a threshold power that is required to lift the water to the tank.

Using this procedure, the authors have optimized and assessed the profitability of different types of more complex PV irrigation systems. They applied this methodology to an olive orchard farm [22] and to a greenhouse farm for growing vegetables in the south of Spain [24].

In the first case, the authors proposed combining the methodology discussed in this section together with a deficit irrigation approach. This new approach to PV irrigation design, termed Photovoltaic Opportunity Irrigation, proved to be very efficient both from a technical and economic point of view as it improved the efficiency of irrigation water, the indices of energy used, and the NPV of the system. The results found in this work show that significant reductions in the PP of the PV system could be achieved by using the proposed methodology. The economically optimal designs provided by the model were not achieved for a complete irrigation of the crop but for a deficit one. This implied that not only a reduction in the investment costs of the PV system but also some water savings (from 4% to 6% in the study case), which is very important in areas with water scarcity.

In the second case, the authors concluded that stand-alone direct pumping irrigation systems were a technical and economically feasible alternative to irrigate greenhouse crops, provided that an appropriate design of the irrigation system was carried out. Particularly, the number of irrigation sectors was a variable that significantly affected the system profitability.

Table 9.4 Daily Simulation of a Photovoltaic Pumping System Composed of a Fixed Pump and a Tank

HORA	Irrad. directa (W/m²)	Irrad. difusa (W/m²)	Irrad. global (W/m²)	Vector solar (x)	Vector solar (y)	Vector solar (z)	PS * n	Corrección PS * n	Corrección Vector solar (z)	Irrad. Directa beta (W/m²)	Irrad. Difusa beta (W/m²)	Irrad. Refleja da beta (W/m²)	Irradiancia global beta (W/m²)	Pot. 1 (W)	Pot. 2 (W)	¿Existe bombeo?	Minutos bombeo al dia
–12.00	0.00	0.00	0.00	0.00	–0.29	–0.96	–0.97	0.00	0.00	0.00	0.00	0.00	0.00	0.00	0.00	0.00	0.00
–11.65	0.00	0.00	0.00	–0.09	–0.29	–0.95	–0.97	0.00	0.00	0.00	0.00	0.00	0.00	0.00	0.00	0.00	m3 riego al me s
–11.30	0.00	0.00	0.00	–0.17	–0.28	–0.95	–0.96	0.00	0.00	0.00	0.00	0.00	0.00	0.00	0.00	0.00	
–10.95	0.00	0.00	0.00	–0.25	–0.27	–0.93	–0.94	0.00	0.00	0.00	0.00	0.00	0.00	0.00	0.00	0.00	
–10.60	0.00	0.00	0.00	–0.33	–0.25	–0.91	–0.91	0.00	0.00	0.00	0.00	0.00	0.00	0.00	0.00	0.00	0.00
–10.25	0.00	0.00	0.00	–0.41	–0.23	–0.88	–0.88	0.00	0.00	0.00	0.00	0.00	0.00	0.00	0.00	0.00	
–9.9	0.00	0.00	0.00	–0.49	–0.20	–0.85	–0.84	0.00	0.00	0.00	0.00	0.00	0.00	0.00	0.00	0.00	
–9.55	0.00	0.00	0.00	–0.56	–0.17	–0.81	–0.79	0.00	0.00	0.00	0.00	0.00	0.00	0.00	0.00	0.00	
–9.2	0.00	0.00	0.00	–0.62	–0.14	–0.77	–0.74	0.00	0.00	0.00	0.00	0.00	0.00	0.00	0.00	0.00	
–8.85	0.00	0.00	0.00	–0.69	–0.10	–0.72	–0.68	0.00	0.00	0.00	0.00	0.00	0.00	0.00	0.00	0.00	
–8.5	0.00	0.00	0.00	–0.74	–0.06	–0.67	–0.61	0.00	0.00	0.00	0.00	0.00	0.00	0.00	0.00	0.00	
–8.15	0.00	0.00	0.00						0.00	0.00	0.00		0.00	0.00	0.00	0.00	
–7.8	0.00															0.00	
–3.6																0.00	
–3.25	34.11	115.03	149.14						0.26	72.19			181.51	499.16	449.24	0.00	
–2.9	47.71	136.17	183.89	–0.64	0.70	0.31	0.62	0.62	0.31	94.60	127.05	2.46	224.12	616.32	554.69	0.00	
–2.55	62.04	155.37	217.40	–0.58	0.73	0.36	0.68	0.68	0.36	117.42	144.96	2.91	265.29	729.56	656.60	0.00	
–2.2	76.37	172.45	248.82	–0.51	0.76	0.40	0.73	0.73	0.40	139.72	160.90	3.33	303.96	835.85	752.27	0.00	
–1.85	90.01	187.28	277.29	–0.43	0.79	0.43	0.77	0.77	0.43	160.58	174.73	3.72	339.03	932.34	839.11	0.00	
–1.5	102.34	199.73	302.07	–0.36	0.81	0.46	0.80	0.80	0.46	179.19	186.35	4.05	369.59	1016.38	914.74	0.00	
–1.15	112.77	209.70	322.48	–0.28	0.83	0.48	0.83	0.83	0.48	194.81	195.66	4.32	394.78	1085.65	977.09	0.00	
–0.8	120.85	217.11	337.96							206.81	202.57	4.52					
9.7	0.00	0.00	0.00							0.00							
10.05	0.00	0.00	0.00	0.46	–0.21	–0.86	–0.86	0.00	0.00	0.00	0.00						
10.4	0.00	0.00	0.00	0.38	–0.24	–0.89	–0.89	0.00	0.00	0.00	0.00	0.00	0.00				
10.75	0.00	0.00	0.00	0.30	–0.26	–0.92	–0.92	0.00	0.00	0.00	0.00	0.00	0.00	0.00	0.00	0.00	
11.15	0.00	0.00	0.00	0.21	–0.27	–0.94	–0.95	0.00	0.00	0.00	0.00	0.00	0.00	0.00	0.00	0.00	
11.55	0.00	0.00	0.00	0.11	–0.28	–0.95	–0.97	0.00	0.00	0.00	0.00	0.00	0.00	0.00	0.00	0.00	
12	0.00	0.00	0.00	0.00	–0.29	–0.96	–0.97	0.00	0.00	0.00	0.00	0.00	0.00	0.00	0.00	0.00	

REFERENCES

[1] World Health Organization and UNICEF, Water for Life, WHO/UNICEF Joint Monitoring Programme for Water Supply and Sanitation, 2005, ISBN 92 4 156293 5.

[2] IFPRI, Global Nutrition Report 2016: From Promise to Impact: Ending Malnutrition by 2030, IFPRI, Washington, DC, 2016.

[3] https://yearbook.enerdata.net/ (consultada en marzo de 2017).

[4] P. Droege, Renewable energy and the city: urban life in an age of fossil fuel depletion and climate change, Bull. Sci. Technol. Soc. 22 (2) (2002) 87−99.

[5] M. El-Fadel, R. Chedid, M. Zeinati, W. Hmaidan, Mitigating energy-related GHG emissions through renewable energy, Renew. Energy 28 (8) (2003) 1257−1276.

[6] REH Sims, Renewable energy: a response to climate change, Sol. Energy 76 (1−3) (2004) 9−17.

[7] A. Longo, A. Markandya, M. Petrucci, The internalization of externalities in the production of electricity: willingness to pay for the attributes of a policy for renewable energy, Ecol. Econ. 67 (1) (2008) 140−152.

[8] G.L. Talbot, L′intégration spatiale et temporelle du partage des ressources dans un système agroforestier noyers-céréales : une clef pour en comprendre la productivité? (Ph.D. thesis), Université Montpellier II-Sciences et Techniques du Languedoc, 2011.

[9] B. Kuemmel, V. Langer, J. Magid, A. De Neergaard, J.R. Porter, Energetic, economic and ecological balances of a combined food and energy system, Biomass Bioenergy 15 (4−5) (1998) 407−416.

[10] A. Goetzberger, A. Zastrow, On the coexistence of solar-energy conversion and plant cultivation, Int. J. Sol. Energy 1 (1) (1982) 55−69.

[11] H. Marrou, J. Wery, L. Dufour, C. Dupraz, Productivity and radiation use efficiency of lettuces grown in the partial shade of photovoltaic panels, Eur. J. Agron. 44 (2013) 54−66.

[12] H. Marrou, L. Guilioni, L. Dufour, C. Dupraz, J. Wery, Microclimate under agrivoltaic systems: is crop growth rate affected in the partial shade of solar panels? Agric. For. Meteorol. 177 (2013) 117−132.

[13] C. Dupraz, H. Marrou, G. Talbot, L. Dufour, A. Nogier, Y. Ferard, Combining solar photovoltaic panels and food crops for optimising land use: towards new agrivoltaic schemes, Renew. Energy 36 (10) (2011) 2725−2732.

[14] P.C. Pande, A.K. Singh, S. Ansari, S.K. Vyas, B.K. Dave, Design development and testing of a solar PV pump based drip system for orchards, Renew. Energy 28 (2003) 385−396.

[15] A.G. Bhave, Potential for solar water-pumping systems in India, Appl. Energy 48 (1994) 197−200.

[16] A. Chaurey, P.M. Sadaphal, D. Tyaqi, Experiences with SPV water pumping systems for rural applications in India, Renew. Energy 3 (1993) 961−964.

[17] E. Mahmoud, H. Nather, Renewable energy and sustainable developments in Egypt: photovoltaic water pumping in remote areas, Appl. Energy 74 (2003) 141−147.

[18] Y. Yu, J. Liu, H. Wang, M. Liu, Assess the potential of solar irrigation systems for sustaining pasture lands in arid regions—a case study in Northwestern China, Appl. Energy 88 (2011) 3176−3182.

[19] A.R. Al Ali, S. Rehman, S. Al Agili, M.H. Al-Omari, M. Al Fayezi, Usage of photovoltaic in an automated irrigation system, Renew. Energy 23 (2001) 17−26.
[20] A. Mokeddem, A. Midoun, D. Kadri, S.S. Hiadsi, I.A. Raja, Performance of a directly-coupled PV water pumping system, Energy Convers. Manag. 52 (2011) 3089−3095.
[21] A. Hamidat, B. Benyoucef, T. Hartani, Small-scale irrigation with photovoltaic water pumping system in Sahara regions, Renew. Energy 28 (2003) 1081−1096.
[22] R. López-Luque, J. Reca, J. Martínez, Optimal design of a standalone direct pumping photovoltaic system for deficit irrigation of olive orchards, Appl. Energy 149 (2015) 13−23.
[23] S.S. Chandel, M. Nagaraju Naik, R. Chandel, Review of solar photovoltaic water pumping system technology for irrigation and community drinking water supplies, Renew. Sustain. Energy Rev. 49 (September 2015) 1084−1099.
[24] J. Reca, C. Torrente, R. López-Luque, J. Martínez, Feasibility analysis of a standalone direct pumping photovoltaic system for irrigation in Mediterranean greenhouses, Renew. Energy (2016).
[25] R. Posadillo, R. López Luque, A sizing method for stand-alone PV installations with variable demand, Renew. Energy 33 (5) (2008) 1049−1055.
[26] R. Sen, S.C. Bhattacharyya, Off-grid electricity generation with renewable energy technologies in India: an application of HOMER, Renew. Energy 62 (2014) 388−398. https://doi.org/10.1016/j.renene.2013.07.028.
[27] J. Carroquino, R. Dufo-López, J.L. Bernal-Agustín, Sizing of off-grid renewable energy systems for drip irrigation in Mediterranean crops, Renew. Energy 76 (2015) 566−574. http://doi.org/10.1016/j.renene.2014.11.069.
[28] G. Panayiotou, S. Kalogirou, S. Tassou, Design and simulation of a PV and a PV−Wind standalone energy system to power a household application, Renew. Energy 37 (2012) 355−363. https://doi.org/10.1016/j.renene.2011.06.038.
[29] A. Hamidat, B. Benyoucef, Systematic procedures for sizing photovoltaic pumping system, using water tank storage, Energy Policy 37 (2009) 1489−1501. http://doi.org/10.1016/j.enpol.2008.12.014.
[30] K. Meah, S. Ula, S. Barrett, Solar photovoltaic water pumping—opportunities and challenges Renew, Sustain. Energy Rev. 12 (2008) 1162−1175. http://doi.org/10.1016/j.rser.2006.10.020.
[31] K. Benlarbi, L. Mokrani, M.S. Nait-Said, A fuzzy global efficiency optimization of a photovoltaic water pumping system, Sol. Energy 77 (2004) 203−216. https://doi.org/10.1016/j.solener.2004.03.025.
[32] A.A. Ghoneim, Design optimization of photovoltaic powered water pumping systems, Energy Convers. Manag. 47 (2006) 1449−1463. https://doi.org/10.1016/j.enconman.2005.08.015.
[33] Z. Glasnovic, J. Margeta, A model for optimal sizing of photovoltaic irrigation water pumping systems, Sol. Energy 81 (2007) 904−916. https://doi.org/10.1016/j.solener.2006.11.003.
[34] P.E. Campana, H. Li, J. Yan, Dynamic modelling of a PV pumping system with special consideration on water demand, Appl. Energy 112 (2013) 635−645. https://doi.org/10.1016/j.apenergy.2012.12.073.

[35] X. Gao, J. Liu, J. Zhang, J. Yan, S. Bao, H. Xu, et al., Feasibility evaluation of solar photovoltaic pumping irrigation system based on analysis of dynamic variation of groundwater table, Appl. Energy 105 (2013) 182–193. https://doi.org/10.1016/j.apenergy.2012.11.074.

[36] A. Baille, C. Kittas, N. Katsoulas, Influence of whitening on greenhouse microclimate and crop energy partitioning, Agric. For. Meteorol. 107 (4) (2001) 293–306.

[37] C. Kittas, N. Katsoulas, A. Baille, Influence of aluminized thermal screens on greenhouse microclimate and night transpiration, Acta Hort. ISHS 614 (2003) 387–392. http://www.actahort.org/books/614/614_58.htm.

[38] J.C. López, A. Baille, S. Bonachela, J. Pérez-Parra, Analysis and prediction of greenhouse green bean (*Phaseolus vulgaris* L.) production in a mediterranean climate, Biosyst. Eng. 100 (2008) 86–95. http://doi.org/10.1016/j.biosystemseng.2008.02.006.

[39] A.J. Callejón-Ferre, F. Manzano-Agugliaro, M. Díaz-Pérez, A. Carreño-Ortega, J. Pérez-Alonso, Effect of shading with aluminised screens on fruit production and quality in tomato (*Solanum lycopersicum* L.) under greenhouse conditions, Span. J. Agric. Res. 7 (1) (2009) 41–49.

[40] E. Kittas, A.D. Baille, N. Katsoulas, N. Rigakis, M.M. González-Real, Effects of cover optical properties on screenhouse radiative environment and sweet pepper productivity, Biosyst. Eng. 122 (2014) 115–126. http://doi.org/10.1016/j.biosystemseng.2014.04.001.

[41] M. Kadowaki, A. Yano, F. Ishizu, T. Tanaka, S. Noda, Effects of greenhouse photovoltaic array shading on Welsh onion growth, Biosyst. Eng. 111 (2012) 290–329.

[42] J. Pérez-Alonso, M. Pérez-García, M. Pasamontes-Romera, A.J. Callejón-Ferre, Performance analysis and neural modelling of a greenhouse integrated photovoltaic system, Renew. Sustain. Energy Rev. 16 (2012) 4675–4685. http://doi.org/10.1016/j.rser.2012.04.002.

[43] P.J. Sonneveld, G.L.A.M. Swinkels, J. Campen, B.A.J. van Tuijl, H.J.J. Janssen, G.P.A. Bot, Performance results of a solar greenhouse combining electrical and thermal energy production, Biosyst. Eng. 106 (1) (2010) 48–57.

[44] P.J. Sonneveld, G.L.A.M. Swinkels, B.A.J. van Tuijl, H.J.J. Janssen, J. Campen, G.P.A. Bot, Performance of a concentrated photovoltaic energy system with static linear Fresnel lenses, Sol. Energy 85 (3) (2011) 432–442.

[45] R. Ureña-Sánchez, A.J. Callejón-Ferre, J. Pérez-Alonso, A. Carreño-Ortega, Greenhouse tomato production with electricity generation by roof-mounted flexible solar panels, Sci. Agric. 69 (4) (2012) 233–239.

[46] A. Yano, A. Furue, M. Kadowaki, T. Tanaka, E. Hiraki, M. Miyamoto, F. Ishizu, S. Noda, Electrical energy generated by photovoltaic modules mounted inside the roof of a north–south oriented greenhouse, Biosyst. Eng. 103 (2009) 228–238. http://doi.org/10.1016/j.biosystemseng.2009.02.020.

[47] A. Yano, M. Kadowaki, A. Furue, N. Tamaki, T. Tanaka, E. Hiraki, Y. Kato, F. Ishizu, S. Noda, Shading and electrical features of a photovoltaic array mounted inside the roof of an east–west oriented greenhouse, Biosyst. Eng. 106 (2010) 367–377. http://doi.org/10.1016/j.biosystemseng.2010.04.007.

[48] M. Biancardo, K. Taira, N. Kogo, H. Kikuchi, N. Kumagai, N. Kuratani, I. Inagawa, S. Imoto, J. Nakata, Characterization of microspherical semi-transparent solar cells and modules, Sol. Energy 81 (2007) 711–716. http://doi.org/10.1016/j.solener.2006.10.009.

[49] A. Yano, M. Onoe, J. Nakata, Prototype semi-transparent photovoltaic modules for greenhouse roof applications, Biosyst. Eng. 122 (2014) 62–73. http://doi.org/10.1016/j.biosystemseng.2014.04.003.
[50] J. Keller, R.D. Bliesner, Sprinkle and Trickle Irrigation, AVI Book. Van Nostrand Reinhold, New York, 1990.
[51] R.G. Allen, L.S. Pereira, D. Raes, M. Smith, Crop evapotranspiration. Guidelines for computing crop water requirements, in: FAO Irrigation and Drainage Paper 56, FAO, Rome, 1998.

FURTHER READING

[1] Y.S. Mohammed, M.W. Mustafa, N. Bashir, Hybrid renewable energy systems for off-grid electric power: review of substantial issues, Renew. Sustain. Energy Rev. 35 (2014) 527–539. https://doi.org/10.1016/j.rser.2014.04.022.

This page intentionally left blank

CHAPTER

10 Scalar and Vector Control of Induction Motor for Online Photovoltaic Pumping

Imene Yahyaoui[1], **Alvaro Serna Cantero**[2]
University Carlos 3 of Madrid, Madrid, Spain[1]*; University of Valladolid, Valladolid, Spain*[2]

CHAPTER OUTLINE

1. Introduction **336**
2. Modeling of the System Components **337**
3. Scalar Control **338**
4. The Vector Control **339**
4.1 Estimation of the Torque and the Flux 339
4.2 Selection of the Regulators 340
4.3 Calculation of the Electric Speed Reference 341
5. Results and Discussion **342**
6. Conclusion **346**
Annex **346**
References **347**

NOMENCLATURE

C_{em}	Electromagnetic torque (N·m)
C_l	Resistive torque (N·m)
f_b	Base frequency (Hz)
IM	Induction machine
i_s	Stator current (A)
i_{sd}	Direct component of the stator current (A)
i_{sq}	Quadratic component of the stator current (A)
J	Inertia moment (kg·m^2)
l_s	Cyclic stator reluctance (H)
MPPT	Maximum Power Point Tracking
P_{pv}	Photovoltaic power (W)
PVPS	Photovoltaic water Pumping Systems
PWM	Pulse Width Modulation
r_r	Rotor phase resistance (**Ω**)

Advances in Renewable Energies and Power Technologies. https://doi.org/10.1016/B978-0-12-812959-3.00010-1
Copyright © 2018 Elsevier Inc. All rights reserved.

r_s	Stator phase resistance (**Ω**)
V	Volume of the pumped water (m^3)
V_r	Rotor voltage (V)
V_{rd}	Direct component of the rotor voltage (V)
V_{rq}	Quadratic component of the rotor voltage (V)
V_s	Stator voltage (V)
V_{s0}	Base voltage (V)
V_{sd}	Direct component of the stator voltage (V)
V_{sq}	Quadratic component of the stator voltage (V)
w_g	Slip pulsation (rad/s)
w_s	Stator pulsation (rad/s)
φ_s	Stator flux (Wb)
φ_r	Rotor flux (Wb)
φ_{rd}	Direct component of the rotor flux (Wb)
φ_{rq}	Quadratic component of the rotor flux (Wb)
Ω	Mechanical speed (rad/s)

1. INTRODUCTION

In remote areas in Tunisia, traditional systems are used for agriculture, such as the diesel engine pumps, to extract water from wells. These systems are easy to install; however, they present some major inconvenience because they involve frequent repairs and refueling, and often the diesel is not available in these areas. Furthermore, the use of fossil fuels causes environmental problems such as the emission of carbon dioxide (CO_2) into the atmosphere. However, there is a great potential of both solar energy source and underground water reserve, which is encouraging for an off-grid photovoltaic water pumping system (PVPS). The main purpose of this study is to provide water for agricultural applications using clean energy.

Over the past few years, in this area, research interests are essentially related to the modeling [1−4], optimization [5], and the adaptation system [6] of the PVP supply. According to equipment needs, many others researches were focused on PV pumping from sizing points, based on the potential of solar energy and water demand [7]. Other works of PVPS concentrated on the pump performances [8]. The same works of different PVPS were studied in different sites [9,10]. Other investigators established strategies to ensure optimum energy management of PV systems [11−13]. Therefore, numerous algorithms are advanced to predict climatic parameters performance throughout daylight.

DC motors were first used because they provide easy operation with low-cost power conversion [14,15]. Operational pumping systems have revealed that these types of pumps need regular maintenance. To overcome this weakness, brushless permanent-magnet motors have been suggested [16]. Nevertheless, this solution is restricted for low-power PV systems. The induction motor−based PV pumping systems offer an alternative for a more efficient and maintenance-free system [17].

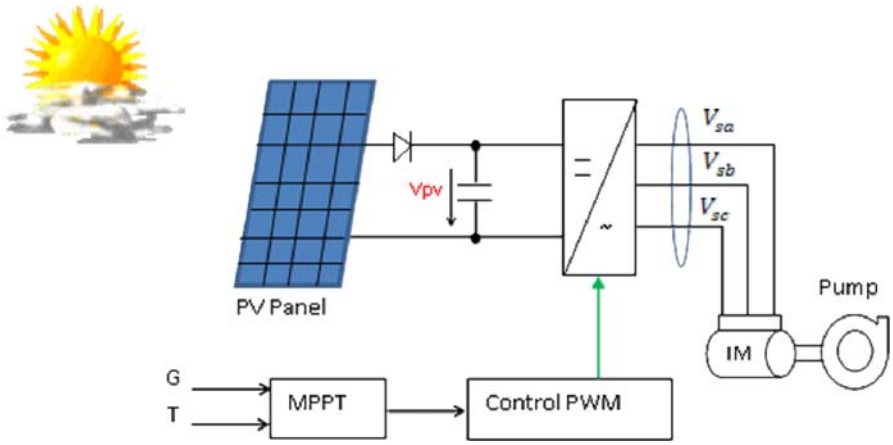


FIGURE 10.1

Online photovoltaic water pumping system principle.

This paper presents a comparison between the scalar and the vector methods, in terms of power, daily cumulative water and the overall efficiency of each PVPS, when controlling an asynchronous motor that drives an online water pump. The pump is supplied only with a photovoltaic panel that provides maximum power thanks to the maximum power point tracking (MPPT) algorithm (Fig. 10.1). The system components are modeled in Section 2. In Section 3, the scalar control used for controlling the asynchronous machine is presented. The vector control is detailed in depth in Section 4. Section 5 illustrates the results and discussion. Finally, Section 6 is the chapter conclusion.

2. MODELING OF THE SYSTEM COMPONENTS

As it has been mentioned previously, the system studied here is composed of photovoltaic panels, a water pump driven by an asynchronous machine. Using the measured temperature and solar radiation, the photovoltaic voltage and current at maximum power point (MPP) are expressed by [18]:

$$V_{pv} = \left(12 + 0.07 * \left(T + \frac{G}{40} - 25\right) - 0.8 * 1.2e^{-3} * \frac{G}{1000}\right) * \left(T + \frac{G}{40} - 25\right) + 3.35 * \left(\frac{G}{1000} - 1\right) \tag{10.1}$$

$$i_{pv} = \left(3.33 + 1.4e^{-3} * \left(\frac{G}{1000}\right)\right) * \left(T + \frac{G}{40} - 25\right) + 3.35 * \left(\frac{G}{1000} - 1\right) \tag{10.2}$$

The motor pump adopted is an asynchronous machine. The motor mode and vector transformation in the asynchronous machine circuits provide the dynamic model of the asynchronous motor in the $d-q$ reference frame (Eq. 10.3) [19,20]:

$$\begin{cases} \overline{V_s} = V_{sd} + jV_{sq} = r_s\overline{I_s} + \dfrac{d}{dt}\overline{\varphi_s} + jw_s\overline{\varphi_s} \\ \overline{V_r} = V_{rd} + jV_{rq} = r_r\overline{I_r} + \dfrac{d}{dt}\overline{\varphi_r} + jw_g\overline{\varphi_r} \end{cases} \tag{10.3}$$

In addition, the machine flux is expressed as follows:

$$\begin{cases} \overline{\varphi_s} = l_s\overline{I_s} + m\overline{I_r} \\ \overline{\varphi_r} = l_r\overline{I_r} + m\overline{I_s} \end{cases} \tag{10.4}$$

The associated motion equation is given by Eq. (10.5) [20]:

$$\frac{d}{dt}\Omega = p\frac{1}{J}(C_{em} - C_l) \tag{10.5}$$

It is considered that the machine is coupled to a centrifugal pump having a load torque C_l, which can be expressed as [20]:

$$C_l = k\Omega^2 \tag{10.6}$$

The electromagnetic torque is given by Eq. (10.7) [21].

$$C_{em} = p\left(\frac{m}{l_r}\varphi_{dr}i_{qs} - \varphi_{qr}i_{ds}\right) \tag{10.7}$$

3. SCALAR CONTROL

The principle of the scalar control method consists in maintaining $\frac{V_s}{f_s}$ constant. This allows maintaining the flux constant. The torque control is done through the slip variation. In permanent state, the expression of the maximum torque is given by Eq. (10.8):

$$C_{em} = \frac{3p}{2N_r}\left(\frac{V_s}{w_s}\right)^2 \tag{10.8}$$

where V_s is given (using phase diagram) by Eq. (10.9) [22].

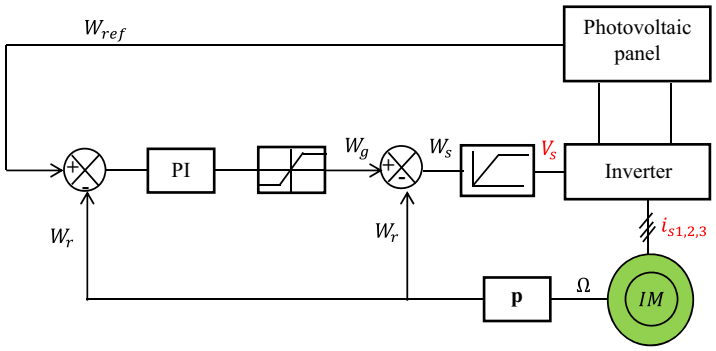


FIGURE 10.2

The block diagram of a scalar control of the induction machine.

$$V_s = \frac{\sqrt{2}}{3} I_{s(re)} r_s + \sqrt{\left(\frac{v_{s0} f_s}{f_b}\right)^2 + \frac{2}{9}\left(I_{s(re)} r_s\right)^2 - \left(I_s r_s\right)^2} \tag{10.9}$$

Fig. 10.2 presents the regulation method of the machine speed by reconstituting the stator pulsation.

4. THE VECTOR CONTROL

4.1 ESTIMATION OF THE TORQUE AND THE FLUX

In this case, the asynchronous motor is controlled by vector control with a rotor flux orientation. In fact, the torque control is made by calculating the desired components i_{qs} and i_{ds} of the stator current. It is maximum for a given current if $\varphi_{qr} = 0$ is imposed. During the operation, the rotor flux is positioned to coincide with the d-axis component (i.e., $\varphi_{dr} = \varphi_r$ and $\varphi_{qr} = 0$). Thus, it becomes possible to control the torque independently by acting on the q-axis stator current, whereas the rotor flux can be controlled with the d-axis stator current. Hence, by keeping the rotor flux constant, the motor torque is directly controlled, the expression of the rotor flux is then given by Eq. (10.10):

$$\varphi_{rd} = \frac{m}{1 + \tau_r s} i_{sd} \tag{10.10}$$

Consequently, the electromagnetic torque C_{em} is proportional to the quadratic stator current i_{sq}. Then, the torque can be expressed by [23]:

$$C_{em} = p \frac{m}{l_r} \varphi_r i_{sq} \tag{10.11}$$

4.2 SELECTION OF THE REGULATORS

The regulators used are PI type whose transfer functions are given by:

$$R(s) = \frac{K_p(1+\tau_p s)}{\tau_p s} \tag{10.12}$$

For the selection of the regulator parameters, the method of zeros compensation is adopted [24]. The flux regulator output allows the direct stator current i_{sd} to be generated, using Eq. (10.10). The transfer function relating the current to the voltage of the direct stator component is given by Eq. (10.13). The regulation scheme is given by Fig. 10.3.

$$H_1(s) = \frac{i_{sd}(s)}{v_{sd^*}(s)} = \frac{\dfrac{1}{\left(r_s + \frac{m^2}{l_r \tau_r}\right)}}{1 + \dfrac{k_s}{\left(r_s + \frac{m^2}{l_r \tau_r}\right)} s} \tag{10.13}$$

Using Eq. (10.11), the torque regulation ensures the regulation of the quadrature stator current i_{sq}. The transfer function relating the current to the voltage of the quadrature stator component is given by Eq. (10.14) with its principle described by Fig. 10.4:

$$H_2(s) = \frac{i_{sq}(s)}{v_{sq}(s)} = \frac{\dfrac{1}{\left(r_s + \frac{m^2}{l_r \tau_r}\right)}}{1 + \dfrac{k_s}{\left(r_s + \frac{m^2}{l_r \tau_r}\right)} s} \tag{10.14}$$

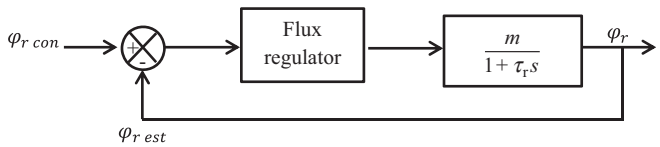


FIGURE 10.3

Principle of flux regulation.

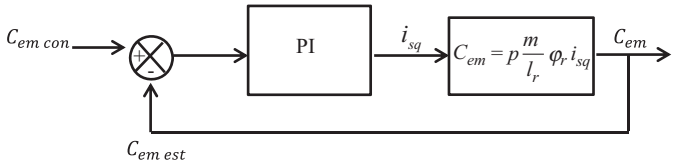


FIGURE 10.4

Principle of the torque regulation.

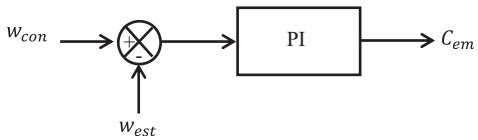


FIGURE 10.5

Principle of speed regulation.

The pump resistive torque depends on the squared speed. Thus, the elaboration of the transfer function relating the electromagnetic torque variation to the electric speed variation must be done around an operating point (Fig. 10.5). This transfer function is given by Eq. (10.15):

$$H(s) = \frac{\Delta\Omega(s)}{\Delta C_{em}(s)} = \frac{\dfrac{1}{2k_l\Omega_0}}{1 + \dfrac{J}{2k_l\Omega_0}s} \tag{10.15}$$

4.3 CALCULATION OF THE ELECTRIC SPEED REFERENCE

To evaluate the speed reference, losses in the stator are taken into consideration. In fact, the power balance of the asynchronous machine is given by Eq. (10.16) [24]:

$$P_l = P_{pv} - \frac{3}{2}r_s I_s^2 \tag{10.16}$$

Consequently, for the vector control, the rotor pulsation can be evaluated from:

$$P_l = C_{em}\Omega_s = C_{em}\frac{w_s}{p} \tag{10.17}$$

where

$$C_{em} = k_l\ \Omega^2 \tag{10.18}$$

Thus, Eq. (10.17) becomes

$$P_l = \frac{k_l}{p^3}\ (w + w_g)\ w^2 \tag{10.19}$$

Moreover, the stator current is a function of the direct and quadrature current:

$$I_s = \sqrt{i_{sd}^2 + i_{sq}^2} \tag{10.20}$$

where

$$i_{sd} = \frac{\varphi_{rd}}{m} \tag{10.21}$$

$$i_{sq} = \frac{2}{3}\frac{l_r\, k_l}{p^3 m\ \varphi_r} w^2 \tag{10.22}$$

Using Eq. (10.23) [24]:

$$w_g = \frac{m}{\tau_r}\frac{1}{\varphi_r} i_{sq} \tag{10.23}$$

Eq. (10.16) may be written as follows:

$$a\, w^4 + b\, w^3 + c = 0 \tag{10.24}$$

where

$$a = \frac{12}{18p^6} r_s \left(\frac{l_r k_l}{m\varphi_r}\right)^2 + \frac{2}{3}\frac{k^2}{p^6}\frac{r_r}{\varphi_r^2} \tag{10.25}$$

$$b = \frac{k_l}{p^3} \tag{10.26}$$

$$c = \frac{3}{2} r_s \left(\frac{\varphi_r}{m}\right)^2 - P_{pv} \tag{10.27}$$

The resolution of Eq. (10.24) allows deducing the reference electric speed. The comparison results of both control methods are detailed in Section 5.

5. RESULTS AND DISCUSSION

With the aim of evaluating the proposed field-oriented control rule for the vector control and comparing it with the scalar control approach, simulations were carried out, using data measured from the target location (Sfax, Tunisia). The nominal value for the reference value of the rotor flux values $\varphi_{rd} = -0.36$ Wb and $\varphi_{rq} = 0$ Wb are selected.

Fig. 10.6A and B demonstrate the evolution of the radiance and the photovoltaic power corresponding to a typical sunny day (October 22, 2016). Figs. 7–9 show, respectively, the curves of the mechanical power, stator pulsation, and stator voltage responses, using the scalar control, using the data measured in three different days in Summer, Autumn, and Winter. These figures show that the scalar control allows a good function of the induction machine but it is not possible to operate at the MPP points.

Figs. 10–12 show the characteristics of the mechanical power, electric speed, and the rotor flux responses, using the vector control for the selected days. With the aim of testing the effectiveness of the suggested method (vector control), the simulation for 3 days is performed, allowing therefore the radiance and temperature to change. It is clear that in rapid changing in atmospheric conditions, the panel is able to operate around the optimal value. The obtained curves demonstrate the viability of the suggested structure. In Figs. 10–12, the flux magnitude is retained

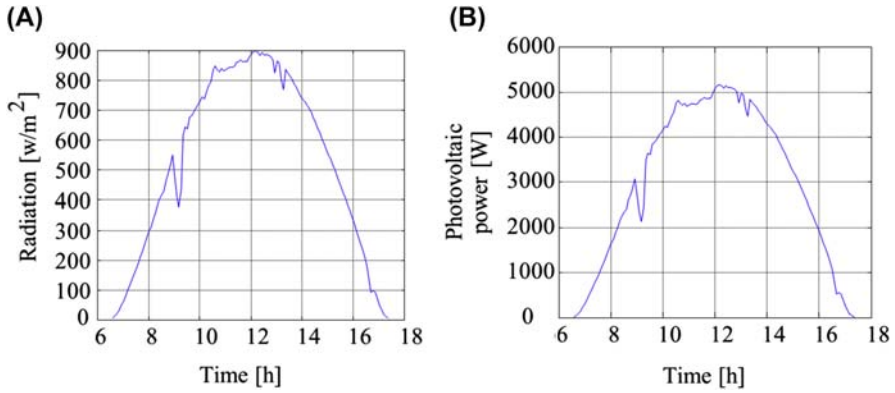


FIGURE 10.6

Photovoltaic characteristics for October 22, 2010. (A) Solar radiation, (B) Photovoltaic power.

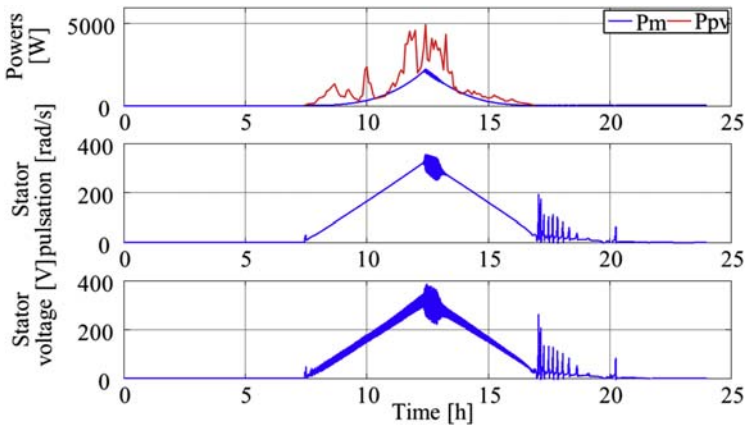


FIGURE 10.7

Evolution using the scalar control for December 6, 2016.

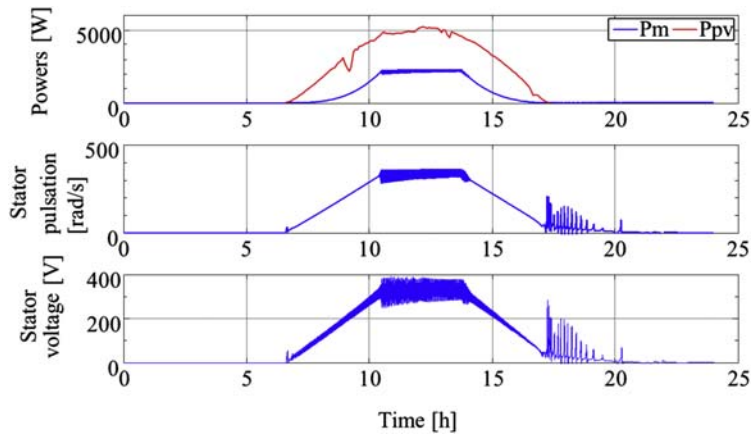


FIGURE 10.8

Evolution using the scalar control for October 22, 2016.

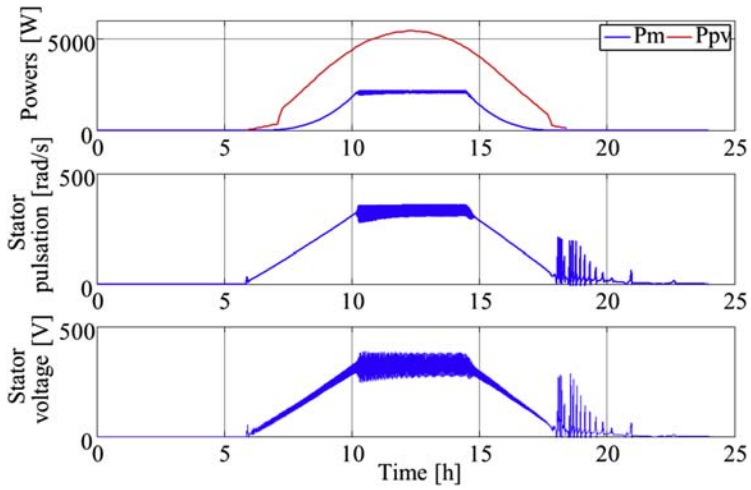


FIGURE 10.9

Evolution using the scalar control for August 22, 2016.

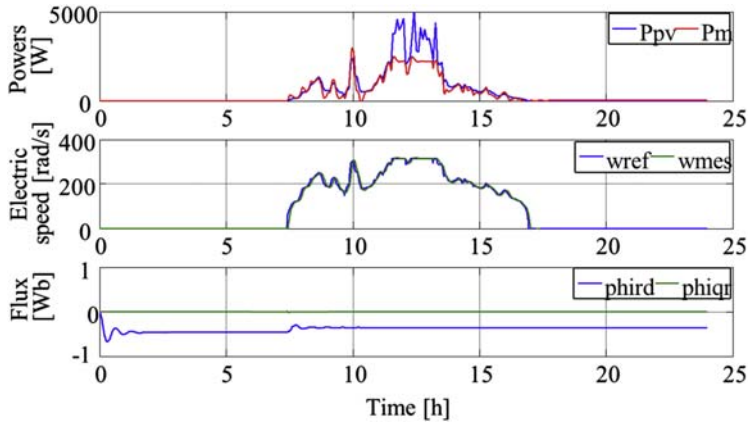


FIGURE 10.10

Evolution using the vector control for December 6, 2016.

at its nominal value of −0.36 Wb. Moreover, these figures show that the rotor pulsation meets perfectly with its reference.

The useful power of the centrifugal pump is expressed by Eq. (10.28) [20]:

$$P_u(t) = \eta P_l = \rho g H q(t) \tag{10.28}$$

where ρ is the density (kg/m^3); g is the acceleration of gravity (m^2/s), H is the height of rise (m), $q(t)$ is the flow (m^3/s), P_l is the absorptive power, which is obviously a mechanical power on the shaft coupled to the pump and η is the pump efficiency.

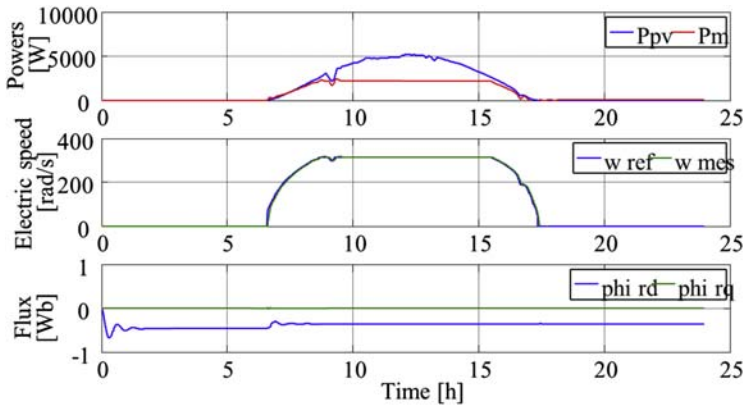


FIGURE 10.11

Evolution using the vector control for October 22, 2016.

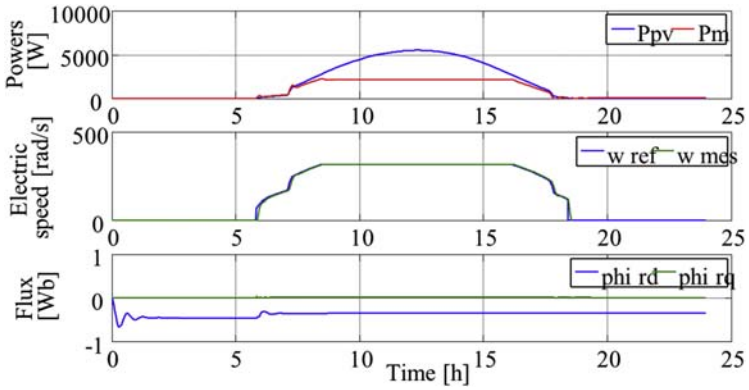


FIGURE 10.12

Evolution using the vector control for August 22, 2016.

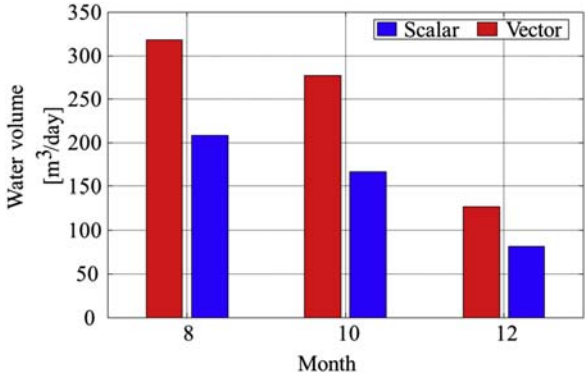


FIGURE 10.13

Water volume comparison.

Table 10.1 Water Volume Pumped Using the Scalar and Vector Control Methods

Season	Volume Obtained With Scalar Control (m^3 per day)	Volume Obtained With Vector Control (m^3 per day)
Hot season	208.9	317.8
Moderate season	166.9	277.45
Cold season	81.72	127.4

Fig. 10.13 and Table 10.1 illustrates the pumped water volume obtained using the scalar and vector control in the three seasons: cold, medium, and hot seasons. The results show that, using the vector control method, the pumped volume is clearly higher than using the scalar method.

6. CONCLUSION

An optimal process of a photovoltaic pumping system based on an induction machine was detailed. The goal was to ensure maximum motor efficiency after extracting maximum photovoltaic power with MPPT method. A comparative study was carried out on two control methods: scalar and the vector control. The simulation results show the increase of both the daily pumped quantity and pump efficiency, reached by the vector control. The investigation of the vector control with cheap available electronic instruments still is an objective for generalizing and spreading the use of photovoltaic energy in water pumping applications.

ANNEX

Table A Parameters of the Asynchronous Machine

Nominal voltage [V]	220/380 V	Stator resistance [Ω]	2.3
Nominal stator current [A]	21	Rotor resistance [Ω]	2.3
Nominal power [kW]	4.5	Stator mutual inductance [H]	0.462
Nominal torque [Nm]	28	Rotor mutual inductance [H]	0.462
Nominal speed [tr/mn]	1435	Inertia moment [kg·m^2]	0.0049
Pairs poles number 2			

REFERENCES

[1] A.H. Fanny, B.P. Dougherty, M.W. Davis, Measured Performance of Building Integrated Photovoltaic Panels. Solar Energy: The Power to Choose, Forum 2001, Washington, DC.

[2] M. Xu, R.V.N. Melnik, U. Borup, Modelling anti-islanding protection devices for photovoltaic systems, Renew. Energy 29 (2004) 2195–2216.

[3] H. Kawamura, K. Naka, N. Yonekura, Simulation of I–V characteristics of a PV module with shaded PV cells, Sol. Energy Mater Sola Cells 75 (2003) 613–621.

[4] O. Gergaud, B. Multon, H. Ben Ahmed, Analysis and experimental validation of various photovoltaic system models, in: Seventh international ELECTRIMACS Congress, MontréAl, August 2002.

[5] W. De Soto, S.A. Klein, W.A. Beckman, Improvement and validation of a model for photovoltaic array performance, Sol. Energy 80 (1) (2006) 78–88.

[6] M.A. Ramli, S. Twaha, K. Ishaque, Y.A. Al-Turki, A review on maximum power point tracking for photovoltaic systems with and without shading conditions, Renewable and Sustainable Energy Reviews 67 (2017) 144–159.

[7] E.S. Hrayshat, M.S. Al-Soud, Z. Li, L. Lu, Potential of solar energy development for water pumping in Jordan, Renew. Energy 29 (2004) 1393e9.

[8] A. Munir, A.A. Al-Karaghouli, A.A.J. Al-Douri, A PV pumping station for drinking water in a remote residential complex, Desalination 209 (2007) 58–63.

[9] H. Hadi, Photovoltaic Water Pump System, Course of intelligent mechanical system engineering, Kochi University of Technology, 2003. Pakistan in partial fulfillment of the requirement for the degree of Ph.D.

[10] A. Hadj Arab, F. Chenlo, K. Mukadam, J.L. Balenzategui, Performance of PV water pumping systems, Renew. Energy (1999) 18.

[11] C. Ben Salah, M. Chaabene, M. Ben Ammar, Multi-criteria fuzzy algorithm for energy management of a domestic photovoltaic panel, Renew. Energy 33 (2008) 993–1001.

[12] K.-S. Jeong, W.-K. Lee, C.-S. Kimm, Energy management strategies of a fuel cell/battery hybrid system using fuzzy logics, J. Power Sources 145 (2) (2005) 319–326 [Electr Power Energy Syst 2007; 29: 783–95].

[13] A. Hajizadeh, M. Aliakbar Golkar, Intelligent power management strategy of hybrid distributed generation system, Electr. Power Energy Syst. 29 (2007) 783–795.

[14] J. Appelbaum, Starting and steady state characteristics of DC motor powered by solar cell generator, IEEE Trans Energy Conv 1 (1) (1986) 17–25.

[15] J. Appelbaum, M.S. Sarme, The operation of permanent magnet DC motor powered by common source of solar cells, IEEE Trans Energy Conv 4 (4) (1989) 635–642.

[16] C.L.P. Swamy, et al., Dynamic performance of a permanent magnet DC motor powered by a PV array for water pumping, Sol. Energy Mat. Sol. Cell 36 (995) (1995) 187–200.

[17] S.R. Bhat, A. Pittet, B.S. Sonde, Performance optimization of induction motor-pump using photovoltaic energy source, IEEE Trans. Ind. App 23 (6) (1987) 995–1000.

[18] M. Chaabane, M. Ben Ammar, Neuro-fuzzy dynamic model with Kalman filter to forecast irradiance and temperature for solar energy systems, Renew. Energy 33 (7) (July 2008) 1435–1443.

[19] X. Gong, M. Kulkarni, Design optimization of a large scale rooftop photovoltaic system, Sol. Energy 78 (2005) 362–374.

[20] S. Souhir, M. Chaabane, M.B.A. Kamoun, Energy management algorithm for an optimum control of a photovoltaic water pumping system, Appl. Energy 86 (2009) 2671−2680.
[21] M.A. Khalfa, Commande vectorielle indirecte d'une pompe centrifuge photovoltaïque au fil de soleil, Revue des Energies renouvelables CICME'08 Sousse (2008) 163−175.
[22] A.M. Garcia, T.A. Lipos, A new induction motor V/f control method capable of high-performance regulation at low speeds, IEEE Trans. Ind. Appl. 34 (4) (July/August 1998).
[23] R. Chenni, L. Zarour, A. Bouzid, T. Kerbache, Comparative study of photovoltaic pumping systems using a permanent magnet synchronous motor (PMSM) and an asynchronous motor (ASM), Rev. Energ. Ren 9 (2006) 17−28.
[24] M.N. Mansouri, N. Ghanmi, M.F. Mimouni, Commande et analyse des performances d'une station de pompage photovoltaïque fonctionnant en régime optimal, Rev. Energ. Ren. 11N°1 (2008) 1−17.

CHAPTER

Energy Management for PV Installations

11

Djamila Rekioua
Laboratoire LTII, University of Bejaia, Bejaia, Algeria

CHAPTER OUTLINE

1. Introduction 350
2. Photovoltaic Principle, Cells Technologies, and Efficiencies 351
2.1 Photovoltaic Principle 351
2.2 Photovoltaic Cell Efficiency 351
3. Energy Management for Photovoltaic Installations 352
3.1 Photovoltaic Systems with Storage 352
3.1.1 Photovoltaic Systems with Battery Storage 352
3.2 Other Structures 359
3.2.1 Photovoltaic Systems with Fuel Cells 359
3.2.2 Photovoltaic System with Wind Turbine and Battery Storage 364
4. Conclusions 366
References 367

NOMENCLATURE

G	Solar irradiance, W/m^2
I_{sc}	Short circuit current, A
I_{pv}	PV current, A
K_1, K_2, K_3 and K_4	Switches
P_{batt}	Battery power, W
P_{elec}	Electrolyzer Power, W
P_{in}	Input power, W
P_{load}	Load power
P_{out}	Output power, W
R_{aux}	Auxiliary load
S_{pv}	Solar module surface, m^2
T_a	Ambient temperature, °C)
V_{oc}	Open circuit voltage, V
V_{pv}	PV voltage, V

Advances in Renewable Energies and Power Technologies. https://doi.org/10.1016/B978-0-12-812959-3.00011-3
Copyright © 2018 Elsevier Inc. All rights reserved.

Greek Letters

ΔP	Available power
η_{pv-max}	Maximum Photovoltaic efficiency

List of Abbreviations

AC	Alternate current
DC	Direct current
EM	Energy management
FC	Fuel cell
FF	Fill factor
HRES	Hybrid renewable energy sources
MSMSS	Multi-sources multi-storage systems
PEMFC	Proton exchange membrane fuel cells
SOC	State of Charge
SOC_{min}	Minimum State of Charge
SOC_{max}	Maximum State of Charge
STC	Standard Tests Conditions
RES	Renewable energy systems

1. INTRODUCTION

The term "photovoltaic" refers to the photovoltaic effect discovered by Alexandre Edmond Becquerel in 1839 [1]. Photovoltaic solar energy is the electricity produced by transforming part of the solar radiation using a photovoltaic cell. Photovoltaic cells are manufactured with semiconductor materials produced from a very pure material, such as silicon. These materials emit electrons when subjected to the action of light. These are ejected from the material and in a closed circuit, thereby producing electricity [2]. Most people know about photovoltaic, wind, and some other renewable energy sources, but because of their nonlinearity, hybrid energy systems are proposed to overcome this problem with important improvements. In general, hybridization consists of combining several energy sources and storage units within the same system to optimize the production and energy management (EM). In review papers, they can be found under the following names: hybrid renewable energy sources (HRESs) [3–9] or multisources multistorage systems (MSMSSs) [10–12].

To control the power exchange between the different sources, EM strategies must be used. This chapter is focused on EM control of renewable energy systems (RESs). There are different methods proposed in literature [11–38]. Each method differs from another in the control algorithm. Most of them are based on On/Off switches that can be resolved using conventional or intelligent algorithms [36–38]. Others are based only on batteries or supercapacitors state of charge (SOC) [35]. In all cases, the mathematical model is generally based on power balance equation.

2. PHOTOVOLTAIC PRINCIPLE, CELLS TECHNOLOGIES, AND EFFICIENCIES

2.1 PHOTOVOLTAIC PRINCIPLE

The photovoltaic cells use the photoelectric effect to produce direct current by absorption of solar radiation. This effect allows the cells to directly convert the light energy of the photons into electricity by using a semiconductor material carrying electrical charges [2]. The semiconductor material has two parts (Fig. 11.1), one having an excess of electrons (type N) and the other a deficiency of electrons (type P) [4].

2.2 PHOTOVOLTAIC CELL EFFICIENCY

An individual cell produces very little electrical power. To produce more power, the cells are assembled to form a panel. Several cells connected in series increase the voltage for the same current, while the connection in parallel increases the current while maintaining the voltage. The output current and thus the power will be proportional to the panel area. Efficiency in photovoltaic panels is the ability of a panel to convert sunlight into energy. This value is important to choose the correct panels for a specific photovoltaic system application. The photovoltaic efficiency is given as [4]:

$$\eta_{pv} = \frac{P_{out}}{P_{in}} = \frac{V_{pv} \cdot I_{pv}}{S_{pv} \cdot G} \tag{11.1}$$

where, P_{out} is the output power; P_{in} is the input power; V_{pv} and I_{pv} are, respectively, PV voltage and current; S_{pv} is the solar module surface; and G is the solar irradiance.

Under STCs ($G = 1000\ W/m^2$, $T_a = 25°C$), the maximum efficiency will be calculates as:

$$\eta_{pv-max} = \frac{P_{pv-max}}{P_{in}} = \frac{V_{pv-max} \cdot I_{pv-max}}{S_{pv} \cdot G_{STC}} = \frac{V_{pv-max} \cdot I_{pv-max}}{S_{pv} \cdot 1000} \tag{11.2}$$

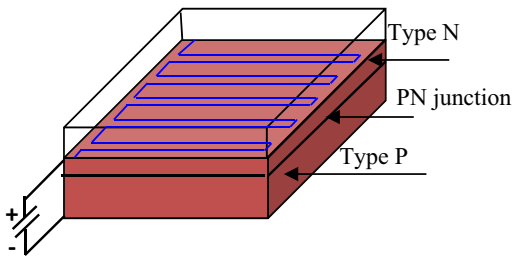


FIGURE 11.1

Photovoltaic cell technology.

The fill factor describes how square the $I_{pv}-V_{pv}$ curve is. It is defined as follows:

$$FF = \frac{P_{pv-max}}{V_{oc} \cdot I_{sc}} = \frac{V_{pv-max} \cdot I_{pv-max}}{V_{oc} \cdot I_{sc}} \tag{11.3}$$

where V_{oc} and I_{sc} are, respectively, the open-circuit voltage and short-circuit current.

So, the maximum efficiency can be expressed as:

$$\eta_{pv-max} = \frac{FF \cdot V_{oc} \cdot I_{sc}}{S_{pv} \cdot 1000} \tag{11.4}$$

The most efficient solar panels commercially available today have solar panel efficiency just above 20%.

3. ENERGY MANAGEMENT FOR PHOTOVOLTAIC INSTALLATIONS

3.1 PHOTOVOLTAIC SYSTEMS WITH STORAGE

3.1.1 Photovoltaic Systems with Battery Storage

The structure generally includes a PV generator, DC/DC converters, a battery bank, and an inverter supplying a stand-alone load. The schematic structure can be represented as in Fig. 11.2 [35].

The key decision factors for the EM strategies are the power P_{pv} provided by PV panels and the SOC of the batteries. The use of the management allows producing maximum power from the PV array, protect the batteries against overcharge, and deep discharge and satisfy the energy needs.

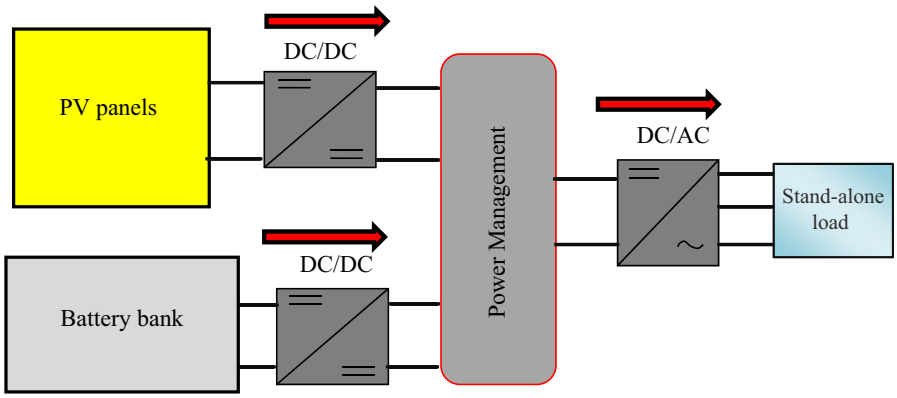


FIGURE 11.2

Schematic PV system with battery storage.

3.1.1.1 First Structure of PMC

In this structure, it has used only three switches K_1, K_2, and K_3 (Fig. 11.3). The switch K_1 is used for the photovoltaic power flow while the second switch K_2 is used for the battery power flow and the third one K_3 is used for both photovoltaic and batteries for the compensation mode.

The available power (ΔP) given by the balance equation between photovoltaic power and load power is calculated as [36]:

$$\Delta P = P_{pv} - P_{load} \tag{11.5}$$

According to the mathematical value of the available power (ΔP), it will obtain two cases. If $\Delta P \geq 0$, the load will be supplied by PV panels while the batteries are charging. In the second case, where $\Delta P < 0$, the PV power can be null or insufficient to feed the load; so batteries are added to satisfy the power load (Table 11.1).

Depending on the different tests on ΔP, P_{pv}, and SOC, the system operates in one of the following modes (Fig. 11.4). In this first structure, five different modes are observed, which are the following:

Mode 1: In this mode, the photovoltaic power (P_{pv}) is quite sufficient to supply the load and charge the batteries (so $\Delta P \geq 0$ and $SOC < SOC_{max}$).

Mode 2: The power supplied by PV panels is insufficient ($0 < P_{pv} < P_{load}$); in this case, the power of the batteries is added to satisfy the power load demand ($SOC > SOC_{min}$). It is the compensation mode, so $P_{load} = P_{pv} + P_{bat}$.

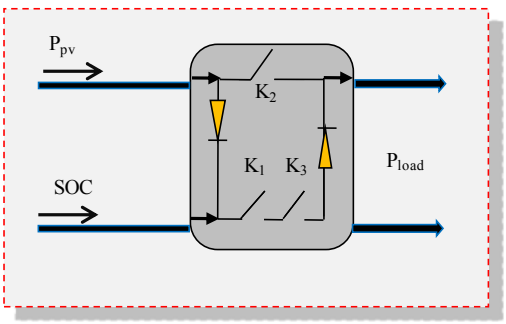


FIGURE 11.3

Energy management based on three switches (PV/battery system).

Table 11.1 Different Cases of the Available Power in the First Configuration (PV/Battery System)

	ΔP	Load	Batteries
Case 1	≥	Supplied by PV	Charging
Case 2	<	Supplied by batteries	Discharging

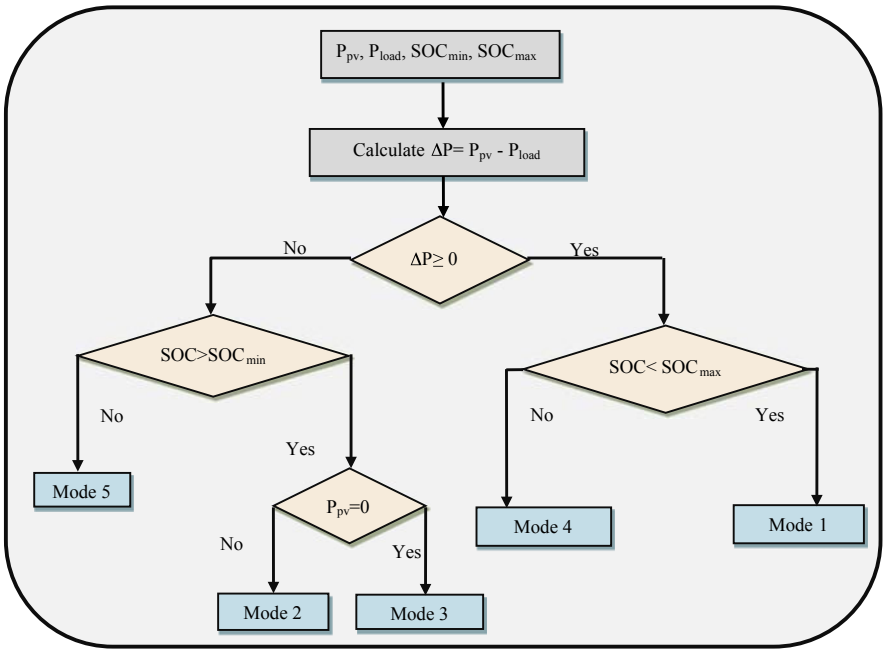


FIGURE 11.4

Energy management strategy of the PV/battery system.

Mode 3: This mode is operating when no energy provides from the photovoltaic generator ($\Delta P < 0$), so batteries alone supply the load ($SOC > SOC_{min}$).

Mode 4: The photovoltaic power is sufficient and batteries are completely charging so the disconnection of the batteries is necessary to protect them ($SOC = SOC_{max}$).

Mode 5: In this mode, there is no production from the PV generator and the batteries are discharged, so the load will be disconnected ($SOC = SOC_{min}$).

The different modes depend on the three switches K_1, K_2, and K_3. Mathematically, it can obtain two power n combinations (2^n), which correspond to eight ($2^3 = 8$) cases (Table 11.2).

After simplifications, it is possible to obtain the Table 11.3.

But practically only five cases can be exploitable (Table 11.4).

The different powers can be expressed in terms of the different switches considered as Boolean values (0 or 1) as:

$$P_{pv} = \left(\overline{K}_1 \cdot K_2 \cdot \overline{K}_3 + \overline{K}_1 \cdot K_2 \cdot K_3 + K_1 \cdot K_2 \cdot \overline{K}_3\right) \cdot P_{pv} \tag{11.6}$$

$$P_{batt} = \left(\overline{K}_1 \cdot \overline{K}_2 \cdot K_3 + \overline{K}_1 \cdot K_2 \cdot K_3\right) \cdot P_{batt} \tag{11.7}$$

Table 11.2 Mathematically Cases Based on Three Switches of PV/Battery System

Switches				Powers		
K_1	K_2	K_3	Modes	P_{pv}	P_{batt}	P_{load}
0	0	0	Mode 5	0	0	0
0	0	1	Mode 3	0	P_{batt}	P_{batt}
0	1	0	Mode 4	P_{pv}	0	P_{pv}
0	1	1	Mode 2	P_{pv}	P_{batt}	$P_{pv} + P_{batt}$
1	0	0	X	X	X	X
1	0	1	X	X	X	X
1	1	0	Mode 1	P_{pv}	0	P_{pv}
1	1	1	X	X	X	X

Table 11.3 Simplified Table in the Case of Three Switches (PV/Battery System)

Switches				Powers		
K_1	K_2	K_3	Modes	P_{pv}	P_{batt}	P_{load}
0	0	0	Mode 5	0	0	0
0	0	1	Mode 3	0	P_{batt}	P_{batt}
0	1	0	Mode 4	P_{pv}	0	P_{pv}
0	1	1	Mode 2	P_{pv}	P_{batt}	$P_{pv} + P_{batt}$
1	1	0	Mode 1	P_{pv}	0	P_{pv}

Table 11.4 Real Cases Based on Three Switches of PV/Battery System

Modes	Sources	ΔP	SOC	K1	K2	K3	P_{load}
Mode 1	PV	≥ 0	$SOC < SOC_{max}$	1	1	0	P_{pv}
Mode 2	PV + Battery	<0	$SOC > SOC_{min}$	0	1	1	$P_{pv} + P_{batt}$
Mode 3	Battery	<0	$SOC > SOC_{min}$	0	0	1	P_{batt}
Mode 4	PV	≥ 0	$SOC = SOC_{max}$	0	1	0	P_{pv}
Mode 5	/	<0	$SOC = SOC_{min}$	0	0	0	0

These equations can be minimized to:

$$P_{pv} = (K_2 + K_1) \cdot P_{pv} \tag{11.8}$$

$$P_{batt} = (K_3 + K_1) \cdot P_{batt} \tag{11.9}$$

Therefore, the load power is given as:

$$P_{load} = (K_2 + K_1) \cdot P_{pv} + (K_3 + K_1) \cdot P_{batt} \tag{11.10}$$

3.1.1.2 Second Structure of PMC

In this structure, four switches (K_1, K_2, K_3, and K_4) have been used. The fourth switch is used to store the power excess, if there is, in a derivate load or an auxiliary source (Fig. 11.5).

The available power ΔP (Eq. (11.1)) has to be determinate. According to its mathematical value, it is noticed in three cases. If $\Delta P > 0$, the load will be supplied by PV panels while the batteries are charging and if there will be an excess of power, it will be dissipated through a dump load, hence, the need of adding the fourth switch K_4 (Fig. 11.5). In the second case, where $\Delta P < 0$, the load is supplied only by batteries until their discharging, and in the last case, where $\Delta P = 0$, the load will be supplied only by PV panels (Table 11.5).

The EM strategy of PV/battery system based on four switches can be represented in the following flowchart (Fig. 11.6). Depending on the different tests on ΔP, P_{pv}, P_{load}, and SOC, the system operates in one of the different modes.

Mode 1: In this mode, the photovoltaic power ($P_{pv} > P_{load}$) is quite sufficient to supply the load and charge batteries.

Mode 2: The power supplied by PV panels is insufficient ($0 < P_{pv} < P_{load}$); in this case, the power of batteries is added to satisfy the power load demand. It is the compensation mode.

Mode 3: This mode is operating when no energy provides from the PV generator ($P_{pv} = 0$), so the batteries alone supply the load.

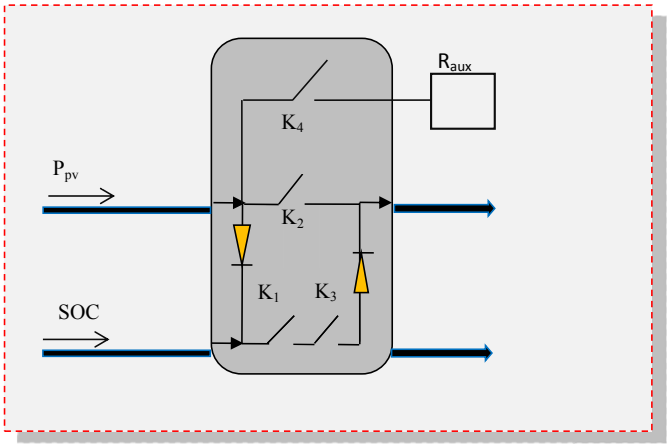


FIGURE 11.5

Power management based on four switches (PV/battery system).

Table 11.5 Different Cases of the Available Power in the Second Configuration of PV/Battery System

	ΔP	Load	Batteries
Case 1	>	Supplied by PV	Charging
Case 2	<	Supplied by batteries	Discharging
Case 3	=0	Supplied by PV	—

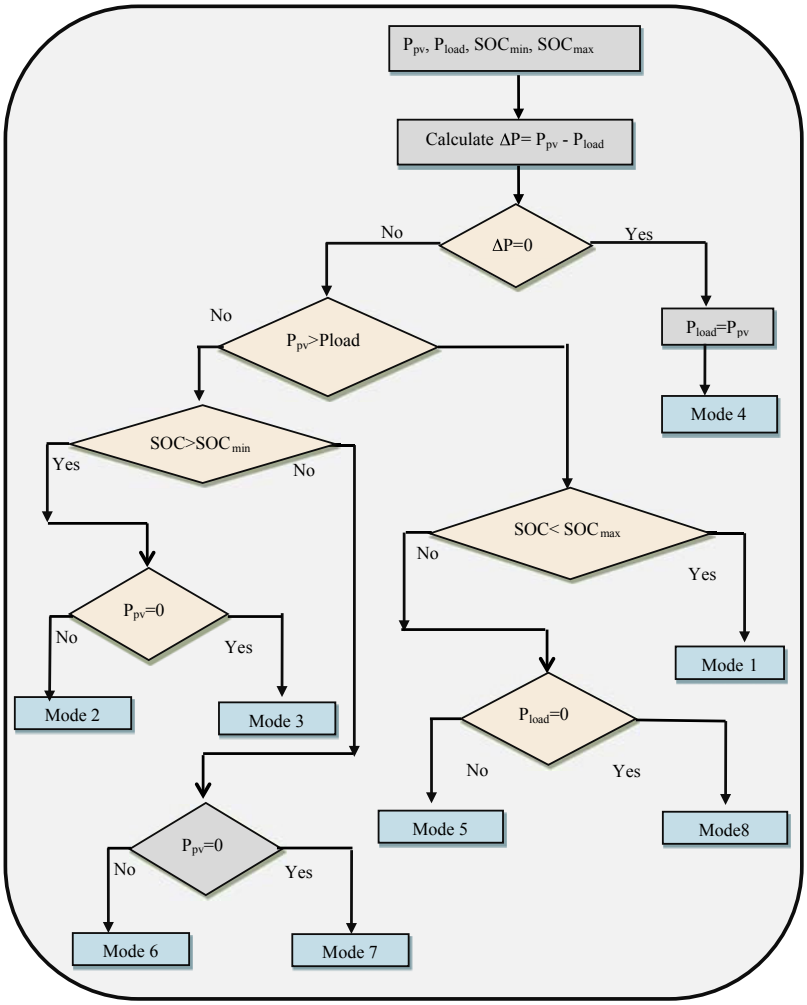


FIGURE 11.6

Energy management strategy of PV/battery system based on four switches.

Mode 4: The PV power is sufficient ($\Delta P = 0$ and $P_{pv} = P_{load}$), batteries are completely charging so the disconnection of the batteries is necessary to protect them.

Mode 5: The produced photovoltaic power ($P_{pv} > P_{load}$) is sufficient to supply the load and batteries are fully charged ($SOC = SOC_{max}$), so the excess energy will be dissipated in a derivate load or in an auxiliary source.

Mode 6: The produced photovoltaic power is insufficient to supply the load ($P_{pv} < P_{load}$) and the batteries are discharged ($SOC < SOC_{min}$).

Mode 7: In this case, there is no PV power production (during night or cloudy day $P_{pv} = 0$) and batteries are completely discharged, so the load will be disconnected ($P_{load} = 0$).

Mode 8: The produced photovoltaic power ($P_{pv} > P_{load}$) is sufficient to supply the load and batteries are fully charged ($SOC = SOC_{max}$), but the load is disconnected, so the excess energy will be dissipated in a derivate or dump load.

The different modes depend on the four switches K_1, K_2, K_3, and K_4. Mathematically, it can obtain 16 ($2^4 = 16$) cases (Table 11.6). It is noticed that the four first modes are the same than those in the first structure.

After simplifications, we obtain the Table 11.7.

The eight real modes are given in Table 11.8.

Table 11.6 Mathematically Cases Based on Four Switches of PV/Battery System

Switches					Powers				
K_1	K_2	K_3	K_4	Modes	P_{pv}	$P_{batt\text{-}discharge}$	P_{batt_charge}	P_{aux}	P_{load}
0	0	0	0	Mode 7	0	0	0	0	0
0	0	0	1	Mode 8	P_{pv}	0	0	0	P_{pv}
0	0	1	0	Mode 3	0	P_{batt}	0	0	P_{pv}
0	0	1	1	X	X	X	X	X	X
0	1	0	0	Mode 4	P_{pv}	0	0	0	0
0	1	0	1	Mode 5	P_{pv}	0	0	0	P_{pv}
0	1	1	0	Mode 2	P_{pv}	P_{batt}	0	0	$P_{pv} + P_{batt}$
0	1	1	1	X	X	X	X	X	X
1	0	0	0	Mode 6	P_{pv}	0	1	0	P_{pv}
1	0	0	1	X	X	X	X	X	X
1	0	1	0	X	X	X	X	X	X
1	0	1	1	X	X	X	X	X	X
1	1	0	0	Mode 1	P_{pv}	0	1	0	P_{pv}
1	1	0	1	X	X	X	X	X	X
1	1	1	0	X	X	X	X	X	X
1	1	1	1	X	X	X	X		X

Table 11.7 Simplified Table Based on Four Switches of PV/Battery System

Switches					Powers		
K_1	K_2	K_3	K_4	Modes	P_{pv}	P_{batt}	P_{load}
0	0	0	0	Mode 7	0	0	0
0	0	0	1	Mode 8	P_{pv}	0	P_{batt}
0	0	1	0	Mode 3	0	P_{batt}	P_{pv}
0	1	0	0	Mode 4	P_{pv}	0	P_{pv}
0	1	0	1	Mode 5	P_{pv}	0	P_{pv}
0	1	1	0	Mode 2	P_{pv}	P_{batt}	$P_{pv} + P_{batt}$
1	0	0	0	Mode 6	P_{pv}	0	P_{pv}
1	1	0	0	Mode 1	P_{pv}	0	P_{pv}

The different powers can be expressed in terms of the different switches as:

$$P_{pv} = \left(\overline{K}_1 \cdot \overline{K}_2 \cdot \overline{K}_3 \cdot K_4 + \overline{K}_1 \cdot K_2 \cdot \overline{K}_3 \cdot \overline{K}_4 + \overline{K}_1 \cdot K_2 \cdot \overline{K}_3 \cdot K_4 + \overline{K}_1 \cdot K_2 \cdot K_3 \cdot \overline{K}_4 + K_1 \cdot K_2 \cdot \overline{K}_3 \cdot \overline{K}_4\right) \cdot P_{pv} \tag{11.11}$$

$$P_{batt-discharge} = \left(\overline{K}_1 \cdot \overline{K}_2 \cdot K_3 \cdot \overline{K}_4 + \overline{K}_1 \cdot K_2 \cdot K_3 \cdot \overline{K}_4\right) \cdot P_{batt} \tag{11.12}$$

$$P_{batt-charge} = \left(K_1 \cdot \overline{K}_2 \cdot K_3 \cdot \overline{K}_4 + K_1 \cdot K_2 \cdot \overline{K}_3 \cdot \overline{K}_4\right) \cdot P_{batt} \tag{11.13}$$

$$P_{deriv} = \left(\overline{K}_1 \cdot \overline{K}_2 \cdot \overline{K}_3 \cdot K_4 + \overline{K}_1 \cdot K_2 \cdot \overline{K}_3 \cdot K_4\right) \cdot P_{pv} \tag{11.14}$$

These equations can be minimized to:

$$P_{pv} = (K_1 + K_2 + K_4) \cdot P_{pv} \tag{11.15}$$

$$P_{batt-discharge} = K_3 \cdot P_{batt} \tag{11.16}$$

$$P_{batt-charge} = K_1 \cdot P_{batt} \tag{11.17}$$

Therefore, the load power is given as:

$$P_{load} = (K_1 + K_2 + K_4) \cdot P_{pv} + K_3 \cdot P_{batt-discharge} \tag{11.18}$$

3.2 OTHER STRUCTURES

3.2.1 Photovoltaic Systems with Fuel Cells

In this structure, four switches (K_1, K_2, K_3, and K_4) have been used. The fourth switch is used to store in a derivate load [37,38] (Fig. 11.7).

According to the value of ΔP, three cases are noticed. If $\Delta P > 0$, the load will be supplied by the PV panel and the surplus PV energy is stored in the form of hydrogen by the electrolyzer, hence, the need for adding the fourth switch K_4 (Fig. 11.8). In the

Table 11.8 Real Cases Based on Four Switches of PV/Battery System

Modes	Sources	ΔP	SOC	P_{batt}	P_{aux}	P_{load}
Mode 1	PV	$P_{pv} > P_{load}$	$SOC < SOC_{max}$	Charge	0	P_{pv}
Mode 2	PV + Battery	$0 < P_{pv} < P_{load}$	$SOC > SOC_{min}$	Discharge	0	$P_{pv} + P_{batt}$
Mode 3	Battery	$P_{pv} = 0$	$SOC > SOC_{min}$	Discharge	0	P_{batt}
Mode 4	PV	$P_{pv} = P_{load}$	$SOC = SOC_{max}$	Charge	0	P_{pv}
Mode 5	PV	$P_{pv} > P_{load}$	$SOC = SOC_{max}$	Charge	ΔP	P_{pv}
Mode 6	PV	$P_{pv} < P_{load}$	$SOC < SOC_{min}$	Discharge	0	0
Mode 7	/	$P_{pv} = 0, P_{load} = 0$	$SOC = SOC_{min}$	Discharge	0	0
Mode 8	PV	$P_{pv} > P_{load}$	$SOC = SOC_{max}$	Charge	ΔP	P_{pv}

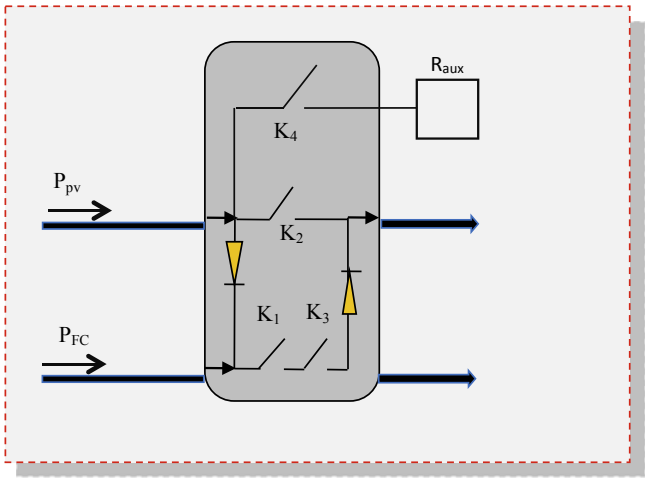


FIGURE 11.7

Energy management of PV/FC system based on four switches.

second case, where $\Delta P < 0$, the deficit energy can be taken from hydrogen by the fuel cells. In the last case, where $\Delta P = 0$, the load will be supplied by PV panels (Table 11.9).

Depending on the different tests ΔP, P_{pv}, and P_{FC}, the system operates in one of the following modes (Table 11.10).

Mode 1: In this mode, the photovoltaic power ($P_{pv} > P_{load}$) is quite sufficient to supply the load and the excess energy will be stored in hydrogen by an electrolyzer ($P_{Load} = P_{pv}$, $P_{ele} = \Delta P$).

Mode 2: The power supplied by PV is insufficient ($0 < P_{pv} < P_{load}$); in this case, the power of fuel cells is added to satisfy the power demand. It is the compensation mode ($P_{load} = P_{pv} + P_{FC}$).

Mode 3: This mode is operating when no energy provides from the PV generator ($P_{pv} = 0$), so fuel cells alone supply the load ($P_{load} = P_{FC}$).

Mode 4: The PV power is sufficient ($\Delta P = 0$ and $P_{pv} = P_{load}$).

Mode 5: In this case, there is no PV energy production (during night $P_{pv} = 0$) and fuel cells are not powered by hydrogen, the load is disconnected ($P_{load} = 0$).

Mode 6: The photovoltaic power produced is insufficient to supply the load ($P_{pv} < P_{load}$) and the power fuel cells is zero ($P_{FC} = 0$, $P_{load} = 0$, so $P_{elec} = P_{pv}$).

The different modes depend on the four switches K_1, K_2, K_3, and K_4 (Table 11.10). Mathematically, it can obtain 16 cases (Table 11.10).

After simplification, we obtain the Table 11.11 and 11.12.

The EM strategy of PV/FC system based on four switches can be represented in the following flowchart (Fig. 11.8).

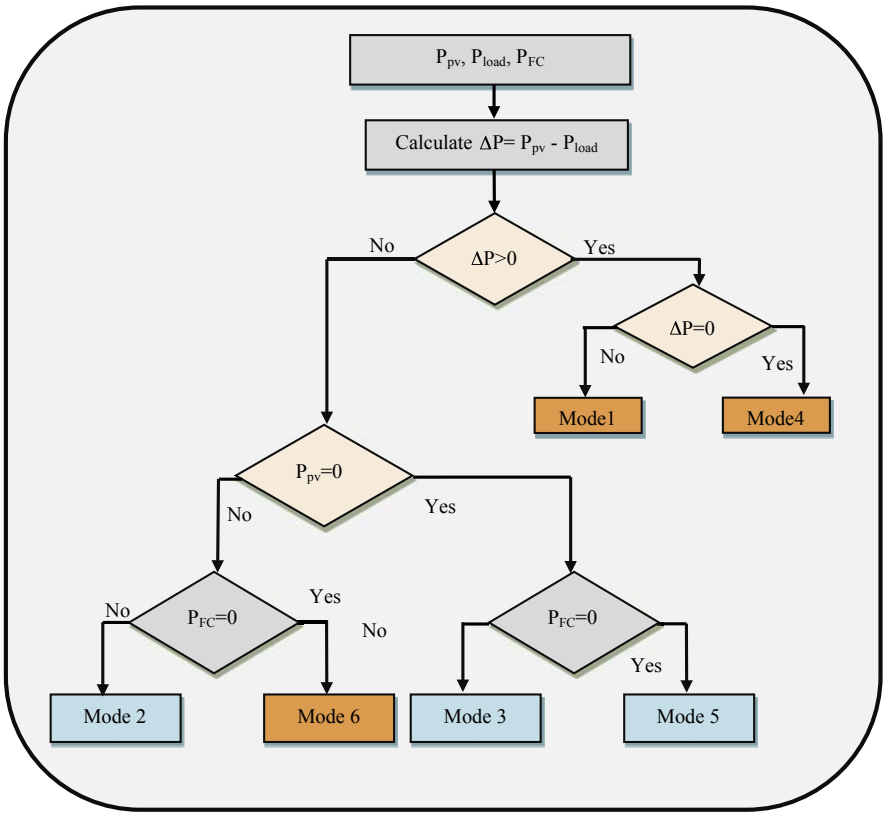


FIGURE 11.8

Energy management strategy of PV/FC system based on four switches.

Table 11.9 Different Cases of the Available Power in PV/FC System

	ΔP	Load	Electrolyzer
Case 1	>	Supplied by PV	$P_{elec} = \Delta P$
Case 2	<	Supplied by fuel cells	0
Case 3	= 0	Supplied by PV	0

The different powers can be expressed in terms of the different switches as:

$$P_{pv} = \left(\overline{K}_1 \cdot K_2 \cdot \overline{K}_3 \cdot \overline{K}_4 + \overline{K}_1 \cdot K_2 K_3 \cdot \overline{K}_4 + K_1 \cdot K_2 \cdot \overline{K}_3 \cdot K_4\right) \cdot P_{pv} \tag{11.19}$$

$$P_{FC} = \left(\overline{K}_1 \cdot \overline{K}_2 \cdot K_3 \cdot \overline{K}_4 + \overline{K}_1 \cdot K_2 K_3 \cdot \overline{K}_4\right) \cdot P_{FC} \tag{11.20}$$

$$P_{elec} = \left(K_1 \cdot K_2 \cdot \overline{K}_3 \cdot K_4\right) \cdot P_{pv} \tag{11.21}$$

Table 11.10 Mathematically, Cases Based on Three Switches of PV/Fuel Cells System

Switches					Powers			
K_1	K_2	K_3	K_4	Modes	P_{pv}	P_{FC}	P_{load}	P_{elec}
0	0	0	0	Mode 7	0	0	0	0
0	0	0	1	x	x	x	x	x
0	0	1	0	Mode 3	0	P_{FC}	P_{FC}	0
0	0	1	1	X	X	X	X	x
0	1	0	0	Mode 4	P_{pv}	0	P_{pv}	0
0	1	0	1	Mode 5	0	0	0	0
0	1	1	0	Mode 2	P_{pv}	P_{FC}	$P_{pv} + P_{FC}$	0
0	1	1	1	X	X	X	X	x
1	0	0	0	Mode 6	P_{pv}	0	0	P_{pv}
1	0	0	1	X	X	X	X	x
1	0	1	0	X	X	X	X	x
1	0	1	1	X	X	X	X	x
1	1	0	1	Mode 1	P_{pv}	0	P_{pv}	P_{pv}
1	1	0	1	X	X	X	X	x
1	1	1	0	X	X	X	X	x
1	1	1	1	X	X	X	X	x

Table 11.11 Simplified Table Based on Four Switches of PV/Fuel Cells System

Switches					Powers			
K_1	K_2	K_3	K_4	Modes	P_{pv}	P_{FC}	P_{load}	P_{elec}
0	0	0	0	Mode 7	0	0	0	0
0	0	1	0	Mode 3	0	P_{FC}	P_{FC}	0
0	1	0	0	Mode 4	P_{pv}	0	P_{pv}	0
0	1	0	1	Mode 5	0	0	0	0
0	1	1	0	Mode 2	P_{pv}	P_{FC}	$P_{pv} + P_{FC}$	0
1	0	0	0	Mode 6	P_{pv}	0	0	P_{pv}
1	1	0	1	Mode 1	P_{pv}	0	P_{pv}	P_{pv}

These equations can be minimized to:

$$P_{pv} = (K_2 + K_1) \cdot P_{pv} \tag{11.22}$$

$$P_{FC} = (K_3) \cdot P_{FC} \tag{11.23}$$

$$P_{elec} = (K_4) \cdot P_{pv} \tag{11.24}$$

Table 11.12 Real Cases Based on Four Switches of PV/FC System

Modes	Sources	ΔP	P_{pv}	P_{FC}	P_{elec}	P_{load}
Mode 1	PV	$P_{pv} > P_{load}$	P_{pv}	0	ΔP	P_{pv}
Mode 2	PV + Fuel cells	$0 < P_{pv} < P_{load}$	P_{pv}	P_{FC}	0	$P_{pv} + P_{FC}$
Mode 3	Fuel cells	$P_{pv} = 0$	0	P_{FC}	0	P_{FC}
Mode 4	PV	$P_{pv} = P_{load}$	P_{pv}	0	0	P_{pv}
Mode 5	PV	$P_{pv} = 0$	0	0	0	0
Mode 6	PV	$P_{pv} < P_{load}$	P_{pv}	0	P_{pv}	0

3.2.2 Photovoltaic System with Wind Turbine and Battery Storage

The main power is the summation of the two renewable sources P_{renew} [5], which can be written as:

$$P_{Renew} = P_{pv} + P_{Wind} \tag{11.25}$$

And then the available power will be:

$$\Delta P = P_{Renew} - P_{load} \tag{11.26}$$

According to the value of ΔP, we will obtain two cases. If $\Delta P \geq 0$, the load will be supplied by the two renewable energy sources (solar and wind). In the second case, where $\Delta P < 0$, the power PV can be null or insufficient to feed the load; so, the battery storage is added to satisfy the power load (Table 11.13).

The EM strategy of wind turbine/battery system based on three switches can be represented in the following flowchart (Fig. 11.9).

Mode 1: In this mode, the photovoltaic power (P_{Renew}) is quite sufficient to supply the load and charge the batteries ($\Delta P \geq 0$ and $SOC < SOC_{max}$).

Mode 2: The power supplied by the two renewable sources is insufficient ($0 < P_{Renew} < P_{load}$), in this case, the power of batteries is added to satisfy the power demand ($SOC > SOC_{min}$). It is the compensation mode.

Mode 3: This mode is operating when no energy is provided from the two renewable sources ($\Delta P < 0$), so the batteries alone supply the load ($SOC > SOC_{min}$).

Mode 4: The power of the two renewable sources is sufficient and batteries are completely charging so the disconnection of the batteries is necessary to protect them ($SOC = SOC_{max}$).

Mode 5: In this mode, there is no production from the two renewable sources and the batteries are discharged. The load is disconnected ($SOC = SOC_{min}$)

Table 11.13 Different Cases of the Available Power in PV/Wind/Battery System

	ΔP	Load
Case 1	$\geq$	Supplied by renewable energy sources
Case 2	$<$	Supplied by battery storage

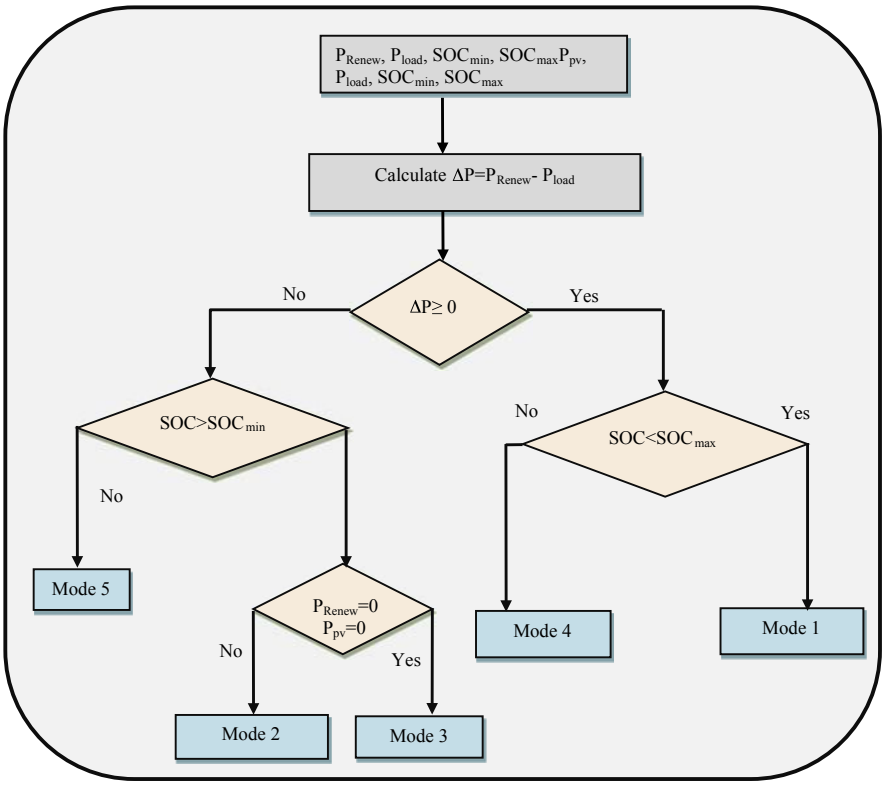


FIGURE 11.9

Energy management strategy of PV/wind system with battery storage.

The different modes depend on the three switches K_1, K_2, and K_3. Mathematically, it results in eight cases (Table 11.14).

After simplification, we obtain the Table 11.15:

But only five cases can be exploitable as real cases (Table 11.16)

The different powers can be expressed in terms of the different switches as:

$$P_{Renew} = \overline{K}_1 \cdot K_2 \cdot \overline{K}_3 + \overline{K}_1 \cdot K_2 \cdot K_3 + K_1 \cdot K_2 \cdot \overline{K}_3 \tag{11.27}$$

$$P_{batt} = \overline{K}_1 \cdot \overline{K}_2 \cdot K_3 + \overline{K}_1 \cdot K_2 \cdot K_3 \tag{11.28}$$

These equations can be minimized to:

$$P_{Renew} = K_2 + K_1 \tag{11.29}$$

$$P_{batt} = K_3 \tag{11.30}$$

Therefore, the load power is given as:

$$P_{load} = (K_2 + K_1) \cdot P_{Renew} + K_3 \cdot P_{batt} \tag{11.31}$$

Table 11.14 Mathematically Cases Based on Three Switches of PV/Wind Turbine/Battery System

Switches			Modes	Powers		
K_1	K_2	K_3		P_{Renew}	P_{batt}	P_{load}
0	0	0	Mode 5	0	0	0
0	0	1	Mode 3	0	P_{batt}	P_{batt}
0	1	0	Mode 4	P_{Renew}	0	P_{Renew}
0	1	1	Mode 2	P_{Renew}	P_{batt}	$P_{Renew} + P_{batt}$
1	0	0	X	X	X	X
1	0	1	X	X	X	X
1	1	0	Mode 1	P_{Renew}	0	P_{Renew}
1	1	1	X	X	X	X

Table 11.15 Simplified Table in the Case of Three Switches of PV/Wind Turbine/Battery System

Switches			Modes	Powers		
K_1	K_2	K_3		P_{Renew}	P_{batt}	P_{load}
0	0	0	Mode 5	0	0	0
0	0	1	Mode 3	0	P_{batt}	P_{batt}
0	1	0	Mode 4	P_{Renew}	0	P_{Renew}
0	1	1	Mode 2	P_{Renew}	P_{batt}	$P_{Renew} + P_{batt}$
1	1	0	Mode 1	P_{Renew}	0	P_{Renew}

Table 11.16 Real Cases Based on Three Switches of PV/Wind Turbine/Battery System

Modes	Sources	ΔP	SOC	K_1	K_2	K_3	P_{load}
Mode 1	PV + Wind	≥ 0	$SOC < SOC_{max}$	1	1	0	P_{Renew}
Mode 2	PV + Wind + Battery	<0	$SOC > SOC_{min}$	0	1	1	$P_{Renew} + P_{batt}$
Mode 3	Battery	<0	$SOC > SOC_{min}$	0	0	1	P_{batt}
Mode 4	PV + Wind	≥ 0	$SOC = SOC_{max}$	0	1	0	P_{Renew}
Mode 5	/	<0	$SOC = SOC_{min}$	0	0	0	0

4. CONCLUSIONS

In this chapter, EM structures have been presented. In each structure, PV generators are chosen to be the main source while others are used to obtain the compensation

mode. The hybridization of PV source with an energy storage system or another source can provide steady-state energy to the load during cloudy days or during night and can improve dynamic response during transients.

These EM algorithms are simple, flexible, and can be applied to other sources or other storage and even to various applications such as electric vehicles, pumping water, electrification.

REFERENCES

[1] Solar Energy at Home, http://www.solar-energy-at-home.com/photovoltaic-solar-power.html.

[2] How do Photovoltaics Work? https://science.nasa.gov/science-news/science-at-nasa/2002/solarcells.

[3] M. Fadaeenejad, M.A.M. Radzi, M.Z.A. AbKadir, H. Hizam, Assessment of hybrid renewable power sources for rural electrification in Malaysia, Renew. Sustain. Energy Rev. 30 (February 2014) 299−305.

[4] D. Rekioua, E. Matagne, Optimization of photovoltaic power systems: modelization, simulation and control, in: Green Energy and Technology, Springer, 2012.

[5] D. Rekioua, Wind power electric systems: modeling, simulation and control, in: Green Energy and Technology, Springer, 2014.

[6] N. Mezzai, D. Rekioua, T. Rekioua, K. Idjdarane, S. Bacha, Modeling of hybrid photovoltaic/wind/fuel cells power system, Int. J. Hydrogen Energy 39 (27) (September 12, 2014) 15158−15168.

[7] Z. Mokrani, D. Rekioua, T. Rekioua, Modeling, control and power management of hybrid photovoltaic fuel cells with battery bank supplying electric vehicle, Int. J. Hydrogen Energy 39 (27) (September 12, 2014) 15178−15187.

[8] D. Rekioua, S. Bensmail, N. Bettar, Development of hybrid photovoltaic-fuel cell system for stand-alone application, Int. J. Hydrogen Energy 39 (3) (2014) 1604−1611.

[9] S. Aissou, D. Rekioua, N. Mezzai, T. Rekioua, S. Bacha, Modeling and control of hybrid photovoltaic wind power system with battery storage, Energy Convers. Manage. 89 (1) (January 2015) 615−625.

[10] H. Fang, J. Zhang, J. Gao, Optimal operation of multi-storage tank multi-source system based on storage policy, J. Zhejiang Univ.-Sci. A 11 (8) (2010) 571−579.

[11] J. Becker, C. Schaeper, D.U. Sauer, Energy management system for a multi-source storage system electric vehicle, in: 2012 IEEE Vehicle Power and Propulsion Conference (VPPC), Seoul, South Korea.

[12] P. Mancarella, Multi-energy systems: an overview of concepts and evaluation models, Energy (February 2014) 1−35.

[13] S. Koohi-Kamali, N.A. Rahim, H. Mokhlis, Smart power management algorithm in microgrid consisting of photovoltaic, diesel, and battery storage plants considering variations in sunlight, temperature, and load, Energy Convers. Manage. 84 (August 2014) 562−582.

[14] A. Rabhi, J. Bosch, A. Elhajjaji, Energy management for an autonomous renewable energy system, Energy Procedia 83 (December 2015) 299−309.

[15] S. Gaurav, C. Birla, A. Lamba, S. Ganesan, Energy management of PV-battery based microgrid system, Procedia Technol. 21 (2015) 103−111.

[16] J. Seigneurbieux, G. Robin, H. Ben Ahmed, B. Multon, Optimization with energy management of PV battery stand-alone systems over the entire life cycle, in: 21st European Photovoltaic Solar Energy Conference and Exhibition, Dresden, September 2006.
[17] H. Kanchev, D. Lu, F. Colas, V. Lazarov, B. Francois, Energy management and operational planning of a microgrid with a PV-based active generator for smart grid applications, IEEE Trans. Industr. Electron. 58 (10) (October 2011) 4583−4592.
[18] S.N. Singh, A.K. Singh, Rural home energy management by fuzzy control model for solar (PV)-grid/DG power system in India, J. Electr. Control Eng. 2 (1) (2012) 29−33.
[19] P.J.R. Pinto, C.M. Rangel, A power management strategy for a stand-alone photovoltaic/fuel cell energy system for a 1 kW application, in: Hydrogen Energy and Sustainability - Advances in Fuel Cells and Hydrogen Workshop 3rd Seminar International Torres Vedras (Portugal) April 29-30, 2010.
[20] T. Balamurugan, S.Manoharan, Optimal power flow management control for grid connected photovoltaic/wind turbine/diesel generator (GCPWD) hybrid system with batteries, Int. J. Renew. Energy Res. 3 (4) (2013) 819−826.
[21] Y. Jaganmohan Reddy, Y.V. Pavan Kumar, K. Padma Raju, A. Ramsesh, PLC based energy management and control design for an alternative energy power system with improved power quality, Int. J. Eng. Res. Appl. (IJERA) 3 (3) (May-Jun 2013) 186−193.
[22] B. Belvedere, M. Bianchi, A. Borghetti, C. Alberto Nucci, M. Paolone, A. Peretto, A microcontroller-based power management system for standalone micro grids with hybrid power supply, IEEE Trans. Sustain. Energy 3 (3) (July 2012) 422−431.
[23] K. Sekar, V. Duraisamy, Efficient energy management system for integrated renewable power generation systems, J. Sci. Industr. Res. 74 (June 2015) 325−329.
[24] G.V. Santos, F.H. de Oliveira, A.F. Cupertino, T.A. Pizziollo, H.A. Pereira, Power flow management in hybrid power system using flatness based control, in: 2013 IEEE PES Conference on Innovative Smart Grid Technologies (ISGT Latin America), April 15-17, 2013, pp. 1−6.
[25] C. Serir, D. Rekioua, N. Mezzai, S. Bacha, Supervisor control and optimization of multi-sources pumping system with battery storage, Int. J. Hydrogen Energy 41 (45) (2016) 20974−20986.
[26] M. Al-Norya, M. El-Beltagya, An energy management approach for renewable energy integration with power generation and water desalination, Renew. Energy 72 (December 2014) 377−385.
[27] R. Miceli, Energy management and smart grids, Energies 6 (2013) 2262−2290.
[28] C. Sudipta, D.W. Manoja, M.G. Simoes, Distributed intelligent energy management system for a single-phase high-frequency AC micro grid, IEEE Trans. Ind. Electron 54 (1) (February 2007) 97−109.
[29] O.O. Mengi, I.H. Altas, A new energy management technique for PV/wind/grid renewable energy system, Int. J. Photoenergy (2015) 1−19.
[30] V. Courtecuisse, J. Sprooten, B. Robyns, M. Petit, B. Francois, J. Deuse, A methodology design a fuzzy logic based supervision hybrid renewable energy systems, Math. Comput. Simul. 81 (2) (2010) 208−224.
[31] K.S. Jeong, W.Y. Lee, C.S. Kim, Energy management strategies of a fuel cell/battery hybrid system using fuzzy logic, J. Power Sources 145 (2) (2005) 319−326.
[32] N. Karami, N. Moubayed, R. Outbib, Energy management for a PEMFC−PV hybrid system, Energy Convers. Manage. 82 (June 2014) 154−168.

[33] D. Ipsakis, S. Voutetakis, P. Seferlis, F. Stergiopoulos, C. Elmasides, Power management strategies for a stand-alone power system using renewable energy sources and hydrogen storage, Int. J. Hydrogen Energy 34 (16) (2009) 7081−7095.
[34] P. García, J.P. Torreglosa, L.M. Fernández, F. Jurado, Optimal energy management system for stand-alone wind turbine/photovoltaic/hydrogen/battery hybrid system with supervisory control based on fuzzy logic, Int. J. Hydrogen Energy 38 (33) (2013) 14146−21415.
[35] W. Andari, S. Ghozzi, H. Allagui, A. Mami, Design, modeling and energy management of a PEM fuel cell/supercapacitor hybrid vehicle, Int. J. Adv. Comput. Sci. Appl. 8 (1) (2017).
[36] F. Zaouche, Z. Mokrani, D. Rekioua, Control and energy management of photovoltaic pumping system with battery storage, in: 4rd International Renewable and Sustainable Energy Conference (IRSEC'16), November 14-18, 2016 Marrakech, Morocco.
[37] N. Mebarki, T. Rekioua, Z. Mokrani, D. Rekioua, S. Bacha, PEM fuel cell/battery storage system supplying electric vehicle, Int. J. Hydrogen 41 (2016) 1−13.
[38] Z. Mokrani, D. Rekioua, N. Mebarki, T. Rekioua, S. Bacha, Energy management of battery-PEM fuel cells hybrid energy storage system for electric vehicle, in: 4rd International Renewable and Sustainable Energy Conference (IRSEC'16), November 14−18, 2016 Marrakech, Morocco.

This page intentionally left blank

PART

PVT Energy

2

This page intentionally left blank

www.TechnicalBooksPDF.com

CHAPTER

Concentrating Solar Power 12

José J.C.S. Santos[1], José C.E. Palacio[2], Arnaldo M.M. Reyes[2], Monica Carvalho[3], Alberto J.R. Freire[4], Marcelo A. Barone[1]

Department of Mechanical Engineering, Federal University of Espírito Santo, Vitória, Brazil[1]; Department of Mechanical Engineering, Federal University of Itajubá, Itajubá, Brazil[2]; Department of Renewable Energy Engineering, Federal University of Paraíba, João Pessoa, Brazil[3]; Department of Control Engineering and System Analysis, Université Libre de Bruxelles, Brussels, Belgium[4]

CHAPTER OUTLINE

1. Introduction 373
2. Solar Energy Resources: Sun Characteristics and Solar Radiation 377
3. Concentrating Solar Power Plants 381
4. Solar Thermal Energy Storage 391
5. Thermodynamic and Economic Study 395
References 401

1. INTRODUCTION

Concentrating solar power (CSP) is the power generated in solar power systems that use solar concentrators to convert solar energy into heat and then the produced heat is converted into power. CSP systems use very different technology than photovoltaic (PV) systems. They use the sun as heat energy source instead of the photon energy of the sun used by PV systems. CSP plants use mirrors or lenses to concentrate a large area of sunlight, or solar thermal energy, onto a small area. Electricity is generated when the concentrated light drives a heat engine, usually a steam turbine cycle, connected to an electrical power generator. The thermal energy concentrated can be stored and used to produce electricity when it is needed. Most power plants use solar concentrator together with some form of fossil fuel burners to increase the amount of thermal heat source.

The four main types of solar concentrator systems are parabolic trough, power tower, linear Fresnel, and dish. All of them use thermal energy from the sun to generate mechanical energy in a heat engine to drive electrical generator do produce electricity. The dish concentrates thermal energy, generally used in Stirling engine systems. The parabolic trough, linear Fresnel, and power tower are technologies

Advances in Renewable Energies and Power Technologies. https://doi.org/10.1016/B978-0-12-812959-3.00012-5
Copyright © 2018 Elsevier Inc. All rights reserved.

for CSP systems based on Brayton or Rankine cycles. The basic and general process for conversion of solar thermal energy to electric energy in the concentrated power plants is shown schematically in Fig. 12.1.

Energy is recovered by solar collectors, which are mechanical devices that capture radiant solar energy and convert it to useful thermal energy. This energy can be stored (if appropriate or required) and converted to satisfy electricity, thermal, or mechanical energy demands. Different types of solar collectors can be applied, depending on the application.

There are nonconcentrating and concentrating types of solar collectors. The former uses the same area to intercept and absorb solar radiation. However, the concentrating solar collectors used in CSP plants usually have concave reflecting surfaces to intercept and concentrate solar radiation into a small receiving area, thereby increasing radiation flow. Parabolic troughs, solar towers in heliostat field, linear Fresnel reflectors (LFRs), and parabolic dishes (PDs) are the main technologies used in the concentrating solar thermal power plants, due to the production of high-temperature heat. Fig. 12.2 represents the concept involved in the solar concentrator: (1) parabolic trough, (2) PD, (3) power tower, and (4) linear Fresnel.

As sunlight is not always available, an energy storage system is required to extend the working hours of a solar energy plant to satisfy energy demands during the nighttime, for example. Integration of energy storage systems with CSP technologies enables the prolongation of the operation hours of solar power plants and could mitigate the dependence and direct relationship between CSP technologies and

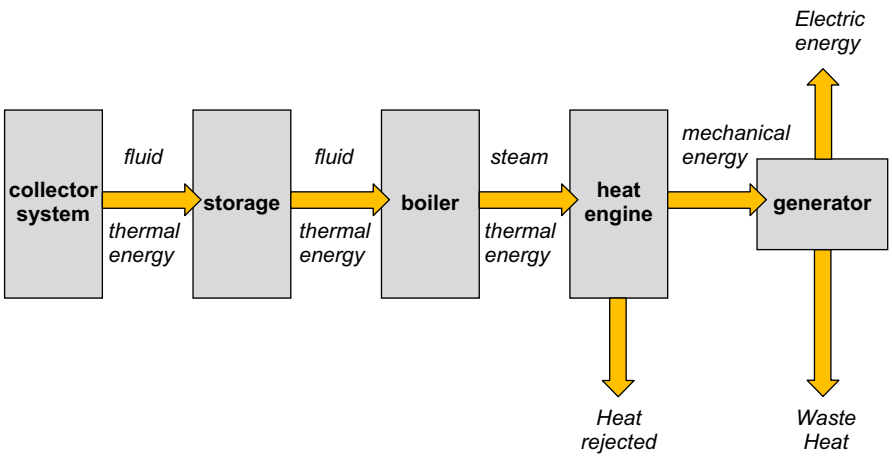


FIGURE 12.1

A generic concentrating solar power plant.

Courtesy L. Witmer, Overview of Solar Thermal Power Systems | EME 811: Solar Thermal Energy for Utilities and Industry [WWW Document], Pennsylvania State Univ., 2017. URL: https://www.e-education.psu.edu/eme811/node/682.

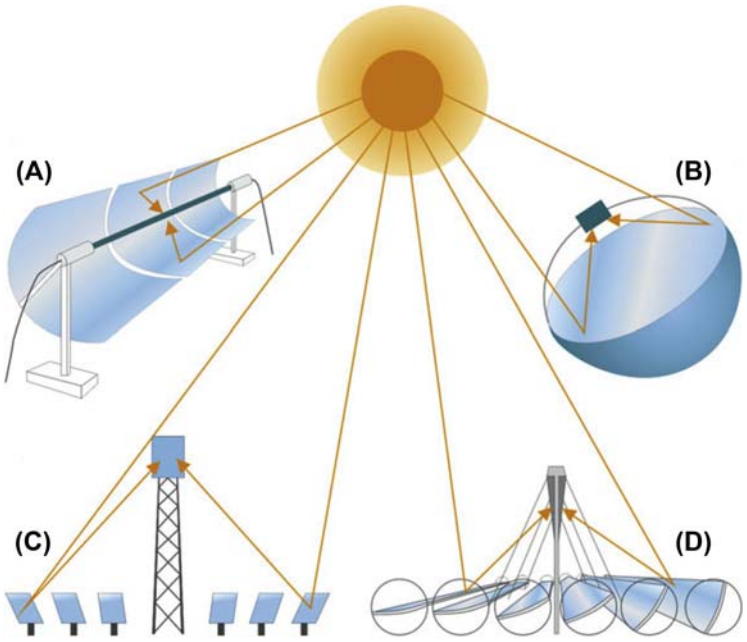


FIGURE 12.2

Solar collectors: (A) parabolic troughs; (B) parabolic dishes; (C) tower; and (D) linear Fresnel reflectors.

Courtesy R. Guerrero-Lemus, J.M.M. Martínez-Duart, Concentrated solar power, in: Renewable Energies and CO_2, Springer-Verlag, London, 2013, pp. 135–151.

climatic conditions, such as clouds or low solar irradiation. Short-term thermal storage systems, with a 1-h capacity, can be used to ensure the production of energy on a cloudy day. Despite clear benefits, most of the early operating pilot and commercial solar power plants lacked significant thermal storage, typically relying on steam or oil accumulators for thermal inertia.[1] For large-scale power plant applications, the use of battery storage has not been explored due to economic limitations.

Table 12.1 compares the main CSP technologies, considering storage integration possibilities, advantages, and disadvantages: parabolic trough collector (PTC), LFR, solar power tower with heliostat field, and PD.

In a heat engine, power conversion efficiency is theoretically limited by Carnot's efficiency and is related to the quality of energy, and thus temperature, of the thermal energy supply. In an electricity generation system based on solar energy, the high-quality thermal energy required must be supplied by the collectors. Solar collectors are affected by energy losses (reflection, glazing absorption, convective heat transfer,

[1]P. Gauché, J. Rudman, M. Mabaso, W.A. Landman, T.W. von Backström, A.C. Brent, System value and progress of CSP, Sol. Energy. 152 (2017) 106–139

Table 12.1 Comparison Between Different Concentrating Solar Power (CSP) Technologies

CSP Technology	Storage Integration Possibility	Advantages	Disadvantages
PTC	Possible	• Relatively low installation cost • Large experimental feedback	• Relatively large area occupied • Low thermodynamic efficiency due to low operating temperature
LFR	Possible	• Relatively low installation cost	• Low thermodynamic efficiency due to low operating temperature
SPT	Highly possible with low storage cost.	• High thermodynamic efficiency due to high operating temperature	• Large space area occupied • Relatively high installation cost • High heat losses
PD	Difficult	• Relatively small area occupied • High thermodynamic efficiency due to high operating temperature	• Relatively high installation cost • Little experimental feedback

LFR, *linear Fresnel reflector;* PD, *parabolic dish;* PTC, *parabolic trough collector;* SPT, *solar power tower.*

Modified from U. Pelay, L. Luo, Y. Fan, D. Stitou, M. Rood, Thermal energy storage systems for concentrated solar power plants, Renew Sustainable Energy Rev. 79 (2017) 82–100.

and thermal radiation) whenever the collector output temperature rises. This occurs because the collector is influenced by the local environmental conditions. Efficiency increases along with the temperature of the hot reservoir, but high temperatures could decrease the efficiency of solar collectors; a trade-off analysis must be carried out to determine the optimum operation point for the power plant.

Fig. 12.3 shows the combined heat engine efficiency and absorber efficiency for different CSP technologies. Fig. 12.3 shows that the concentration ratio always increases the global plant efficiency, and that there is a trade-off relationship between the two efficiencies (heat engine + absorber), leading to optimum operation temperatures.

Although there are various technical options available for CSP technology, some of them did not reach development level of industrial maturity. Some of them are only concepts being developed in laboratories, R&D, or demonstration.[2] Recently, some authors conducted a survey on websites, identifying the current situation and future trends in CSP plants, the type, the use, duration, and type of energy

[2]EASAC, Concentrating Solar Power: Its Potential Contribution to a Sustainable Energy Future, 2011.

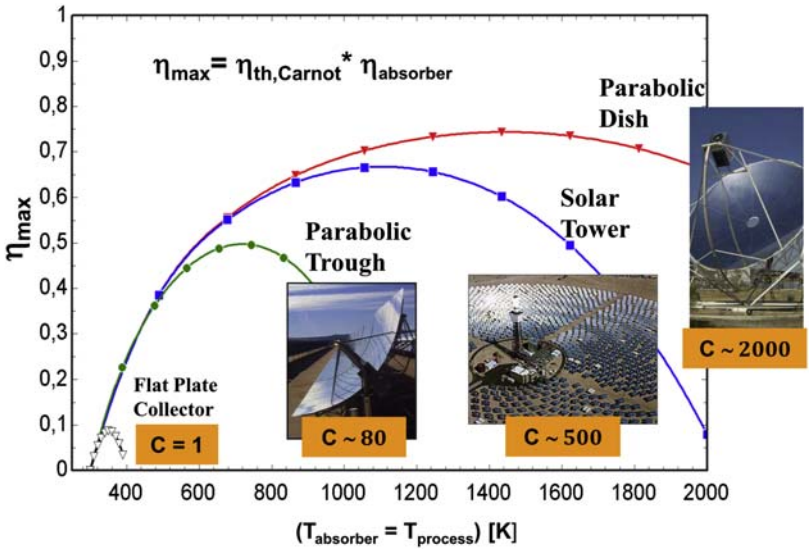


FIGURE 12.3

Theoretical thermal efficiency for different collector technologies.

Courtesy B.B. Hoffschmidt, Receivers for Solar Tower Systems [WWW Document], 2014. URL: http://sfera2.sollab.eu/networking/announcement-summer-schools/summer-schools/summer-school-presentation-2014.

storage as well as the average electrical power produced by the plants.[3] They found the utilization of backup system (hybridization) when solar radiation intensity is low and when a quick response is needed. Fossil or renewable fuels can be used, but solar PV is occasionally used.

2. SOLAR ENERGY RESOURCES: SUN CHARACTERISTICS AND SOLAR RADIATION

The Sun was formed 4.6 billion years ago and is estimated to last 5 billion more. It is the main source of energy for all processes in the Earth–atmosphere system, constituting more than 99.9% of this system. The main characteristics of the Sun are as follows[4]:

- It is a luminous gaseous star, with a diameter of 1.39×10^6 km (100 times that of the Earth), surface area of 6.08×10^{12} km^2, and a mass of 1.989×10^{30} kg (300,000 times that of the Earth); its density is more than 100 times that of water.

[3]U. Pelay, L. Luo, Y. Fan, D. Stitou, M. Rood, Thermal energy storage systems for concentrated solar power plants, Renew. Sustain. Energy Rev. 79 (2017) 82–100.
[4]N. Armaroli, V. Balzani, Energy for a Sustainable World: From the Oil Age to a Sun-Powered Future, Wiley-VCH, Weinheim, Germany, 2011.

- Its chemical composition is ~91.20% of hydrogen and 8.70% of helium, and less than 2% is accounted for by other elements such as oxygen, carbon, iron, sulfur, and neon.
- It emits energy in the form of electromagnetic radiation (photons), which propagates radially in space, traveling at the speed of light in the vacuum ($c = 300{,}000$ km/s). The propagation is in all directions through space or some medium, although a material medium is not needed (as in the case of conduction and convection) to propagate, independently of its wavelength (λ) and frequency (θ), but there is a well-defined relationship between these three elements: $c = \lambda \cdot \theta$. However, the speed, intensity, and direction of its energy flow are affected by the presence of matter, such as Earth's atmosphere. A photon takes only about 8 min to travel from the photosphere to the Earth. Once photon gets into our planet, its unique atmosphere and peculiar sea and land surface work out the incoming radiation. This complex pattern of reflection, absorption, scattering, and reabsorption effects is one of the countless prerequisites that makes possible life on Earth because, among others, it prevents the highest energy radiation (ultraviolet and others rays) from reaching the surface and it warms the planet to a comfortable 15°C average temperature.
- The solar mass that is irradiated per second into space in the form of high-energy particles and electromagnetic radiation is approximately 5.6×10^{35} GeV ($1\ \text{eV} = 1.6 \times 10^{-19}$ J).

The average distance between Sun and Earth is 149.6×10^6 km, known as the Astronomical Unit (UA), which varies because the Earth's trajectory is an elliptical; presenting extreme values between 147.05×10^6 km (Perihelio), and 152.14×10^6 km (Afelio), the points closest to and farthest from the Sun, respectively (Fig. 12.4).

The Sun's energy is generated within the core by nuclear reactions, the most important one involving four protons of hydrogen, which combine to form a nucleus of helium. Approximately 650×10^6 t/s of hydrogen is converted into approximately 646×10^6 t/s of helium. According to Einstein's equation ($E = mc^2$), a power of about 3.9×10^{26} J/s (W) of nuclear energy is delivered, that is, about 1 million times our current global primary energy consumption per year (as a further comparison, a 1000 MW coal or nuclear power plant converts 0.130 kg of matter into energy in 1 year). The Sun's temperature is about 14×10^6 K in the core and 5760 K in the surface. For simplified calculations of engineering, it is common to adopt for the temperature of the Sun the approximate value of 6000 K. The largest amount of radiant energy in the Sun is concentrated in the visible and near visible range of the spectrum: visible light 43%, near-infrared 49%, ultraviolet 7%, and other ranges 1%.

Solar energy advantages are—apart from being free—the low impact of its installation because it does not involve gas or acoustic pollution; it is also a simple installation, which requires minimal maintenance. The energy obtained can be used directly in numerous applications, from street lamps to satellites. It can be stored in

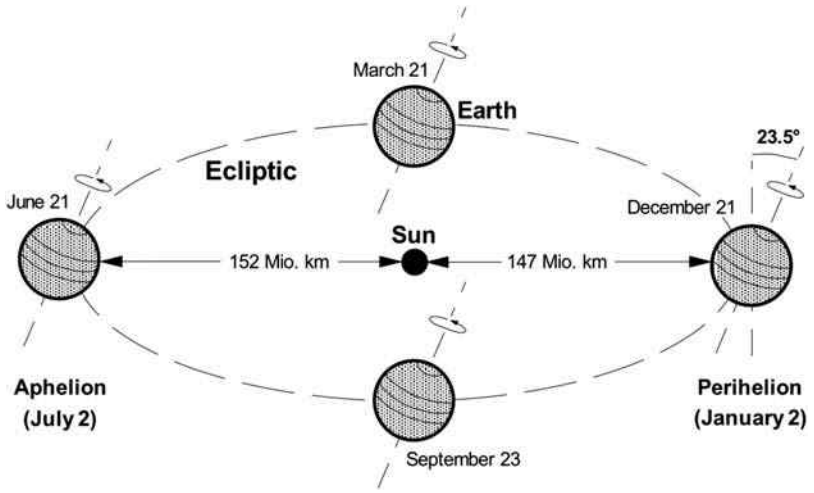


FIGURE 12.4

Elliptical orbit of the Earth around the Sun.

Courtesy M. Kaltschmitt, W. Streicher, A.A. Wiese, Renewable Energy: Technology, Economics and Environment, Springer, Berlin, Heidelberg, 2007.

accumulators and used as a power supply in homes, especially in areas with a low population density. Its main drawback is that it is not very competitive at the moment because its performance is not yet very high, and the installation of solar power plants requires large initial investments and very wide spaces that are usually desert and distant, generating a negative visual impact in very open spaces.

Irradiance is the magnitude used to describe the incident power per unit area of all types of electromagnetic radiation. There is no single value of it, because the Earth−Sun distance is not constant. The unit of irradiance is kW/m^2, or W/m^2. The irradiance differs from the term "irradiation," which is the energy per unit area: kWh/m^2. Its value is determined by the irradiance versus time curve, that is, the area under the curve.

Insolation is the accumulation of average energy over a period of time (day, month, annual, seasonal). It is the same irradiance, but considering an average time of permanence on a surface. Monthly values and the average in a year, for a specific place,[5] are shown in Fig. 12.5.

For works, projects, and solar energy installation executions, technicians and engineers have been using the expression "solar peak hour," meaning the greatest heat in an area or city and in a known time or period of time. Therefore, the amount of insolation received in a solar panel photovoltaic (or any solar collector) in 1 h is

[5]M. Kaltschmitt, W. Streicher, A.A. Wiese, Renewable Energy: Technology, Economics and Environment, Springer, Berlin, Heidelberg, 2007.

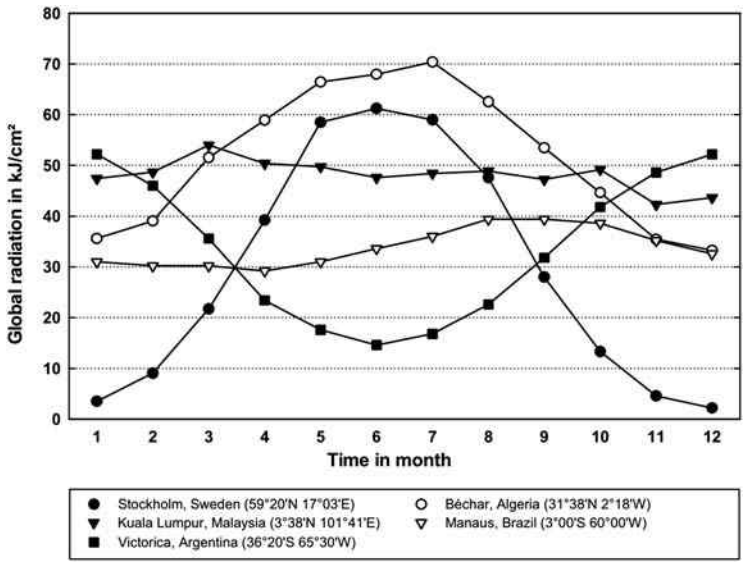


FIGURE 12.5

Monthly insolation values in a year.

Courtesy M. Kaltschmitt, W. Streicher, A.A. Wiese, Renewable Energy: Technology, Economics and Environment, Springer, Berlin, Heidelberg, 2007.

known as solar peak hour or simply pick hour, whose generalized units are as follows: 1 h solar peak = 1000 Wh.

The radiation received at the Earth's surface consists of direct and scattered (plus reflected) short-wavelength radiation plus long-wavelength radiation from sky and clouds, originating as thermal emission or by reflection of thermal radiation from the ground. Direct radiation is defined as the radiation that has not experienced scattering in the atmosphere, so that it is directionally fixed, coming from the disk of the Sun. Scattered radiation is, then, the radiation that experienced scattering processes in the atmosphere. In practice, it is often convenient to treat radiation that has experienced only forward scattering processes together with the unscattered radiation, and thus direct and scattered radiation are defined as radiation coming from or not coming from the direction of the Sun. A fraction of the incoming solar radiation is reflected back into space. This fraction is called the albedo of the Earth–atmosphere system. Its medium value is about 0.35. This is composed of about 0.2 from reflection on clouds, 0.1 from reflection on cloudless atmosphere (particles, gases), and 0.05 from reflection on the Earth's surface. If there were no air, obviously all the radiation would be direct, and our eye would receive no radiation (the sky would be black). Clouds diffuse solar radiation more strongly than dry air; therefore on a cloudy day all the radiation that we get will be diffuse radiation. On a typical clear day, the direct radiation is several times greater than the diffuse one.

In the characterization of the solar radiation incident on the Earth, to estimate the solar potential, several factors intervene, which includes climatic conditions (which influence the degree of cloudiness, atmospheric turbidity, prevailing wind, etc.), time of the year, the latitude of the place, and orientation of the receiving surface. Variations of the sunburst are relatively small, compared with other factors that determine it to a greater extent, such as the transparency of the atmosphere (defines albedo, direct light, and diffuse light), the duration of light day (determines the energy reaching a particular point during the day), and the angle with which the sun's rays fall on the Earth (the more perpendicular the rays fall on a surface, the greater the energy uptake). Of course, the distribution of the solar energy that arrives at the Earth is not uniform. The abovementioned factors lead to the solar irradiance on the surface of the Earth being between 900 and 1000 W/m^2.

The solar energy that arrives at the Earth is distributed as follows[6]:

- Reflected by the atmosphere into outer space: 30%, 0.52×10^{14} kW;
- Used in heating the atmosphere: 47%, 0.80×10^{14} kW;
- Used in the evaporation of the oceans: 23%, 0.40×10^{14} kW;
- Used to generate atmospheric disturbances, such as wind: 0.0037×10^{14} kW;
- Used in photosynthesis: 0.0004×10^{14} kW.

Thus, 47% of the incident solar energy reaches the Earth's surface (31% do so directly and the other 16% after being diffused by dust, water vapor, and air molecules). The rest of the solar energy, 53%, does not reach the surface of the Earth, because 15% is absorbed by the troposphere (water, ozone, and clouds), 23% is reflected by clouds, 7% is reflected by the soil, 2% is absorbed by the stratosphere, mainly by ozone, and the remaining 6% is the energy diffused by the atmosphere that is directed toward the sky.[7]

Solar radiation data are supplied to the public in the form of tables, maps, and computational tools. The SWERA (Solar and Wind Energy Resource Assessment) Project of the United Nations Environmental Programs Group, on the http://en.openei.org/apps/SWERA/ website, offers free information.

3. CONCENTRATING SOLAR POWER PLANTS

To convert solar energy into power, the radiation may concentrate on a point or on a line, where thermal energy is transferred to the heat transfer fluid (HTF). Considering these two types of concentration (on a point or on a line), CSP plants can be classified in two main designs: parabolic trough and power tower.

[6]See footnote 5.
[7]P. Fernández Díez, Procesos Termosolares en Baja, Media y Alta Temperatura [WWW Document], n.d. URL: http://www.mariloureiro.net/ciencia/EnerSolarTermica/SolarPROCESOSTERMO/Solar1.pdf.

Parabolic trough consists of long curved mirrors that concentrate sunlight on a liquid inside a tube that runs parallel to the mirror. The liquid heat is generally used to produce steam that drives a steam turbine. Power towers use fields of mirrors to concentrate sunlight on the top of central towers, in which the intense heat, generally carried by molten salts, boils water, and the steam then drives turbines.

Another type of CSP plant, although not yet broadly in use, is the PD. This system focuses the sunlight on a single point. Dish concentrating technology uses a Stirling engine to produce power. A Stirling engine produces power by way of mirrors that reflect sunlight on the outside of the engine.

Similar to parabolic troughs, concentrating LFR systems use multiple flat mirrors to concentrate solar sunlight onto the receiver tube. The same concept is applied where the liquid running in the heated tube is used to boil water and drive a steam turbine. Both these technologies are based on linear solar concentration.

Solar fields that use trough systems (Fig. 12.6), or shaped like a giant "U" that are connected in long lines, capture the sun's energy with large parabolic mirrors, tracking the sun's movement throughout the day. When the sun's heat is reflected off the mirror, the curved shape sends most of the reflected heat onto a receiver pipe that is filled with a specific HTF. The thermal energy from the heated fluid generates steam to drive a conventional steam turbine. Once the fluid transfers its heat, it is recirculated into the system for reuse. Steam is also cooled, condensed, and reused in the steam cycle. Heated fluid in trough systems can also provide heat to thermal storage systems, which can be used to generate electricity at times when the sun is not shining.

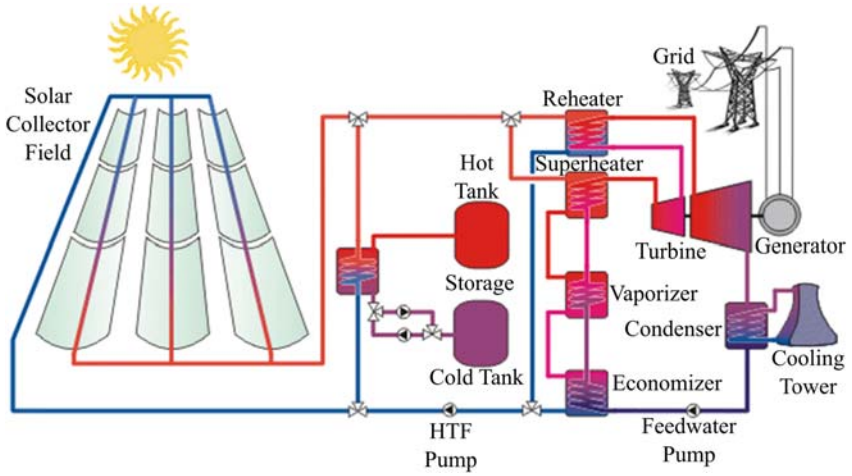


FIGURE 12.6

Scheme of a parabolic trough power plant.

Courtesy V. Quaschning, Solar thermal power plants: technology fundamentals, Renew. Energy World (2003) 109–113.

The efficiency of a solar thermal power plant is the product of the collector field and steam-cycle efficiencies. The collector efficiency depends on the sunlight incidence angle and the temperature in the absorber tube and can reach values up to 75%. Field losses are usually under 10%. Altogether, solar thermal trough power plants can reach annual efficiencies of ~15%. The steam-cycle efficiency (~35%) has the most significant influence on the overall efficiency. Central receiver systems, such as solar thermal power plants, can reach higher temperatures and therefore achieve higher efficiencies.

Power towers use large, flat mirrors called heliostats to reflect sunlight onto a solar receiver at the top of a central tower (Fig. 12.7). In a direct steam power tower, water is pumped up the tower, to the receiver, and heated to ~540°C. The superheated steam then powers a conventional steam turbine. In this case, heat is transferred from the receiver to the power block, via steam. Some power towers use molten salt instead of water and steam. Hot molten salt can be used immediately to generate steam and then electricity by means of a steam turbine driving an electric generator, or it can also be stored and used later.

There are also pressurized air receivers. In this case, a compressor pressurizes air to ~15 bar; a transparent glass dome covers the receiver and separates the absorber from the environment. Inside the pressurized receiver, air is heated up to 1100°C, which then drives a gas turbine (connected to the compressor and to a generator that produces electricity). Waste heat from the gas turbine goes to a recovery boiler and drives a steam-cycle process. The combined gas and steam turbine processes can

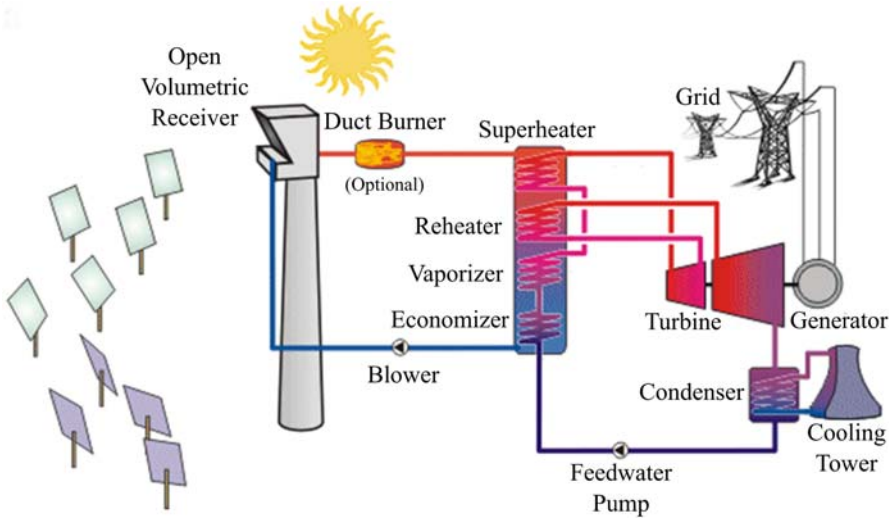


FIGURE 12.7

Solar thermal tower power plant with steam turbine cycle.

Courtesy V. Quaschning, Solar thermal power plants: technology fundamentals, Renew. Energy World (2003) 109–113.

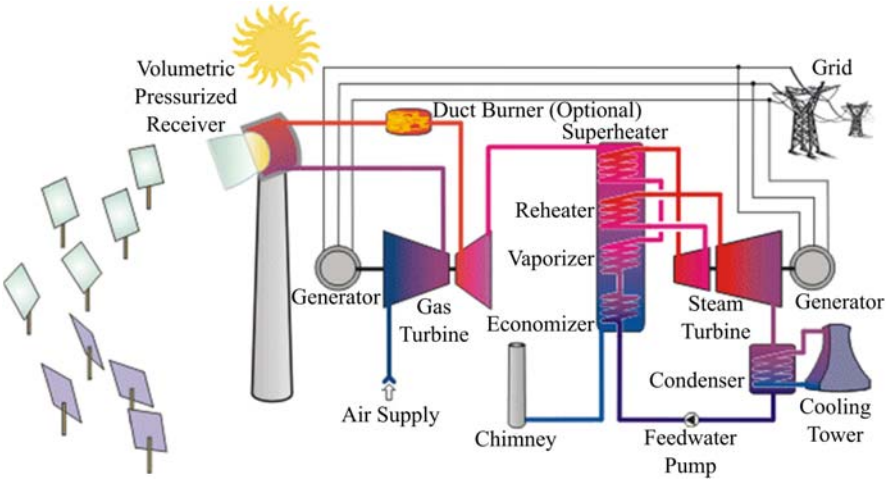


FIGURE 12.8

Solar thermal tower power plant with pressurized receiver using combined gas and steam turbine cycle.

Courtesy V. Quaschning, Solar thermal power plants: technology fundamentals, Renew. Energy World (2003) 109–113.

reach efficiencies over 50%, whereas the efficiency of a simple steam turbine cycle is only 35%. Therefore, solar system efficiencies of over 20% are possible (Fig. 12.8).

The heliostat typically constitutes ~50% of the energy system costs, and therefore it is important to optimize its design, size, weight, manufacturing volume, and performance. These are important design variables, approached differently by developers, to minimize cost.

Energy storage is viewed as the next game changer in the power sector. Medium-term thermal storage systems, with 5-h capacity per day, can be used to cover periods of peak demands at nighttime. Long-term storage systems present thermal storage capacity between 8 and 16 h, enabling the base load operation of power plants all night and in the early hours of the day, when required.[8] In a CSP plant, thermal energy is stored before being converted to electricity. As a result, the round-trip efficiency of CSP thermal storage can be close to 100%, much higher than any electricity storage technology. However, CSP thermal energy storage (TES) can only store thermal energy produced from the solar field, as opposed to other storage technologies that can store electricity produced from any source.

The most common TES systems currently in use or under construction are based on sensible heat storage using molten salts or synthetic oils. Some of the main

[8]See footnote 1.

large-scale TES configurations for CSP plants are two-tank direct systems, two-tank indirect systems, and single-tank thermocline systems. The two-tank direct system essentially consists of two tanks filled with molten salt, at different temperatures and fullness levels.

The two main types of two-tank direct systems are direct and indirect TES systems. In the direct system, salt is the HTF and the storage medium at the same time (Fig. 12.9). In an indirect system, thermal storage is decoupled from the HTF loop of the solar receiver, via a heat exchanger (Fig. 12.10).

Single-tank thermocline systems store thermal energy in a solid medium—most commonly, silica sand—located in a single tank. At any time during operation, a portion of the medium is at high temperature, and a portion is at low temperature. The hot- and cold-temperature regions are separated by a temperature gradient or thermocline. A high-temperature HTF flows into the top of the thermocline, exiting at the bottom at a low temperature.

This process moves the thermocline downward and adds thermal energy to be stored in the system. Reversing the flow moves the thermocline upward and removes thermal energy from the system, which can be used to generate steam and electricity. Buoyancy effects create thermal stratification of the fluid within the tank, which helps stabilize and maintain the thermocline (Fig. 12.11).

The use of a solid storage medium and only one tank reduces the cost of this system, in comparison with two-tank systems. This system was demonstrated at the Solar One power tower, where steam was the HTF and mineral oil was the storage fluid. Table 12.2 shows operational solar thermal facilities with TES systems.

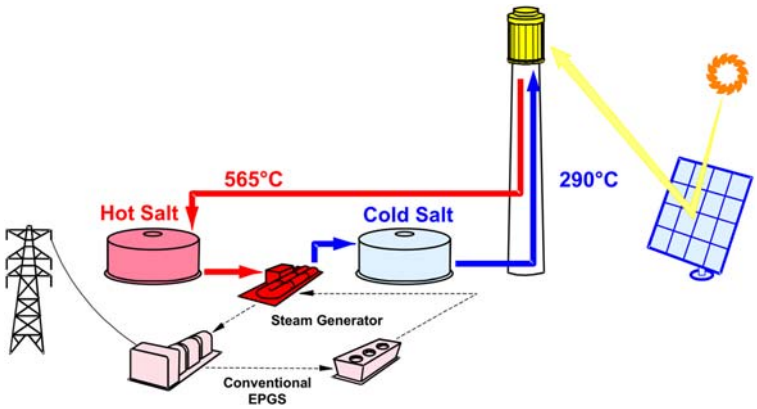


FIGURE 12.9

Solar tower plant with two-tank direct storage system.

Courtesy T. Bauer, N. Breidenbach, N. Pfleger, D. Laing, M. Eck, Overview of Molten Salt Storage System and Material Development for Solar Thermal Power Plants, American Solar Energy Society, 2012, p. 8.

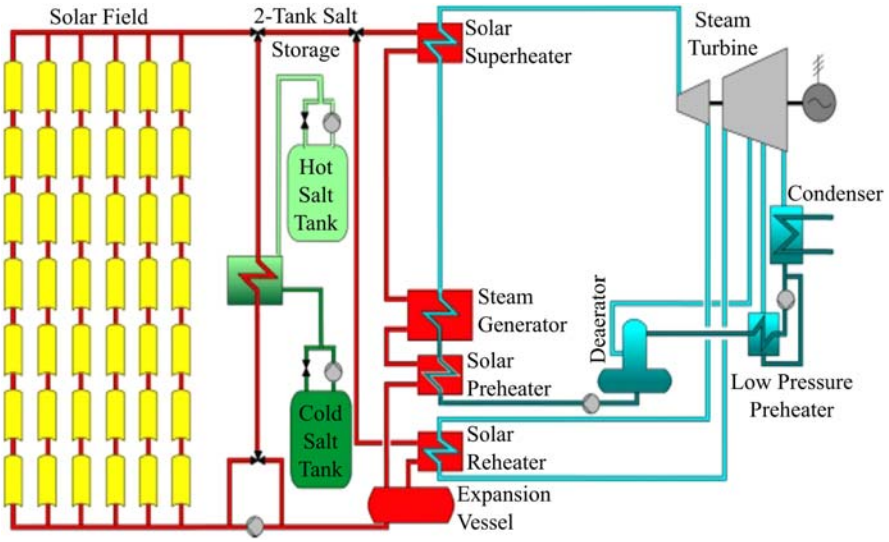


FIGURE 12.10

Schematic flow diagram of a parabolic trough power plant with two-tank molten salt storage.

Courtesy U. Herrmann, M. Geyer, D. Kearney, Overview on thermal storage systems. Work. Therm. Storage Trough Power Plants (2006).

Fig. 12.12 shows a comparison of TES configurations commonly used in CSP plants, according to technological maturity and annual solar-to-electricity efficiency. Table 12.3 presents the related technical options available for each CSP technology.

Parabolic troughs (PT-oil) and Tower (T) plants using T-SaS and T-SHS are available in commercial application stages; meanwhile Towers using T-AR and Linear Fresnel with superheated steam as HTF are currently under transition to commercial applications. PDs are at the demonstration stage.

The amount of solar energy harnessed is a function of the solar collector orientation, and therefore, efficient solar energy harvesting can only occur with the assistance of a solar tracking system. A mobility platform can ensure the movement of the solar collector system, so that it can follow the sun and harness solar energy during the day. This solar tracking mobility platform plays a crucial role in the development of solar energy applications, especially in high-temperature solar concentration systems that directly convert the solar energy into thermal or electrical energy. In these systems, high precision tracking is required to ensure that the solar collector is capable of harnessing the maximum amount of solar energy throughout the day. Some solar tracking platforms designs are shown in Fig. 12.13.

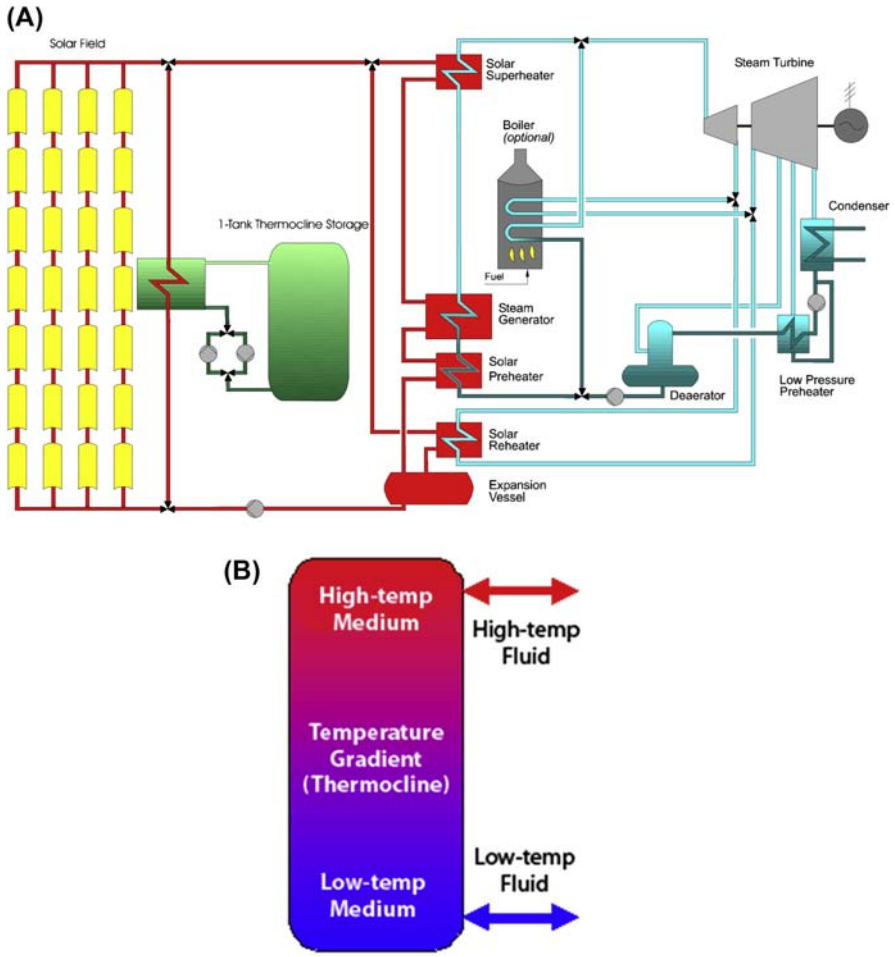


FIGURE 12.11

Single-tank thermocline system: (A) Installation scheme of a parabolic through power plant, with single-tank storage system; (B) Single-tank thermocline thermal energy storage system.

Courtesy U. Herrmann, M. Geyer, D. Kearney, Overview on thermal storage systems. Work. Therm. Storage Trough Power Plants (2006).

Any solar tracking platform with electronic control system must be designed for the continuous orientation or positioning of the solar harvesting means with respect to the sun vector. The solar tracking platform and control system for a solar harvesting means should be able to control and manage the physical movements of the solar collector with high accuracy.

Table 12.2 Operational Solar Thermal Facilities With Thermal Energy Storage Systems

Project	Type	Storage Medium	Nominal Temperature (°C)		Storage Concept	Plant Capacity	Storage Capacity
			Cold	Hot			
SSPS-DCS test facility Almeria, Spain	Parabolic trough	Santotherm 55	225	295	Single-tank thermocline	1.2 MWth	5 MWht
Nevada Solar One Nevada, USA	Parabolic trough	Dowtherm A	318	393	Oversized field piping	64 MWe	0.5 h
Holaniku at Keahole Point Hawaii, USA	Parabolic trough	Water	n.a.	200	Indirect storage	2 MWth, 500 kWe	2 h
Planta Solar-10 Sevilla, Spain	Central receiver	Pressurized water	240	260	Steam accumulator	11 MWe	50 min/ 20 MWht
Planta Solar-20 Sevilla, Spain	Central receiver	Pressurized water	n.a.[a]	250 –300	Steam accumulator	20 MWe	50 min
La Florida Badajoz, Spain	Parabolic trough	Molten solar salt	292	386	2-tank indirect	50 MWe	7.5 h
Andasol-1 Granada, Spain	Parabolic trough	Molten solar salt[b]	292	386	2-tank indirect	50 MWe	7.5 h/ 1010 MWht
Andasol-2 Granada, Spain	Parabolic trough	Molten solar salt[b]	292	386	2-tank indirect	50 MWe	7.5 h/ 1010 MWht
Extresol-1 Badajoz, Spain	Parabolic trough	Molten solar salt[b]	292	386	2-tank indirect	50 MWe	7.5 h/ 1010 MWht
Manchasol-1 Ciudad Real, Spain	Parabolic trough	Molten solar salt[b]	292	386	2-tank indirect	50 MWe	7.5 h

Manchasol-2 Ciudad Real, Spain	Parabolic trough	Molten solar salt[b]	292	386	2-tank indirect	50 MWe	7.5 h
La Dehesa Badajoz, Spain	Parabolic trough	Molten solar salt[b]	292	386	2-tank indirect	50 MWe	7.5 h
Puerto Errado 1 Murcia, Spain	Linear Fresnel	Saturated steam	n.a.[a]	270	Steam accumulator	1.4 MWe	n.a.[a]
Archimede Sicily, Italy	Parabolic trough	Molten solar salt[b]	290	550	2-tank direct	5 MWe	8 h/100 MWht
Torresol Gemasolar Seville, Spain	Central receiver	Molten solar salt[b]	292	565	2-tank direct	17 MWe	15 h
Dahan Beijing, China	Central receiver	Saturated steam/oil	220	350	Combined steam accumulator/concrete	1 MWe	1 MWht

[a] n.a., *not available.*
[b] *Molten solar salt = 60% sodium nitrate/40% potassium nitrate.*
From S. Kuravi, J. Trahan, D.Y. Goswami, M.M. Rahman, E.K. Stefanakos, Thermal energy storage technologies and systems for concentrating solar power plants, Prog. Energy Combust. Sci. 39 (2013) 285–319.

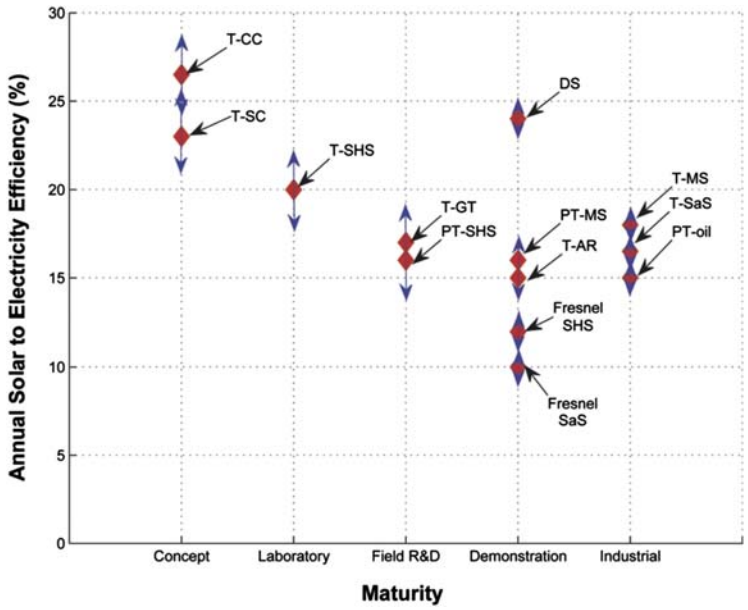


FIGURE 12.12

Annual solar-to-electricity efficiency as a function of development level.

Courtesy EASAC, Concentrating Solar Power: Its Potential Contribution to a Sustainable Energy Future, 2011.

Table 12.3 Technical Options Available for Each Concentrating Solar Power (CSP) Technology

CSP Technology	Technical Options
Linear Fresnel systems (F)	Fresnel SaS: saturated steam as HTF
	Fresnel SHS: superheated steam as HTF
Parabolic troughs (PT)	PT-oil: oil as HTF and molten salt storage
	PT-SHS: superheated steam as HTF
	PT-MS: molten salt as HTF and storage
Towers (T)	T-SaS: saturated steam as HTF
	T-SHS: superheated steam as HTF
	T-MS: molten salt as HTF and storage
	T-AR: ambient pressure air as HTF and Rankine cycle
	T-GT: pressurized air as HTF and Brayton cycle
	T-SC: supercritical cycle
	T-CC: pressurized air as HTF and combined cycle
Parabolic dishes (DSs)	DS: helium Stirling cycle

HTF, *heat transfer fluid.*

From EASAC, Concentrating Solar Power: Its Potential Contribution to a Sustainable Energy Future, 2011.

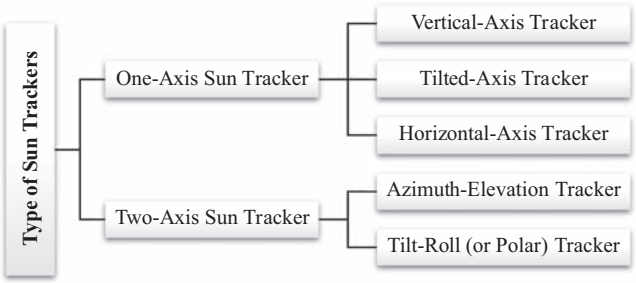


FIGURE 12.13

Some solar tracking platforms.

Reproduced from Adapted K.-K. Chong, C.-W. Wong, General Formula for On-Axis sun-tracking system, in: R. Manyala (Ed.), Solar Collectors and Panels, Theory and Applications, Sciyo, 2010.

4. SOLAR THERMAL ENERGY STORAGE

Solar thermal storage (STS) refers to the accumulation of energy collected by a given solar field for its later use. In the context of this chapter, STS technologies are installed to provide the solar plant with partial or full dispatchability, so that the plant output does not depend strictly in time on the input, i.e., the solar irradiation. STSs are TES systems where the source of heat is provided by the solar field, capturing the excess of energy not directly converted into power or other useful utility. As such, most TES technologies known can be adapted and have been adopted in solar applications, in particular for power production. A detailed review on this topic can be found in the literature.[9–12]

The selection of an STS is determined by a set of physical, chemical, environmental, and economic properties[11]:

- Energy density of the storage material
- Heat transfer and mechanical properties
- Chemical compatibility and stability

[9]A. Gil, M. Medrano, I. Martorell, A. Lázaro, P. Dolado, B. Zalba, L.F. Cabeza, State of the art on high temperature thermal energy storage for power generation. Part 1 - Concepts, materials and modellization, Renew. Sustain. Energy Rev. 14 (2010) 31–55.

[10]M. Medrano, A. Gil, I. Martorell, X. Potau, L.F. Cabeza, State of the art on high-temperature thermal energy storage for power generation. Part 2 – Case studies, Renew. Sustain. Energy Rev. 14 (2010) 56–72.

[11]S. Kuravi, J. Trahan, D.Y. Goswami, M.M. Rahman, E.K. Stefanakos, Thermal energy storage technologies and systems for concentrating solar power plants, Prog. Energy Combust. Sci. 39 (2013) 285–319.

[12]M. Liu, N.H. Steven Tay, S. Bell, M. Belusko, R. Jacob, G. Will, W. Saman, F. Bruno, Review on concentrating solar power plants and new developments in high temperature thermal energy storage technologies, Renew. Sustain. Energy Rev. 53 (2016) 1411–1432.

- Thermodynamic reversibility
- Environmental impact
- Thermal losses
- Cost

To these properties one may add automation and control[13] and health and safety requirements as factors that influence the performance of STS when integrated in a given solar plant. Efforts made toward enhancement of a particular property often results in trade-off situations. For instance, effort in heat transfer improvements brings about normally a cost increase. Thus, designing and operating STS is not always an off-the-shelf pick-up process.

The classification of STS is generally done considering two characteristics: the nominal or maximum temperature, which affects the maximum overall efficiency of the system, and the nature of the energy storage process regarding the materials and equipment used.

As for the temperature, TES can be classified as low, medium, and high temperature storage systems. Low temperature TES for heat storage for domestic application (heating or sanitary hot water) are in the range of 40−90°C. Medium temperature TES, up to 300°C, can be used, for example, in process heat applications[14] and power production in Organic Rankine Cycles (ORCs).[15] However, in solar applications where electric power is the goal, discharge temperatures must remain above 400°C for Rankine cycles and 600°C for Brayton cycles to overall efficiencies be economically attractive. Thus, not only the solar field collectors should ensure high output temperatures (HTF temperature leaving the solar field), but also HTF and storage materials should interact such that energy and exergy losses during the various heat transfer processes are minimized and their working life guaranteed, as explained later in the chapter. Table 12.4 summarized the temperature range achieved and sought to be achieved by several solar field technologies.[16]

Regarding the nature of the STS, two main elements constitute and define these storage systems, namely, the HTF, and the storage material. Depending on the configuration, they can be in direct contact, separated, or be the same.

The catalog of storage media increases with ongoing research, and an exhaustive enumeration is out of the scope of this chapter. In general, media are classified by their operating state (solid, liquid, gas, or a combination) and the physical and

[13]See footnote 12.
[14]R. Tamme, T. Bauer, J. Buschle, D. Laing, H. Müller-Steinhagen, W.-D. Steinmann, Latent heat storage above 120°C for applications in the industrial process heat sector and solar power generation, Int. J. Energy Res. 32 (2008) 264−271.
[15]R. Chacartegui, L. Vigna, J.A. Becerra, V. Verda, Analysis of two heat storage integrations for an Organic Rankine Cycle Parabolic trough solar power plant, Energy Convers. Manag. 125 (2016) 353−367.
[16]See footnote 12.

Table 12.4 Temperature (°C) of the Heat Transfer Fluid for Different Collector Technologies

		Tower			
	Parabolic Trough	Current	Volumetric Receiver	Dish-Stirling	Linear Fresnel
Source	Commercial	Commercial	Demonstration	Demonstration	Commercial
Ref. [9]	290–550	250–650	–	550–750	250–390
Ref. [12]	290–390	290–565	–	550–750	250–390
	393[a]	565[a]	1000[b]	–	–

[a] *Maximum achieved.*
[b] *Goal value.*

chemical transformations in the experiment. According to the literature,[1] there are three types of TES considering the process of storage and the corresponding medium:

- sensible energy storage;
- latent energy storage; and
- thermochemical storage.

Considering the mobility of the storage material, a classification applicable to latent and thermochemical heat can be drawn.[17] Storage media that are allowed or forced to flow, e.g., through pipes or heat exchangers, are considered *active* storage systems. On the other hand, when storage media are confined permanently in a tank or container, the system is considered *passive*, also known as regenerators. With some exceptions, only liquid-type sensible heat STS can be used in the active configuration.

In general, HTFs do not store significant volumes of energy, nor they produce work; they only carry the energy from one element of the plant to the next. This is the case of mineral or synthetic oils that circulate along PTCs. In some cases, HTF work as storage material, as shown below for molten salts. Working fluids such as water or steam can, in certain cases, be used to collect and store the bulk of the energy stored. HTF connects thermally the storage with the rest of the plant, namely, the solar field and the power block.

Regarding the topology of the system, one or more tanks can be used to store the medium, being common the single-tank system, also known as thermocline tank due to the temperature distribution in the volume arising from density differences, and the two-tank system, where the medium flows from one tank to the other as the charge and discharge take place. Alternative configurations[18] have been proposed

[17] See footnote 9.
[18] See footnote 12.

such as the split tank and the cascade tank arrangement which, because of the additional complexity, enjoy currently a marginal penetration.

Sensible heat storage consists in the increase through heat transfer of the kinetic energy of the molecules of the storage medium, which translates in a temperature increase. Molten salts, synthetic oils, concrete, packed bed, or pressurized water is the most common storage medium.

Latent energy storage makes use of the enthalpy difference of a given substance between two physical states or phases. The use of phase change materials (PCMs) is characteristic of this storage type. Sharma et al. provides a review on PCMs for TES.[19]

This third type of TES relies on reversible endothermic chemical reactions[20] fostered by the addition/retrieval of energy to/from a substance. Heat is the motive source of the endothermic reactions, in contrast with other chemical energy storage options such as water electrolysis to obtain hydrogen gas, which requires electricity.

The decision of providing a solar plant with a storage system responds almost completely to economical criteria. In exceptional cases, flexibility of operation and base load needs will influence the final design of the plant, but sizing of the storage will also be determined by a process of cost optimization.

For solar plant without storage and without external inputs of conventional energy such as natural gas, the levelized cost of energy is a function of the capital investment and the operating costs and revenues. Investment may take place in different instants of the life of the plant, but a great share will take place during the construction of the plant.

The cost of STS depends on three main terms: (1) the cost of the containers, storing material, and the HTF; (2) the cost of the required heat exchangers; and (3) the cost of the space that the STS occupies[20]. Estimated costs of TES in solar plants with commercial technologies are reproduced in Table 12.5.

What storage makes possible is mainly to increase the flexibility of the plant and to run the equipment for longer hours at the nominal operating point. Flexibility or dispatchability means that one can generate electricity not strictly when the sun shines, but when electricity has more value. The economics of the plant improve when the elements of the power block operate steadily, which reduces mechanical and thermal fatigue typical cyclical operation.

Thus, it is important to notice that the cost of a storage technology does not suffice to establish their cost-effectiveness, which is determined by its performance (efficiency, durability, etc.) within a specific plant design. Sizing and operation of STS systems require the use of simulation tools to ensure that both the storage and the rest of the plant behave within the technical and economical boundaries of the project.

[19]A. Sharma, V.V. Tyagi, C.R. Chen, D. Buddhi, Review on thermal energy storage with phase change materials and applications, Renew. Sustain. Energy Rev. 13 (2009) 318–345.
[20]See footnote 9.

Table 12.5 Examples of Thermal Energy Storage Costs

Type	Configuration	Storage Material	Heat Transfer Fluid	ΔT(K)	Capital Costs ($/kWh$_{th}$)
Sensible	Two-tank	Molten salt	Same as storage material	300	28.21
Sensible	Two-tank	Liquid sodium	Same as storage material	300	48.48
Sensible	Thermocline	Quartz/ sand	Molten salt (solar salt)	300	20.26
Latent	EPCM	Chloride salt	Air	300	19.74
Latent	Coil-in-tank	Carbonate salt	SCO_2 or liquid sodium	300	21

From M. Liu, N.H. Steven Tay, S. Bell, M. Belusko, R. Jacob, G. Will, W. Saman, F. Bruno, Review on concentrating solar power plants and new developments in high temperature thermal energy storage technologies, Renew. Sustain. Energy Rev. 53 (2016) 1411–1432.

Research studies and more detailed engineering works can often be carried out with tools such as Matlab®/Simulink, Modelica, or Visual Basic. Specific components may require the use of specific finite element method software such as ANSYS-Fluent. ASPEN PLUS, APROS, or DYMOLA (Modelica) has been widely used for modeling and simulation of complete solar plants, storage included, because of the flexibility of their component libraries and the possibility to integrate detailed control systems.[21,22]

5. THERMODYNAMIC AND ECONOMIC STUDY

To evaluate a 3-MW parabolic trough power plant using an ORC, a thermodynamic and an economic study were carried out.

The primary system evaluated is an ORC, constituted by its main components: pump, evaporator, turbine, and condenser, as shown in Fig. 12.14. The working fluid is saturated at the outlet of the condenser (3–4), then is compressed by the pump (4–1), flows to the evaporator, where it receives heat from the solar source until reaching saturated vapor (2–22), and is finally expanded in the turbine for the generation of useful work (22–3).

The solar energy system is constituted of a set of parabolic cylindrical collectors that receive solar radiation and uses it to heat an HTF that circulates within a system in

[21]See footnote 9.
[22]F. Alobaid, N. Mertens, R. Starkloff, T. Lanz, C. Heinze, B. Epple, Progress in dynamic simulation of thermal power plants, Prog. Energy Combust. Sci. 59 (2017) 79–162.

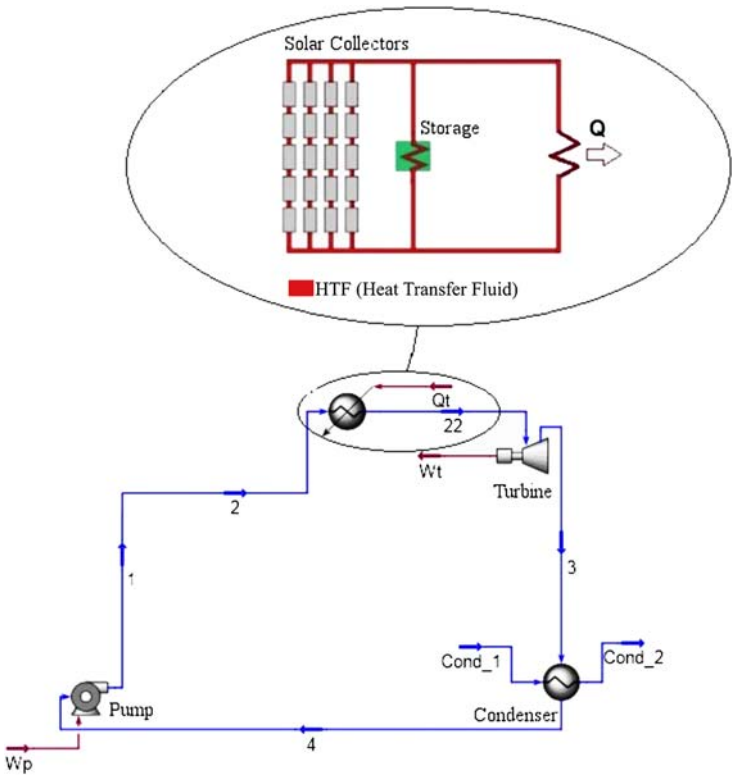


FIGURE 12.14

Scheme of the hybrid solar–geothermal power plant simulated in the Hysys software.

interconnected tubes. During the high radiation hours, most of this energy is directly transferred to the power system, and the remaining energy is accumulated in the storage (for utilization during low radiation hours). Energy transference to the power cycle is accomplished through a heat exchanger located before the turbine inlet.

The main parameters considered in the simulation are shown in Table 12.6. To calculate the required area for the parabolic cylindrical solar collector to satisfy the complementary heat requirements, the basic parameter to be considered is the thermal efficiency of the solar collector.

The thermal efficiency, "η," of a PTC is the captured or gained useful energy divided by the incident radiation on the aperture plane, as shown in Eq. (12.1).[23]

[23]C. Echevarría López, Diseño de un colector cilindro parabólico compuesto con aplicación para el calentamiento de agua, Univ. Piura. Universidad de Piura, 2012.

Table 12.6 Main Parameters Considered in the Simulation

Variable	Value	Unit
Organic Rankine Cycle System		
Ambient temperature	25	°C
Pinch temperature differential	10	°C
Condensation temperature	40	°C
Organic fluid flow	51.4	kg/s
Power generated	3000	kWe
Inlet turbine pressure	2857	kPa
Inlet turbine temperature	120	°C
Outlet turbine pressure	500	kPa
Outlet temperature pressure	61.5	°C
Solar Collector System		
Overall conversion efficiency of the solar circuit	71.69	%
Full load time of the storage system	6.0	h
Full load time of the power cycle operating directly with solar energy	6.0	h
Thermal flow utilized for the simulated storage system	*Hitec Solar Salt*	
Performance Parameters Calculated		
Produced electrical power	3	MWe
Heat required	21,250	MWth
Thermal efficiency	14	%

$$\eta = \frac{Q_u}{A_a I} \tag{12.1}$$

where η is the thermal efficiency of the collector; Q_u is the useful power (W); A_a is the aperture area of the collector (m^2); and I is the solar radiation absorbed in the aperture plane (W/m^2).

The modification of Eq. (12.1) yields Eq. (12.2):

$$A_a = \frac{Q_u}{\eta I} \tag{12.2}$$

The National Laboratory of Renewable Energy of the United States, within its software *Solar Advisor Model* (SAM), version 2014-01-14, utilizes a value of 0.7169 for the conversion efficiency of a PTC. This software was developed to help evaluate performance and costs of PV and solar concentrating systems.

During sun hours (6 h were considered), the thermal power at the outlet of the solar field must satisfy the demand of the power system (ORC) and also provide thermal energy for the storage system (also 6 h). Therefore, 50% of the heat at the outlet of the solar field goes to the power cycle and 50% goes to the storage system. This means that during sun hours, the thermal power at the outlet of the solar field must be double the requirements for the ORC. The value of heat in Eq. (12.2) is double the heat required for power generation. From Eq. (12.2), and using $\eta = 0.7169$, the values of aperture areas for PTC were calculated in function of local solar radiation.

As shown in Eq. (12.2), if the value of the heat exiting the collector is fixed, the necessary collector area is inversely proportional to solar radiation. This is why the value of solar radiation is fundamental for the development of projects involving solar energy.

However, the required land area for installation of solar collectors is higher than the aperture area of collectors. This value varies approximately between three to four times the aperture area of collectors. The land area is greater because there is a distance between collectors besides the required space for pipes and other accessories of the system. Table 12.7 shows the land area required for the installation of solar collectors, adopting a value three times higher than the collector area (A_a), for several radiation values (I).

Table 12.8 shows the costs associated with a solar system based on PTC. These values are based on technical report NREL/TP-550-47605 (July 2010), of the National Laboratory of Renewable Energy of the United States.[24]

The 2014 version of SAM software utilizes a more recent value, which was adopted here in: USD 270/m^2 for the solar field.

With the solar collector areas calculated in Table 12.7 and the costs presented in Table 12.8, final costs were calculated, as shown in Table 12.9.

For the ORC-solar system that considered average radiation (450−550 W/m^2), the costs associated with the solar system represent over 96% of total costs, while the components of the ORC system corresponded to under 4%. Local improvement costs were responsible for 5% of total costs, solar field costs corresponded to 55% of total costs, the HTF system contributed with 18%, and the storage system with 22% of total costs.

From these values, the cost per kW installed was calculated for different radiation levels, and the main results are presented in Fig. 12.15.

[24]C. Turchi, Parabolic Trough Reference Plant for Cost Modeling With the Solar Advisor Model (SAM), 2010.

Table 12.7 Required Area for Parabolic Trough Collector Installation, in Function of Solar Radiation, for a 3 MWe Organic Rankine Cycle-Solar System

I (W/m^2)	A_a (m^2)	Land Area (Ha)
150	395,198	119
200	296,398	89
250	237,119	71
300	197,599	59
350	169,371	51
400	148,199	44
450	131,733	40
500	118,559	36
550	107,781	32
600	98,799	30
650	91,200	27
700	84,685	25
750	79,040	24
800	74,100	22
850	69,741	21
900	65,866	20
950	62,400	19
1000	59,280	18

Table 12.8 Costs Utilized Within Software Solar Advisor Model (SAM) for the Reference Parabolic Trough Collector System

Direct Cost	Value Utilized in SAM 2010	Unit
Local improvements	25	USD/m^2
Solar field	295 (270[a])	USD/m^2
SHTF system	90	USD/m^2
Storage	80	USD/kWh-t[a]

[a] *In the 2014-01-14 version of the SAM software the cost of the solar field was changed to 270 $/m^2. From C. Turchi, Parabolic Trough Reference Plant for Cost Modeling With the Solar Advisor Model (SAM), 2010.*

From Fig. 12.15 it can be seen that the costs per kW vary between 13,053 and 56,162 USD/kW. As all calculations were carried out in function of solar radiation, the importance of this parameter at the time of designing solar-based generation systems is highlighted, as well as its impact on the overall costs of the systems.

The costs presented in USD/kW are specific for the power cycle studied herein (3 MWe), and results could vary if a different cycle is simulated.

Table 12.9 Costs for the Parabolic Trough Collector System, in Function of Solar Radiation, for a 3 MWe Organic Rankine Cycle-Solar System

I (W/m^2)	Costs for Local Improvements (USD)	Costs of Solar Field (USD)	Costs of HTF System (USD)	Costs of Storage System (USD)	Total Costs (USD)
150	9.879.946	106.703.417	35.567.806	14.227.122	166.378.292
200	7.409.960	80.027.563	26.675.854	14.227.122	128.340.499
250	5.927.968	64.022.050	21.340.683	14.227.122	105.517.824
300	4.939.973	53.351.709	17.783.903	14.227.122	90.302.707
350	4.234.263	45.730.036	15.243.345	14.227.122	79.434.766
400	3.704.980	40.013.782	13.337.927	14.227.122	71.283.811
450	3.293.315	35.567.806	11.855.935	14.227.122	64.944.179
500	2.963.984	32.011.025	10.670.342	14.227.122	59.872.473
550	2.694.531	29.100.932	9.700.311	14.227.122	55.722.896
600	2.469.987	26.675.854	8.891.951	14.227.122	52.264.915
650	2.279.988	24.623.866	8.207.955	14.227.122	49.338.931
700	2.117.131	22.865.018	7.621.673	14.227.122	46.830.944
750	1.975.989	21.340.683	7.113.561	14.227.122	44.657.356
800	1.852.490	20.006.891	6.668.964	14.227.122	42.755.467
850	1.743.520	18.830.015	6.276.672	14.227.122	41.077.329
900	1.646.658	17.783.903	5.927.968	14.227.122	39.585.651
950	1.559.991	16.847.908	5.615.969	14.227.122	38.250.991
1000	1.481.992	16.005.513	5.335.171	14.227.122	37.049.798

HTF, *heat transfer fluid.*

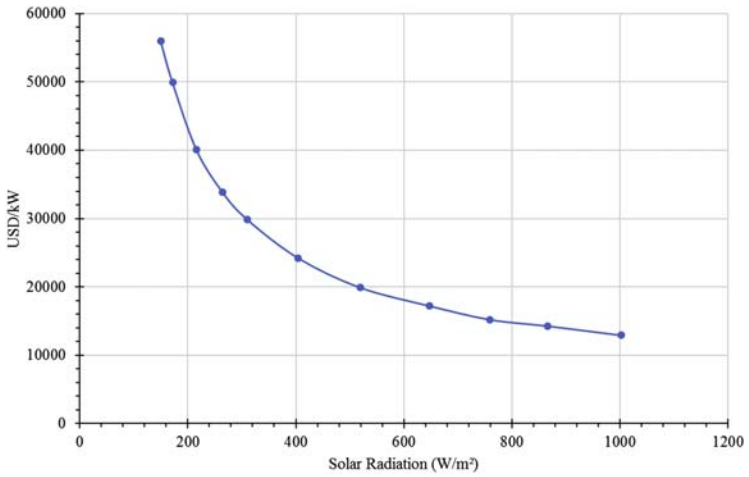


FIGURE 12.15

USD costs per kW installed, in function of solar radiation.

REFERENCES

[1] L. Witmer, Overview of Solar Thermal Power Systems | EME 811: Solar Thermal Energy for Utilities and Industry [WWW Document], Pennsylvania State Univ., 2017. URL: https://www.e-education.psu.edu/eme811/node/682.

[2] R. Guerrero-Lemus, J.M. Martínez-Duart, Concentrated solar power, in: Renewable Energies and CO_2, Springer-Verlag, London, 2013, pp. 135−151.

[3] U. Pelay, L. Luo, Y. Fan, D. Stitou, M. Rood, Thermal energy storage systems for concentrated solar power plants, Renew. Sustain. Energy Rev. 79 (2017) 82−100.

[4] B. Hoffschmidt, Receivers for Solar Tower Systems [www Document], 2014. URL: http://sfera2.sollab.eu/networking/announcement-summer-schools/summer-schools/summer-school-presentation-2014.

[5] M. Kaltschmitt, W. Streicher, A. Wiese, Renewable Energy: Technology, Economics and Environment, Springer, Berlin, Heidelberg, 2007.

[6] V. Quaschning, Solar thermal power plants: technology fundamentals, Renew. Energy World (2003) 109−113.

[7] T. Bauer, N. Breidenbach, N. Pfleger, D. Laing, M. Eck, Overview of Molten Salt Storage System and Material Development for Solar Thermal Power Plants, American Solar Energy Society, 2012, p. 8.

[8] U. Herrmann, M. Geyer, D. Kearney, Overview on thermal storage systems, Work. Therm. Storage Trough Power Plants (2006).

[9] S. Kuravi, J. Trahan, D.Y. Goswami, M.M. Rahman, E.K. Stefanakos, Thermal energy storage technologies and systems for concentrating solar power plants, Prog. Energy Combust. Sci. 39 (2013) 285−319.

[10] EASAC, Concentrating Solar Power: Its Potential Contribution to a Sustainable Energy Future, 2011.

[11] K.-K. Chong, C.-W. Wong, General formula for On-Axis sun-tracking system, in: R. Manyala (Ed.), Solar Collectors and Panels, Theory and Applications, Sciyo, 2010.
[12] M. Liu, N.H. Steven Tay, S. Bell, M. Belusko, R. Jacob, G. Will, W. Saman, F. Bruno, Review on concentrating solar power plants and new developments in high temperature thermal energy storage technologies, Renew. Sustain. Energy Rev. 53 (2016) 1411−1432.
[13] C. Turchi, Parabolic Trough Reference Plant for Cost Modeling With the Solar Advisor Model (SAM), 2010.

CHAPTER

Photovoltaic Cooking 13

Antonio Lecuona-Neumann, José I. Nogueira, Mathieu Legrand
Departamento de Ingenierá Térmica y de Fluidos, Universidad Carlos III de Madrid, Madrid, Spain

CHAPTER OUTLINE

1. Introduction 403
1.1 Energy and Cooking 404
1.2 Cooking With Wood and the Associated Health Problems 405
1.3 Cooking With Wood and the Associated Environmental Problems 406
1.4 Cooking With Solar Energy 406
2. Solar Cooking Possibilities 407
3. Fundamentals of Cooking 409
4. Thermal Model of a Photovoltaic Cooker 409
4.1 Some Results of the Model 411
5. Heat Storage (Thermal Energy Storage) With Solar Cooking 414
5.1 Sensible Heat Thermal Energy Storage 414
5.2 Latent Heat Thermal Energy Storage 416
6. Photovoltaic Solar Cookers 416
7. Conclusions 421
Acknowledgments 421
References 421
Further Reading 425

1. INTRODUCTION

Cooking is essential for humankind. Raw food is difficult to eat and digest and can be insecure. Only some vegetables and fruits are appropriate to be eaten raw if properly manipulated [1]. In wide areas of the world, water for drinking needs to be boiled. This is essential to avoid deadly infections, mainly in developing countries and where nontreated water is used. Preparation of sanitary hot water (SHW) is also needed to fight illnesses. This means that thermal energy is essential in human life.

Advances in Renewable Energies and Power Technologies. https://doi.org/10.1016/B978-0-12-812959-3.00013-7
Copyright © 2018 Elsevier Inc. All rights reserved.

1.1 ENERGY AND COOKING

A heat source well above water boiling temperature is currently used for cooking, classically burning flames. In developed countries, modern forms of energy are used to make cooking fast, clean, and controllable. Mainly fossil fuels are burned, but recently natural gas or liquefied petroleum gases (LPGs, butane, and propane) are preferred. In the most developed countries, there is a tendency to use electricity to produce heat, either through the Joule effect or by means of microwave ovens or induction ranges. The energy consumption and cost of cooking for an average family are generally small in comparison to heating, air conditioning, and other electricity consumption by home appliances, exception made for the low-income users [2]. This justifies consuming the more expensive option, electricity, because of its ease of use and high availability. In the poorest situation, such as in developing nations, and especially in the country and periurban areas, almost only firewood is burned for cooking, either gathered directly from nature or procured from local markets, in addition to residues from landfill or from agriculture.

According to the International Energy Agency, about 3 billion people worldwide depend on burning solids for cooking [3]. More than 95% of these people are either in Sub-Saharan Africa or in developing Asia, and around 80% are in rural areas [4]. A common first evolution from this status is shifting from firewood to charcoal as it is lighter, more compact and inert, burns with fewer fumes, and gives a higher and more consistent heating effect. Because of this, it is much preferred in urban and periurban areas, although starting and stopping cooking is cumbersome too. Conversion of wood into charcoal wastes at least two-thirds and up to nine-tenths of the heating content in wood, needing on average 5−7 kg of dry wood for producing 1 kg of charcoal. The sustainable use of charcoal indicates that the net CO_2 released to the atmosphere by charcoal production and end combustion is neutral. But its manufacture is very polluting and increases user cost. It is well known that in many places charcoal use causes deforestation, e.g., Haiti. Using coal worsens indoor pollution and adds net CO_2 to the atmosphere. Transition to liquid fuels such as kerosene and paraffin oil reduces ash and indoor fumes substantially but its supply tends to be irregular in many rural areas. Their cost is high, around 5−15 times that of firewood, although the average efficiency of paraffin cook stoves is around twice that of those using firewood or charcoal. Bioalcohol and other liquid biofuels, such as plants oil, have not reached widespread use for cooking because of high cost and complex production. Burning LPGs is the following step forward toward safety, cooking control, and air cleanliness. They are costly and scarce in many undeveloped areas despite government's tendency to sponsor LPGs for helping low-income families. Access to grid electricity is even worse in those areas and probably it will not be available in the foreseeable future in many small and remote communities because of investment cost. Use of electricity is very clean and controllable but its production by burning fuels signifies emissions of pollutants to the atmosphere elsewhere.

A detailed study on choices for domestic fuels within this framework is that by Bisu et al. [5].

In some regions, the cost of firewood can be higher than the cost of the food itself, raising food safety issues.

Biomass amounts to around 10% of world primary energy consumption (firewood, agricultural residues, dung, and waste). The World Health Organization estimated that the use of biomass fuels and charcoal for cooking and heating accounts for 10%−15% of global energy use [6]. It is the fourth energy source at world level behind oil, coal, and natural gas and can be around 80% of primary energy consumption in undeveloped countries. Precise data are difficult to gather because of the noncommercial nature of the directly collected biomass. Firewood used worldwide for household cooking is around 50% of the total, according to diverse sources.

Obtaining biogas in anaerobic digesters from collectible soft organic residues is one possibility of distributing a clean and renewable fuel for small communities [7]. In some places, feedstock and manure biomass consumption compete with fertilizers; but in other areas, its use as fuel is a way to manage excessive biological residues, e.g., Chen et al. [8]. In periurban areas, digesters seem inappropriate because of space requirement, odors, and insects.

1.2 COOKING WITH WOOD AND THE ASSOCIATED HEALTH PROBLEMS

One main problem with combustion in poor dwellings is indoor air pollution; actually, it is common smoke. Toxic gases are produced, such as carbon monoxide (CO), unburned and partially burned hydrocarbons (noncondensing hydrocarbons), and flying particles (ash, tar, and cinder). This is a problem also for not-so-low-income dwellings [9]. Breathing this polluted air daily leads to illnesses, including stroke, ischemic heart disease, chronic obstructive pulmonary disease, and lung cancer [10−12] among others. For the poorest dwellings, an effective chimney is frequently nonexistent but only small ventilating apertures. Two to four million premature deaths worldwide per year are attributed to this cause [13,14], decreasing GDP, e.g., Naciones Unidas/OCDE [15].

Indoor domestic air pollution is higher as a result of the low efficiency of the cook stoves used, mainly open fire and frequently on the floor (three-stones cooker). The energy efficiency is typically not higher than 15% of the lower heating value of wood [16]. This translates into an increased amount of hot fumes. Because these are used for indoor space heating and eventually smoking hanged meat, this method does not promote ventilation. Mainly children and women breathe polluted air for a prolonged period. Also, they spend many hours gathering wood, which is difficult in the initial stages of economic development, and augments risks of accidents, kidnapping, being prone to attack by wild animal, and being affected by articular lesions. This duty also precludes children going to school. Cultural and gender issues can aggravate this problem [17].

1.3 COOKING WITH WOOD AND THE ASSOCIATED ENVIRONMENTAL PROBLEMS

Deforestation is another consequence of nonrenewable firewood collection and even more if charcoal is obtained [18,19].

The immediate step for helping people in reducing firewood consumption is doubling the efficiency of the primitive cook stoves by using improved versions. Basically, they enclose the flame in a re-radiating insulated environment that promotes complete combustion and directs hot combustion fumes toward the cooking pot(s) to enhance heat transfer [20]. Many models of improved cook stoves are available, made of clay pottery, can sheets, welded steel, or a combination of them, either constructed in place or in remote factories [21]. Large dissemination campaigns have been endeavored for improved cook stoves implementation, reporting good results, but still, firewood is necessary [4,22]. Air pollution and greenhouse gases emission are also reduced but not eliminated, raising doubts about the efficacy of these initiatives in the long term. In their study, Lacey et al. [23] indicate the benefits of complete abatement of domestic solid fuel burning "Abatement in China, India, and Bangladesh contributes to the largest reduction of premature deaths from ambient air pollution, preventing 198,000 (102,000−204,000) of the 260,000 (137,000−268,000) global annual avoided deaths in 2050.□ In Sub-Saharan Africa, about 730 million people cook with solid fuels, according to the study by the International Energy Agency [24]. The shift to charcoal in urban areas in combination with population growth could increase the pressure on declining forests for firewood consumption.

Combustion cooking forms a non-negligible source of atmospheric greenhouse gases. In the study by Xu et al. [25], different measures to reduce the carbon footprint of cooking are reviewed.

1.4 COOKING WITH SOLAR ENERGY

The use of solar energy for cooking eliminates the air pollution, use of scarce firewood, its cost, and burden [26]. Many energy-poor areas in the world are very sunny [27] [28]. Despite the much-studied advantages of solar cooking, it is still underused [29].

Almost all the existent solar cookers are of the thermal type. They share some characteristics with the more advanced photovoltaic (PV) solar cookers that eventually will replace them. This is why they are presented first.

The use of solar energy dates back to ancient times, although cooking with the sun seemed too inconvenient. Even nowadays it is not much used, although several millions of solar thermal cookers have been deployed. Many people do not realize that it is actually possible. Billions of people still do not have access to modern forms of energy so that the potential benefits are huge, including fighting against global climate change. Nowadays solar thermal cookers are low cost and convenient for an individual size, family size, and even community size. There are facilities for cooking several thousand meals a day, all with solar thermal technologies. In India

and in other countries there are food processors that use solar cookers in their operations [30,31]. Elsewhere in the world, solar restaurants use only the sun to cook meals [32]. Outdoors space requirement for solar thermal cookers is high because, in addition to sun collection, space is required for food preparation. Nevertheless, in periurban areas, it is still possible [33], especially with innovative PV cookers (more on that in the following sections).

Direct exposure of food to solar irradiance, with a maximum of around 1 kW/m^2 at midday, is not strong enough to elevate temperatures so that cooking is performed, only drying happens. Special devices have to be employed to reach cooking temperatures under the sun, actually using either or both of the following techniques:

- **Heat retention**. This means protecting the cooking utensil with a greenhouse effect cover. This is produced by windows made of glass, which is transparent to solar rays but opaque for infrared spontaneous self-radiation. A sealed cover also keeps the hot air and steam from escaping. In nontransparent sides of the cover, conventional heat insulation needs to be implemented using wool, glass fibers, foams, dry grass or leaves, etc.
- **Optical solar concentration** by means of mirrors and lenses. They increase the irradiance (W/m^2) impacting in the utensil containing food. From another point of view, optical concentration allows the heat losing area to be much smaller than the solar collecting area, increasing efficiency.

The combination of both techniques forms a contemporary *thermal solar cooker* of the thermal type. Some examples are shown in Figs. 13.3 and 13.4. Convenient features are the possibility of being constructed with local tools, elements and techniques, even scrap materials, and not needing much maintenance but ordinary cleaning. Solar thermal cookers:

- Can use the traditional metallic pots as utensils, only requiring to paint their exterior black to absorb sun rays.
- They are preferred for helping displaced people (e.g., refugees) and are preferred over fueled cookers for the null fire risk they offer and for not requiring supplies. Some solar cookers are very light and foldable, thus portable.
- In developed countries, forest fires consume natural spaces every year, sometimes caused by barbecuing. If they are replaced by effective solar cookers not only the fire risk is eliminated in parks and forest rest areas but also cooking with the sun forms an educational experience about sustainability.

2. SOLAR COOKING POSSIBILITIES

Conventional solar cookers are thermal. This means that the sun rays are impacting on an absorbing surface where they are instantly dissipated as heat that is transferred to the food. Figs. 13.3 and 13.4 show some examples. The heat transfer to the food can be direct or can be diverted to an additional body that stores it for a delayed use,

constituting the *indirect solar cookers*. Obviously, the heat storage must be at a higher temperature than that needed for cooking.

Another possibility is to transform the sun's energy into electricity by means of a PV solar panel. This electricity can be easily transported using cables to a remote (indoor) ohmic resistance put in contact with the food or even submerged in it. This makes a PV solar cooker. Its main inconvenience is the low efficiency of the available solar panels ($\eta \cong 10\% - 15\%$) and its cost. Big advantages are needing only some roof space and sharing space in the kitchen.

Let us assume a single representative meal for a small family composed of 0.5 kg of rice and 1.5 kg of water. Rice has a specific heat that is not much smaller than that of water so that 2 kg of water can be safely assumed.

Bringing 2 L of water from ambient temperature $T_a = 25°\text{C}$ to boiling, $T_{bo} \sim 100°\text{C}$ requires an output heat amounting $Q = m_w c_w \Delta T = 2\ \text{kg} \times 4.2\ \text{kJ/kg K} \times 75\ \text{K} = 630\ \text{kJ}$. Assuming that 37% of the total amount is lost to ambient (energy efficiency $\eta = 0.63$, only attainable with advanced electric or solar cookers) $\approx 1\ \text{MJ} \approx 0.28\ \text{kWh}$ of heat is required as input. Less efficient cooking may represent up to twice this energy consumption and three stone cookers four times. On the other hand, reducing the water content, during the cooking time, Fig. 13.2, requires boiling approximately half of this water (~ 1 kg) for a representative recipe. This means an output of $Q = m_{bo} L_{bo,w} = 1\ \text{kg} \times 2.26\ \text{MJ/kg} = 2.3\ \text{MJ} = 0.64\ \text{kWh}$. Now applying larger heat losses during boiling, because of a higher average temperature than during heating, makes about $3.7\ \text{MJ} = 1.0\ \text{kWh}$ input energy required for just boiling, indicating the high energy consumption for reducing the water content in the food, common for traditional recipes such as rice cooking. Let us assume 1.0 kWh total energy input. During the central hours of a sunny day, $G = 1\ \text{kW/m}^2$ of solar irradiance is available, assuming $\eta = 35\%$ efficiency of a 1.5-m^2 solar collecting surface of a solar thermal cooker, makes cooking last to about 1.2 h, fairly long time. For a PV panel, this time doubles as its efficiency is about half of this amount. Thus, recipes needing to evaporate less water jointly with techniques to enhance efficiency are necessary.

Solar cooking shares with other solar technologies its variability, making solar cooking impossible during cloudy days. Moreover, dinner and breakfast cannot be cooked on time for the lack of sun at those times. This makes both *heat retention* on the food itself and *thermal energy storage* (TES) in an additional body very important to delay in time cooking some hours [34]. This means keeping the food hot enough so that residual cooking continues with no energy output, just using the stored thermal energy. For that, a high thermal insulation is required. Nowadays, these techniques are not much developed, exception made of the *hay baskets* [35–38] and experimental prototypes.

The dramatic price reduction of PV panels [39] offers the possibility for indoor solar cooking with renewable electricity at an affordable cost, which is relevant not only for isolated communities but also for periurban areas. Financial help is required as its amortization by not consuming any fuel can take many years. At the same time, PV opens the possibilities for home off-grid electrification, allowing

telecommunication, lamp charging, cold production for food and medicines preservation, etc., as their consumption is smaller than that required for cooking. Thus, highly appreciated commodities are offered. Some studies have analyzed the strategy of starting modern energy supply for illumination and mobiles charging to 1.2 billion people who are without grid access worldwide and 1 billion more with erratic access. This can be achieved by deploying solar home systems of pico-power size PV (1−10 W peak of electricity, W_p) [40] and even expanding them to supply radios, TVs, and fans with 100-W peak PV systems. In some studies, like that by Phadke [41], the basic needs of cooking, water sterilization, SHW, and food preservation are not considered in this kind of campaigns, surprisingly as these are the basic needs. The very important sterilization of surgical instruments using solar energy in remote locations has also received some attention [42].

3. FUNDAMENTALS OF COOKING

Cooking requires reaching at least temperatures T above 70°C for some time. Otherwise, pathogens survive and cooking does not happen. Humid food preservation needs higher temperatures. Reaching the required temperature inside of solids is delayed from the instant this temperature is reached in the surrounding liquid. When cooking with combustion or with electricity, the power delivered to the food is so high (0.5−2 kW) that this is seldom a problem and boiling water ($T_{bo} \approx 100$°C at sea level) is the current practice to guarantee sterilization and increase fluid agitation by bubbling. Frying, toasting, and barbequing require higher temperatures.

Low-temperature cooking at $T < 100$°C is possible and convenient to minimize heat losses to the surroundings, while tenderness and flavor can be enhanced [43−46]. But at higher temperatures, cooking is faster and operates in a different way because some chemical reactions appear (e.g., browning by Maillard reaction) so that a high temperature is a basic parameter for some recipes. Reducing water or oil addition in a classical recipe and increasing cooking time is current practice in solar cooking, but not always. This obliges people to change their cooking habits, which is not always easy, especially in a poor and noninstructed environment, even taking into account the benefit of the time recovered from avoiding firewood collection.

To understand the many possibilities that solar cooking offers, a simple thermal model seems useful.

4. THERMAL MODEL OF A PHOTOVOLTAIC COOKER

The net transient heat transfer to a single body $\dot{Q}_{tr}$ [W] causes its temperature T to change along time t and/or evaporate water. For simplicity, we consider the utensil

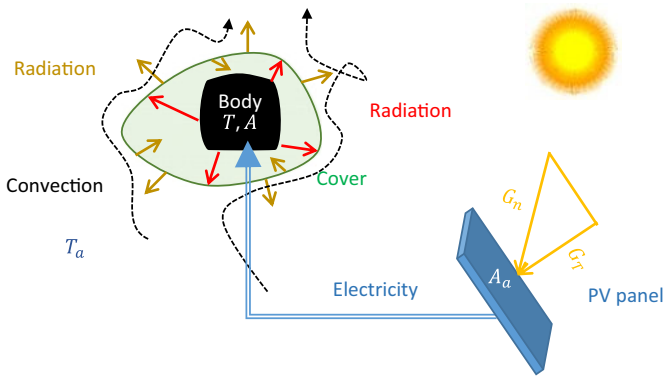


FIGURE 13.1

Scheme of a photovoltaic (PV) solar cooker indicating thermal losses.

(pot), food, and added water (sauce) as a lumped single body at a homogeneous temperature T above ambient $> T_a$ [K], owing to the small Biot number (Fig. 13.1). Cooking chemical reactions take negligible energy when compared with heating and boiling energies.

The net power delivered to the food by a PV system is proportional to the aperture active area of the PV panel A_a times the incident solar irradiance G_T normal to A_a and times the overall efficiency η_{PV} between the panel and the delivery ohmic resistance in contact with the food. The energy balance can be formulated as:

$$\dot{Q}_{tr} = C_{b+c}\frac{\mathrm{d}T}{\mathrm{d}t} = \overbrace{A_a G_T \eta_{\mathrm{PV}}}^{\text{PV heat}} - \overbrace{\mathrm{UA}(T - T_a)}^{\text{Heat loss}\dot{Q}_{l,\ \mathrm{dry}}} - \overbrace{\dot{m}_{bo} L_{bo}}^{\text{Enthalpy loss by evaporation or boiling}} \qquad \overbrace{\qquad\qquad}^{\dot{Q}_{tr,\ \mathrm{dry}}} \tag{13.1}$$

In Eq. (13.1):

- C_{b+c} is the heat capacity of the body (food, water, and utensil) and cover, respectively; $C_{b+c} = \overbrace{C_f + C_w + C_u + C_c}^{\text{Utensil}}$ [47]. $C = c \times m$, where c is the specific heat of mass m. An insulating cover usually is at an intermediate temperature between body and ambient; thus, its thermal capacity C_c [J/K] is a fraction $\delta_c < 1$ of its real one C_{cover}.
- A $\left[\mathrm{m}^2\right]$ is the area for heat losses, with the following subscripts: by conduction$_{cond}$, convection$_{conv}$, and radiation$_{rad}$. Normally, it is considered the external utensil area (see Fig. 13.1).
- G_T is the tilted solar irradiance $\left[\mathrm{W/m}^2\right]$, normal to the aperture surface, in-plane or with null incidence angle [48].

- $U\ \left[\mathrm{W/m^2\ K}\right]$ is the global heat transfer coefficient through A [47], including the cover as a barrier toward ambient. Generically, $U = U_{cond} + U_{conv} + U_{rad}$ as they act in parallel.
  - U_{conv}. It increases with $T - T_a$ for natural (free) convection. For forced convection, it increases with wind velocity v_w.
  - U_{rad} increases with body temperature and can be much reduced by a glass single- or double-layered cover, being generally $U_{conv,\,air} \approx U_{rad,\,amb} \approx 5 - 20\ \mathrm{W/K\ m^2}$ when cooking at $T_{ext} = 100°\mathrm{C}$ and no wind.

  A representative value for the parameter U considering either convection or radiation toward ambient is that of a sphere into air, as the detailed shape of a compact body does not have much influence either to convection or to radiation heat transfer.

  For elements in series (i.e., several layers in a single path), $\mathrm{UA} = \left[\sum_i (U_i A_i)^{-1}\right]^{-1}$, so that the smallest U controls the overall value. This is why a layer of thermal insulation $\left(U_{\mathrm{in}} \sim 0.1 - 1\ \mathrm{W/K\ m^2}\right)$ as a cover is usually devised to dominate the value of U from the body to ambient, and this method significantly reduces heat loss.
- $\dot{m}_{bo}\ [\mathrm{kg/s}]$ is the mass flow rate of evaporated liquid from the foodstuff, typically water_w, whose phase change enthalpy is very high $L_{bo,w} = 2.26\ \mathrm{MJ/kg}$.
  - For $T < T_{bo}$, there is evaporation, $\dot{m}_{bo}$ is proportional to the liquid−air interphase area, grows rapidly with T and liquid−gas agitation, and it is smaller when liquid contains dissolved or suspended nonvolatile substances, e.g., salt or oil, according to the Dühring's law.
  - For $T = T_{bo}$, boiling heat balances net heat applied so that $\dot{m}_{bo} L_{bo,w} = \dot{Q}_{tr,\mathrm{dry}}$ and temperature stabilizes. The resulting concentration of less volatile components increases boiling temperature.

4.1 SOME RESULTS OF THE MODEL

The temperature versus time evolution during cooking is sketched in Fig. 13.2. At the beginning, when $T = T_a$, the heating power $\dot{Q}_{tr}$ is maximum, as losses are null. As temperature increases, losses increase reducing the net heating power down to null when losses equal gain at what is called stagnation temperature. Actually, if all terms in Eq. (13.1) are constant except T and t, one can integrate Eq. (13.1) with no evaporation neither boiling in a time period between (t_1, T_1) and (t_2, T_2) (Fig. 13.2):

$$\frac{T_{st,\mathrm{dry}} - T_2}{T_{st,\mathrm{dry}} - T_1} = \exp\left(-\frac{t_2 - t_1}{t^*_{coo}}\right);\ t^*_{coo} \doteq \frac{C_{b+c}}{\mathrm{UA}};\ \dot{Q}_{tr} = A_a G_T \eta_{\mathrm{PV}}\ \frac{T_{st,\mathrm{dry}} - T}{T_{st,\mathrm{dry}} - T_a} \quad (13.2)$$

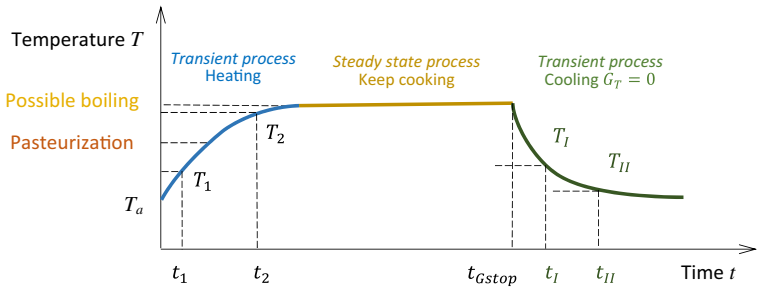


FIGURE 13.2

Representative temperature–time evolution starting and ending at ambient temperature.

- $T_{st,\text{dry}}$ is the dry stagnation temperature, formulated in Eq. (13.4) with the simplification of $U = U|_{T=T_{st}}$, meaning this constancy along the whole heating process, as a simplification.
- t^*_{coo} is the characteristic cooling time at the same operating conditions than heating but with $G_T = 0$. Eq. (13.5), also considering constancy during cooling.

Both parameters can be considered for an average value during heating $\overline{U}$, between T_1 and T_2, so that the parameters, previously considered constant, can be now only piecewise constant.

Maximum temperature is reached when $\frac{dT}{dt} = 0$:

- If there is boiling, according to Eq. (13.1):

$$\dot{m}_{bo} = \frac{A_a G_T \eta_{\text{PV}} - U|_{T=T_{bo}} A (T_{bo} - T_a)}{L_{bo,w}} \tag{13.3}$$

- For no boiling or evaporation (requiring a pot cover or no significant amount of water in the food), the steady-state *dry stagnation temperature* is obtained:

$$T_{st,\text{dry}} = T_a + \frac{A_a G_T \eta_{\text{PV}}}{U|_{T=T_{st}} A} \tag{13.4}$$

In Fig. 13.2, when $t > t_{\text{stop } G}$ it corresponds to $G_T = 0$ (dusk, heavy cloud, or indoors); cooling rate $\frac{dT}{dt} < 0$ is maximum in magnitude at the higher temperature and slows down as ambient temperature is approached. Integrating Eq. (13.1) with all the parameter constants excepting t and T between period (t_I, T_I) and (t_{II}, T_{II}) (Fig. 13.2), one gets:

$$\frac{T_{II} - T_a}{T_I - T_a} = \exp\left(- \frac{t_{II} - t_I}{t^*_{coo}} \right) \tag{13.5}$$

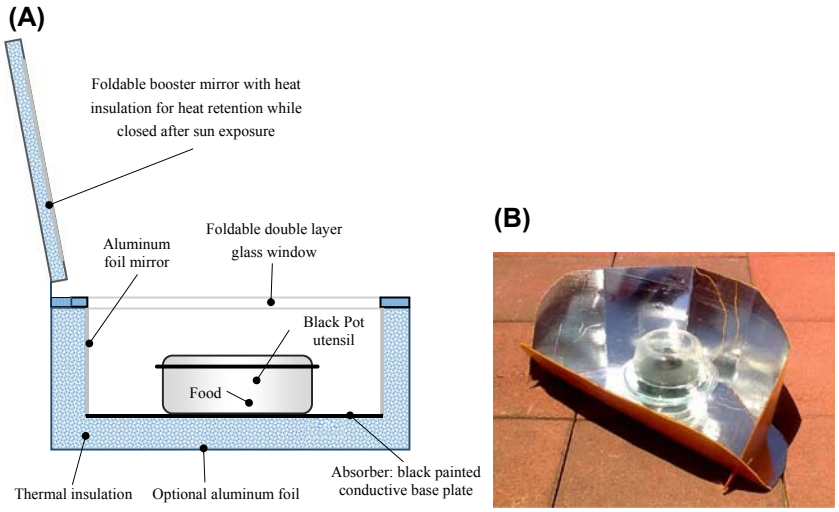


FIGURE 13.3

(A) Section of a generic solar box oven containing a single pot. (B) A Cookit type solar thermal cooker made of cardboard and aluminum foil. Scrap washing machine windows as greenhouse cover and thermocouples for testing.

In Eq. (13.4) the characteristic cooling time can be a function of the overtemperature, t^*_{coo} $t^*_{coo} = t^*_{coo}T - T_a$. A further simplification is when it is considered constant all over the cooling process.

Thermal insulation reduces U to something slightly larger than the value of the insulation $U_{\text{in}} = \frac{k_{\text{in}}}{l}$ where the *heat conductivity* of the current insulating material is $k_{\text{in}} = (0.04 - 0.05)\ \text{W/K m}$ and l is the thickness of the insulation layer. Just $l = 5$ cm gives $U_{\text{in}} = 1\ \text{W/K m}^2 \ll U_{conv+rad,air}$.

The average water heating power $\overline{\dot{Q}}_{tr}$ and efficiency $\overline{\eta}$ during heating can be calculated between: (1) a temperature slightly higher than T_a to avoid cooling water, $T_{1,hea}$, and (2) a temperature $T_{2,hea}$ slightly lower than T_{bo} to limit appreciable mass loss m_{bo} because of evaporation:

$$\overline{\dot{Q}}_{tr} = C_w \frac{T_{2,hea} - T_{1,hea}}{t_{2,hea} - t_{2,hea}}; \quad \overline{\eta}_{hea} = \frac{\overline{\dot{Q}}_{tr} + \overbrace{m_{bo}L_{bo}}^{\text{Optional}}}{G_T A_a}; \quad \overbrace{\overline{\eta}_{bo}}^{\substack{\text{Steady-state} \\ \text{at } T = T_{bo}}} = \frac{m_{bo}L_{bo}}{G_T A_a t_{bo}} \quad (13.6)$$

In this equation, the boiling efficiency η_{bo} during a time t_{bo} has been introduced, although it is seldom used.

Generally, a constant G_T is required to obtain consistent results; thus, central hours of the day are typically used for testing.

When cooling in the shadow with no evaporation, Eq. (13.1) reduces to:

$$U = -\frac{C_{b+c}}{A(T - T_a)} \frac{\mathrm{d}T}{\mathrm{d}t} \tag{13.7}$$

This equation indicates that by deriving the $T - t$ evolution one can obtain U as a function of T, or alternatively $U = U\langle T - T_a \rangle$, requiring always to specify A. C_{b+c} can be experimentally evaluated with a constant known power, such as with an electrical resistance under adiabatic conditions. In Lecuona-Neumann [49] and Lecuona et al. [50] more details are explained.

Pressure pots maintain a higher than atmospheric pressure inside it during boiling, resulting in an increased T_{bo}, reducing the time for cooking, at the expense of slightly higher sensible heat loss. A pressure pot/cooker is necessary, more expensive than an atmospheric pot.

5. HEAT STORAGE (THERMAL ENERGY STORAGE) WITH SOLAR COOKING

Cooking time extension is performed currently by wrapping the pot containing the already finished or partly cooked food with a insulating cover that commonly is located indoors. Also, they allow maintaining the food warm for some hours thus ready to serve. This practice is also known as *heat retention*. Down to 70°C cooking continues appreciably, performing what is called *fireless* or *thermal cooking* [43–46]. In locations where training on the topic has been performed, ordinary baskets filled with hollow materials are useful and become popular. It is enough to fill the baskets with used clothes, hay, or dry leaves [43–46]. They insulate not very well as they allow steam and hot air transpiration, but in contrast, this avoids mold formation. Low-temperature cooking is a fashionable tendency nowadays in developed countries [43–46]. A better option is to construct highly insulating indoor covers, as shown in Fig. 13.4.

There are two additional possibilities to extend or to delay cooking after sunset or to allow cooking during cloudy periods in a day – sensible and latent TES.

5.1 SENSIBLE HEAT THERMAL ENERGY STORAGE

Storing sensible heat (elevating temperature) in the food is not enough to keep it warm for hours, neither is it enough to avoid ruining cooking during a prolonged cloudy period. This limitation can be overcome by heating an additional mass of material at an elevated temperature that continuously or later is put in contact with the food. If this mass has stored enough heat at enough elevated temperature, it could even cook by itself, what is called *delayed cooking* [51]. This means a slower heating during the morning under the sun until the cooking temperature has been reached in the storage mass and cooking in parallel with further charging. Introducing the TES in an insulating cover maintains its cooking capacity for typically several hours and

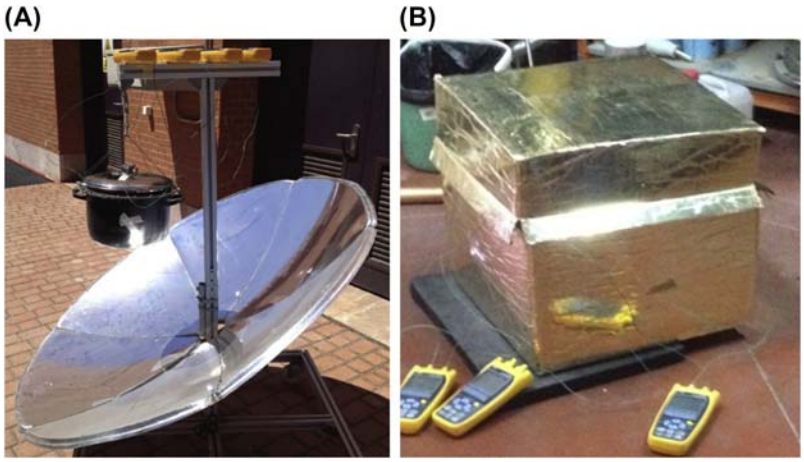


FIGURE 13.4

(A) Thermal energy storage (TES) utensil with phase-change material (PCM) between outer and inner coaxial pots, being charged on a high-concentration thermal solar cooker of the paraboloidal dish type, model Icogen, in a testing campaign. (B) Insulating cover for keeping heat for an indoor use of the charged TES utensil, made of a cardboard box, plastic metalized film, and polyurethane foam.

even 1 day. If this thermal "battery" cools down to a temperature lower than 70°C, still SHW can be produced with it.

Integrating Eq. (13.7) for $t > t_{G\ \text{stop}}$ (Fig. 13.2) considering the utensil and cover in contact with the TES and neglecting evaporation, the temperature results in a similar expression than Eq. (13.5):

$$\frac{T_{II} - T_a}{T_I - T_a} = \exp\left[- \frac{\text{UA}}{C_{b+c+\text{TES}}} \left(t_{II} - t_I\right)\right] \tag{13.8}$$

This makes $t^*_{coo,\text{TES}} = \frac{m_{\text{TES}} c_{\text{TES}} + C_{b+c}}{\text{UA}}$ the time when initial overtemperature $T_I - T_a$ reduces by a factor $\text{e}^{-1} = 0.368$. If desiring $t^*_{coo,\text{TES}} \approx 10 - 20$ h, a large mass m_{TES} is required of a material with large enough specific heat c_{TES}.

Putting the food in contact with the TES performs cooking. Storage in sand, used engine oil, rocks or cast iron has been attempted, but always the mechanisms involved is sensible heating s, so that to store a significant amount, high temperatures are needed, resulting in a low efficiency of the solar cooker η_{hea} (Eq. 13.5) when charging with the sun. Also during storage losses will be higher. If bringing to boil a mass of water m_w at 25°C with a mass of TES m_{TES}, a temperature above 100°C, ΔT_{TES} is required, it can be calculated with an adiabatic heat balance between both masses, neglecting the heat capacity of the utensil and cover: $\Delta_{\text{TES},S} = \frac{m_w c_w}{m_{\text{TES}} c_{\text{TES}}} (100 - 25)^\circ\text{C}$. As $\frac{c_w}{c_{\text{TES}}} \approx 1 - 10$ (exception made for liquid

ammonia) either large m_{TES} or/and Δ_{TES} are needed. Storing heat in water or any other volatile liquid is inconvenient because of vapor pressure growth. Storing heat in hot oil accelerates its degradation and gum formation, besides producing odors.

5.2 LATENT HEAT THERMAL ENERGY STORAGE

Better choice than sensible heat TES is latent heat TES with *phase change materials* (PCMs) [52,53]. Some implementations are reported in Sharma et al. [54] and Lecuona-Neumann [49]. Melting the PCM stores energy at a constant temperature, which is given back when solidifying. If melting occurs above 100°C, it allows boiling water when heat is restituted in solidifying the PCM. Acetanilide has been attempted as PCM [55]. The sugar alcohol erythritol $_{ER}$ is a good choice, with phase change at $T_{\mathrm{PC}} = 118°\mathrm{C}$ and involving $L_{\mathrm{PCM},ER} = 340\ \mathrm{kJ/kg}$, amount similar to the one of ice. It is eatable and is massively produced as a noncaloric sugar at an indicative retail price of 5 €/kg. Performing again the above-mentioned adiabatic heat balance with two identical TES masses, a reduction of overtemperature required for latent heat storage of $\Delta T_{\mathrm{TES},l} = \frac{L}{c_{\mathrm{TES}}}$ is obtained. For erythritol, it is around a descent of 120−250°C as $c_{\mathrm{TES},ER} = 1.38\ \mathrm{kJ/K\ kg}$ when solid and 2.76 kJ/K kg when liquid [49], resulting in a great advantage over sensible TES. The mass of PCM required to adiabatically heat up to the boiling temperature a mass of cold water m_w only by phase change is $m_{\mathrm{TES}} = \frac{m_w c_w}{L_{\mathrm{TES}}}\ 75°\mathrm{C} \approx m_w$ using erythritol. Some numerical studies can be found in Lecuona et al. [34] and Tarwidi et al. [56]. Experimental results are shown in Lecuona-Neumann [49]. An essay on figures of merit for TES solar cookers can be found in Lecuona et al. [50].

With the currently available PCMs, heat conductivity has to be enhanced using submerged metal fins, sponges, or particles, as the heat conductivity of PCMs is not high enough, e.g., $k_{ER} = 0.733/0.326\ \mathrm{W/K\ m}$ as solid or liquid. Issues still under review are PCM subcooling and thermal degradation [57]. One topic up to now not much studied is the separation of the PCM from the container walls when contracting as a result of solidification.

6. PHOTOVOLTAIC SOLAR COOKERS

PV solar cookers have been attempted elsewhere [58], using large solar panels and heavy lead−acid batteries. In this section, an ongoing research for the development of a cost-effective PV solar cooker is described and its principles described for engineers and entrepreneurs to bring the ideas to a reliable product for developing countries.

The basic design is an isolated electric system (Fig. 13.5). A PV solar panel is fixed on the roof, eventually with some periodic adjustment of its orientation for better gathering sun rays. Cables transport DC electricity to the kitchen. Batteries or preferably TES serve as storage for delayed cooking. Hydrogen-based electric

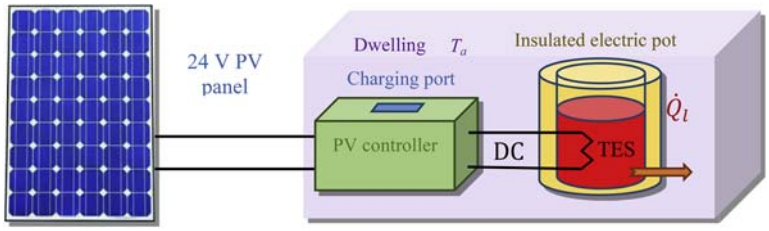


FIGURE 13.5

Layout of a stand-alone photovoltaic (PV) solar cooker with no batteries, using an electronic controller including a charging port for externals.

generation, storage, and ulterior burning have been studied [59] but its application in developing countries seems too far in the future because of cost.

Nowadays solar panels are massively produced with a retail price per watt peak (@ $G_n = 1\ \mathrm{kW/m^2}$ and $T_a = 25°\mathrm{C}$) of the order of 0.7−1.0 €/$\mathrm{W_p}$ down to 0.5 €/$\mathrm{W_p}$ for large quantities. The largest silicon panels with $A_a \approx 2\ \mathrm{m^2}$ yield around 300−315 $\mathrm{W_p}$, at 12 or 24 V nominal. This power is equivalent to the net power of a thermal solar cooker of family size with the advantage of making possible a high thermal insulation of the pot because of not having to devise apertures to the sun light around the pot. This defines the possibility of clean and sustainable cooking indoors and also provides surplus electricity for other home uses (25 $\mathrm{W_p}$ are typically considered enough for illumination and mobile charging). Deep cycle lead−acid batteries match the panel cost for 2.5 kWh nominal charging capacity of which only around 1/10 to no more than half of it can be used for storage to avoid operational life reduction. Lead−acid batteries have a short duration, $\sim 10^3$ charging cycles, and are polluting residues if abandoned. The power here considered is enough for cooking a meal on a sunny day and adequate for the yearly average daily production of 1.5−1.7 kWh of the fixed stand-alone panel in northern Africa, as a reference, according to Photovoltaic Geographical Information System [28]. This level of production will enter the dwelling into the official classification of "access to electricity" as more than 500 kWh per year will be possible. A complement will be required for cloudy days. Doubling the PV panel will add more availability but no additional changes will be required if the controller copes with the double intensity. Two additional devices are needed for a feasible solar cooker: (1) a pot containing a resistance (electrical pot or boiler) with enough heat insulation that allows cooking with this power level and (2) a PV panel controller without batteries, which is not currently in practice.

AC electrical pots including a microprocessor with 1−1.2 kW maximum power are available at 30−100 € retail price in the international market with 5−6 L capacity. They incorporate washable inner liners, insulated lid, and double wall, thus heat is insulated and even capable of acting as a moderate pressure cooker. Eventually, its

heat insulation can be improved with fiberglass matt. An independent electrical resistance for a nominal 24 V/300 W or even with a 600 W additional plug needs to be added in the heating base plate, thus eliminating the necessity of a DC/AC inverter for PV electricity and corresponding energy losses $\sim$10%. This way the pot retains the capacity of using the grid AC electricity when available. This electricity can be also solar if in a later time a solar power plant feeds the community [60,61].

For an efficient DC supply, a PV panel controller is needed to match its $I - V$ characteristic to heat the fixed resistance R to capture the maximum power under different irradiances, either along the day or in cloudy periods (Fig. 13.6). Otherwise, points indicated with a cross will be the operational points with the fixed resistance, producing less energy at part load.

The result is shown in Fig. 13.6.

The simplest control technique is an input feedback electronic circuit for constant-voltage operation of the panel, using duty cycle modulation, eventually with correction for sun irradiance and panel temperature. No smoothing of the output voltage is advisable so that when the circuit is open the constant voltage is applied to the constant resistance. A better technique is based on a switching converter microcontroller-based circuit that iteratively tracks the maximum power point in a continuous way [62]. The absence of battery makes current commercial controllers not useful. In the study by Lecuona-Neumann et al. [63], there is a description of a PV cooker with neither a battery nor an inverter, using a commercial electric pot. The power of such device $\left(A_a \approx 2\ \mathrm{m}^2\right)$ would be enough to serve also as a micro power plant [41]. For houses in developed countries, the programmable electric pot could be a modern appliance for sustainable kitchen practice and even a valued

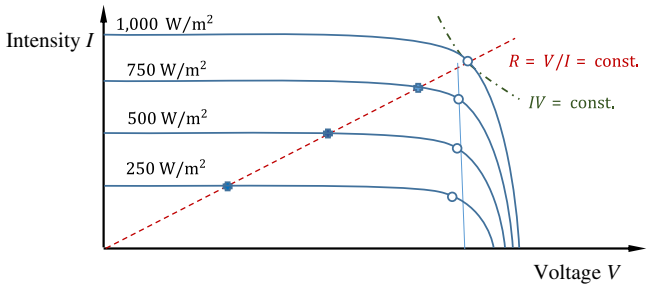


FIGURE 13.6

Intensity—voltage curves of a solar panel at four different normal irradiances and constant temperature. The *dash-dot line* is for constant maximum power. Maximum power point (MPP) control operation is shown with *hollow circles*. *Dashed line* indicates the $I - V$ relationship of a fixed load resistance R matched at peak irradiance. *Cross points* are matches with constant R operation without control. *Thin line* indicates $V =$ const. controlled operation.

accessory for rapid deployment emergency houses. PCM TES can be an optional add-on block inside the pot for delayed cooking.

As an example, one can use Eq. (13.3) for $T_{st,\mathrm{dry}}$ and assuming a 5-cm thickness of a typical insulation matt, such as fiberglass, and 30-cm size cylindrical pot, the insulation UA is much smaller than the UA for radiation and convection to the surrounding, thus it is dominant. As mentioned above $U_{\mathrm{in}} = 1\ \mathrm{W/m^2K}$. Let us assume central hours of a clear day with the PV panel not exactly oriented to the sun, then:

$$T_{st,\mathrm{dry}} = T_a + \frac{A_a G_T \eta_{\mathrm{PV}}}{U_{\mathrm{in}} A} = 25^{\circ}\mathrm{C} + \frac{\overbrace{2\ \mathrm{m}^2\ 600\ \frac{\mathrm{W}}{\mathrm{m}^2}\ 0.15}^{Q_s=240\ \mathrm{W\ electrical\ input}}}{1\ \frac{\mathrm{W}}{\mathrm{m^2K}}\ \underbrace{3.1416\left(\frac{0.3^2}{2}\ \mathrm{m}^2 + 0.3\ \mathrm{m} \times 0.3\ \mathrm{m}\right)}_{0.424\ \mathrm{m}^2}}$$

$$= 596^{\circ}\mathrm{C} \tag{13.9}$$

Obviously, this temperature will not be reached as evaporation and boiling will limit it, and increase of external U, but this calculation indicates that with a good enough insulation, cooking with a 2 m^2 PV panel is possible and boiling can occur. If U were half of this value, still the dry stagnation temperature would be high. The rate of water boiling can be estimated, according to Eq. (13.3):

$$\dot{m}_{bo,w} = \frac{A_a G_T \eta_{PV} - U|_{T=T_{bo}} A (T_{bo} - T_a)}{L_{bo,w}}$$

$$= \frac{240\ \mathrm{W} - 1\frac{\mathrm{W}}{\mathrm{m^2\ K}} 0.424\ \mathrm{m}^2 (100-25)^{\circ}\mathrm{C}}{2.26\frac{\mathrm{MJ}}{\mathrm{kg}}} = 0.33\frac{\mathrm{kg}}{\mathrm{h}} \tag{13.10}$$

This is a modest rate, so that excess water has to be avoided to not have a prolonged boiling time.

The cooling characteristic time is obtained according to Eq. (13.2) and assuming m_{b+c} as the mass of 2 L of water, thus only relying on heat retention on the food:

$$t^*_{coo} \doteq \frac{C_{b+c}}{\mathrm{UA}} = \frac{2\ \mathrm{kg} \times 4.18\ \frac{\mathrm{kJ}}{\mathrm{kg\ K}}}{1\ \frac{\mathrm{W}}{\mathrm{m^2K}}\ 0.424\ \mathrm{m}^2} = 5.5\ \mathrm{h} \tag{13.11}$$

If the starting temperature were that of boiling, after this time the food temperature would be, according to Eq. (13.5):

$$T_{II} = T_a + (T_I - T_a)\exp\left(-\frac{t_{\mathrm{II}} - t_{\mathrm{I}}}{t^*_{coo}}\right) = 25^{\circ}\mathrm{C} + \frac{75^{\circ}\mathrm{C}}{\mathrm{e}} = 53^{\circ}\mathrm{C} \tag{13.12}$$

This temperature would be perfect for serving.

Let us assume an applied PV power of $Q_S = 240$ W and the mentioned parameters assumed constant along the heating process. This is representative of the central hours in a clear day, when $G_T \eta_{\mathrm{PV}}$ can be considered constant for simplicity. The evaporation and boiling can be estimated using the Antoine equation for water saturation pressure $p_{s,w}\langle T\rangle$ and assuming the evaporation water mass flow $\dot{m}_{bo,w}$ proportional to it and equal to the net dry power at $T_{bo,w} = 100°\mathrm{C}$ when $p_{s,w} = 1$ atm.

$$p_{s,w}\langle T\rangle = \frac{10^{\left(8.07131 - \frac{1730.63}{\frac{T}{\mathrm{K}} - 39.724}\right)}}{760}\ \mathrm{atm} \tag{13.13}$$

This means open air evaporation of the heated water. Thus,

$$\dot{m}_{bo,w}\langle T\rangle = \frac{Q_S - \mathrm{UA}(100\ °\mathrm{C} - T_a)}{L_{bo,w}} \frac{p_{s,w}\langle T\rangle}{1\ \mathrm{atm}} \tag{13.14}$$

This limits the time evolution of the water temperature to 100°C, using the finite difference system of equations for increments in temperature ΔT and mass m_w during time increment Δt:

$$\Delta T = \frac{\Delta t}{m_w\langle t\rangle c_w}\left[Q_S - \mathrm{UA}(T - T_a) - \dot{m}_{bo,w}\langle T\rangle L_{bo,w}\right];\ \Delta m_w = -\dot{m}_{bo,w}\langle T\rangle \Delta t \tag{13.15}$$

Fig. 13.7 shows the results. For the herewith used value of $U = 1.0\ \mathrm{W/m^2K}$, one can appreciate that cooking $(T > 70°\mathrm{C})$ starts 40 min after the beginning and boiling starts at around 2 h after beginning. Cooking continues until about 4 h. Now evaporation reduces cooling characteristic time about 1 hour, resulting in $t^*_{coo} = 4.5$ h. Water loss during boiling is 0.33 kg/h, coinciding with Eq. (13.10). The water weight loss is 0.809 kg when $T = 70°\mathrm{C}$ during the cooling process,

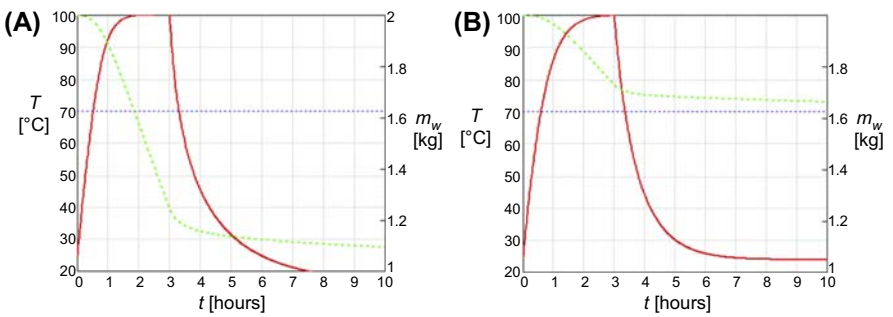


FIGURE 13.7

Water temperature and mass of water time evolution considering evaporation and saturated boiling. Cooling ($G_T = 0$) starts after 3 h in the same utensil, as described. The *blue dot line* (black in print versions) indicates start of cooking. (A) $U = 1.0\ \mathrm{W/m^2K}$. (B) $U = 5.0\ \mathrm{W/m^2K}$.

end of cooking. Just evaporation becomes difficult as a result of using a thermally insulated lid or/and reducing boiling by a pressure cooker this amount can be much reduced. A higher value of the overall heat transfer coefficient and $U = 5.0\ \mathrm{W/m^2K}$ can be representative of a thinner insulation, some thermal bridges and a moist insulation. One can appreciate in Fig. 13.7 the slower heating and the faster cooling and the slightly shorter cooking time, not actually reaching boiling. Correspondingly, there is a substantial smaller water loss. During cooling, time–temperature evolution is different in both cases. In both cases, one can appreciate that the equilibrium temperature at the end of cooling is lower than ambient temperature $T_a = 25°\mathrm{C}$ owing to the cooling effect of evaporation, down to a temperature that is an equilibrium of evaporation with heat input from ambient.

7. CONCLUSIONS

Solar cooking offers possibilities of reducing the burning of biomass for cooking, which causes pain, illnesses, and deforestation in one-third of world population in the developing countries.

PV panels offer a great potential for indoor cooking and also for bringing renewable electricity to homes, not only in isolated communities but also in periurban regions.

PCM-based TES offers the possibility of getting rid of current technology batteries and the associated cost, burden, and pollution.

Simple electronics for control makes possible the circuit manufacture and maintenance on site.

Preliminary modeling results are encouraging and serve to demonstrate the feasibility of the rapidly evolving PV technology to help a sustainable development.

ACKNOWLEDGMENTS

The partial funding by the CYTED research project RED TEMÁTICA 717RT0535 “ALMACENAMIENTO DE ENERGÍA SOLAR PARA COMUNIDADES AISLADAS” is much appreciated. The authors express the gratitude to the several students that have collaborated into the testing campaigns of the solar cookers developed in the laboratory, especially to Manuel Manchado and Alberto Barbero. Also to the technicians Manuel Santos, David Díaz and Israel Pina for their support on the machine shop.

REFERENCES

[1] D.W. Sun, Thermal Food Processing, second ed., CRC Press, Boca Raton, 2012.
[2] J.H. Tiffany, R. Morawicki, Energy consumption during cooking in the residential sector of developed nations: a review, Food Policy 40 (2013) 54–63.
[3] IEA, International Energy Agency, World Energy Outlook 2010, IEA, Paris, France, 2010.

[4] IEA, International Energy Agency, *Role of sustainable energy in ending poverty*, (n.d.). http://www.iea.org/topics/energypoverty/.
[5] D. Bisu, A. Kuhe, A. Iortyer, Urban household cooking energy choice: an example of Bauchi metropolis, Nigeria, Energ. Sustain. Soc. 6 (15) (2016), https://doi.org/10.1186/s13705-016-0080-1.
[6] World Health Organization, Fuel for life: household energy and health, World Health Organization, Geneva, 2006. https://www.cabdirect.org/cabdirect/abstract/20063133325.
[7] N. Abadi, K. Gebrehiwot, K. Techane, Links between biogas technology adoption and health status of households in rural Tigray, Northern Ethiopia, Energy Policy 101 (2017) 284−292, https://doi.org/10.1016/j.enpol.2016.11.015.
[8] Y. Chen, W. Hu, P. Chen, R. Ruan, Household biogas CDM project development in rural China, Renew. Sustain. Energy Rev. 67 (2017) 184−191, https://doi.org/10.1016/j.rser.2016.09.052.
[9] J. Logue, B. Singer, Energy impacts of effective range hood use for all U.S. residential cooking, HVAC&R Res. 20 (2) (2014) 264−275, https://doi.org/10.1080/10789669.2013.869104.
[10] K.R. Smith, Health, energy, and greenhouse-gas impacts of biomass combustion in household stoves, Energy Sustain. Dev. 1 (4) (1994) 23−29.
[11] M. Subramanian, Global health: deadly dinners, Nature 509 (2014) 548−551.
[12] Z.A. Nasir, F. Murtaza, I. Colbeck, Role of poverty in fuel choice and exposure to indoor air pollution in Pakistan, J. Integr. Environ. Sci. 12 (2) (2015) 107−117, https://doi.org/10.1080/1943815X.2015.1005105.
[13] W. Foell, S. Pachauri, D. Spreng, H. Zerriffi, Household cooking fuels and technologies in developing economies, Energy Policy 39 (2011) 7487−7496, https://doi.org/10.1016/j.enpol.2011.08.016.
[14] World Health Organization, Household air pollution and health, 2017. Retrieved from Fact sheet No. 292, http://www.who.int/mediacentre/factsheets/fs292/en/.
[15] Naciones Unidas/OCDE, in: CEPAL (Ed.), Evaluaciones del desempeño ambiental, Perú, Naciones Unidas/OCDE, Santiago, Chile, 2016. http://repositorio.cepal.org/bitstream/handle/11362/40171/S1600313_es.pdf?sequence=1.
[16] K.B. Sutar, M.R. Ravi, A. Ray, Biomass cookstoves: a review of technical aspects, Renew. Sustain. Energy Rev. 41 (2015) 1128−1166.
[17] C. Ong, Choice of energy paths: its Implications for rural energy poverty in less developed countries, Soc. Nat. Resour. 28 (7) (2015) 733−748, https://doi.org/10.1080/08941920.2015.1020583.
[18] M. Tucker, Can solar cooking save the forests? Ecol. Econ. 1 (1999) 77−89.
[19] J.C. Allen, D.F. Barnes, The causes of deforestation in developing countries, Ann. Assoc. Am. Geogr. 75 (2) (1985) 163−184, https://doi.org/10.1111/j.1467-8306.1985.tb00079.x.
[20] D. Still, J. Kness, Capturing HEAT: Five Earth-Friendly Cooking Technologies and How to Build Them, second ed., (available en: http://www.aprovecho.org/lab/pubs/arcpubs ed.). Aprovecho Research Center, 80574 Hazelton Road, Cottage Grove, Oregon, USA, 20xx.
[21] ClimateTechWiki, Improved cook stoves, in: W. van der Gaast (Ed.), (n.a.). http://www.climatetechwiki.org/technology/imcookstoves.
[22] International Energy Agency (OECD-IEA), Energy Poverty How to Make Energy Access Universal?, International Energy Agency, Paris, 2010.

[23] F. Lacey, D. Henze, C. Lee, A. van Donkelaar, R. Martin, Transient climate and ambient health impacts due to national solid fuel cookstove emissions, Proc. Natl. Acad. Sci. U.S.A. 114 (February 23, 2017) 1269−1274, https://doi.org/10.1073/pnas.1612430114.
[24] International Energy Agency, in: R. Priddle (Ed.), Africa Energy Outlook, International Energy Agency (OECD-IEA), Paris, France, 2014. Retrieved from: http://www.iea.org/.
[25] Z. Xu, D. Sun, Z. Zhang, Z. Zhu, Research developments in methods to reduce carbon footprint of cooking operations: a review, Trends Food Sci. Technol. 44 (1) (2015) 49−57, https://doi.org/10.1016/j.tifs.2015.03.004.
[26] Solar Cookers International, in: Solar Cookers International Network, S.C. International, 2016. http://solarcooking.wikia.com/wiki/Scheffler_Community_Kitchen.
[27] SOLARGIS, in: SOLARGIS, SOLARGIS, 2010−2016. http://solargis.info/imaps/.
[28] Institute for Energy and Transport, PVGIS. European Commission Center for Joint Research, (n.a.). http://re.jrc.ec.europa.eu/pvgis/.
[29] J. MacClancy, Solar Cooking? Why is it not yet global? Food Cult. Soc. 17 (2) (2014) 301−318.
[30] Solar Food Processing Network, Solar Food Processing Network, 2017. http://www.solarfood.org/.
[31] International Solar Energy Society, Solar Food Processing, International Solar Energy Society (ISES), Freiburg, 2009. Retrieved from: www.ises.org.
[32] Restaurante Solar Delicias del Sol Villaseca, Vicuña, Chile, Restaurante Solar Delicias del Sol Villaseca, 2016. https://www.facebook.com/pages/Restaurant-Solar-Delicias-Del-Sol-Villaseca/254951814584007.
[33] H.M. Toonen, Adapting to an innovation: solar cooking in the urban households of Ouagadougou (Burkina Faso), Phys. Chem. Earth, Parts A/B/C 34 (1−2) (2009) 65−71.
[34] A. Lecuona, J.I. Nogueira, R. Ventas, M.C. Rodríguez-Hidalgo, M. Legrand, Solar cooker of the portable parabolic type incorporating heat storage based on PCM, Appl. Energy 111 (2003) 1136−1146, https://doi.org/10.1016/j.apenergy.2013.01.083.
[35] Solar Cookers International Network, Heat-Retention Cooking, (n.a.). http://solarcooking.wikia.com/wiki/Heat-retention_cooking.
[36] Solar Cookers International Network, Parabolic Solar Cooker Designs, (n.a.). http://solarcooking.wikia.com/wiki/Parabolic_solar_cooker.
[37] Solar Cookers International Network, Solar Panel Cooker Designs, (n.a.). http://solarcooking.wikia.com/wiki/Solar_panel_cooker_designs.
[38] Solar Cookers International Network, Solar Trough Cooker Designs, (n.a.). http://solarcooking.wikia.com/wiki/Solar_trough_cooker_designs.
[39] UnderstandSolar.com, Cost of Solar Panels Over Time, 2016. https://understandsolar.com/cost-of-solar/#cost.
[40] V. Salas, Stand-alone photovoltaic systems, in: N. Pearsal (Ed.), The Performance of Photovoltaic (PV) Systems, Woodhead Publishing, 2017, pp. 251−296, https://doi.org/10.1016/B978-1-78242-336-2.00009-4.
[41] A. Phadke, Powering a Home with just 25 watts of Solar PV: Super-Efficient Appliances Can Enable Expanded Off-Grid Energy Service Using Small Solar Power Systems, Ernest Orlando Lawrence Berkeley National Laboratory, Berkeley, CA, 2015 (2015) LBNL-175726, Berkeley.
[42] E. González-Mora, E. Rincón-Mejía, D. Lawrence, Using a new solar sterilizer for surgical instruments as a solar oven for cooking. *CYTEF 2016 − VIII Congreso Ibérico | VI Congreso Iberoamericano de las Ciencias y Técnicas del Frío* (p. n.a.). Coimbra: SECYTEF, 2016 http://secytef.upct.es/. Retrieved from: http://www.adai.pt/event/event/home/index.php?target=home&defLang=4&event=2.

[43] Wikipedia, Low Temperature Cooking, (15 August 2017). https://en.wikipedia.org/wiki/Low-temperature_cooking.
[44] Wikipedia, Slow Food, (1 October 2017). https://en.wikipedia.org/wiki/Slow_Food.
[45] Wikipedia, Thermal Cooking, (4 October 2017). https://en.wikipedia.org/wiki/Thermal_cooking.
[46] Wikipedia, Wonderbag, (4 July 2017). https://en.wikipedia.org/wiki/Wonderbag.
[47] F.P. Incropera, et al., Fundamentals of Heat and Mass Transfer, John Wiley & Sons, Hoboken, New Jersey, USA, 2007.
[48] J.A. Duffie, W.A. Beckman, Solar Engineering of Thermal Processes, John Wiley & Sons, Hoboken, New Jersey, USA, 1991.
[49] A. Lecuona-Neumann, Cocinas solares. Fundamentos y aplicaciones. Herramientas de lucha contra la pobreza energética, Marcombo, Barcelona, Spain, 2017.
[50] A. Lecuona, J.I. Nogueira, C. Vereda, R. Ventas, Solar cooking figures of merit. Extension to heat storage, in: A. Méndez-Vilas (Ed.), Materials and Processes for Energy: Communicating Current Research and Technological Developments, Formatex Research Center, 2013, pp. 134−141. http://www.formatex.info/energymaterialsbook/.
[51] K. Schwarzer, M. Vieira da Silva, Solar cooking system with or without heat storage for families and institutions, Sol. Energy 75 (1) (2003) 35−41.
[52] A. Sharma, V. Tyagi, C. Chen, D. Buddhi, Review on thermal energy storage with phase change materials and applications, Renew. Sustain. Energy Rev. 13 (2009) 318−345.
[53] B. Zalba, J.M. Marín, L.F. Cabeza, H. Mehling, Review on thermal energy storage with phase change: materials, heat transfer analysis and applications, Appl. Therm. Eng. 23 (2003) 251−283.
[54] S.D. Sharma, D. Buddhi, L.R. Sawhney, A. Sharma, Design, development and performance evaluation of a latent heat storage unit for evening cooking in a solar cooker, Energy Convers. Manage. 41 (2000) 1497−1508.
[55] A. Chaudhary, A. Kumar, A. Yadav, Experimental investigation of a solar cooker based on parabolic dish collector with phase change thermal storage unit in Indian climatic conditions, J. Renew. Sustain. Energy 5 (12) (2013), https://doi.org/10.1063/1.4794962.
[56] D. Tarwidi, D. Murdiansyah, N. Ginanja, Performance evaluation of various phase change materials for thermal energy storage of a solar cooker via numerical simulation, Int. J. Renew. Energy Dev. 5 (3) (2016) 199−210, https://doi.org/10.14710/ijred.5.3.199-210.
[57] A. Shukla, D. Buddhi, R. Sawhney, Thermal cycling test of few selected inorganic and organic phase change materials, Renew. Energy 33 (2008) 2606−2614.
[58] S. Joshu, A. Jani, Certain analysis of a solar cooker with dual Axis sun tracker, in: 2013 Nirma University International Conference on Engineering (NUiCONE), IEEE, 2013.
[59] E. Topriska, M. Kolokotroni, Z. Dehouche, D. Novieto, E. Wilson, The potential to generate solar hydrogen for cooking applications: case studies of Ghana, Jamaica and Indonesia, Renew. Energy 95 (2016) 495−509, https://doi.org/10.1016/j.renene.2016.04.060.
[60] Price Waterhause Coopers, Electricity Beyond the Grid. Accelerating Access to Sustainable Power for All, Price Waterhouse Coopers, 2016. www.pwc.com/utilities.
[61] A. Condé, We Can Bring Electricity to All of Africa in Just 10 Years, World Economic Forum, January 13, 2017. Retrieved from World Economic Forum Annual Meeting 2017: https://www.weforum.org/agenda/2017/01/we-can-bring-electricity-to-all-of-africa-in-just-ten-years?utm_content=buffer4595a&utm_medium=social&utm_source=twitter.com&utm_campaign=buffer.

[62] V. Salas, E. Olías, A. Barrado, A. Lázaro, Review of the maximum power point tracking algorithms for stand-alone photovoltaic systems, Sol. Energy Mater. Sol. Cells 90 (11) (2006) 1555−1578, https://doi.org/10.1016/j.solmat.2005.10.023.
[63] A. Lecuona-Neumann, M. Sanchez-Bodas, R. Ventas-Garzón, Propuesta de cocina solar fotovoltaica. Análisis simplificado, in: CYTEF (Ed.), VIII Iberian Congres/VI Iberian Congress on Refrigeration Sciences and Technology, CYTEF, Coimbra, 2016, p. 597. Retrieved from: file:///C:/Users/ANTONIO/AppData/Local/Temp/Rar$EXa0.107/CYTEF2016%20-%20Proceedings/CYTEF2016_proceedings/CYTEF2016_proceedings/others/4.Chapter08.html.

FURTHER READING

[1] H.Z. Abou-Ziyan, Experimental investigation of tracking paraboloid and box solar cookers under Egyptian environment, Appl. Therm. Eng. 18 (1998) 1375−1394.
[2] alSol, Cocina Solar alSol 1.4., (n.d.). http://alsol.es/productos/cocina-alsol-1-4/.
[3] American Society of Agricultural and Biological Engineers, ASAE Standard S-580.1 Testing and Reporting Solar Cooker Performance, Standard, ASABE, St. Joseph, Michigan, USA, 2013.
[4] American Society of Agricultural Engineers, Standard ASAE S580 JAN 03 Testing and Reporting Solar Cooker Performance, ASAE 2950, St. Joseph, MI, USA, 2003, pp. 49085−49659.
[5] P. Arveson, Wikipedia, 2011. Retrieved from Solar cooker: http://en.wikipedia.org/wiki/File:HotPot_d.PNG.
[6] Blazing Tube, Retrieved from BlazingTubeSolarAppliance: Blazingtubesolar.com, 2015 http://blazingtubesolar.com/index.html.
[7] BMZ aktuell 060, ECSCR. Second International Solar Cooker Test − Summary of Results, Bundesministerium fur wirtschaftliche Zusammenarbeit und Entwicklung, Bonn, 1994.
[8] D. Buddhi, S. Sharma, A. Sharma, Thermal performance evaluation of a latent heat storage unit for late evening cooking in a solar cooker having three reflectors, Energy Convers. Manage. 44 (2003) [809]−[817].
[9] Bureau of Indian Standards (BIS), Indian Standard-Solar Cooker, IS 13429, Manak Bhawan, New Delhi, 1992.
[10] Bureau of Indian Standards (BIS), Indian Standards IS 13429: Solar Cooker e Box Type, First Revision, BIS, Manak Bhawan, New Delhi, 2000.
[11] CERCS, Comite europeen pour la recherche sur la cuisson solair, Syst. Solaires 104 (1994) 33−52 (Paris).
[12] A. Chandak, S.K. Somani, P.M. Suryaji, Comparative analysis of SK-14 and PRINCE-15 solar concentrators, in: Proceedings of World Congress on Engineering vol. III, 2011 (Londres).
[13] A.A. El-Sebaii, A. Ibrahim, Experimental testing of a box-type solar cooker using the standard procedure of cooking power, Renew. Energy 30 (2005) 1861−1871.
[14] H.P. Garg, Solar Cookers, in: H.P. Garg (Ed.), Advances in Solar Energy Technology. Volume 3 Heating, Agricultural and Photovoltaic Applications of Solar Energy, Springer, Amsterdam, The Netherlands, 1987, pp. 1−61.
[15] GOSUN, Gosun Sport, (n.a.). Retrieved from Gosun: https://www.gosunstove.com/products/gosun-sport.

[16] M. Grupp, T. Merkle, M. Owen-Jones, Second International Solar Cooker Test, European Committee for Solar Cooking Research & Synopsis, 1994. Route d'Olmet, F-34700 Lodeve, France.
[17] GTZ, M. Grupp, et al., Solarkocher in Entwicklungsländern: (Solar cookers in developing countries), Eschborn, 1999. http://www.giz.de.
[18] S. Kumar, Estimation of design parameters for thermal performance evaluation of box-type solar cooker, Renew. Energy 30 (2005) 1117−1126.
[19] S. Kumar, T.C. Kanpal, S.C. Mullick, Optical efficiency and stagnation test on a paraboloidal solar cooker, in: Proceedings of Indian National Solar Energy Convention, 1990, pp. 105−109 (Udaipur).
[20] S. Kumar, T.C. Kandpal, S.C. Mullick, Heat losses from a paraboloid concentrator solar cooker: experimental investigations on effect of reflector orientation, Renew. Energy 3 (8) (1993) 871−876.
[21] R. Kumar, R.S. Adhikari, H.P. Garg, A. Kumar, Thermal performance of a solar pressure cooker based on evacuated tube solar collector, Appl. Therm. Eng. 21 (2001) 1699−1706.
[22] G. Kumaresan, V. Vigneswaran, S. Esakkimuthu, R. Velraj, Performance assessment of a solar domestic cooking unit integrated with thermal energy storage system, J. Energy Storage 6 (2016) 70−79, https://doi.org/10.1016/j.est.2016.03.002.
[23] A. Kundapur, C.V. Sudhir, Proposal for a new world standard for testing solar cookers, J. Eng. Sci. Technol. 4 (3) (2009) 272−281.
[24] P.J. Lahkar, A review of the thermal performance parameters of box type solar cookers and identification of their correlations, Renew. Sustain. Energy Rev. 14 (6) (2010) 1615−1621.
[25] S. Mahavar, N. Sengar, P. Rajawat, M. Verma, P. Dashora, Design development and performance studies of a novel single family solar cooker, Renew. Energy 47 (2012) 67−76.
[26] M. Manchado-Megía, Caracterización de una cocina solar parabólica, Universidad Carlos III de Madrid, INgeniería Térmica y de Fluidos, Leganés, Madrid, España, 2010.
[27] S.C. Mullick, T.C. Kandpal, A.K. Saxena, Thermal test procedure for box type solar cooker, Sol. Energy 39 (4) (1987) 353−360.
[28] S.C. Mullick, T.C. Kandpal, S. Kumar, Thermal test procedure for a paraboloid concentrator solar cooker, Sol. Energy 46 (3) (1991) 139−144.
[29] PVGIS, Photovoltaic Geographical Information System, EC, European Commission, 2001−2008. http://re.jrc.ec.europa.eu/pvgis/apps3/pvest.php.
[30] A. Saxena, P. Varun, G. Srivastav, A thermodynamic review on solar box type cookers, Renew. Sustain. Energy Rev. 15 (2011) 3301−3318.
[31] A.V. Sonune, S.K. Philip, Development of a domestic concentrating cooker, Renew. Energy 28 (2003) 1225−1234.
[32] US Environmental Protection Agency, The Water Boiling Test (WBT) Version 4.2.2, Cookstove Emissions and Efficiency in a Controlled Laboratory Setting. US EPA, Partnership for Clean Indoor Air (PCIA), Global Alliance for Clean Cookstoves (GACC), Aprovecho Research Center (ARC), (n.d.) http://www.aprovecho.org.
[33] Xuaxo, Wikipedia, 2007. Retrieved from Solar Cooker: https://commons.wikimedia.org/wiki/File:Solar_oven_Portugal_2007.jpg.
[34] F. Yettou, B. Azoui, A. Malek, A. Gama, N. Panwar, Solar cooker realizations in actual use: an overview, Renew. Sustain. Energy Rev. 37 (2014) 288−306, https://doi.org/10.1016/j.rser.2014.05.018.

[35] http://atlascuisinesolaire.free.fr. A. B. Wikipedia, 2010. Retrieved from Solar cooker: https://en.wikipedia.org/wiki/File:Parabole_de_cuisson_solaire_Scheffler_coccion_solar_cooking.jpg.
[36] http://www.atlascuisinesolaire.com/photos-cuisine-solaire.php. Wikipedia, 2014. Retrieved from Solar cooker: http://en.wikipedia.org/wiki/File:ALSOL.jpg.

This page intentionally left blank

PART

Wind Energy

3

This page intentionally left blank

www.TechnicalBooksPDF.com

CHAPTER

Wind Energy FACTS Applications and Stabilization Schemes

14

Erhab Youssef[1], Adel Sharaf[2], Amr Amin[1], Adel El Samhey[1]

Electrical Power and Machines Department, Helwan University, Cairo, Egypt[1]; Electrical and Electronics Engineering Department, New Brunswick University, Fredericton, NB, Canada[2]

CHAPTER OUTLINE

1. Introduction 433
2. Wind Farm Configuration 434
2.1 Fixed-Speed Wind Energy Conversion System 434
2.2 Variable-Speed Wind Energy Conversion System 435
2.3 Wind Doubly Fed Induction Generators 436
3. Issues of Integrating Wind Energy Into the Grid: An Overview 438
3.1 Issue of Voltage Regulation and Power Quality 439
3.1.1 Low-Voltage Ride-Through Capability 439
4. Different FACTS Schemes and Applications 441
4.1 FACTS Applications 441
5. Wind Energy in Egypt 441
6. Wind Farm Modeling 443
6.1 Wind Turbine Modeling 444
6.2 Modeling of Self-Excited Induction Generator 446
6.3 Static Synchronous Compensator Modeling 447
6.4 Proposed Controller Design 449
6.4.1 Modeling of the Pitch Angle Controller 449
6.4.2 Modeling of the Reactive Power Controller 449
6.5 Simulation Results 450
6.5.1 Variable Wind Speed 450
6.5.2 Three-Phase Fault 451
6.5.3 Voltage Sag With Severe Wind Speed Variation 454
7. Conclusions 458
Appendix 458
References 459

Advances in Renewable Energies and Power Technologies. https://doi.org/10.1016/B978-0-12-812959-3.00014-9
Copyright © 2018 Elsevier Inc. All rights reserved.

NOMENCLATURE

Variables and parameters

A	Rotor swept area
A_g	Wind gust amplitude
C_p	Power coefficient
$E_{O,abc}$	Inverter output voltage
E_{Od}, E_{Oq}	Inverter voltage (d−q frame)
i_{dc}	Current at dc side
I_{Od}, I_{Oq}	Inverter current (d−q frame)
L_s	Leakage inductance transformer
m	Modulation index
P, Q	Active and reactive power
P_m	Mechanical power
R_m	Maximum radius of wind turbine
R_s	Transformer resistance
S	Switching function
T_{eg}	End time of the wind gust
T_{sg}	Time start of the wind gust
U_{dc}	The voltage at dc side
Vsa	Phase voltage at the supply side
V_w	Wind speed
Vwa	First wind speed
Vwg	Wind speed gust component
Vwr	Wind speed ramp component
Vwt	Wind speed turbulence
X	Transformer reactance
α	Phase angle
β	Pitch angle
θ	The angular speed of the voltage supply
λ	Tip speed ratio
ρ	Air mass density
ω_m	Angular shaft speed

Subscripts

a, b, c	a, b, c Frame
d	Direct axis
dc	Direct current
e	Electrical value
g	Grid
m	Mechanical value
q	Quadrature axis
s	Supply

1. INTRODUCTION

Worldwide, the development of wind power is dramatic. The number of wind power installations will roughly double in the upcoming 5 years, in accordance with the Global Wind Energy Council. China will be the principal participant of wind power installation, however with important contributions from Europe and United States. The United States recommends that a much stronger enterprise emerge, setting the stage as a result of the rapid increase in the advent in the last few years. New markets are developing across Africa, Asia, and Latin America, as a result of the increase in market from the previous decade. In Asia, China is leading in the production of wind power followed by India; however, market is growing rapidly in countries such as Indonesia, Vietnam, the Philippines, Pakistan, and Mongolia [1].

The first market in Africa to pass the 1000-MW value in 2014 has been South Africa. Egypt, Morocco, Ethiopia, and Kenya will be the dominant developing markets. Brazil will be the prime player in Latin America, followed by Chile and Uruguay, and a potentially great market is just now opening in Argentina. The annual installed capacity by region during the period 2007−15 is shown in Fig. 14.1 [1].

Nowadays, the integration of renewable energy sources (i.e., solar, wind, wave and tidal systems, etc.) into the grid is experiencing rapid increase. The high penetration of these sources could present a significant impact on the grid. Consequently, enhancement the power system stability and quality and reliability are the main area of research interest.

Flexible AC Transmission Systems (FACTS) devices improve the performance of power system. FACTS comprise a family of shunt, series, and hybrid devices. Modern smart grid dynamics will comprise a green renewable energy and distribute

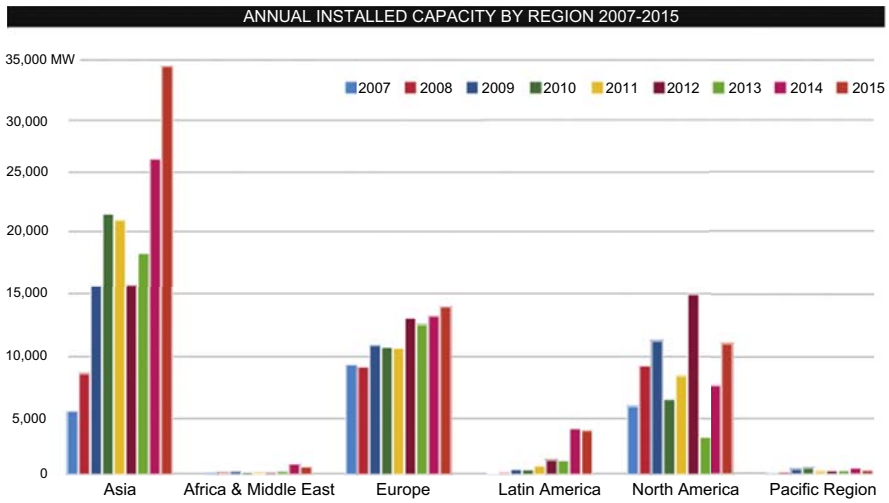


FIGURE 14.1

Annual installed capacity by region 2007−15 [1].

generation and FACTS stabilization. In order to filter devices to alleviate severe voltage instability and enhance power factor and for energy-efficient utilization using switched FACTS-based devices, dynamic control systems are fully utilized [2].

This chapter will present the wind farm schemes and FACTS. The operation of the fixed-speed wind farm and its control for active power will be demonstrated in detail. The operation and control of static synchronous compensator (STATCOM) are presented. Simulation is carried out to study the performance of the proposed system with STATCOM at variable wind speed and a three-phase to ground short-circuit fault. MATLAB®/SIMULINK Software is used to validate the proposed system.

2. WIND FARM CONFIGURATION

The modern wind turbine system consists of the turbine rotor, gearbox, generator, transformer, and possible power electronics as illustrated in Fig. 14.2. The wind power is converted to mechanical power by aerodynamics. The wind power is proportional to the cube of the wind speed, and so, there are different methods to control the mechanical power at wind gust to avoid the breakdown of a wind tower. These methods are stall control, active stall control, and pitch control. For the stall control, the position of the blade is fixed but stall of the wind appears along the blade at higher wind speed. Meanwhile, in the active stall the blade angle is controlled to make stall along the blades. Regarding the pitch control, the blades are turned out of the wind when the wind speed is high by changing the pitch angle of blades.

Two types of wind energy conversion systems (WECS) can be distinguished, namely fixed-speed and variable-speed turbines.

2.1 FIXED-SPEED WIND ENERGY CONVERSION SYSTEM

In this type, the speed of wind turbine is determined by the frequency of the grid, number of poles, number of induction generators, and the gearbox ratio. The

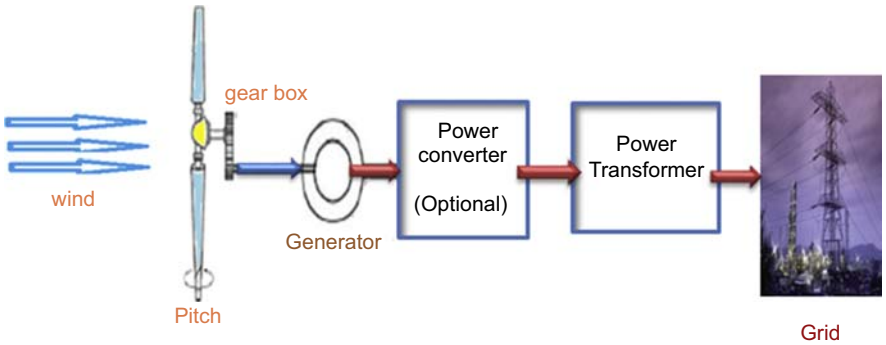


FIGURE 14.2

Main components of a wind turbine system.

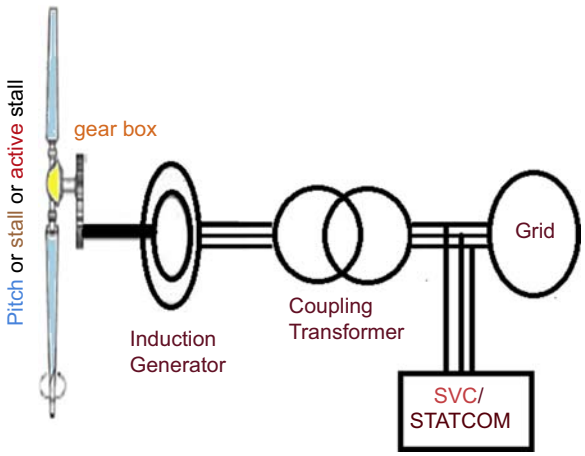


FIGURE 14.3

Frequently used fixed-speed WECS.

aerodynamic control of blades is essential to improve the complete system operation. The most common wind turbine systems of this type are illustrated in Fig. 14.3. Using induction generators will keep an almost fixed speed (variation of 1%−2%). The voltage regulation requirements can be improved by a STATCOM or SVC [3]. Modeling of the fixed-speed WECS is presented in detail in this chapter.

2.2 VARIABLE-SPEED WIND ENERGY CONVERSION SYSTEM

In this type, the wind turbine can store the varying wind power as rotational energy by controlling the speed of the turbine. Thus, the stress on the mechanical structure is minimized, and the generated power becomes smoother than that in fixed-speed WECS concept. The aerodynamic control of wind turbine keeps the mechanical power at nominal value by using the Maximum Power Point Tracking technique [4]. The wind turbine speed control is achieved by adding a variable resistance in the rotor of induction generator as presented in Fig. 14.4A. This allows a speed range of 2%−4%. Another method to get variable speed is by using a full- and partial-scale power converter with a wound-rotor induction generator.

Fig. 14.4B shows a medium-scale power converter with a wound rotor induction generator called doubly fed induction generator (DFIG). In this type, a partial power converter is connected to the rotor via slip rings to control the rotor currents. If the generator is operating above synchronous speed, the generated power is delivered through both the rotor and the stator. Meanwhile, if the generator is operating subsynchronously, the electrical power is only delivered into the rotor from the grid. The variation of speed is 60% and synchronous speed might be obtained using a power converter of 30% of the nominal power of generator [5]. The active and reactive power control of DFIG is discussed in detail in the next section.

The full-scale WECS consists of a full-scale power converter connected between the generator and grid as shown in Fig. 14.4C. In this concept, there is a flexible control in the mechanical power generated by the wind turbine. The squirrel cage induction

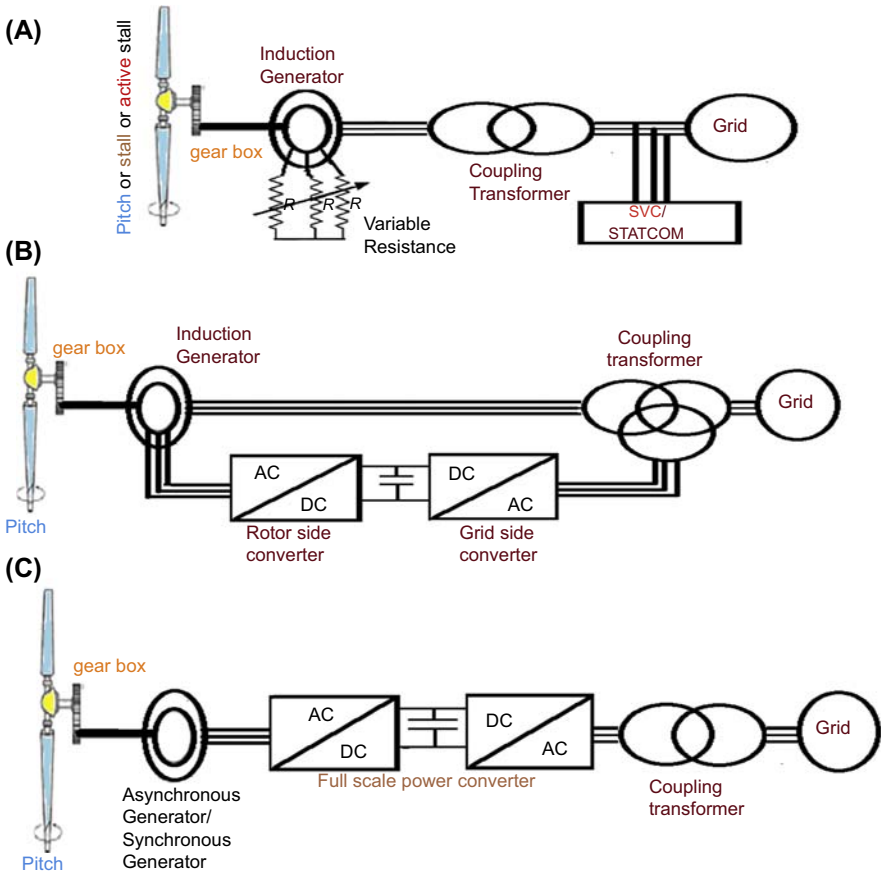


FIGURE 14.4

Variable-speed wind energy conversion system (WECS). (A) Wound rotor induction generator with variable resistance, (B) doubly fed induction generator WECS, (C) full-scale converter WECS.

machine, synchronous generator, or permanent magnet synchronous generator has been used as a solution. The main advantages of this concept compared to the DFIG are the absence of the slip ring or gear box, the full power control and speed controllability, and better grid support. However, there are drawbacks for this type such as the high cost of power electronic converter and the higher power losses in the converter [5].

2.3 WIND DOUBLY FED INDUCTION GENERATORS

Nowadays, the wind-DFIG is the most adopted solution in variable-speed wind-WECS and has been in use since the 2000s. The partial-scale power converters that are connected to DFIG could control the frequency and current in the rotor to obtain variable-speed range to satisfactory level. The two-level back-to-back converter (2L-B2B) voltage source converter is the widely used converter topology

for DFIG. Because the power rating requirement for the converter is limited, the rating is 30% of the generating power of DFIG [6].

The main advantage of 2L-B2B voltage source converter is fully controlled by active and reactive power with a simple structure and few components, which contribute to well-proven robust performance and cost. The schematic control structure of DFIG is divided into three parts:

1. Wind turbine controller
2. Grid-side converter
3. Rotor-side converter

Fig. 14.5 shows the control structure of a wind turbine-DFIG. For the wind turbine controller, the pitch angle controller is used and is only active in higher wind speeds such as wind gust. For rated wind speed below the high wind speed and above the cut-in wind speed, the wind turbine tries to produce as much power as possible, with fixed pitch angle. The value of the pitch angle should be optimal to generate maximum power at variable wind speed. The pitch controller supports an efficient tool of regulating the aerodynamic power and loads produced by the rotor at higher wind speeds, so that the design limits are not exceeded [8].

The grid-side PWM converter is responsible for the regulation of the DC-link voltage to be constant, regardless of the direction and magnitude of the rotor power, whereas the grid current is kept sinusoidal as also the reactive power control that flows between the grid and the grid side converter by setting the reactive power reference.

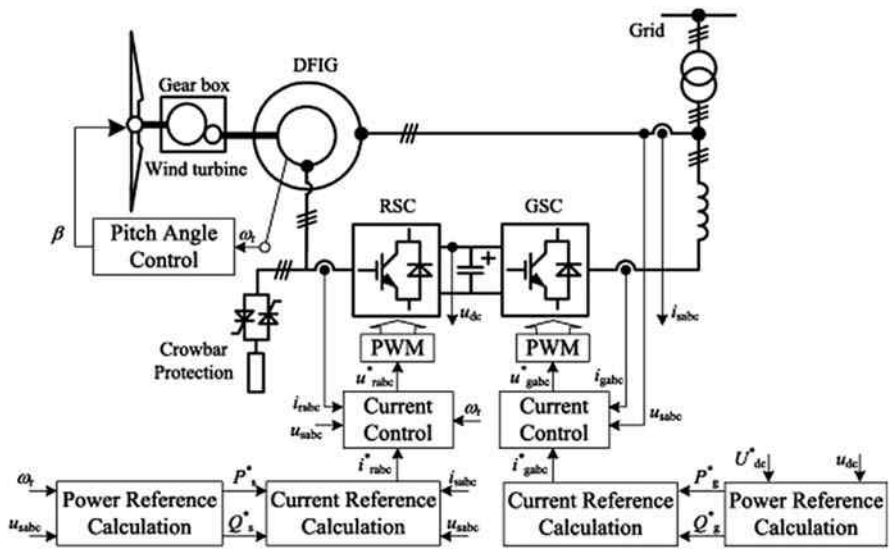


FIGURE 14.5

The schematic control structure of a DFIG.

From Niancheng Zhou, Fangqing Sun, Qianggang Wang, Xiaoxiao Meng, A flexible power control strategy for rotor-side converter of DFIG under unbalanced grid voltage sags, International Journal of Electrical Power & Energy Systems, Volume 90, September 2017, Pages 64–75

The PWM converter rotor side operates to control the active and reactive power of the stator side. The active power reference for the side of the stator is obtained from a look-up table at a given rotor speed of the generator. This gives the optimal power tracking for maximum energy capture from the wind.

The crowbar is used for protecting the rotor and grid converter of DFIG from the high current faults. Because during a fault, the windings of rotor are short-circuited by a group of resistors, the current of short circuit will flow through this crowbar only rather than the converter. The crowbar can be done by adding a group of resistors to the windings of rotor using bidirectional thyristors [9].

When the crowbar is connected, different actions could be done as follows. The First, the wind turbine conversion system and the grid converter can be disconnected from the grid (islanding mode) [10]. The wind turbine is possible to be in operation and the converter will disconnect from the rotor, which is the second action. In this case, the generator operates like an induction machine with rotor resistance. The third action is the whole wind turbine is kept connected to the grid. So, the wind turbine can be restored to the normal operation immediately after clearing the fault. The wind turbine can also support the grid during the dip. Even this dip lasts for a longer time as mentioned in the grid code [15].

3. ISSUES OF INTEGRATING WIND ENERGY INTO THE GRID: AN OVERVIEW

The fluctuation and changeable features of wind energy have a severe impact on the grid performance. So, nowadays, the grid codes reflect the issues of high penetration of wind energy connected to the power grid, and they just apply some basic issues for the wind turbines. More advanced grid interconnection features will be applied for large-scale wind farm also [11].

The influence of wind turbine integration on power systems and the advanced solutions of realizing a smart operation and power quality for the power systems are discussed with the following issues:

- Active power balance
- The fluctuation and quality of voltage

Active power balance and the penetration scales of wind power are increasing. Consider Denmark as an example. The average penetration levels are 20%−30% through peak value of penetration level up to 100% of the system load. The production of wind farms fluctuates with the wind speed; meanwhile, the electrical grid must sustain a balance between the supply and the demand. The effects of fluctuating wind power on the stability of power system and quality are vital issues. Active power balance issue can be realized by several methods [12], as follows:

- Enhancement of the wind speed forecast

- Provision of regulating and reserve power from the large-scale wind farms and other generation units (main power station and combined heat and power units).
- Management of consumers loads
- Storage energy technologies

The storage system can be organized locally for each wind turbine unit and centrally for several wind turbines. The storage energy systems could be like a battery, supercapacitor, flywheel, or even combined energy storage systems. This depends on the cost and the needed amount of energy and control dynamics.

- Formation of proper power exchange agreements to utilize the regulating power control in neighboring power systems.

3.1 ISSUE OF VOLTAGE REGULATION AND POWER QUALITY

The principal source of voltage instability in the network is the reactive power; it also increases the power losses. WECS is equipped with induction generators that consume reactive power at no load, the consumption of reactive power is roughly 35%−40% of the rated active power and increases to about 60% at the rated power.

In the normal operational mode, the voltage quality of a wind turbine or a wind farm can be evaluated using the following parameters [13]:

The voltage at steady state, where the voltage at the point of common coupling (PCC) should be maintained within its limits for the continuous production of power.

Voltage flickers (during operation and due to switching)

Fluctuations in the voltage system (more exactly in its root mean square (RMS) value) may cause observable light flicker. It depends on the magnitude and frequency of the fluctuation. In this case, the type of disturbance is called voltage flicker. The flicker emissions related to wind turbines have two types. The first type is the flicker emission during continuous operation and the second type is because of generator and capacitor switching. Frequently, one or the other will be prime. The permissible flicker limits are determined by individual utilities.

The rapid variations in the wind power output during generator switching and capacitor switching produce the variations in the RMS value of the voltage also. At a defined rate and magnitude, the variations cause flickering of the electric light.

To prevent flicker emission from damaging the voltage quality, the operation units should not cause excessive voltage flicker. International Electrotechnical Commission 61000-4-15 appropriates a flicker meter that can measure the flicker directly [11].

3.1.1 Low-Voltage Ride-Through Capability

Low-Voltage Ride-through Capability (LVRT) is the ability of wind generators to remain in service during a voltage dip caused by a fault. The Transmission System Operators (TSOs) assess some strict requirements on the wind parks, for comprising the reactive power control and ride-through capability.

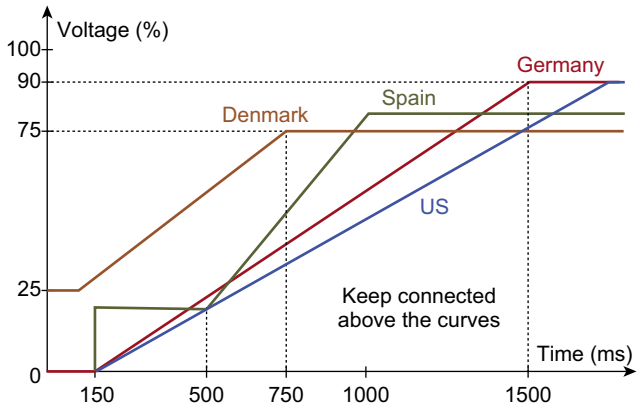


FIGURE 14.6

Voltage profile for LVRT capability of the wind turbines [14].

Adapted from https://www.hindawi.com/journals/ijp/2013/257487/#B2

In most countries, the TSOs have issued strict grid supporting for the wind farm under grid faults. As shown in Fig. 14.6 [14], the boundaries with various grid voltage dip amplitudes and the proper disturbing time are set for a wind farm. The wind farm should also provide reactive power (up to 100% current capacity) to participate in the voltage recovery at grid voltage sag disturbance. Fig. 14.7 illustrates the amount of reactive current required versus the grid voltage amplitude by the German and Danish grid codes [15]. So, STATCOM is widely used in wind farm application to support the strict requirements of grid code.

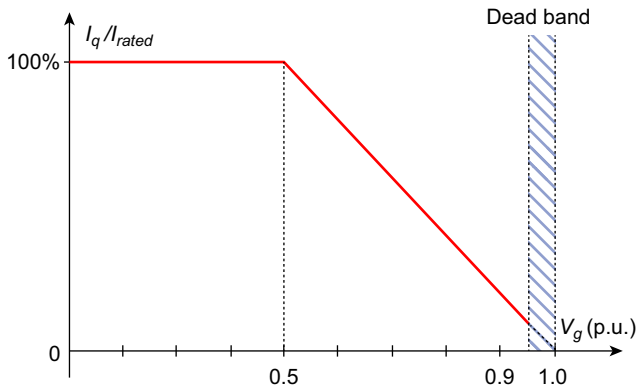


FIGURE 14.7

The requirements of reactive current for a wind farm during grid sags by the German and Danish grid codes [15].

From Yongheng Yang, Wenjie Chen Frede Blaabjerg, Advanced Control of Photovoltaic and Wind Turbines Power Systems, Advanced and Intelligent Control in Power Electronics and Drives pp 41–89"

4. DIFFERENT FACTS SCHEMES AND APPLICATIONS

The FACTS devices have been used during the last 3 decades and provide better utilization of existing systems. FACTS are used to control the transmission line power flow, voltage control, transient stability improvement, and oscillation damping as shown in Table 14.1. FACTS are divided into three types (series, shunt, combined devices). Table 14.1 also shows a comparison between several types of FACTS devices at each problem as shown in the figure.

4.1 FACTS APPLICATIONS

FACTS has been the focal device in power system, because of the applicability to enhance the stability of power system voltage, angle, and frequency stability. More studies have discussed the performance of STATCOM for improving the voltage stability and for integrating the wind farm into the grid.

Many studies based on distribution FACTS and control devices have been applied to enhance the problems of power quality in the distribution system. These problems are voltage dips, harmonics, unbalance reactive power compensation, etc. The control devices custom is DSTATCOM, UPFC, and DVR [16].

A microgrid is a form of a grid that is integrated with a variety of distributed generation technology and power electronics technology. It consists of microsources and hybrid loads with storage energy devices. As an autonomous entity, the micro-grid has two modes of operation islanded and parallel operation [17].

At present, the microsources in the microgrid mainly comprise solar energy, biomass energy, wind energy, and so on. They are connected to the microgrid by advanced power converter units. However, these power converter units have a high degree of flexibility, although it brings some hidden dangers to the system stability because of its low inertia [18].

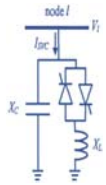
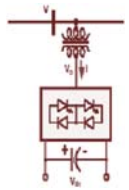
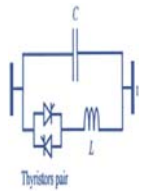
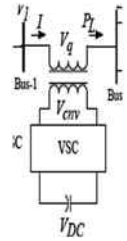
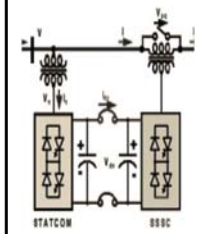
Obviously, novel D-FACTS devices are connected to AC/DC buses as a dynamic compensator. Modulated power filter compensators are demonstrated as AC-side FACTS devices, which are used for stabilization of the voltage buses, improving the power factor, and mitigating the harmonic distortion. In addition, a green plug filter compensator is presented as DC-side FACTS devices, where it is connected to DC buses [19].

5. WIND ENERGY IN EGYPT

The most promising sites in Egypt for wind energy area is Zafarana. which lies on the east coast of Red Sea zone. In addition, it is characterized by a high wind speed of average 10 m/s at 40 m above the ground level, low turbulence, flat area, and high capacity factor. It is planned to implement 3000 MW by 2022 [20].

In this study, Vestas (V47) wind farm is investigated, which is located at the Zafarana site at 6.5 km distance from a 220-kV substation, which is presented as

Table 14.1 Different FACTS Applications

FACTS Devices					
Connection Type	**Shunt**		**Series**		**Combined**
Technology	**Traditional/Advanced**		**Traditional/Advanced**		**Advanced FACTS**
Device **Problem**	**SVC (TSR)**	**STATCOM** **D-STATCOM**	**TCSC** **TSSC**	**SSSC (DVR)**	**UPFC**
Voltage control steady state	**	**	***	**	***
Voltage control dynamic	**	**	***	**	***
Phase balancing steady state	**	**	*	*	***
Transient stability	***	**	**	*	**
Power flow steady state	***	***	**	**	**
Circuit diagram					

*, *low influence*; **, *medium influence*; ***, *strong influence*.
D-STATCOM, *distributed STATCOM*; DVR, *dynamic voltage restorer*; SSSC, *static synchronous series capacitor*; STATCOM, *static synchronous compensators*; SVC, *static var compensator*; TCR, *thyristor controlled reactor*; UPFC, *unified power flow controller*.

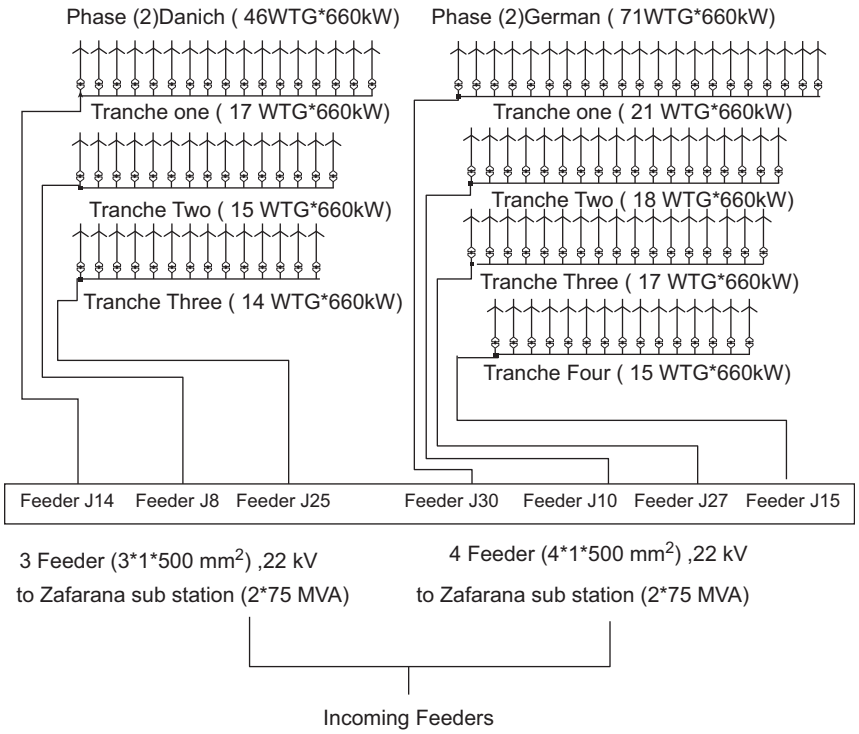


FIGURE 14.8

Schematic diagram of Zafarana wind farm.

the PCC. The total capacity of the wind farm is 77.22 MW as shown in Fig. 14.8. It consists of 117 wind induction generators. Each unit includes a 660-kW wind turbine, an induction generator with fixed capacitor 250 kVAr and a step-up transformer. This transformer is used to step up the voltage from the standard level of wind turbine generators at 690 V to the level of collector bus at 22 kV.

6. WIND FARM MODELING

In this chapter, the dynamic modeling of fixed-speed WECS (pitch control) is presented. A voltage source converter with sinusoidal pulse width modulation (SPWM) technique based on STATCOM is modeled and analyzed. Vector control of STATCOM is used to stabilize grid connection of wind turbines under variable wind speed and three-phase fault disturbance. MATLAB®/SIMULINK is used to validate the proposed model of a wind farm with STATCOM as shown in the Fig. 14.9. The proposed system data in Appendix section.

As a result, the system is large and needs a long time to simulate with the network, aggregation model is used to simulate three-feeders only.

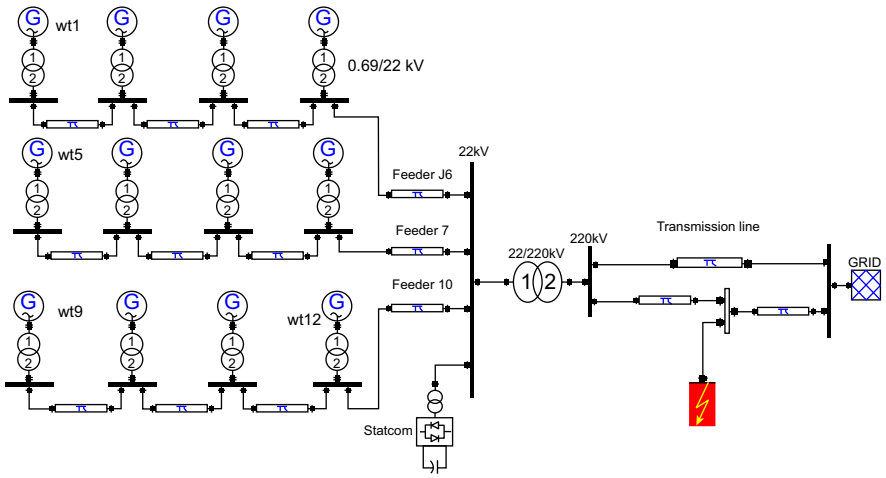


FIGURE 14.9

Schematic diagram of the proposed system.

6.1 WIND TURBINE MODELING

Normally, a simplified modeling of the wind turbine rotor is used when the electrical performance of the system is the main point. The numerical relation between wind speed and mechanical power extracted is calculated from the following equation:

$$P_{\mathrm{m}} = 0.5\rho A C_{\mathrm{p}} V^3 \tag{14.1}$$

where ρ, the density of air mass; V_{w}, wind speed; A, rotor swept area; C_{p}, a power coefficient that representing the percentage of the extracted power from the aerodynamic power in the wind by a practical wind turbine.

The power coefficient C_{p} value is calculated from nonlinear function [21].

$$C_{\mathrm{p}} = 0.22\left(\frac{116}{\lambda_{\mathrm{i}}} - 0.4\beta - 5\right)\mathrm{e}^{\frac{-12.5}{\lambda_{\mathrm{i}}}} \tag{14.2}$$

with

$$\frac{1}{\lambda_{\mathrm{i}}} = \frac{1}{\lambda + 0.08\beta} - \frac{0.035}{1 + \beta^3} \tag{14.3}$$

where β is pitch angle and λ is tip speed ratio and defined as:

$$\lambda = r_{\mathrm{m}}\omega_{\mathrm{m}}/\nu \tag{14.4}$$

where r_{m} is the maximum radius of the rotating wind turbine in m, ω_{m} is the mechanical angular velocity of the turbine in rad/s, and ν is the wind speed in m/s.

The angular velocity ω_{m} is obtained from the rotational speed n by the equation:

$$\omega_{\mathrm{m}} = 2\pi n/60 \tag{14.5}$$

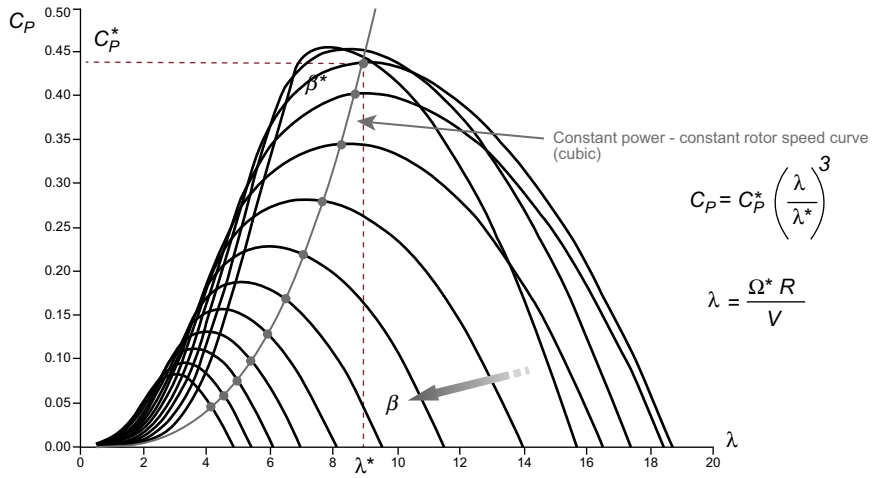


FIGURE 14.10

Power coefficient versus tip speed ratio for different values of pitch angle [4].

The variation of C_p with λ is shown in Fig. 14.10.

The model of wind speed contains a source that generates the signal of wind speed to be applied to the wind turbine. This signal consists of four components, that is, the wind speed mean, a ramp wind speed, a wind gust, and turbulence [22].

The wind gust is characterized by three parameters as demonstrated below:

- The amplitude of wind gust A_g [m/s].
- Time start of the wind gust T_{sg} [s].
- End time of the wind gust T_{eg} [s].

The following equations are provided for wind gust model [22]:

$$Vwg = \begin{cases} 0 & t \ll T_{sg} \\ A_g\left(1 - \cos(2 * \Pi * (t - T_{sg})/D_g\right) & T_{eg} \leq t \geq T_{sg} \\ 0 & t \gg T_{eg} \end{cases} \tag{14.6}$$

where D_g is the time duration of the wind gust [s], which equals to $(T_{eg} - T_{sg})$.

MATLAB/SIMULINK program supports composite wind model that considers the wind as composed of four parts as follows:

$$vw(t) = vwa + vwr(t) + vwg(t) + vwt(t) \tag{14.7}$$

where *vwa* is first wind speed, *vwr* is ramp component of wind speed, *vwg* is gust component of wind speed, and *vwt* is wind speed turbulence. Fig. 14.11 shows the wind speed distribution.

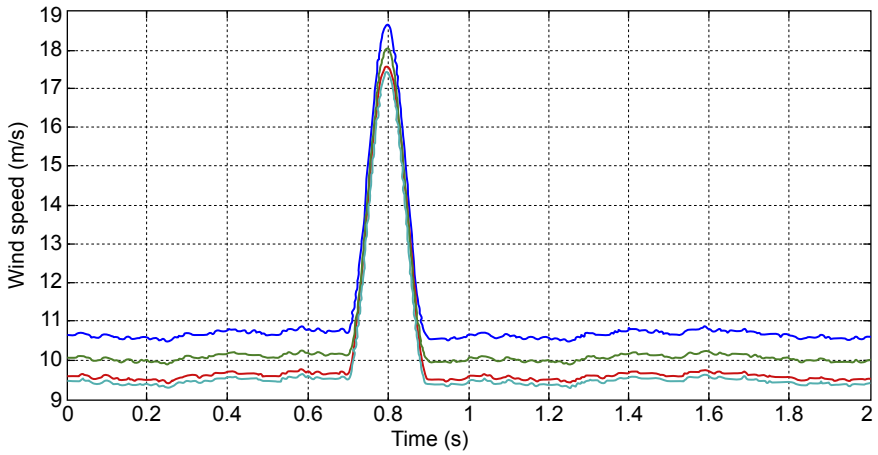


FIGURE 14.11

Wind speed distribution (composite model).

6.2 MODELING OF SELF-EXCITED INDUCTION GENERATOR

SimPower Systems blocks are used to model the Self-Excited Induction Generator (SEIG) (squirrel cage). The aggregation model is studied to simulate three feeders with each feeder having 16 turbines. WECS is simulated as shown in Fig. 14.12 where the wind turbine is connected to SEIG, a three-phase capacitor bank is

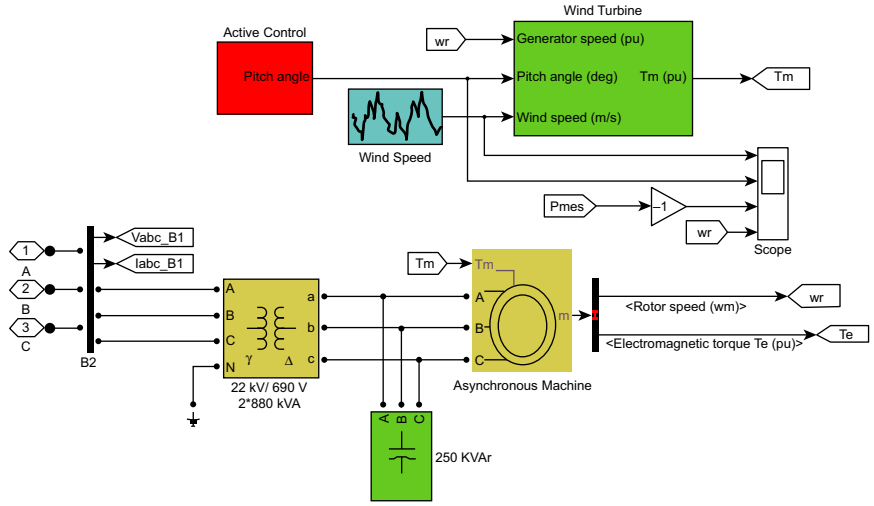


FIGURE 14.12

Simulation diagram of WECS using MATLAB/SIMULINK.

connected to the stator terminal of induction generator, and the step-up transformer is connected to step up the voltage from the standard level of wind turbine generators at 690 V to the level of collector bus at 22 kV.

6.3 STATIC SYNCHRONOUS COMPENSATOR MODELING

The power circuit of three-level inverter STATCOM is demonstrated in Fig. 14.13. In this arrangement, a three-level inverter refers to the negative and positive voltage levels including zero. These appear in the output line voltage of inverter; thus, two capacitors are connected to the dc side. The inverter is connected to the supply system through a transformer.

STATCOM operates in two modes—capacitive and inductive mode—that depends on the voltage level at the bus coupling. In other words, when Vsa is greater than Ea1 (a fundamental component of the inverter output), STATCOM absorbs reactive power (inductive mode), and when Vsa is lower than Ea1, STATCOM generates reactive power (capacitive mode).

Mathematical models of STATCOM can be described according to the study by Jayam et al. [23] with the assumption that harmonic components are negligible. The switching function S can be represented as follows:

$$S_{a,b,c} = \sqrt{\frac{2}{3}}\ m \begin{bmatrix} \sin(wt+\alpha) \\ \sin\left(wt-\frac{2\pi}{3}+\alpha\right) \\ \sin\left(wt+\frac{2\pi}{3}+\alpha\right) \end{bmatrix} \tag{14.8}$$

where, m is modulation index $m = \frac{E_{O,peak}}{U_{dc}}$ and α is the phase angle which indicates the phase difference between the voltage source and the output voltage of the inverter.

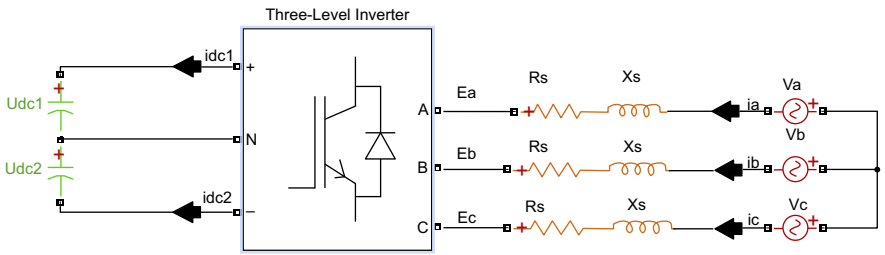


FIGURE 14.13

Power circuit of the three-level inverter.

As for the output voltage of the inverter, the DC voltage side can be expressed as follows:

The voltage inverter is described as follows:

$$E_{\mathrm{O,abc}} = SU_{\mathrm{dc}} \tag{14.9}$$

$$I_{\mathrm{dc}} = S^T I_{\mathrm{abc}} \tag{14.10}$$

$$\begin{bmatrix} E_{\mathrm{oa}}(t) \\ E_{\mathrm{ob}}(t) \\ E_{\mathrm{oc}}(t) \end{bmatrix} = \frac{1}{3}\begin{bmatrix} 2 & -1 & -1 \\ -1 & 2 & -1 \\ -1 & -1 & 2 \end{bmatrix}\left\{ \begin{bmatrix} S_{11}\cdot S_{11} \\ S_{21}\cdot S_{22} \\ S_{31}\cdot S_{32} \end{bmatrix} U_{\mathrm{dc1}} - \begin{bmatrix} S_{13}\cdot S_{14} \\ S_{23}\cdot S_{24} \\ S_{33}\cdot S_{34} \end{bmatrix} U_{\mathrm{dc2}} \right\} \tag{14.11}$$

with S_{kI} connection function, referring to the switch state, $S_{kI} = 1$ if the switch is closed and 0 in open switch. K: number of the arms (k = 1, 2, 3). I: number of the switches for the arm ($I = 1, 2, 3, 4$).

To summarize, the switching state and the operating device shown in the following table is used.

$$S_{\mathrm{a}} = \left\{ \begin{array}{ll} 1 & \{\text{if} \quad S_{11} \text{ and } S_{12} \text{ are ON}\} \\ 0 & \{\text{if} \quad S_{12} \text{ and } D(0-a) \text{ or } S_{13} \text{ and } D(0-a') \text{ are ON}\} \\ -1 & \{\text{if} \quad S_{13} \text{ and } S_{14} \text{ are ON}\} \end{array} \right\} \tag{14.12}$$

- The DC voltage side is modeled by

$$\begin{bmatrix} \dfrac{\mathrm{d}U_{\mathrm{dc1}}}{\mathrm{d}t} \\ \dfrac{\mathrm{d}U_{\mathrm{dc2}}}{\mathrm{d}t} \end{bmatrix} = \frac{1}{C}\begin{bmatrix} i_{\mathrm{dc1}} \\ -i_{\mathrm{dc2}} \end{bmatrix} \tag{14.13}$$

$$i_{\mathrm{dc1}} = S_{11}\cdot S_{12} i_{\mathrm{a}} + S_{21}\cdot S_{22} i_{\mathrm{b}} + S_{31}\cdot S_{32} i_{\mathrm{c}} \tag{14.14}$$

$$i_{\mathrm{dc2}} = S_{13}\cdot S_{14} i_{\mathrm{a}} + S_{23}\cdot S_{24} i_{\mathrm{b}} + S_{33}\cdot S_{34} i_{\mathrm{c}} \tag{14.15}$$

ABC equations are converted to d−q frame. As a result, the d−q frame is simple to study the analysis and the decouple control using Park's transformation. The full model equation can be summarized in the d−q frame as follows:

$$\begin{bmatrix} \dfrac{\mathrm{d}i_{\mathrm{d}}}{\mathrm{d}t} \\ \dfrac{\mathrm{d}i_q}{\mathrm{d}t} \\ \dfrac{\mathrm{d}U_{\mathrm{dc}}}{\mathrm{d}t} \end{bmatrix} = \begin{bmatrix} \dfrac{-R_{\mathrm{s}}}{L_{\mathrm{s}}} & w \\ -w & \dfrac{-R_{\mathrm{s}}}{L_{\mathrm{s}}} \\ \dfrac{E_{\mathrm{Od}}}{2C} & \dfrac{E_{\mathrm{Oq}}}{2C} \end{bmatrix}\begin{bmatrix} i_{\mathrm{d}} \\ i_{\mathrm{q}} \\ 0 \end{bmatrix} + \frac{1}{L_{\mathrm{s}}}\begin{bmatrix} E_{\mathrm{Od}} - V_{\mathrm{sd}} \\ E_{\mathrm{Oq}} - V_{\mathrm{sq}} \\ 0 \end{bmatrix} \tag{14.16}$$

Furthermore, reactive and active power of STATCOM at bus inverter can be calculated as

$$P = \frac{3\,E_a\,V_s}{X}\sin(\alpha) \tag{14.17}$$

$$Q = \frac{3\,V_s}{X}(E_a\cos(\alpha) - V_s) \tag{14.18}$$

6.4 PROPOSED CONTROLLER DESIGN

6.4.1 Modeling of the Pitch Angle Controller

From Eqs. (14.2) and (14.3), it can be summarized that the optimal pitch angle equals zero below the nominal wind speed and increases gradually when the wind speed increases above nominal rate. This observation greatly simplifies pitch control.

Moreover, the pitch angle cannot change instantly, but only at a limited rate, which may be quite low because of the size of the rotor blades of modern wind turbines and also protects the blade drives from rapid mechanical actions. The change rate of the pitch angle has a maximum range from 3 to 10/s, depending on the wind turbine size. Furthermore, because the blade pitch angle can only change slowly, the pitch angle controller operates with a sampling frequency, which is in the range of 1−3 Hz. In Fig. 14.14, the pitch angle controller is depicted.

Hence, using this controller type (Proportional and Integral controller) PI, the rotor speed can increase up to its nominal value by 20%, depending on the wind turbine size. However, a proportional controller is used, because

- A insignificant overspeeding of the rotor above its nominal value can be allowed and poses no problems for the construction of wind turbine;
- Because of the varying wind speed, the system is not ever in the steady state, so that the advantage of an integral controller to obtain zero steady-state error is not appropriate [22].

6.4.2 Modeling of the Reactive Power Controller

This controller regulates the voltage bus at the wind farm PCC under various disturbances. The exchange of reactive power between STATCOM and ac system can be

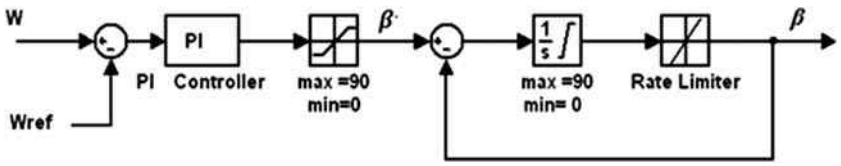


FIGURE 14.14

Pitch angle controller.

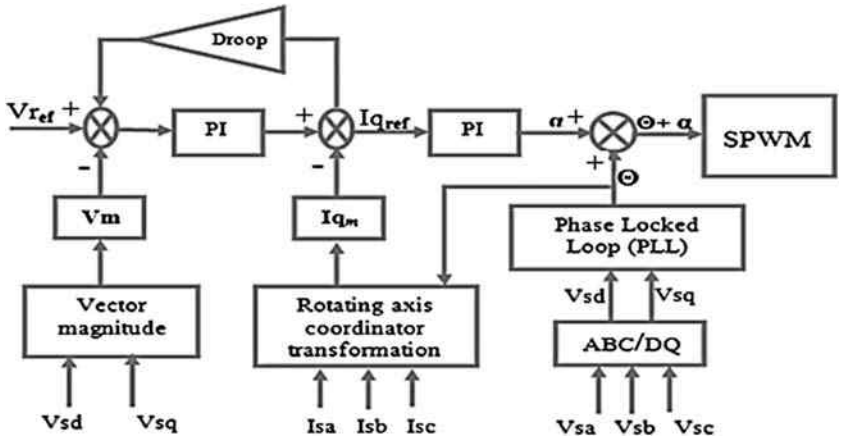


FIGURE 14.15

Schematic diagram of the proposed controller.

controlled by the phase angle α. The reactive and active power requirements are calculated using Eqs. (14.15) and (14.16).

The goals in the controller design process include both transient excursion suppression and proper regulations in steady-state operation. Fig. 14.15 presents the structure of the proposed controller in detail.

This circuit consists of the transformation of the measured three-phase voltage and current of the PCC bus to the d−q frame. It gives the voltage and current in the d−q frame. The vector of measured voltage is required to get the amount of current, which is compared with the measured current to find the required angle control α. The phase difference angle α (the output of PI controller) is added to the phase angle Θ that is the voltage bus of the PCC and is calculated from the Phase-Locked Loop.

SPWM technique is used for the generation of switching pulses of the three-level inverter with modulation index 1.01 and frequency carrier ratio 21.

6.5 SIMULATION RESULTS

Simulation is carried out to investigate the performance of WECS with STATCOM at variable wind speed and a three-phase to ground short-circuit fault. Results of Digital Simulation are carried out using the MATLAB/SIMULINK Software Environment.

6.5.1 Variable Wind Speed

This section shows the main results of the models described at variable wind speed. Where the mean wind speed is changed from 9.5 to 11 m/s at start followed by wind gust starting at $t = 2$ s and ending after 10 cycles, it has a peak value=16 m/s, as shown in Fig. 14.16.

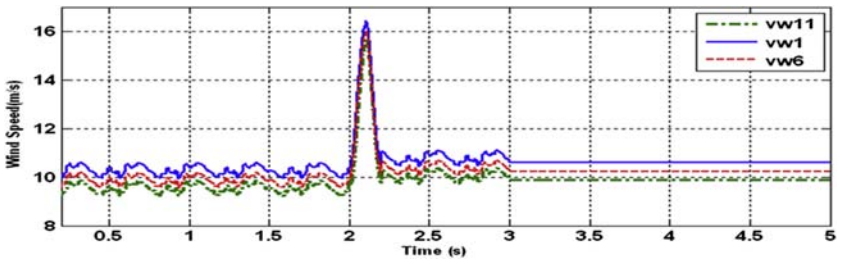


FIGURE 14.16

Wind speed for wt1, wt6, and wt11.

The value of wind speed is changed from feeder to another because of the shadow effect of the tower. It is obvious that the rotor would accelerate because of the rising mechanical power caused by increasing wind speed. The wind-sensor less output feedback controller generated a pitch angle command as soon as the wind speed began to increase as illustrated in Figs. 14.17 and 14.18. Also, the increased output power of wind turbine1 converted from aerodynamic power after gust was another benefit of the controller. Increasing power leads to increase in reactive power, as illustrated in Fig. 14.19 to support the voltage at the PCC at this disturbance.

6.5.2 Three-Phase Fault

Three-phase to ground short-circuit fault is applied to the system at the midpoint of the transmission lines. The fault starts at 0.9 s and tripped after 100 ms. The three-phase fault is the worst disturbance event to the generation system because it causes shutdown station in case a voltage recovery became unstable, and the rotor speed accelerates. Thus, the ability of generation system to be stable after tripping faults depends on the reactive power requirement of the system. STATCOM has a robust

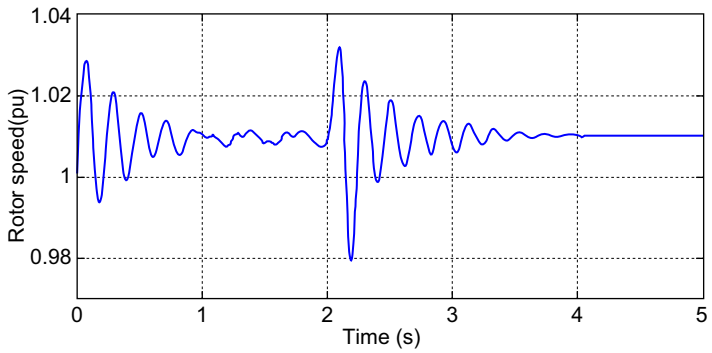


FIGURE 14.17

Rotor speed of wind turbine 1.

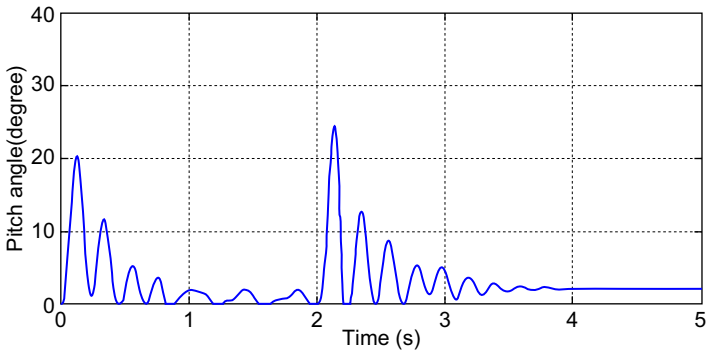


FIGURE 14.18

Pitch angle for wind turbine 1.

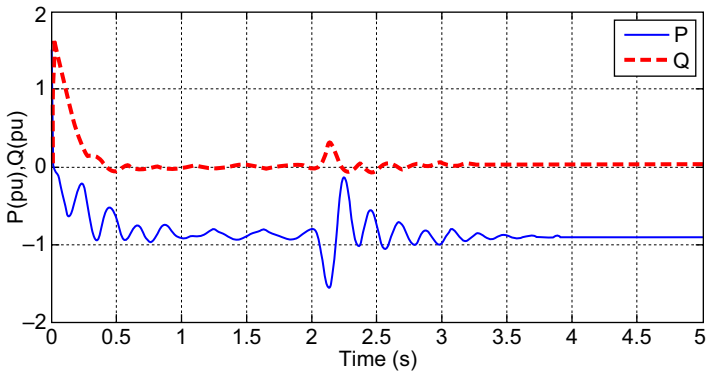


FIGURE 14.19

Active and reactive power for wind turbine 1.

control of reactive power as presented in Fig. 14.20B, where the voltage at PCC is more stable. The rotor speed has less acceleration and is damping for all wind turbines, as presented in Fig. 14.20A and the electrical torque of induction generator also as figured out in Fig. 14.20B.

Figs. 14.21 and 14.22 illustrate the response of active and reactive power at PCC during a fault. Active power reduces to zero power almost, and after clearing fault, it also reduces as a result of the acceleration of the wind turbine speed. Moreover, it causes overspeed, which leads to disconnect in the wind farm to overspeed case. With respect to reactive power at the PCC point, before fault, it has almost zero value. After clearing the fault, the system has drawn 0.6 PU to recover voltage because of the acceleration of the rotor speed. STATCOM helps the active power to be stable and generate active power after clearing fault at zero reactive power at PCC.

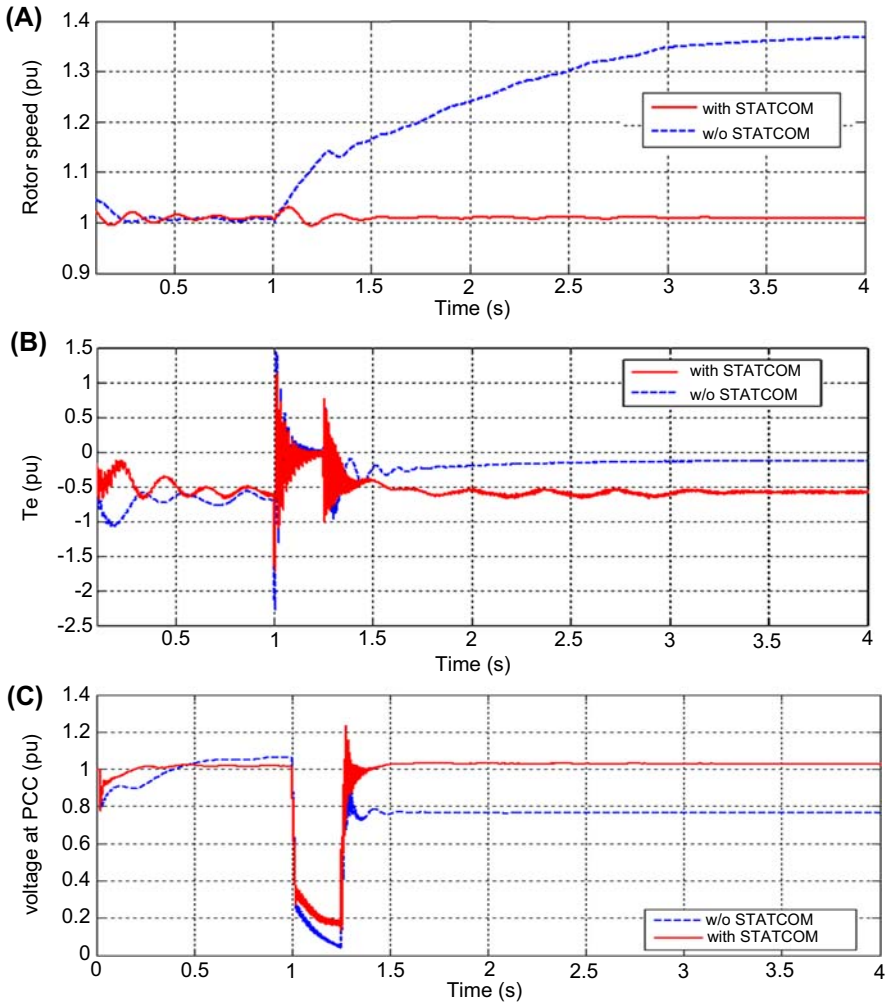


FIGURE 14.20

The behavior of wind farm at low-voltage ride-through. (A) Rotor speed for wt1, (B) electrical torque for wt1, and (C) the voltage at PCC.

The current control of STATCOM is presented in Fig. 14.23A and B. These figures show that the reference current is required to define the amount of injection current to the system at the disturbance. The phase angle between the PCC voltage bus and inverter voltage bus is positive (leading mode/capacitive mode) because the PCC voltage is less than the STATCOM voltage. The voltage at dc link is dropped at this mode as shown in Fig. 14.23C because the reactive power flows

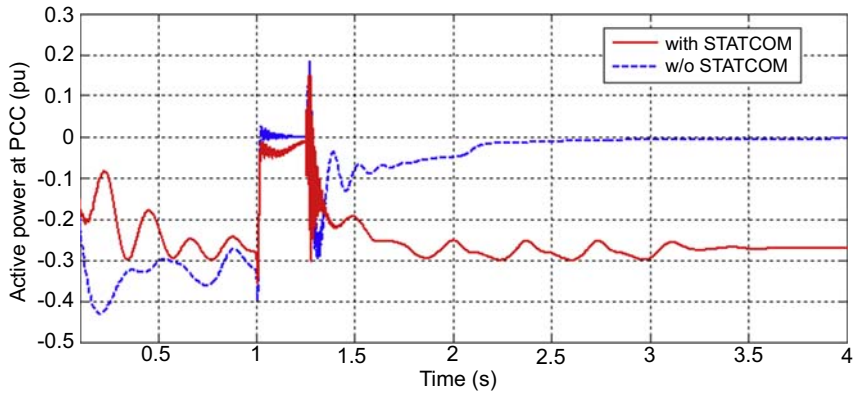


FIGURE 14.21

Active power at PCC.

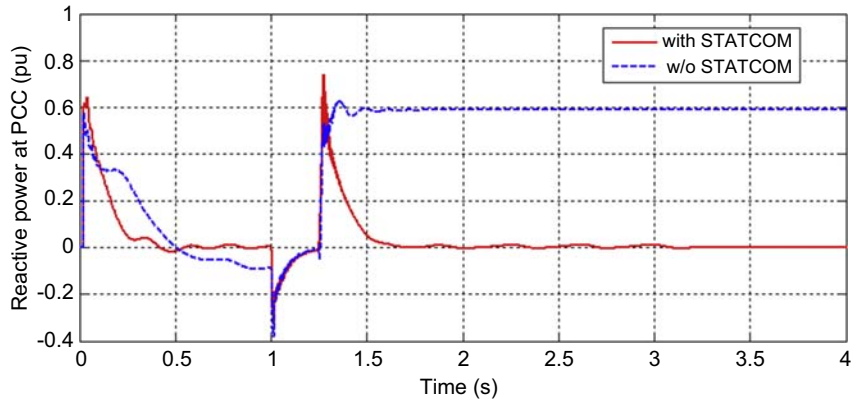


FIGURE 14.22

Reactive power at PCC.

from dc side to ac side (inverter mode). The active power and generated reactive power of STATCOM are presented in Fig. 14.23D. STATCOM operates as a reactive power source (capacitive), to recover the PCC voltage to maintain the stability of the wind energy system.

6.5.3 Voltage Sag With Severe Wind Speed Variation

In this case, voltage sag is applied to voltage grid with ±10% starting at 1.5 s at ending after five cycles. As shown in Fig. 14.24A, when the voltage grid raised up to 10% of rated value, the increase in the voltage at PCC of wind farm occurred because of the increase of reactive power. Without STATCOM, the voltage at PCC

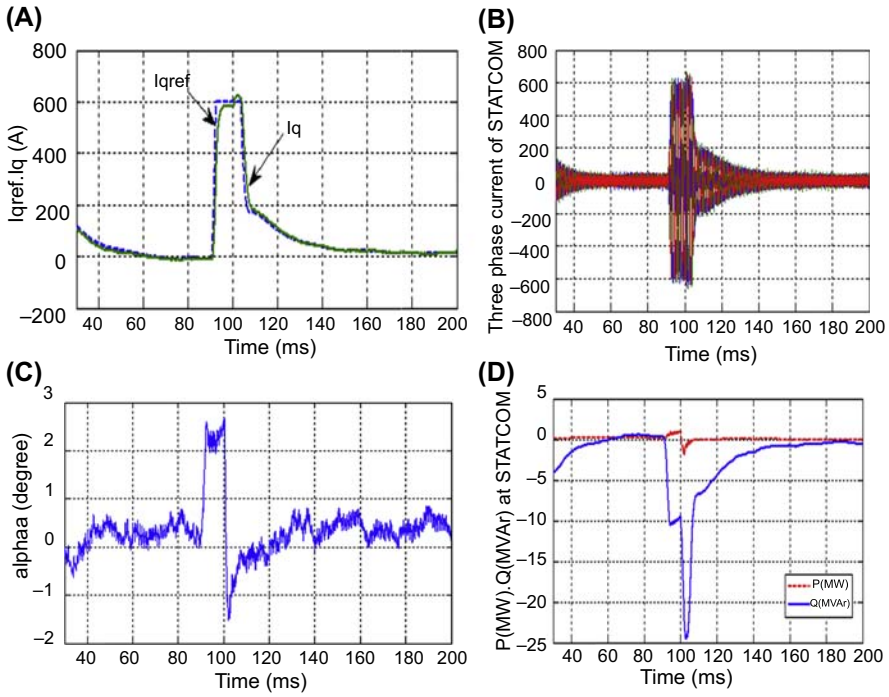


FIGURE 14.23

STATCOM variables. (A) STATCOM current Iqref, Iq, (B) three-phase STATCOM current, (C) variation of alpha (degree) and (D) reactive and active power of STATCOM.

goes to overvoltage, and in this event, the bus voltage will go outage. Meanwhile, when the STATCOM is connected to the PCC bus, STATCOM operates as an inductive source and absorbs the extra reactive power to keep the voltage at PCC within its limit and stable. A similarly, when the grid voltage drops to 10%, the PCC voltage drops to 0.9 PU and it is a critical value. STATCOM enhances the voltage regulation of the wind farm PCC by supporting the required reactive power (capacitive mode).

The variables of the reactive power controller of the STATCOM are illustrated in Fig. 14.25 during this disturbance. According to the reference current control, STATCOM operates in two modes—inductive and capacitive mode—to enhance the voltage of wind farm at PCC and to maintain it more stable.

To check the viability of the pitch controller, the variable wind speed with ±50% is applied to the system. When the wind speed increases to 14 m/s, the pitch angle controller operates to limit the excessive power by increasing the pitch angle as demonstrated in Fig. 14.26B. Similarly, if the wind speed is below the rated wind speed of the turbine, the pitch angle is decreased to zero angle and the developed power from a wind turbine is almost zero as shown in Fig. 14.26C and in this case, the generator operates as an induction motor.

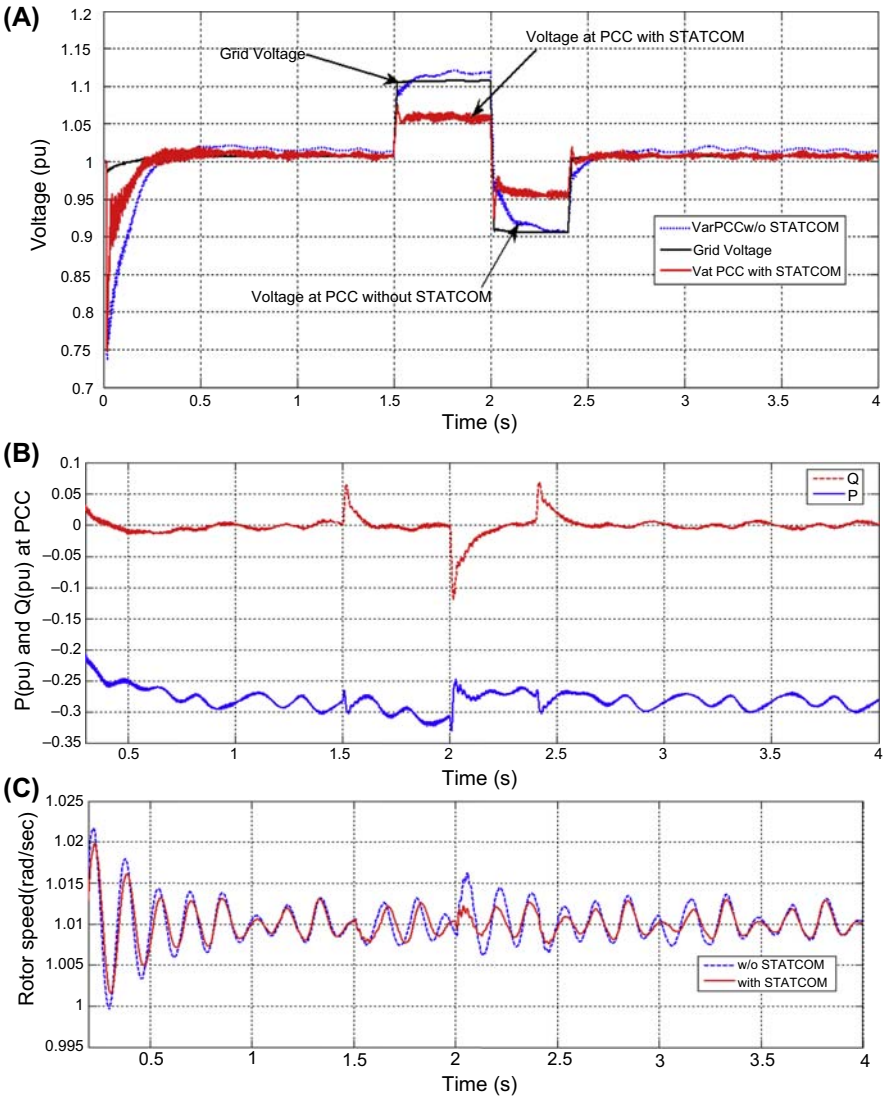


FIGURE 14.24

Voltage sag at grid side starting at 1.5 s and lasting at 2.5 s. (A) The voltage at PCC, (B) active and reactive power at PCC, and (C) rotor speed for wt1.

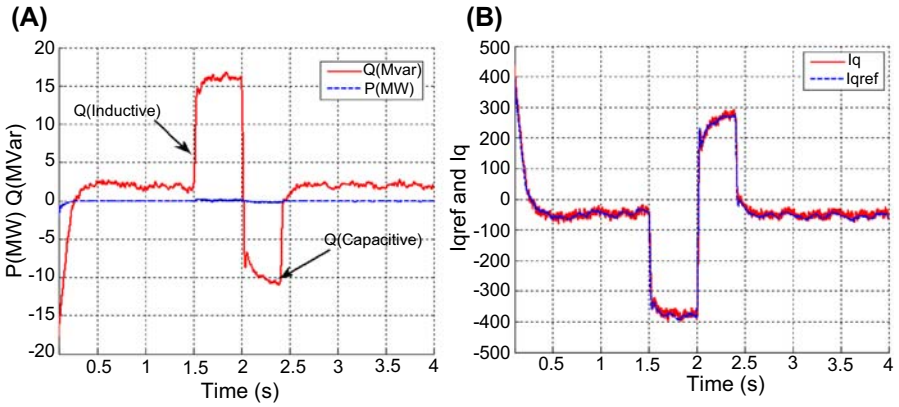


FIGURE 14.25

STATCOM parameters at grid voltage sag. (A) Reactive power for STATCOM and (B) Iqref and Iq variables.

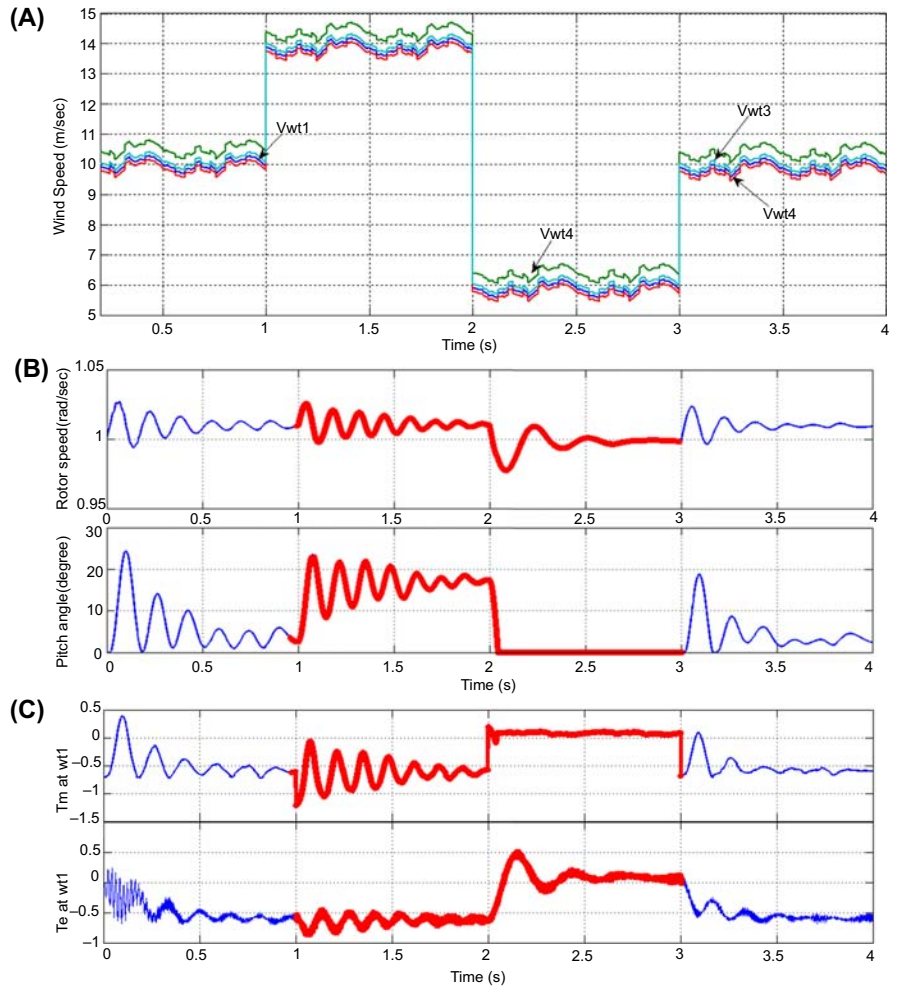


FIGURE 14.26

The behavior of wind farm at various of wind speeds for all turbines. (A) Wind speed for wt1, wt2, wt3, and wt4. (B) Rotor speed for wt1 and Pitch angle at wt1. (C) Mechanical torque and electrical torque T_m, T_e. (D) Reactive and active and power at PCC. (E) Wind farm voltage at PCC.

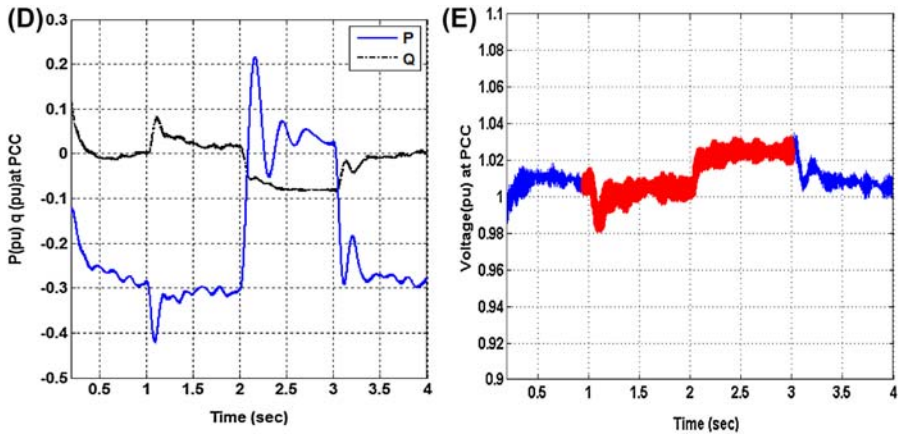


FIGURE 14.26

continued

7. CONCLUSIONS

Integration of large-scale wind power into power systems presents many new challenges. WECS are required to have an excellent controllability like the conventional power stations. This chapter analyzed the detailed model of the wind farm, in addition to studying the effect of the STATCOM on the fault ride-through capability of the fixed−wind speed turbines. First, the steady-state models of the wind farm, including the STATCOM model as a reactive power source and pitch angle control, were developed. Then, the effect of the STATCOM on the stability of the Squirrel Cage Induction Generator (SCIG) was investigated by MATLAB/SIMULINK at the fault ride-through. A STATCOM control system has been successfully designed to stabilize the voltage bus and the ability of wind farm to be in operation at the fault ride-through.

APPENDIX

Wind Turbine Data	
Rotor diameter	47 m
Nominal wind speed	11 m/s
Gear box ratio	52.6514
Generator Data	
Rated power	660 kW
Rated voltage	690 V

Rated frequency	50 Hz
Resistance of stator	0.0092 Ω
Inductance of stator	0.1686 H
Resistance of rotor	0.0121 Ω
Inductance of rotor	0.1446 H
Mutual inductance	5.6863 H
Inertia of rotor generator	18.03 kg s
Poles pairs number	2
LV/MV transformers	880 kVA, 0.69/22 kV, 690V
MV/HV transformer	75 MVA, 22/220 kV
Underground cables wind turbines impedance (Ω/km)	$0.325 + 0.121j$
The length of the feeder	650 m
Impedance of feeder	$0.08 + 0.102j$ (Ω/km)
Transmission line	$0.01273 + 0.293\,j$ (Ω/km)
SATCOM Data	
Resistance of transformer	0.1128 Ω
Reactance of transformer	2.0973 Ω
DC-link capacitance	2500 μF
Controller Parameters	
For STATCOM	
Proportional gain (kp)	0.099
Integral time constant	0.495 s
For Wind Turbine	
Proportional gain (kp)	840
Integral time constant	0.0067

REFERENCES

[1] GWEC, Global wind report 2015 | GWEC, Wind Energy Technology (2016) [Online]. Available: http://www.gwec.net/global-figures/wind-energy-global-status/.

[2] A.M. Sharaf, F.H. Gandoman, FACTS based stabilization for smart grid applications, Int. J. Electr. Comput. Electron. Commun. Eng. 4 (2014) 1726−1730.

[3] E. Muljadi, C.P. Butterfield, J. Chacon, H. Romanowitz, Power Quality Aspects in a Wind Power Plant Preprint Power Quality Aspects in a Wind Power Plant, 2006.

[4] E.B.H.YOUSSEF, Performance Optimization of Wind Generators Connected to the Grid, Helwan university, Engineering Faculty, 2011.

[5] Y. Amirat, M. Benbouzid, B. Bensaker, R. Wamkeue, The state of the art of generators for wind energy conversion systems, Electromotion 14 (4) (2007) 163−172.

[6] F. Blaabjerg, K. Ma, Future on power electronics for wind turbine systems, IEEE J. Emerg. Sel. 1 (2013).

[7] R. Pena, J. Clare, G. Asher, Doubly fed induction generator using back-to-back PWM converters and its application to variable-speed wind-energy generation, IEE Proc. Electric Power Appl. 143 (1996).

[8] T. Sun, Z. Chen, F. Blaabjerg, Flicker study on variable speed wind turbines with doubly fed induction generators, IEEE Trans. Energy 20 (2005).
[9] J. Morren, S. De Haan, Ridethrough of wind turbines with doubly-fed induction generator during a voltage dip, IEEE Trans. Energy 20 (2005).
[10] A. Dittrich, A. Stoev, Comparison of fault ride-through strategies for wind turbines with DFIM generators, Power Electron. Appl. 2005 (2005).
[11] Z. Chen, Issues of connecting wind farms into power systems, in: IEEE/PES Transmission & Distribution Conference & Exposition: Asia and Pacific, 2005, pp. 1−6.
[12] Z. Chen, F. Blaabjerg, Wind farm—a power source in future power systems, Renew. Sustain. Energy Rev. 13 (2009).
[13] A. Gupta, A. Shandilya, Challenges of integration of wind power on power system grid: a review, Int. J. Emerg. Technol. 4 (2014).
[14] M. Tsili, S. Papathanassiou, A review of grid code technical requirements for wind farms, IET Renew. Power Gener. 3 (2009).
[15] D. Energinet, Technical Regulation 3.2. 5 for Wind Power Plants with a Power Output Greater than 11 kW, 2010.
[16] A.M. Sharaf, A.A. Abdelsalam, A FACTS based static switched filter compensator for voltage control and power quality improvement in wind smart grid, IJPE 4 (1) (2012) 41−57.
[17] Y.-H. Chen, S.-Y. Lu, Y.-R. Chang, T.-T. Lee, M.-C. Hu, Applied Energy, vol. 103, Elsevier, 2013.
[18] H.A. Gabbar, A.A. Abdelsalam, A.M. Sharaf, PSO-based control optimisation of microgrid with D-FACTS, Int. J. Power Energy Convers. 7 (1) (2016) 21.
[19] A.M. Sharaf, A.A. Abdelsalamy, A novel facts based dynamic voltage compensation scheme for smart electric grid stabilization and efficient utilization, in: 2011 24th Canadian Conference on Electrical and Computer Engineering(CCECE), 2011, pp. 000042−000047.
[20] M.M.A. Mahfouz, A.M. Amin, E.B. Youssef, Improvement the integration of Zafarana wind farm connected to egyptian unified power grid, in: Proceedings of the Universities Power Engineering Conference, vol. 2011, 2011. Janua.
[21] J.G. Slootweg, S.W.H. De Haan, H. Polinder, W.L. Kling, General model for representing variable speed wind turbines in power system dynamics simulations, IEEE Trans. POWER Syst. 18 (1) (2003).
[22] S. Kumar Bisoyi □, R.K. Jarial, R.A. Gupta, Modeling and Analysis of Variable Speed Wind Turbine Equipped with PMSG, 2014.
[23] A.P. Jayam, N.K. Ardeshna, B.H. Chowdhury, Application of STATCOM for improved reliability of power grid containing a wind turbine, in: 2008 IEEE Power and Energy Society General Meeting − Conversion and Delivery of Electrical Energy in the 21st Century, 2008, pp. 1−7.

CHAPTER

Doubly Fed Induction Generator in Wind Energy Conversion Systems

15

Domingos S.L. Simonetti[1], **Arthur E.A. Amorim**[1], **Flávio D.C. Oliveira**[2]

Electrical Engineering Department, Federal University of Espirito Santo, Vitória, Brazil[1]; *Computation and Electronics Engineering Department, Federal University of Espirito Santo, São Mateus, Brazil*[2]

CHAPTER OUTLINE

1. Introduction 462
1.1 Historical Review of Doubly Fed Induction Generator Technology 462
1.2 Structure 462
1.3 Doubly Fed Induction Generator Singularities 464
2. Modeling 465
2.1 Doubly Fed Induction Machine 465
2.2 The Static Model 467
2.2.1 Equivalent Circuit 467
2.2.2 Referring Rotor to Stator 467
2.2.3 Doubly Fed Induction Machine Operation Modes 468
2.3 The Dynamic Modeling 470
2.3.1 Reference Frame Transformation 470
2.3.2 Dynamic Modeling 471
2.4 Model for Grid Disturbances 472
2.4.1 The Complex Vector Representation 472
2.4.2 Doubly Fed Induction Generator Behavior Under Symmetrical Voltage Dips 472
3. Control System 476
3.1 Vector Control 477
3.2 Control of Grid Side Converter 477
3.3 Control of Rotor Side Converter 478
4. Power Electronic Converters 480
4.1 The Back-to-Back Voltage Source Converter 480
4.2 The Crowbar and the Chopper 481
4.3 New Trends/Novel Structures 482
5. Low-Voltage Ride-Through 483
5.1 Effects of Voltage Dip on Doubly Fed Induction Generator 483
5.2 Grid Code Requirements 486

Advances in Renewable Energies and Power Technologies. https://doi.org/10.1016/B978-0-12-812959-3.00015-0
Copyright © 2018 Elsevier Inc. All rights reserved.

5.3 Crowbar Protection 487
5.4 Complementary Protection 487
5.4.1 Pitch Angle Control 487
5.4.2 Chopper Circuit 487
5.5 Alternative Solutions 488
5.5.1 Control Strategies 488
5.5.2 Hardware Solutions 488
References 489

1. INTRODUCTION

1.1 HISTORICAL REVIEW OF DOUBLY FED INDUCTION GENERATOR TECHNOLOGY

Wind energy conversion system (WECS) has experienced an expressive development in the past few years. New technologies on turbines, machines, drives, and protection devices have been developed and these devices have been improved progressively. The machine used to convert mechanical rotational energy into electrical energy is the core of any WECS. According to the machine chosen, all other devices are affected; fixed- or variable-speed turbine, power electronic converter type, and the respective power, protections used, and so forth.

Doubly fed induction generator (DFIG) moves together with this technology development. DFIG is nothing more but a wound rotor induction machine, used for years in the past for application requiring speed control. However, working as a generator this machine enables an important feature: it can produce power both in subsynchronous and supersynchronous speeds. Because of this trait, wind turbine is able to operate in a wide range of velocities with high efficiency.

As a characteristic of DFIG, to generate power in subsynchronous speed, the rotor consumes energy. On the other hand, when it is in supersynchronous speed the rotor generates power. Besides that, the frequency of currents produced or consumed in rotor circuit varies according to the rotor speed. To provide the means of such behavior, a bidirectional power electronic converter is used in rotor circuit to be this variable source or load to machine rotor, depending on operation speed. Previously, current source inverter was used, as presented in Smith and Nigim [1]. Nonetheless, this topology produces very poor quality current and has several issues when operating near synchronous speed. To deal with these problems, Pena, Clare, and Asher [2] propose the use of two pulse width modulation (PWM) voltage source converters in a back-to-back structure. The performance with this arrangement is relevant, and it is still used in modern WECS.

1.2 STRUCTURE

The structure of a DFIG-based WECS is formed basically by the wind turbine, the gear box, the wound rotor induction machine, and the back-to-back converter, as

shown in Fig. 15.1. Other peripheral devices are very common, such as the passive filter, the crowbar resistances, and the chopper circuit.

One of the most important advances in WECS technology was the use of variable-speed wind turbines. It is well established that for each wind speed, there is a rotor speed that maximizes power production, as a function of power coefficient [3]. Once wind speed has several variations along the day, this improvement allows a better power extraction, increasing WECS efficiency. The use of variable-speed turbines was only possible because of the advances in power electronics and favored the propagation of DFIG-based WECS.

As wind turbines commonly operate in low speeds and the DFIG turns pretty faster, it is necessary to use a gear box to couple these machine shafts. The transmission is one of the most critical drawbacks of DFIG system, producing losses and requiring frequent maintenance.

As stated before, DFIG is a wound rotor induction machine. This machine is very well-known and there are numerous models to represent its behavior, depending on the analysis conducted. Some of this models used for a better understanding of DFIG will be presented further. Basically, in WECS applications, stator is directly connected to the grid, while rotor is connected to a back-to-back converter.

As a result of the DFIG rotor characteristic of having power being provided or consumed, depending on the situation, the power converter used has to be bidirectional. Besides that, it has to operate with different frequencies in each side, a fixed one (50 or 60 Hz) on the grid side and a variable one on rotor side, determined by the wind speed and the best operation point. It is also desired that this converter produces good quality currents and voltages, with low harmonic content, to prevent machine depreciation and to ensure good energy quality indexes provided to the grid. More details on power electrics converter topologies and features will be presented below.

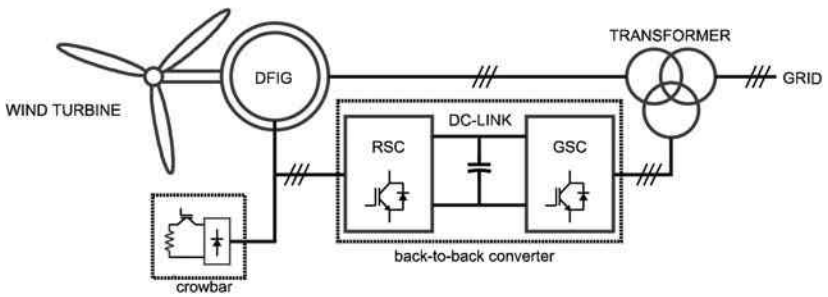


FIGURE 15.1

Doubly fed induction generator (DFIG) basic structure. *GSC*, grid side converter; *RSC*, rotor side converter.

Source: Author.

DFIG stator and rotor voltages usually are not equal because of the machine transformation ratio. Also the produced voltage values do not match the grid voltage. Hence, a three-winding transformer is used to couple these three voltages.

With voltage source converters, to guarantee proper operation, it is necessary to use a passive filter, with dominant inductive behavior. Also, these converters produce voltage harmonics that can disturb other sensitive equipment connected near the wind farm if a proper filter is not adopted to prevent them from flowing [4]. There are countless possibilities for filter design, from filter order, topology, and quality factor to materials used in inductors core.

DFIG is especially susceptible to grid voltage disturbances. To prevent the converter from damages deriving from these transients, some protection devices are commonly applied. To protect converter's switches against high currents on rotor circuit, crowbar resistances are employed. These resistances are normally disconnected from the circuit and when a fault is detected they are inserted in parallel to rotor, providing an alternative path to currents, instead of flow through the converter. A chopper circuit is another protection which prevents high voltages on the converter's DC link. This device consists of a switchable resistance in parallel to DC-link capacitor, which is activated when its voltages surpasses safe values, wasting the extra energy.

1.3 DOUBLY FED INDUCTION GENERATOR SINGULARITIES

Some characteristics of DFIG distinguish it from other WECS. The most important one concerns the converter. Despite using the so-called, full converter—that is, a converter that deals with the full power produced by the turbine—DFIG uses a partial converter—which controls the total power, but just a part of it passes through the converter.

In DFIG system the converter is placed in rotor circuit, while the stator is directly connected to the grid. With this configuration, as will be stated further, only a fraction of the power, proportional to machine slip, will pass through the converter. This is recognized as the main advantage of DFIG system—for the same wind turbine power its converter is reduced, to around 25%, in comparison with other technologies, reducing costs, size, and weight.

Other advantages of DFIG are its wide speed range operation, from 60% up to 110% of rated speed and also the fact that this is an extremely reliable and simple construction machine. On the other hand, this structure leads to some issues for DFIG-based WECS: the machine is directly connected to the grid, which make it extremely susceptible to grid disturbances and faults [5].

Another peculiarity of DFIG is the presence of brushes on rotor circuit. They are necessary to make contact with rotor wounds that, obviously, are turning. This is a drawback, once the brushes need constant maintenance and are a source of failures.

In the following sections, characteristics of DFIG modeling and control will be discussed. Also, the power electronic converters used in WECS equipped with DFIG are presented. In addition, a brief review of new trends on DFIG ride-through to grid disturbances is outlined.

2. MODELING

2.1 DOUBLY FED INDUCTION MACHINE

The doubly fed induction machine (DFIM) is a wound rotor induction machine and has a construction very similar to the traditional squirrel-cage machine. In a concise way, it consists of two three-phase winding sets: stator and rotor, as shown in Fig. 15.2.

The application of symmetric three-phase voltages along with the spatial distribution of the windings in the stator produces a rotating magnetic field in the air gap. Such magnetic field is seen as a time-variant field by each rotor winding, in which AC voltages are induced. The induced rotor voltage and its frequency are proportional to the difference between the stator flux speed and the mechanical rotor speed. In DFIM, rotor windings are also fed by another source, through brushes, which enable some singularities in the machine behavior.

Denoting ω_s as the angular frequency of stator voltages (rad/s) and p as the pairs of poles of the DFIM, the angular frequency of rotor voltages, ω_r, is given by Eq. (15.1):

$$\omega_r = \omega_s - \omega_m \tag{15.1}$$

where ω_m is the angular speed at shaft,

$$\omega_m = \frac{p \cdot V_{\text{RPM}}}{60} \tag{15.2}$$

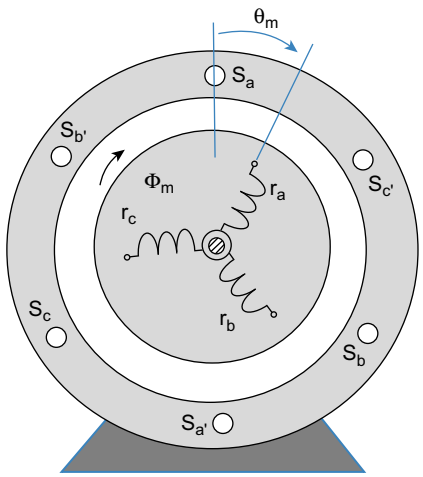


FIGURE 15.2

Simplified doubly fed induction machine. ω_m, mechanical rotational speed at shaft (RPM); s_a, s_b, s_c, r_a, r_b, r_c, stator and rotor windings for phases *a*, *b*, *c* respectively; Φ_m, magnetizing flux.

Source: Author.

The slip is defined as the relation between angular frequencies of rotor and stator voltages:

$$s = \frac{\omega_r}{\omega_s} = \frac{\omega_s - \omega_m}{\omega_s} \rightarrow \omega_r = s \cdot \omega_s \tag{15.3}$$

According to the slip, three different operating modes are possible for the DFIM:

Subsynchronous operation: $\omega_m < \omega_s \Rightarrow s > 0$
Synchronous operation: $\omega_m = \omega_s \Rightarrow s = 0$
Supersynchronous operation: $\omega_m > \omega_s \Rightarrow s < 0$

The stator and rotor voltage equations for a, b, and c windings can be described as in Eq. (15.4) [6]:

$$\begin{aligned} \left[v_{s,abc}\right] &= R_s\left[i_{s,abc}\right] + \frac{d}{dt}\left[\lambda_{s,abc}\right] \\ \left[v_{r,abc}\right] &= R_r\left[i_{r,abc}\right] + \frac{d}{dt}\left[\lambda_{r,abc}\right] \end{aligned} \tag{15.4}$$

and

$$\begin{bmatrix} \lambda_{s,abc} \\ \lambda_{r,abc} \end{bmatrix} = \begin{bmatrix} [L_s] & [L_{sr}] \\ [L_{rs}] & [L_r] \end{bmatrix} \times \begin{bmatrix} i_{s,abc} \\ i_{r,abc} \end{bmatrix} \tag{15.5}$$

where

$$[L_s] = \begin{bmatrix} L_{\sigma s} + L_{ms} & -\frac{1}{2}L_{ms} & -\frac{1}{2}L_{ms} \\ -\frac{1}{2}L_{ms} & L_{\sigma s} + L_{ms} & -\frac{1}{2}L_{ms} \\ -\frac{1}{2}L_{ms} & -\frac{1}{2}L_{ms} & L_{\sigma s} + L_{ms} \end{bmatrix}$$

$$[L_r] = \begin{bmatrix} L_{\sigma r} + L_{mr} & -\frac{1}{2}L_{mr} & -\frac{1}{2}L_{mr} \\ -\frac{1}{2}L_{mr} & L_{\sigma r} + L_{mr} & -\frac{1}{2}L_{mr} \\ -\frac{1}{2}L_{mr} & -\frac{1}{2}L_{mr} & L_{\sigma r} + L_{mr} \end{bmatrix} \tag{15.6}$$

$$[L_{sr}] = [L_{rs}]^T = L_m \begin{bmatrix} \cos\theta_m & \cos\left(\theta_m + \frac{2\pi}{3}\right) & \cos\left(\theta_m - \frac{2\pi}{3}\right) \\ \cos\left(\theta_m - \frac{2\pi}{3}\right) & \cos\theta_m & \cos\left(\theta_m + \frac{2\pi}{3}\right) \\ \cos\left(\theta_m + \frac{2\pi}{3}\right) & \cos\left(\theta_m - \frac{2\pi}{3}\right) & \cos\theta_m \end{bmatrix}$$

where $v_{s,abc}$ and $v_{r,abc}$, stator and rotor voltages for phases a, b, and c respectively; $i_{s,abc}$ and $i_{r,abc}$, stator and rotor c for phases a, b, c; R_s and R_r, stator and rotor resistances; $L_{\sigma s}$, $L_{\sigma r}$, stator leakage and rotor leakage inductance; L_{ms}, L_{mr}, stator to stator and rotor to rotor mutual inductance; L_m, maximum value of the stator−rotor mutual inductance.

The drawback of this complete *abc* representation is that a large set of equations are derived needing much effort to accomplish the analysis.

2.2 THE STATIC MODEL

The steady-state−equivalent electric circuit of the machine is developed through physics equations that describe the machine behavior. This modeling allows an evaluation of machine performance and its operating modes.

2.2.1 Equivalent Circuit

A representative steady-state −equivalent electric circuit of the DFIM is obtained considering the following assumptions:

- The stator and the rotor are connected in the star configuration;
- The stator is powered by the grid with constant and balanced three-phase AC voltage amplitude and constant frequency;
- The rotor is powered by the grid with constant and balanced three-phase AC voltage amplitude and constant frequency;

Fig. 15.3 represents one phase of the stator and rotor three-phase windings.

2.2.2 Referring Rotor to Stator

The magnetic field of the stator rotates at a speed synchronized to the grid frequency. The magnetic field of the rotor rotates synchronized to rotor currents frequency. Despite this, at the machine air gap the rotor field is superimposed to the mechanical

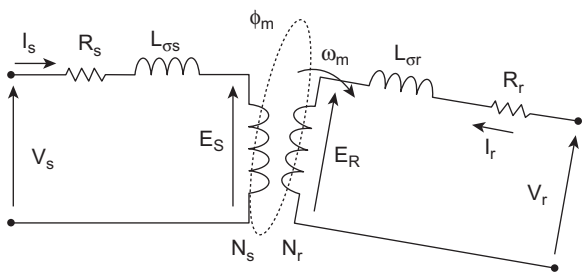


FIGURE 15.3

Steady-state−equivalent electric circuit. I_s, stator current; E_S, induced electro-magnetic force in the stator; I_r, rotor current; L_M, magnetizing inductance, $L_M = 3L_{ms}/2$; N_s, N_r, stator and rotor winding's number of turns.

Source: Author.

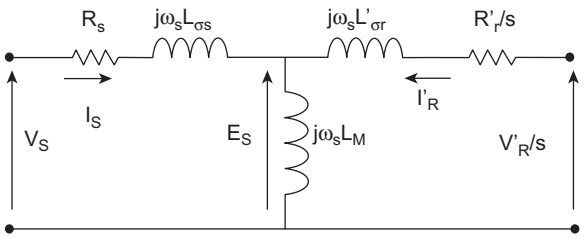


FIGURE 15.4

Steady-state—equivalent circuit of the doubly fed induction machine referred to the stator with stator frequency. $a = \frac{N_s}{N_r}$; $R'_r = a^2 R_r$; $L'_{\sigma r} = a^2 L_{\sigma r}$; $V'_r = aV_r$; $I'_r = \frac{I_r}{a}$.

Source: Author.

speed. Therefore, stator windings see the rotor field at its own synchronous frequency. In this way, to perform the analysis, it is advantageous to represent all circuits referred to stator as presented in Fig. 15.4 [7].

2.2.3 Doubly Fed Induction Machine Operation Modes

DFIM can operate as a generator as well as a motor in both subsynchronous or supersynchronous speeds.

The relation between stator and rotor power can be deduced, considering that the sum of the active power (P) in a closed system is equal to zero ($\sum P = 0$). Considering P_m as the shaft mechanical power, P_S the stator active power, P_R the rotor active power, and P_{loss} the active power losses (copper losses, neglecting core losses), we have:

$$P_m = P_S + P_R + P_{loss} \tag{15.7}$$

It is well known that [7]:

$$P_R = -s \cdot P_S \tag{15.8}$$

So, neglecting power losses ($P_{loss} \approx 0$):

$$P_m = (1 - s) \cdot P_S \tag{15.9}$$

2.2.3.1 Motor Operation ($P_m > 0$)

The machine is delivering mechanical power and receiving electric power from grid, as shown in Fig. 15.5.

Speed	P_m	P_S	P_R
Subsynchronous: $s > 0$ and $\omega_m < \omega_s$	$P_m > 0$	$P_S > 0$	$P_R > 0$
Supersynchronous: $s < 0$ and $\omega_m > \omega_s$	$P_m > 0$	$P_S > 0$	$P_R < 0$

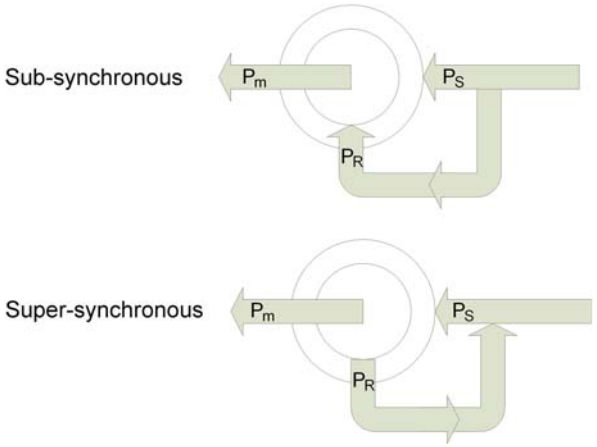


FIGURE 15.5

Active power flow representation for motor operation.

Source: Author.

2.2.3.2 Generator Operation ($P_m < 0$)

The machine is receiving mechanic power and delivering electric power from grid, as shown in Fig. 15.6:

Speed	P_m	P_S	P_R
Subsynchronous: $s > 0$ and $\omega_m < \omega_s$	$P_m < 0$	$P_S < 0$	$P_R > 0$
Supersynchronous: $s < 0$ and $\omega_m > \omega_s$	$P_m < 0$	$P_S < 0$	$P_R < 0$

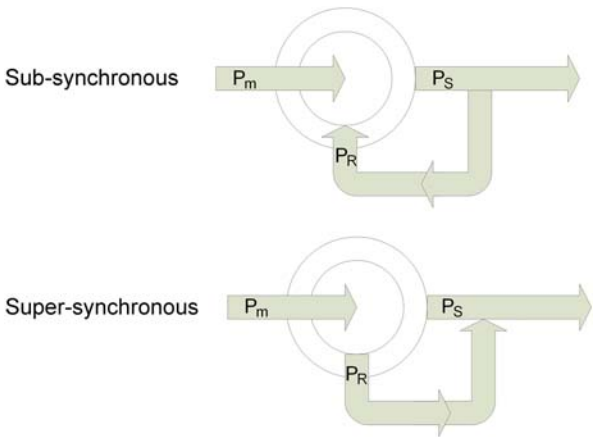


FIGURE 15.6

Active power flow representation for operation as generator.

Source: Author.

2.3 THE DYNAMIC MODELING

Although the steady-state model is useful to understand and for calculus under steady-state, transient operation requires a more complete model to represent the asymmetric coupling effects. In the *abc* frame, a large set of equations are derived needing much effort to accomplish the analysis.

2.3.1 Reference Frame Transformation

Consider the equations of a symmetric three-phase system:

$$\begin{aligned} x_A(t) &= X\cdot\cos(\omega\cdot t+\phi) \\ x_B(t) &= X\cdot\cos\left(\omega\cdot t+\phi\ -\frac{2\pi}{3}\right) \\ x_C(t) &= X\cdot\cos\left(\omega\cdot t+\phi+\frac{2\pi}{3}\right) \end{aligned} \tag{15.10}$$

As the symmetric three-phase system is linearly dependent $(x_a(t) = -x_b(t) - x_c(t))$, it can be represented by an equivalent two-phase orthogonal system, as shown in Fig. 15.7. The new reference frame is also called $\alpha\beta$ transformation, $x_a(t)$, $x_b(t)$, and $x_c(t)$ are transformed to $x_\alpha(t)$ and $x_\beta(t)$.

This representation transforms the models and their equations in simpler elements than the classic three-phase model. In the $\alpha\beta$ frame, $x_\alpha(t)$ and $x_\beta(t)$ can be composed in a time-dependent phasor $x_{\alpha\beta}(t)\angle\theta$. The mathematical transformation is given by Eq. (15.11):

$$\begin{bmatrix} x_\alpha \\ x_\beta \end{bmatrix} = \frac{2}{3}\cdot\begin{bmatrix} 1 & \frac{-1}{2} & \frac{-1}{2} \\ 0 & \frac{\sqrt{3}}{2} & \frac{-\sqrt{3}}{2} \end{bmatrix}\cdot\begin{bmatrix} x_a \\ x_b \\ x_c \end{bmatrix} \tag{15.11}$$

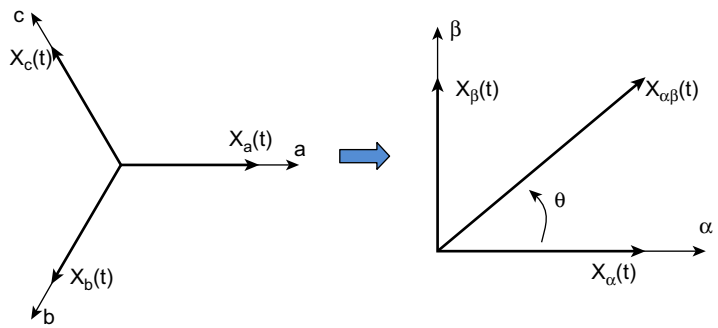


FIGURE 15.7

$\alpha\beta$ Frame.

Source: Author.

Then, one step ahead is to compose the $\alpha\beta$ system at a generic two-phase frame, the so-called dq frame (Park transformation). The generic dq frame can be fixed and coincident to the $\alpha\beta$ frame, or can rotate at any angular speed, but usually it is grid synchronized ($\phi = \omega t$). Fig. 15.8 shows $\alpha\beta$ and dq frame, and Eqs. (15.12) and (15.13) present $\alpha\beta \rightarrow dq$ transformation tied to the grid voltages, considering $v_a = \sqrt{2} \cdot V_{\text{RMS}} \cdot \cos(\omega t)$.

$$\begin{bmatrix} x_d \\ x_q \end{bmatrix} = \begin{bmatrix} \cos\phi & \text{sen}\phi \\ -\text{sen}\phi & \cos\phi \end{bmatrix} \cdot \begin{bmatrix} x_\alpha \\ x_\beta \end{bmatrix} \tag{15.12}$$

$$\varnothing = \omega_s t$$

$$v_{s,\alpha} = v_a$$

$$\begin{bmatrix} v_{s,d} \\ v_{s,q} \end{bmatrix} = \begin{bmatrix} \sqrt{2V_{\text{rms}}} \\ 0 \end{bmatrix} \tag{15.13}$$

2.3.2 Dynamic Modeling

The grid-synchronized dq transformation can be applied to the set of equations given by Eqs. (15.4)–(15.6), generating a simpler but effective complete dynamic circuit model, which is shown in Fig. 15.9.

Neglecting the power losses associated with the stator and rotor resistances, the powers and electromagnetic torque (T_{em}) equation are given by Eqs. (15.14)–(15.18).

$$P_s = \frac{3}{2}\left(v_{s,d} i_{s,d} + v_{s,q} i_{s,q}\right) \tag{15.14}$$

$$P_r = \frac{3}{2}\left(v_{r,d} i_{r,d} + v_{r,q} i_{r,q}\right) \tag{15.15}$$

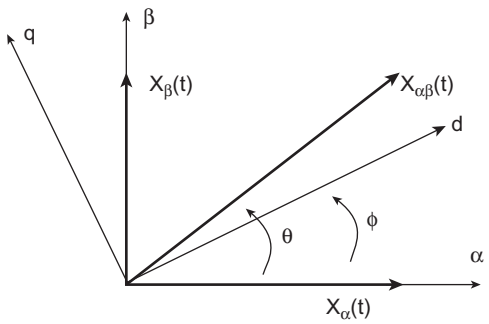


FIGURE 15.8

$\alpha\beta \rightarrow dq$ Transformation.

Source: Author.

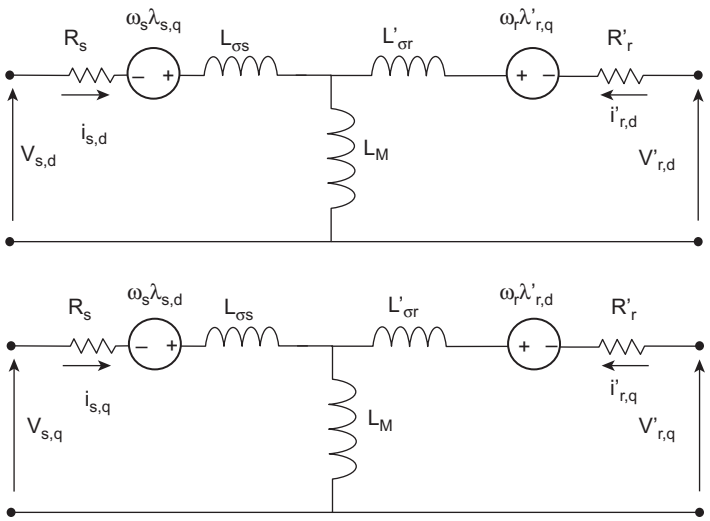


FIGURE 15.9

The *dq* equivalent circuit. $\lambda_{s,d} = (L_{\sigma s} + L_M)i_{s,d} + L_M i'_{r,d}$; $\lambda_{s,q} = (L_{\sigma s} + L_M)i_{s,q} + L_M i'_{r,q}$; $\lambda'_{r,d} = (L'_{\sigma r} + L_M)i'_{r,d} + L_M i_{s,d}$; $\lambda'_{r,q} = (L'_{\sigma r} + L_M)i'_{r,q} + L_M i_{s,q}$.

Source: Author.

$$Q_s = \frac{3}{2}\left(v_{s,q}i_{s,d} - v_{s,d}i_{s,q}\right) \tag{15.16}$$

$$Q_r = \frac{3}{2}\left(v_{r,q}i_{r,d} - v_{r,d}i_{r,q}\right) \tag{15.17}$$

$$T_e = \frac{3}{2}\frac{p}{2}L_M\left(i_{s,q}i'_{r,d} - i_{s,d}i'_{r,q}\right) \tag{15.18}$$

2.4 MODEL FOR GRID DISTURBANCES

2.4.1 The Complex Vector Representation

Considering v_a, v_b, and v_c, a symmetric set of three-phase voltages, namely $v_a(t) = \sqrt{2}V_{\text{rms}}\cos(\omega t)$, $v_\alpha(t)$, and $v_\beta(t)$ from Eq. (15.11), can be composed as a time-dependent phasor, $v_{\alpha\beta}(t) \angle \theta$ in a polar form. Considering the Euler formula, the phasor can be expressed as a complex vector:

$$v_{s,\alpha\beta}(t)\angle\varnothing = \overrightarrow{v_s} = \sqrt{2}V_{\text{rms}}e^{j\omega_s t} \tag{15.19}$$

2.4.2 Doubly Fed Induction Generator Behavior Under Symmetrical Voltage Dips

Among all fault situations, the symmetrical one is that which leads to higher fault currents. This is because the analysis carried out here only considers this situation.

When a voltage dip happens, there is an imbalance between the former magnetic flux operating on machine and the new imposed stator voltage. With this abrupt change on grid voltage, two flux components, named forced and natural, arise in the magnetic flux. The forced component is proportional to the new grid voltage, while the natural component represents the transitory phase between these two states, describing machine demagnetization process. The transient operation of the stator flux induces high voltages on the rotor circuit, which is very dangerous for the power electronics converter connected to the rotor.

The stator flux linkage Ψ_s, using complex vector representation, can be obtained from:

$$\frac{d\vec{\psi}_s(t)}{dt} = \vec{v}_s(t) - R_S \cdot \vec{i}_s(t) \tag{15.20}$$

The generator is initially considered at normal operation, and at $t = 0$ s, a voltage dip occurs with depth D, as shown in Fig. 15.10. Eq. (15.21) describes the grid voltage before and after the voltage dip.

$$\vec{v}_s(t) = \begin{cases} V_p \cdot e^{j \cdot \omega_s \cdot t} & t < 0\ s \\ (1 - D) \cdot V_p \cdot e^{j \cdot \omega_s \cdot t} & t \geq 0\ s \end{cases} \tag{15.21}$$

The ordinary differential equation solution is divided into two terms, the homogeneous solution, Eq. (15.22) and the particular solution, Eq. (15.23):

$$\vec{\psi}_{s\,h}(t) = \frac{D \cdot V_p}{j \cdot \omega_s} e^{-t/\tau_s}, \quad \forall t \geq 0 \tag{15.22}$$

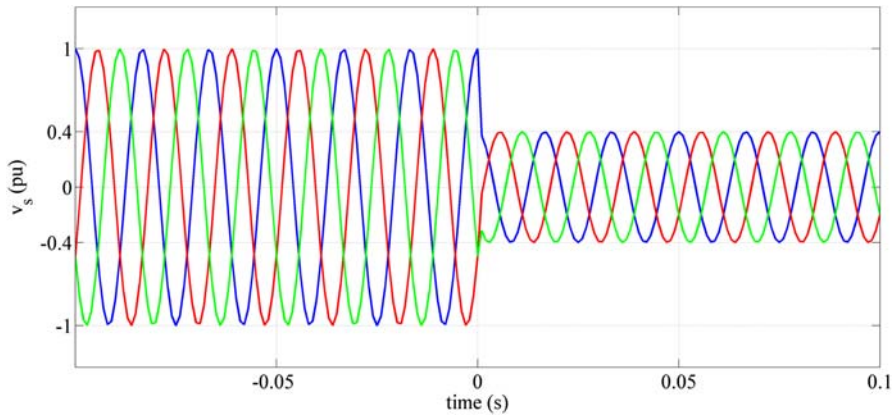


FIGURE 15.10

Voltage dip.

Source: Author.

$$\vec{\psi}_{s\,p}(t) = \frac{(1-D)\cdot V_p}{j\cdot\omega_s} e^{j\cdot\omega_s\cdot t}, \quad \forall\ t \geq 0 \tag{15.23}$$

The homogeneous solution of the magnetic flux is a transient flux and the particular solution is the steady-state component. When the voltage dip occurs, the stator flux has its dynamic as shown in Fig. 15.11 and is described by Eq. (15.24).

$$\vec{\psi}_s(t) = \begin{cases} \dfrac{V_p}{j\cdot\omega_s} e^{j\cdot\omega_s\cdot t} & t < 0 \\ \dfrac{(1-D)\cdot V_p}{j\cdot\omega_s} e^{j\cdot\omega_s\cdot t} + \dfrac{D\cdot V_p}{j\cdot\omega_s} e^{-t/\tau_s} & t \geq 0 \end{cases} \tag{15.24}$$

where

$$\tau_s = \frac{L_S}{R_S}$$

The induced electromagnetic force in the rotor circuit is obtained from Eq. (15.25):

$$\vec{e}_r(t) = \frac{1}{a}\frac{L_m}{L_S}\frac{d\vec{\psi}_r(t)}{dt} \tag{15.25}$$

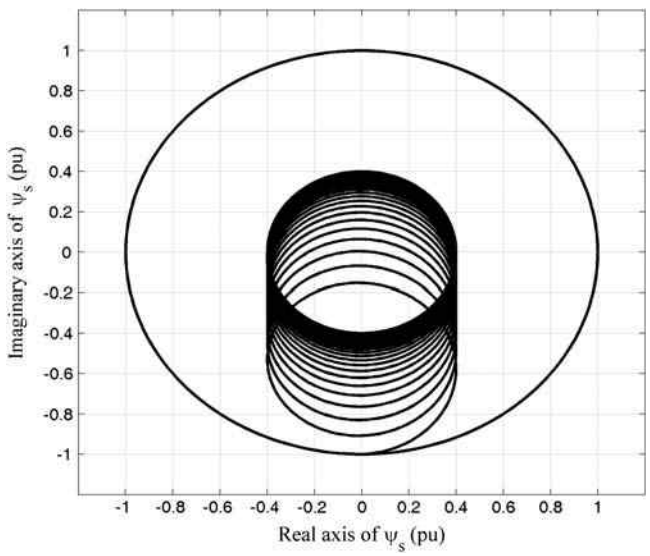


FIGURE 15.11

Stator flux trajectory with *D* voltage dip.

Source: Author.

But the rotor flux Ψ_r is given by:

$$\overrightarrow{\psi}_r(t) = \overrightarrow{\psi}'_s(t) = \overrightarrow{\psi}_s(t)\cdot e^{-j\cdot\omega_m\cdot t}$$

$$= \begin{cases} \dfrac{V_p}{j\cdot\omega_s} e^{j\cdot\omega_r\cdot t} & t < 0 \\ \dfrac{(1-D)\cdot V_p}{j\cdot\omega_s} e^{j\cdot\omega_r\cdot t} + \dfrac{D\cdot V_p}{j\cdot\omega_s} e^{-j\cdot\omega_m\cdot t}\cdot e^{-t/\tau_s} & t \geq 0 \end{cases} \tag{15.26}$$

Using both equations, the induced electromagnetic force in the rotor is obtained as follows:

$$\overrightarrow{e}_r(t) = \begin{cases} \dfrac{1}{u}\dfrac{L_m}{L_S} V_p\cdot s\cdot e^{j\cdot\omega_r\cdot t} & t < 0 \\ \dfrac{1}{u}\dfrac{L_m}{L_S} V_p\cdot\left[(1-D)\cdot s\cdot e^{j\cdot\omega_r\cdot t} - D\cdot(1-s)\cdot e^{-j\cdot\omega_m\cdot t}\cdot e^{-t/\tau_s}\right] & t \geq 0 \end{cases} \tag{15.27}$$

From this last deduction, it can be seen that the induced internal rotor voltage because of a stator voltage dip presents two superposed frequencies, one is function of the slip frequency and the other is associated to the rotational mechanical speed.

The Fig. 15.12 shows the simulation result of the internal voltage e_r of a 2 MW DFIG under a 50% voltage dip. The induced rotor voltage is more than twice its steady-state value. It is possible to see the two superposed frequencies commented

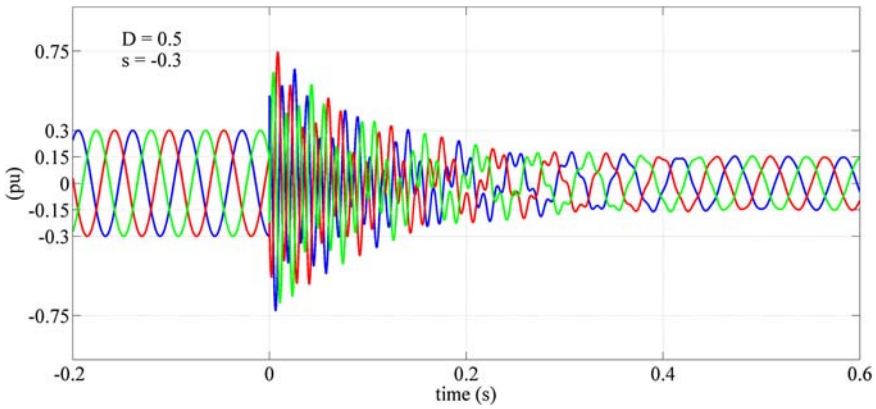


FIGURE 15.12

Rotor-induced voltage during a voltage dip.

Source: Author.

above. This overvoltage produces high-value currents in the rotor circuit, which can seriously damage the rotor converter if some action is not taken.

3. CONTROL SYSTEM

Control system has the task to extract maximum power from the wind. This dynamic control of the DFIG is executed by the adequate control of the power converter. The converter enables variable-speed operation of the wind turbine, decoupling rotor mechanical speed from the power system electrical system. Typically, the behavior of a wind turbine power extraction from wind speed is described by the curves in Fig. 15.13.

For each wind speed, there is a curve of the generator power in function of the generator speed. The maximum power curve can be extracted connecting the maximum Cp points of each curve; the control system aim is to keep the turbine on this curve as the wind varies. However, converter has a limited capacity; thus, it is not possible to obtain optimum power extraction over all wind speeds. It is common to have on wind turbines the curve divided in sections. For very low wind speeds (A-B) the system operates at a constant rotational speed. In section (B-C), the system follows the optimal curve, until machine limitation, when Cp diverges from its optimal point (C-D). For very high wind speeds (D-E), aerodynamic control limits the power extraction to ensure safe conditions for torque in the shafts.

DFIG control is completely done through its rotor, where the power electronic converter is connected. The converter is a back-to-back type, formed by two voltage source converters linked by a DC capacitor. The rotor side converter (RSC) controls

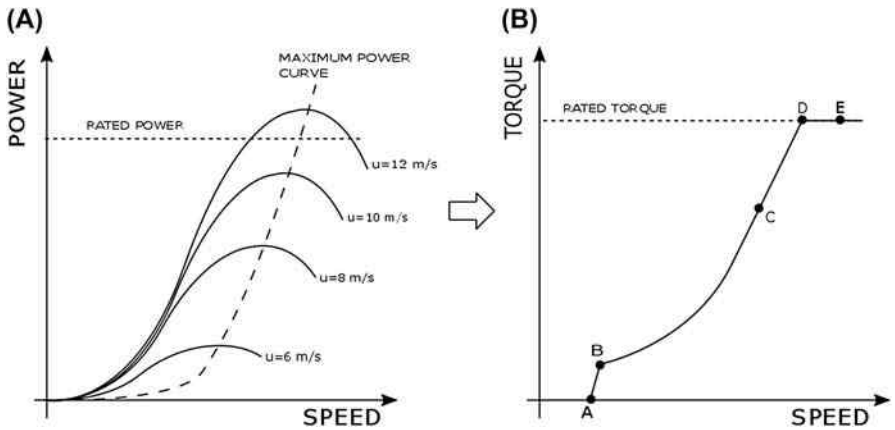


FIGURE 15.13

Wind turbine characteristic for maximum power extraction.

Source: Author.

the DFIG's rotor currents. By these currents, it is possible to control the power flow on machine's stator. In turn, the grid side converter (GSC) controls DC-link voltage and reactive power flow between converter and electrical power system. DC-link capacitor insulates both sides of the back-to-back and damps power fluctuation, acting as an inertia for the rotor power flow.

The control system is primordial for the proper operation of any machine drive; in WECS it is not different. The control of DFIG has to ensure system stability and optimal operation. To do so, there are several variables to be kept controlled in established set points, such as torque, active and reactive powers, and also magnitudes related to the GSC, such as the reactive power and the DC bus voltage. Control system has the task to receive all these references and determine the voltages to be generated in both sides of the back-to-back converter.

3.1 VECTOR CONTROL

The most common strategy for a grid-connected DFIG is the vector control, which is very similar to the widespread classical vector control employed in induction machine drives. As explained in the previous section, if the machine is represented in a synchronous reference frame (dq), active and reactive stator power can be controlled independently, by means of direct and quadrature current. To ensure this decoupled control, it is very important to correctly align the dq reference frame. In the literature, two orientations are discussed, each one has advantages and disadvantages; the first is called flux orientation and the second voltage orientation.

Following the legacy of machine drive's vector control, flux orientation was the first option in DFIG control. With this approach, the machine stator flux is estimated and aligned to the d axis of the reference frame. Another option, discussed later, is the grid voltage orientation. A phase-locked loop is used to detect the angle of the fundamental voltage, which is aligned to the reference frame axis. Both options are equivalent if the stator voltage and flux are stable. In general, stator resistance is very small and the voltage drop on it is negligible, which made both reference frames coincident. Applications using these approaches are found in literature.

The differences are noted during transition, when the phase shift between the stator voltage and the flux are not precisely 90 degrees anymore. Also, Petersson [8] compares both orientation techniques performance and proves that voltage orientation is always stable, although flux orientation may destabilize vector control depending on the d-axis component of the current.

3.2 CONTROL OF GRID SIDE CONVERTER

As shown in Fig. 15.1, one part of the back-to-back converter is called the GSC. GSC is in charge to control DC-link voltage and reactive power flux between the converter and the electrical grid. This is done by means of a cascade control loop,

as shown in Fig. 15.14. In an external loop, these variables are set as references, compared with its measured values and the control gives the reference currents to the internal loop. In the internal loop, reference currents are compared to the measured ones to set the voltages to be produced by converter. To decouple d and q components of control system, a feed-forward loop inserts these compensations on reference voltage.

Usually, proportional integral (PI) controllers are used in both internal and external loops. Basically, the outer loop has two distinct characteristics, one for DC-link voltage control and other to reactive power exchange. DC-link voltage control is done by the balance of active power flowing through GSC and RSC. The relation between the DC-voltage and the current is established by the DC-link capacitance. Reactive power is calculated by measured currents and voltages and is filtered before being inserted in the control loop. For the inner loop, the plant is modeled by the difference between the grid voltage and the converter voltage in filter impedance, which enables PI controller design for better results in currents dynamics.

3.3 CONTROL OF ROTOR SIDE CONVERTER

Active and reactive power flow between the stator and grid are controlled by the RSC. As in GSC, these variables are controlled by means of cascade control loops, as shown in Fig. 15.15. In the same way, external loop set references, compare with measured values and the control gives the reference currents to the internal loop. Internal loop compares reference currents with measured values to set the voltages to

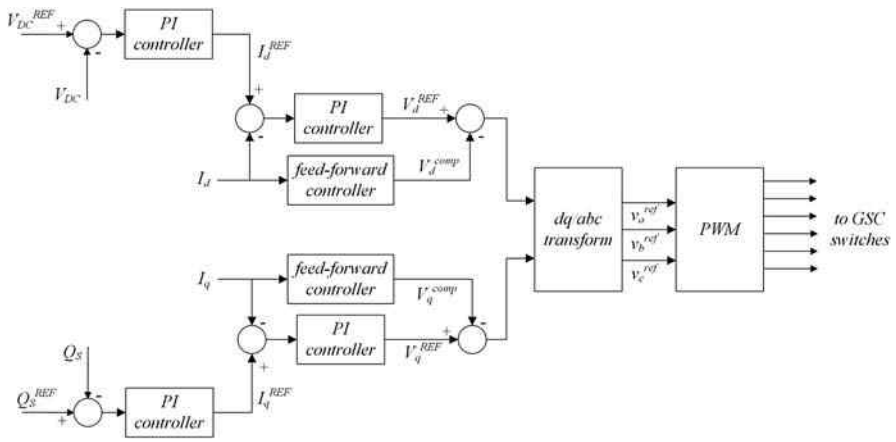


FIGURE 15.14

Control loop for grid side converter.

Source: Author.

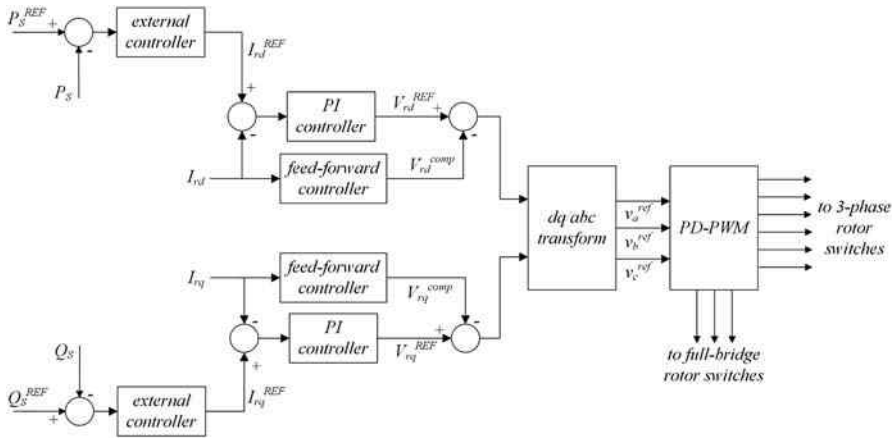


FIGURE 15.15

Control loop for rotor side converter.

Source: Author.

be produced by converter. Feed-forward controllers insert compensations to decouple d and q components in the voltages.

Eqs. (15.4) and (15.5) show the relation between stator and rotor variables. Active and reactive powers in stator are determined by voltages and currents on stator, and the voltages are fixed by electrical grid. Power is controlled by controlling the currents. The stator currents, in turn, can be controlled by rotor currents, which are produced by the RSC. Thus, rotor current control is the ultimate goal of RSC control loops.

According to the *dq* model of DFIG, the reference rotor currents can be evaluated to generate the desired stator power, as shown in Fig. 15.16.

Also, according to the model, oriented by stator voltage, the equations of rotor voltages can be written as:

$$v_{r,d} = R_r i_{r,d} - \omega_r \sigma L_r i_{r,q} + \sigma L_r \frac{d}{dt} i_{r,d} + \frac{L_m}{L_s} \frac{d}{dt} \lambda_{s,d} \tag{15.28}$$

$$v_{r,q} = R_r i_{r,q} - \omega_r \sigma L_r i_{r,d} + \sigma L_r \frac{d}{dt} i_{r,q} + \omega_r \frac{L_m}{L_s} \lambda_{s,d} \tag{15.29}$$

where

$$\sigma = 1 - \frac{L_m^2}{L_s \cdot L_r}$$

These equations are used to model the plant for the inner loop controller design. The last term depends only on stator voltage; thus, it is seen as a perturbation from the control point of view. The cross terms are compensated by feed-forward controllers.

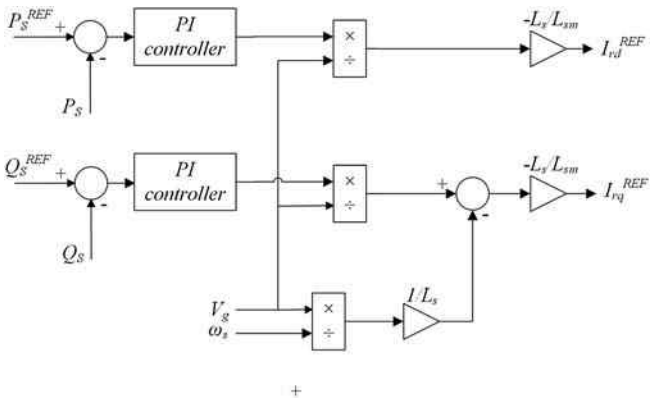


FIGURE 15.16

External control loop for power control.

Source: Author.

4. POWER ELECTRONIC CONVERTERS

The key to correctly operate the induction machine as a double-fed generator is the electronic converter required to connect the rotor terminals to the grid. The converter has the function of adjusting rotor frequency to the frequency of the grid and, at the same time, provides control of active and reactive power that is sent to the line. The converter is about 30% of rated DFIG power. Besides the interconnection structure, other topologies are present in the rotor circuit to protect the main converter.

The most common solution to connect both DFIG rotor and stator (grid) is the well known back-to-back voltage source converter, allowing a four-quadrant operation.

4.1 THE BACK-TO-BACK VOLTAGE SOURCE CONVERTER

The back-to-back structure is composed of two voltage-source converters linked by the same DC-bus [9]. Fig. 15.17 shows the structure using a two-level PWM converter.

The converter is able to synthesize voltages matching rotor requirements on the rotor side and grid requirements on the other side. Despite the fact that usually the stator−rotor turns ratio boosts the rotor voltage with respect to the stator voltage, the slip range of operation is between −0,3 and +0,3, and a not high voltage value is needed to be synthesized on the rotor side. On the grid side, a transformer connection matches voltage values to grid.

Drive signals are generated using sinusoidal PWM (SPWM) (voltage references compared with triangular carrier at switching frequencies), or using space vector modulation (SVPWM). The first is of simpler achievement, but the converter

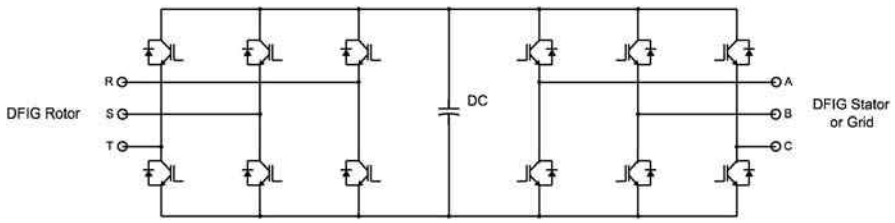


FIGURE 15.17

Two three-phase inverters back to back connected. *DFIG*, doubly fed induction generator.

Source: Author.

potential is subutilized. Some improvement can be done using third-harmonic injection technique. On the other hand, SVPWM allows a better voltage synthesis and better converter utilization but it is more toilsome to implement.

In the last few years, preference has been given to employ neutral-point clamped converters (NPC), in medium-to-high power converters [10]. The NPC, shown in Fig. 15.18, is a multilevel converter that presents lower harmonics in the synthesized voltage, less voltage stress for the same converter compared to the conventional on, and high efficiency.

4.2 THE CROWBAR AND THE CHOPPER

The crowbar is a cost-effective structure to protect the back-to-back converter against high circulating currents during severe voltage dips. As has been shown previously, during a voltage dip, a transient voltage of high value is induced from stator to rotor circuit. This induced voltage leads to high currents on the rotor circuit.

To protect the structure, an alternative current path is created between the DFIG rotor and the RSC, as shown in Fig. 15.1. The main topologies to implement such path are shown in Fig. 15.19. As soon as a voltage dip is detected, drive signals

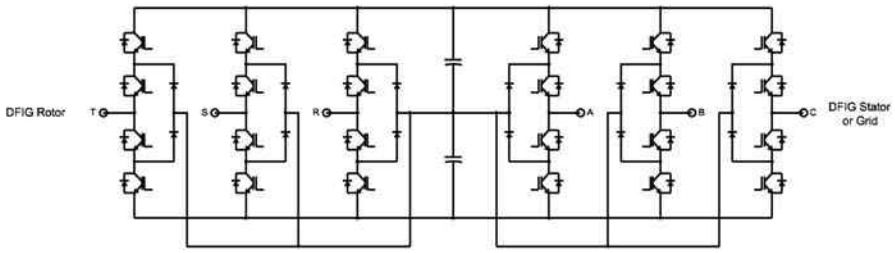


FIGURE 15.18

Neutral-point clamped converters in a back-to-back connection. *DFIG*, doubly fed induction generator.

Source: Author.

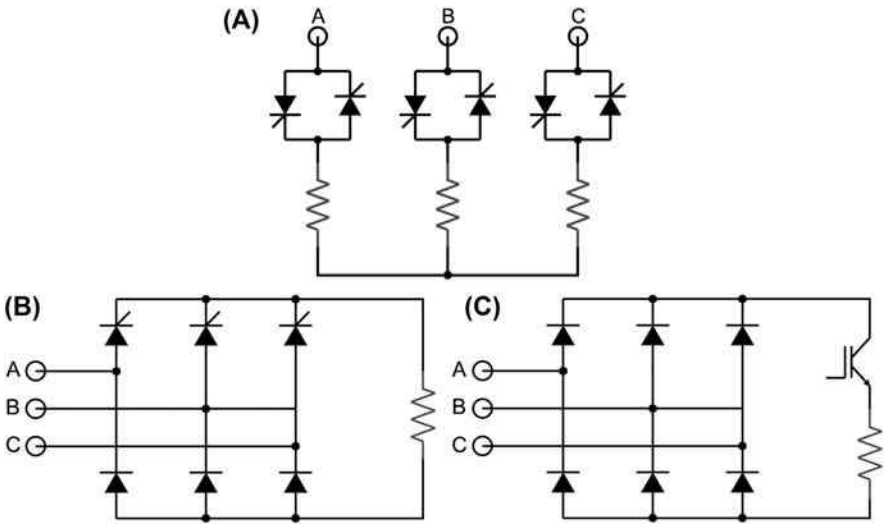


FIGURE 15.19

Topologies for crowbar implementation. (A) with SCR, (B) with SCR + Diodes, (C) with Diodes + IGBT.

Source: Author.

to RSC are turned off, and the crowbar is turned on. At the time the transient finishes, the crowbar is disconnected and the drive signals can be sent again to RSC [11]. The deactivation of the RSC is a drawback of this solution, because the DFIG loses its controllability [12].

Because of the fact that thyristors and diodes support well over current values, topologies (A) and (B) are more robust but are not fully controllable. The topology employing the insulated gate bipolar transistor (IGBT) is fully controllable (it turns on and off exactly with the drive signal), but is more sensitive to overcurrent and overvoltages.

The chopper, shown in Fig. 15.20, is required to protect the converter from overvoltages in the DC link. Such overvoltage can occur mainly during voltage dips. As the drive signals to RSC are cancelled, the converter acts as a diode bridge rectifier. If the voltage at crowbar terminals is greater than DC-voltage, the diode-bridge conducts, delivering power to the capacitor of the DC-link. If the capacitor voltage surpasses a safe limit, the chopper is triggered to discharge the capacitor.

4.3 NEW TRENDS/NOVEL STRUCTURES

The rated power of wind DFIG machines is increasing more and more. To deal with this new reality, novel solutions are being proposed. Matrix converters are being considered [13]; their main advantage is the absence of DC capacitors. Modular

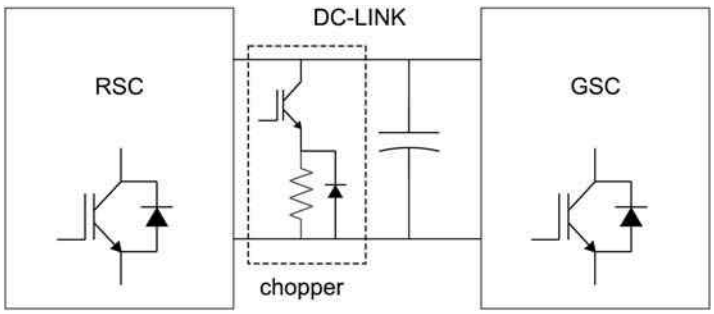


FIGURE 15.20

Chopper circuit. *GSC*, grid side converter; *RSC*, rotor side converter.

Source: Author.

multilevel converters are easy to implement and, using present devices, can process higher power [14]. Parallel connection of converters also can deliver more power in a modular way [13].

5. LOW-VOLTAGE RIDE-THROUGH

5.1 EFFECTS OF VOLTAGE DIP ON DOUBLY FED INDUCTION GENERATOR

As stated in the sections above, the voltage dip is a great issue for the DFIG to deal with. The converter is the most susceptible part of a DFIG-based WECS; hence, the major worries concern voltage dips supportability. The effects of a voltage dip without any countermeasure are tremendous. As in the study by Erlich, Wrede, and Feltes [15], an analysis of this phenomenon is evaluated in this condition. Fig. 15.21 presents the impact of an 80% voltage dip in the most important variables of DFIG—stator voltage; stator, rotor, and GSC currents; DC-link voltage; and stator power.

With the abrupt change in stator voltage, Fig. 15.21 shows that DC components increase the stator currents, as explained before. On the rotor side, these DC components appear as a high-frequency component surpassing the steady-state currents on this circuit. It could be noticed that the levels reached by the rotor currents are extremely higher than the nominal ones. This is unfeasible to deal because of converter switches limitations.

When these high currents flow into the converter, they cause the DC-link voltage to increase. Even if the capacitor is acting in inertia, it is not capable to considerably reduce this behavior on the voltage. Without other countermeasures, DC-link voltage can reach two times its rated value, which is far beyond capacitor and switch design limits.

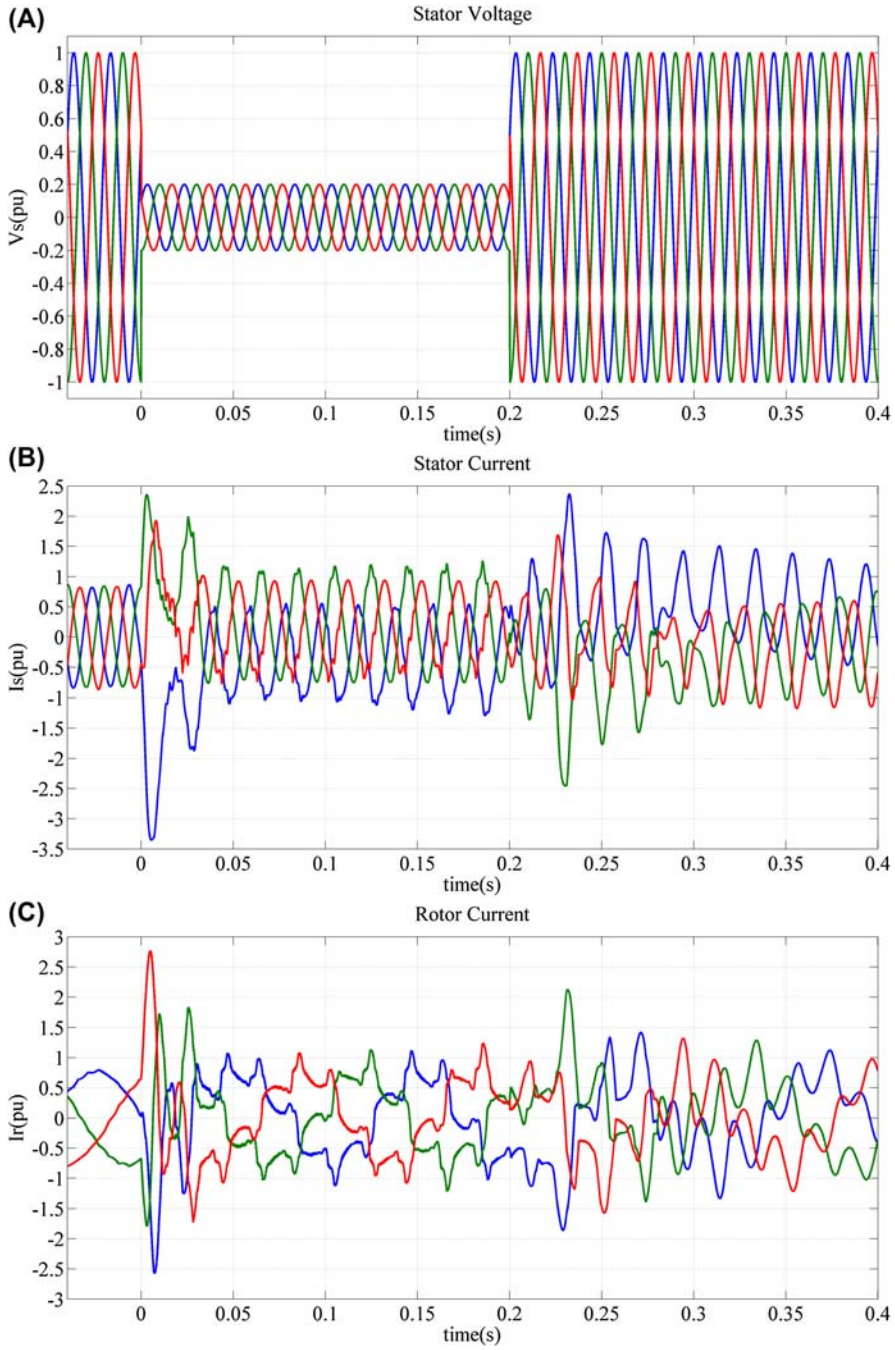


FIGURE 15.21

Effect of voltage dip on a doubly fed induction generator. (A) Stator voltage, (B) stator current, (C) rotor current, (D) GSC current, (E) DC-link voltage, (F) stator active and reactive power.

Source: Author.

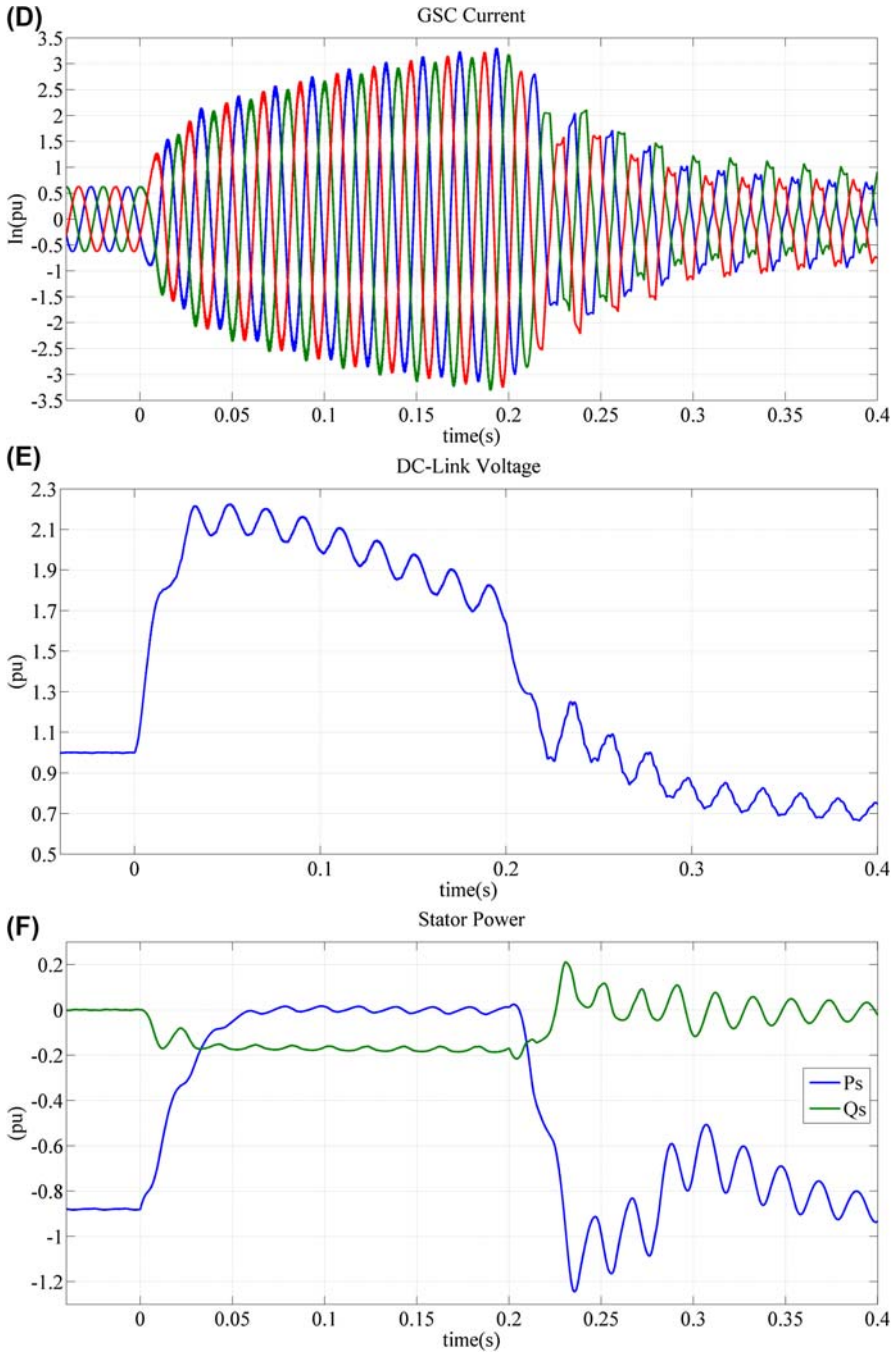


FIGURE 15.21 cont'd.

If there is no change in control operation, GSC will try to stabilize DC-link voltage. To do so, it will force currents far beyond switches' rated values, as shown in the figure. However, even with these attempts, DC-link voltage could not be controlled.

5.2 GRID CODE REQUIREMENTS

In the past, wind turbines were allowed to disconnect from the grid when faults occurred. They were considered as a large industrial load and were subjected to the same standards These requirements aim to protect the machine itself and prevent from islanding operation. Thus, the old codes allowed the disconnection during grid faults, which contributes to the dip.

Nowadays, because of the increasing penetration of these sources in electrical power system, national grid codes understand that they must contribute to the stability during these disturbances, as any other power source. For the proper operation of electrical power system, it is essential that all generators connected to the grid support and help to mitigate oscillations in voltage and frequency. A simultaneous disconnection of a large amount of wind turbines at the same time may collapse system stability in that region.

As stated before, the voltage dips are especially problematic to the WECS. Thus, there are specific requirements in each national grid code concerning wind turbines supportability during these faults, and the codes show the regions that the turbine shall still stay connected with. These regions are determined by the depth of the voltage dip and its duration [16]. IEC 61400−21 [17] states tests to be applied to a wind turbine, as detailed in Table 15.1.

Table 15.1 IEC 61400−21 Voltage Dip Tests

Case	Voltage Magnitude After the Dip (pu)	Positive Sequence Voltage Magnitude (pu)	Duration (s)
VD1—Three-phase symmetric voltage dip	0.90 ± 0.05	0.90 ± 0.05	0.50 ± 0.02
VD2—Three-phase symmetric voltage dip	0.50 ± 0.05	0.50 ± 0.05	0.50 ± 0.02
VD3—Three-phase symmetric voltage dip	0.20 ± 0.05	0.20 ± 0.05	0.20 ± 0.02
VD4—Phase−phase voltage dip	0.90 ± 0.05	0.95 ± 0.05	0.50 ± 0.02
VD5—Phase−phase voltage dip	0.50 ± 0.05	0.75 ± 0.05	0.50 ± 0.02
VD6—Phase−phase voltage dip	0.20 ± 0.05	0.60 ± 0.05	0.20 ± 0.02

Source: Author.

In addition, to help voltage restoration during a fault, some countries demand that WECS provide reactive power for the grid. Inserting reactive power, DFIG will operate with leading power factor and help the voltage to increase. Grid codes have, also, curves to determine the amount of reactive current to be injected, according to the voltage dip depth.

5.3 CROWBAR PROTECTION

In a general way, crowbar is a widely used device in power electronics circuit protection against overvoltages. In DFIG-based WECS, the term describes any device that provides an alternative path to the currents, diverting then from the RSC, through a low-resistance circuit. It is activated when any sign of a fault is detected, such as overcurrent in the rotor, low stator voltage, or overvoltage in the DC-link. The activation of Crowbar protection is temporary; it means during normal operation Crowbar is off, during a fault it is activated, and after the fault clearance it is turned off again.

The use of crowbar in wind turbines is reported even before the grid code requirements for WECS low-voltage ride-through. There are some variations in the implementation of this technology, as discussed before. However, because of its simplicity and as it is a well-known and reliable solution, it remains being the main solution in many wind farms all over the world.

Despite its wide-spread utilization, Crowbar presents some disadvantages. When it is activated, the machine is no longer controlled by the RSC—which means it lost control for this period. Also, the power system seems DFIG as a wound rotor machine with a high rotor resistance and a very high slip. This configuration consumes much reactive power from a grid already disturbed, making it even more difficult for the voltage to be restored. In addition, as crowbar is a resistance, much energy is wasted within its activation.

5.4 COMPLEMENTARY PROTECTION

5.4.1 Pitch Angle Control

One of the issues during a voltage dip is that the power cannot be delivered to the electrical grid. This method uses a control that regulates the angle between the blades and the wind force [18]. This way, the power extraction from the wind is reduced preventing major damages to the WECS. However, this variation in blade angles, especially in large turbines, demands much time compared with electrical transients.

This approach has been applied in almost every WECS as a solution for steady-state condition, together with another technique with faster response, which will act during the transient phase. The pitch angle control, alone, is not able to accomplish grid code requirements and protect DFIG system.

5.4.2 Chopper Circuit

To protect DC-link, the most common protection is the chopper circuit. It consists of a resistance in parallel with DC-bus capacitor, which is switched on when high

voltage is detected [19]. This resistance enables an alternative path to hazardous currents in the capacitor and regulates its voltage. Usually, chopper circuit is placed as a complementary circuit to the crowbar protection.

5.5 ALTERNATIVE SOLUTIONS

Because of the theme relevance, a great number of solutions were and are being proposed. Some of these solutions have already been well established and implemented on wind turbines, many others still need maturation and substantiation. In general, a comprehensive fault ride-through technique should pursue the following main goals:

- Minimize the voltage drop at the generator
- Divert or negate rotor overcurrent
- Produce appropriate power output during faults.

5.5.1 Control Strategies

Many works propose ride-through improvement by using control strategies of the rotor currents produced by the power electronic converter.

Some strategies inject currents by RSC to oppose natural and negative sequence components of magnetic flux [20], or in counterphase with stator currents [21], and thus limit the currents levels on the converter circuit. The great benefit of this kind of solution is that no additional hardware is used, which considerably reduces costs. However, these proposals still have to improve its current limitation and the reactive power consumption during the fault. Also, all these methods have a great dependence on machine parameters to adequate control operation, which in practice reduces reliability, once these parameters vary over time and cannot be ever precisely measured.

5.5.2 Hardware Solutions

Because of the great relevance of the fault supportability issue and the drawbacks of both crowbar solutions and control strategies, alternative hardware solutions have been proposed in literature. The idea behind these proposals is that if an external power electronic device is used to compensate the faulty grid voltage, any protection method in the DFIG system can be left out.

One of the most prominent solution is the Dynamic Voltage Restorer (DVR), which is a voltage source converter connected in series to the grid to correct faulty line voltages. There are several topologies for DVR implementation [22] and many works attest that this proposal is feasible as a protection for WECS, both in squirrel-cage generators [23] as in DFIG systems [24].

Lately, solutions applying superconductive materials have been proposed. These materials have singular characteristics of resistance and inductance change during fault conditions, which are used in DFIG benefit. Some of them implement Superconducting Magnetic Energy Storage to protect the whole wind farm [25] or in individual DFIG [26], others propose resistive Superconductor Fault Current Limiter placed in the point of connection between DFIG and the grid [27] or in the rotor

circuit [28]. However, the superconductor material needs a cryogenic system to operate and none of the proposals experimentally demonstrate its performance.

The disadvantages of any of these hardware solutions are the cost and the reduction of system reliability with the increase in the number of electronic devices, although, much research has been made on new proposals on topologies, technologies, and on their control to enhance DFIG performance during grid faults.

REFERENCES

[1] G.A. Smith, K.A. Nigim, Wind-energy recovery by a static Scherbius induction generator, IEE Proc. C 128 (6) (1981).

[2] R. Pena, J.C. Clare, G.M. Asher, Doubly fed induction generator using back-to-back PWM converters and its application to variable-speed wind-energy generation, IEE Proc.-Electr. Power Appl. 143 (3) (1996) 231−241.

[3] J.G. Slootweg, et al., General model for representing variable speed wind turbines in power system dynamics simulations, IEEE Trans. Power Syst. 18 (1) (2003) 144−151.

[4] R. Teodorescu, M. Liserre, P. Rodriguez, Grid Converters for Photovoltaic and Wind Power Systems, vol. 29, John Wiley & Sons, 2011.

[5] H. Polinder, et al., Trends in wind turbine generator systems, IEEE J. Emerg. Sel. Top. Power Electron. 1 (3) (2013) 174−185.

[6] P.C. Krause, O. Wasynczuk, S. Sudhoff, Analysis of Electric Machinery and Drive Systems, IEEE Press, 2002.

[7] A.E. Fitzgerald, et al., Electric Machinery, vol. 5, McGraw-Hill, New York, 2003.

[8] A. Petersson, Analysis, Modeling and Control of Doubly-Fed Induction Generators for Wind Turbines, Chalmers University of Technology, 2005.

[9] J.M. Carrasco, et al., Power-electronic systems for the grid integration of renewable energy sources: a survey, IEEE Trans. Ind. Electron. 53 (4) (2006) 1002−1016.

[10] M. Liserre, et al., Overview of multi-MW wind turbines and wind parks, IEEE Trans. Ind. Electron. 58 (4) (2011) 1081−1095.

[11] K.E. Okedu, et al., Wind farms fault ride through using DFIG with new protection scheme, IEEE Trans. Sustain. Energy 3 (2) (2012) 242−254.

[12] M. Benbouzid, S. Muyeen, F. Khoucha, An up-to-date review of low-voltage ride-through techniques for doubly-fed induction generator-based wind turbines, Int. J. Energy Convers. 3 (1) (2015) 1−9.

[13] V. Yaramasu, et al., High-power wind energy conversion systems: state-of-the-art and emerging technologies, Proc. IEEE 103 (5) (2015) 740−788.

[14] F. Blaabjerg, K. Ma, Future on power electronics for wind turbine systems, IEEE J. Emerg. Sel. Top. Power Electron. 1 (3) (2013) 139−152.

[15] I. Erlich, H. Wrede, C. Feltes, Dynamic behavior of DFIG-based wind turbines during grid faults, in: Power Conversion Conference-Nagoya, 2007. PCC'07, IEEE, 2007.

[16] M. Tsili, S. Papathanassiou, A review of grid code technical requirements for wind farms, IET Renew. Power Gener. 3 (3) (2009) 308−332.

[17] Standard, IEC 61400−61421, Measurement and Assessment of Power Quality of Grid Connected Wind Turbines, 2001.

[18] T. Senjyu, et al., Output power leveling of wind turbine generator for all operating regions by pitch angle control, IEEE Trans. Energy Convers. 21 (2) (2006) 467−475.

[19] G. Pannell, et al., Evaluation of the performance of a DC-link brake chopper as a DFIG low-voltage fault-ride-through device, IEEE Trans. Energy Convers. 28 (3) (2013) 535−542.
[20] S. Xiao, et al., An LVRT control strategy based on flux linkage tracking for DFIG-based WECS, IEEE Trans. Ind. Electron. 60 (7) (2013) 2820−2832.
[21] F.K.A. Lima, et al., Rotor voltage dynamics in the doubly fed induction generator during grid faults, IEEE Trans. Power Electron. 25 (1) (2010) 118−130.
[22] J.G. Nielsen, F. Blaabjerg, A detailed comparison of system topologies for dynamic voltage restorers, IEEE Trans. Ind. Appl. 41 (5) (2005) 1272−1280.
[23] D. Ramirez, et al., Low-voltage ride-through capability for wind generators based on dynamic voltage restorers, IEEE Trans. Energy Convers. 26 (1) (2011) 195−203.
[24] C. Wessels, F. Gebhardt, F.W. Fuchs, Fault ride-through of a DFIG wind turbine using a dynamic voltage restorer during symmetrical and asymmetrical grid faults, IEEE Trans. Power Electron. 26 (3) (2011) 807−815.
[25] A.M. Shiddiq Yunus, M.A.S. Masoum, A. Abu-Siada, Application of SMES to enhance the dynamic performance of DFIG during voltage sag and swell, IEEE Trans. Appl. Supercond. 22 (4) (2012) 5702009.
[26] W. Guo, L. Xiao, S. Dai, Enhancing low-voltage ride-through capability and smoothing output power of DFIG with a superconducting fault-current limiter−magnetic energy storage system, IEEE Trans. Energy Convers. 27 (2) (2012) 277−295.
[27] M.E. Elshiekh, D.-E.A. Mansour, A.M. Azmy, Improving fault ride-through capability of DFIG-based wind turbine using superconducting fault current limiter, IEEE Trans. Appl. Supercond. 23 (3) (2013) 5601204.
[28] F. Oliveira, et al., Enhancing LVRT of DFIG by using a superconducting current limiter on rotor circuit, Energies. 9 (1) (2015) 16.

CHAPTER

Modeling and Characterization of a Wind Turbine Emulator

16

Imene Yahyaoui[1], **Alvaro S. Cantero**[2]
University Carlos 3 of Madrid, Madrid, Spain[1]*; University of Valladolid, Valladolid, Spain*[2]

CHAPTER OUTLINE

1. Introduction **491**
2. Description and Qualities of Wind Energy **492**
2.1 Definition of Wind Energy 492
2.2 Main Components of the Wind Turbine 493
3. Types of Wind Turbines **494**
3.1 Vertical-Axis Wind Turbines 494
3.2 Horizontal-Axis Wind Turbines 495
4. Modeling of the Wind Turbine **495**
5. Principle of Wind Turbine Emulator **499**
5.1 Modeling and Simulation of the Wind Emulator 500
5.2 Mechanical Speed Control 502
6. Results and Interpretations **502**
7. Conclusion **507**
References **507**

1. INTRODUCTION

The intense industrialization of the last decades (1990–2010) and the multiplication of electric devices have led to a considerable increase in the needs of the electrical energy [1]. In response to this growing demand, industrialized countries have essentially relied on nuclear power plants. In fact, this energy source has the advantage of not to cause atmospheric pollution unlike thermal power stations; however, the risk of nuclear accidents, waste treatment, and landfilling are real problems that make this energy unattractive for future generations [2].

In view of these problems, and to limit the use of nuclear power plants, some countries have turned to new forms of renewable energy [3]. For instance, wind energy is not a substitute for conventional sources but complementary to the energy used. Indeed, the potential energy of the movement of air masses represents a consistent deposit of energy [4].

Advances in Renewable Energies and Power Technologies. https://doi.org/10.1016/B978-0-12-812959-3.00016-2
Copyright © 2018 Elsevier Inc. All rights reserved.

Since the use of the windmill, the technology of wind turbines is being enhanced [4]. It was in the early 1940s that real prototypes of wind turbines with blade profiles have successfully been used to generate electricity. In this sense, several technologies are used to capture wind energy (vertical- or horizontal-axis sensor) [5]. In addition to the mechanical properties of the wind turbine, the conversion efficiency of mechanical energy into electrical energy is very important [4,5]. Indeed, synchronous and asynchronous machines are used for this purpose [6]. The control of these machines and their possible interfaces to the network must make a maximum of energy over a widest possible range of wind speed variation possible to be extracted, in such a way to improve the profitability of wind power installations.

The spread of the use of wind turbines has led researchers in electrical engineering to study how to improve the efficiency of the electromechanical conversion and quality of energy supplied by wind turbines. In this context, this chapter focuses on the realization of wind turbine emulators. This is based on DC motors, which are controlled to reproduce the mechanical behavior of wind turbines. This allows to study the behavior of wind turbines following the weather condition variations, in particular, the wind speed. Thus, the chapter is organized as follows: after the introduction, the second section is concerned with the definition of the wind energy. The third section deals with the types of wind turbines. The modeling of the wind turbine is studied in depth in Section 4. Section 5 presents the principle of the wind turbine emulator. Finally, Section 6 summarizes the simulation results.

2. DESCRIPTION AND QUALITIES OF WIND ENERGY

2.1 DEFINITION OF WIND ENERGY

A wind turbine is a device that transforms a part of the kinetic energy of the wind (fluid in motion) into available mechanical energy on a transmission shaft and then into electrical energy via a generator [7] (Fig. 16.1). In fact, wind energy is a nondegraded renewable energy, is geographically diffuse, and is in correlation with the season (electric power is much more demanded in winter, and it is often during this period that the average wind speed is high). Furthermore, it produces

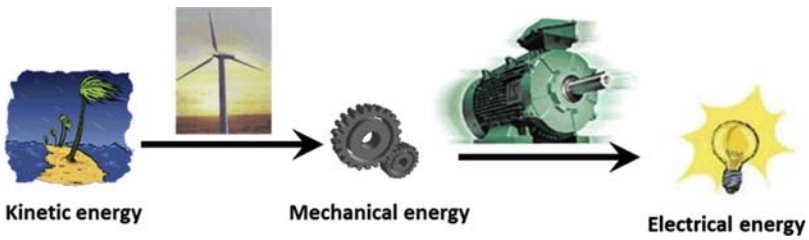


FIGURE 16.1

Energy conversion: from kinetic to electrical energy.

no atmospheric discharge or radioactive waste [6,7]. However, it is random in time, and its capture remains complex and requires large masts and blades (up to 60 m for several megawatts) in clear areas to avoid turbulence [8].

The materials required for the manufacture of wind turbine elements (nacelle, blades, and multiplier) must be technologically advanced and are therefore expensive. The installations can be carried out not only on land but also increasingly at sea (offshore wind farms), where the presence of wind is more regular. Wind turbines are thus less visible and cause less noise nuisance [9].

In addition to the visual aspect of wind turbines, their impact on the environment is reduced: a very small rate of the total area of the site on which it is located is used by the wind turbine, which allows the sites to retain their industrial or agricultural activities [9]. Their noise pollution is also relatively low. Indeed, the level sound of a wind turbine is 50 dB at 150 m and becomes imperceptible beyond 400 m.

The criteria for choosing a wind farm are based on several conditions. In particular, the efficiency of a wind turbine depends on its location. This is strongly related to the constancy of speed and the direction of wind [9]. Indeed, the wind speed must be acceptable and contained in the area where the wind turbine operates properly and without fear of destruction [10,11]. In addition, the axis of rotation of the wind turbine must be maintained, as far as possible, parallel to the wind direction to obtain an optimal efficiency. In this sense, offshore facilities are very responsive because of the constant wind speed, and these sites are much more windy and the mechanical stresses are much lower [12,13]. In addition, the accessibility to the electricity network is a very important criterion because the network connected to the wind turbines must be able to support the energy produced [12,13].

The wind turbines are generally divided into three categories, according to their nominal power: small power wind turbines ($<$40 KW), medium-power wind turbines (40$-$1 MW), and high-power wind turbines ($>$1 MW) [14,15].

2.2 MAIN COMPONENTS OF THE WIND TURBINE

There are several possible configurations of wind turbines. However, a conventional wind turbine consists generally of three main elements: first, the mast, which is a steel tube or a wire mesh, used to avoid disturbances near the ground. However, the amount of material implementation is a nonnegligible cost and the weight must be limited. Therefore, a compromise consists in taking a mast of a size slightly greater than the diameter of the wind turbine rotor [16,17].

The second element of a wind turbine is the nacelle, which brings together all the mechanical elements allowing to couple the wind turbine's electric generator: slow and fast shafts, bearings, and multiplier. The disc brake, which is different from the aerodynamic brake, makes stopping the system in case of possible overloading. The generator which is generally composed of a synchronous or asynchronous machine and hydraulic or electric steering of the blades (aerodynamic brake) and the nacelle

(necessary to keep the surface swept by the wind turbine perpendicular to the wind direction) in addition to the air or water cooling system, anemometer, and the electronic system of the wind turbine management [18,19].

The rotor is formed by the blades assembled in their hub. For wind turbines, the number of blades typically varies from 1 to 3, the three-bladed rotor (Danish concept) being by far the most widespread because it represents a good compromise between the cost, vibration behavior, visual pollution, and noise [18].

Fixed speed rotors are often equipped with a blade orientation system, allowing the generator (usually an asynchronous squirrel-cage machine) to operate on the synchronism and to be connected directly to the network without power electronics device. This system combines simplicity and low cost [19].

However, variable speed rotors are often less expensive because the steering device of the blades is simplified or deleted. However, a power electronics interface between the generator and the network or load is required. The blades are characterized mainly by their geometry, which will depend on the aerodynamic performance and materials (currently, composite materials such as glass, and more recently carbon fibers are used much because they combine lightness and good mechanical resistance) [9].

3. TYPES OF WIND TURBINES

There are two types of wind turbines: vertical-axis and horizontal-axis wind turbines, which are detailed in the following sections.

3.1 VERTICAL-AXIS WIND TURBINES

This type of wind turbine has been the subject of much research. It has the advantage of not requiring a system for orienting the blades and possessing a mechanical part (multiplier and generator) at the ground, therefore facilitating the operations of maintenance. On the other hand, some of these wind turbines must be trained at start-up, which represents a drawback for the mat, because it receives strong mechanical constraints, making these types of wind turbines abandoned by manufacturers (except for the low power) in favor of horizontal-axis wind turbines [5].

Vertical-axis wind turbines were the first structures developed to produce the electricity, paradoxically in contradiction with the traditional windmill with horizontal axis. They have the advantage of having the control members and the generator at the ground level, which make them so easily accessible. Many variants have been tested since the 1920s, and many of them have been unsuccessful, but two structures have been well industrialized [5]:

- The Savonius rotor (named after its inventor) in which operation is based on the principle of "differential drag" used in anemometers: the efforts exerted by the faces of a hollow body are of different intensity, which then generates a motor torque making the assembly to rotate. The effect is reinforced by the circulation of air between two half-cylinders, which increase the motor torque [20].

- The cyclically variable wind turbines with the most widespread structure being that of Darrieus (French engineer who filed the patent in the early 1930s). Their operation is based on the fact that a profile placed in airflow according to different angles is subjected to forces with variable direction and intensity, which generates a motor torque causing the rotation of the device [21]. These forces are created by the combination of the proper displacement speed of the profile and the wind speed. This means that the rotation of the device cannot start on its own. When it is stationary, the wind turbine must be launched by an ancillary device (use of the generator as a motor, for example).

Although some major industrial projects have been carried out, vertical-axis wind turbines remain marginal and little used and currently abandoned. Indeed, the presence of the energy sensor near the ground exposes it to turbulence and wind gradient, which reduces its effectiveness. They are also exposed to aeroelasticity problems due to constraints they undergo. Finally, the surface they occupy on the ground is very important for high powers [22].

3.2 HORIZONTAL-AXIS WIND TURBINES

Horizontal-axis wind turbines are much more widely used, even if it requires a mechanism for orienting the blades. This type of aero generators is characterized by a higher aerodynamic yield than the vertical one. Moreover, it starts autonomously and has low elements at the ground level [23].

Indeed, horizontal-axis wind turbines are based on the ancestral wind. They are made up of several blades that are aerodynamically shaped like airplane wings. In this case, lift is not used to maintain an aircraft in flight, but for generating a driving torque causing rotation. The number of blades used for electric power generation typically varies between 1 and 3; with three blades, there is a compromise between the power coefficient, the cost, and the speed of rotation of the wind sensor [23]. This type of wind turbine has gained the upper hand over those with vertical. Moreover, they are less expensive and less exposed to mechanical stresses, and the position of the receiver at several tens of meters of the ground favors the efficiency. In this study, we will consider the case of horizontal-axis wind turbines, for the advantages listed earlier [23].

4. MODELING OF THE WIND TURBINE

Wind energy comes from the kinetic energy of the wind. If we consider an air column of length dl and density ρ, moving with a velocity V_1, the kinetic energy dE of this column is given by Eq. (16.1) [24]:

$$dE = \frac{\ell S_1 V_1^2 dl}{2} \tag{16.1}$$

By replacing dl with $V_1\,dt$, we obtain the expression of the wind power before the wind turbine P_m [24]:

$$P_m = \frac{\ell S_1 V_1^3}{2} \tag{16.2}$$

Let V_1 be the wind velocity before passing the turbine and V_2 the velocity after passing (Fig. 16.2). The wind speed across the turbine is the average of the two speeds. Thus, the mass m of an air column, having a density ℓ and of section S_1, passing through the surface of the blades is given by Eq. (16.3) [24]:

$$m = \frac{\ell S_1 (V_1 + V_2)}{2} \tag{16.3}$$

The extracted power P_{aer} is expressed by half the product of the mass and the decrease of the wind speed (Newton's second law). It is given by the following expression (16.4):

$$P_{aer} = \frac{m\left(V_1^2 - V_2^2\right)}{2} \tag{16.4}$$

By replacing m by its expression, given by Eq. (16.3), in Eq. (16.4), we obtain:

$$P_{aer} = \frac{\ell S_1 (v_1 + v_2)\left(v_1^2 - v_2^2\right)}{4} \tag{16.5}$$

The ratio between the power extracted from the wind and the kinetic power is given by Eq. (16.6):

$$\frac{P_{aer}}{P_m} = \frac{\left(1 + \left(\frac{v_1}{v_2}\right)\right)\left(1 - \left(\frac{v_1}{v_2}\right)^2\right)}{2} \tag{16.6}$$

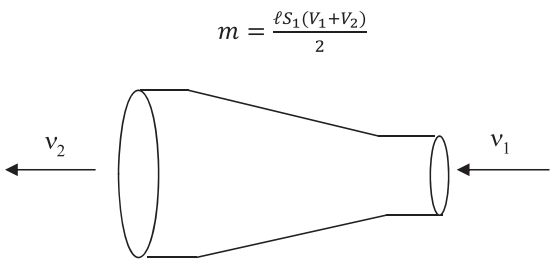


FIGURE 16.2

Diagram showing the variation of the wind speed before and after passage through the wind turbine.

This ratio is known as the power coefficient or Betz C_p coefficient. The characteristic corresponding to Eq. (16.6) is given by Fig. 16.3.

The power coefficient characteristic has a maximum, which is the image of the maximum ratio between the power extracted from the wind and the power before passing by the wind turbine. Indeed, this coefficient explains the fact that a wind turbine allows to recover only a part of the wind power because the flow cannot have a zero speed after its passage through the turbine (otherwise, this would means to "stopping the wind").

For a given wind velocity, we want the power supplied to be maximum, which corresponds to an optimum value of λ_1, giving the maximum coefficient of Betz. The curve giving $C_p(\lambda_1)$ does not exceed a maximum equal to 0.59: this is the limit of Betz.

In this study, we have chosen to model a 1.5-kW wind turbine. It is a three-bladed wind turbine with a radius of 1.5 m. To simulate the behavior of the wind turbine, it is necessary to determine the torque that the latter exerts on the mechanical shaft. Indeed, the aerodynamic power P_{aer} is given by the expression (16.7):

$$P_{aer} = \frac{P_{aer}}{P_m} P_m = C_p(\lambda_1) P_m \tag{16.7}$$

By replacing P_m with its expression given by Eq. (16.2), P_{aer} becomes:

$$P_{aer} = \frac{1}{2} C_p(\lambda_1) \ell S_1 v_2^3 \tag{16.8}$$

For small power wind turbines, the wind direction is characterized by an angle θ called angle of attack, which is the angle that the wind direction makes with the rotation axis of the wind turbine rotor [3]. Then, v_2 can be expressed by:

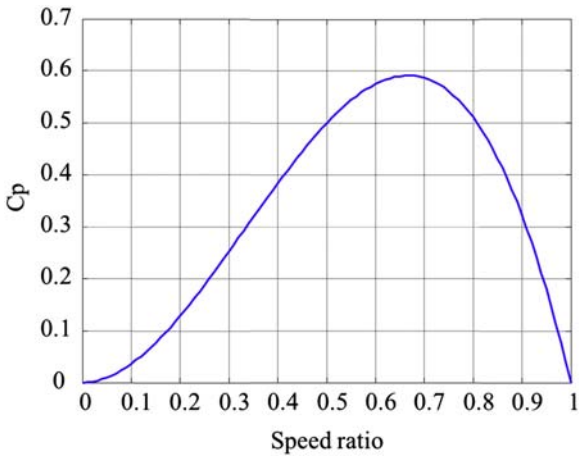


FIGURE 16.3

Power coefficient versus the speed ratio v_1/v_2.

$$v_2 = v_2 \cos\theta \tag{16.9}$$

The aerodynamic power then becomes:

$$P_{aer} = \frac{1}{2}\ell S_1 c_p(\lambda_1) v_2^3 \cos\theta^3 \tag{16.10}$$

Thus, the power supplied is a function of the cube of the wind speed, which is why the sites are first chosen according to the wind speed. The aerodynamic torque is therefore given by Eq. (16.11):

$$C_{aer} = \frac{1}{2}\ell S_1\, c_p(\lambda_1) R \frac{v_2^2}{\lambda_1}\cos^3\theta \tag{16.11}$$

Several types of the power coefficient modeling can be found in the literature. These models are often valid for a specific wind turbine. Nevertheless, the pattern of curve networks is generally the same and the modeling handicap can be lifted. For the modeling of the aerodynamic pair, we adopt the expression given by Eqs. (16.12) and (16.13) [24].

$$C_p(\lambda_1, ß) = 0.5176\left[\frac{116}{\lambda_i} - 0.4ß - 5\right]e^{\frac{-21}{\lambda_i}}0.0068\lambda_1 \tag{16.12}$$

$$\frac{1}{\lambda_i} = \frac{1}{\lambda_1 + 0.08ß} - \frac{0.0035}{ß^3 + 1} \tag{16.13}$$

Indeed, Eq. (16.12) is used in the polynomial form (Eq. 16.14) and presented in Fig. 16.4:

$$C_p(\lambda_1) = a_5\lambda_1^5 + a_4\lambda_1^4 + a_3\lambda_1^3 + a_2 9410^{-3}\lambda_1^2 + a_1\lambda_1 + a_0 \tag{16.14}$$

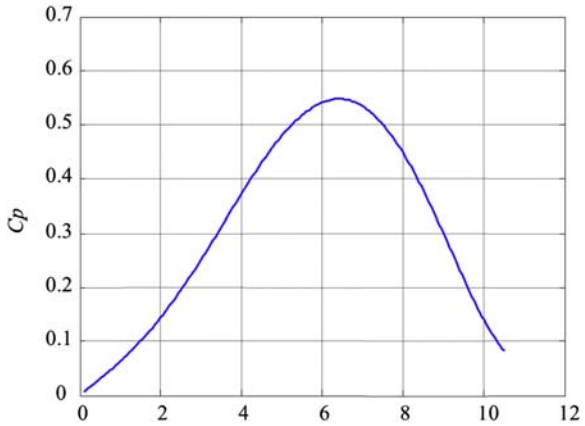


FIGURE 16.4

Betz coefficient using the polynomial representation.

$$C_{aer} = \frac{1}{2}\frac{C_p(\lambda_1)}{\lambda_1}\ell RS\,{}_1v_2^2(\cos\theta)^3 \tag{16.15}$$

The curve characteristics of the mechanical torque as a function of the mechanical angular velocity of the turbine for different wind speed values and for a zero pitch angle (β) give the results presented in Fig. 16.5.

5. PRINCIPLE OF WIND TURBINE EMULATOR

The principle of the wind emulator consists in calculating, for a given wind speed, the desired speed, which is the wind torque image. The comparison of this speed to the measured speed of the DC motor allows the PWM signal, input of the chopper feeding the DC motor through a PI controller, to be generated.

A control loop makes it possible to adopt, at each iteration, the voltage control of the DC motor armature. The possibility of disturbances making the wind not constant can occur and causes fluctuations. This is why we have also modeled the dynamic behavior of the wind by a transfer function [24].

$$\Theta(v_2) = a_5v_2^5 + a_4v_2^4 + a_3v_3^3 + a_2v_2^2 + a_1v_2 + a_0 \tag{16.16}$$

$$H(p) = \frac{1}{1.3p^2 + p + 1} \tag{16.17}$$

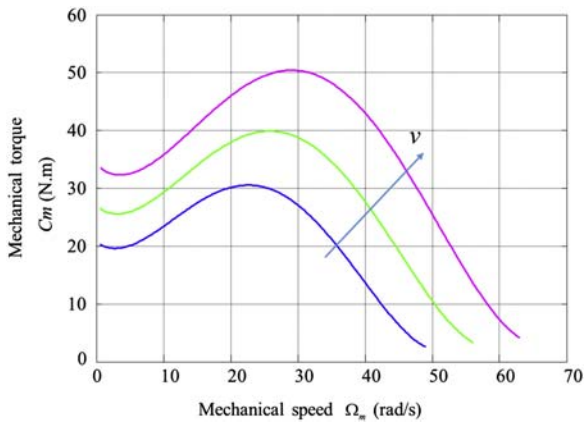


FIGURE 16.5

Mechanical torque versus mechanical speed for different wind speed values v_2.

5.1 MODELING AND SIMULATION OF THE WIND EMULATOR

An essential step for the implementation of the wind turbine emulator is to study its behavior in both steady state and transient regime. To do this, we proceed to the first step of our work to model the global chain of the emulator (wind turbine model and DC motor). In fact, the DC motor is the simplest machine to control, which requires only choppers or rectifiers (Fig. 16.6).

In this study, the DC motor model with a separate excitation is considered. Therefore, the inductor flux φ_f is constant (Eq. 16.18).

$$\Phi_f = K_\Phi i_f \tag{16.18}$$

At the terminals of the armature:

$$U_a = R_a i_a + L_a \frac{di_a}{dt} + E \tag{16.19}$$

where

$$E = K_\Phi \Omega_m \tag{16.20}$$

K_Φ, the torque.

The armature current evolution is given by Eq. (16.21):

$$\frac{di_a}{dt} = \frac{1}{L_a}(U_a - R_a i_a - K_\Phi \Omega_m) \tag{16.21}$$

At the terminals of the inductor, the voltage U_f is constant, consequently, I_f is constant and is equal to (16.22):

$$I_f = \frac{U_f}{R_f} \tag{16.22}$$

The slow dynamics of the DC motor is governed by Eq. (16.23):

$$J\frac{d\Omega_m}{dt} + f\Omega_m = C_m - C_r \tag{16.23}$$

where f, the friction; C_r, the resistant torque.

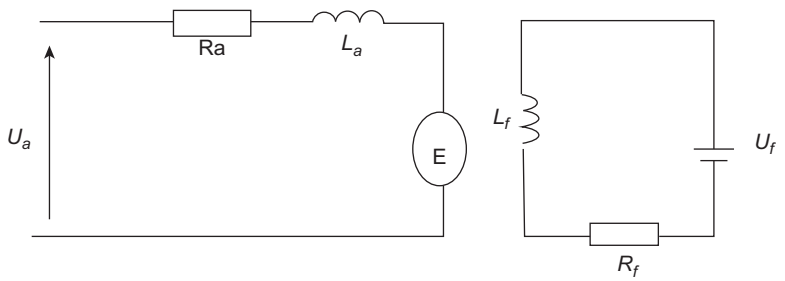


FIGURE 16.6

Simplified schema of a DC motor.

The mechanical torque C_m is given by:

$$C_m = K_\Phi i_a \tag{16.24}$$

The command adopted is a voltage control of the armature. Eqs. (16.21) and (16.23) are represented in the space state by:

$$\left[\dot{X}\right] = [\mathrm{A}][\mathrm{X}] + [\mathrm{B}]\mathrm{U} + [\mathrm{C}]\mathrm{W} \tag{16.25}$$

where

$$[\mathrm{X}] = [i_a\ \Omega]^t; \quad [\mathrm{A}] = \begin{bmatrix} \frac{-R_a}{L_a} & \frac{-K_\Phi}{L_a} \\ \frac{K_\Phi}{J} & \frac{-f}{J} \end{bmatrix}; \quad [\mathrm{B}] = \begin{bmatrix} \frac{1}{L_a} \\ 0 \end{bmatrix}; \quad \mathrm{U} = U_a; \quad [\mathrm{C}] = \begin{bmatrix} 0 \\ \frac{-1}{J} \end{bmatrix}; \quad \mathrm{W} = C_r$$

$$pi_a = \frac{1}{L_a}(U_a - R_a i_a - K_\Phi \Omega_m) \tag{16.26}$$

$$p\Omega_m = \frac{1}{J}(C_m - C_r - f\Omega_m) \tag{16.27}$$

$$i_a = \frac{U_a - K\Omega_m}{R_a + L_a p} \tag{16.28}$$

$$\Omega_m = \frac{KI_a - C_r}{Jp + f} \tag{16.29}$$

The direct current motor can thus be expressed by a second-order linear system having for control and disturbing inputs, respectively, U_a and C_r and for output the mechanical speed Ω_m.

The open-loop transfer function of the DC motor is given by:

$$H_0(p) = \frac{K_\Phi}{fR_a + K_\Phi^2} \Bigg/ \left(\frac{JL_a}{fR_a + K_\Phi^2} p^2 + \frac{(R_a J + fL_a)}{fR_a + K_\Phi^2} p + 1 \right) \tag{16.30}$$

It can be written as a function of the electrical constant τ_e and the mechanical constant τ_m. The function is given by Eq. (16.31):

$$H_0(p) = \frac{K}{(1 + \tau_e p)(1 + \tau_m p)} \tag{16.31}$$

5.2 MECHANICAL SPEED CONTROL

To have the same rotational speed as that of the wind turbine, a PI regulator is used, which makes it possible to generate the voltage and must be injected into the DC motor armature. Thus, the PI regulator is chosen since the proportional acts on the speed and the integrator decreases on the static error. The regulator $R(p)$ is given by Eq. (16.32):

$$R(p) = K_p + \frac{K_i}{p} = K_p\left(\frac{1+\tau_p}{\tau_p}\right) \tag{16.32}$$

6. RESULTS AND INTERPRETATIONS

In this paragraph, the principle of the emulator using Matlab®-Simulink is presented (Fig. 16.7), followed by the simulation results.

The mechanical speed of the corresponding turbine at a wind speed of 7 m/s is equal to 39.14 rad/s. This is shown in Figs. 16.8–16.12.

Fig. 16.8 shows the mechanical reference velocity and the steady-state velocity and shows that they coincide.

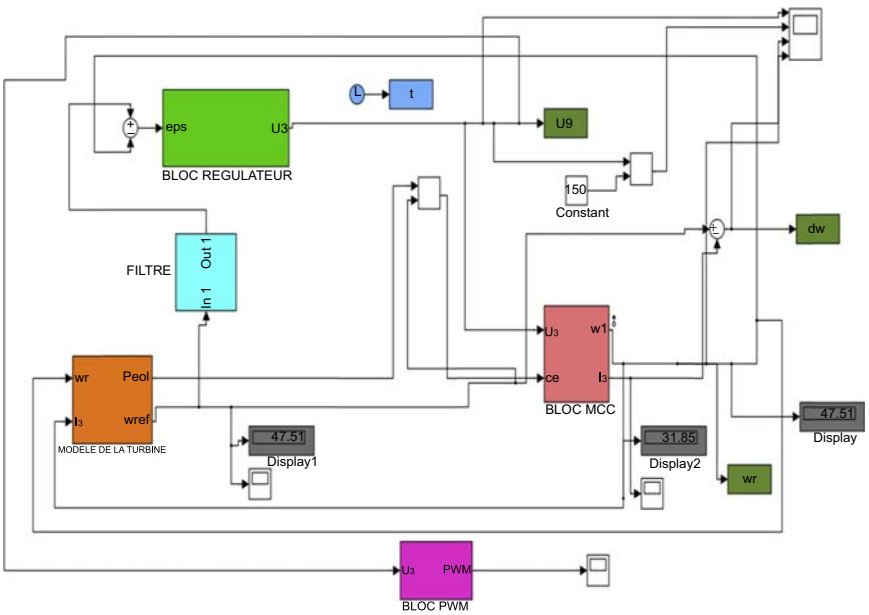


FIGURE 16.7

Schema of the emulator simulation.

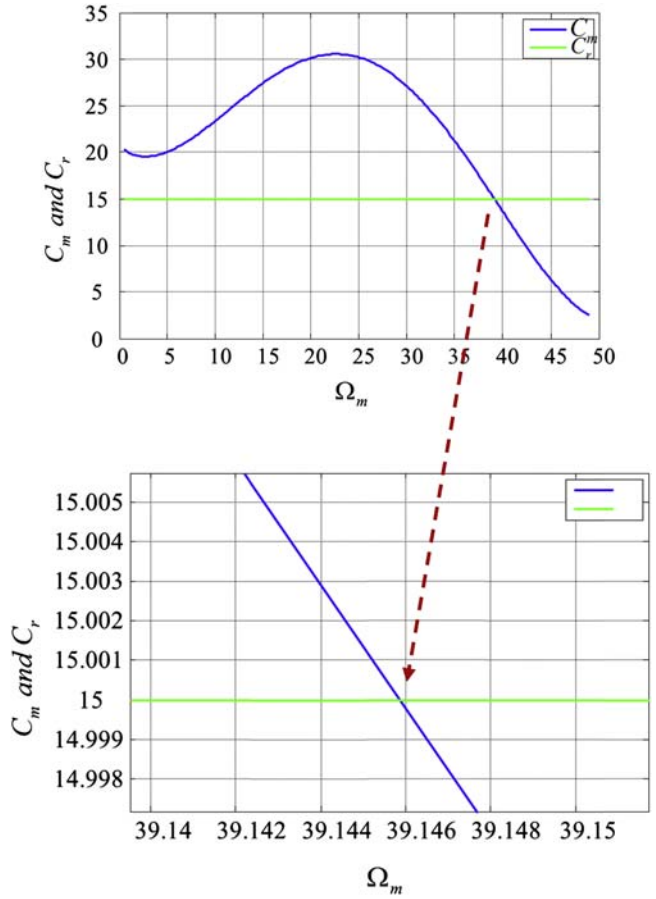


FIGURE 16.8

Diagram showing the mechanical torque C_m at the resistive torque C_r as a function of the mechanical speed Ω_m for $V_2 = 7$ m/s.

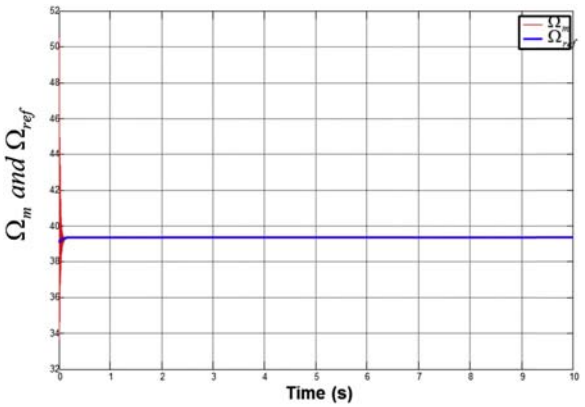


FIGURE 16.9

Reference and measured mechanical speed.

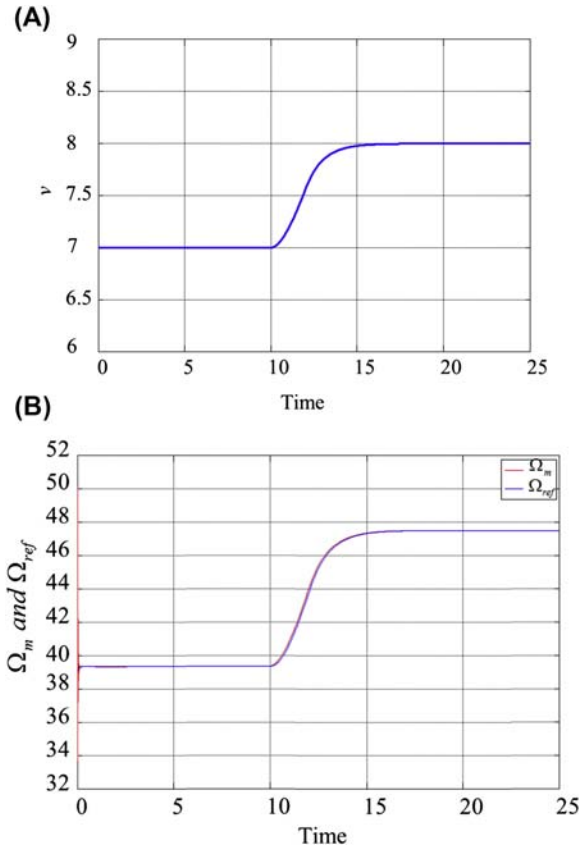


FIGURE 16.10

Simulation results in dynamic system.

By applying a wind speed step from 7 to 8 m/s, the mechanical reference velocity and the regulated velocity are similar. This confirms the efficiency of the PI regulator used.

Fig. 16.10B shows the turbine speed following the application of a wind step from 7 to 8 m/s (Fig. 16.10A). It is shown that the rotation speed of the DC motor follows the turbine rotation speed, which is considered as reference speed.

Fig.16.10C gives the armature current I_a as a function of time. The simulation results show that the current is proportional to the torque of the wind turbine (Fig.16.10D). Indeed, by varying the wind speed at constant torque, the armature current remains virtually constant according to Eq. (16.28).

The application of a wind speed step from 7 to 8 m/s produces a voltage variation U_a of the DC armature (see Fig. 16.10E). This variation, compared with a triangular

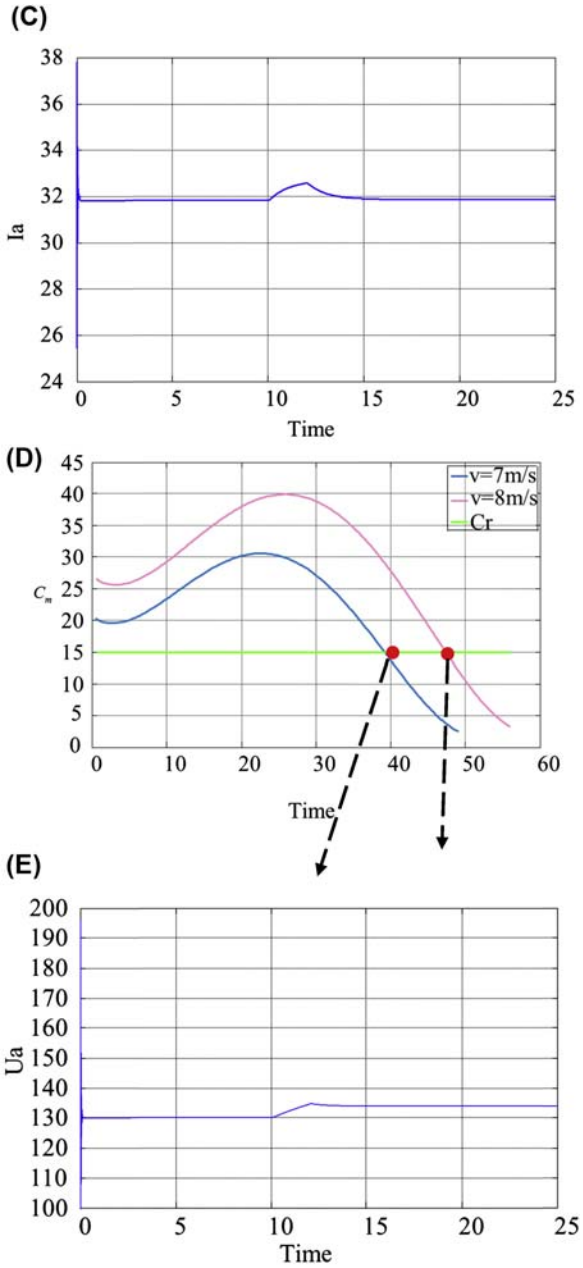


FIGURE 16.10 cont'd.

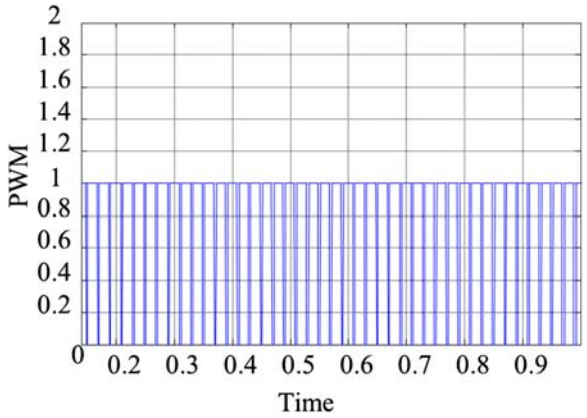


FIGURE 16.11

Pulse width modulation (PWM) signal as a function of time.

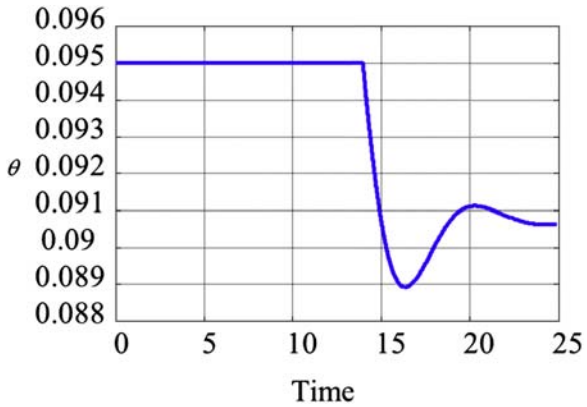


FIGURE 16.12

Angle of attack θ as a function of time following a wind step.

signal, gives the signal PWM, which, applied to the input of the chopper feeding the armature of the DC motor is given by Fig. 16.11.

The variation of the angle of attack at a step of wind speed v_2 taking into account the static and dynamic behavior of the wind shows that this angle decreases as the wind speed increases; this confirms the influence of the angle in small wind turbines. The angle of attack is illustrated in Fig. 16.12.

7. CONCLUSION

In 2000−17 there has been increasing interest in improving energy production based on renewable energy sources. Wind energy is one of the most important renewable sources, for its advantages of being nonpolluting, reliable, and not too expensive.

Difficulties in controlling weather lead researchers in the wind energy fields to carry out simulators on which the tests will be easier. In this study, a wind turbine emulator is tested by simulation using a DC motor that reproduced exactly the behavior of a small power wind turbine. The control of the DC motor has been tested dynamically by changing the wind speed.

REFERENCES

[1] P. Fan, Z. Ouyang, C. Basnou, J. Pino, H. Park, J. Chen, Nature-based solutions for urban landscapes under post-industrialization and globalization: Barcelona versus Shanghai, Environ. Res. 156 (2017) 272−283.

[2] G.J. Youinou, Powering sustainable low-carbon economies: some facts and figures, Renew. Sustain. Energy Rev. 53 (2016) 1626−1633.

[3] V. Khare, S. Nema, P. Baredar, Solar−wind hybrid renewable energy system: a review, Renew. Sustain. Energy Rev. 58 (2016) 23−33.

[4] J.S. González, R. Lacal-Arántegui, A review of regulatory framework for wind energy in European Union countries: current state and expected developments, Renew. Sustain. Energy Rev. 56 (2016) 588−602.

[5] A.E. Craig, J.O. Dabiri, J.R. Koseff, Low order physical models of vertical axis wind turbines, J. Renew. Sustain. Energy 9 (1) (2017), 013306.

[6] C. Carunaiselvane, T.R. Chelliah, Present trends and future prospects of asynchronous machines in renewable energy systems, Renew. Sustain. Energy Rev. 74 (2017) 1028−1041.

[7] D. Grieve, U.S. Patent No. 9,410,534, U.S. Patent and Trademark Office, Washington, DC, 2016.

[8] B.K. Kirke, B. Paillard, Predicted and measured performance of a vertical axis wind turbine with passive variable pitch compared to fixed pitch, Wind Eng. 41 (1) (2017) 74−90.

[9] R. Pillai, S. Narayanan, G. Swindale, Benefits and Challenges of a Grid Coupled Wound Rotor Synchronous Generator in a Wind Turbine Application, 2016. Technical Information from Cummins Generator Technologies, Issue number: WP102. Last visited.

[10] N.J. Stone, A Synthesis of Approaches for Wind Turbine Amplitude Modulation Data Analysis, 2016.

[11] W. La Cava, K. Danai, L. Spector, P. Fleming, A. Wright, M. Lackner, Automatic identification of wind turbine models using evolutionary multiobjective optimization, Renew. Energy 87 (2016) 892−902.

[12] M. Strach-Sonsalla, M. Stammler, J. Wenske, J. Jonkman, F. Vorpahl, Offshore wind energy, in: Springer Handbook of Ocean Engineering, Springer International Publishing, 2016, pp. 1267−1286.

[13] J. Abiassi, U.S. Patent No. 9,476,409, U.S. Patent and Trademark Office, Washington, DC, 2016.

[14] S.A. Jafari, S. Hassanli, K.C. Kwok, Performance analysis of a small wind turbine mounted inside a tall building, in: 18th Australasian Wind Engineering Society Workshop, July 6−8, 2016, Serafino Convention Centre, McLaren Vale, South Australia, Australia, July 2016.
[15] P. Maguire, Impact of Averaging Period on a Medium-Scale Wind Turbine Power Curve and Prediction of Annual Energy Production, 2016. Doctoral dissertation, Kalamazoo College).
[16] F.P.G. Márquez, J.M.P. Pérez, A.P. Marugán, M. Papaelias, Identification of critical components of wind turbines using FTA over the time, Renew. Energy 87 (2016) 869−883.
[17] T. Pahn, R. Rolfes, J. Jonkman, Inverse load calculation procedure for offshore wind turbines and application to a 5-MW wind turbine support structure, Wind Energy 20 (2017).
[18] M. Mooney, G. Maclaurin, Transportation of Large Wind Components: A Review of Existing Geospatial Data (No. NREL/TP-6A20-67014), NREL (National Renewable Energy Laboratory (NREL), Golden, CO (United States), 2016.
[19] E. Hao, C. Liu, Evaluation and comparison of anti-impact performance to offshore wind turbine foundations: Monopile, tripod, and jacket, Ocean. Eng. 130 (2017) 218−227.
[20] S.C. Goh, S.R. Boopathy, C. Krishnaswami, J.U. Schlüter, Tow testing of Savonius wind turbine above a bluff body complemented by CFD simulation, Renew. Energy 87 (2016) 332−345.
[21] F. Balduzzi, A. Bianchini, R. Maleci, G. Ferrara, L. Ferrari, Critical issues in the CFD simulation of Darrieus wind turbines, Renew. Energy 85 (2016) 419−435.
[22] D.B. Araya, T. Colonius, J.O. Dabiri, Transition to bluff-body dynamics in the wake of vertical-axis wind turbines, J. Fluid Mech. 813 (2017) 346−381.
[23] X. Liu, C. Lu, S. Liang, A. Godbole, Y. Chen, Vibration-induced aerodynamic loads on large horizontal axis wind turbine blades, Appl. Energy 185 (2017) 1109−1119.
[24] T. Ouyang, A. Kusiak, Y. He, Modeling wind-turbine power curve: a data partitioning and mining approach, Renew. Energy 102 (2017) 1−8.

Index

'*Note*: Page numbers followed by "f" indicate figures and "t" indicate tables.'

A

Absorber efficiency, 376, 377f
Absorption coefficient alpha, 14, 14f
AC electrical pots, 417–418
AC load prediction, 280
Active power balance, 438–439
Aero generators, 495
Aggregation, 122
Agrivoltaic production approach, 296
Air pollution, 406
Albedo, 380
Alternative current (AC), 297
Ambient temperature, 271
Anaerobic digesters biogas, 405
Analytical hierarchy process (AHP), 61–62
Angle of incidence, 320
Annual energy balance, 299
Annual solar-to-electricity efficiency, 386, 390f
Antireflection coating, 30–32, 33f
Arrays, 240–243
Artificial neural networks (ANNs), 102–103, 103f, 118
Astronomical Unit (UA), 378
Auger recombination, 12
Automatic supervision strategies, 237–240
Autoregressive integrated moving-average (ARIMA) model, 102
Autoregressive moving-average (ARMA) model, 101–102
Azimuthal, 321f

B

Band impurity band Shockley–Read–Hall non-radiative recombination, 12
Band to band radiative recombination, 12
Battery model, 128–130, 128f
Beam irradiance, 321
Betz C*p* coefficient, 497
Bioalcohol, 404–405
Biomass, 405
Blades, 494
Boolean values, 354
Boost-based lossless self controlled photovoltaic units
  exact I–V characteristic, 183–184, 184f
  exact P–V characteristic, 183–184, 184f
  FEMPValgorithm, 183–184
  I–V and P–V characteristics, 181–182, 181f
  time-varying parameter, 182–183
Boost converter model, 130–131, 131f
Boost switch driver circuit, 141f, 142
Breathing, 405
Buck-based lossless self-controlled photovoltaic units, 187–190, 188f
  curve of equation, 186
  hyperbole of equation, 186
  I_{MAX}, 184–185
  I–V characteristic, 185–186, 186f
  P–V characteristic, 185–186, 186f
Buoyancy effects, 385

C

Carbon dioxide (CO2), 336
Carnot's efficiency, 375–376
Central maximum power point tracking (CMPPT)
  adopted ordering rule, 178
  bulk voltage compensation network, 177
  grid-connected inverter system, 164–167, 166f
  inverter outer feedback loop, 175–176
  inverter outer voltage feedback loop, 179
  mismatching operating conditions, 177
  peak to peak amplitude, 176–177
  sampling instants, 175–176
  staircase reference voltage, 175–176, 175f
  steady-state condition, 178–179
  voltage reference value, 166–167
Centrifugal pump, 344
Chemical composition, 378
Chronic obstructive pulmonary disease, 405
Clarity index, 322–323
Clean energy, 336
Clouds diffuse solar radiation, 380
Coal worsens indoor pollution, 404–405
Combustion cooking, 406
Complementary protection, 487–488
  chopper circuit, 487–488
  pitch angle control, 487
Compressor pressurizes air, 383–384
Concentrating solar power (CSP), 259
  absorber efficiency, 376, 377f
  albedo, 380
  annual solar-to-electricity efficiency, 386, 390f
  Astronomical Unit (UA), 378
  buoyancy effects, 385

Concentrating solar power (CSP) (*Continued*)
Carnot's efficiency, 375−376
chemical composition, 378
clouds diffuse solar radiation, 380
compressor pressurizes air, 383−384
CSP technologies, 374−375
dish, 373−374
Earth−atmosphere system, 377−378
electricity, 373
electromagnetic radiation, 378−379
elliptical orbit, 378, 379f
energy, 374
fossil fuel burners, 373
fossil/renewable fuels, 376−377
gas/acoustic pollution, 378−379
gas and steam turbine process, 383−384, 384f
heat engine, 375−376
heat engine efficiency, 376, 377f
heliostats, 383−384
hot- and cold-temperature regions, 385
hybridization, 376−377
insolation, 379, 380f
irradiance, 379
LFR, 375
linear Fresnel, 373−374
linear Fresnel reflectors (LFRs), 374
luminous gaseous star, 377
operational solar thermal facilities, 388t−389t
parabolic dishes (PDs), 374
parabolic trough, 373−374, 381−382, 382f
parabolic trough collector (PTC), 375
photovoltaic (PV) systems, 373
plants, 381−387
power towers, 373−374, 381−382, 383f
scattered radiation, 380
simulation parameters, 396, 397t
single-tank thermocline systems, 385, 387f
Solar Advisor Model (SAM), 398
Solar and Wind Energy Resource Assessment (SWERA) project, 381
solar collectors, 375−376
solar energy, 373
solar energy resources, 377−381
solar mass, 378
Solar One power tower, 385
solar peak hour, 379−380
solar power tower, 375
solar radiation, 377−381
solar thermal storage (STS), 391−395
active storage, 393
classification of, 392
cost, 394
flexibility/dispatchability, 394
HTF, 392
latent and thermochemical heat, 393
latent energy storage, 393−394
operation, 394
Organic Rankine Cycle (ORC), 392
passive storage, 393
phase change material (PCM), 394
properties, 392
selection, 391−392
sensible energy storage, 393
sensible heat storage, 394
sizing, 394
storage material, 392
storage media catalog, 392−393
TES technologies, 391
thermochemical storage, 393
thermocline tank, 393−394
solar tracking mobility platform, 386, 391f
solid storage medium, 385
sun characteristics, 377−381
technical options, 386, 390t
technologies, 375, 376t
thermal energy, 373
thermal energy storage (TES), 384−385
thermodynamic and economic studies, 395−399
two-tank direct systems, 385, 385f
two-tank indirect systems, 385, 386f
Constant-current maximum power point tracking, 118
Constant-voltage maximum power point tracking, 117
Control switches, 129−130, 130f, 130t
Control system, 476−479, 476f
grid side converter control, 477−478, 478f
phase-locked loop, 477
proportional integral (PI) controllers, 478
rotor side converter control, 478−479, 479f
vector control, 477
Conventional solar cookers, 407−408
Crowbar, 438
Cyclically variable wind turbines, 495

D

Dark P−N junction diode, 15
field region formation, 15−16, 15f
ideal dark I−V characteristics
excess electrons and holes, forward-biased diode, 16, 17f
reverse saturation current, 16−18
total diode current, 16−18
real dark diode characteristics, 18−19, 19f

DC motors, 336
Deep cycle leadeacid batteries, 417
Deforestation, 406
Defuzzification, 122
Delayed cooking, 414–415
Depth of discharge *(dod)*, 259
  batteries, 270, 281
  energy management, 283f
  Kalman filter, 283
  optimal range, 270
  optimal values, 278–279
  parameter value, 261–262
  PV and battery storage, 276
Deterministic PSO (DPSO), 123
Diesel engine (DE) model, 262–263, 263f, 263t
Diesel generator (DG) model, 262–264, 262f
Diffuse irradiance, 321, 324
Diffusion current, 11–12
Diffusion length, 12
Direct-coupled method, 117
Direct current (DC) motors, 296–297
Direct irradiance, 324
Direct pumping, 300, 301f, 314–319
Disc brake, 493–494
Discharge control batteries bank depth, 280
Distributed maximum power point tracking (DMPPT)
  boost-based LSCPVU, 164–166, 165f
  buck-based LSCPVU, 164–166, 165f
  and central maximum power point tracking (CMPPT)
    buck-boost converter, 167–168
    commercial PV inverters, 170
    HMPPTF technique, 180–201
    hybrid MPPT (HMPPT) technique, 169–170
    k-th LSCPVU, 167–168
    k-th PV module, 167–168
    N LSCPVUs, 167–168
    OFF subinterval, 167–168
    P–V characteristics, 167–168, 168f, 170f
    SolarWorld SW225 PV modules, 167–168, 169t
Doping, 10, 10f
Doubly fed induction generator (DFIG) technology
  alternative solutions, 488–489
  complementary protection, 487–488
    chopper circuit, 487–488
    pitch angle control, 487
  control strategies, 488
  control system, 476–479, 476f
    grid side converter control, 477–478, 478f
    phase-locked loop, 477
    proportional integral (PI) controllers, 478
    rotor side converter control, 478–479, 479f
    vector control, 477
doubly fed induction machine (DFIM), 465–467, 465f
dynamic modeling, 470–472
  definition, 471–472
  grid-synchronized *dq* transformation, 471, 471f
  reference frame transformation, 470–471, 470f
Dynamic Voltage Restorer (DVR), 488
grid disturbances model
  complex vector representation, 472
  stator flux, 474, 474f
  symmetrical voltage dips, 472–476, 473f
hardware solutions, 488–489
historical review, 462
insulated gate bipolar transistor (IGBT), 482
low-voltage ride-through
  crowbar protection, 487
  grid code requirements, 486–487, 486t
  voltage dip, 483–486, 484f
maturation, 488
modeling, 465–476
neutral-point clamped converters (NPC), 481
power electronic converters, 480–483
  back-to-back voltage source converter, 480–481, 481f
  chopper, 481–482, 483f
  crowbar, 481–482, 482f
  new trends/novel structures, 482–483
pulse width modulation (PWM) voltage, 462
singularities, 464
space vector modulation (SVPWM), 480–481
static model, 467–469
  doubly fed induction machine operation modes, 468–469
  equivalent circuit, 467, 467f
  generator operation, 469, 469f
  motor operation, 468, 469f
  rotor to stator, 467–468, 468f
stator and rotor voltages, 464
structure, 462–464, 463f
substantiation, 488
symmetric three-phase voltages, 465
two three-phase winding sets, 465
variable-speed turbines, 463
wind energy conversion system (WECS), 462
wound rotor induction machine, 462–463

Doubly fed induction machine (DFIM), 465–467, 465f
Drift current density, 11
Dry stagnation temperature, 412
"Dump load", 212–213
Dynamic modeling, 470–472
  definition, 471–472
  grid-synchronized *dq* transformation, 471, 471f
  reference frame transformation, 470–471, 470f
Dynamic Voltage Restorer (DVR), 488

E

Earth–atmosphere system, 377–378
Einstein equation, 11–12
Electrical energy, 492–493, 492f
Electricity, 373
Electrolyzer, 359–361
Electromagnetic radiation, 378–379
Elementary semiconductors
  covalent bonds in, 9, 9f
Elevated tank pumping, 300, 300f, 313–314
Elevation angles, 321f
Elimination and choice translating reality (ELECTRE), 63
Elliptical orbit, 378, 379f
Energy, 374
Energy balance, 327
Energy gap, 9, 10f
Energy generation technology, 308
Energy management (EM)
  hybrid renewable energy sources (HRESs), 350
  multisources multistorage systems (MSMSS), 350
  photovoltaic, 350
  photovoltaic cell efficiency, 351–352
  photovoltaic installations, 352–365
    available power (ΔP), 353, 357t
    battery storage, 364–365
    battery storage, PV system, 352–359, 352f
    electrolyzer, 359–361
    four switches, 359
    fuel cells, PV systems, 359–363
    hydrogen, 359–361
    PMC first structure, 353–356
    PMC second structure, 356–359
    PV/FC system, 361, 362f, 362t
    three switches, 353, 353f
    wind turbine, 364–365
  photovoltaic principle, 351, 351f
  renewable energy systems (RESs), 350
  state of charge (SOC), 350
Energy storage system (ESS), 211
European Center for Medium-RangeWeather Forecasts (ECMWF), 104

F

FACTS, 441
  applications, 441, 442t
Fault detection procedures
  automatic supervision and diagnosis, 245–247, 246f–247f
  supervision and diagnosis, 247–250, 249t
Fill factor (FF), 302–303
Firewood, 404–405
Fixed speed rotors, 494
Fixed-speed wind energy conversion system, 434–435, 435f
Fixed/tracked collector plane, 324–325
Flat plate modules, 42–43, 43f
Flexible active power control
  power-limiting control algorithm, 220–221, 220f–221f
  power ramp-rate control algorithm, 221–222, 222f–223f
  power reserve control algorithm, 222–224, 224f–225f
Flexible power control
  control algorithm modification, 213–214, 213f–214f
  installing flexible loads, 212–213, 212f
  integrating energy storage systems, 211–212, 211f
Forecast accuracy evaluation
  comparisons, 87–89
  graphic tools, 89
  mean absolute error (MAE), 91
  mean absolute percentage error, 91
  mean bias error (MBE), 90
  mean square error (MSE), 91
  predicted *vs.* measured global irradiations, 89, 90f
  root mean square error (RMSE), 91, 93f
  skill scores, 92
  solar irradiance, 92
  "trivial" forecast methods, 92
Forecast error, 84, 86
Forecasting
  cost of intermittency, 85–86
  forecast accuracy evaluation
    comparisons, 87–89
    graphic tools, 89
    mean absolute error (MAE), 91
    mean absolute percentage error, 91
    mean bias error (MBE), 90

mean square error (MSE), 91
predicted *vs.* measured global irradiations, 89, 90f
root mean square error (RMSE), 91, 93f
skill scores, 92
solar irradiance, 92
"trivial" forecast methods, 92
and influences, production cost, 86–87, 88f–89f
intermittent and stochastic renewable energy production
production/consumption balance, 79–81
renewable production and impact, 81–83
reliability and accuracy, 104–106, 105f–106f
renewable energy forecasting, 106–108
solar and wind forecast, 83–85, 84f
solar forecasting, 6 H and days ahead, 104
temporal horizon and resolution, 93f–94f
forecasting time horizon *vs.* temporal resolution, 94, 94f
NWP-based methods, 95
PV power forecast, 95
satellite imagery-based methods, 95
sky images-based methods, 95
time series-based methods, 95
very short-term forecasting, 0 to 6 H
satellite cloud image, 96–99, 99f–100f
stochastic learning methods/time series-based method, 99–103
total sky imagery (TSI), 96, 97f–98f
Fossil fuel burners, 373
Fossil/renewable fuels, 376–377
Fuzzification, 122
Fuzzy inference system (FIS), 134
Fuzzy logic controller (FLC), 121–122
aggregation stage, 134–135
defuzzification stage, 134
digital devices, 132
fuzzy inference system (FIS), 134
HC technique, 132
1 inputs, 1 output, and 7 MFs each, 132–134, 133f
linguistic variables, 134
MATLAB/Simulink, 134
surface function, 135, 135f
two inputs and one output with seven-membership functions, 132–134, 133t

G

Gas/acoustic pollution, 378–379
Geographical information system (GIS), 58, 64
Global warming, 296
Gradual depletion, 296
Greenhouse gases emission, 406
Greenhouse rooftops, 308, 308f
Grid code requirements, 486–487, 486t
Grid-connected inverter system, 166–167, 166f
Grid-connected plants, 299
Grid-connected PV systems (GCPVSs), 231
active power control strategies for, 208–209, 208f
automatic supervision system, 232
control structure, 217, 217f–218f
grid voltage fluctuation, 210
limited-frequency regulation capability, 210
overloading, 209–210
system diagram, 214–217, 215f–217f
Grid disturbances model
complex vector representation, 472
stator flux, 474, 474f
symmetrical voltage dips, 472–476, 473f
Grid-side converter, 437
Grid-side PWM converter, 437
Grid voltage fluctuation, 210

H

Hardware solutions, 488–489
Heat conductivity, 413
Heat engine, 375–376
efficiency, 376, 377f
Heat retention, 407–408
Heat storage, 414–416
Heliostats, 383–384
High accuracy irradiance measurement, 108
Hill climbing MPPT technique, 121–122, 121f
HMPPTF technique
advantages, 194
central maximum power point tracking, 190–195
climbing–based refinement phases, 190–192
distributed maximum power point tracking, 190–195
exact and approximate I–V and P–V characteristics, LSCPVUs
boost-based lossless self controlled photovoltaic units, 181–184
buck-based lossless self-controlled photovoltaic units, 187–190
buck–boost based lossless self-controlled photovoltaic units, 184–187
exact I–V characteristics, 190–192, 191f–194f
exact P–V characteristics, 192–193, 192f–193f
FEMPValgorithm, 192–193
numerical simulations concerning hybrid maximum power point tracking techniques, 196f

HMPPTF technique (*Continued*)
case I, 195–199, 196t, 197f–199f
case II, 199–201, 200f–201f
Horizontal-axis wind turbines, 495
Hot- and cold-temperature regions, 385
Hot-spots
back-connected bypass protection diodes, 40–41, 41f
reverse characteristics, 39–40, 40f
weak p–n junction region, 39–40, 40f
Hybridization, 376–377
Hybrid maximum power point trackings (HMPPTS), 167–201
central maximum power point trackings (CMPPTS) technique, 175–180
modified P&O distributed maximum power point tracking technique
k-th LSCPVU, 171–173
N LSCPVUs, 174
P–V characteristics, 171–173, 172f
working principle, 171–173
worst-case (lowest) value, 174
Hybrid photovoltaic/batteries bank/ diesel generator system
economics, 284–290
cost analysis, 284
general specifications, 284, 285t
investment and operational cost, 284
energy management, 277–284
AC load prediction, 280
case studies, 279–284
control strategy, 278–279
discharge control batteries bank depth, 280
Kalman filter, 283
normalized mean bias error (NRMSE), 282, 282f
process, 280–281
results, 282–284
schemes, 278–279
load investigated description, 265–266, 266t–267t, 268f
loss of load probability (LLP) parameter, 265
renewable energy system optimization process, 266–276
ambient temperature, 271
methodology, 269–270
objective function, 267–269
optimal values, 275t
optimization constraints, 269
particle swarm optimization, 270–271
population and iteration, PSO algorithm conversion, 272, 273f–274f
result and discussion, 271
results summary, 272–276
sun solar radiation, 271
sizing, 264–276
Hybrid renewable energy sources (HRESs), 350
Hybrid renewable energy system modeling, 260f
battery model, 259
case studies, 276
cost, 286–290
diesel engine (DE) model, 262–263, 263f, 263t
diesel generator model, 262–264, 262f
discharge batteries depth, 286–290
dod parameter, 261–262
economics, 276, 276f–279f
excitation system model, 264, 264f
lead-acid battery model, 261–262, 261f
maximum power point trackers, 261
photovoltaic cell model, 260–261, 260f
pollution, 286–290
sizing, 286–290
synchronous generator, 263–264
Hydraulic simulation, 315
Hydrogen-based electric generation, 416–417

I

Incident solar radiation “insolation”, 6–7, 7f
Incremental conductance (IncCond) technique, 118–119, 120f
Indirect solar cookers, 407–408
Indoor domestic air pollution, 405
Insolation, 379, 380f
Insulated gate bipolar transistor (IGBT), 482
Integrating energy storage systems, 211–212, 211f
Intermittent and stochastic renewable energies systems (ISRES), 78
accurate prediction, 85
evaluation and forecasting, 85
individual prediction errors, 84
power variations, 85
production/consumption balance
electrical dispatching center, 79, 80f
electrical network, 79
electricity production plant characteristics, 79, 80t
power ramp rate, 79
power system, 81
reliable forecasting method, 87
renewable production and impact constraints, 81–83
penetration rate, 83
solar and wind resources, 81, 82f

variability, 81, 82f
"unpredictable" variations, 85
Intermittent renewable energy production rate, 78, 78t
International Energy Agency (IEA), 233
Inverter, 243–244, 309–310, 311f
Irradiance, 379
Irrigation system, 300
Isolated electric system, 416–417, 417f
I–V characteristics
effective collection region, 23, 23f
equivalent circuit, 26, 26f
photocurrent, 23–24
photogeneration rate, 22–23
photon flux, 22–23
photovoltaic (PV) array
mismatched cells, module, 38–39
module, 36–38, 36f–37f
and *P–V* characteristics, 26, 27f
semiconductor material, cutoff wavelength, 24, 25f
spectral irradiance, 22–23
superposition, 25, 25f
superposition principle, 21–22

K

Kalman filter, 283

L

Latent heat thermal energy storage, 416
Limited-frequency regulation capability, 210
Linear Fresnel, 373–374
Linear Fresnel reflectors (LFRs), 374
Liquefied petroleum gas (LPG), 404
Liquid fuels transition, 404–405
Load investigated description, 265–266, 266t–267t, 268f
Load model, 128–130
Lossless SCPVU (LSCPVU), 164–166
Loss of load probability (LLP) parameter, 265
Low-temperature, 409
Low-voltage ride-through capability (LVRT), 439–440, 440f
crowbar protection, 487
Luminous gaseous star, 377
Lung cancer, 405
LVRT. *See* Low-voltage ride-through capability (LVRT)

M

Malnutrition affects, 296
MATLAB/SIMULINK Software, 434, 443, 445, 446f
Maturation, 488
Maximum power point (MPP), 116, 163–164, 337–338, 418–419, 418f
Maximum power point tracking (MPPT), 218–220, 219f, 261, 337, 337f
components, 116–117
constant-current MPPT, 118
constant-voltage MPPT, 117
direct-coupled method, 117
fuzzy logic controller (FLC), 122
hill climbing MPPT technique, 121–122, 121f
incremental conductance (IncCond) technique, 118–119, 120f
parasitic capacitance algorithm, 120
Particle Swarm Optimization (PSO) MPPT technique, 122–124
Perturb-and-Observe (P&O) technique, 118, 119f
photovoltaic source, 163–164
PV energy system, 116–117, 117f
Ripple Correlation Control (RCC), 120
Mean absolute error (MAE), 91
Mean bias error (MBE), 90
Mean square error (MSE), 91
Mechanical power, 342
Mechanical speed control, 502
Mechanical torque, 503f
Microconverters, 163–164
Microinverters, 163–164
Mismatch power loss (MML), 148–150, 151f
Mobility, 11
Modeling solar cells, 240–243, 241f
Model Output Statistics (MOS), 104, 107–108
Module-dedicated DC/AC converters, 163–164
Module-dedicated DC/DC converters, 163–164
Modules
circuit and device simulation, 45–54
failure modes, 43–44, 44f
glassing factor, 44–45
MOSFET IRFP260N, 34
MSMSS. *See* Multisources multistorage systems (MSMSS)
Multicriteria decision-making (MCDM), 58
analytical hierarchy process (AHP), 61–62
elimination and choice translating reality (ELECTRE), 63
fuzzy methods, 63–64
outranking methods, 63
Technique for Order Preference by Similarity to Ideal Solution (TOPSIS), 63
weighted linear combination (WLC), 62–63
Multisources multistorage systems (MSMSS), 350

N

Nacelle, 493–494
National Centers for Environmental Prediction (NCEP), 104
National Digital Forecast Database (NDFD), 104
Net metering, 299
Neutral-point clamped converters (NPC), 481
Newton's second law, 496
NI-USB 6008, 34–35
Nominal power, 310
Noncompensating emitters, 314–315
Nonhydrostatic atmospheric models, 108
Nonshading conditions, PV system
  experimental work
    hardware implementation, boost circuit, 138–140, 139f–140f
    sensors and driver circuits, 142–144
  simulation
    battery model, 128–130, 128f
    boost converter model, 130–131, 131f
    charging control, 129–130, 130f
    control switches, 129–130, 130f, 130t
    E and ΔE calculation, 131–132, 132f
    fuzzy logic controller model, 132–135
    load model, 128–130
    Matlab/Simulink program, 124, 125f
    photovoltaic cell model, 124–128
  simulation results
    battery and control switch models, 137, 139f
    FLC system, 137, 138f
    Matlab code, 135
    output power from PV system, 136–137, 137f
    Simulink model, 135–136, 136f
Normalized mean bias error (NRMSE), 282, 282f
Novel D-FACTS, 441
NRMSE. *See* Normalized mean bias error (NRMSE)
n-type Si, 10

O

Ohm's law, 11
One-axis tracker, 305–306, 305f, 306t
One-diode model, 125–126, 126f
On-farm irrigation network, 312–319
Open circuit voltage, 301–302
Open-loop transfer function, 501
Operational pumping systems, 336
Operational solar thermal facilities, 388t–389t
Optical solar concentration, 407
Optimization constraints, 269
Overloading, 310

P

Parabolic dishes (PDs), 374
Parabolic trough, 373–374, 381–382, 382f
Parabolic trough collector (PTC), 375
Parameter extraction techniques, 244
Parasitic capacitance algorithm, 120
Park's transformation, 448
Partial shadowing, 39
Particles, 122
Particle swarm optimization (PSO), 259, 270–271
  Deterministic PSO (DPSO), 123
  particles, 122
  problem, 124
  self-confidence, range: 1.5–2, 122–123
  swarm-confidence, range: 2–2.5, 122–123
Peak power (PP), 302, 302f
Performance ratio (PR), 233
Persistence model, 101
Perturb-and-Observe (P&O) technique, 118, 119f
Phase change material (PCM), 416
Photocurrent, 23–24
Photon generation process, 13, 14f
Photons, 13
Photovoltaic (PV) array, 4
  constant-voltage MPPT, 117
  direct-coupled method, 117
  power *versus* voltage (P–V) characteristic, 163–164
  solar modules, 5
Photovoltaic (PV) capacity, 231
Photovoltaic cell efficiency, 351–352
Photovoltaic cell model
  crystalline silicon, 124
  Kirchhoff's current law, 126–127
  materials, 124
  one-diode model, 125–126, 126f
  Simulink model, 127, 127f
  two-diode model, 125, 125f
Photovoltaic cooking
  AC electrical pots, 417–418
  air pollution, 406
  anaerobic digesters biogas, 405
  bioalcohol, 404–405
  biomass, 405
  breathing, 405
  charcoal, 404–405
  chronic obstructive pulmonary disease, 405
  coal worsens indoor pollution, 404–405
  combustion cooking, 406
  conventional solar cookers, 407–408
  cultural and gender issues, 405
  deep cycle leadeacid batteries, 417

deforestation, 406
delayed cooking, 414–415
dry stagnation temperature, 412
energy, 404–405
financial help, 408–409
firewood, 404–405
fundamentals, 409
greenhouse gases emission, 406
heat conductivity, 413
heat retention, 407–408
heat storage, 414–416
hydrogen-based electric generation, 416–417
indirect solar cookers, 407–408
indoor domestic air pollution, 405
isolated electric system, 416–417, 417f
latent heat thermal energy storage, 416
liquefied petroleum gas (LPG), 404
liquid fuels transition, 404–405
low-temperature, 409
lung cancer, 405
maximum power point (MPP), 418–419, 418f
optical solar concentration, 407
phase change material (PCM), 416
photovoltaic solar cookers, 416–421
sanitary hot water (SHW), 403
simplest control technique, 418–419
solar cooking, 407–409
solar energy, 406–407
solar thermal cookers, 407
temperature *versus* time evolution, 411–412, 412f
thermal energy storage (TES), 408, 414–416, 415f
thermal insulation, 413
thermal model, 409–414
thermal solar cooker, 407
toxic gases, 405
wood and associated environmental problems, 406
World Health Organization, 405
Photovoltaic cost reduction, 231–232, 232f
Photovoltaic effect, 124
Photovoltaic irrigation systems
agriculture, 296
agrivoltaic production approach, 296
alternative current (AC), 297
angle of incidence, 320
annual energy balance, 299
azimuthal and elevation angles, 321f
beam irradiance, 321
clarity index, 322–323
classification, 297–300
climate change, 296
Collares-Pereira and Rabl formula, 323–324
components, 301–319
definition, 311–319
design, 326–328
diffuse irradiance, 321, 324
direct current (DC) motors, 296–297
direct irradiance, 324
direct pumping, 300, 301f, 314–319
discharge-head-efficiency, 312
distortion waveform, 310
earth–sun geometry, 319–326
efficiency, 310
electric power generated, 325–326
elevated tank pumping, 300, 300f, 313–314
energy balance, 327
energy generation technology, 308
fixed/tracked collector plane, 324–325
global warming, 296
gradual depletion, 296
greenhouse rooftops, 308, 308f
grid-connected plants, 299
hydraulic simulation, 315
input data and initialization, 326–327
inverter, 309–310, 311f
irrigation system, 300
irrigation water requirements calculation, 327
malnutrition affects, 296
materials and technical solutions, 308
modeling and simulation, 319–326
net metering, 299
nominal operating point, 317
nominal power, 310
noncompensating emitters, 314–315
on-farm irrigation network, 312–319
operating point calculation, 327
overloading, 310
partial shading, 308
photovoltaic modules, 301–304, 302f
arrangement, 303–304, 304f
energy conversion efficiency, 303
fill factor (FF), 302–303
open circuit voltage, 301–302
peak power (PP), 302, 302f
short-circuit current, 301
photovoltaic (PV) power plants, 301–310
power calculations, 325–326
powering plant, 298–299
PP values and other design parameters, 328
pumping systems, 297, 312
PV modules, 308, 309f
reflected irradiance, 322, 324

Photovoltaic irrigation systems (*Continued*)
self-consumption, 299
solar irradiance components, 321–325, 322f
solar position, 319–320
solar radiation modeling, 319–326
solar rays, 320
solar tracking systems, 304–307
driving motor, 307
mechanism, 304–306, 305f
one-axis tracker, 305–306, 305f, 306t
solar tracker control, 307
two-axis trackers, 306, 307f
stand-alone plants, 298
subsystem, 297
system curve, 314
technical and economic performance, 328
total irradiance, 324
water balance, 327
Photovoltaic modules, 240–243, 301–304, 302f
arrangement, 303–304, 304f
energy conversion efficiency, 303
fill factor (FF), 302–303
open circuit voltage, 301–302
peak power (PP), 302, 302f
short-circuit current, 301
Photovoltaic (PV) system, 5f, 301–310, 373
active power control strategies, 208–209
applications, 116
arrays, 240–243
automatic supervision strategies, 232, 237–240, 239f
battery storage, 5
flexible active power control
power-limiting control algorithm, 220–221, 220f–221f
power ramp-rate control algorithm, 221–222, 222f–223f
power reserve control algorithm, 222–224, 224f–225f
flexible power control
control algorithm modification, 213–214, 213f–214f
installing flexible loads, 212–213, 212f
integrating energy storage systems, 211–212, 211f
grid-connected PV systems, 209–210
inverter model, 243–244
modeling solar cells, 240–243, 241f
nonshading conditions
experimental work, 137–144
simulation, 124–135
parameter extraction techniques, 244
performance parameters
miscellaneous losses, 233
normalized thermal losses, 235
performance ratio (PR), 233
possible faults and origins, 233, 234t
thermal effects, 233
photovoltaic modules, 240–243
power conditioning circuits, 5
power converter technology and control
control structure, grid-connected PV systems, 217, 217f–218f
maximum power point tracking algorithms, 218–220, 219f
system diagram, grid-connected PV systems, 214–217, 215f–217f
power-limiting control (PLC), 208–209
power ramp-rate control (PRRC), 209
power reserve control (PRC), 209
PVarray, 4
simulation tools, 244–245
supervision and diagnosis of, 235–237, 236t, 237f
terminal voltage, 116, 116f
Photovoltaic water pumping system (PVPS)
carbon dioxide (CO2), 336
centrifugal pump, 344
clean energy, 336
cold seasons, 346
DC motors, 336
direct/quadrature current, 341–342
hot seasons, 346
induction motor–based PV pumping systems, 336
maximum power point (MPP), 337–338
maximum power point tracking (MPPT) algorithm, 337, 337f
mechanical power, 342
medium seasons, 346
operational pumping systems, 336
pump resistive torque, 341
radiance, 342
rotor pulsation, 341–344
scalar control, 338–339
stator current, 341–342
stator pulsation, 342
stator voltage responses, 342
system components modeling, 337–338
torque control, 338–339
vector control, 339–342
electric speed reference, 341–342
flux regulation, 339, 340f
regulators selection, 340–341

speed regulation, 341, 341f
torque regulation, 339, 340f
transfer function, 340
water volume comparison, 345f
Pitch angle controller, 449, 449f
Power coefficient, 497
Power control functionalities, 208–209
Power electronic converters, 480–483
back-to-back voltage source converter, 480–481, 481f
chopper, 481–482, 483f
crowbar, 481–482, 482f
new trends/novel structures, 482–483
Powering plant, 298–299
Power-limiting control (PLC), 208–209, 220–222, 220f–223f
Power reserve control (PRC), 209, 222–224, 224f–225f
Power supply circuits, 140f, 142
Power towers, 373–374, 381–382, 383f
Proposed controller, 449–450, 450f
p-type Si, 10
Pulse width modulation (PWM) voltage, 462
Pumping systems, 297, 312
Pump resistive torque, 341
PV arrays
failure modes, modules, 43–44, 44f
flat plate modules, 42–43, 43f
glassing factor, modules, 44–45
hot-spots
back-connected bypass protection diodes, 40–41, 41f
reverse characteristics, 39–40, 40f
weak p–n junction region, 39–40, 40f
I–V characteristics
mismatched cells, module, 38–39
module, 36–38, 36f–37f
measurement data and practical considerations, 41–42, 41f
solar cell array, 41f, 42
PV current-sensing circuit, 141f, 143–144
PV effect
P–N solar cell
e–h pairs, 21
front metallization, 20, 20f
illustration of, 20, 21f
metal-semiconductor, 21
photovoltaic effect, 20, 21f
solar cell construction, 20, 20f
PV voltage-sensing circuit, 141f, 142–143
PWM converter rotor side, 438

R

Reactive power controller, 449–450
Recombination mechanisms, 12
Reference/measured mechanical speed, 503f
Reflected irradiance, 322, 324
Renewable energy forecasting
high accuracy irradiance measurement, 108
Model Output Statistics (MOS), 107–108
nonhydrostatic atmospheric models, 108
now-casting, 106–107
Renewable energy system optimization process, 266–276
Ripple Correlation Control (RCC), 120
Root mean square error (RMSE), 91
Rotor, 494
Rotor pulsation, 341–342
Rotor-side converter, 437

S

Sampling instants, 175–176
Sandia Array Performance Model (SAPM), 243
Sanitary hot water (SHW), 403
Satellite cloud image, 96–99, 99f–100f
Savonius rotor, 494
SC. *See* Solar constant (SC)
Scalar control, 338–339
Scaled persistence model, 101
Scattered radiation, 380
Self-consumption, 299
Self-controlled PV unit (SCPVU), 164–166
Self-excited induction generator (SEIG), 446–447, 446f
Semiconductor currents, 11–12, 11f
Semiconductors
amorphous, 8
atomic arrangements, 8
crystalline, 8
currents, 11–12, 11f
doping and conductivity, 10–11, 10f
electrical characteristics, 8
energy gap E_g and intrinsic concentration N_I, 9, 9f–10f
excess of, electrons and holes, 12, 12f
optical properties
absorption coefficient alpha, 14, 14f
light intensity, absorption coefficient alpha, 13, 13f
longer wavelength photons, 14–15
photoelectric effect, 12–13
photon generation process, 13, 14f
photons, 13
polycrystalline, 8

Semiconductors (*Continued*)
recombination mechanisms, 12
structures for, 8, 8f
Severe wind speed variation, 454–455, 456f–457f
Shadowing, 39
Short-circuit current, 301
Silicon, 9
Simplest control technique, 418–419
Simulation parameters, 396, 397t
Simulation tools, 244–245
Single-tank thermocline systems, 385, 387f
Sinusoidal pulse width modulation (SPWM), 443
"Smart load", 212–213
Smart maximum power point tracker
mismatch power loss (MML), 148–150, 151f
partial shading effect, 144f, 151f
generated power *vs.* terminal voltage, 148, 151f
output power *vs.* terminal voltage, 147, 148f–149f
20 series with one shaded PV cell, 145–147, 146f
shaded cell with voltage and radiation, 144–145, 146f
shaded PV cell among 20 series PV cells, 145–147, 147f
total generated power along with terminal voltage, 147–148, 150f
two P–V cells without bypass, 144–145, 145f
simulation of proposed systems, 156f
cosimulation, Simulink and PSIM, 152, 153f
E and ΔE calculation, inputs, 152, 152f
MPSO and FLC, 153, 155f
output signal from FLC, 152, 152f
PV modules and boost converter, 152, 153f
simulation parameters, each PV module in PSIM, 152, 154t
Solar Advisor Model (SAM), 398
Solar and Wind Energy Resource Assessment (SWERA) project, 381
Solar cells
array, 41f, 42
conversion efficiency
defined, 27
fill factor (FF), 27
R_{sh}, I–V solar cell characteristics, 27, 28f
R_s, I–V solar cell characteristics, 27, 28f
temperature effect, 29, 29f
dark P–N junction diode, 15–19
functions, 19–20
heterotype junctions, 15
homotype p–n junctions, 15
I–V characteristics, 21–27
manufacturing, 34
measurement results and practical considerations
antireflection coating, 30–32, 33f
material, 30, 30f
size, 29–30
spectral response, 30, 31f
thickness, Si-solar cells, 30, 31f
mismatch, 38–39
module, 36–38, 36f–37f
multi-junction, 15
PV effect, P–N solar cell
e–h pairs, 21
front metallization, 20, 20f
illustration of, 20, 21f
metal-semiconductor, 21
photovoltaic effect, 20, 21f
solar cell construction, 20, 20f
semiconductors properties. *See* Semiconductors
and solar panels testing, 34–35, 35f
Solar cells and modules
circuit-level simulation
case studies, 48–49, 49t, 50f
mathematical modeling, 45, 46t
parameter extraction, 45–46, 47t
PSpice model, 46–48
Technology Computer Aided Design (TCAD) simulation
electrical and optical characterization, 52–53, 53f
n^+ emitter sidewall surfaces, 53–54, 54t
novel npn solar cell structure, 50, 51f
npn solar cell structure using SILVACO/Athena, 51–52, 52f
SILVACO device simulator, 49–50
Solar cell string, 36
Solar collectors, 375–376
Solar constant (SC), 5
Solar cooking, 407–409
Solar energy, 373, 406–407
resources, 377–381
Solar irradiance, 92
components, 321–325, 322f
Solar irradiation, 67, 67f
Solar mass, 378
Solar One power tower, 385
Solar panels
testing, 34–35, 35f
Solar peak hour, 379–380
Solar photovoltaic land suitability
dealing with uncertainties, 65
geographical information system (GIS), 58, 64

multicriteria decision-making (MCDM), 58–64
research studies, 58, 59t–61t
utility-size solar photovoltaic (PV) site suitability, 58, 61f
Solar position, 319–320
Solar power tower, 375
Solar PV power plants site selection
criteria for
air temperature, 67–68
decision criteria, 65, 66t–67t
solar irradiation, 67, 67f
restriction factors, 68–69, 68t, 69f
solar photovoltaic land suitability
geographical information system (GIS), 58, 64
multicriteria decision-making (MCDM), 58–64
research studies, 58, 59t–61t
uncertainties, 65
utility-size solar photovoltaic (PV) site suitability, 58, 61f
unsuitable sites, 68–69
Solar radiation modeling, 319–326, 377–381
air mass 1 (AM1), 6
Air Mass Zero (AM0), 6
astronomical unit, 5
black body radiation, 5
human consumption, 4
power spectral distribution, 5, 6f
solar constant (SC), 5
spectral irradiance, 5
Solar rays, 320
Solar thermal cookers, 407
Solar thermal storage (STS), 391–395
active storage, 393
classification of, 392
cost, 394
flexibility/dispatchability, 394
HTF, 392
latent and thermochemical heat, 393
latent energy storage, 393–394
operation, 394
Organic Rankine Cycle (ORC), 392
passive storage, 393
phase change material (PCM), 394
properties, 392
selection, 391–392
sensible energy storage, 393
sensible heat storage, 394
sizing, 394
storage material, 392
storage media catalog, 392–393
TES technologies, 391
thermochemical storage, 393
thermocline tank, 393–394
Solar tracker control, 307
feedback controllers, 307
open-loop controllers, 307
Solar tracking mobility platform, 386, 391f
Solar tracking systems, 304–307
driving motor, 307
mechanism, 304–306, 305f
one-axis tracker, 305–306, 305f, 306t
solar tracker control, 307
two-axis trackers, 306, 307f
SolarWorld SW225 PV modules, 167–168, 169t
Solid storage medium, 385
Space vector modulation (SVPWM), 480–481
Spectral irradiance, 5
Speed regulation, 341, 341f
Stand-alone plants, 298
STATCOM. *See* Static synchronous compensator (STATCOM)
State of charge (SOC), 350
Static model, 467–469
doubly fed induction machine operation modes, 468–469
equivalent circuit, 467, 467f
generator operation, 469, 469f
motor operation, 468, 469f
rotor to stator, 467–468, 468f
Static synchronous compensator (STATCOM), 434, 440, 443, 444f, 447–449, 447f
Stator current, 341–342
Stator pulsation, 342
Stator/rotor voltages, 464
Stator voltage responses, 342
Substantiation, 488
Sun characteristics, 377–381
Sun's energy, 378
Sun solar radiation, 271
Sun's temperature, 378
Symmetric three-phase voltages, 465

T

Technique for Order Preference by Similarity to Ideal Solution (TOPSIS), 63
Thermal energy, 373
Thermal energy storage (TES), 384–385, 414–416, 415f
Thermal insulation, 413
Thermal model, 409–414
Thermal solar cooker, 407
Thermodynamic and economic studies, 395–399
Three-phase fault, 451–454, 453f–455f

Torque regulation, 339, 340f
Total irradiance, 324
Total sky imagery (TSI), 96, 97f–98f
Toxic gases, 405
Transfer function, 340
Transmission shaft, 492–493
"Trivial" forecast methods, 92
Two-axis trackers, 306, 307f
Two-diode model, 125, 125f
Two-level back-to-back converter (2L-B2B), 436–437
Two-tank direct systems, 385, 385f
Two-tank indirect systems, 385, 386f
Two three-phase winding sets, 465

V

Variable speed rotors, 494
Variable-speed turbines, 463
Variable-speed wind energy conversion system, 435–436, 436f
Variable wind speed, 450–451, 451f
Vector control, 339–342
  electric speed reference, 341–342
  flux regulation, 339, 340f
  regulators selection, 340–341
  speed regulation, 341, 341f
  torque regulation, 339, 340f
  transfer function, 340
Vertical-axis wind turbines, 494–495
Vestas (V47) wind farm, 441–443
Voltage at steady state, 439
Voltage dip, 483–486, 484f
Voltage flickers, 439
Voltage regulation and power quality, 439–440

W

Water balance, 327
Weighted linear combination (WLC), 62–63
Wind doubly fed induction generators, 436–438, 437f
Wind energy
  active power balance, 438–439
  crowbar, 438
  Egypt, 441–443
  FACTS, 441
    applications, 441, 442t
    novel D-FACTS, 441
  fixed-speed wind energy conversion system, 434–435, 435f
  grid-side converter, 437
  grid-side PWM converter, 437
  low-voltage ride-through capability (LVRT), 439–440, 440f
  MATLAB/SIMULINK Software, 434, 443, 445, 446f
  Park's transformation, 448
  pitch angle controller, 449, 449f
  proposed controller, 449–450, 450f
  PWM converter rotor side, 438
  reactive power controller, 449–450
  rotor-side converter, 437
  self-excited induction generator (SEIG), 446–447, 446f
  severe wind speed variation, 454–455, 456f–457f
  sinusoidal pulse width modulation (SPWM), 443
  static synchronous compensator (STATCOM), 434, 440, 443, 444f, 447–449, 447f
  three-phase fault, 451–454, 453f–455f
  TSO, 440
  two-level back-to-back converter (2L-B2B), 436–437
  variable-speed wind energy conversion system, 435–436, 436f
  variable wind speed, 450–451, 451f
  Vestas (V47) wind farm, 441–443
  voltage at steady state, 439
  voltage flickers, 439
  voltage regulation and power quality, 439–440
  wind doubly fed induction generators, 436–438, 437f
  wind farm configuration, 434–438, 434f
  wind farm modeling, 443–455
  wind speed distribution, 445, 446f
  wind turbine, 438
    controller, 437
    modeling, 444–445, 445f
  Zafarana wind farm, 441–443, 443f
Wind energy conversion system (WECS), 462
Wind farm configuration, 434–438, 434f
Wind farm modeling, 443–455
Wind speed distribution, 445, 446f
Wind turbine, 364–365, 438
Wind turbine emulator
  aero generators, 495
  Betz C*p* coefficient, 497
  blades, 494
  components, 493–494
  cyclically variable wind turbines, 495
  definition, 492–493
  description, 492–494
  disc brake, 493–494
  electrical energy, 492–493, 492f

fixed speed rotors, 494
horizontal-axis wind turbines, 495
interpretations, 502–506
mechanical speed control, 502
mechanical torque, 503f
modeling, 495–501
nacelle, 493–494
Newton's second law, 496
open-loop transfer function, 501
power coefficient, 497
principle, 499–502
qualities, 492–494
reference/measured mechanical speed, 503f
rotor, 494
Savonius rotor, 494
schema, 502f
simulation, 500–501, 504f
transmission shaft, 492–493
types, 494–495
variable speed rotors, 494
vertical-axis wind turbines, 494–495
Wound rotor induction machine, 462–463

Z

Zafarana wind farm, 441–443, 443f

This page intentionally left blank

Advances in Renewable Energies and Power Technologies

Volume 1 Solar and Wind Energies

Advances in Renewable Energies and Power Technologies: Volume 1: Solar and Wind Energies examines both the theoretical and practical elements of renewable energy sources, such as photovoltaics, solar, photothermal and wind energies. Yahyaoui and a team of expert contributors present the most up-to-date information and analysis on renewable energy generation technologies in this comprehensive resource. This volume covers principles and methods of each technology, implementation analysis, management and optimization, and related economic advantages and limitations, in addition to recent case studies and models of each technology.

Advances in Renewable Energies and Power Technologies: Volume 1: Solar and Wind Energies is a valuable resource for anyone working in renewable energy or wanting to learn more about theoretical and technological aspects of the most recent inventions and research in the field.

Key Features

- Offers a comprehensive guide to the most advanced contemporary renewable power generation technologies written by a team of top experts
- Discusses the energy optimization, control and limitations of each technology, as well as a detailed economic study of the associated costs of implementation and management
- Includes global case studies and models to exemplify the technological possibilities and limitations of each power generation method

About the Editor

Dr. Imene Yahyaoui obtained her electrical engineering and Master's degrees in electric conversion and renewable energies from the University of Sfax, Tunisia. She has a PhD in Systems and Process Engineering from the Industrial Engineering School of the University of Valladolid, Spain. She performed her postdoc at the Electric Engineering Department of the Federal University of Espiritu Santo, Brazil. She is currently a postdoctoral researcher at the Electric Engineering Department of the University Carlos III of Madrid (UC3M), Spain.

ELSEVIER

elsevier.com/books-and-journals

ISBN 978-0-12-812959-3

9 780128 129593